Investigation into the behaviour of displacement piles under cyclic and seismic loads

Emilio E. Saldivar Moguel

02

A thesis submitted to the University of London
Imperial College of Science, Technology, and Medicine
in partial fulfillment of the requirements for the degree of
Doctor of Philosophy in the Faculty of Engineering
and the Diploma of Imperial College



ABSTRACT

Recent research at Imperial College (IC) has focused on obtaining insights into the mechanics of displacement pile behaviour. The research allowed Jardine and Chow (1996) to propose an effective stress approach to design driven piles to sustain static loads in clay and sand. Their research also recognized that the effects of cyclic loads required further investigation.

The Thesis presents research into the behaviour of displacement piles in clays when subjected to cyclic and seismic axial loads. The aim of the research is to improve knowledge concerning the dynamic capacity of friction piles, especially in relation to their static capacity. The research focuses on instrumented building case histories from Mexico City (MC) where an important number of friction pile foundations failed during the September 19 1985 earthquake.

The initial stage of the research consists of the estimation of the static pile capacity from the application of the IC Pile Design Method (ICPDM), which is validated for MC clays using a database of static pile load tests. In order to assist in the design method validation, the research includes an original Ring Shear laboratory study.

In the case histories considered, the seismic axial pile loads are determined using a dynamic structural programme, in which earthquake accelerations recorded (in post 1985 events) at basement level on instrumented buildings are fed in as prescribed motions at the model supports. The analyses are then extended to cover pile loads developed during the 1985 earthquake.

Conclusions on the response of the piles in the case histories are inferred (i) by comparing the computed seismic axial pile loads with the static capacity predicted by the ICPDM, and (ii) from the occurrence (or not) of building settlements during the earthquake under study. Other data from cyclic pile tests undertaken in MC are combined with the Author's analytical results to develop an Interaction Diagram that is proposed as a tool for the design of piles subjected to cyclic loading in MC. The cyclic pile response is considered in terms of effective stress processes.

Acknowledgements

The National Council for Science and Technology "CONACYT" (Mexico) sponsored this research. I am very grateful for their support.

I am indebted to my main supervisor, Prof. Richard Jardine, for his support throughout my studies. Prof. Jardine's suggestions shaped many ideas in this Thesis. I am also grateful to Dr. Sarada Sarma and Dr. Julian Bommer who helped at different stages in my studies. The structural analyses were carried with much help from Dr. Rui Pinho from the Engineering Seismology section at Imperial College.

I would like to thank all the engineers who responded to my endless request for information, particularly Mr. Marcos Orozco and Mr. Rene Contreras. The soil samples and building information were provided by a multiplicity of organisations and institutes in Mexico, unfortunately space prevents individual acknowledgement, but their names are mentioned in the text.

My thanks are due to the fellow students: Jun-ho Shin, Graham Taylor, Adam Pellew, Rolf Hamm, Julio Colmenares, Kieran Dineen, Mark Cunningham, Rob Nyren, Reinaldo Rolo, Felix Schroeder, Vincent Nyambayo, Kirsty Boydell, Peter Bourne Webb, Angeliki Grammatikopoulus, Konstantinos Georgiadis, Monica Melgarejo, Stuart Hardy, Philip Smith, Jan Franzius, Apiniti Jotisankasa, and Raphael Monroy. Thanks also to the academics at IC, especially Lidija Zdravkovic and Jamie Standing, to Sue Feller and the technicians.

Many thanks to my non-geotechnical friends specially Marie Aimée Dinan, Miguel Hernandez and Carlos Romero. Marie Aimée's company made of the most difficult period of the PhD, actually the most beautiful, fulfilling time.

I thank and dedicate this work to my family, source of love, inspiration, strength, and unconditional support, if I am something it is due to them. Thanks to God.

Table of contents

ABSTRACT **2**

ACKNOWLEDGEMENTS **3**

TABLE OF CONTENTS **4**

LIST OF FIGURES **11**

LIST OF TABLES **20**

LIST OF SYMBOLS AND ABBREVIATIONS **24**

CHAPTER 1

INTRODUCTION **28**

1.1 PILES UNDER DYNAMIC CYCLIC LOADS 28

1.2 PREVIOUS INVESTIGATIONS 28

1.3 OUTLINE OF THE RESEARCH 29

1.4 CONTENT OF THE THESIS 31

CHAPTER 2

AXIAL BEHAVIOUR OF DISPLACEMENT PILES IN CLAY **33**

2.1 DEFINITIONS 34

2.2 STATIC PILE BEHAVIOUR (IMPERIAL COLLEGE RESEARCH) 35

2.2.1 Installation *36*

2.2.2 Equalisation *38*

2.2.3 Pile response to static loading *42*

2.3 IMPERIAL COLLEGE DESIGN APPROACH FOR STATIC CAPACITY OF DISPLACEMENT PILES IN CLAYS 45

2.3.1 Shaft capacity *45*

2.3.2 Base capacity *46*

2.3.3 Overall reliability *47*

2.3.4 Traditional design procedure in Mexico City *47*

2.4 PILE RESPONSE MECHANISM DURING CYCLIC LOADING 48

2.4.1 Pore pressure behaviour *51*

2.4.2 Radial stress behaviour 53
2.4.3 Shear stress behaviour 54
2.5 PILE CAPACITY RESPONSE TO CYCLIC LOADING 56
2.5.1 Effects of load cycles on pile capacity 56
2.5.2 Loading rate effect on pile capacity 58
2.5.3 Effects of load cycling on subsequent pile capacity 60
2.6 PILE LOAD-DISPLACEMENT RESPONSE TO CYCLIC LOADING 62
2.6.1 Effects of load cycles on pile load-displacement response 62
2.6.2 Loading rate effect on pile load-displacement response 63
2.6.3 Effects of cycling on subsequent test load-displacement response 64
2.7 DESIGN OF DISPLACEMENT PILES UNDER AXIAL CYCLIC LOADING 65
2.7.1 Current practice in the design of displacement piles under dynamic loads 65
2.7.2 Review of the design codes for piles under dynamic loads 66
2.7.3 Analytical tools 68
2.8 INTERACTION DIAGRAMS 71
2.9 PILE CAPACITY RESPONSE WITH TIME 72

CHAPTER 3

SUBSOIL CONDITIONS IN MEXICO CITY 74

3.1 GEOLOGY OF THE VALLEY OF MEXICO 74
3.2 GEOTECHNICAL ZONING OF MEXICO CITY 77
3.3 INDEX PROPERTIES 80
3.4 MECHANICAL PROPERTIES 83
3.4.1 Yield stress ratio (YSR) 83
3.4.2 Undrained shear strength 85
3.4.3 Comparison with in situ vane tests (sampling effects) 90
3.4.4 Triaxial effective stress path tests 92
3.4.5 One dimensional compressibility and intrinsic properties 96
3.5 DYNAMICAL PROPERTIES 105
3.5.1 Low-strain shear modulus (G_{max}) 105
3.5.2 Large-strain shear modulus 107
3.5.3 Shear modulus degradation by fatigue 109
3.5.4 Damping ratio (ζ) 111
3.5.5 Stress-strain behaviour 112
3.5.6 Pore water pressure 115
3.6 REGIONAL SUBSIDENCE 116

CHAPTER 4

SHEAR STRENGTH OF MEXICO CITY CLAY ON RING SHEAR 118

4.1 SHEARING MODES 119

4.1.1 Clay-to-clay shearing 119

4.1.2 Effects of displacement rate on shearing modes 122

4.1.3 Clay-to-interface shearing 125

4.2 APPARATUS AND TESTING PROCEDURE 126

4.2.1 Ring shear principle 126

4.2.2 Bishop ring shear apparatus 127

4.2.3 Bromhead ring shear apparatus 129

4.2.3 Interface characteristics 130

4.3 SAMPLE CHARACTERISTICS 131

4.4 MEXICO CITY CLAY RESPONSE TO RING SHEAR TESTING 133

4.4.1 Apparatuses and Interface material effects 134

4.4.2 Normal effective stress and overconsolidation ratio effects 139

4.4.3 Rate of displacement effects 142

4.4.4 Characterisation of MC clay in the ring shear 147

4.5 DIRECT SHEAR TESTS 149

CHAPTER 5

VALIDATION OF THE IC PILE DESIGN METHOD FOR MEXICO CITY 151

5.1 DESCRIPTION OF THE DATABASE 151

5.2 MODIFICATION OF THE ICPDM FOR SQUARE CROSS SECTION PILES 154

5.2.1 Effects of cross section geometry on pile behaviour 154

5.2.2 Development of equivalent radius, shaft perimeter and base area 157

5.3 PERFORMANCE OF THE ICPDM 158

5.4 COMPARISON OF THE ICPDM VS. MEXICO CITY TRADITIONAL DESIGN METHOD 164

CHAPTER 6

BASE REACTIONS ON CASE HISTORIES 166

6.1 PRINCIPLES OF THE PROPOSED SEISMIC STRUCTURAL ANALYSIS 167

6.1.1 Proposed methodology of analysis 167

6.1.2 De-coupling of SSI subsystems 169

6.1.3 Characteristics included in motions recorded at the basement of buildings 170

6.2 CHARACTERISTICS OF THE PROGRAM OF STRUCTURAL ANALYSIS 173

6.2.1 Material models 174

6.2.2 Geometric non-linearity (Changes in stiffness due to deformations) *176*
6.2.3 Solution procedure *177*
6.2.4 Post-processing of results *178*
6.3 CHARACTERISTICS OF THE STRUCTURAL MODELS 178
6.4 PROCEDURE TO UPGRADE RECORDS TO 1985 MICHOACAN EARTHQUAKE CHARACTERISTICS 183
6.4.1 Description of the procedure *183*
6.4.2 Upgrading of 1995 Copala records to 1985 Michoacan earthquake characteristics *185*
6.5 CASE HISTORIES 187

CHAPTER 7

THE BASE REACTIONS DEVELOPED ON THE JAL BUILDING DURING SEISMIC SHAKING 189

7.1 A GENERAL DESCRIPTION OF THE JAL BUILDING 189
7.2 STRUCTURAL CONFIGURATION AND MATERIAL CHARACTERISTICS 190
7.3 FOUNDATION CONFIGURATION 191
7.4 INSTRUMENTATION AND INPUT MOTIONS 193
7.5 BEHAVIOUR OF THE BUILDING DURING EARTHQUAKES 196
7.6 MODELLING 199
7.6.1 JAL building model description *199*
7.6.2 Bare frame *200*
7.6.3 Frame with masonry walls *204*
7.6.4 Frame with concrete walls *208*
7.6.5 Analysis *211*
7.7 BASE REACTION UNDER THE 1995 COPALA EARTHQUAKE 213
7.7.1 Static reactions *213*
7.7.2 Seismic base reactions under the 1995 Copala earthquake – Masonry model *215*
7.8 BASE REACTIONS UNDER THE 1985 MICHOACAN EARTHQUAKE 219
7.8.1 General response of the models *219*
7.8.2 Forces under upgraded motions *219*

CHAPTER 8

THE BASE REACTIONS DEVELOPED ON THE PC BUILDING DURING SEISMIC SHAKING 223

8.1 A GENERAL DESCRIPTION OF THE PC BUILDING 223
8.2 STRUCTURAL CONFIGURATION AND MATERIAL CHARACTERISTICS 224
8.3 FOUNDATION CONFIGURATION 225
8.4 INSTRUMENTATION AND INPUT MOTIONS 226

8.5 BEHAVIOUR OF THE BUILDING DURING EARTHQUAKES 229
8.6 MODELLING 231
8.6.1 PC building model description *231*
8.6.2 Original frame *232*
8.6.3 Selected frame *236*
8.6.5 Analysis *240*
8.7 BASE REACTION FOR THE 1995 COPALA EARTHQUAKE 240
8.7.1 Static reactions *240*
8.7.2 Seismic base reactions for the Selected model under 1995 Copala earthquake *241*
8.8 BASE REACTIONS FOR THE 1985 MICHOACAN EARTHQUAKE 243
8.8.1 General response of the models *243*
8.8.2 Reactions under amplified motions *244*

CHAPTER 9

THE BASE REACTIONS DEVELOPED ON THE PCC BUILDING DURING SEISMIC SHAKING 247

9.1 A GENERAL DESCRIPTION OF THE PCC BUILDING 247
9.2 STRUCTURAL CONFIGURATION AND MATERIAL CHARACTERISTICS 248
9.3 FOUNDATION CONFIGURATION 249
9.4 INSTRUMENTATION AND INPUT MOTIONS 252
9.5 BEHAVIOUR OF THE BUILDING DURING EARTHQUAKES 255
9.6 MODELLING 257
9.6.1 PCC building model description *257*
9.6.2 Primary frame under Colima event *258*
9.6.3 Structural model of the frame under simulated Copala event *262*
9.6.4 Analysis *266*
9.7 BASE REACTION FOR THE 1995 COPALA EARTHQUAKE 267
9.7.1 Static reactions *267*
9.7.2 Seismic base reactions under the 1995 Copala earthquake *268*
9.8 BASE REACTIONS FOR THE 1995 MICHOACAN EARTHQUAKE 270
9.8.1 General response of the models *270*
9.8.2 Reactions under amplified motions *270*

CHAPTER 10

FACTORS INVOLVED IN THE COMPUTATION OF PILE FORCES ON THE CASE HISTORY BUILDINGS 273

10.1 PREVIOUS STUDIES ON THE PILE - RAFT LOAD DISTRIBUTION IN MEXICO CITY 273

10.1.1 Finite element analysis of La Azteca building in Mexico City 274
10.1.2 Instrumented piled raft foundation – static response 275
10.1.3 Instrumented piled raft foundation in Mexico City – seismic response 279
10.2 PROPOSED METHODOLOGY FOR THE ANALYSIS OF THE PILE-RAFT LOAD DISTRIBUTION 284
10.2.1 Principles of the pile-raft load sharing analysis on the case histories 284
10.2.2 Flexibility Matrix approach 285
10.2.3 Stiffness of a single pile 287
10.2.4 Pile group stiffness using the Equivalent Pier approach 289
10.3 PREDICTION OF THE PILE-RAFT LOAD SHARING IN THE CASE HISTORY BUILDINGS 290
10.3.1 Static capacity of the case history piles 290
10.3.2 Compensation analyses 291
10.3.3 Pile raft load distribution for the case histories 291
10.4 PROCESSING OF THE AXIAL SEISMIC BASE REACTIONS 294
10.4.1 JAL Building 295
10.4.2 PC Building 297
10.4.3 PCC Building 300
10.5 ASSESSMENT OF THE FOUNDATION LATERAL STABILITY 301
10.5.1 Passive earth pressure contribution 302
10.5.2 Pile lateral resistance contribution 304
10.6 KINEMATIC FORCES ON PILES 306

CHAPTER 11

RELATIONSHIPS BETWEEN STATIC AND DYNAMIC AXIAL PILE CAPACITIES 307

11.1 STUDIES INCLUDED IN THE INTERACTION DIAGRAM FOR MEXICO CITY 308
11.1.1 JAL Building pile data 310
11.1.2 PC Building pile data 314
11.1.3 Jaime, Resendiz and Romo cyclic pile tests 318
11.1.4 Girault cyclic pile test 319
11.1.5 Mendoza, Romo, Calderon, and Rodriguez instrumented piled foundation 320
11.2 INTERACTION DIAGRAM FOR MEXICO CITY 322
11.2.1 Summary of the data used to develop an Interaction Diagram for driven piles in Mexico City 322
11.2.2 Failure countours in the ID for Mexico City 325
11.2.3 Dynamic versus static pile capacity 329
11.3 ANALYSIS OF RESULTS ACCORDING TO THE STATE OF THE KNOWLEDGE 331
11.3.1 Effects of load cycles on pile response 331
11.3.2 Loading rate effect on pile response 333
11.3.3 Test sequence effect on pile response 335
11.4 IMPLICATIONS FOR SEISMIC DESIGN OF PILES IN MC 336

11.4.1 Application of the interaction diagram to the seismic design of piles *336*

11.4.2 The importance of the static pile design on the seismic pile design based on ID *337*

11.4.3 Implications for the structural analysis of buildings *338*

CHAPTER 12

CONCLUSIONS **339**

12.1 PILE RESPONSE TO CYCLIC LOADING 339

12.2 MEXICO CITY CLAY PROPERTIES 340

12.2.1 Intrinsic properties study *340*

12.2.2 Ring Shear study *341*

12.3 VALIDATION OF THE IMPERIAL COLLEGE DESIGN METHOD 341

12.4 DYNAMIC STRUCTURAL ANALYSIS OF CASE HISTORIES 342

12.5 SEISMIC LOADS AND INTERACTION DIAGRAM 343

12.6 ANALYSIS OF THE SEISMIC PERFORMANCE OF PILES IN MEXICO CITY 344

12.7 IMPLICATIONS FOR SEISMIC DESIGN OF PILES 344

12.7.1 Application of the interaction diagram on the seismic design of piles *344*

12.7.2 Implications of the seismic design of piles based on an ID for the static design of piles and the structural analysis of buildings *345*

12.8 RECOMMENDATIONS FOR FUTURE RESEARCH 346

REFERENCES **347**

APPENDIX A

DATABASE OF LABORATORY TESTS ON MEXICO CITY CLAY **371**

APPENDIX B

APPLICATION OF THE IMPERIAL COLLEGE PILE DESIGN METHOD TO THE WD58A TENSION PILE RESEARCH RESULTS **378**

B1 INTRODUCTION 378

B2 EVALUATION OF PILE CAPACITY 379

APPENDIX C

APPLICATION OF THE IMPERIAL COLLEGE PILE DESIGN METHOD TO THE PILES OF THE CASE HISTORY BUILDINGS **391**

List of Figures

Chapter 2

FIG. 2.1 DEFINITION OF CYCLIC PARAMETERS (AFTER BRIAUD AND FELIO, 1986) 35

FIG. 2.2 MEAN VARIATIONS IN NORMALISED RADIAL TOTAL STRESS WITH NORMALISED HEIGHT (LEHANE, 1992) 37

FIG. 2.3 CHANGES IN RADIAL TOTAL STRESS DURING EQUALISATION (CHOW, 1997) 38

FIG. 2.4 VARIATIONS OF NORMALISED σ_R' WITH TIME (CHOW, 1997) 39

FIG. 2.5 TRENDS FOR K_C WITH YSR AND H/R IN CLAYS (LEHANE, 1992) 41

FIG. 2.6 INFLUENCE OF H/R ON σ_{RC}' (CHOW, 1997). 41

FIG. 2.7 VARIATIONS IN LOCAL SHEAR STRESSES WITH LOCAL PILE DISPLACEMENTS; COMPRESSION TESTS ON FAST-JACKED PILES (CHOW, 1997) 43

FIG. 2.8 EFFECTIVE STRESS PATHS FOR FIRST TIME LOADING TESTS ON FULLY EQUALISED PILES 43

(LEHANE, 1992). 43

FIG. 2.9 EVOLUTION OF EARTH AND PORE PRESSURE DURING LONG-TERM CYCLIC TEST Q_{MAX}/Q_{ULT}= 0.62, Q_{MIN}/Q_{ULT}= 0.04 (KARLSRUD AND HAUGEN, 1985) 52

FIG. 2.10 LOAD TRANSFER AND PORE WATER PRESSURE VERSUS NUMBER OF LOAD CYCLES (GROSCH AND REESE, 1980) 53

FIG. 2.11 VARIATIONS IN RADIAL TOTAL STRESS RECORDED FOR LONG TERM AND AFTER CYCLIC LOAD TEST (BOGARD AND MATLOCK, 1998B) 54

FIG. 2.12 LOAD DISTRIBUTION CURVES FROM CYCLIC TEST LOADS (PUECH AND JEZEQUEL, 1980) 55

FIG. 2.13 MAXIMUM AND MINIMUM τ_{RZ} DISTRIBUTION AT TWO STAGES DURING HAGA TEST (JARDINE, 1991 FROM KARLSRUD AND HAUGEN, 1983). 56

FIG. 2.14 SLOW AND QUICK PENETRATION TESTS (JAIME ET AL., 1990) 59

FIG. 2.15 RESULTS OF STATIC AND CYCLIC LOAD TESTS (BOGARD AND MATLOCK, 1990A) 60

FIG. 2.16 AVERAGE SHEAR STRENGTH AGAINST PILE HEAD DISPLACEMENT BEFORE AND AFTER CYCLIC TEST (CHOW, 1997) 61

FIG. 2.17 TYPICAL LOAD-DISPLACEMENT RESPONSE FROM STATIC TESTS (KARLSRUD AND HAUGEN, 1985) 62

FIG. 2.18 EXAMPLES OF EVOLUTION OF ACCUMULATED AVERAGE DISPLACEMENT, D_A, AND DISPLACEMENT AMPLITUDE, D_C, DURING CYCLIC TESTS (KARLSRUD AND HAUGEN, 1985) 63

FIG. 2.19 EFFECT OF CYCLIC PRE-SHEARING ON PERMANENT DISPLACEMENT ACCUMULATION OF SMALL-SCALE MODEL PILES (BOUCKOVALAS, 1996) 64

FIG. 2.20 IDEALISED DISCRETE ELEMENT SYSTEM FOR DYNAMIC PILE RESPONSE (BEA AND AUDIBERT, 1979) 69

FIG. 2.21 QUASI 3D FINITE ELEMENT MODEL OF PILE-SOIL RESPONSE (FINN, ET AL., 1997) 70

FIG. 2.22 CYCLIC INTERACTION DIAGRAM FROM HAGA TENSION PILE TESTS (JARDINE, 1991 AFTER KARLSRUD AND HAUGEN, 1983). 71

FIG. 2.23 PILE CAPACITY RECOVERY WITH ELAPSED TIME (HJORT AND CARRILLO, 1985) 72

FIG. 2.24 INCREMENT ON PILE CAPACITY WITH TIME (MARSAL AND MASARI, 1962) 73

CHAPTER 3

FIG. 3.1 BASIN OF THE VALLEY OF MEXICO (ZEEVAERT, 1988) 75
FIG. 3.2 EVOLUTION OF THE LAKES IN THE VALLEY OF MEXICO (JAIME, 1987) 76
FIG. 3.3 GEOLOGICAL CROSS SECTION ALONG THE VALLEY OF MEXICO (MOOSER, 1990) 77
FIG. 3.4 GEOTECHNICAL ZONING OF MEXICO CITY (JAIME, 1987) 78
FIG. 3.5 CONTOURS OF EQUAL DEPTH OF THE "DEEP DEPOSITS" (TARANGO SAND II) IN MEXICO CITY (ROMO, ET AL. 1988) 79
FIG. 3.6 MC CLAY ON THE PLASTICITY CHART (MARSAL AND MAZARI, 1962) 81
FIG. 3.7 TYPICAL PROFILES OF PIEZOMETRIC LEVELS, σ_{vy}', S_{UU} AND CPT TEST IN MEXICO CITY (AFTER SANTOYO AND GUTIERREZ, 1990) 84
FIG. 3.8 RELATIONSHIP BETWEEN THE YIELD AND OVERBURDEN STRESSES (ZEEVAERT, 1983) 85
FIG. 3.9 S_U^{CIC} / S_U^{UU} RATIO VS. CONSOLIDATION PRESSURE 86
FIG. 3.10 S_U^{CIC} / P_P' VS. NORMALISED CONSOLIDATION PRESSURE FOR MC CLAY 87
FIG. 3.11 S_U^{CIC} / P_P' VS. OCR FOR MC CLAY 87
FIG. 3.12 ISOTROPIC $(S_U/P_0')_{OC} / (S_U/P_0')_{NC}$ VS. OCR FOR MC CLAY AND CLAYS OF DIFFERENT PLASTICITY 87
FIG. 3.13 RATE EFFECT ON MEXICO CITY CLAY UNDRAINED SHEAR STRENGTH (AFTER ALBERRO AND SANTOYO, 1973) 89
FIG. 3.14 COMPARISON OF ISOTROPICALLY NORMALLY CONSOLIDATED TRIAXIAL TESTS (ROJAS, ET AL. 1987) 92
FIG. 3.15 COMPARISON OF ANISOTROPICALLY NORMALLY CONSOLIDATED TRIAXIAL TESTS (ROJAS, ET AL., 1987) 94
FIG. 3.16 EXTENSION AND COMPRESSION DRAINED TESTS (ROJAS, ET AL., 1987) 95
FIG. 3.17 STRESS PATHS FOR NC AND OC TESTS ON MC CLAY SAMPLES (GIRALDO, 1996) 95
FIG. 3.18 DEVIATOR STRESS AND PORE PRESSURE IN NC AND OC TESTS (GIRALDO, 1996) 96
FIG. 3.19A INTACT, REMOULDED AND RECONSTITUTED COMPRESSIBILITY CURVE FOR MC CLAY 97
FIG. 3.19B INTACT, REMOULDED AND RECONSTITUTED COMPRESSIBILITY CURVE FOR MC CLAY 98
FIG. 3.20 INTRINSIC COMPRESSION LINES FOR MC CLAY 100
FIG. 3.21 BURLAND (1990) AND NAGARAJ, ET AL. (1986) INTRINSIC PROPERTY CORRELATIONS VS. MC CLAY MEASURED INTRINSIC PROPERTIES 101
FIG. 3.22 IN SITU VOID INDEX FOR TWO NORMALLY CONSOLIDATED PROFILES IN MEXICO CITY 102
FIG. 3.23 SENSITIVITY FROM OEDOMETER TEST 103
FIG. 3.24 SENSITIVITY OF MEXICO CITY CLAY (MARSAL AND MAZARI, 1962) 105
FIG. 3.25 EFFECT OF EFFECTIVE CONFINING STRESS AND PLASTICITY INDEX ON MC CLAY G_{MAX} (ROMO, 1995) 106
FIG. 3.26 G VS. γ FOR MC CLAY (ROMO, 1995) 108
FIG. 3.27 G REDUCTION MEASURED IN CLAYS IN THE LABORATORY (DOBRY AND VUCETIC, 1988) 109
FIG. 3.28 G MODULUS DEGRADATION FOR MC CLAY FROM CYCLIC TRIAXIAL TESTS (ROMO, 1995) 110
FIG. 3.29 ζ RANGE MEASURED IN CLAYS IN THE LABORATORY (DOBRY AND VUCETIC, 1988) 112
FIG. 3.30 INITIAL SHEAR STRESS AND CYCLIC ONE- AND TWO- WAY LOADING EFFECTS ON VOLCANIC CLAY

(ISHIHARA, 1996) 113
FIG. 3.31 EFFECTS OF CONFINING STRESS ON THE DYNAMIC STRENGTH OF A VOLCANIC CLAY (ISHIHARA, 1996) 114
FIG. 3.32 EFFECT OF CYCLIC TRIAXIAL LOADING ON PERMANENT DEFORMATION (ROMO, 1995) 115
FIG. 3.33 DYNAMIC STRESS VS. PLASTIC DEFORMATION RELATIONSHIP FOR TRIAXIAL TESTS ON MC CLAY (ROMO, 1995) 115

CHAPTER 4

FIG. 4.1 LUPINI, ET AL. (1981) INTERPRETATION OF SLIDING SHEARING IN LONDON CLAY (48% CLAY FRACTION) 119
FIG. 4.2 LUPINI, ET AL. (1981) INTERPRETATION OF TURBULENT SHEARING, MATERIAL WITH 27% CLAY FRACTION 120
FIG. 4.3 LUPINI, ET AL. (1981) INTERPRETATION OF TRANSITIONAL SHEARING, MATERIAL WITH 40% CLAY FRACTION 121
FIG. 4.4 RESIDUAL SHEAR MECHANISM AS A FUNCTION OF PARTICLE PACKING AND CLAY FRACTION. S1 AREA REPRESENT POSSIBLE SLIDING SHEAR WHEN SOIL IS FAILED AGAINST A SMOOTH INTERFACE (LEMOS AND VAUGHAN, 2000 AFTER LUPINI, ET AL., 1981) 122
FIG. 4.5 SUMMARY OF THE OBSERVED RATE-DEPENDET PHENOMENA FOR RESIDUAL STRENGTH (TIKA, ET AL., 1996) 123
FIG. 4.6 VARIATION OF FAST RESIDUAL STRENGTH WITH AN INCREASING RATE OF DISPLACEMENT (TIKA, 1989) 124
FIG. 4.7 GENERAL LAYOUT AND DETAILS OF SAMPLE ASSEMBLY FOR THE BISHOP RING SHEAR APPARATUS (BISHOP, ET AL. 1971) 128
FIG. 4.8 SIDE VIEW AND SECTION THROUGH SAMPLE TURRET FOR BROMHEAD RING SHEAR APPARATUS (WYKEHAM AND FARRANCE HANDBOOK) 130
FIG. 4.9 CPT PROFILES FOR PIEDAD AND CHAPULTEPEC SITES (TGC, GEOTECNIA) 132
FIG. 4.10 PHOTOMICROGRAPHS OF SILT SIZED SHELLS AND SHELL FRAGMENTS IN MC CLAY (LEFT), AND LARGE AND SMALL MICROFOSSILS AND CLAY FLOCS (RIGHT) (MESRI ET AL., 1975) 133
FIG. 4.11 PHOTOMICROGRAPH OF CLAY-SIZED FRACTION OF MC CLAY SHOWING FILM CLAY MINERAL PARTICLES (LOWER RIGHT) AND FINE FRAGMENTS OF MICRO-ORGANISMS (MESRI, ET AL., 1975) 133
FIG. 4.12 COMPARISON OF PEAK ANGLES OF SHEARING FROM BROMHEAD AND BISHOP APPARATUS 136
FIG. 4.13 COMPARISON OF RESIDUAL ANGLES OF SHEARING FROM BROMHEAD AND BISHOP APPARATUS . 136
FIG. 4.14 COMPARISON OF BROMHEAD AND BISHOP RING SHEAR TEST RESULTS FOR SAMPLE M15-1 137
FIG. 4.15 COMPARISON OF BROMHEAD AND BISHOP RING SHEAR TEST RESULTS FOR SAMPLE M16-2 138
FIG. 4.16 NORMAL EFFECTIVE STRESS AND OVERCONSOLIDATION EFFECTS ON SAMPLE M16-2. SOIL-TO-CONCRETE TEST WITH FAST PRE-SHEARING, FOUR STAGES 140
FIG. 4.17 NORMAL EFFECTIVE STRESS AND OVERCONSOLIDATION EFFECTS ON SAMPLE M16-2. SOIL-TO-CONCRETE TEST WITH FAST PRE-SHEARING, FOUR INDIVIDUAL STAGES 140
FIG. 4.18 NORMAL EFFECTIVE STRESS AND OVERCONSOLIDATION EFFECT ON SAMPLE M13-4. SOIL-TO-SOIL TEST FOUR STAGES WITH CUMULATIVE DISPLACEMENT 141
FIG. 4.19 NORMAL EFFECTIVE STRESS AND OVERCONSOLIDATION EFFECT ON SAMPLE M13-4. SOIL-TO-SOIL

TEST FOUR INDIVIDUAL STAGES 142
FIG. 4.20 FAST SHEARING RESPONSE ON SOIL-TO-SOIL TEST OF SAMPLE C13-4 143
FIG. 4.21 FAST SHEARING RESPONSE ON SOIL-TO-STEEL TEST OF SAMPLES C13-4 144
FIG. 4.22 FAST SHEARING RESPONSE ON SOIL-TO-SOIL TEST OF SAMPLES M15-1 145
FIG. 4.23 VARIATION OF FAST RESIDUAL / SLOW RESIDUAL WITH RATE OF SHEARING 146
FIG. 4.24 SOIL-TO-STEEL FAST SHEARING RESPONSE OF SAMPLE M15-1 146
FIG. 4.25 DATABASE OF PEAK INTERFACE SOIL-TO-STEEL FRICTION ANGLES, TESTS INCLUDE FAST SHEARING PULSES, EXTENDED FROM RAMSEY, ET AL. (1998) 148
FIG. 4.26 DATABASE OF RESIDUAL INTERFACE SOIL-TO-STEEL FRICTION ANGLES, TESTS INCLUDE FAST SHEARING PULSES, EXTENDED FROM RAMSEY, ET AL. (1998) 149
FIG. 4.27 DETAIL OF INITIAL PLATEAU FOR RING SHEAR TESTS IN MC CLAY SAMPLE 13-4 SOIL-TO-SOIL BISHOP APPARATUS TEST 149

CHAPTER 5

FIG. 5.1 TYPICAL TEST RESULT FOR LINEA 4 PILE TESTS 152
FIG. 5.2 SHAPES AND DIMENSIONS OF JAIME ET AL'S MODEL PILES (JAIME, ET AL., 1991) 155
FIG. 5.3 NORMALISED PILE CAPACITY VS. PILE/BOREHOLE AREA RATIO (JAIME, ET AL. 1991) 156
FIG. 5.4 COMPARISON OF SIMPLE PLATE, B/W = 6.8, AND SIMPLE PILE NORMALISED EXCESS PORE PRESSURES (AUBENY, 1992 FROM COWLEY, 1998) 157
FIG. 5.5 IC DESIGN METHOD PREDICTION VS. MEASURED PILES CAPACITIES 160
FIG. 5.6 IC PILE DESIGN METHOD RESPONSE WITH L/D RATIO 160
FIG. 5.7 IC PILE DESIGN METHOD RESPONSE WITH YSR 161
FIG. 5.8 IC PILE DESIGN METHOD RESPONSE WITH S_T 161
FIG. 5.9 COMPUTED AND MEASURED α VS. S_U AND API (1986) AND TOMLINSON (1957) SUGGESTED VALUES 162
FIG. 5.10 β VS. DEPTH OF PENETRATION FOR COMPUTED AND MEASURED CAPACITIES AND MEYERHOF (1976) SUGGESTED VALUES 162
FIG. 5.11 INFERRED τ_{RZ} VALUES VS. PILE LENGTH 163
FIG. 5.12 CALCULATED AND INFERRED A VS. S_U/σ_{v0}' RATIO, WITH IDENTIFIED OVERPREDICTED AND UNDERPREDICTED TESTS 163

CHAPTER 6

FIG. 6.1 DYNAMIC SOIL-STRUCTURE INTERACTION CONCEPT 167
FIG. 6.2 FOURIER SPECTRA OF BASEMENT ACCELERATION AND PILE FORCES (MENDOZA, ET AL. 1998) 169
FIG. 6.3 DE-COUPLING OF SUBSYSTEMS (WOLF, 1985) 170
FIG. 6.4 PHYSICAL INTERPRETATION OF KINEMATIC AND INERTIAL INTERACTION (WOLF, 1985) 171
FIG. 6.5 KINEMATIC AND INERTIAL INTERACTION MOTIONS (WOLF, 1985) 172
FIG. 6.6 LOADING AND UNLOADING PATHS OF BILINEAR KINEMATIC MODEL (IZZUDDIN, 1991) 174
FIG. 6.7 LOADING SURFACES FOR MULTI-SURFACE PLASTICITY MODEL (ELNASHAI AND IZZUDDIN, 1993) 174
FIG. 6.8 UNIAXIAL STRESS-STRAIN RELATIONSHIP FOR CONCRETE (MARTINEZ-RUEDA, 1997) 175
FIG. 6.9 UNIAXIAL STRESS-STRAIN RELATIONSHIP WITH ACTIVE CONFINEMENT (MANDER, ET AL., 1988) 176

FIG. 6.10 DISCRETISATION OF RC SECTIONS (PINHO, 2000) 177
FIG. 6.11 FLEXURAL WALL SECTION (IZZUDDIN AND ELNASHAI, 1993) 177
FIG. 6.12 DESCRIPTION OF MODEL FOR MASONRY WALLS 180
FIG. 6.13 ANALYSIS OF RECORD UPGRADING TO 1985 CONDITIONS 184
FIG. 6.14 LOCATION OF THE STUDIED BUILDINGS IN A ISO-PERIOD PLAN (AFTER MURIA, 1997) 188

CHAPTER 7

FIG. 7.1 ELEVATION AND PLAN VIEWS OF THE JAL BUILDING (MURIA AND DEL TORO, 1998) 190
FIG. 7.2 JAL BUILDING PILE FOUNDATION SOLUTION 192
FIG. 7.3 PLAN OF JAL BUILDING FOUNDATION (PROVIDED BY DR. D. MURIA) 192
FIG. 7.4 SHEAR WAVE VELOCITY (V_s) PROFILE AND CONE PENETRATION RESISTANCE (Q_c) AT SCT SITE (MELI, ET AL., 1998) 193
FIG. 7.5 OVERVIEW OF THE BUILDING INSTRUMENTATION (MELI ET AL. 1998) 194
FIG. 7.6 RECORDS FROM THE 1995 COPALA EARTHQUAKE (GAMBOA AND MURIA, 1996) 196
FIG. 7.7 ACCELEROGRAM AT ROOF CENTER FOR THE 94-3 EVENT, AND THE CORRESPONDING TIME EVOLUTION OF THE NATURAL FREQUENCIES IN THE L AND T DIRECTIONS (MELI, ET AL., 1998) 198
FIG. 7.8 JAL BUILDING, BARE FRAME CONFIGURATION 200
FIG. 7.9 RECORDED AND PREDICTED ROOF ACCELERATION, BARE FRAME 201
FIG. 7.10 FOURIER SPECTRA OF RECORDED AND PREDICTED ROOF ACCELERATION, BARE FRAME 202
FIG. 7.11 COMPUTED AND INFERRED ROOF LATERAL DISPLACEMENTS, BARE FRAME 202
FIG. 7.12 COMPUTED AND INFERRED DRIFT INDEXES, BARE FRAME 203
FIG. 7.13 JAL BUILDING, MASONRY FRAME CONFIGURATION 204
FIG. 7.14 RECORDED AND PREDICTED ROOF ACCELERATION, MASONRY FRAME 205
FIG. 7.15 FOURIER SPECTRA OF RECORDED AND PREDICTED ROOF ACCELERATION, MASONRY FRAME 205
FIG. 7.16 PREDICTED AND INFERRED FROM RECORDS LATERAL DISPLACEMENTS, ... 206
MASONRY FRAME 206
FIG. 7.17 PREDICTED AND INFERRED DRIFT INDEXES, MASONRY FRAME 207
FIG. 7.18 JAL BUILDING, RC WALL FRAME CONFIGURATION 208
FIG. 7.19 RECORDED AND PREDICTED ROOF ACCELERATIONS, RC WALL FRAME 209
FIG. 7.20 FOURIER SPECTRA OF RECORDED AND PREDICTED ROOF ACCELERATIONS, RC WALL FRAME 209
FIG. 7.21 PREDICTED AND INFERRED LATERAL DISPLACEMENT, RC WALL FRAME 210
FIG. 7.22 PREDICTED AND INFERRED DRIFT INDEXES, RC WALL FRAME 211
FIG. 7.23 INITIAL STATIC LOAD DISTRIBUTION AT THE BASE OF THE STUDIED CONFIGURATIONS 214
FIG. 7.24 TIME-HISTORY OF CALCULATED FORCES AT THE BASE OF THE MASONRY FRAME 215
FIG. 7.25 MAXIMUM AND MINIMUM LOAD UNDER THE COPALA EVENT – MASONRY FRAME 215
FIG. 7.26 FOURIER SPECTRA OF FORCES AT BASE – MASONRY FRAME 216
FIG. 7.27 MAXIMUM LOADS FOR THE THREE CONFIGURATIONS OF THE UNDER STUDY 217
FIG. 7.28 MINIMUM LOAD FOR THE THREE CONFIGURATIONS UNDER STUDY 217
FIG. 7.29 RATIOS OF THE BASE REACTION FOURIER SPECTRA FOR THE THREE FRAME CONFIGURATIONS UNDER STUDY 218
FIG. 7.30 MAXIMUM AND MINIMUM REACTIONS FOR BARE FRAME UNDER AMPLIFIED MOTIONS 220

FIG. 7.31 MAXIMUM AND MINIMUM REACTIONS - MASONRY FRAME UNDER AMPLIFIED MOTIONS 220

CHAPTER 8

FIG. 8.1 ELEVATION AND PLAN VIEWS OF PC BUILDING (AFTER ALCANTARA, ET AL. , 1999) 224
FIG. 8.2 PC BUILDING PILE FOUNDATION SOLUTION 225
FIG. 8.3 FOUNDATION PLAN AND PILE LOCATION IN THE PC BUILDING 226
FIG. 8.4 OVERVIEW OF THE BUILDING INSTRUMENTATION (ALCANTARA, ET AL. 1999) 227
FIG. 8.5 INPUT RECORDS FOR PC DYNAMIC ANALYSIS (19-09-1995 EVENT) 229
FIG. 8.6 ROOF (PCAC) VS. BASEMENT (PCSC) SPECTRAL RATIOS FOR PC BUILDING 230
FIG. 8.7 SLAB AND BEAM EFFECTIVE WIDTH DETAILS 231
FIG. 8.8 PC BUILDING, ORIGINAL FRAME CONFIGURATION 233
FIG. 8.9 RECORDED AND PREDICTED ROOF ACCELERATION, ORIGINAL FRAME 234
FIG. 8.10 FOURIER SPECTRA OF RECORDED AND PREDICTED ROOF ACCELERATIONS, ORIGINAL FRAME 234
FIG. 8.11 PREDICTED AND INFERRED HORIZONTAL ROOF DISPLACEMENTS, ORIGINAL FRAME 235
FIG. 8.12 PREDICTED AND INFERRED DRIFT INDEXES, ORIGINAL FRAME 235
FIG. 8.13 PC BUILDING, SELECTED FRAME MODEL CONFIGURATION 236
FIG. 8.14 RECORDED AND PREDICTED ACCELERATION TIME HISTORIES, SELECTED FRAME 237
FIG. 8.15 FOURIER SPECTRA OF RECORDED AND PREDICTED ROOF ACCELERATION, SELECTED FRAME 237
FIG. 8.16 PREDICTED AND INFERRED LATERAL DISPLACEMENTS, SELECTED FRAME 238
FIG. 8.17 COMPUTED AND INFERRED FROM RECORDS DRIFT INDEXES, SELECTED FRAME 239
FIG. 8.18 STATIC LOAD DISTRIBUTION AT THE FRAME BASE 241
FIG. 8.19 TIME-HISTORY OF CALCULATED REACTIONS AT THE BASE OF THE SELECTED FRAME DURING THE COPALA 1995 EARTHQUAKE 242
FIG. 8.20 MAXIMUM AND MINIMUM LOAD FOR 1995 COPALA EVENT – SELECTED FRAME 242
FIG. 8.21 FOURIER SPECTRA OF BASE REACTIONS BASE – SELECTED FRAME 243
FIG. 8.22 MAXIMUM AND MINIMUM SEISMIC REACTIONS IN THE ORIGINAL FRAME FOR INPUT COPALA MOTION UNDER $\lambda = 1$ AND 3 244
FIG. 8.23 MAXIMUM AND MINIMUM SEISMIC REACTIONS IN THE SELECTED FRAME FOR INPUT COPALA MOTION UNDER $\lambda = 1$ AND 3 245

CHAPTER 9

FIG. 9.1 ORIGINAL ELEVATION AND PLAN VIEWS OF THE PCC BUILDING (REYES, ET AL., 1995) 248
FIG. 9.2 REINFORCEMENT OF THE PCC BUILDING (REYES, ET AL., 1995) 249
FIG. 9.3 FOUNDATION PLAN AND ORIGINAL FRICTION PILES (RODRIGUEZ, 1991) 250
FIG. 9.4 PLANT VIEW OF THE PCC BUILDING FOUNDATION WITH THE LOCATION OF NEW END BEARING PILES (RODRIGUEZ, 1991) 251
FIG. 9.5 WATER CONTENT AND FAST TRIAXIAL UNDRAINED SHEAR STRENGTH FROM SOIL PROFILE AT PCC BUILDING SITE (REYES AND LUCO) 252
FIG. 9.6 LOCATION OF ACCELEROMETERS AT THE PCC BUILDING (REYES, ET AL., 1995) 253
FIG. 9.7 LONGITUDINAL ACCELERATIONS AT F6 LOCATION FOR COPALA AND COLIMA EVENTS (REYES, ET AL., 1997) 254

FIG. 9.8 AMBIENT VIBRATION TESTS ON PCC BUILDING (RODRIGUEZ, 1991) 255
FIG. 9.9 COMPARISON BETWEEN RIGID BASE AND COMPLETE SYSTEM RESPONSE (REYES AND LUCO) 256
FIG. 9.10 EFFECT OF FOUNDATION DEPTH ON GROUND MOTION (ROMO, 1995) 257
FIG. 9.11 PCC BUILDING, PRIMARY FRAME CONFIGURATION 259
FIG. 9.12 RECORDED AND PREDICTED ROOF ACCELERATION, PRIMARY FRAME 260
FIG. 9.13 FOURIER SPECTRA FOR THE RECORDED AND PREDICTED ROOF ACCELERATIONS, PRIMARY FRAME 260
FIG. 9.14 PREDICTED AND INFERRED HORIZONTAL ROOF DISPLACEMENTS, PRIMARY FRAME 261
FIG. 9.15 COMPUTED AND INFERRED DRIFT INDEXES, PRIMARY FRAME 262
FIG. 9.16 ORIGINAL AND MODIFIED LONGITUDINAL BASEMENT INPUT MOTION FROM THE COLIMA EVENT 263
FIG. 9.17 PCC BUILDING, IMPLEMENTED FRAME CONFIGURATION 264
FIG. 9.18 PREDICTED AND RECORDED ACCELERATION TIME HISTORIES AT ROOF FOR THE IMPLEMENTED MODEL UNDER THE COPALA EVENT. 265
FIG. 9.19 FOURIER SPECTRA OF PREDICTED ROOF ACCELERATION, IMPLEMENTED FRAME 265
FIG. 9.20 PREDICTED DRIFT INDEXES, IMPLEMENTED FRAME 266
FIG. 9.21 STATIC LOAD DISTRIBUTION AT THE BASE OF THE PRIMARY AND IMPLEMENTED MODELS 268
FIG. 9.22 TIME-HISTORY OF PREDICTED BASE REACTIONS IN THE IMPLEMENTED FRAME UNDER THE COPALA EVENT 269
FIG. 9.23 MAXIMUM AND MINIMUM REACTIONS AT THE BASE OF THE IMPLEMENTED FRAME UNDER THE COPALA EARTHQUAKE 269
FIG. 9.24 MAXIMUM AND MINIMUM SEISMIC REACTIONS IN THE PRIMARY FRAME FOR COPALA MOTION UNDER $\lambda = 1$ AND 5 271
FIG. 9.25 MAXIMUM AND MINIMUM SEISMIC REACTIONS IN THE IMPLEMENTED FRAME FOR COPALA MOTION UNDER $\lambda = 1$ AND 5 271

CHAPTER 10

FIG. 10.1 BASEMENT LAYOUT FOR LA AZTECA BUILDING (HEMSLEY, 2000) 275
FIG. 10.2 IMPULSORA BRIDGE INSTRUMENTED SUPPORT (MENDOZA, ET AL., 2000B) 276
FIG. 10.3 IMPULSORA BRIDGE FOUNDATION PLAN VIEW AND INSTRUMENTATION LAYOUT (MENDOZA, ET AL., 1998) 277
FIG. 10.4 LONG TERM STATIC PILE-RAFT LOAD DISTRIBUTION FOR IMPULSORA BRIDGE (MENDOZA, 1998) 278
FIG. 10.5 JANUARY, 1997 EVENT AND LONG TERM RECORDED PRESSURES AT THE SOIL-RAFT CONTACT OF THE IMPULSORA BRIDGE (MENDOZA, ET AL., 1998) 280
FIG. 10.6 PILE LOAD RECORDED ON IMPULSORA BRIDGE DURING JANUARY, 1997 EVENT (MENDOZA, ET AL., 1997) 281
FIG. 10.7 JANUARY, 1997 EVENT AND LONG TERM PILE LOADS ON IMPULSORA BRIDGE (MENDOZA, ET AL., 1998) 282
FIG. 10.8 PILE LOAD AND CELL PRESSURES ON THE IMPULSORA BRIDGE FOUNDATION DURING THE JUNE 1999 EVENT (MENDOZA, ET AL., 2000A) 283
FIG. 10.9 SETTLEMENTS ON THE IMPULSORA BRIDGE FOUNDATION (MENDOZA, ET AL., 2000A) 283

FIG. 10.10 LOAD DISPLACEMENT RESPONSE OF COMPENSATED FOUNDATION RAFTS 284
FIG. 10.11 SETTLEMENT INTERACTIONS BETWEEN SINGLE PILE AND CAP (RANDOLPH, 1983) 286
FIG. 10.12 CONCEPT OF EQUIVALENT PIER METHOD (HORIKOSHI AND RANDOLPH, 1999)..... 289
FIG. 10.13 DEFINITION OF PARAMETERS FOR THE ANALYSIS OF CYCLIC BASE REACTIONS 294
FIG. 10.14 BASE REACTION FROM MASONRY MODEL UNDER TWICE AMPLIFIED INPUT MOTION..... 296
FIG. 10.15 BASE REACTIONS FROM SELECTED MODEL UNDER INPUT MOTION AMPLIFIED THREE TIMES..... 298
FIG. 10.16 BASE REACTION FROM IMPLEMENTED MODEL UNDER FIVE TIMES AMPLIFIED COPALA INPUT MOTION..... 301
FIG. 10.17 SOIL REACTIONS TRANSMITTED TO THE FOUNDATION DURING LATERAL LOADING 302
FIG. 10.18 FAILURE MODES FOR RESTRAINED PILES (BROMS, 1964) 305

CHAPTER 11

FIG. 11.1 NORMALIZED PILE LOADS FOR THE JAL BUILDING MASONRY FRAME MODEL UNDER THE COPALA (1995) EARTHQUAKE..... 313
FIG. 11.2 NORMALIZED PILE LOADS FOR THE JAL BUILDING BARE FRAME MODEL UNDER THE MICHOACAN (1985) EARTHQUAKE..... 313
FIG. 11.4 PILE LOADS FOR THE PC BUILDING SELECTED FRAME MODEL UNDER THE COPALA EARTHQUAKE 317
FIG. 11.5 CYCLIC PILE TESTS ON MEXICO CITY CLAY PRESENTED IN A CYCLIC INTERACTION DIAGRAM FRAMEWORK..... 320
FIG. 11.6 FRAME LOADS FROM PILE LOADS 322
FIG. 11.7 JAL AND PC BUILDING FRAME LOADS AND CYCLIC PILES TEST RESULTS IN MC 323
FIG. 11.8 NUMBER OF CYCLES TO FAILURE UNDER DIFFERENT CONSTANT CYCLIC LOAD COMBINATIONS FOR 4 MC CLAY SAMPLES (OVANDO, ET AL., 1993) 325
FIG. 11.9 INFORMATION USED TO DEVELOPED THE ID FOR MC AND INTERPOLATION POINTS THROUGH USE OF SURFER PROGRAMME – DATA FROM SEISMIC AND SLOWER CYCLIC TESTS NOT NORMALIZED FOR LOADING RATE..... 326
FIG. 11.10 PROPOSED ID FOR MC FOR 84.8 TON/SEC ($0.45Q_{ULT}$/SEC) LOADING RATE (2.3 SEC PERIOD) ... 327
FIG. 11.11 EXAMPLE OF SURFER OUT PUT DATA USED TO DEVELOP THE FAILURE CONTOURS FOR THE SLOW LOADING RATE ID..... 328
FIG. 11.12 ID EXTRAPOLATING FOR SLOW CYCLIC OR STATIC LOADING – WITH 22 HRS NOMINAL LOADING 328
FIG. 11.13 CYCLIC AMPLITUDE AND DISPLACEMENTS FROM STATIC AND CYCLIC TESTS, AFTER JAIME, ET AL. (1990) 330
FIG. 11.14 LOAD-DISPLACEMENT RESPONSE FOR JAIME, ET AL. (1990) TEST PROGRAM..... 335

APPENDIX B

FIG. B1 MOISTURE CONTENT VS DEPTH PROFILE (AUDIBERT AND HAMILTON, 1998)..... 382
FIG. B2 SUBMERGED UNIT WEIGHT VS DEPTH PROFILE (AUDIBERT AND HAMILTON, 1998) 382
FIG. B3 SAMPLE 40, DEPTH 62.0 FT.....383

FIG. B4 SAMPLE 61, DEPTH 122 FT 384
FIG. B5 SAMPLE 79, DEPTH 169.5 FT 384
FIG. B6 SAMPLE 90, DEPTH 199.5 FT 385
FIG. B7 SAMPLE 101, DEPTH 229.5 FT 385
FIG. B8 SENSITIVITY PROFILE (AUDIBERT AND HAMILTON, 1998) 386
FIG. B9 YIELD STRESS PROFILE (BOGARD AND MATLOCK, 1998A) 386
FIG. B10 SUMMARY OF WD58A TEST RESULTS AND IC PREDICTIONS 387

List of Tables

CHAPTER 2

TABLE 2.1 SUMMARY OF IMPERIAL COLLEGE PILE RESEARCH SITES (JARDINE, ET AL., 1998) 36
TABLE 2.2 SUMMARY OF RESEARCH STUDY PILE RESPONSE TO CYCLIC LOADING 50
TABLE 2.3 INCREMENT OF PILE CAPACITY WITH TIME (MARSAL AND MASARI, 1962) 73

CHAPTER 3

TABLE 3.1 MINERAL COMPONENTS OF MC CLAY ACCORDING TO THE PARTICLE SIZE (PERALTA, 1989) 81
TABLE 3.2 CIC VS. UU SHEAR STRENGTH RATIOS (JAIME, ET AL. 1988) 85
TABLE 3.3 NORMALLY CONSOLIDATED VS. OVER-CONSOLIDATED UNDRAINED SHEAR STRENGTHS (GIRALDO, 1996) 86
TABLE 3.4 CONSOLIDATED UNDRAINED TRIAXIAL TESTS AT DIFFERENT STRAIN RATES DURING FAILURE STAGE (ALBERRO AND SANTOYO, 1973) 89
TABLE 3.5 VANE TEST VS. UNDRAINED TRIAXIAL TEST SHEAR STRENGTHS (MARSAL AND MAZARI, 1962) 91
TABLE 3.6 V_S AT OVERCONSOLIDATED AND VIRGIN (NC) TEXCOCO LAKE (JAIME, 1987) 106
TABLE 3.7 V_S AT XOCHIMILCO CHALCO LAKE ZONE (NC) - TLAHUAC DEPORTIVO SITE (JAIME, 1987)..... 106
TABLE 3.8 EFFECTS OF INCREASING VARIOUS FACTORS ON G_{MAX}, G/G_{MAX} AND DAMPING RATIO (ζ) FOR NORMALLY CONSOLIDATED AND MODERATELY OVERCONSOLIDATED CLAYS (DOBRY AND VUCETIC, 1988) 107
TABLE 3.9 PROGRESSIVE SETTLEMENTS AT THE OLD DOWNTOWN AREA OF MC (JAIME, 1987) 116
TABLE 3.10 RATE OF SETTLEMENT AT VARIOUS ZONES OF MC, 1970-1977 (JAIME, 1987)..... 116

CHAPTER 4

TABLE 4.1 CONCRETE AND STAINLESS STEEL INTERFACE DESCRIPTION..... 131
TABLE 4.2 CHARACTERISTICS OF SAMPLES USED IN RING SHEAR TESTS..... 131
TABLE 4.3 PEAK ANGLES AND ASSOCIATED DISPLACEMENTS FOR COMPARATIVE BROMHEAD AND BISHOP TESTS 135
TABLE 4.4 RESIDUAL ANGLES AND ASSOCIATED DISPLACEMENTS FOR COMPARATIVE BROMHEAD AND BISHOP TESTS[57] 135
TABLE 4.5 SAMPLES USED TO EXPAND IC RING SHEAR DATABASE 148

CHAPTER 5

TABLE 5.1 SUMMARY OF THE PILE TEST DATABASE 152
TABLE 5.2 DETAILS OF THE DATABASE PILE TESTS 153
TABLE 5.3 APPROACHES ANALYSED BY COWLEY FOR THE R_{EQ} OF SQUARE PILES 158
TABLE 5.4 SUMMARY OF RESULTS FROM THE VALIDATION OF THE ICPDM FOR MEXICO CITY CONDITIONS 159
TABLE 5.5 STATISTICAL RESULTS OF THE VALIDATION 159

TABLE 5.6 ICPDM VS. TOTAL STRESS METHOD FOR MEXICO CITY CONDITIONS 165
TABLE 5.7 STATISTICAL RESULTS FOR ICPDM AND TOTAL STRESS α=1. 165

Chapter 6

TABLE 6.1 VARIABILITY IN MAIN ANALYSIS AND DESIGN INPUT PARAMETERS DURING A STRUCTURAL SEISMIC STUDY (FEMA, 1995) 182
TABLE 6.2 CHARACTERISTICS OF THE COPALA 1995 AND MICHOACAN 1985 EARTHQUAKES 186
TABLE 6.3 SUMMARY OF JAL RECORDS AMPLIFICATION ANALYSIS 186
TABLE 6.4 DATABASE OF INSTRUMENTED BUILDINGS ON FRICTION PILES 187

Chapter 7

TABLE 7.1 MAIN SEISMIC EVENTS RECORDED AT JAL BUILDING 195
TABLE 7.2 ESTIMATED EXPERIMENTAL PARAMETERS FOR JAL BUILDING (AFTER MURIA AND DEL TORO, 1998) 197
TABLE 7.3 PREDICTED AND INFERRED ABSOLUTE MAXIMUM LATERAL DISPLACEMENTS AND DRIFTS, BARE FRAME UNDER COPALA EVENT 201
TABLE 7.4 PREDICTED AND INFERRED MAXIMUM ABSOLUTE LATERAL DISPLACEMENTS AND DRIFT INDEXES, MASONRY FRAME UNDER COPALA EVENT 207
TABLE 7.5 PREDICTED AND INFERRED MAXIMUM LATERAL DISPLACEMENTS AND DRIFTS, RC WALL FRAME 210
TABLE 7.6 SUMMARY OF PREDICTED AND RECORDED RESPONSE OF JAL BUILDING 212
TABLE 7.7 INITIAL FORCES ON EACH MODEL CONFIGURATION AND MAXIMUM AND MINIMUM SEISMIC FORCES DURING THE COPALA EARTHQUAKE EXPRESSED AS PERCENTAGE OF INITIAL STATIC FORCES .. 214
TABLE 7.8 RESPONSE OF BARE FRAME MODEL TO AMPLIFIED INPUT MOTION 219
TABLE 7.9 RESPONSE OF MASONRY FRAME MODEL TO AMPLIFIED INPUT MOTION 219
TABLE 7.10 AMPLIFICATION RATIOS FOR BARE FRAME UNDER UPGRADED INPUT MOTIONS 221
TABLE 7.11 AMPLIFICATION RATIOS FOR MASONRY FRAME UNDER UPGRADED INPUT MOTIONS 221

Chapter 8

TABLE 8.1 MAXIMUM REGISTERED ACCELERATIONS AT PC BUILDING, CM/S^2 (ALCANTARA, ET AL., 1999) 228
TABLE 8.2 RECORDED RESPONSE OF THE PC BUILDING (MURIA VILA, 1997) 230
TABLE 8.3 MAXIMUM PREDICTED AND INFERRED HORIZONTAL DISPLACEMENTS AND DRIFT INDEXES FOR THE ORIGINAL FRAME MODEL UNDER COPALA EVENT 236
TABLE 8.4 MAXIMUM LATERAL DISPLACEMENTS AND DRIFTS INDEXES, SELECTED FRAME UNDER COPALA EVENT 239
TABLE 8.5 RATIOS OF THE MAXIMUM AND MINIMUM SEISMIC LOADS TO THE STATIC LOADS 241
TABLE 8.6 RESPONSE OF THE ORIGINAL MODEL TO THE CALIBRATION COPALA MOTION UNDER λ = 1, 3, AND 5 243
TABLE 8.7 RESPONSE OF THE SELECTED MODEL TO THE CALIBRATION COPALA MOTION UNDER λ = 1, AND 3 244

TABLE 8.8 SPECTRAL RATIOS OF FORCES FOR ORIGINAL FRAME UNDER AMPLIFIED MOTIONS 245
TABLE 8.9 SPECTRAL RATIOS OF FORCES FOR SELECTED MODEL UNDER AMPLIFIED MOTIONS 245

Chapter 9

TABLE 9.1 MAXIMUM LONGITUDINAL ACCELERATIONS (CM/S^2) AT PCC BUILDING FOR THE COPALA AND COLIMA EARTHQUAKES (REYES, ET AL., 1997) 253
TABLE 9.2 RECORDED FUNDAMENTAL FREQUENCIES FOR PCC BUILDING (REYES AND LUCO) 256
TABLE 9.3 MAXIMUM COMPUTED AND INFERRED DISPLACEMENTS AND DRIFT INDEXES 261
TABLE 9.4 MAXIMUM PREDICTED LATERAL DISPLACEMENTS AND DRIFTS INDEXES, IMPLEMENTED FRAME 266
TABLE 9.5 RATIOS OF THE MAXIMUM AND MINIMUM SEISMIC LOADS PREDICTED UNDER THE COPALA EVENT AGAINST THE STATIC LOADS 268
TABLE 9.6 RESPONSE OF THE PRIMARY MODEL TO THE COPALA MOTION UNDER λ= 1 AND 5 270
TABLE 9.7 RESPONSE OF THE IMPLEMENTED MODEL TO THE COPALA MOTION UNDER λ = 1, 3, AND 5 270

CHAPTER 10

TABLE 10.1 EARTHQUAKES USED BY MENDOZA ET AL. TO CHARACTERIZE THE IMPULSORA BRIDGE SEISMIC RESPONSE (MENDOZA, ET AL., 1997, 1998, AND 2000A) 279
TABLE 10.2 COMPUTED PILE CAPACITY FOR THE PILES OF THE CASE HISTORY BUILDINGS 291
TABLE 10.3 SUMMARY OF COMPENSATED FOUNDATION WORKING CONDITIONS 291
TABLE 10.4 PERCENTAGE OF THE TOTAL BUILDING WEIGHT CARRIED BY THE PILES IN THE JAL, PC AND PCC BUILDINGS FOUNDATIONS 292
TABLE 10.5 SUMMARY OF PROCESSED BASE REACTIONS ON BARE FRAME JAL BUILDING UNDER NORMAL AND AMPLIFIED INPUT MOTIONS 296
TABLE 10.6 SUMMARY OF PROCESSED BASE REACTION ON MASONRY FRAME JAL BUILDING UNDER NORMAL AND AMPLIFIED INPUT MOTION AND ELASTIC ANALYSIS CONDITIONS 297
TABLE 10.7 SUMMARY OF PROCESSED REACTIONS ON ORIGINAL FRAME PC BUILDING UNDER NORMAL AND AMPLIFIED INPUT MOTIONS 299
TABLE 10.8 SUMMARY OF PROCESSED BASE REACTIONS ON SELECTED FRAME PC BUILDING UNDER NORMAL AND AMPLIFIED INPUT MOTIONS 300
TABLE 10.9 PASSIVE EARTH PRESSURE RESISTANCES ON THE CASE HISTORY BUILDINGS 304

Chapter 11

TABLE 11.1 PILES AXIAL CAPACITY BIASES AND UNCERTAINTIES (API, DRAFT 1998) 307
TABLE 11.2 PILE LOADS (KN) FOR THE JAL BUILDING BARE FRAME MODEL UNDER THE COPALA AND THE AMPLIFIED INPUT MOTIONS 311
TABLE 11.3 PILE LOADS (KN) FOR THE JAL BUILDING MASONRY FRAME MODEL UNDER CALIBRATION COPALA AND AMPLIFIED INPUT MOTIONS 312
TABLE 11.4 PILE LOADS (KN) FOR THE PC BUILDING ORIGINAL FRAME MODEL UNDER CALIBRATION COPALA AND AMPLIFIED INPUT MOTIONS 315
TABLE 11.5 PILE LOADS (KN) FOR THE PC BUILDING SELECTED MODEL UNDER CALIBRATION COPALA AND

AMPLIFIED INPUT MOTIONS 316
FIG. 11.3 PILE LOADS FOR THE PC BUILDING ORIGINAL FRAME MODEL UNDER THE 1985 MICHOACAN EARTHQUAKE 317
TABLE 11.6 SUMMARY OF THE CYCLIC PILE TESTS CARRIED OUT IN MEXICO CITY CLAY BY JAIME, ET AL. (1988) 319
TABLE 11.7 RECORDED PILE LOADS IN MENDOZA, ET AL. INSTRUMENTED FOUNDATION 321
TABLE 11.8 PILE CHARACTERISTIC LOADS AND FRAME MEAN LOADS FOR JAL AND PC BUILDINGS 323
TABLE 11.9 FAILURE LOADS FOR JAIME, ET AL. AND GIRAULT CYCLIC PILE TESTS 324
TABLE 11.10 NORMALIZED DYNAMIC PILE CAPACITIES WITH AND WITHOUT RATE EFFECTS 330

APPENDIX A

TABLE A1 SUMMARY OF LABORATORY TESTS ON MEXICO CITY CLAY SAMPLES 372
TABLE A2 SUMMARY OF BROMHEAD RING SHEAR TEST RESULTS 373
TABLE A3 BISHOP RING SHEAR TEST RESULTS ON SAMPLE CHAPULTEPEC 13-4 374
TABLE A4 BISHOP RING SHEAR TEST RESULTS ON SAMPLE CHAPULTEPEC 14-2 375
TABLE A5 BISHOP RING SHEAR TEST RESULTS ON SAMPLE PIEDAD 15-1 376
TABLE A6 BISHOP RING SHEAR TEST RESULTS ON SAMPLE PIEDAD 16-2 377

APPENDIX B

TABLE B1 SPREAD SHEET B1 – 1999 OTC PAPER ANALYSIS 388
TABLE B2 SPREAD SHEET B2 – 2000 ANALYSIS 389
TABLE B3 SPREAD SHEET B3 – 2000 ANALYSIS (PROGRESSIVE FAILURE) 390

APPENDIX C

TABLE C1 JAL BUILDING PILE CAPACITY 392
TABLE C2 PC BUILDING PILE CAPACITY 393

List of symbols and abbreviations

A_g	plan area of a pile group as a block
A_{pp}	cross sectional area of a pile pre-driven borehole
A_{tp}	cross sectional area of a pile; or total cross-sectional area of the piles in a group
$C_{\alpha e}$	coefficient of secondary consolidation
CAC	anisotropically consolidated compression test
C_c	compressibility
C_c^*	intrinsic compressibility
CIC	isotropically consolidated compression tests
CLA	Centre line average roughness parameter
COV	coefficient of variation
CPT	cone penetration test
c_{rh}	linear coefficient of consolidation
C_s	swelling index
c_v	coefficient of consolidation
D	depth of a foundation box
d	pile head vertical displacement
d_a	average permanent pile displacement
d_c	cyclic pile displacement
d_{eq}	diameter of a equivalent pier
e	void ratio
E_{eq}	Young's modulus of a equivalent pier
e_{LL}	void ratio at liquid limit
EP	epicentral distance
E_{sav}	average soil Young's modulus along pile shaft
E_{sb}	soil Young's modulus of bearing stratum below pile tip
E_{sl}	soil Young's modulus at level of pile tip
esp	effective stress path
e_{100}^*	intrinsic void ratio at 100 kPa
G	equivalent linear shear modulus
G_{ave}	average shear modulus of soil along pile length
G_b	shear modulus of soil below the level of pile base
G_b'	soil modulus at a depth of $L_p+d^*d_{eq}$
G_c	soil cyclic stiffness
G_{cp}	pile cyclic stiffness
G_l	shear modulus at pile length depth

G_{max}	low strain shear modulus
G_s	soil secant stiffness
G_{sp}	pile secant stiffness
h	height above the pile tip; or soil stratum thickness
h/R	normalized height above pile tip
ICL	Intrinsic Compression Line
I_L	liquidity index
I_v	void index
I_{v0}	in situ void index
$[k_c]$	stiffness matrix of a structural subsystem
K_c	equalised earth pressure coefficient
K_i	installation earth pressure coefficient
K_0	in situ earth pressure coefficient
K_p	stiffness of a pile group
K_{pr}	overall stiffness of a piled raft foundation
K_r	stiffness of a foundation raft
LL	liquid limit
L_p	pile length
MC	Mexico City
$[M_c]$	mass matrix of a subsystem
m_v	coefficient of volume compressibility
NTC	Complementary Technical Norms to the construction code in Mexico City
OCR	Overconsolidation ratio
p_a	active earth pressure
P_c'	mean effective pressure
PI	plasticity index
p_{lim}	pressuremeter limit value
p_0'	mean consolidation pressure
P_p	load on piles in a piled raft fundation or mean preconsolidation pressure
p_p	passive earth pressure
P_r	load carried by a foundation raft in a piled raft foundtion
P_t	load at pile head
P_u	pile capacity obtained when pre-boring is carried out
P_{us}	pile capacity without preboring
Q	pile load
Q_a	mean cyclic pile load
q_b	pile end bearing resistance
Q_c	cyclic pile load

q_c	CPT end resistance
Q_{max}	maximum peak cyclic load
Q_s	pile shaft capacity
q_u	intact sample unconfined compression strength
Q_{ult}	ultimate pile capacity
q_{ur}	remoulded sample unconfined compression strength
q_v	soil strength from vane test
q_{vult}	soil ultimate strength from vane test
R or r_p	pile radius
R_a	Centre line average roughness parameter
r_b	radius of pile base
R_{eq}	equivalent pier radius
r_m	the maximum radius of influence of an individual pile
r_r	average radius of a foundation raft
SCL	Sedimentation Compression Line
S_t	clay sensitivity
S_u	soil undrained shear strength
S_{ur}	remoulded undrained shear strength
S_u^{CIC}	undrained shear strength in isotropically consolidated compression triaxial test
S_{uNC}	undrained shear strength from normally consolidated triaxial test
S_{uOC}	undrained shear strength from overconsolidated triaxial test
T	time factor
t	cyclic degradation parameter
u	pore pressure
u_c	response of a subsystem
u_f	motion at the surface of the free field
u_0	in situ pore pressure
u_s	acceleration or displacement time history
u_s^i, u_0^i	motions originated from the inertial interaction
u_s^k, u_0^k	motions originated from the kinematic interaction
u_s^t, u_0^t	total motion
UU	unconsolidated undrained
v_s	shear wave propagation velocity
w_{pr}	average settlement of a piled foundation raft
w_t	pile head settlement
YSR	yield stress ratio
α_{cp}	raft-pile interaction factor
δ'	soil-steel interface friction angle

δ_p	peak interface friction angle
δ_r	residual friction angle
δ_t	cyclic degradation index
δ_{ult}	ultimate interface friction angle
ε_1	axial strain
ε_v	volumetric strain
ϕ'	angle of shearing resistance
ϕ_R'	residual angle of shearing resistance
γ	shear strain
η	ratio of under-ream for underreamed piles
λ	pile-soil stiffness ratio
ν_{soil}	Poisson's ratio of soil
ρ	E_{sav} / E_{sl}; or G_{ave}/G_l; or soil density
σ_1	major principal stress
σ_3	minor principal stress
σ_r	radial total stresses
σ_r'	radial effective stress
σ_{rc}'	equalised radial effective stress
σ_{rf}'	radial effective stress at failure
σ_{ri}	installation radial total stresses
σ_{v0}'	free field vertical effective stress
σ'_{vy}	effective yield stress
τ	shear stress
τ_{rzf}	local shear stress at failure
τ_{rzi}	local shear stress during installation
ξ	E_{sl} / E_{sb}; or G_l/G_b
ζ	measure of radius of influence of pile; or damping ratio
ζ_c	damping ratio of a subsystem

CHAPTER 1

INTRODUCTION

1.1 Piles under dynamic cyclic loads

Piles are used in foundation engineering to transfer structural loads to deeper, more competent soil strata. Pre-cast concrete friction piles attached to foundation boxes are a common foundation solution for buildings taller than 5 storeys in Mexico City (MC).

Piles can be subjected to static and cyclic loads. Although the potential negative and positive effects of cyclic loading on pile capacity have been a concern since the 1970's, the current design procedures hardly take cyclic effects into account. The reasons for the lack of a general approach for the cyclic design of piles are: (i) the small number of documented pile failures during cyclic loading; and (ii) the lack of research into the pile cyclic response. This emphasizes the need for the following issues to be addressed: (i) the basic mechanics of the response of piles to cyclic loading; and (ii) the need for a rational method for the design of piles subjected to cyclic loading.

Two main hypotheses have been proposed to explain the assumed good performance of piles under cyclic loading: (i) the positive rate effects associated with rapid cyclic loading out-weigh the cyclic damage and result in a pile capacity during earthquakes that could be higher than the static pile capacity; and (ii) the pile foundations are statically over-designed.

1.2 Previous investigations

Imperial College (IC) has developed a research focus on better understanding the static behaviour of piles. The research carried out by Jardine (1985), Bond (1989), Lehane (1992) and Chow (1997), enabled Jardine and Chow (1996) to propose a design method for closed and open-ended piles driven in sand and clay. Based on effective stress principles, the design method is termed the IC Pile Design Method (ICPDM).

The axial cyclic behaviour of displacement piles has been subjected to diverse studies. Natural scale field tests include: Bogard and Matlock (1998); Jaime, et al. (1990);

Karlsrud and Haugen (1985); and Puech and Jezequel (1980); among others. Laboratory experiments and small scale field tests include: Bouckovalas (1996); Grosch and Reese (1980); and Holmquist and Matlock (1976); among others. At IC Bond (1989), Lehane (1992) and Chow (1997) carried out limited cyclic tests using the instrumented IC Pile.

In MC, the analysis of piled foundation failures produced by the 19 September 1985 earthquake showed that there was no clear understanding of the response of compensated piled foundations to seismic loads (Auvinet and Mendoza, 1986). As a result, research into the seismic behaviour of piled foundation was undertaken that focussed on:

i) Dynamic properties of the MC clay (Romo, 1995; and Dobry and Vucetic, 1988)
ii) Soil structure interaction and seismic site response effects (Romo, 1995; and Seed, et al., 1988)
iii) Pile-raft load transfer mechanism under static and seismic conditions (Mendoza, et al., 1998 and 2000b)
iv) Response of friction piles to cyclic dynamic loading (Jaime, et al., 1988)

Most of this research has been completed. The current research necessities include:

i) Detailed documentation of case histories ranging from good to poor performance of piled foundations under earthquake loading
ii) Systematic evaluation of analysis procedures against a number of case histories or physical models
iii) Refinement of analysis/design procedures.

1.3 Outline of the research

The aim of this Thesis is to develop a simple approach to include cyclic pile behaviour in the cyclic design of piles. The focus is on improving the present understanding of the dynamic pile capacity, especially its relation to their static capacity. The research deals with documented case histories ranging from good to poor performance under earthquake loading in MC, which was chosen since an important number of friction pile foundations failed during the September 19, 1985 earthquake.

The research is based in the determination of dynamic seismic axial loads on piles

acting on 3 case history instrumented buildings on friction piles (JAL, PC and PCC buildings). The building seismic loads are predicted using a non-linear dynamic structural programme (ADAPTIC; Izzuddin and Elnashai, 1989) in which earthquake accelerations recorded at basement level on the instrumented buildings are fed in as prescribed motions at the model supports.

The dynamic axial pile loads determined from the structural analyses are compared to the static pile capacity obtained from the application of the ICPDM. The design method was validated for MC clays using a database of static pile load tests from different locations around the clayey zone in the city. Quantitative assessment shows that the ICPDM is free from significant bias and more reliable than the existing design method recommended by MC design code.

The comparison of the computed seismic axial pile loads against the static capacity predicted by the ICPDM, and the occurrence (or not) of excessive building settlements during the earthquake under study, are used to evaluate the relationship between static and dynamic pile capacities.

The results from the building case histories, and cyclic pile tests available in the literature, enabled the development of an Interaction Diagram (ID) for MC. The ID facilitates the study of piles subjected to cyclic loading, including the effects of number of cycles, rate of loading, mean and cyclic loads, and load direction. The ID is proposed as a tool to include seismic loading conditions to the design of friction piles.

In order to assist in this study, the research incorporated the characterization of MC diatomaceous silty clay, including:

i) A critical review of its static and dynamic properties.
ii) The determination of MC clay's intrinsic properties as defined by Burland (1990).
iii) A Ring Shear laboratory study using different interface materials, rates of shearing, and consolidation states.

The following topics, related to the comparison between the static capacity and the seismic pile loads on the case histories, were also included:

i) Study of the dependency of the base reactions on the structural configuration and structural modelling technique
ii) Analysis of the soil-structure-interaction effects on the response of buildings and in

the proposed analysis procedure

iii) Descriptions of both the models and the actual structures' seismic behaviours.

iv) Analysis of the pile-raft load sharing, the foundation lateral seismic stability, kinematic forces on piles, and pile group effects

v) Variations in pile capacity with loading rate, load direction and number of cycles.

1.4 Content of the thesis

Chapter 2 presents a literature review of the axial behaviour of displacement piles on clay. The static behaviour is described from the IC research standpoint. The pile response during cyclic loading is reviewed by examining the pore pressure, radial stress, and the shear stress responses during field and laboratory cyclic pile tests. The pile cyclic capacity and load-displacement responses to load cycles, loading rate effect, and test sequence are also presented. The chapter includes the description of the ICPDM, the pile design method applied in MC, and the current state of the practice for the design of displacement piles under dynamic cyclic loads.

Chapter 3 describes the subsoil conditions in MC, comprising the static and dynamic properties. A study of MC clay intrinsic properties is included.

Chapter 4 presents the characterisation of MC clay response during ring shear testing based upon the framework developed by Lupini, et al. (1981). The responses to the following varibles were studied: (i) Bromhead and Bishop ring shear apparatus; (ii) interface materials; (iii) normal effective stress and overconsolidation ratios; and (iv) rate of displacement.

Chapter 5 presents the results of the validation of the ICPDM for MC conditions.

Chapter 6 sets out the principles applied to determine the vertical base reactions in the case history buildings, including: (i) the methodology of analysis; (ii) the structural programme's characteristics; (iii) the structural modelling technique; and (iv) the procedure to upgrade records to 1985 Michoacan earthquake's characteristics.

Chapters 7, 8 and 9 study the vertical base reactions developed during seismic shaking on the JAL, PC and PCC buildings, respectively. The chapters have similar configuration, which includes: (i) description of the structure and foundation layout; (ii) description of the instrumentation and input motions; (iii) evaluation of the seismic

response of the building; (iv) development of the structural models; and (v) description of the base reactions for the calibration and amplified input motions.

Chapter 10 studies the phenomena related to the comparison between static pile capacity and seismic pile forces. Five main issues are discussed: (i) pile-raft load distribution in MC; (ii) efficiency of the pile groups; (iii) foundation seismic lateral stability; (iv) kinematic forces on piles; and (v) distribution of the axial seismic base reactions to obtain forces on single piles.

Chapter 11 presents comparisons between static pile capacities and seismic pile loads to allow the dynamic axial capacity of the piles to be assessed. It includes the ID developed for MC, and the analysis of the results according to the state of knowledge, discussing the practical implications for the seismic design of piles.

Chapter 12 presents the conclusions from the Thesis and makes recommendations for future research.

CHAPTER 2

AXIAL BEHAVIOUR OF DISPLACEMENT PILES IN CLAY

Piles can be subjected to both static and cyclic loads. Static loads are related to gravity forces. Transient and cyclic loads capable of repeatedly subjecting foundations to compression and uplift forces can be induced by wind, earthquakes, waves, moving objects, construction activities, etc.

Relatively few well-documented pile failures have been reported due to cyclic loading in offshore engineering. Pile damage during earthquakes occurred in Japan (Sugimura, et al., 1997), Mexico City in 1985 (Mendoza and Auvinet, 1988), and Los Angeles in 1989 (Earthquake Spectra, 1990). The common opinion appears to be that the dynamic capacity of piles often exceeds the static capacity predicted from standard design criteria. The main uncertainty is about how slow and fast cyclic loading actually influences the capacity of piles.

This chapter presents a review of the available published literature on the behaviour of axially loaded driven piles on clay. The pile response to static load is illustrated using the research carried out during the last few years by Imperial College (IC). Additionally, the Imperial College Pile Design Method (ICPDM), and the traditional design approach used in Mexico City (MC) for the static design of friction piles on clay, are introduced.

The study of pile response to cyclic axial loading[1] is based on a literature review of full-scale field tests. In addition to the load-displacement response, it is also vital to know how the local shear stresses, pore pressures, and normal stresses develop during cycling. Cyclic load tests on instrumented model piles were included in the review as cyclic load tests on instrumented full-scale piles are rare. The analysis starts with the study of the pore pressure, radial stress and shear stress responses during cyclic pile loading. Then, the effects of such responses on pile capacity and stiffness are discussed. Finally, a summary is presented of the current state of practice and code specification for designing piles under axial cyclic loading.

Several shortcomings exists when attempting to draw conclusions concerning pile

---

[1] Large magnitude low frequency load cycles. Brief comments on the response of piles to lateral seismic loading in MC are presented in Chapter 10.

behaviour by reviewing information from a broad database, among them: (i) differences between field cyclic tests and the actual cyclic loading that develops on working piles - especially during a seismic event when the in situ stress state is more complex than that induced during cyclic field pile tests; and (ii) limitations due to the miscellaneous and varied procedures in which the pile tests entered in the database were carried out. Notwithstanding these shortcomings, field pile tests are essential to understand how piles respond under cyclic loading.

2.1 Definitions

Fig. 2.1 illustrates the basic parameters used to describe the typical response of a pile or soil element to cyclic loading. The vertical axis (Y) may represent the shear stress (τ), skin friction, or load in a pile test (Q). The horizontal axis (X) may be the local near shaft shear strain (γ) or pile vertical displacement (d). The cyclic load amplitude (Q_c) is:

$$Q_c = \frac{Y_{\max(0)} - Y_{\min(0)}}{2} \tag{2.1}$$

and the mean load (Q_a) is:

$$Q_a = \frac{Y_{\max(0)} + Y_{\min(0)}}{2} \tag{2.2}$$

Where Y_{max} and Y_{min} are the maximum and minimum load during a specific cycle, respectively. Y_{ult} is the current ultimate capacity that would be available under static loading conditions (Q_{ult}). (If these expressions are evaluated for the horizontal axis, they represent the cyclic displacement (d_c) and the average permanent displacement (d_a), respectively.)

For soil elements the secant stiffness (G_S) and the cyclic stiffness (G_C) are defined as follows[2]:

$$G_{S(N)} = \frac{Y_{\max(N)}}{X_{\max(N)}} \tag{2.3}$$

$$G_{C(N)} = \frac{Y_{\max(N)} - Y_{\min(N)}}{X_{\max(N)} - X_{\min(N)}} \tag{2.4}$$

One-way cycling consists of imposing cyclic loading without shear stress or load

---

[2] The secant and cyclic stiffnesses obtained from the load-displacement record at pile head are termed G_{sp} and G_{cp}, respectively.

reversals. Two-way cycling involves subjecting the soil to positive and negative shear stresses or loads. Cyclic loading is defined as repetitive loading at a frequency that is sufficiently low for no significant inertia forces or radiation damping to arise.

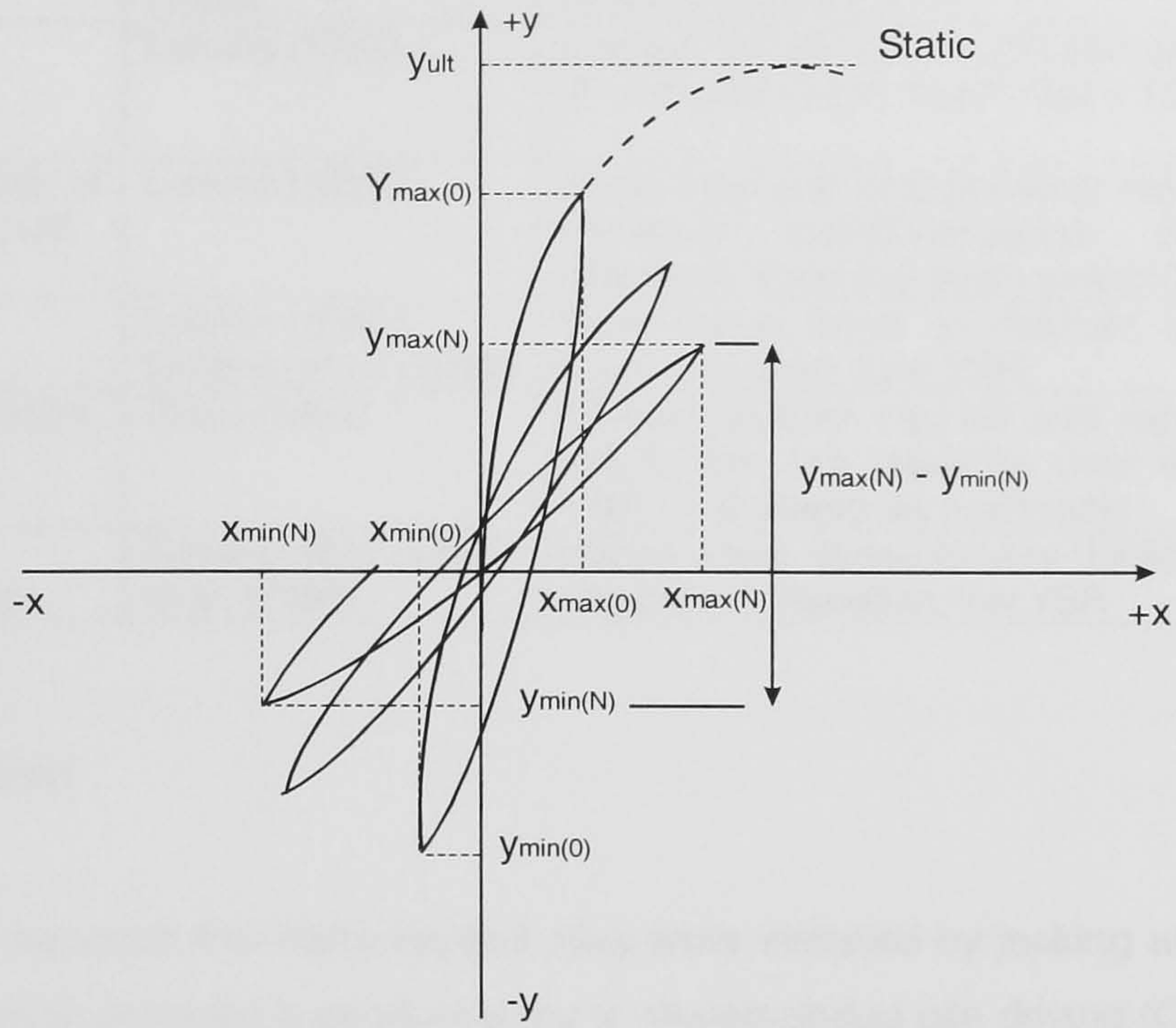


Fig. 2.1 Definition of cyclic parameters (after Briaud and Felio, 1986)

2.2 Static pile behaviour (Imperial College research)

A central feature of the recent research carried out at IC into the static behaviour of displacement piles has been the measurement of the pore pressures, radial total stresses, and local shear stresses developed along the pile shaft. Specially developed gauges were mounted on 6 m to 20 m long, 102 mm diameter, closed ended, steel pipe piles (termed the ICP) and used in test programmes involving a wide range of soil conditions at the six sites identified in Table 2.1 (Jardine, et al., 1998). These measurements allowed a comprehensive study of the effective stresses developed close to the pile shafts at several levels down the length of the pile during installation, long-term equalisation, and load testing to failure. The following sections describe the trends observed for clays, largely presenting a précis of a paper by Jardine, et al. (1998).

Table 2.1 Summary of Imperial College pile research sites (Jardine, et al., 1998)

Site	*Primary reference*	*Soil*
Canons Park, London, England, UK.	Bond (1989), Bond and Jardine (1991), (1995)	London clay: stiff to very stiff, high plasticity Eocene marine clay. Over test depth mean yield stress ratio (YSR) = 33
Cowden, Humberside, England, UK.	Lehane (1992)	Cowden till: stiff to very stiff lean glacial lodgement till. Over test depth mean YSR = 18
Bothkennar, Firth of Forth, Scotland, UK	Lehane (1992)	Carse clay: soft, high plasticity, moderately organic Holocene marine-estuarine clay-silt, lightly cemented. Over test depth mean YSR = 1.8
Labenne, SW France	Lehane (1992), Lehane, et al. (1993)	Dune sand: loose to medium dense, medium sized, Flandrian. Low YSR
Pentre, Shropshire, England, UK.	Chow (1997)	Glacio-lacustrine clay-silt and varved clays: very soft to firm, low plasticity. Over test depth mean YSR = 1.6. Relatively permeable
Dunkirk, Northern France	Chow (1997), Chow, et al. (1996)	Marine sand: dense to very dense shelly medium sized sand, Flandrian; low YSR

2.2.1 Installation

During the IC research the instrumented piles were installed by jacking at a typical rate of 10 mm/s, which provided a good analogy to closed-ended pile driving (Chow, 1997).

2.3.1.1 Shear and radial total stresses

At all the clay sites, the installation radial total stresses (σ_{ri}) and the local shear stresses (τ_{rzi}) showed two trends:

i) The traces with depth of σ_{ri} and τ_{rzi} measurements were soil consistency dependent; they varied in relation to the profiles of CPT end resistance (q_c), or triaxial undrained shear strength (S_{u0}), or pressuremeter limit values (p_{lim}).
ii) The σ_{ri} and τ_{rzi} values mobilised at any particular soil horizon reduced systematically with increasing pile penetration. The total stresses fell systematically as the relative depth of the pile tip increased below the given level.

These two trends are summarised in Fig. 2.2. The figure shows the total radial stresses normalised by the pile end bearing resistance (q_b) during installation (which is close to the CPT tip resistance q_c) plotted against the normalised height above pile tip (h/R), where h is the height above the pile tip and R is the pile radius. At all sites the ratio σ_{ri}/q_b decayed with the h/R ratio.

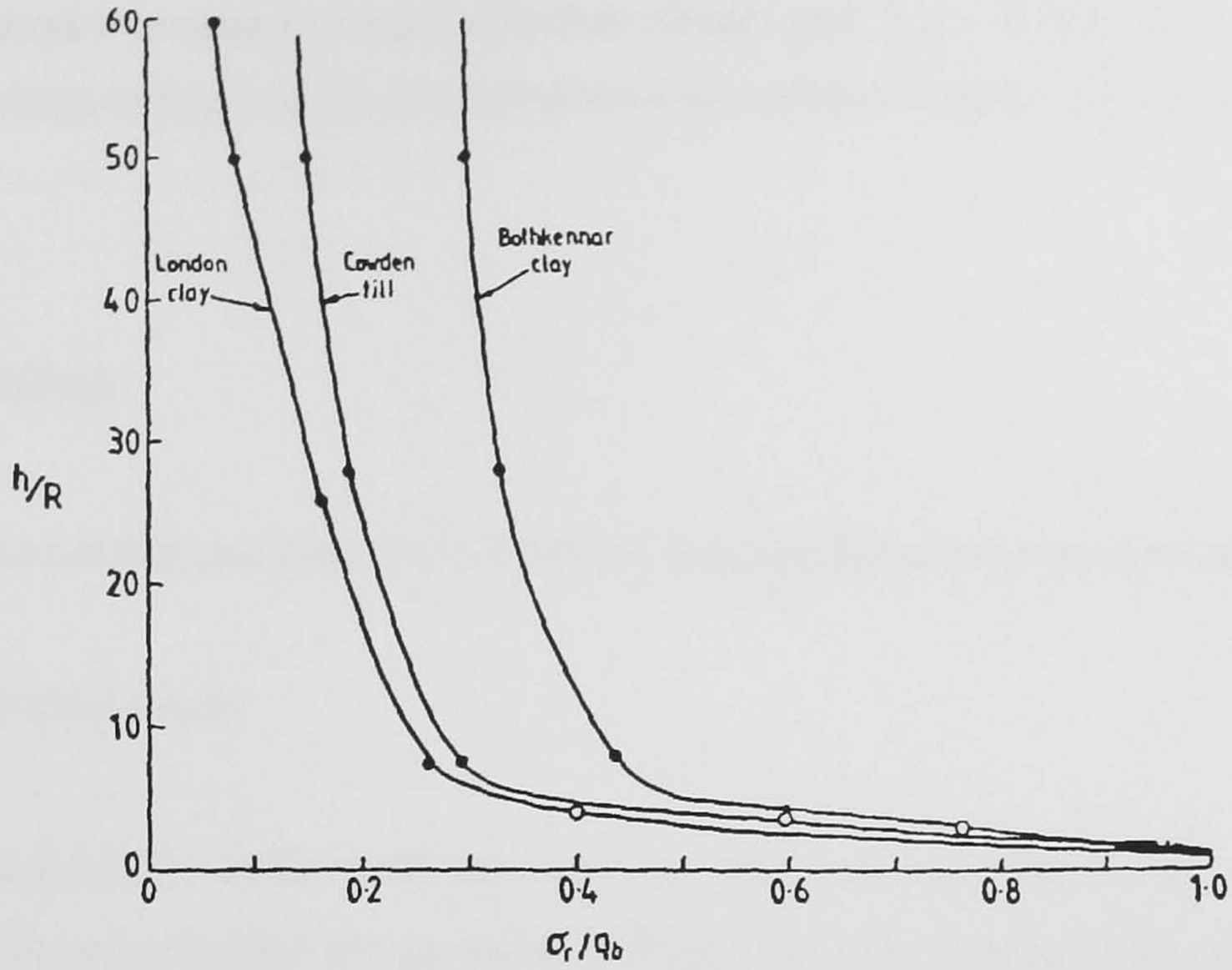


Fig. 2.2 Mean variations in normalised radial total stress with normalised height (Lehane, 1992)

2.2.1.2 Pore pressure

Pore pressure changes during installation resulted from the sum of three components: (i) the increments due to pile penetration (component associated with mean total stress changes); (ii) the shear induced changes in pore pressure (negative for dilatant soils and positive for contractant soils); and (iii) the accumulation of pore pressure due to successive load-unload shearing cycles during installation (Lehane, 1992).

The characteristic responses at each site were related to the yield stress ratio (YSR) of the clays. Positive pressures were recorded at all stages in the Bothkennar clay (mean YSR = 1.8), but negative values were measured close to the pile tip during penetration at Cowden (mean YSR = 18), and along the entire shaft in the high YSR London Clay. Overall, the pore pressure changes showed a comparable dependence on soil consistency and h/R to the σ_{ri} data (Jardine, et al., 1998).

2.2.1.3 Radial effective stress

The radial effective stresses mobilised on the principal displacement shear surface during fast installation also varied with soil type. At Bothkennar, the installation earth pressure coefficient K_i [= ($\sigma_{ri}'/\sigma_{v0}'$)] was always less than the initial free field K_0. Pile installation invoked a highly contractant response in this sensitive, low YSR, clay. In contrast, the stiff and insensitive high YSR Cowden till appeared to dilate strongly,

exhibiting a large increase in mean effective stress and $1.3 < K_i/K_0 < 8$. Even stronger dilation took place in the heavily overconsolidated London Clay at Canons Park (Jardine, et al., 1998).

2.2.2 Equalisation

Monitoring was carried out over the full period required for pore pressure equalisation.

2.2.2.1 Radial total stress

During equalisation the radial total stresses (σ_r) reduced at all three clay sites, with the largest proportional reduction occurring at Bothkennar. The typical relaxations of σ_r after installation are illustrated in Fig. 2.3, where the non-dimensional ratio $H/H_i = (\sigma_r - u_0)/(\sigma_{ri} - u_0)$ is plotted against time (u_0 is the in situ pore pressure). The greatest relative reductions in σ_r take place in the low YSR, sensitive Bothkennar clay. Lehane (1992) showed that the final, fully equalised value of H/H_i decreases systematically with increasing clay sensitivity (S_t) and reducing YSR, and pointed out that this is due to the plastic yielding zone around the pile shaft, which interacts with the surrounding zone of higher stiffness material.

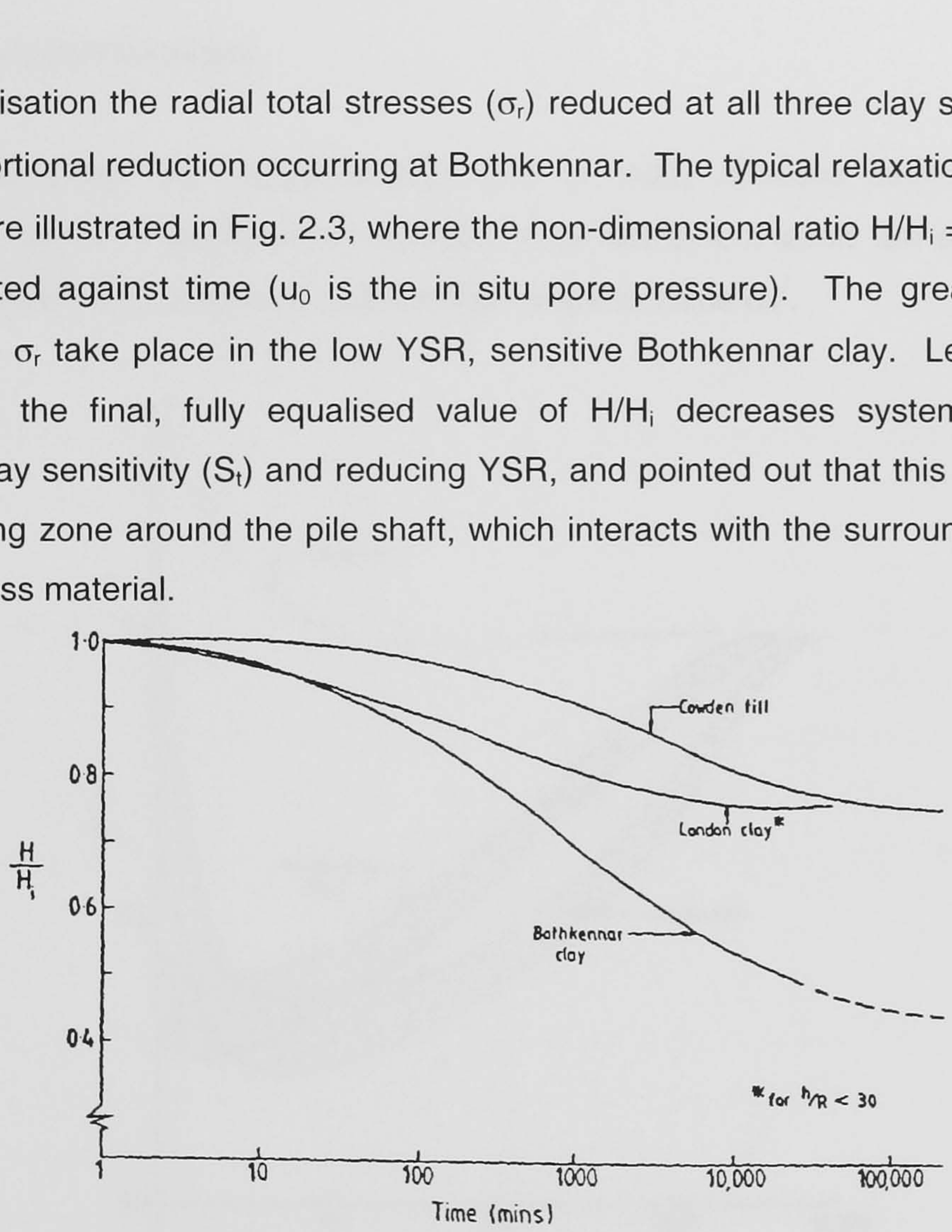


Fig. 2.3 Changes in radial total stress during equalisation (Chow, 1997)

2.2.2.2 Pore pressure

Pore pressures tended to rise immediately after installation for the test piles at Cowden and Bothkennar, giving pronounced short-term maxima before decaying towards hydrostatic values. Similar features were also seen in the deepest layers at Canons Park (Jardine, et al., 1998).

Pore pressure decay rates were invariably faster near to the pile tips, where pore water could flow vertically as well as radially. Simplified consolidation analyses (Lehane, 1992) showed that the equalisation process for closed-ended piles was, for practical purposes, complete when the time factor T reached 100. $T = c_{rh}\, t/R^2$, where: R is the pile radius, t is the elapsed time, and c_{rh} the linear coefficient of consolidation that applies to radial drainage. The c_{rh} values that best fitted the field measurements were relatively high matching the ranges seen in swelling and re-compression laboratory tests (Jardine, et al., 1998).

2.2.2.3 Radial effective stress

Fig. 2.4 summarises the variations with time of radial effective stress (σ_r') during equalisation; the σ_r' measurements recorded at all instrument levels are shown divided by their respective fully equalised radial effective stress value σ_{rc}'.

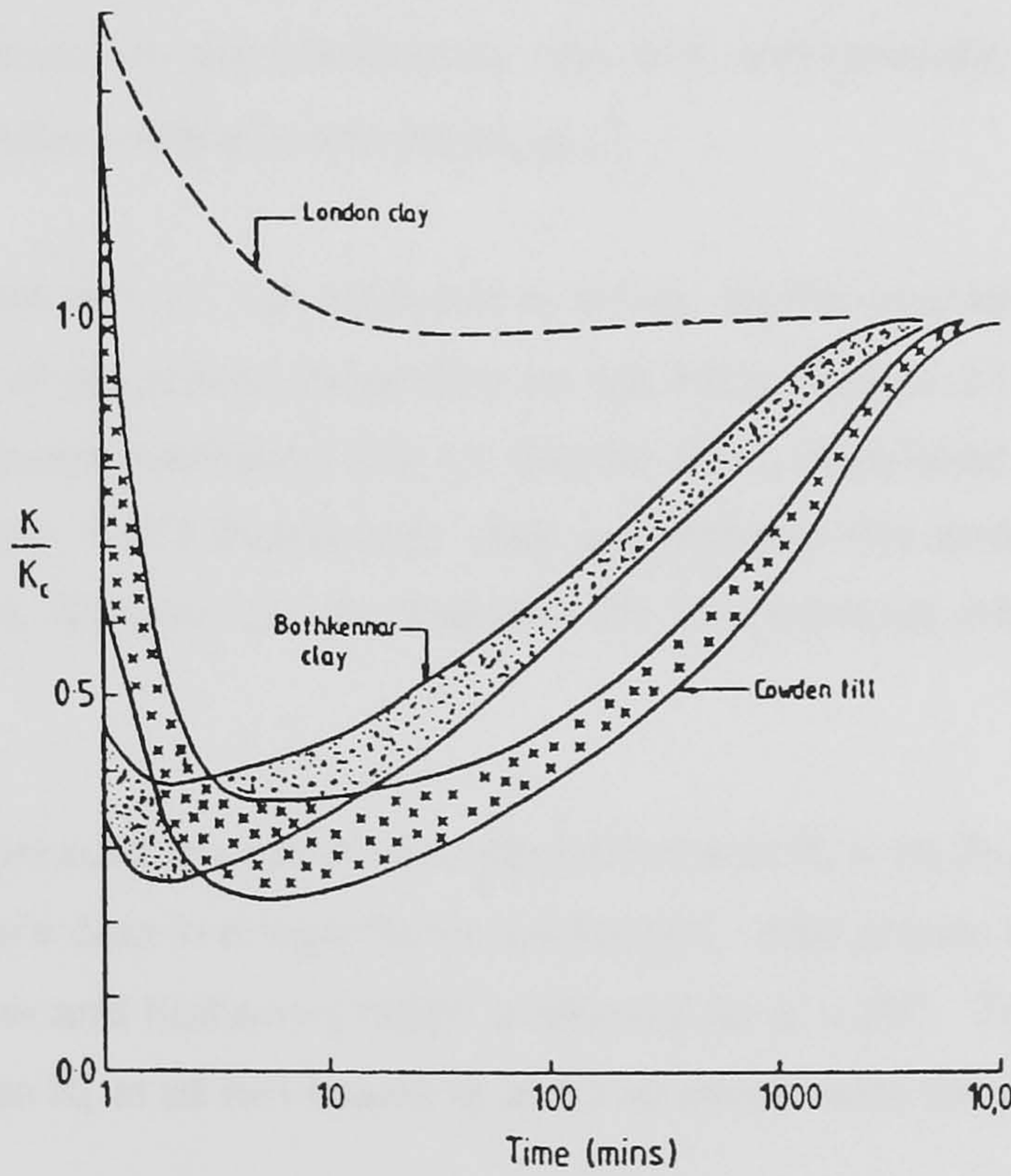


Fig. 2.4 Variations of normalised σ_r' with time (Chow, 1997)

The data fell into well-defined envelopes, from which the IC research group identified the following trends:

i) The overall degree of set-up, $\sigma_{rc}'/\sigma_{ri}'$, decreases with increasing YSR. Large increases in σ_r' were seen during equalisation at Bothkennar; the overall changes

were practically neutral at Cowden; and a significant net reduction in σ_r' took place in the London Clay at Canons Park.

ii) At Cowden, a pronounced short-term minimum was seen followed by a large long-term increase in σ_r'. Faint indications of the same phenomenon were apparent at Canons Park and Bothkennar. Short-term static pile load tests at Cowden confirmed that the reductions in σ_r' corresponded to lower shaft capacities.

The variations of σ_r' with time were negligible at time factors (T) greater than 100; at all three sites the σ_r' traces were within 30% of their final values at T=10.

2.2.2.4 Radial effective stresses after full equalisation

Final equalised radial stresses (σ_{rc}') at Bothkennar were about three times higher than those immediately after installation indicating a large positive overall set-up. At Cowden and Canons Park the changes were smaller and variable with some instruments indicating set-up and others relaxation (Chow, 1997). σ_{rc}' profiles showed similar trends to σ_{ri} with dependence on soil consistency and h/R, and generally increasing with the depth and the effective vertical in situ stress (σ_{v0}').

It was also apparent that σ_{rc}', as measured at similar depths against identical piles, may differ by an order of magnitude depending on the initial ground conditions. The oldest and most heavily overconsolidated clay (at Canons Park) developed the largest stresses and the young (low YSR) Bothkennar clay experienced the smallest. The stiff, but geologically recent, Cowden till falls between the two previous cases (Jardine, et al., 1998).

Lehane (1992) expressed the trends as a dependence of $K_c = (\sigma_{rc}'/\sigma_{v0}')$ on YSR. Fig. 2.5 displays all Lehane's data in a logarithmic scatter plot. Also shown is the K_0 relationship proposed by Mayne and Kulhawy (1982)[3] evaluated for $\phi' = 25^o$. The graph shows that K_c was greater than K_0 at all h/R values in all three cases, with the difference increasing with YSR.

Piles installed to different depths at Cowden and Bothkennar (and Labenne) provided direct proof that K_c reduces as h/R increases, and that the most pronounced changes occur close to the pile tip, where h/R < 20. Fig. 2.6 shows Cowden and Bothkennar cases. A close inspection of the data allowed Lehane (1992) to identify a correlation

[3] $K_0 = (1-\sin\phi')\ YSR^{\sin\phi'}$

between K_c and h/R for any given YSR range.

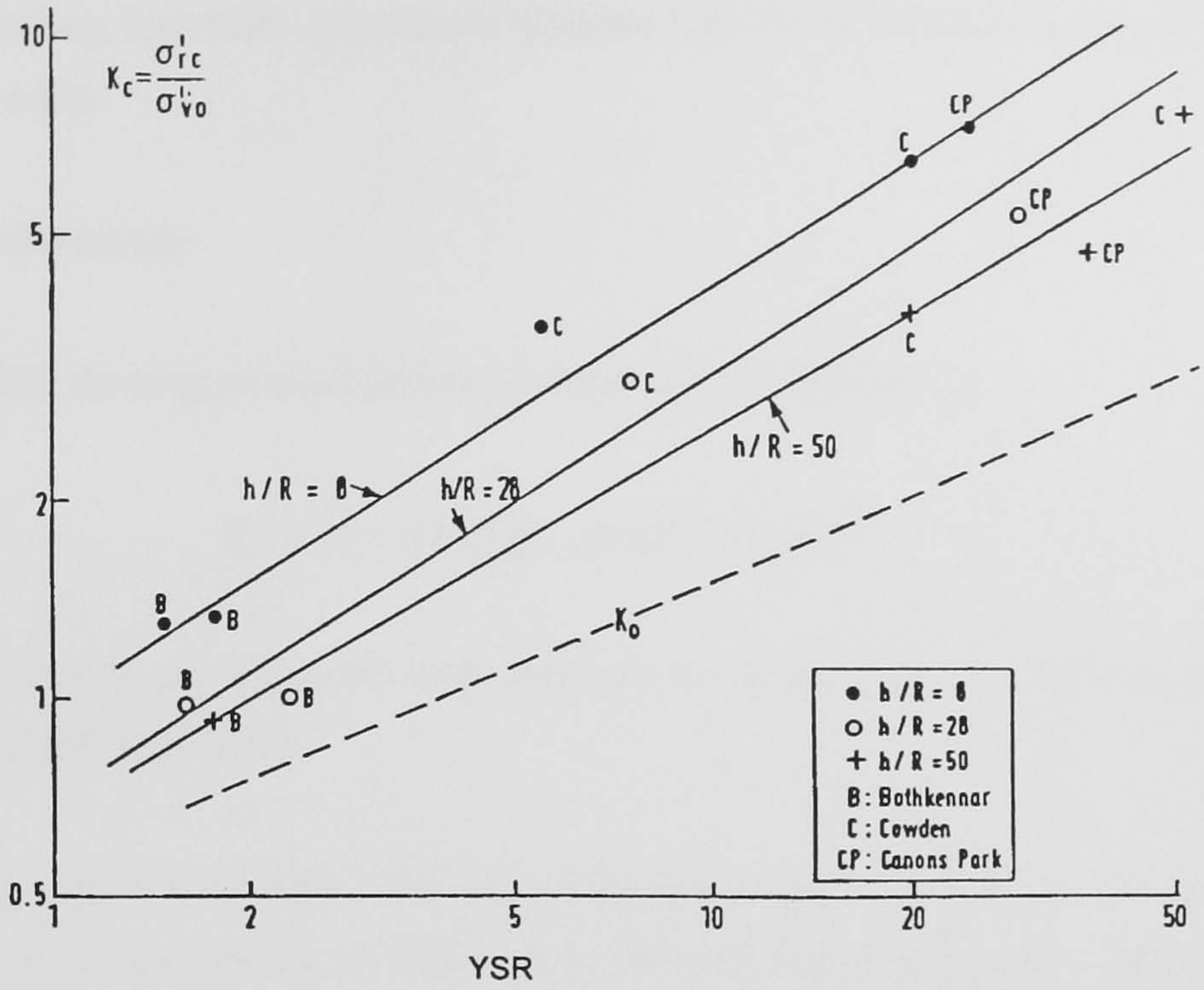


Fig. 2.5 Trends for K_c with YSR and h/R in clays (Lehane, 1992)

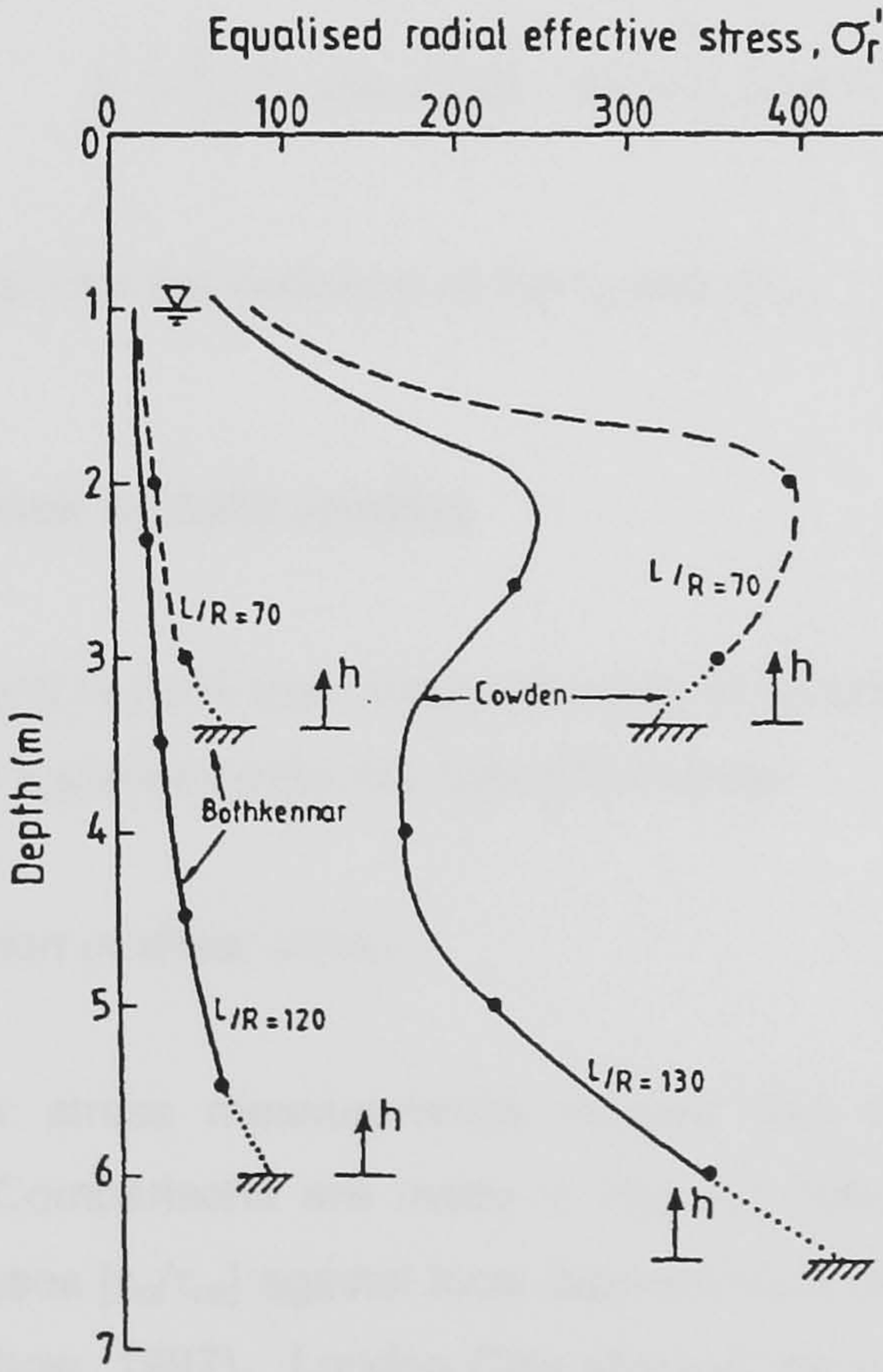


Fig. 2.6 Influence of h/R on σ_{rc}' (Chow, 1997).

No variations in $\sigma_{rc}'/(\sigma_{ri}-u_0)$ ratio were observed along the length of the IC instrumented pile tests though very different values were measured at different sites with similar YSR

values. Lehane (1992) identified sensitivity as a significant factor affecting the soil response and the reason for the above differences in measurements. The K_c values seen in sensitive, low YSR clays were typically half those developed in comparable, but insensitive, soils.

2.2.2.5 Overall trends

Lehane (1992) developed the following overall relationship for K_c:

$$K_c = [2 - 0.625\Delta I_{v0}]YSR^{0.42}(h/R)^{-0.2} \quad (2.5)$$

Lehane found that the equation was accurate to within 20% for 85% of the available instrumented pile test data.

Chow (1997) did not consider the sensitivity parameter I_{v0} used by Lehane as ideal, since it combined the effects of YSR and S_t and was highly dependent on stress history. Chow developed a new S_t parameter independent of YSR (termed ΔI_{vy}) and re-evaluated (2.5) obtaining:

$$K_c = [2.2 + 0.016YSR - 0.87\Delta I_{vy}]YSR^{0.42}(h/R)^{-0.20} \quad (2.6)$$

See section 3.4.5.3 for the definition of the I_{v0} and ΔI_{vy}.

2.2.3 Pile response to static loading

The insights offered by the local measurements of τ_{rz} and σ_r' during first-time load tests to failure on fully equalised piles are described below.

2.3.3.1 Mobilisation of shear stress

The local shear stress measurements showed that all of the IC pile tests failed progressively. Comparisons are made in Fig. 2.7 between the curves of normalised local shear stresses [τ_{rz}/τ_{rzf}] against local displacement (d) for fast-jacked piles tested in compression (Chow, 1997). London Clay showed the stiffest pre-failure response and the largest post-peak reductions in local shaft capacity – this behaviour has important implications for long compressible piles that show progressive failure. Only minor post-peak reductions were seen in the tests performed at Cowden and Bothkennar, the latter

showed the softest and most non-linear response.

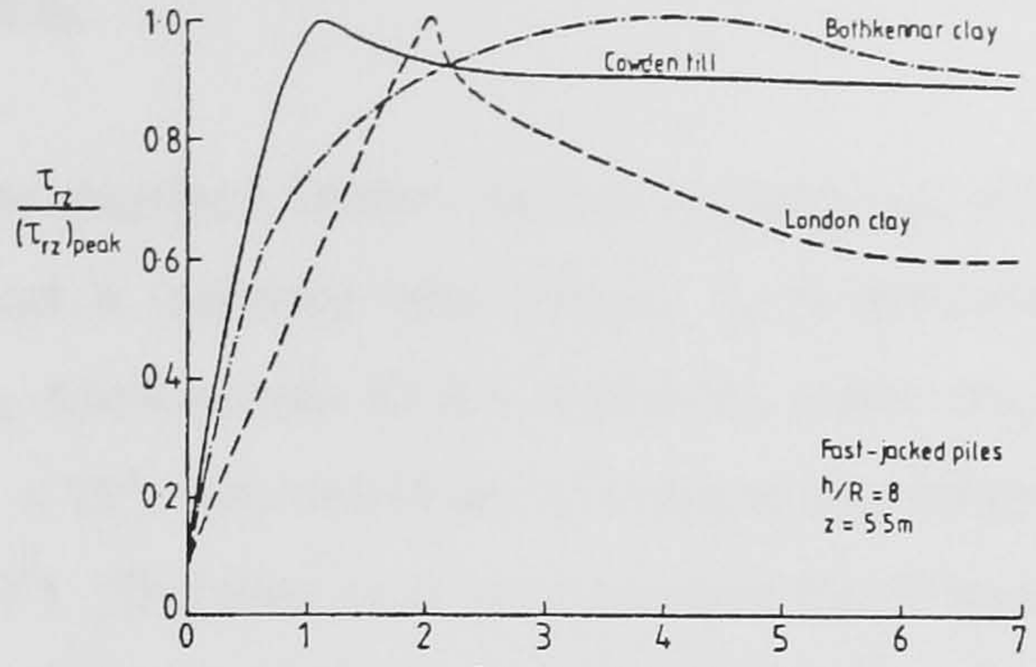


Fig. 2.7 Variations in local shear stresses with local pile displacements; compression tests on fast-jacked piles (Chow, 1997)

At Cowden and Bothkennar the pile response was softer in tension than in compression tests, probably due to the anisotropic soil fabric created during pile installation. No such difference was observed in the London clay (Chow, 1997).

2.2.3.2 Effective stress paths and shaft failure criteria

Fig. 2.8 summarises the normalised effective stress paths for a soil element adjacent to the pile wall during first-time compression and tension tests on fully equalised fast-jacked piles in Cowden till, Bothkennar clay, and London clay. The paths have been plotted using the local measurements of τ_{rz} and σ_r' normalised by σ_{rc}'.

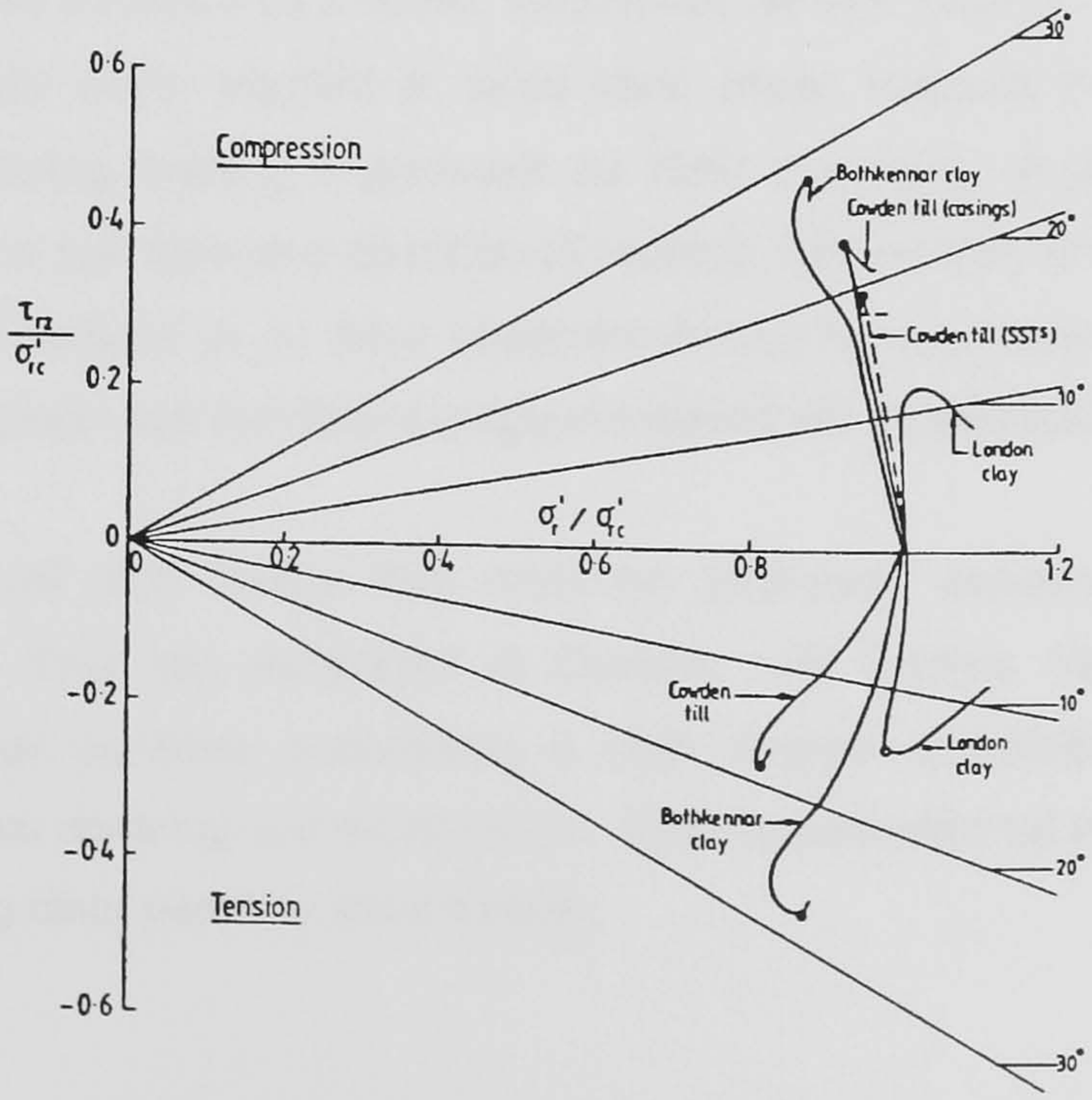


Fig. 2.8 Effective stress paths for first time loading tests on fully equalised piles (Lehane, 1992).

According to Lehane (1992) these stress paths show that the Coulomb law governs local failure, i.e. $\tau_{rzf} = \sigma_{rf}' \tan \delta_f$.

The peak and ultimate interface friction angles (δ_p and δ_{ult}) which apply to local shaft failure in the field cover a relatively wide range; δ_p is associated with the peak local value of τ_{rzf}, while δ_{ult} corresponds to the minimum value observed post peak. The lowest peak angle, $\delta_p = 12^o$, was mobilised in London clay whilst the highest, was seen in Bothkennar clay (29°). The field tests also showed that δ typically reduces from δ_p to δ_{ult} after 5 mm or less local pile-soil slip displacement; δ_{ult} varied from 8° to 28°. The operational values developed locally when the pile reaches overall failure vary between δ_p and δ_{ult}, depending on the degree of progressive failure (Chow, 1997).

The δ values measured during field pile tests showed good agreement with laboratory ring-shear interface tests – when the test procedure represents the normal effective stress level, interface roughness, shearing history, and shearing rate experienced in the field. Fast pre-shearing is usually applied for several metres to simulate pile installation, followed by consolidation and drained shearing (at less than 0.001 mm/s) to simulate slow load testing. Tests without fast shearing often produced lower δ_p.

2.2.3.3 Effective stress changes during loading

The radial effective stresses (σ_r') varied moderately during loading. At all three sites minimum σ_r' values were reached at peak local shear stresses (τ_{rzf}). The relative reduction in σ_r' during loading, expressed as K_f/K_c ($=\sigma_{rf}'/\sigma_{rc}'$), showed only a minor dependence on the soil type and direction of loading, being between 0.8 and 1.0 in all cases. Larger reductions in σ_r' were observed during tension loading, probably as a result of the anisotropic soil conditions produced during pile installation.

Any losses in local skin friction that occurred post-peak appeared to be due to reductions in δ. Trial pits excavated at Cowden and Canons Park confirmed the formation of shear surfaces possessing a high degree of particle alignment that produced a residual shearing soil micro-fabric. Slow-jacked piles fail in a ductile manner without developing clear peaks in shaft friction.

2.3 Imperial College design approach for static capacity of displacement piles in clays

The ICP field research determined how local σ_{rf}' and δ_f at pile shaft vary with a range of parameters. Best-fit equations were developed to predict σ_{rc}' for fully equalised closed-ended piles. The research lead to an explicit pile design method for tubular driven piles in sands and clays[4]. The main features of the design procedure are presented in the following sections.

2.3.1 Shaft capacity

The local radial effective stresses after equalisation (σ_{rc}') developed in clays were found to be controlled by:

i) The free field vertical effective stress σ_{v0}'.
ii) The initial state of the clay, as expressed by the local value of YSR.
iii) The h/R[5] ratio. In practice h/R is limited to a minimum of 8.
iv) The initial sensitivity of the clay, expressed in terms of either the conventional parameter or the parameter ΔI_{vy} (or ΔI_{v0}), which is obtained through oedometer tests.

The corresponding equations for local σ_{rc}' in clays are:

$$\sigma_{rc}' = k_c \sigma_{v0}'$$

$$\textit{where} \qquad k_c = \left[2 - 0.625\Delta I_{v0}\right] YSR^{0.42} \left(h / R^*\right)^{-0.20}$$

or

$$k_c = \left[2.2 + 0.016YSR - 0.87\Delta I_{vy}\right] YSR^{0.42} \left(h / R^*\right)^{-0.20} \qquad (2.7)$$

and

$$\Delta I_{vy} = \log S_t$$

ΔI_{v0} is defined in section 3.4.5.2.

The method also specifies the changes that should be expected in σ_r' as piles are loaded to failure. For clays:

---

[4] The design approach for sands is not presented here.

[5] For open ended piles R is substituted by R*, where: $R^* = (R^2_{outer} - R^2_{inner})^{1/2}$

$$\sigma'_{rf} = 0.8\sigma'_{rc} \tag{2.8}$$

Thus, the local shaft resistance τ_{rzf}, applying the Coulomb failure criterion, is:

$$\tau_{rzf} = \sigma'_{rf} \tan \delta_f \tag{2.9}$$

Where σ_{rf}' is the local σ_r' at failure and δ is the ultimate interface shear friction angle. The external shaft capacity, Q_s, is given by the integral over the pile's surface area of τ_{rzf}.

δ should be measured in interface ring shear tests, as described in section 2.2.3.2. Progressive failure operates where the pile compression reaches the post-peak displacement required to reach residual conditions.

It is now recognised that pile shaft capacities can grow with time due to secondary processes such as pre-failure or bacterial action (Pellew, 2002). The above equations predict the medium term fully equalised pile capacity.

2.3.2 Base capacity

The base capacity of closed-ended piles under short-term loading is often estimated as: $Q_b = q_b A_b = N_c S_u \pi R^2$, where N_c is usually taken as ≈ 9, and the procedure used to determine S_u is not standarised. The ICP tests showed a wide range of ultimate N_c values (from 10 to 22), and a high degree of correlation between q_b and q_c[6].

In the ICPDM, base resistance is computed by relying principally on the local CPT resistance. For closed-ended piles undergoing undrained loading, and where progressive failure is not being modelled explicitly (by a t-z or other numerical analyses), q_b may be taken as $0.8q_c$. When loading rates are slow, and the clay is relatively permeable, drainage permits higher capacities to be reached and the q_b for closed ended piles can rise to $\approx 1.3\ q_c$ (Chow, 1997).

---

[6] The relatively small settlement at shaft failure limits the base contribution to total pile capacity; for long piles in clay the base contribution may be negligible. Tip settlements of between 0.1 and 0.3 times the pile radius are tipically required to develop full base capacity.

2.3.3 Overall reliability

Chow (1997) tested the reliability of the ICPDM for clays against a database of 55 high quality tests on open and closed-ended piles, finding that the approach gave good predictions under a wide range of circumstances. The mean value of $Q_{calculated}/Q_{measured}$ was close to 1.0, and the standard deviation was 0.18. In comparison with the American Petroleum Institute RP2A approach (API, 1993), the IC method was marginally non-conservative but produced less scatter. According to Chow (1997), the new approach was more than twice as reliable as the API.

2.3.4 Traditional design procedure in Mexico City

The Complementary Technical Norms (NTC[7], 2001) developed to regulate pile design in Mexico City (MC) recommend using a variant of the total stress α method to design friction piles – although the use of effective stress based approaches is not discarded entirely. Several researchers advocate the use of the NTC approach, among them Mendoza, et al. (1996), Jaime, et al. (1991), and Resendiz (1964). However, Hjort and Carrillo (1985) have identified (on the basis of the Linea 4 tests presented in Chapter 5 of this thesis) that the α method (taking α=1) overpredicts pile capacity by 30% on average. Hjort and Carrillo (1985) and Zeevaert (1982) advocate the use of effective stress principle to compute pile capacity in MC.

The α method incorporates an empirical correlation between shaft resistance (τ_{rzf}) and the undrained shear strength (S_u) as measured in unconsolidated undrained (UU) triaxial compression tests. The MC code does not specify the type and procedure of sampling, or mention any corrections for sample disturbance or size effects. The empirical correlation is expressed as:

$$\tau_{rzf} = \alpha S_u \tag{2.10}$$

where α has been related directly to S_u as shown in Fig. 5.9. The design code in MC suggests α=1.

There exist further refinements[8] of the α method relating the α parameter to:

---

[7] NTC stand for Normas Tecnicas Complementarias in Spanish

[8] The Author is not aware of any specific study on the applicability of these factors to Mexico City conditions.

i) S_{u0}/σ_{v0}' ratio to allow for soil stress history or YSR (Semple and Rigden, 1984; Randolph and Murphy, 1985)
ii) Pile length (Kraft, et al., 1981)
iii) Progressive failure (Randolph and Murphy, 1985; Chow, 1997).

However, even these variants of the method fail to account explicitly for many of the factors influencing pile capacity, among these: clay sensitivity; the variation of K_c with h/R; pile material or pile end condition; and loading direction or loading rate.

The well-known dependence of S_u on the mode of shearing and sample quality can lead to a wide scatter in the α values. Jardine and Chow (1996) showed that the α based API procedure (essentially Randolph and Murphy's (1985) α variant) leads to a systematic skewing with respect to the length-radius (L/R) ratio and YSR that can lead to unsafe predictions for long offshore piles.

A further problem with the α methods is that the α correlations were derived using the results of average shaft frictions measured in load tests. In order to account for local variations in soil consistency the correlations are often applied incrementally to evaluate local shaft friction. This assumes that the average and local shear stresses are equivalent, whereas the ICP tests have demonstrated that the local shear stress depends on pile tip position and decays rapidly with h/R ratio.

2.4 Pile response mechanism during cyclic loading

A study of the pile response to cyclic loading needs to consider the stress and state changes produced by pile driving, equalisation and loading as reviewed in section 2.2 (Sangrey, 1977; Jardine, 1991). The response to static loading has already been described. The following sections deal with the response to cyclic loading.

The Coulomb law applied to pile design usually ignores the viscous[9] components present during pile installation and dynamic loading, therefore it only appl ies to static conditions (Bond, 1989). However, since in this thesis it is implicit that an effective stress law also governs the cyclic dynamic response of piles, this section focus es in identifying how dynamic cyclic effects modify the factors involved in Coulomb law.

---

[9] Viscous components are those that depend upon velocity.

Piles under cyclic loading may respond with reductions in total radial stresses, variations in pore pressures, or the development of residual fabric failure surfaces, all of which reduce pile capacity. The responses of the pore pressures, and radial and shear stresses during pile cyclic loading are examined in the following sections.

The main factors influencing the behaviour of piles subjected to repeated axial loads are: (i) magnitude of the repeated load (Q_c) as a percentage of the maximum static capacity (Q_{ult}); (ii) number of load cycles; (iii) loading direction (compression, uplift, or both); (iv) soils characteristics; (v) drainage conditions; and (vi) embedded depth (i.e. the role of the mean effective stress level). Particularly affected are: (i) the evolution of the pile top displacement; (ii) the load to failure; and (iii) the load transfer mechanism (Charlie, et al., 1985; Puech and Jezequel, 1980).

Briaud and Felio (1986) defined a maximum peak (Q_{max}) cyclic load called the "threshold" load. Below the threshold no significant decrease in the ultimate static capacity or stiffness is produced, and no unacceptable pile damage (failure) occurs with increasing number of cycles. Above the threshold, cycling can markedly decrease pile capacity and stiffness; large cumulative displacements may develop causing "failure" by plunging or pull-out of the pile. On average for one-way loading the value of this threshold is $Q_{max} = 0.7$ to $0.8\ Q_{ult}$. (During two-way loading the threshold could be $Q_{max} = 0.4\ Q_{ult}$.) Bogard and Matlock (1990b) defined a "strain" threshold, and Charlie, et al. (1985) reported that, in general, this is about 5% of the pile diameter.

The load-displacement response of piles to load cycles shows two mechanisms, these are cyclic shakedown and incremental collapse. During cyclic shakedown the permanent displacements evolve according to a linear logarithmic relationship with respect to number of cycles and tended to stabilise during the later stages of a test. Incremental collapse starts with cyclic stiffness and cyclic displacement remaining practically constant, while permanent displacement accumulates at a steadily decreasing rate. The onset of collapse is identified with a gradual deterioration in the cyclic stiffness followed by a gradual increase in the rate of permanent displacement accumulation.

The Author's database for piles under cyclic loading is presented chronologically in Table 2.2 – the table is used as reference when the tests are described later in the section. The database includes a wide range of soil and test conditions.

Table 2.2 Summary of research study pile response to cyclic loading

Reference	*Soil*
Holmquist and Matlock (1976)	Laboratory model pile segment driven into soft saturated contractive clay.
Grosch and Reese (1980)	Field experiment with a 254 mm long 25.4 mm diameter small-scale pile segments jacked into clay and tested under repeated displacement controlled axial loading. The tests were carried out in soft inorganic, highly plastic clay with thin sand lenses and pockets. No loading period is given.
Puech and Jezequel (1980)	The pile was composed of 7 273 mm OD 6.3 mm wall thickness steel pipe elements. The embedment length was 13 metres in recent marine deposits including compressible silts, loose sands and silty clays.
Kraft, et al. (1981a)	Repeated field compression and uplift loading tests (period of 15 s) on four instrumented pipe pile segments. The pile segments were 356 mm in diameter, approximately 15.25 m long, and were driven to various depths into underconsolidated clay at Empire, Louisiana, USA. Stiff to very stiff, gray, highly plastic clay containing seems of sand, silty sand and sandy silt.
McAnoy, et al. (1982)	A 193 mm diameter, 9.90 m long pile was tested in Boulder clay (glacial till) at Cowden, England. The ground consisted of a thick deposit of uniform overconsolidated, sandy silty clay till, with interposed layers of sand and gravel. The tests were carried out on single piles previously part of a pile group that had been tested in tension for 26330 cycles of low intensity (the higher amplitude was 50% for 11200 cycles). No clear indication of load period is given but is considered to be 10 s.
Karlsrud and Haugen (1985)	16 cyclic pile load tests mainly in tension in Haga sensitive overconsolidated clay (near Oslo, Norway). The instrumented pile (153 mm in diameter and 5.0 m long) was monitored during jacking and subsequent reconsolidation and static and cyclic loading. Load period of 6 s.
Doyle and Pelletier (1985)	Cyclic test in 30-inch pipe pile section driven between 58 and 80 m depth in San Francisco Bay mud (Long Beach, Cal. USA). The soil at the test site was a very stiff to hard silty clay with frequent sand seams below 78 m.
Briaud and Felio (1986)	Based on a database of one-way load controlled laboratory and field tests in clay.
Bond (1988)	Canons Park, London clay: stiff to very stiff, high plasticity Eocene marine clay. Over test depth mean yield stress ratio (YSR) = 33
Bogard and Matlock (1990a)	Field-tests in soft-to-stiff high plasticity clays (Empire, Louisiana) using 3-inch and 1.72-inch diameter probes to simulate pile behaviour under axial static and cyclic (force and displacement controlled) loading. The loading period was approximately 2 minutes.
Bogard and Matlock (1990b)	Field experiments in normally consolidated soft clay at Harvey, Louisiana. Impact driven or jacked pile segment models 3 and 1.72 in diameter – period of 2 minutes.
Jaime, et al. (1990)	30 One-way cycles pile tests in Mexico City.
Lehane (1992)	Test in Bothkennar, Central Scotland on a soft, high plasticity, moderately organic Holocene marine-estuarine clay-silt, lightly cemented. Over test depth mean YSR = 1.8.
Bouckovalas (1996)	Data from scale model pile tests in Nivaa clay, a natural normally consolidated low plasticity metlwater clay from Denmark.
Chow (1997)	The site (Pentre, England) is characterised by a glacio-lacustrine clay-silt and low plasticity varved clays, from very soft to firm. Over test depth, mean YSR = 1.6, and relatively permeable.
Bogard and Matlock (1998 a, b)	Offshore cyclic testing of a 30 inch diameter pile in highly plastic clay 4, 16 and 29 months after driving. The pile was subjected to a cyclic tension test, with mean load equal to one-half the peak load, followed by symmetric loads above and below the bias until the pile failed in tension – no load period is given.

2.4.1 Pore pressure behaviour

It is difficult to synthesize conclusions from the various tests in the database since the experiments were performed in dissimilar profiles (with different drainage conditions) and test characteristics. The relevant responses are:

i) The build up and cyclic variations of pore pressure seem to depend on the rate of loading and drainage conditions.
ii) Pore pressure variations were observed in all the small-scale laboratory experiments, in which the draining conditions are different to those in the field, subjected to failure loading.
iii) Cyclic field tests carried out under diverse test conditions showed small pore pressure variations during cyclic loading.
iv) The pore pressure response is not strongly affected by the soil's initial state of overconsolidation. Jardine (1995) indicates that repeated cycling eventually leads to contraction in all but the densest, or highest OCR, soils.
v) The rate of pore pressure build up is most marked during the first few cycles and reduces with the number of them. In model tests, a load or displacement threshold for pore pressure can be defined.
vi) Briaud and Felio (1986) indicated no excess pore pressures at the soil-pile interface during pile field cyclic loading tests, even during pile capacity degradation.

The field cyclic pile tests reporting pore pressure measurements include:

i) Puech and Jezequel (1980) did not record pore pressure build up during cyclic pile testing at $Q_{max} = 0.62\ Q_{ult}$ (with 14 seconds cyclic loading period).
ii) Chow (1997) reported pore pressure remaining within ±5% of ambient conditions during 40 one-way tension load cycles at $Q_a = 0.43\ Q_{ult}$, $Q_c = 0.34\ Q_{ult}$ with 60 sec cyclic loading period.
iii) McAnoy, et al. (1982) reported no pore pressure changes for one-way cyclic loading under $Q_{max} = 0.60\ Q_{ult}$. There was a slight increase in excess pore pressure during the first 40 cycles for tests under $Q_{max} = 0.80\ Q_{ult}$ but as pull-out increased this pressure dissipated.
iv) Karlsrud and Haugen (1985) observed pore pressure increments during the first 500 cycles of a long term low magnitude cyclic loading test (over first 50 minutes)

and then a gradual reduction to its starting value (Fig. 2.9)[10]. They point out that the decrease in pore pressure is most likely a reflection of soil consolidation with a simultaneous reduction in the rate of pore pressure generation during cycling.

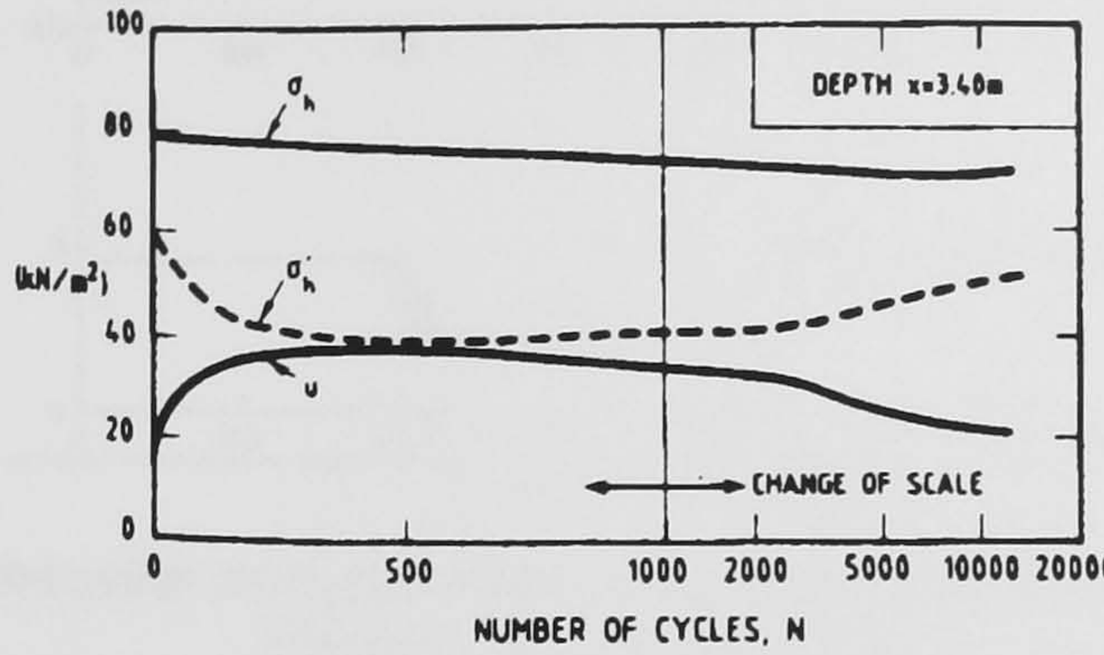


Fig. 2.9 Evolution of earth and pore pressure during long-term cyclic test Q_{max}/Q_{ult}= 0.62, Q_{min}/Q_{ult}= 0.04 (Karlsrud and Haugen, 1985)

Bogard and Matlock (1990a and b) and Grosch and Reese (1980) presented pore water pressure measurements during small-scale laboratory cyclic pile tests. Their main observations are:

i) Build up and cyclic variations of pore pressure occurred at the points where shaft failure developed and pile-soil load transfer reduced. The pore water pressure fluctuations were related to the rate of cyclic shear strength degradation.
ii) The cyclic load threshold for the pore water pressure build-up was the local failure load. The build up was temporary and dissipated when cycling stopped.
iii) Downward displacement resulted in increases in pore water pressure, and upward displacements resulted in decreases in pore water pressure.

Grosch and Reese (1980)'s load transfer and pore water pressure are shown in Fig. 2.10 plotted versus number of load cycles. The figure represents a test under increasingly symmetrical two-way cyclic displacements from ±0.004 in (0.13mm) to ±0.055 in (1.4 mm). At displacement of ±0.02 in (0.5 mm) the pore water pressure decreased slightly, but no fluctuations were observed. Following the initial quarter cycle, at displacements of ±0.033 (0.84 mm), the pore water pressure (and the maximum load transfer) abruptly decreased and began fluctuating. The fluctuations were greater in the first ten cycles and diminished gradually.

---

[10] Note that in Fig. 2.9 σ_r goes down and that σ_r' goes down more. The minimum σ_r' occurs at 500 cycles where it is around 35% less than the initial σ_r'.

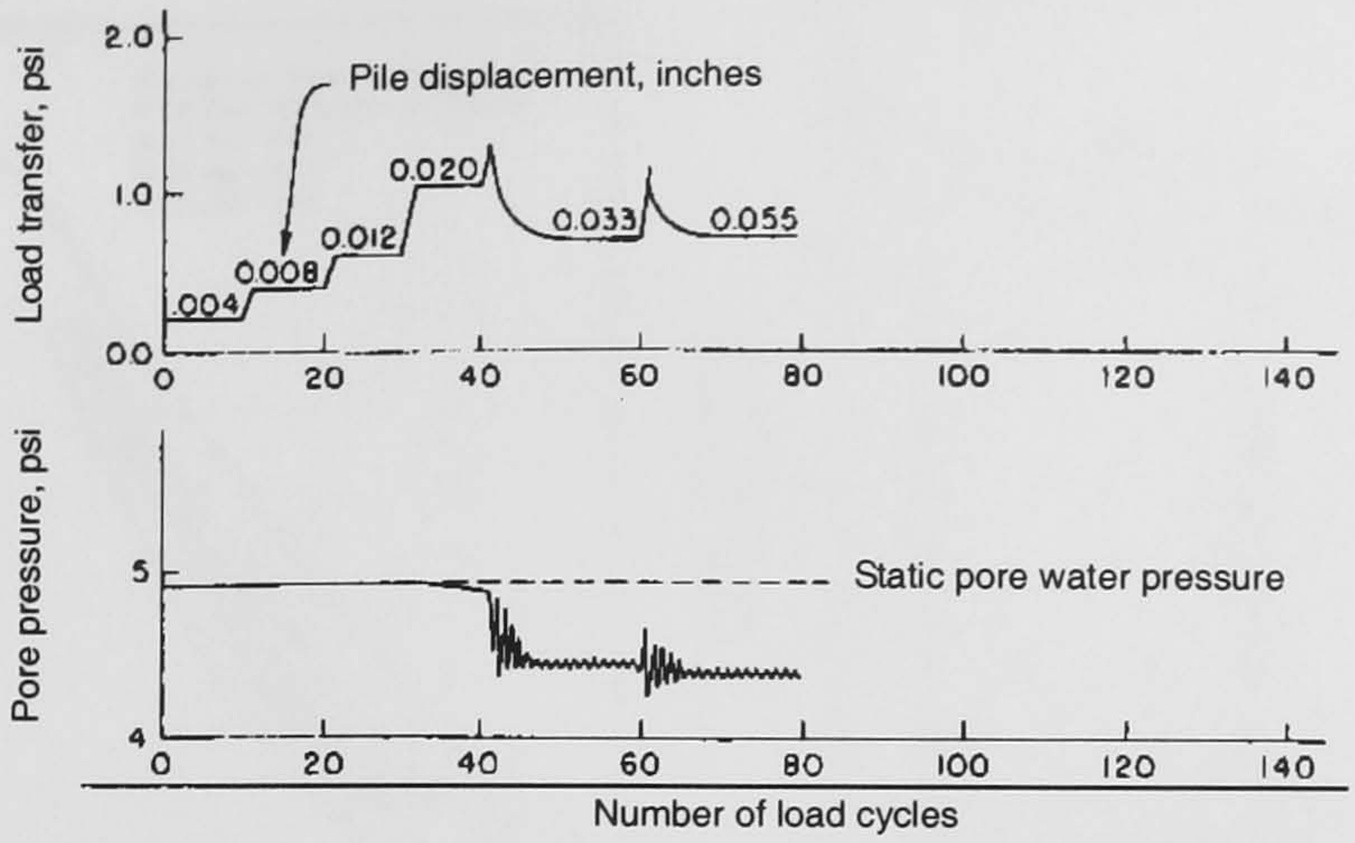


Fig. 2.10 Load transfer and pore water pressure versus number of load cycles (Grosch and Reese, 1980)

2.4.2 Radial stress behaviour

The variation in radial total and effective stresses is a progressive phenomenon that seems to be related to the soil type (OCR and plasticity index), type and amplitude of load, and depth. The effective radial stress can reduce through cyclic loading even when the excess pore pressure generated is practically the same than in static loading, indicating total stress cyclic reductions. Examples of records of radial stress changes are given by:

i) Karlsrud and Haugen (1985) who indicated that the reductions in radial effective stresses were associated with a decrease in total horizontal stress.
ii) Bogard and Matlock (1998b) who reported steady total horizontal stress reductions during at least the first 2 years of stress recording, and sharp reductions after each cyclic test (Fig. 2.11). These reductions were bigger at the top of the pile maybe due to stress reversal.
iii) Chow (1997) who pointed out that radial effective stress rose and shear stress reduced (i.e. became more negative to sustain tension load) with each application of tensile force, and that at the end of each load cycle the stresses returned to their previous values.
iv) Bogard and Matlock (1990a) whose small-scale tests indicated that upon shearing to failure in both tension and compression, a decrease in the lateral effective pressure arose from the pore pressure response.

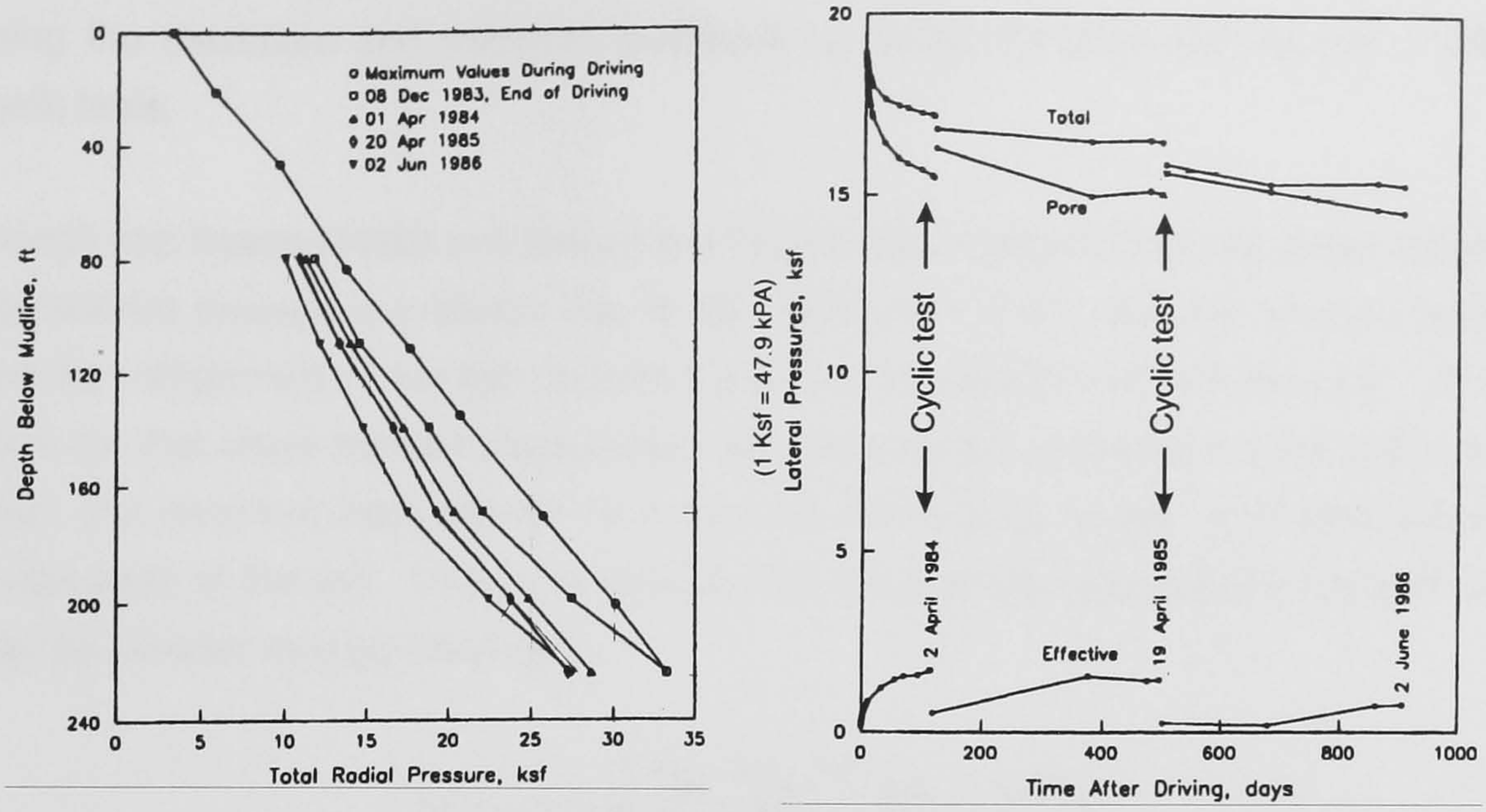


Fig. 2.11 Variations in radial total stress recorded for long term and after cyclic load test (Bogard and Matlock, 1998b)

σ_r' falls generally, with reductions increasing with N and local γ_{rz}. γ_{rz} is much larger for two-way loading than in one-way loading and is related to local the $\Delta\tau_{rz}/\sigma'_{r0}$ ratio. σ_r' may recover when cycling is finished.

2.4.3 Shear stress behaviour

Bogard and Matlock (1998a) and Puech and Jezequel (1980) in NC soils, and Karlsrud and Haugen (1985) in OC soils observed that during high intensity one-way cyclic loading tests the shear stresses at shallow depths exhibited stress reversals. Deeper in the piles, the shear stresses were completely biased to one-way loading (Fig. 2.12). For tension tests this response appears when the unloading of the pile is not transmitted to the lower sections, causing a downward displacement of the upper pile sections that reverse the shear stresses in that zone. This response can be attributed to short period load cycles, which hinder a more complete unloading, acting on long compressible piles.

Shear stress reversal at the top of a pile results in cyclic degradation at shallow depths, and in progressive load transfer from the upper to the lower part of the pile – as recorded by Kraft, et al. (1981a), Puech and Jezequel (1980), and Karlsrud and Haugen (1985). (Kraft, et al. observed that after several cycles this trend was reversed and the upper portion of the pile began to carry more of the load again.) Fig. 2.12 shows load transfer by comparing the load distributions at cycles No. 2 and No. 1500 for a test carried out under $Q_a = 0.42\ Q_{ult}$ and $Q_c = 0.10\ Q_{ult}$. Fig. 2.13 shows similar response

using the maximum and minimum mobilized τ_{rz} during Karlsrud and Haugen (1985) cyclic tests.

Grosch and Reese (1980) and Briaud and Felio (1986) indicated that the shear transfer degradation process is probably due to the destruction of the soil-pile interface bonds and the realignment of the soil particles parallel to the direction of the shearing. (They point out that shear transfer degradation may occur with a decrease in pore pressure.) Thus, the minimum load transfer is a function of the size, shape, and mineralogical composition of the soil. They also indicate that some of the load transfer capacity lost may be restored through thixotropy.

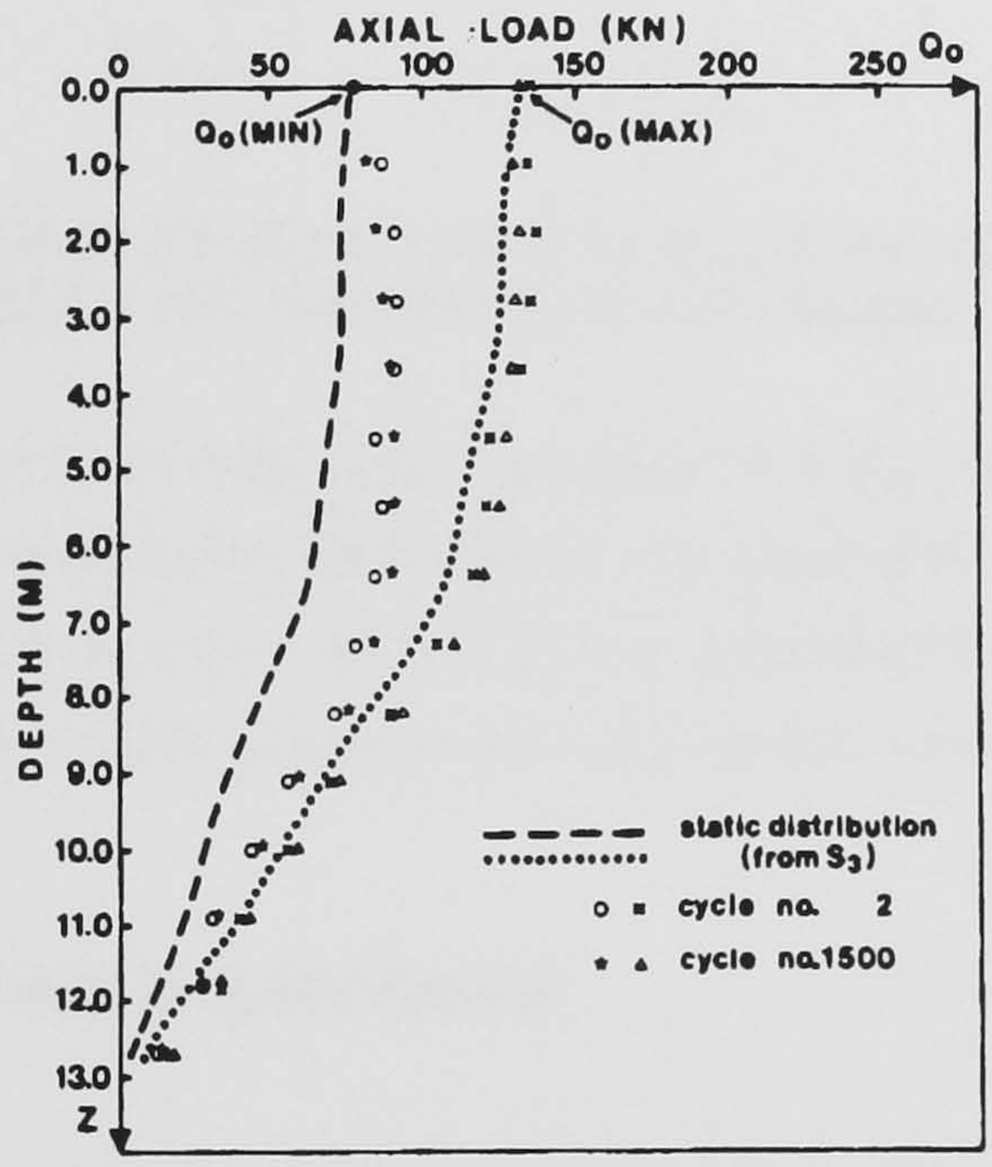


Fig. 2.12 Load distribution curves from cyclic test loads (Puech and Jezequel, 1980)

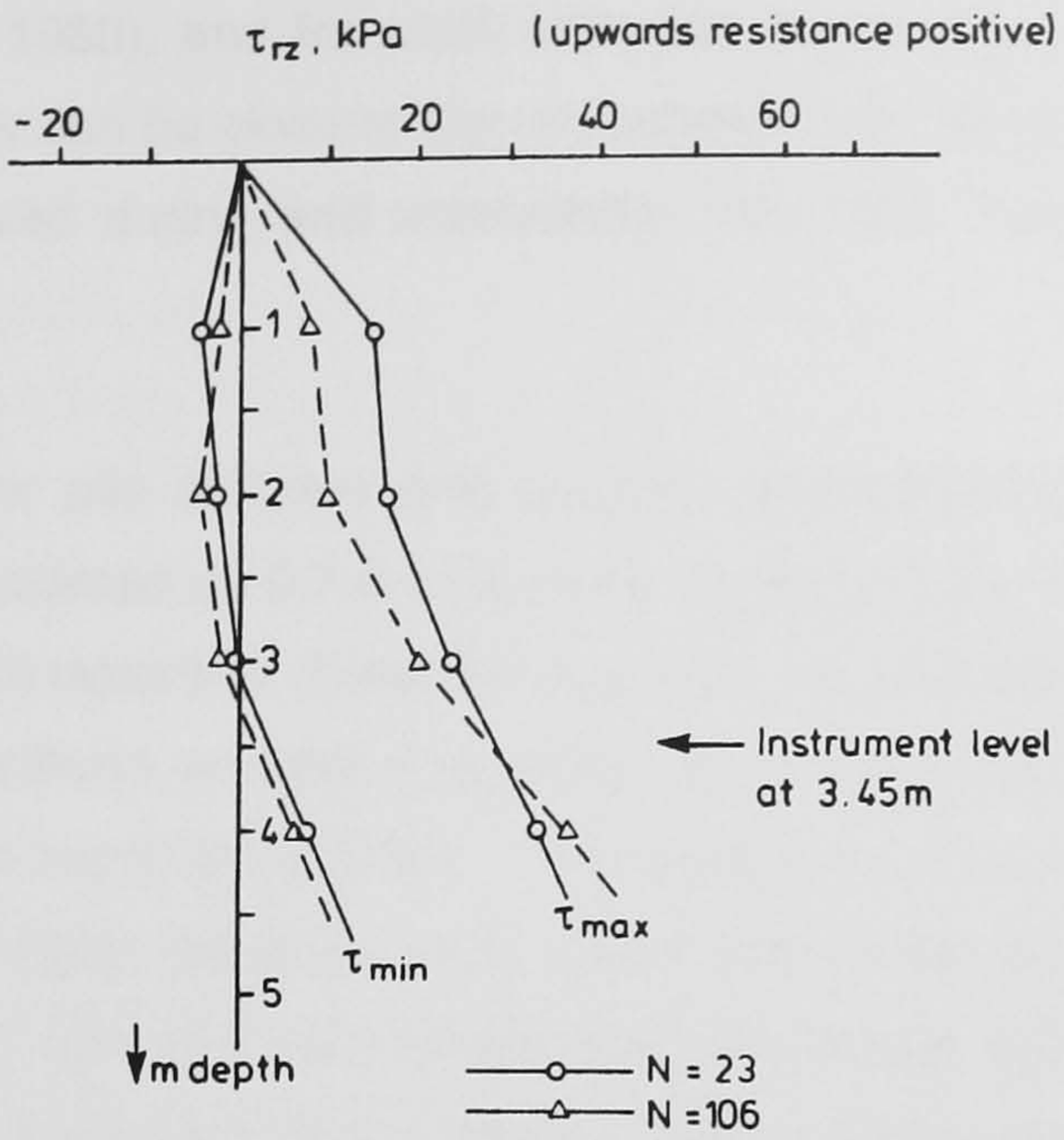


Fig. 2.13 Maximum and minimum τ_{rz} distribution at two stages during Haga test (Jardine, 1991 from Karlsrud and Haugen, 1983).

McAnoy, et al. (1982) - in one-way cyclic load tests at a Q_{max} of 60 and 80% Q_{ult} - and Chow (1997) found a more stable response for OC clays with no significant change in shear stress profiles with number of cycles, and no load shedding during cycling even at failure. (See comments on pore pressure and load transfer responses in section 2.4.1)

2.5 Pile capacity response to cyclic loading

The API RP 2A (1991) document notes that the resultant effect of cyclic loading on pile capacity is primarily influenced by the properties of the pile (e.g. stiffness, length, diameter, material), the soil characteristics (e.g. type, stress history, strain rate, and cyclic degradation characteristics), and the type of loading (e.g. number and magnitude of cycles). The next sections review the effect of these factors on pile cyclic capacity, and load displacement response.

2.5.1 Effects of load cycles on pile capacity

Cyclic loading produces degradation in pile load transfer through the reduction of radial stresses, the destruction of the soil particle bonds, or the generation of a residual failure surface. The loss in shear transfer capacity, when is not produced by residual surfaces, is a temporary phenomenon since is usually regained with time. The value of a fully degraded load transfer is essentially independent of consolidation time and loading rate

(Grosch and Reese, 1980), and for most soils can be as low as 0.40 Q_{ult}. The fully degraded load transfer can be close to the remoulded shear strength or to the minimum shear transfer observed during and immediately after pile installation (Karlsrud and Haugen, 1985).

The threshold Q_{max} for pile stiffness and capacity degradation during one-way cyclic loading is usually considered as 0.7-0.8 Q_{ult} (see section 3.5.5). However, in the cyclic test database there are reports of threshold Q_{max} near Q_{ult}, indicating that the severity of cycling effects is not uniform, and that it depends on load and soil characteristics (mainly in plasticity index, and secondly in OCR). The inspection of the low number of cycles tests indicated that higher plasticity soils seem less susceptible to cyclic loading, perhaps because their more extensive elastic and recoverable regions of behaviour and often lower angles of interface friction (Jardine, 1995). Among the high threshold tests are:

i) In MC, Jaime, et al. (1990) and Girault (1986) indicated a threshold Q_{max} between 1.15 and 1.3 Q_{ult} - the pile loses about 20% Q_{ult} of capacity[11].
ii) Kraft, et al. (1981a) indicated no reduction in static pile capacity for cyclic uplift or compression Q_{max} approximately equal to Q_{ult}.
iii) Karlsrud and Haugen (1985) reported a threshold between 0.73 and 1.0 Q_{ult} – for a maximum of 460 cycles.
iv) Doyle and Pelletier (1985) reported no permanent pile deformations occurred until the pile was cycled 5 times between 25 and 100% Q_{ult}. (10 cycles stages between 25-30%, 25-40%, 25-60%, 25-67%, and 25-83% Q_{ult} had been applied previously).

A threshold during one-way cyclic load between 0.70 and 0.80 Q_{ult} is associated with low plasticity clays (e.g. Bouckovalas, 1996; McAnoy, et al., 1982[12]; and Bergdahl and Hult, 1981[13]).

---

[11] Diaz and Cordoba (1986), using cyclic triaxial tests on MC clay, concluded that the potential loss of soil strength under triaxial cyclic loading depends upon the Q_o/Q_{ult} load ratio: for $Q_o/Q_{ult} < 0.83$, the effect is low; while for $Q_o/Q_{ult} > 0.83$, the loss accelerates. This result coincides with Jaime, et al. pile test results.

[12] Bouckovalas (1996) and McAnoy, et al. (1982) pointed out that the reduction in capacity after cyclic loading was close to that which could be expected if the effective angle of friction of the soil reduced to its residual value.

[13] Bergdahl and Hult (1981) tested a 99 mm square 15 m long wooden pile installed in glacial varved clay at Ska-Edeby, Sweden.

Completely reversing loading leads to earlier deterioration, and a Q_{ult} reduced between 50% and 75%. Among the experiments reporting this response are:

i) Bogard and Matlock (1998a) reported that two-way cyclic tests produced losses between 30% and 50% of the static capacity.
ii) Karlsrud and Haugen (1985) observed that during two-way cyclic loading (for a maximum of 160 cycles), the cyclic capacity reduced by as much as 58% Q_{ult}.
iii) Bogard and Matlock (1990a, b) reported that after 21 cycles of reversed large-displacement, the cyclic degradation of shear transfer capacity reached 40%.
iv) Grosch and Reese (1980) showed that under a constant ±5.5% pile diameter (D) displacement, the load transfer stabilised after 75 cycles at a minimum of 39% of the maximum. In a different test the displacement limits were progressively increased from ±0.4% to ±5.5%D; the threshold displacement was 3.3%D with a reduction of 50% of the peak load transfer after 10 load cycles with no further reduction during additional cycles. For a test where the movement was always in a downward direction but progressively increased from 2%D to 10.8%D, the threshold displacement was 7.5%D, when the peak load transfer reduced in 25%.

2.5.2 Loading rate effect on pile capacity

Kraft, et al. (1981a) pointed out that the dependency of pile response on loading rate may be influenced by: (i) soil properties, (ii) the relative proportion of load carried in end bearing and shaft friction, (iii) pile loading history, and (iv) the Q_a/Q_{ult} ratio, the higher the ratio the lower the rate effect (see section 3.5.5). They also show that inertia effects are not contributing to the observed load rate dependency.

Q_{ult} in clays increases between 5% and 20% for each order of magnitude increase in loading rate, with the greater increases typically applying to softer and highly plastic clays (Dunnavant, et al., 1990). Rate effects decrease with OCR. No single laboratory test can reproduce the rate effects developed by piles, Chow (1997) and Lehane (1992) obtained good agreement from ring shear tests at the same rates, Karlsrud and Haugen (1985) obtained good agreement from undrained triaxial tests; this also appears to apply to MC conditions.

The studies on rate effects on pile capacity have been carried out on diverse pile types and soil characteristics, the database includes:

i) Jaime, et al. (1990) reported 12% capacity increments per order of magnitude increment in loading rate for piles driven in MC (Fig. 2.14)[14]. Marsal and Mazari (1962) reported similar results for other sites in MC.

ii) Kraft, et al. (1981a) tests showed that Q_{ult} may be increased between 40% and 75% if the loading rate is increased by about three orders of magnitude. Kraft, et al. point out that under fast one-way cyclic loading the combined effect of cycling and rate of loading can result in a pile resistance in excess of the static capacity.

iii) Chow (1997) points out that post-peak increases in loading rate from 0.001 to 1.5 mm/min had little or no effect on shaft capacity. However, increases in rate from 1.5 to 15 mm/min produced a rise of ≈8%.

iv) Lehane (1992) reported peak shaft capacity increases of ≈6% when the load testing rate was increased from 1mm/min to 10mm/min.

v) Karlsrud and Haugen (1985) reported that fast static tests carried out in about 10 to 20 seconds gave capacities which were 20-25% larger than a subsequent slower static test completed in 20 to 30 minutes – approximately 9% capacity increase per order of magnitude.

vi) Doyle and Pelletier (1985) report that pile capacity increases approximately 8% per tenfold increase in displacement strain rate.

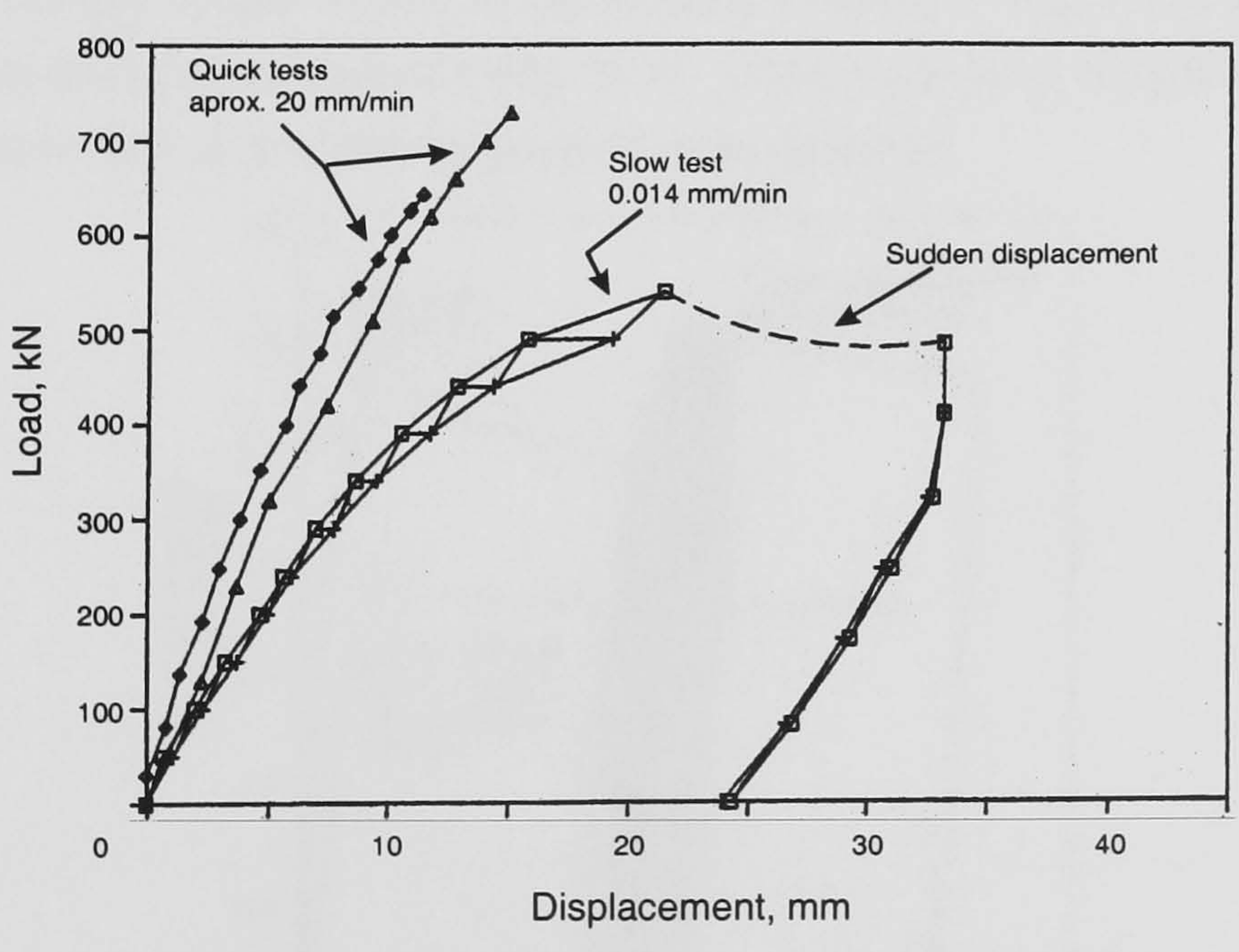


Fig. 2.14 Slow and quick penetration tests (Jaime et al., 1990)

[14] By comparing a test failed under 20 mm/min against a test failed under 0.014 mm/min.

2.5.3 Effects of load cycling on subsequent pile capacity

Cyclic loading influences the capacity of subsequent tests. Residual surfaces, plasticity index, drainage conditions, number of cycles, and load characteristics determine the losses or gains in pile capacity during cyclic loading, with no clear trend against OCR.

Holmquist and Matlock (1976), Charlie, et al. (1985), and Grosch and Reese (1980) indicated that a few additional cycles might erase any strength recovery obtained through reconsolidation after cyclic loading. According to Grosch and Reese, the recovery in load-transfer capacity and subsequent reduction is consistent with combined particle realignment and thixotropy. They also indicated that their minimum values of load transfer recorded in successive cyclic tests were identical because the only change in the soil during the tests was one of alignment of particles, while the size, shape, and mineralogical composition of the particles remained the same.

Research on this topic includes:

i) Bogard and Matlock (1990a) who pointed out that a comparison of the maximum shear stress transfer before and after tension cycling to $Q_{max} < Q_{ult}$ shows that no loss in strength had occurred (Fig. 2.15). Under reversed cycling to shear failure, a loss of 32% on the peak shear stress was observed.

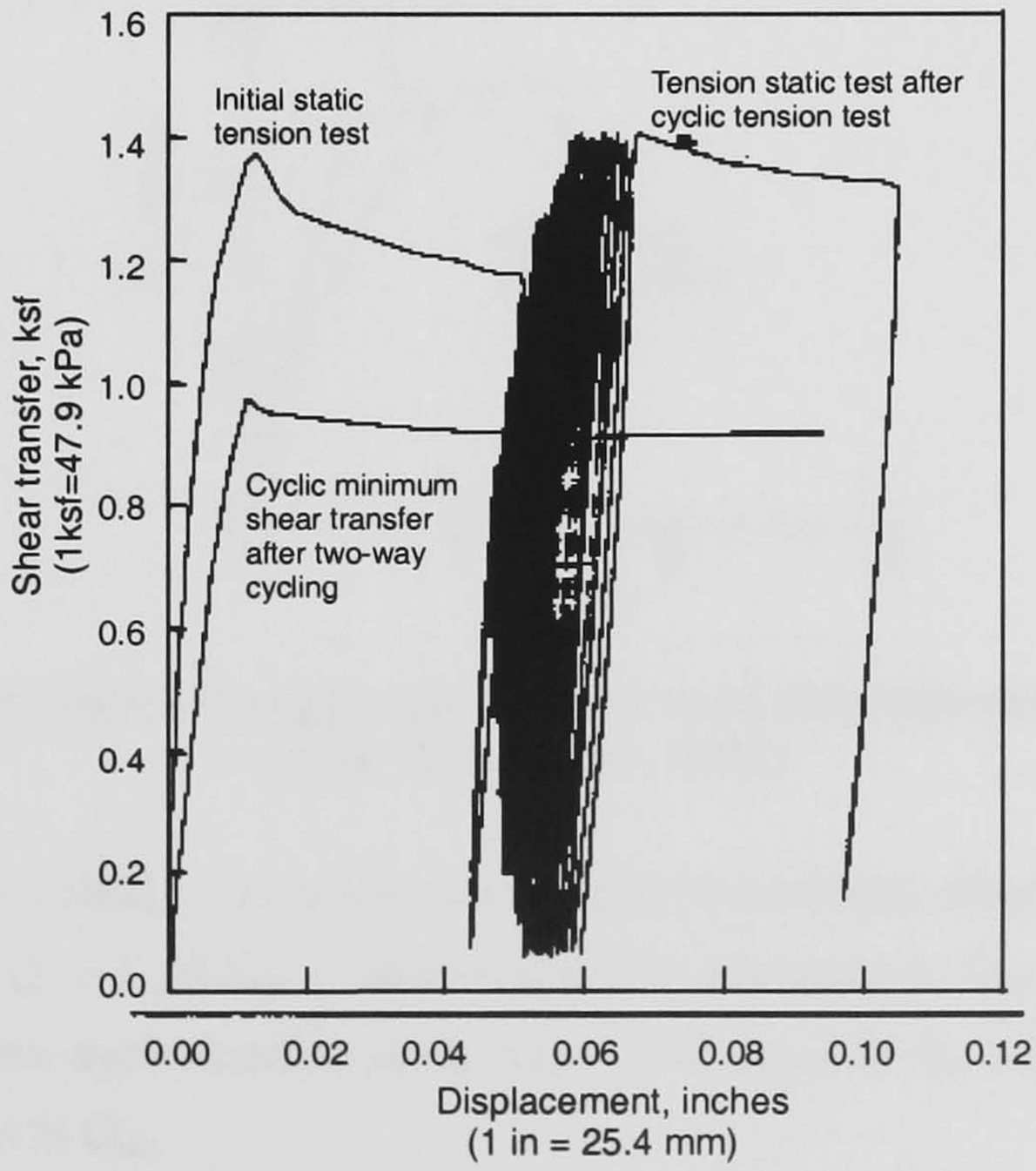


Fig. 2.15 Results of static and cyclic load tests (Bogard and Matlock, 1990a)

ii) Kraft, et al. (1981a) found that static capacities measured after several cyclic failure and re-consolidation periods were up to 25% lower than those developed in previous static tests. They concluded that this probably resulted from residual shear surfaces.

iii) Grosch and Reese (1980) reported that two-way cyclic displacement controlled tests on model piles (running with ±5.5% pile diameter) produced a 60% decrement on static capacity.

iv) Holmquist and Matlock (1976) indicated that one-way cyclic loading at less than 90% Q_{ult} did not significantly affect the pile capacity, but one-way repeated loading at 100% Q_{ult} resulted in a 20% reduction in static capacity. 5 to 50 cycles of repeated two-way loading (depending on confining stress) resulted in a 66% reduction of the static capacity.

v) Chow (1997) compared the mobilisation of shaft resistance in tension tests before and after cycling and found that peak shaft capacity reduced by 9% (Fig. 2.16). By plotting the residual and peak shear stress profiles Chow showed that the latter reduced along the entire pile length, particularly close to the pile tip. Chow indicates that the decrease was due to (i) a reduction in δ_p due to the formation of a residual shear band and (ii) a 25% reduction in σ_{rc}' within the lower section of the pile.

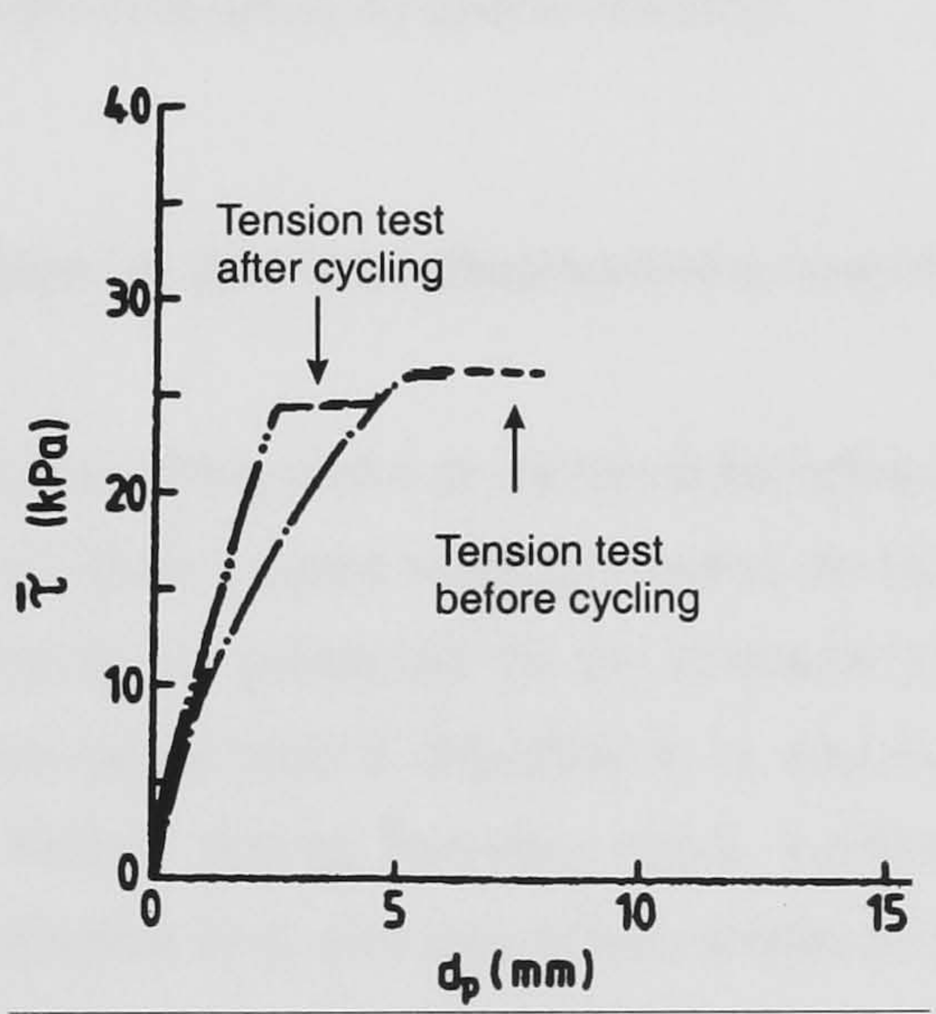


Fig. 2.16 Average shear strength against pile head displacement before and after cyclic test (Chow, 1997)

vi) McAnoy, et al. (1982) - for a test carried out immediately after cycling under Q_a = 0.40 Q_{ult} and Q_c = 0.20 Q_{ult} – observed a 6% decrease in Q_{ult}. An extraction test carried out after cyclic loading under Q_a = 0.40 Q_{ult} and Q_c = 0.40 Q_{ult} showed an 18% reduction in Q_{ult}.

vii) Karlsrud and Haugen (1985)'s pile tests on low OCR sensitive clays indicated that the static load displacement response was very little influenced by one-way cyclic

loading to failure (Fig. 2.17). They also indicated that when reconsolidation is allowed after one-way cyclic loading the static capacity showed an increase relative to an initial static capacity - as was also the case for consecutive static tests.

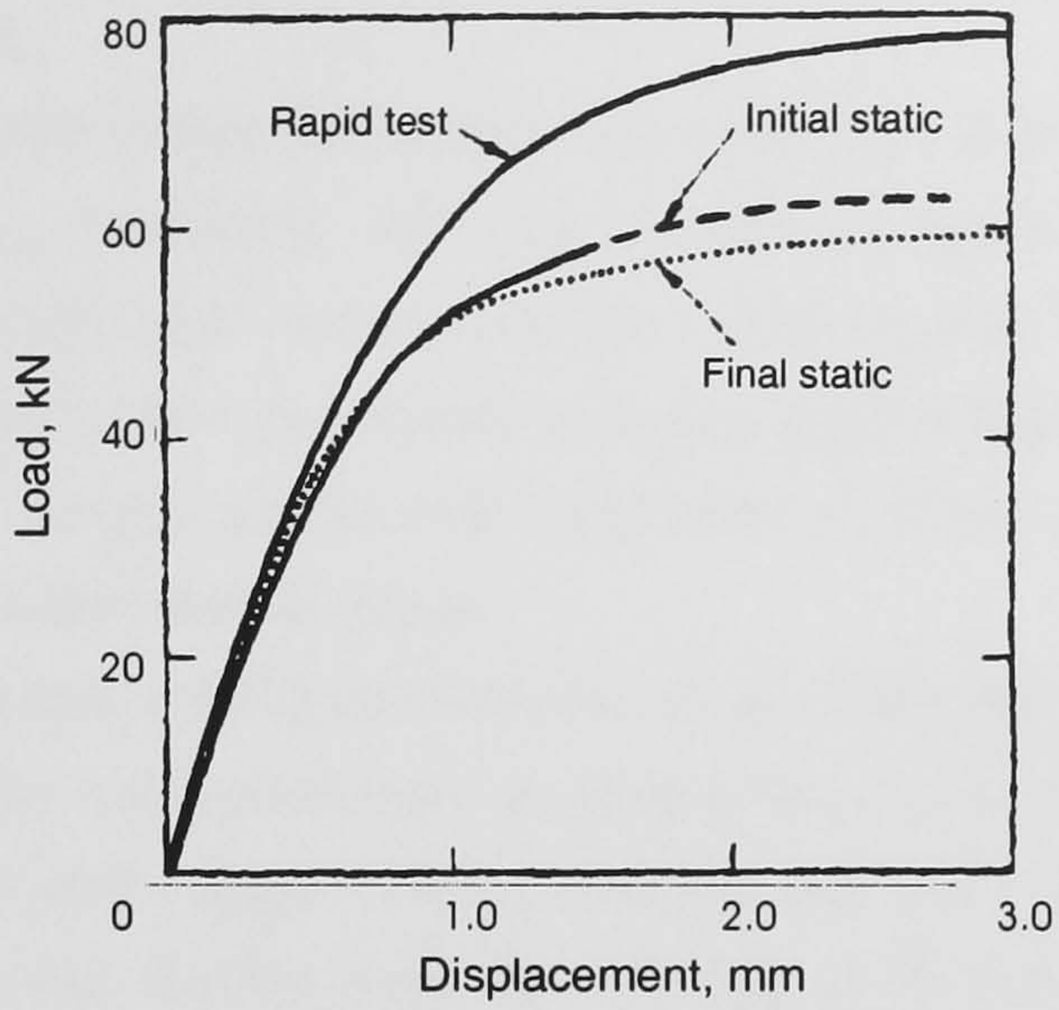


Fig. 2.17 Typical load-displacement response from static tests (Karlsrud and Haugen, 1985)

2.6 Pile load-displacement response to cyclic loading

2.6.1 Effects of load cycles on pile load-displacement response

A pile's response mechanism (shakedown or incremental collapse) and the development of displacement (d_a and d_c) during cyclic loading depend on Q_a and Q_c. Failure in one-way cyclic loading seems to be governed by an increase in the rate of permanent displacement accumulation rather than a reduction in d_c and G_{cp}; with G_{cp} and d_c being mainly related to Q_c. Failure during two-way cyclic loading is characterised by a reduction in G_{cp}, and increments in d_c and rate of accumulation of d_a.

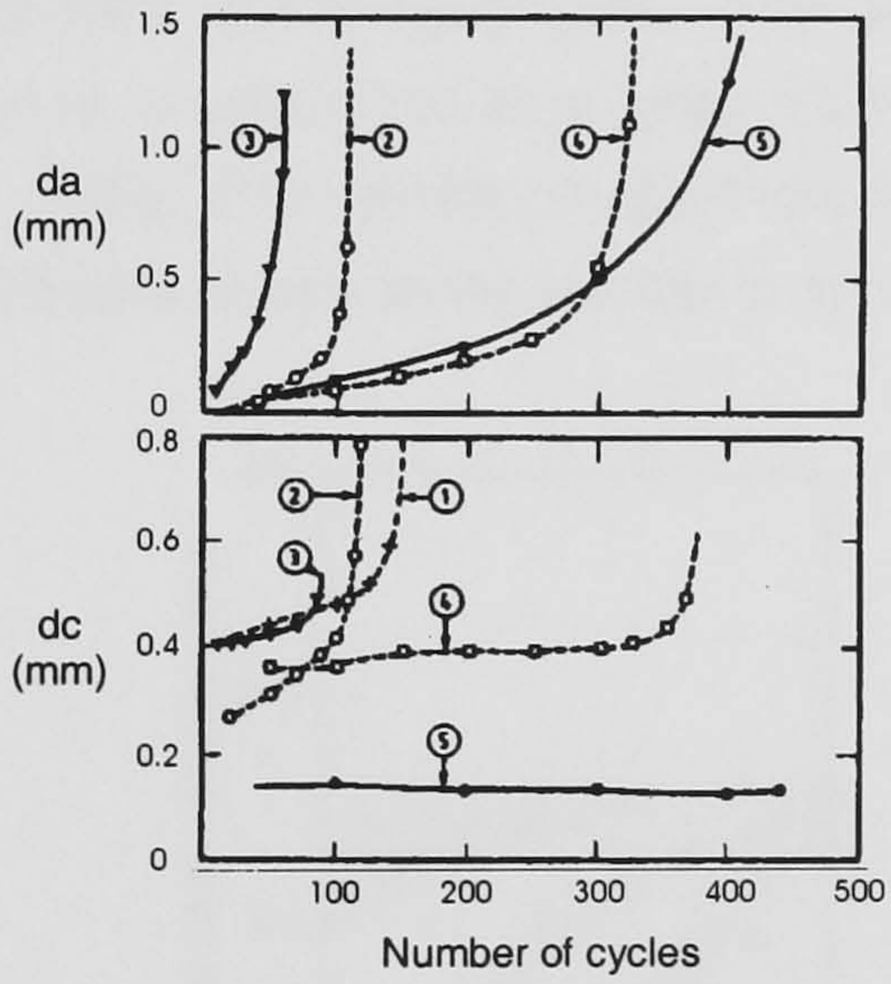
Karlsrud, et al. (1987) pointed out that for one-way loading pile tests the rate of accumulation of d_a is related to the effective time the peak load stays on during each cycle (see Chapter 11). G_{cp} and the rate of accumulation of d_a reduce with the soil's plasticity index. Kraft, et al. (1981a) pointed out that the reloading response for a partially unloaded pile is expected to be stiffer than that for a fully loaded pile.

The research on this topic includes:

i) Kraft, et al. (1981a) and Jaime, et al. (1990) who reported that the rate of accumulation of permanent pile displacement increases substantially for Q_{max} higher than 0.75 to 0.80 Q_{ult}. d_a increased appreciably when Q_{max} approached 1.10 Q_{ult}, at that point there was very little rebound during load cycles. d_a increases with Q_a.

ii) Bouckovalas (1996) presented tension tests under $Q_a = 0.50\ Q_{ult}$ and $Q_c \leq 0.17\ Q_{ult}$ that showed G_{cp} increasing with the number of cycles and finally reaching shakedown. Bouckovalas' tests under $Q_a = 0.50\ Q_{ult}$ and $Q_c \geq 0.31\ Q_{ult}$ showed cyclic stiffness falling with the number of cycles applied (the decrease was gradual during the initial stages but became rapid after a certain number of cycles) and finally reaching incremental collapse.

iii) Karlsrud and Haugen (1985) and McAnoy, et al. (1982) showed cyclic shakedown for one-way cyclic tests performed at various Q_{max} (tests No. 3, 4 and 5 in Fig. 2.18). Karlsrud and Haugen (1985) showed pile tests undergoing completely symmetrical two-way loading (test No. 1 in Fig. 2.18) that failed by incremental collapse. When the loading comprised a non-symmetrical two-way load, both d_a and d_c increased towards failure, and d_a was larger.



Test	Qmax/Qult	Qa/Qult	Qc/Qult	N
1	0.40	0.00	0.40	160
2	0.39	0.10	0.29	100
3	0.83	0.46	0.37	60
4	0.75	0.39	0.36	320
5	0.97	0.26	0.71	460

Fig. 2.18 Examples of evolution of accumulated average displacement, d_a, and displacement amplitude, d_c, during cyclic tests (Karlsrud and Haugen, 1985)

2.6.2 Loading rate effect on pile load-displacement response

Bea (1980) and Charlie, et al. (1985) indicated that a high rate of loading increases the stiffness of deep foundations above that observed in slow, static load tests. Kraft, et al. (1981a) report a 10% to 25% increase in pile-soil stiffness per ten fold of loading rate increment, compared to an 8% increment on axial pile capacity. For Jaime, et al. (1991)'s pile tests in MC, the increment was approximately 20% on stiffness, and 12%

on pile capacity.

2.6.3 Effects of cycling on subsequent test load-displacement response

Static tests carried out after tension one-way cyclic loading showed plastic strain hardening that results in overall load-displacement behaviour that was less non-linear over a large proportion (about 80%) of the capacity, and a displacement to peak that is approximately half of that for an earlier static tests (Chow, 1997; McAnoy, et al., 1982) (Fig. 2.16).

Bouckavalas (1996) indicated that one-way and two-way cyclic pre-testing does not have a significant effect upon the rate of G_{cp} degradation during the initial stages of a subsequent cyclic test, but it slows the rate of permanent displacement accumulation[15]. In Fig. 2.19a, test 8a-I represents a first time cyclic test while tests 8a-II and 8a-III were subjected to cyclic pre-testing. In the figure it is observed that, although the cyclic loading intensity increases from test 8a-I to test 8a-III, the permanent displacements are smaller for tests on pre-tested piles. The same trend is observed in Fig. 2.19b[16], in which test 7a is under first time cyclic loading and test 8a-IV was previously tested cyclically. In Fig. 2.19 the differences in displacements between pre-tested pile and first time loaded piles reduce as the number of cycles increases.

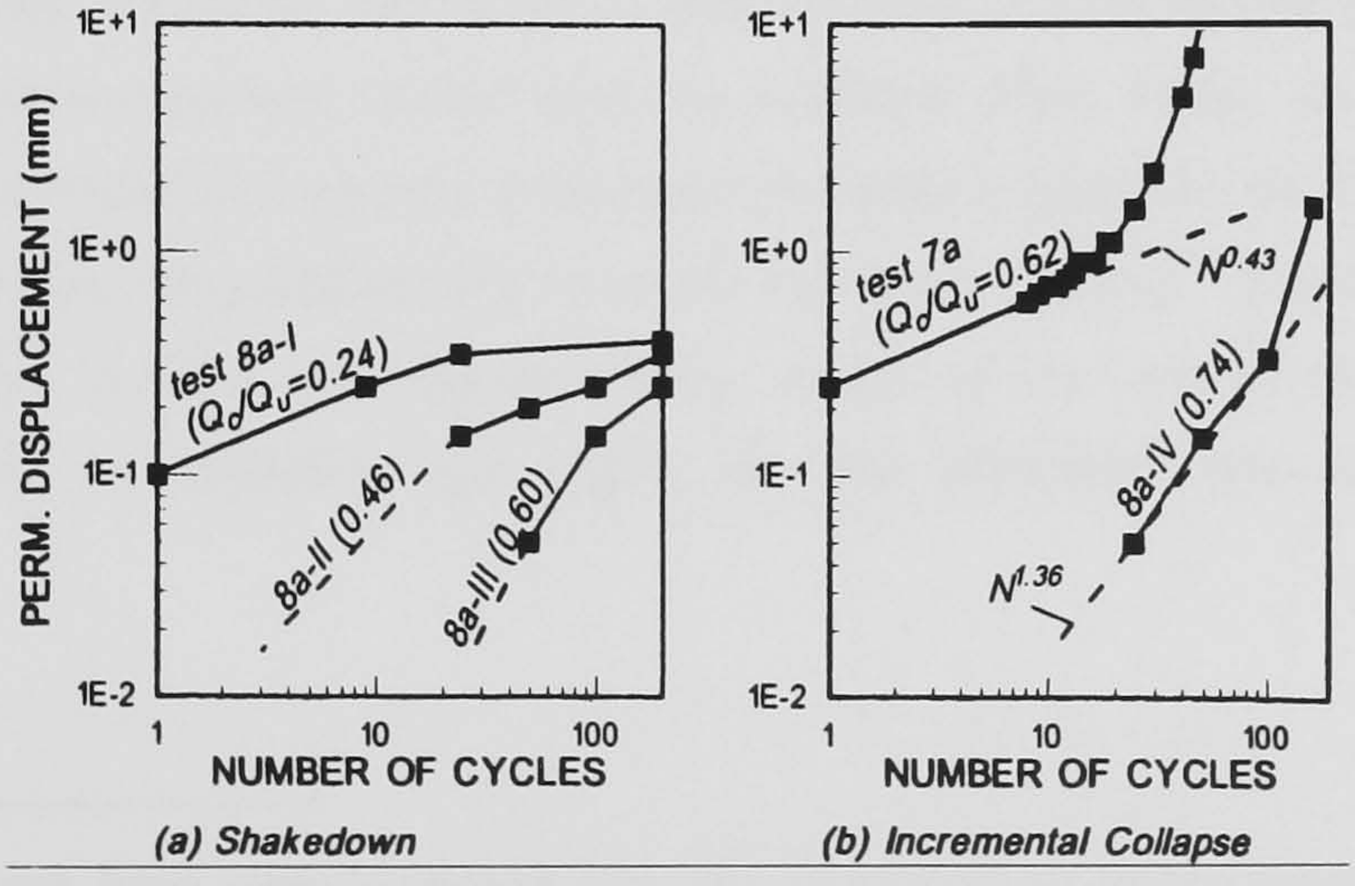


Fig. 2.19 Effect of cyclic pre-shearing on permanent displacement accumulation of small-scale model piles (Bouckovalas, 1996)

Doyle and Pelletier (1985) pointed out that two-way cyclic load levels lower than about

---

[15] The tests were carried out under $Q_a = 0.53Q_{ult}$ and Q_c between 0.23 and 0.37 Q_{ult}. Bouckovalas' Q_c has to be divided by 2 to represent the definition of Q_c used in this Thesis.

[16] The tests in Fig. 2.19b suffered incremental collapse.

0.50 Q_{ult} did not cause further degradation in the load-displacement curve.

2.7 Design of displacement piles under axial cyclic loading

The design process requires relatively simple models that allow parametric studies of the pile geometry and soil properties in order to determine a feasible foundation. More sophisticated analytical tools are generally reserved for verification and fine-tuning of the design.

2.7.1 Current practice in the design of displacement piles under dynamic loads

Despite the considerable number of published experimental studies and theoretical analyses, the factors affecting vertical cyclic pile response are still not fully understood and pile capacity during cyclic loading can only be tentatively quantified. Consequently, there are no design methods for piles under cyclic loads considered adequate for general pile, soil, and load conditions (Bouckovalas, 1996; McAnoy, et al., 1982).

The possible effects of cyclic loading are usually not addressed explicitly in current pile design practice. Although in principle this is unsatisfactory, in practice the remarkably good record of reliability *in offshore* piled foundations indicates that current static pile design procedures, combined with ways of estimating and characterising environmental loads, produce safe cyclically loaded piled foundations (Bea, 1992; and Dunnavant, et al., 1990)[17]. As a result, it is usually assumed that cyclic loading is not a concern as long as the piles possess adequate factors of safety for static loading[18] (Jardine, 1991; Focht and O'Neill, 1985; Grosch and Reese, 1980). Much of the current concern does not centre on safety or reliability, but rather on the efficiency and economy of the foundations.

---

[17] Some researchers have even proposed that piles subjected to design storm loads can have greater axial capacity when cyclic loading effects are considered explicitly than when static procedures are used. Furthermore, they claim that the response is not critical even when the post-cyclic capacity is lower than the static capacity of the foundation, provided the structure can redistribute the loads.

[18] 1.5 is recommended for extreme environmental loading conditions. This factor of safety has been selected based on other implicit foundation and non-foundation considerations, including the probability of the extreme loading event, the duration of extreme loading, etc.

In design practice, those who are concerned about cyclic loading take account of soil degradation effects on axial capacity if either: (i) the transient component of load (Q_{max}) is high (equal to or exceeding about 30% of the static component); or (ii) Q_{max} is greater than about 90% of the static capacity for one-way loading, or 75% of the static capacity in case of two-way loading[19] (Focht and O'Neill, 1985). This practice, which takes little account of cyclic loading effects, should produce inconsistent safety levels between piled structures due to, for example, the difference between the behaviour of piles subjected to one-way and two-way cyclic loading (Karlsrud and Haugen, 1985; Rigden and Semple, 1983).

Bea (1992) gives an example of a pseudo-static design method. He proposes a procedure to estimate the required pile penetration based on a design load (P_t) that is defined as:

$$P_t = \frac{P_c}{(\beta_c)(\beta_r)} + P_m \qquad (2.11)$$

where P_c = maximum cyclic design load; P_m = mean design load; β_c = cyclic-loading factor; and β_r = rate of loading factor.

The empirical nature of this type of procedures has to be acknowledged when applying them to analysis. Mainly because their theoretical and experimental backgrounds do not allow simple extrapolations to pile sizes, soil conditions, and magnitude of static and dynamic loading.

Explicitly incorporating cyclic load factors into the design process will result in a more rational design method (Dunnavant, et al., 1990).

2.7.2 Review of the design codes for piles under dynamic loads

Building codes of practice are classified as either "prescriptive" or "performance" codes (Focht and O'Neill, 1985). Prescriptive codes generally give detailed procedures for assessing pile capacity, and the material and construction quality control; while performance codes specify only how the foundation is to perform and do not outline the details of design and construction. Static pile design codes are prescriptive codes, some with performance basis. The codes of practice for the cyclic pile design are

---

[19] It is assumed that cyclic loading effects become significant only in the case of reversed slip at the pile-soil interface imposed by two-way cyclic loading (Bouckovalas, 1996).

essentially performance based, suggesting an equivalent static calculation and leaving the design to a qualified engineer.

Typical state of the practice design guidelines for piles under cyclic loading are given in the American Petroleum Institute (API) - RP 2A, Eurocode 8, Det Norske Veritas (DNV-OS-C101), and I.S.O. Standards 19900. These codes[20] have been reviewed as part of this research, and the salient points are briefly discussed in the following. Comments on the Mexico City Building Code are also presented.

All the above codes of practice indicate that the foundation should be designed to carry static, cyclic and transient actions. The API, ISO and DNV guidelines also stipulate that the pile deformations should comply with structure serviceability requirements (limits for deformations or vibrations in the structure), which also apply to the response after the design cyclic loading. All the design criteria provided by the codes are based upon static monotonic actions.

The API, ISO and DNV codes[21] specify that, in evaluating the degradation of resistance, the influence of the flexibility of the piles and loading history shall be accounted for – according to the DNV guidelines this should be done "as far as possible". The codes also point out that cyclic loading (including inertial and kinematic loading) can have two effects on the axial capacity: (i) temporary or permanent decreases in load carrying resistance, and/or accumulation of deformation; and (ii) an increase in load-carrying resistance and/or stiffness of the pile due to the rapid application of the load. According to the codes, the resultant influence of cyclic loading on the piles will be a function of the combined effects of the magnitude of the loading, number of cycles, rates of applied loads, the structural characteristics of the pile, the type of soils, and the factors of safety used in the pile design. The DNV code explains the response mechanism by indicating that the cyclic shear stresses may lead to a gradual increase in pore pressure which, in combination with the increase in cyclic and permanent shear strains, may reduce the shear strength of the soil.

The 1987 Complementary Technical Notes (NTC) to the Building Code of MC included the resistance factor $F_R = 0.7\ (1\text{-}s/5)$ for friction piles under the load combination that includes for seismic loading effects. "s", the ratio between the maximum seismic load and the maximum static load on the piles. However, in the 2001 edition of the NTC the

---

[20] All but the Eurocode were developed for offshore conditions.

[21] API RP 2T and the draft of DNV-OS-C105 (2000) deal with Tension Leg Platforms (TLP).

F_R was revised to 0.7, as for the static case, with the emphasis changing to the foundation raft-pile load sharing distribution. This code does not account explicitly for the response of piles to cyclic loading (e.g. the rate and degradation effects and the stress state induced in the soil mass by the seismic waves).

In order to improve the design codes documentation of good and poor pile performance and systematic evaluation of analysis and design procedures against case histories and/or physical models are needed. This thesis addresses this problem.

Regarding the analysis of the foundation-structure system, the Eurocode, ISO and API codes point out that analyses can be based on discrete or continuum models. The DNV code describes briefly general rules for soil-structure interaction analyses.

The Eurocode, API and ISO codes also stipulate that the design of piles subject to cyclic loading should include the following effects:

i) Inertia loading from the superstructure.
ii) Kinematic forces arising from the deformation of the surrounding soil (transient and permanent) due to the passage of seismic waves. The stress produced by this motion may influence pile capacity and stiffness.

The API code indicates that modelling cyclic loading effects explicitly may improve the designers' insight into the relative importance of the loading characteristics. However, the code also notes that extreme care should be exercised in applying this approach since, historically, cyclic effects have been accounted for implicitly. Design methods developed and calibrated on an implicit basis may need extensive modification where explicit algorithms are employed.

2.7.3 Analytical tools

Apart from the static phenomena, the analysis of the cyclic axial pile response requires consideration of the following: (i) an effective stress model of soil cyclic behaviour that links the interface failure criterion to the effect of cycling on shaft capacity; (ii) non-linear stress-strain behaviour of soil at the pile-soil interface, including soil gapping; (iii) loading rate effects; and (iv) changes in ground motions with depth.

The analytical tools can be grouped into two general categories (API, 1991 RP 2A):

a. *Discrete element models.* The soil around the pile is idealised as a series of uncoupled springs or elements attached between the pile and the far field soil (Fig. 2.20). The soil elements are commonly referred to as t-z (shaft resistance-displacement) and q-z (tip resistance-displacement) elements (Kraft, et al., 1981b; Matlock and Foo, 1979; Bea and Audibert, 1979). (For laterally loaded piles, the elements are referred to as p-y or lateral resistance-displacement elements (Mylonakis, 2001; Poulos and Davis, 1980; Randolph and Wroth, 1978; and Coyle and Reese, 1966)). These elements have the ability to simulate non-linearity, inhomogeneity, and hysteretic degradation of the surrounding soil. Linear or non-linear dashpots (velocity dependent resistance) can be placed in parallel and series with the discrete elements to model geometric (radiation) damping and rate of loading effects (Wang, et al., 1998; Poulos, 1989; Bea, et al., 1984). The pile can be modelled as a series of discrete elements (e.g. rigid masses interconnected by springs) or as a continuous rod, behaving in either a linear or non-linear manner). In these models the soil and pile properties can vary with depth.

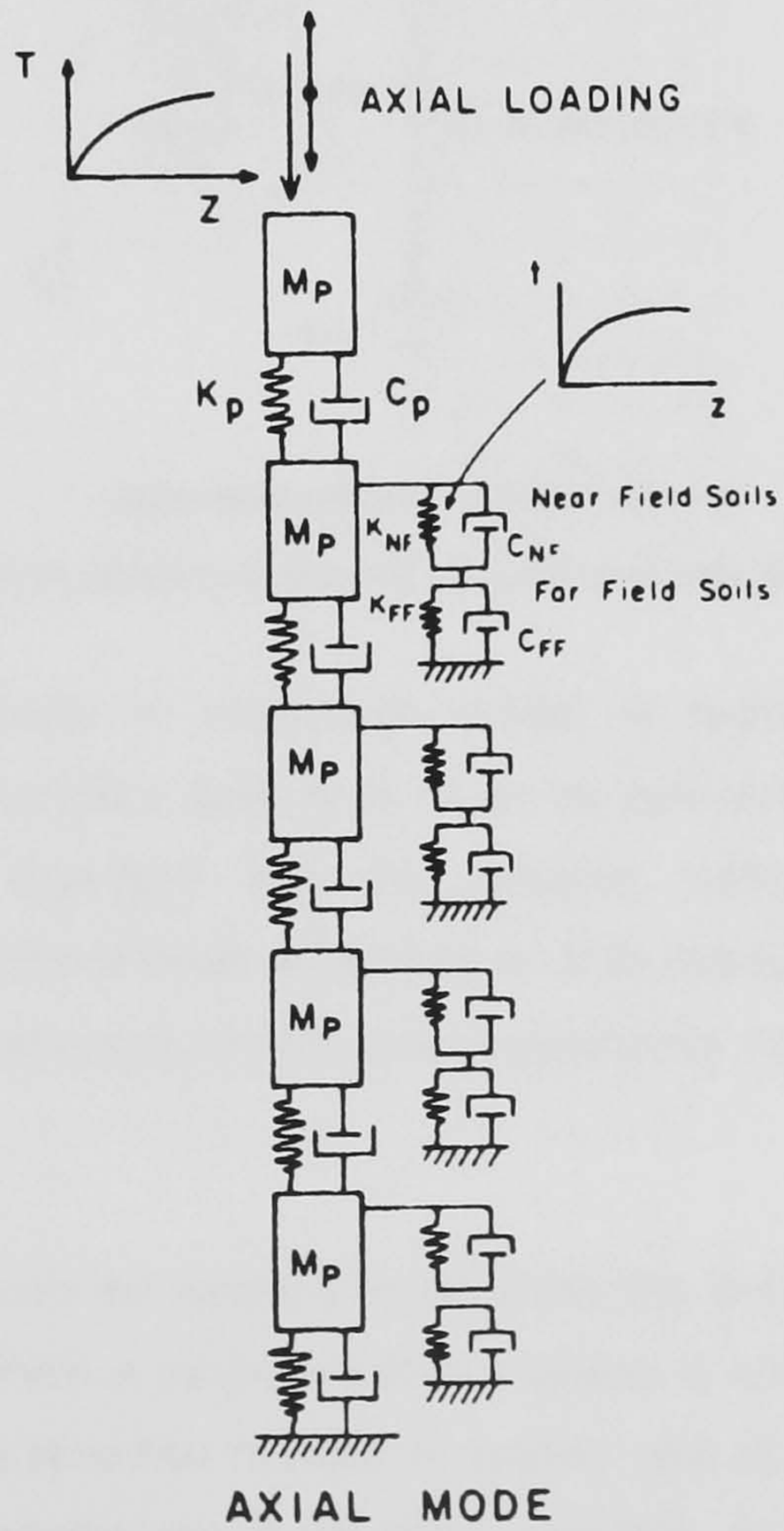


Fig. 2.20 Idealised discrete element system for dynamic pile response (Bea and Audibert, 1979)

Given their versatility, the discrete element models have been heavily used in practical

situations for the evaluation of pile capacity and accumulated displacements following high intensity cyclic loading. However, these analyses usually ignore the interaction that, through the surrounding medium, any other piles in a group might produce (Banerjee and Sen, 1987).

b. *Continuum models*. The soil around the pile is idealised as a continuum attached to the pile (Fig. 2.21). The soil behaviour may incorporate a stress-strain model with non-linearity and heterogeneity; the pile is typically modelled as a continuous rod, behaving in either a linear or non-linear manner. Although these models are limited by the modelling of the boundaries at infinity, these analyses characterise the dynamic behaviour of piles relatively well (including pile installation, set up, and loading history) (Romo, et al., 2000; Finn, et al., 1997; Jardine, 1991; Roesset and Angelides, 1979).

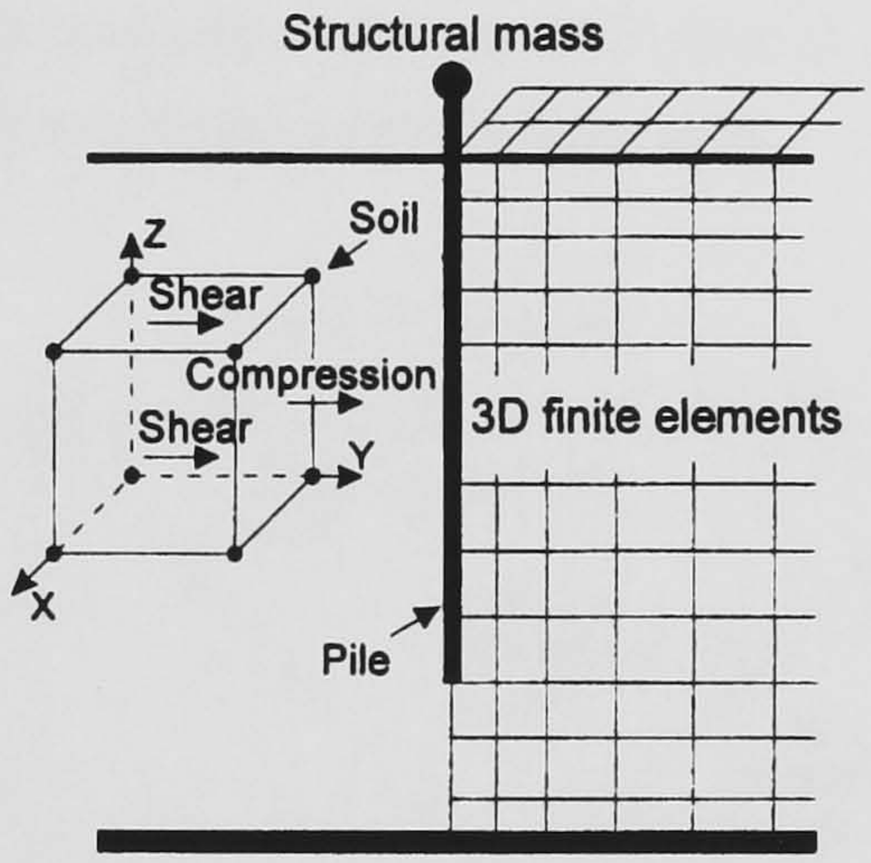


Fig. 2.21 Quasi 3D finite element model of pile-soil response (Finn, et al., 1997)

Once the idealized discrete or continuum model is established and the relevant equations developed, a solution technique must be selected. For simple models, a closed form analytical approach may be possible, otherwise numerical solution techniques such as the finite difference method or finite element method must be used. Discrete element and continuum models are occasionally combined in hybrid models (Bea, et al., 1984).

At least two procedures can be adopted to simulate the cyclic loading of a pile: (i) a single-step analysis, in which a single iterative analysis is carried out to determine the behaviour of a pile after a specified number of cycles; and (ii) a cycle-by-cycle analysis, which is more time-consuming but much more versatile, in that it can accommodate sequences of irregular cyclic loading (Poulos, 1989).

2.8 Interaction diagrams

Cyclic interaction diagrams (ID) consist of contour curves each of which defines combinations of Q_c and Q_a that would cause cyclic failure for a particular number, N, of identical cycles. Since the axes are normalised by Q_{ult}, the diagrams indicate the proportion of the static capacity that could be carried before cyclic failure is reached at a number of cycles (Fig. 2.22 shows half of an ID, the complete ID would include a reciprocal graph to the left).

An ID can be defined from cyclic response analyses (Jardine, 1991; Poulos, 1988) or field tests (Fig. 2.22, Karlsrud and Haugen, 1985; Bea and Audibert, 1979) if the pile is subjected to a full range of combinations of mean and one-way and two-way cyclic loads, and a consistent failure criterion under cyclic loading is applied. The failure criteria can involve the static test failure displacement, d_a after cycling, the change in the accumulation rate of d_a during cycling, or the changes in d_c.

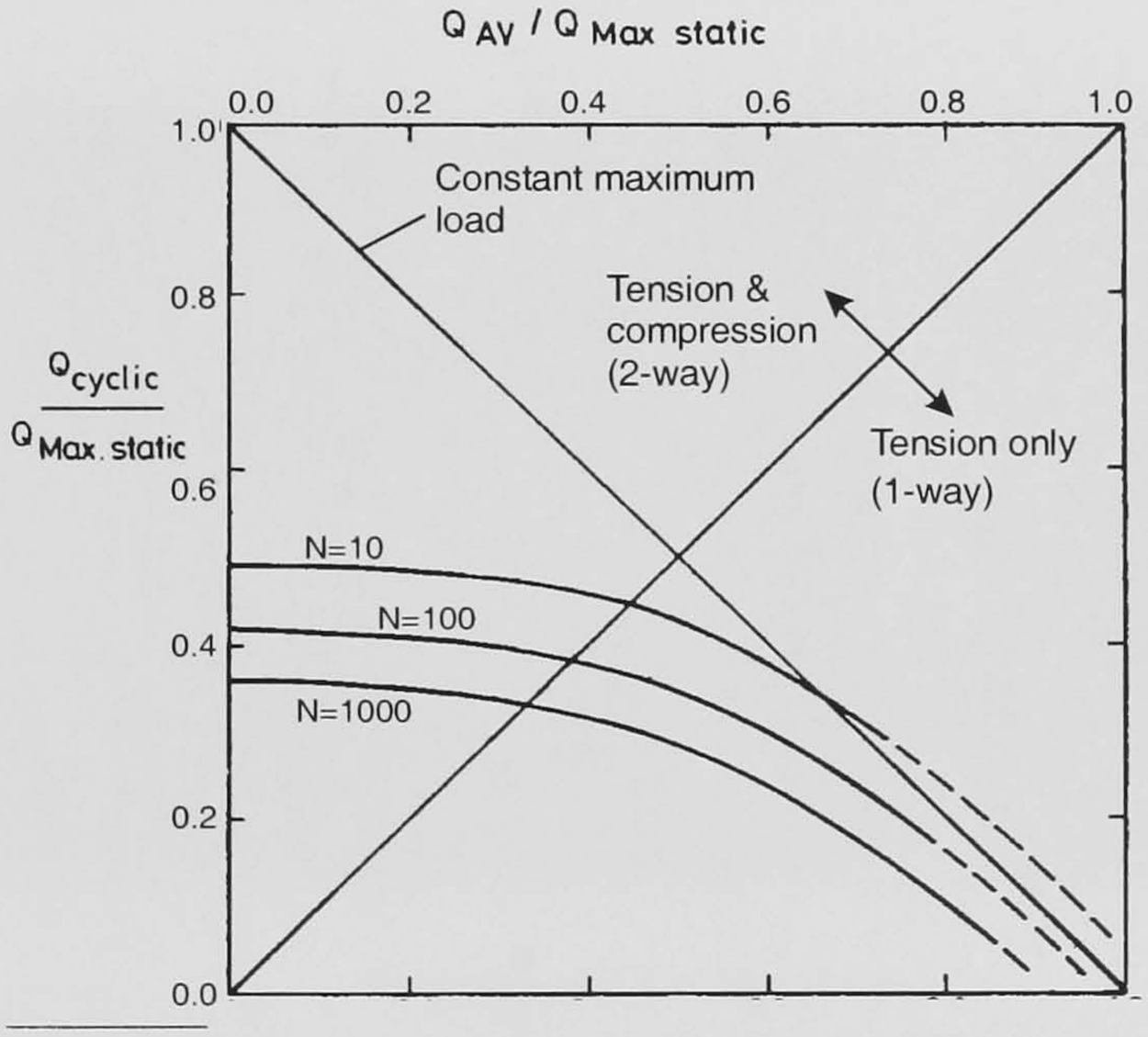


Fig. 2.22 Cyclic interaction diagram from Haga tension pile tests (Jardine, 1991 after Karlsrud and Haugen, 1983).

In an ID the two diagonal lines extending from the origin represent the boundary between one-way and two-way cycling. The orthogonal diagonal lines represent the case of cyclic capacity equal to static capacity. If the system (a soil sample, a pile element or a complete pile) behaves similarly in tension and compression the diagram is symmetrical. If not a second diagram is required to consider the transition from symmetrical tension/compression loads to fully compressive cycling – for the ID presented in Fig. 2.22.

The ID can describe several characteristics of pile response to cyclic loading, including: (i) any tendency for a smaller capacity under two-way cyclic loading than in one-way cyclic loading; and (ii) combinations of Q_c and Q_a that lead to permanent displacements and reductions in shaft capacity but not failure - the "meta-stable region" as described by Poulos (1988).

2.9 Pile capacity response with time

Time is an influential factor in pile capacity. Hjort and Carrillo (1985)[22] carried out repetitive load tests on driven piles in MC using different time intervals between tests (from 16 hours to 53 days)[23]. From the trends of the 13 tested piles presented in Fig. 2.23 Hjort and Carrillo concluded that re-tested piles recover after 1 day between 89% and 99% of the first loading capacity, and between 96% and 100% after 10 days. Hjort and Carrillo ascribe the recovery of capacity to thixotropic effects and consolidation.

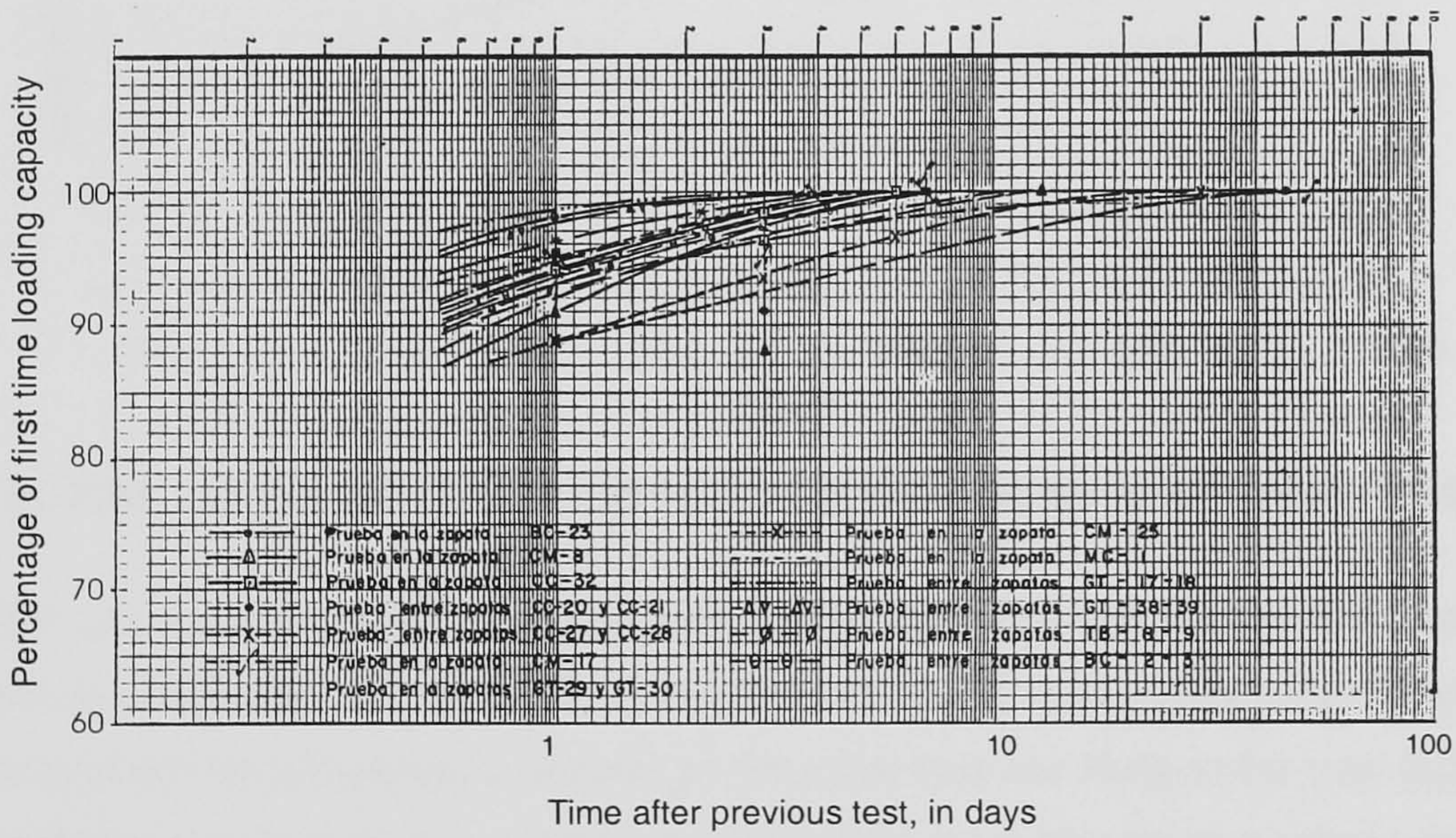


Fig. 2.23 Pile capacity recovery with elapsed time (Hjort and Carrillo, 1985)

Increases in pile capacity with time continue after the 53 days studied by Hjort and Carrillo. The research at IC has identified increments of up to 100% for a 16 years period at Canons Park (Pellew, 2002) and a 30% increment for a 6 months period in Kinnegar, Northern Ireland (Jardine, 2002).

---

[22] Linea 4 pile tests, which are included in the Author's validation of the ICPDM (Chapter 5).

[23] Hjort and Carrillo's goal was to determine the time after driving on which placement of the

An insigth into pile capacity increments over long periods of time in MC was given by Marsal and Masari (1962) who carried out tension tests on a square concrete pile at different times after pile driving. The tests were undertaken on a 10.5 m long pile section of which 4 m were within superficial fill and silts and the rest in MC clay. Table 2.3 and Fig. 2.24 show Marsal and Masari's results.

Table 2.3 Increment of pile capacity with time (Marsal and Masari, 1962)

	1st test	2nd test	3rd test
Mean shaft resistance at peak, kPa	10.8	16.7	17.7
Displacement at peak, mm	10.0	8.0	1.0
Ultimate mean shaft resistance, kPa	9.8	10.8	13.7
Displacement at ultimate resistance, mm	25	80	83
Test time, min	2.8	10.0	22.0
Test time after driving	39 min	47.8 days	248.9 days

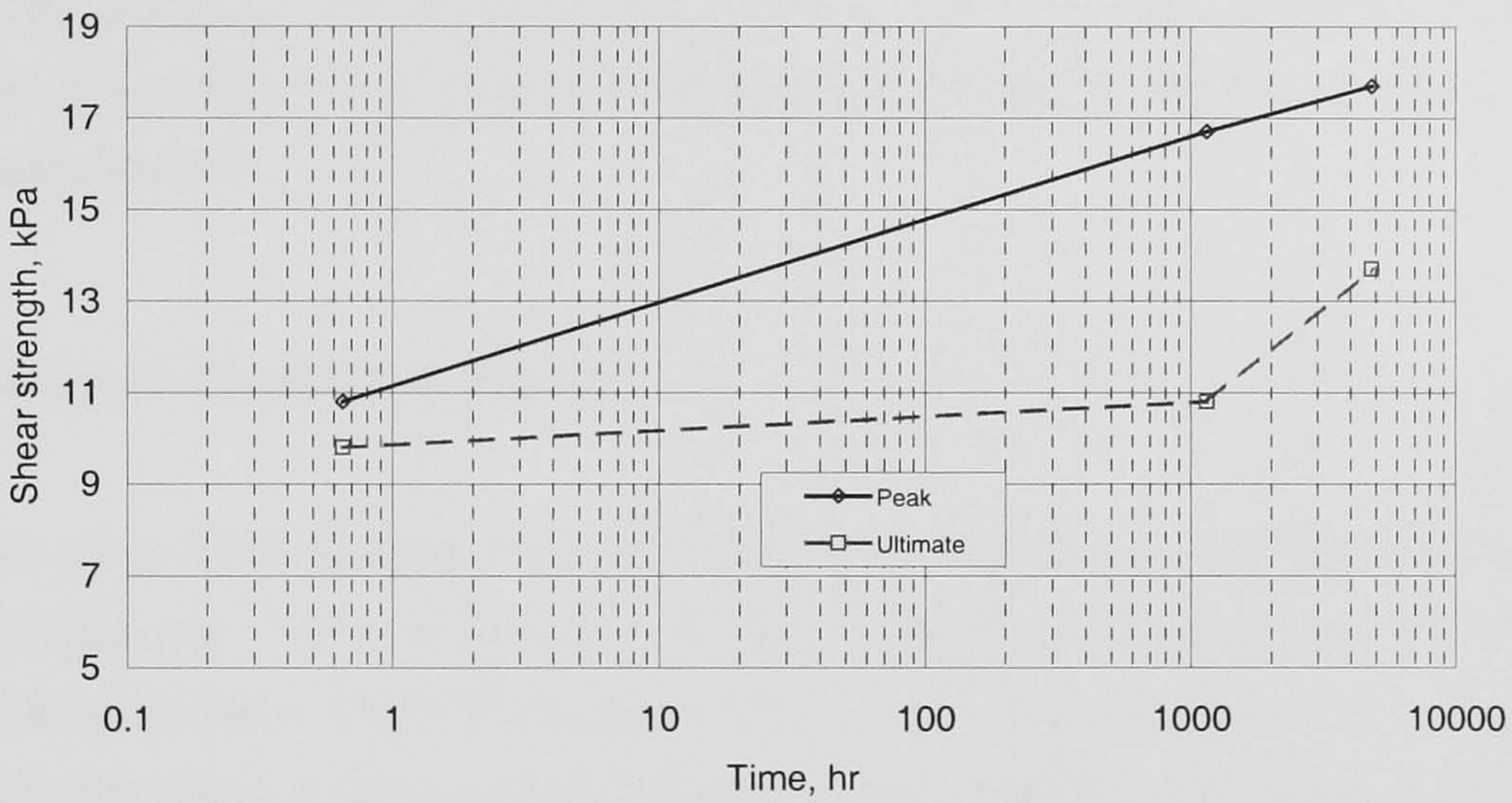


Fig. 2.24 Increment on pile capacity with time (Marsal and Masari, 1962).

After 201 days the increments in peak and residual pile capacities were 64% and 40% respectively. Between 47.8 and 248.9 days the increment in pile peak capacity was 6%. The increments on pile capacity respect to the initial test are likely to be over estimates as the initial test was probably carried out before full pore water pressure and radial total stress equalisation had developed. Marsal and Masari also observed pile capacity increments with time for wood and steel piles.

---

superstructure could commence.

CHAPTER 3

SUBSOIL CONDITIONS IN MEXICO CITY

Fundamental to the development of the research is the characterisation of Mexico City (MC) soils. This chapter summarises the geological origin, depositional conditions, post-depositional changes, mineralogical composition, and the main static and dynamic characteristics of MC soils with emphasis on the clayey soil deposits.

Differences in depositional conditions in the Valley of Mexico (VM) gave rise to clay strata with extreme ranges in the proportions of their constituents. As a result the clays' mechanical behaviour can change every few centimetres. However, since the clays share the same components it is possible to define ranges of typical behaviour, as described in the following sections.

3.1 Geology of the valley of Mexico

The basin of the VM is located at the south end of the Mexican plateau (Mesa de Anahuac or Central plateau). It has an area of 7,160 km^2, a length of 110 km in the N-S direction, and a width of 80 km in the E-W direction (Fig. 3.1). It is a closed basin that is bounded to the east by the plane of Apan and the Nevada Range, which has an altitude of about 5300 m above sea level. In the west and north-west the basin is bordered by the Sierra de las Cruces ranges (Monte Alto and Monte Bajo); to the north it is limited by the Tepotzotlan, Tezontlalpan and Pachuca ranges; and in the south by the Ajusco and Chichinautzin ranges, whose altitude is about 4,000 m above sea level. Inside the valley, the Guadalupe range extends as a peninsula eastward from the centre of the basin (forming the north limit of MC) and in the south, in an east-west direction, runs the Santa Catarina range. The lowest part of the city has an altitude in the order of 2,230 m above sea level (Zeevaert, 1988; Jaime, 1987).

An important feature in the basin was the existence of a network of large shallow lakes created by rivers and creeks that sprang from the surrounding mountains. Among the rivers, Cuatitlan, Tlalnepantla, de los Remedios, Churubusco, Texcoco and de la Compañía stood out. From north to south the lakes were: Zumpango[24], Xaltocan[24], San

---

[24] There still exist portions of the lake

Cristobal, Texcoco[25], Xochimilco and Chalco. The evolution of these lakes from the period of their creation (when the Chichinautzin range obstructed the Alto Amacuzac drain during the Pleistocene) until the end of the nineteenth century is depicted in Fig. 3.2.

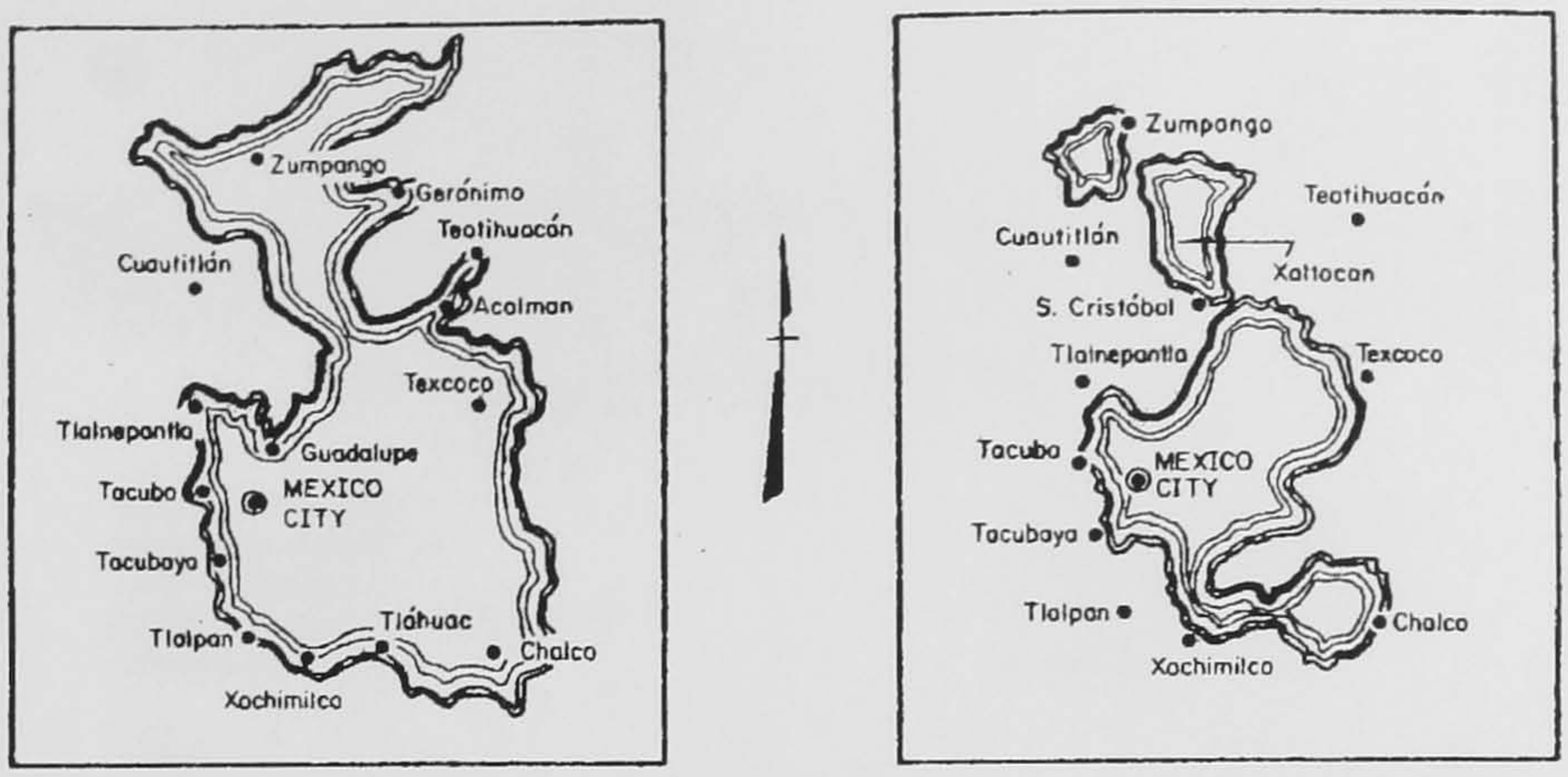


Fig. 3.1 Basin of the Valley of Mexico (Zeevaert, 1988)

The stratigraphic profile of the VM includes an upper layer of lacustrine clayey deposits whose thickness increases from north to south and reaches more than 150 m in the Xochimilco area. Underlaying these deposits there are clastic alluvial deposits, whose depths are between 200 and 350 m in central part of MC, and more than 700 m to the south of the city. Below these deposits there is a Stratified Serie (SS) constituted of strongly consolidated alluvial clastics (stiff clay, compact sand, sandstone and lacustrine limestone). Under the SS there are, successively, lacustrine deposits of the Pliocene and vulcanites of the Miocene and Oligocene. From 1,500 to 3,500 m depth there are Cretaceous marine sediments.

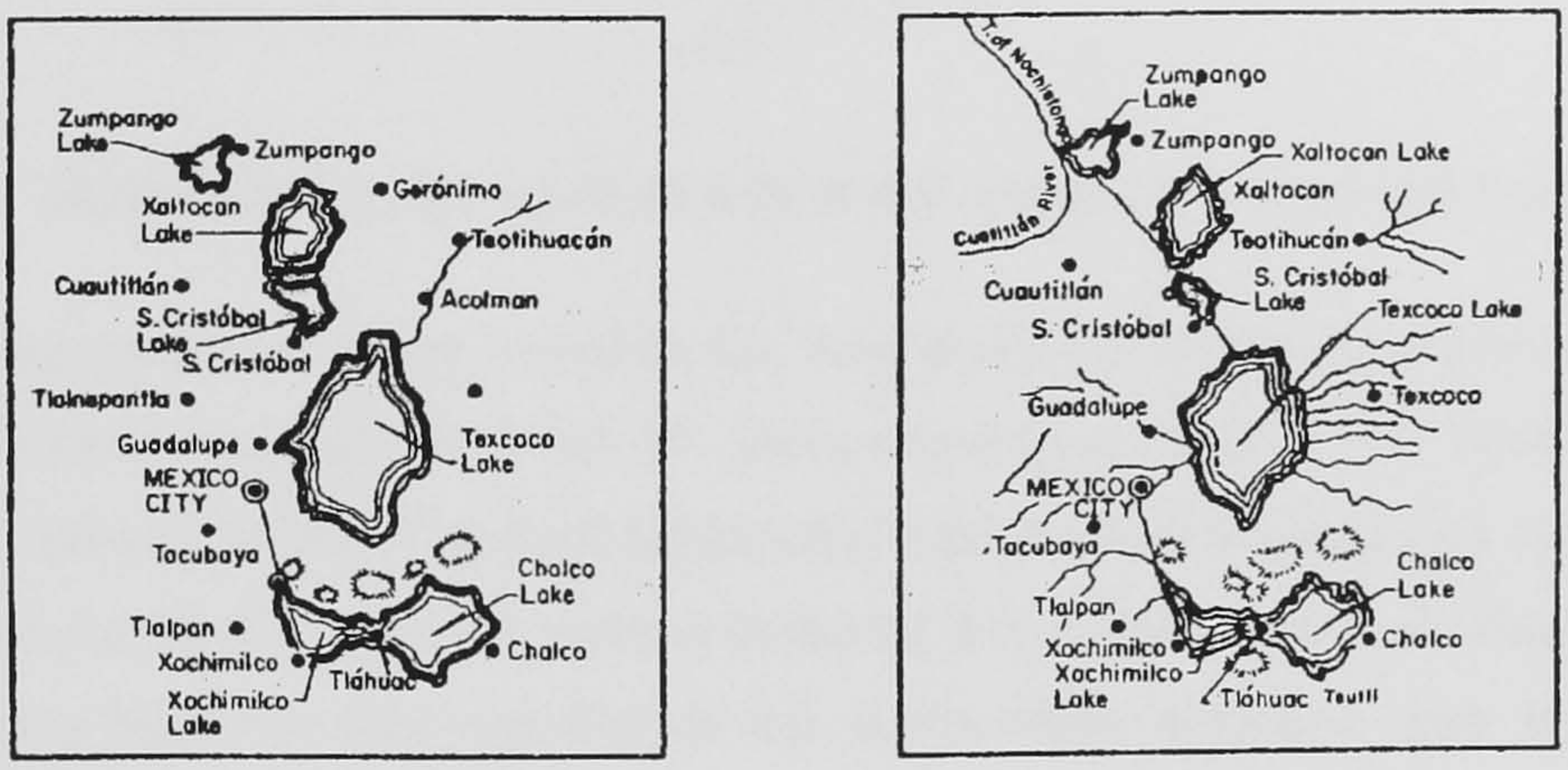
---

[25] Lake with high salinity



Approximate boundaries of the original lake

At the beiginning of the sixteenth century

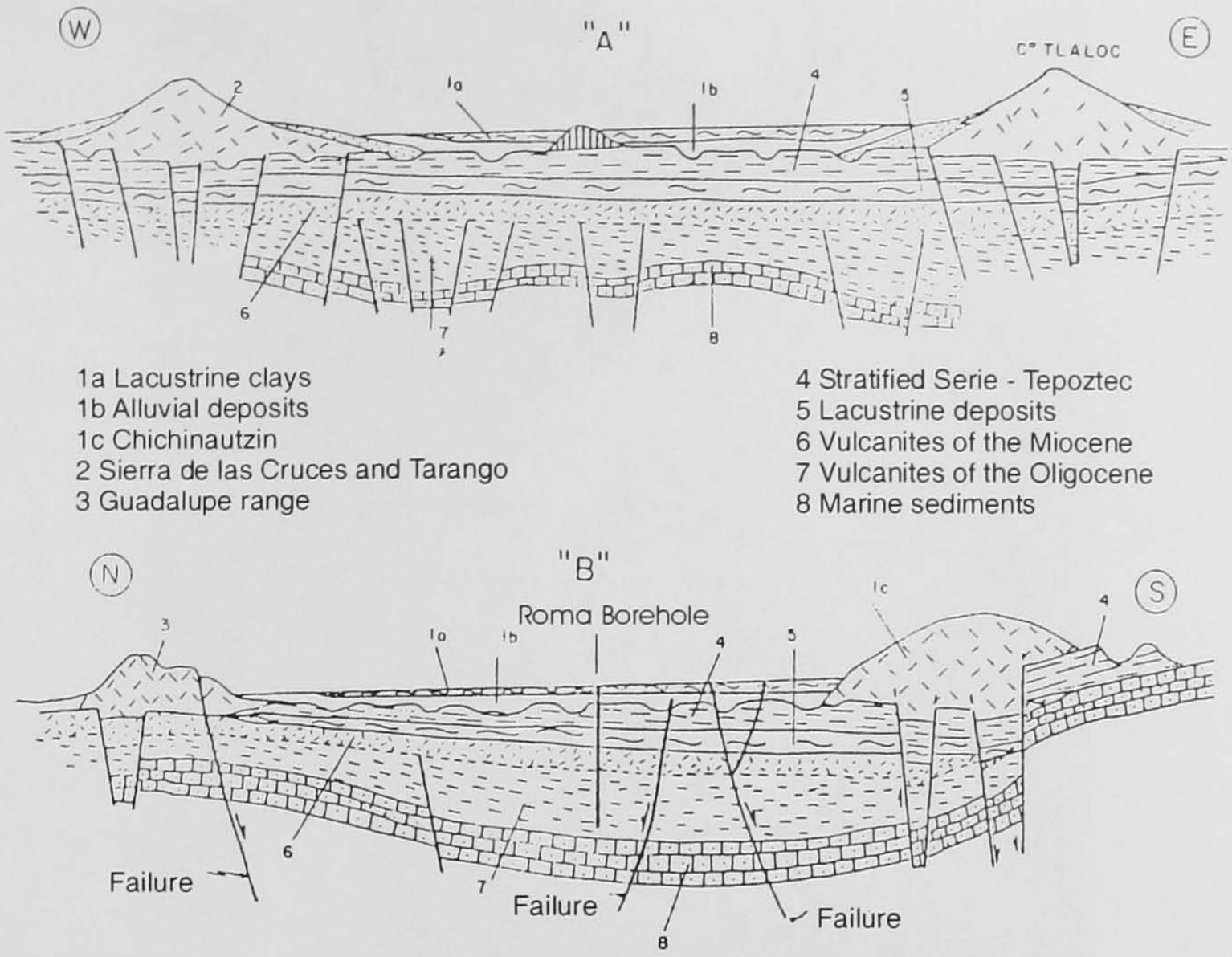


At the beginning of the nineteenth century

In 1889

Fig. 3.2 Evolution of the lakes in the Valley of Mexico (Jaime, 1987)

The sections in Fig. 3.3 show schematically most of the geological elements of the VM. Section "A" crosses through the south of Mexico basin, from the vulcanites of the Sierra de Las Cruces range in the west to the andesitic lava flows of the Nevada Range in the east. Section "B" starts in the west side of the Guadalupe range, which is constituted of vulcanites, crosses the urban plane and the basaltic range of the Chichinautzin and finishes in the Teposteco hill, whose origin is related to the Stratified Serie (Mooser, 1990).



1a Lacustrine clays
1b Alluvial deposits
1c Chichinautzin
2 Sierra de las Cruces and Tarango
3 Guadalupe range
4 Stratified Serie - Tepoztec
5 Lacustrine deposits
6 Vulcanites of the Miocene
7 Vulcanites of the Oligocene
8 Marine sediments

Fig. 3.3 Geological cross section along the Valley of Mexico (Mooser, 1990)

The clay strata originated when volcanic ash was deposited in the lacustrine environment (which contained important colonies of micro-organisms) during the middle to upper Pleistocene (Marsal, 1986). The hard lenses and gravel, sand, silt and silty clay strata that are found interbedded in the clay were created by the transportation of materials (mainly alluvial coming from the disintegration of the surrounding andesitic rock and fine sand sized pyroclastics) and by drought (due to changes in the level of the lakes).

3.2 Geotechnical zoning of Mexico City

The above mentioned factors give notice of a complex stratigraphical profile for the VM. There it is possible to find alluvial and lacustrine strata with different depositional conditions (e.g. variations in organic life and water saline concentration) and different post-depositional processes (e.g. desiccation produced by variations in levels of the lakes, rains and weather during several periods).

In 1959 Marsal and Mazari divided what then was MC into three zones: Hills, Transition and Lake (Marsal, 1986). Because the bulk of the available information was concentrated in the Texcoco lake area, the original definition of the Lake zone only included that lake area. However, due to the expansion of MC, the current official geotechnical zoning (Fig. 3.4) includes in the Lake zone the Xochimilco-Chalco lake, whose profile is different from that in Texcoco lake.

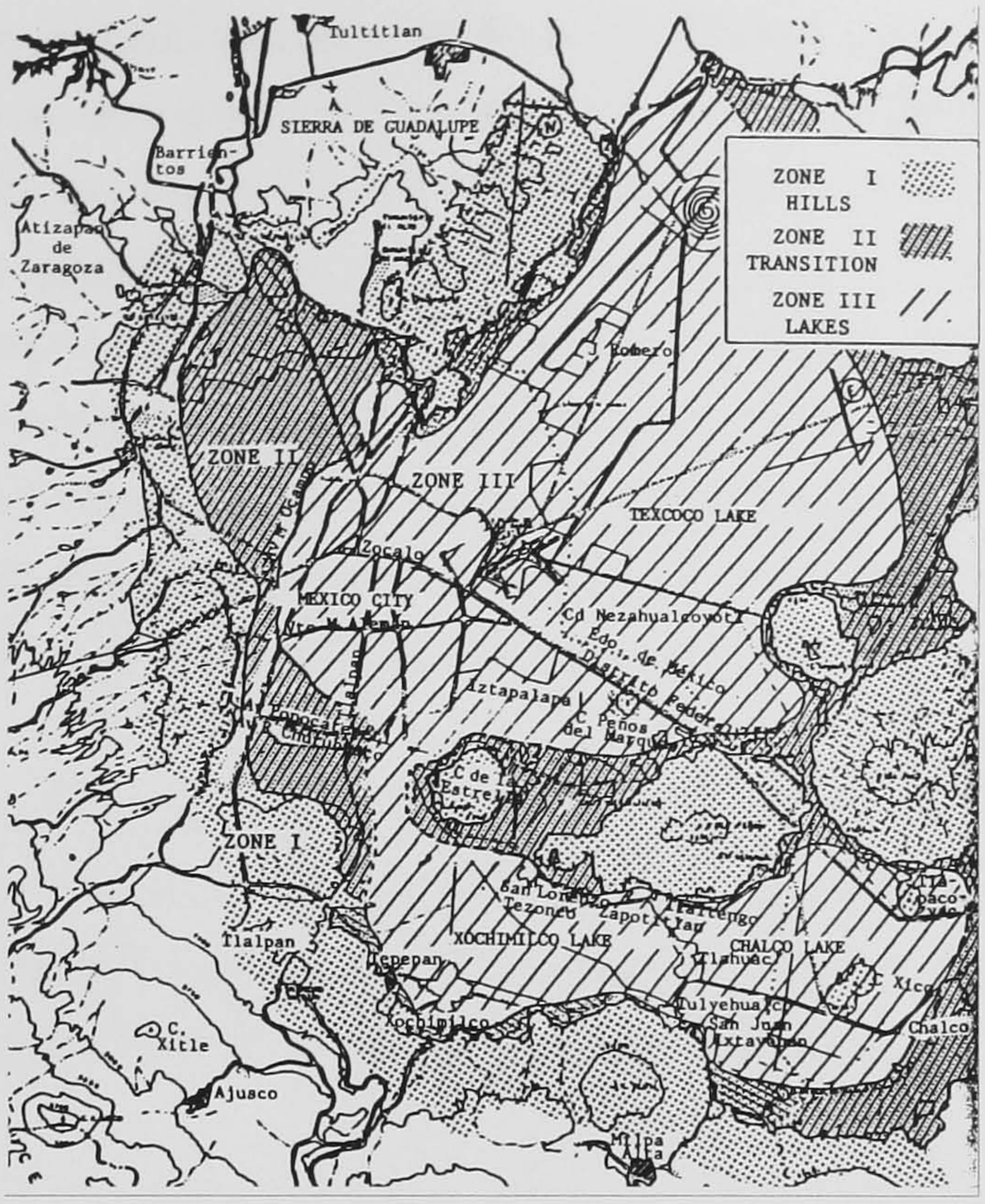


Fig. 3.4 Geotechnical zoning of Mexico City (Jaime, 1987)

The Hill zone, in the western part of the city, is characterized by dense sandy and silty soils, and by well-cemented pumice-type tuffs. In the south, the Hill zone is characterized by the basaltic lava flows of El Pedregal, which have a maximum thickness of about 20 m. Basalt is also found in the eastern region, in the foothills of Santa Catarina and in the vicinity of Chimalhuacan (Fig. 1).

The Transition zone, which extends between the Hill and Lake zones (Fig. 3.4), is typified by drastic stratigraphical variations where it is possible to find layers of dense silty and sandy materials alternating with very soft clay strata - of less than 10 m thick. The transition zone in some sites represents the advancing and receding cycles of the shores of Texcoco and Xochimilco-Chalco lakes; in other sites, it consists of deltaic deposits deriving from the eroded Hill zone materials.

The Texcoco Lake zone profile, where the studies of this research are focused, is composed of a 4 to 6 m thick surface stratum formed from the start of the Holocene and up to recent times. Below this stratum there are 30 to 40 m of the Upper Clay Formation (FAS)[26], which is formed of very soft[27] and compressible silty clay layers interbedded with thin lenses of sand. Below the FAS exists an alluvial stratum of dense andesitic sand,

---

[26] Known as “Tacubaya”

[27] The SPT tool penetrated by self weight at some depths

gravel and silt, with variable cementation given by calcium carbonates and clay, and thickness of up to 5 m - this first hard deposit (named "Tarango Sand I") represents a dry period coincident with the Sangamon interglacial (80,000 years b.p.). This sand stratum overlies the second typical silty clay deposit, which is known as Lower Clay Formation (FAI) or Tarango Clay I, with 4 to 14 m in thickness and high to medium compressibility. Finally, underlying the FAI there are very compact (more than 100 SPT blows/ft) alluvial deposits of cemented silty sands and gravels, called "deep deposits" or Tarango Sand II, whose simplified surface profile is presented in Fig. 3.5 – the figure also shows the Lake zone limits. A typical profile from the Texcoco lake zone is shown in Fig. 3.7.

Due to water pumping from the subsoil in the west side of the Texcoco lake, the clay on this area shows lower water contents and is less compressible. This affected zone, called Pre-loaded zone, is grossly located within the 25 m and the 50 m contour depths of Fig. 3.5; the remainder of the Texcoco lake zone is called Virgin zone.

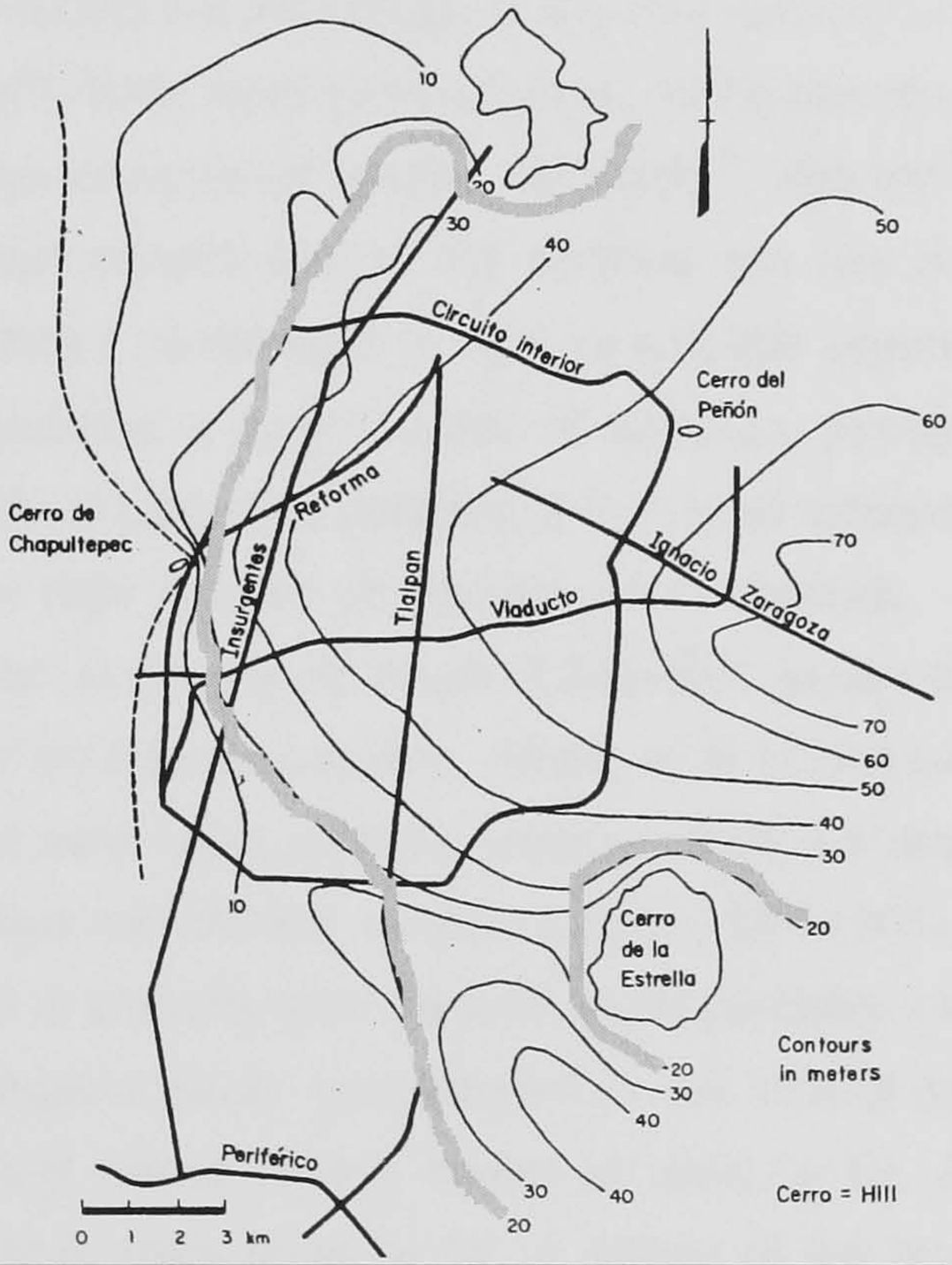


Fig. 3.5 Contours of equal depth of the "deep deposits" (Tarango Sand II) in Mexico City (Romo, et al. 1988)

The zone of Xochimilco-Chalco lakes is characterised by very thick layers of soft clay (somewhat stiffer than Texcoco lake clay) with interbedded thin layers of silty sand, silts and sands. Underlying this clayey deposit, whose thickness may reach in excess of 150 m, there is a lava flow rock that has the characteristics of basalt.

The deep deposits are considered, due to their relative stiffness, as the base of the soil profile in most engineering problems. Romo and Jaime (1986), Romo and Seed (1987, cited by Jaime, 1988) point out that in the evaluation of earthquake-induced ground motions it is sufficiently accurate, for practical applications, to assume that the half-space begins at this elevation - where the last important refractions and reflections of seismic waves take place.

3.3 Index properties

The mineralogical composition mainly determines the size, shape and surface characteristics of the soil particles. These characteristics, along with particle interactions with the fluid phase, control activity, plasticity, swelling, strength and hydraulic conductivity behaviour.

Several authors have studied the mineralogy of the clay forming the Upper clay formation (FAS) of MC. Zeevaert[28] (1949, cited by Mesri, et al., 1975) described it as an organic silty clay that contains large amounts of fossils, ostracods[29], diatoms[30] and volcanic glass. Zeevaert considered that around 40% of the particles are clay sized (50% of which is montmorillonite), and that it contained 5 to 10% of colloidal organic matter. Marsal and Mazari (1962), who analysed a large number of samples, pointed out that MC clay is constituted by 22 to 63% of clay sized particles, 3 to 21% of carbonate content, 1 to 7% of organic matter, and a high content of diatoms and ostracods. Marsal and Mazari's conclusions were similar, in general, to those of Zeevaert, except that they conclude that the clay content "might" be classified as illite. Mesri, et al. (1975) established that the clay consists of 5 to 10% of sand sized particles (most of which are calcareous ooliths), 55 to 65% of silt sized siliceous microfossils, mostly diatoms; 20 to 30% of clay-sized particles of which probably 10% is smectite type material (most probably montmorillonite) and the rest is biogenic or volcagenic silica; and between 5 and 10% of organic matter. Further studies by Leonards and Girault (1961), based on tests by Dr. J. L. White of Purdue University, Lo (1962) from tests done by Dr. J. Moum of the Norwegian Geotechnical Institute, and Gomez-Looh (1987) displayed further discrepancies. Zeevaert's description is the most generally accepted (Diaz-Rodriguez, et al., 1995).

After observing the scatter in the previous analyses, Peralta (1989) carried out electron

---

[28] Based on tests by Dr. R.E. Grim of the University of Illinois

[29] Calcium carbonate

[30] Unicellular plants, algae, with very porous shells made of silica.

microscope and X-ray diffraction analyses on clay samples recovered continuously from a 30 m long soil column. The analysis of 163 representative samples showed an extreme variability on the grain size distribution and mineralogical composition, even in samples spaced no more than five to ten centimetres in depth. Peralta concluded that it was not helpful to quote any definitive percentage of components or dominant clay mineral type and that the disagreement about the mineralogical composition was produced simply because every researcher analysed different material. Peralta classified MC clay as heterogeneous, volcagenic lacustrine clay and summarised the mineralogical components according to the particle size (Table 3.1).

Table 3.1 Mineral components of MC clay according to the particle size (Peralta, 1989)

Total samples	Poorly crystallised clayey material, illite, calcite, dolomite, plagioclase, quartz, cristobalite, hornblende
2-38μm Fraction	Montmorilonite, mica, illite, kaolinite and/or chlorite and clayey material probably poorly crystallised kaolinite. Calcite, dolomite, plagioclase, quartz, cristobalite and hornblende
0.2-2 μm Fraction	Poorly crystallised montmorilonite. Calcite, plagioclase, probably quartz. Cristobalite, probably kaolinite and/or chlorite deficiently crystallised
0.08 to 0.2 μm Fraction	Montmorilonite probably kaolinite and/or chlorite deficiently crystallised

When MC clay Atterberg limits are located in the plasticity chart, they show an extraordinarily extensive cloud of LL and PI values above and below the "A" line (Fig. 3.6), reflecting the variability of components described above.

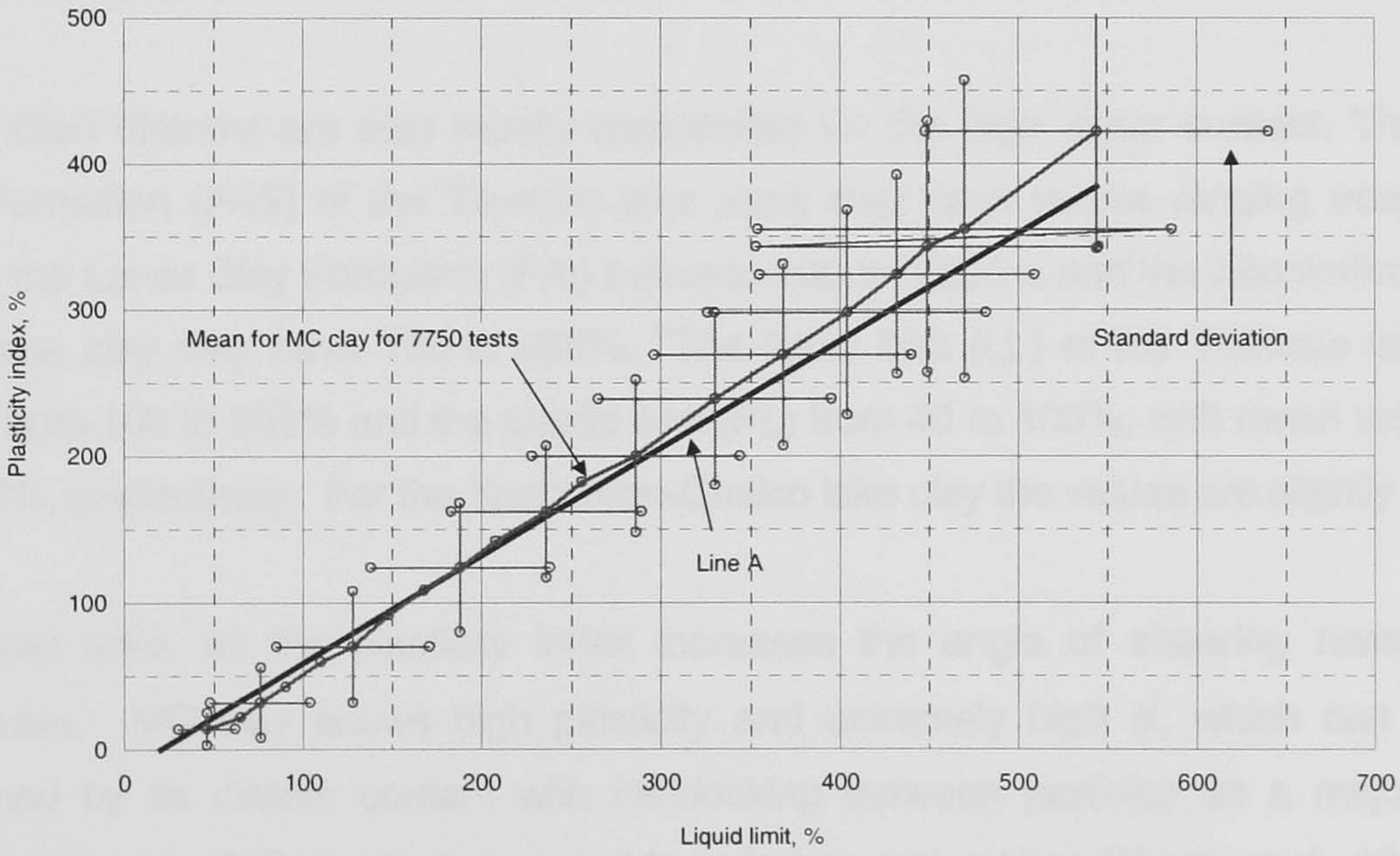


Fig. 3.6 MC clay on the plasticity chart (Marsal and Mazari, 1962)

An idea without disagreement, however, is that the three components that combine to give

MC clay its physical properties are organic matter, skeletal fragments of siliceous diatoms and clay sized active mineral particles.

Mesri, et al. (1975) pointed out that, among these components, the organic content plays the least significant role or at least its influence is overshadowed by the significant characteristics of diatoms and clay sized particles. For example, Mesri, et al. show that even after being treated with hydrogen peroxide (which removes the organic material) MC clay presented a plasticity index of 288% against 350% obtained from a sample in its natural state. In addition Mesri, et al. carried out two consolidation tests using two remoulded samples - one sample in its natural condition and another sample treated with hydrogen peroxide. The results of these tests show that after removal of organic content MC clay stabilized at very high void ratios and that the void ratio-effective stress relationship and low swelling characteristics are not substantially affected. Mesri, et al. concluded that the plasticity, compressibility and secondary consolidation are practically independent from the organic matter fraction. The organic content is responsible for the grey colour tones of fresh MC clay.

Skeletal fragments of diatoms are probably largely responsible for MC clay's unusual physical properties. The porous structure of the diatoms provides an open framework and a very high void ratio (from 4 to 12). The extreme lightness (specific gravity of 2.0) of diatom particles can account for the relatively low specific gravity of MC clay samples (average 2.4 with extreme values of 2.1 and 2.6) and unit weights varying from 11.3 to 12.7 kN/m^3 (Mesri, et al.; 1975).

Water filled diatoms are also mostly responsible for the high water content. The Upper Clay Formation (FAS) of the Texcoco lake zone may have values ranging from 150 to 500%, the Lower Clay Formation (FAI) between 100 and 200% and the Xochimilco-Chalco lake zone clay may have 150 to 350%. The liquid limit (LL) of the Texcoco lake clays range from 100 to 500% and the plastic limit (PL) from 40 to 100%, with mean values 236 and 76%, respectively. For the Xochimilco-Chalco lake clay the values are slightly smaller.

For most soils, as the plasticity index increases the angle of shearing resistance ϕ' decreases. MC clay shows high plasticity and extremely high ϕ', which can only be explained by its diatom content with interlocking between particles as a major factor. Diatoms also give MC clay its cream and fawn to iron-rust colours (Mesri, et al., 1975).

With respect to the clay-sized fraction Mesri, et al. (1975) suggested that it is inter-layered with aluminium, iron and possibly magnesium hydroxide complexes. Mesri, et al. pointed

out that swelling of montmorillonite clays is greatly reduced by interlayer material and that this is entirely consistent with the observed swelling behaviour of MC clay which is typically 10 times smaller than its compression behaviour. Furthermore, Mesri et al. consider that the thixotropic behaviour of MC clay is probably partly due to reorganisation and reorientation of these interlayered materials.

3.4 Mechanical properties

3.4.1 Yield stress ratio (YSR)

Yield stress ratio is the apparent OCR, which generally exceeds the true geological OCR due to ageing and cementing. YSR is defined in terms of σ_{vy}', the one-dimensional effective yield stress shown by undisturbed samples and σ_{v0}' the effective overburden pressure:

$$YSR = \frac{\sigma'_{vy}}{\sigma'_{v0}} \tag{3.1}$$

While ground water is encountered at shallow depth in the VM, it is common to find that the pore-water pressures at depth fall well below hydrostatic values. In the city area extraction (by pumping) of water has created strong reductions in the piezometric levels, particularly close to the first hard sand layer and the deep deposits. The surface water table has remained unaltered due to the permeability gradients within the thick clay deposit. The upper water bearing strata are supplied by inflow from rain and the ruptured present sewage system (Fig. 3.7).

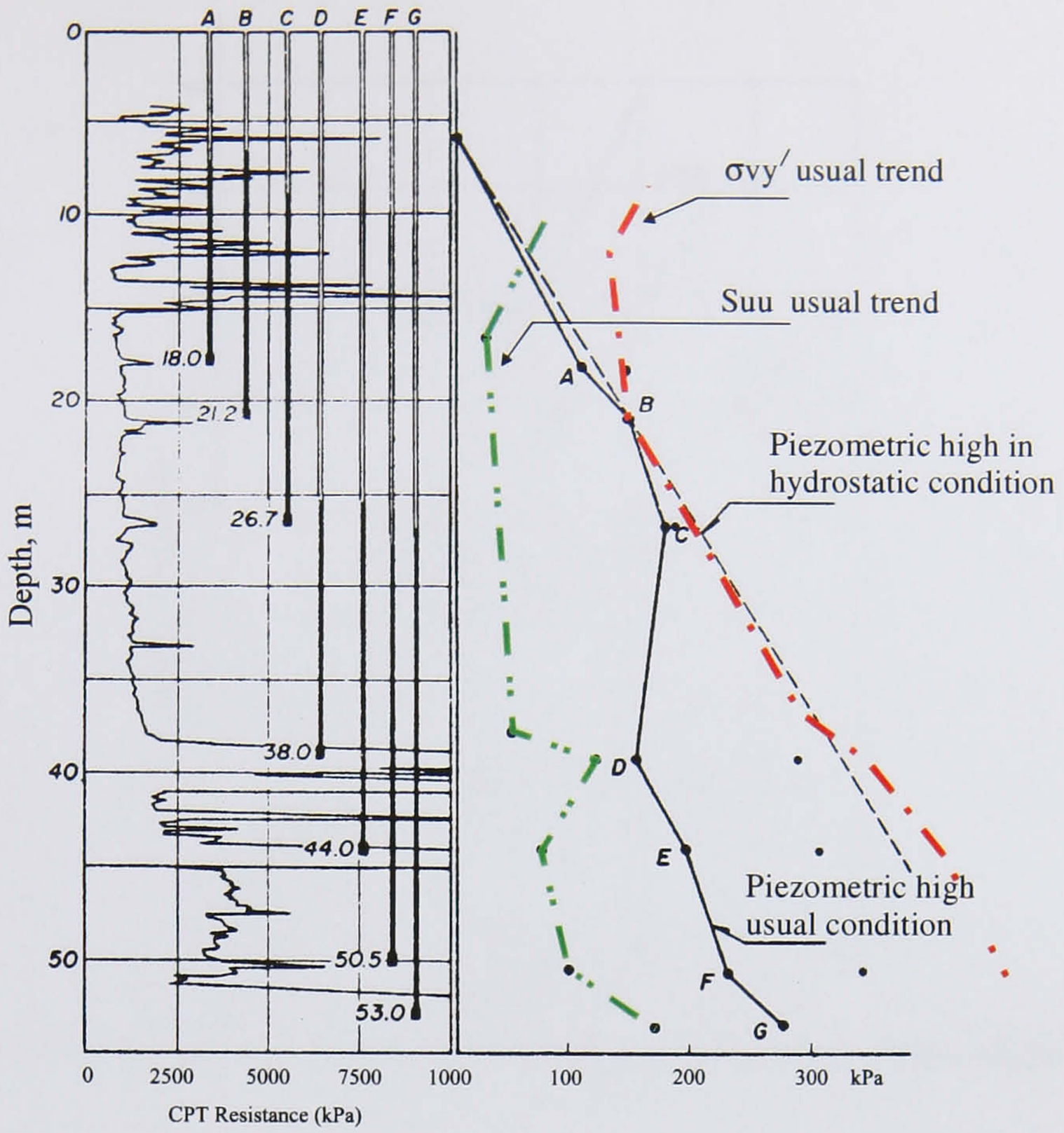


Fig. 3.7 Typical profiles of piezometric levels, σ_{vy}', S_{uu} and CPT test in Mexico City (After Santoyo and Gutierrez, 1990)

Undisturbed MC clay could be considered a geologically normally consolidated deposit. However, determinations of yield stresses through oedometer tests indicate an effective vertical yield stresses σ_{vy}' greater than the current values of σ_{vo}'. These differences may be due to various factors, including ageing[31], water table variation (pumping stopped in some parts of the city in the 1950's), thixotropy and cementation. Fig. 3.8 from Zeevaert (1983) presents relationship between the existing overburden effective stress and the yield stress (critical stress in the graph). Zeevaert pointed out that $\sigma_{vy}' > \sigma_{vo}'$ except at those places where the effective overburden stress had increased markedly recently. Mexico City's typical silty clay hardens under long term sustained loading. Fig. 3.8 shows the recognised Zeevaert's YSR trend for MC clay, giving values in the range 1.4 to 2.0. Zeevaert did not consider sampling disturbance and test method effects in this analysis.

In general, the yield stress profile in the upper clay formation in MC shows a decrement with depth until some few meters from the first sand stratum where it starts growing steadily (Fig. 3.7).

---

[31] More pronounced in more plastic clays.

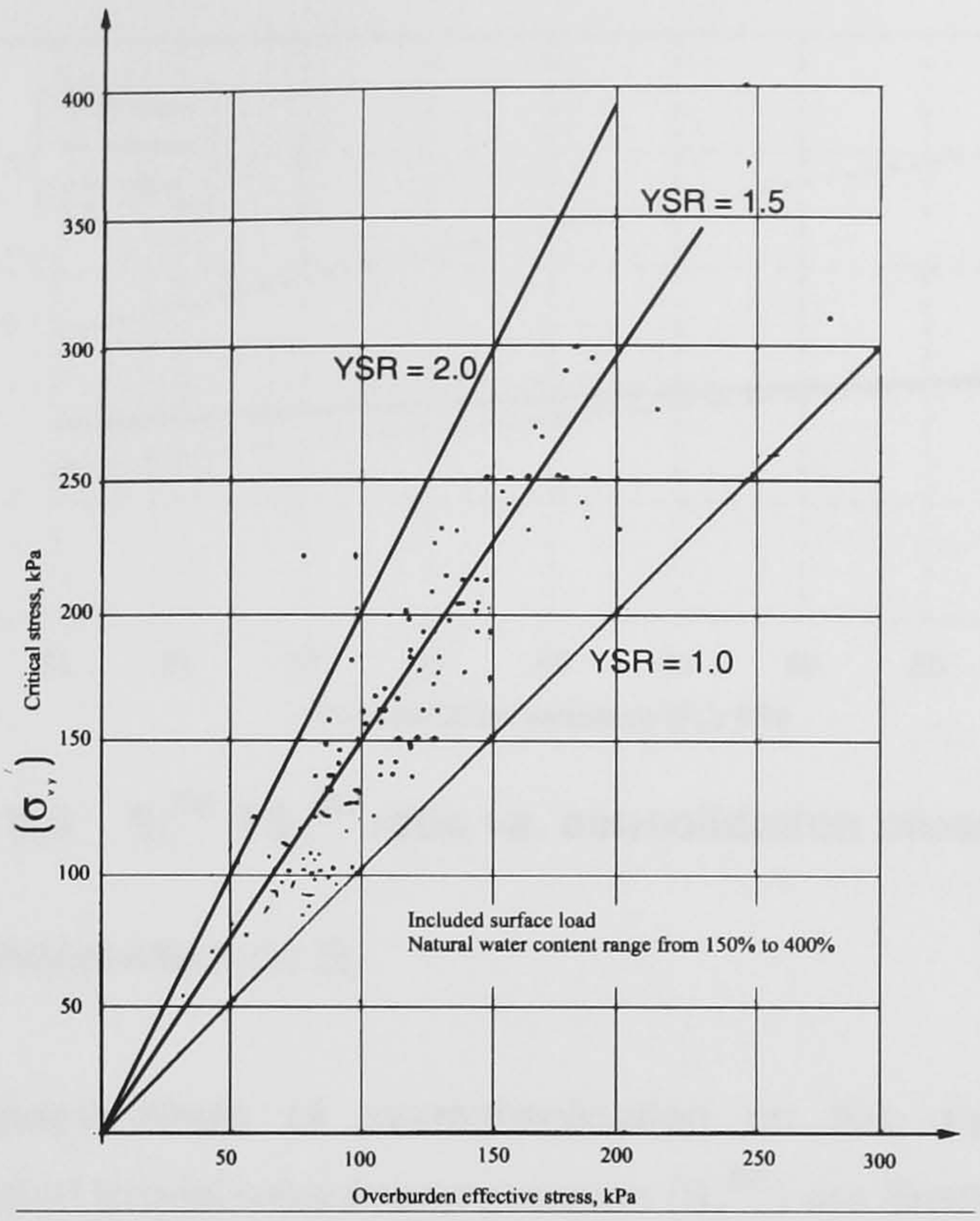


Fig. 3.8 Relationship between the yield and overburden stresses (Zeevaert, 1983)

3.4.2 Undrained shear strength

3.4.2.1 Unconsolidated undrained vs. consolidated undrained shear strength

The ratio between the undrained shear strengths determined in unconsolidated undrained (UU) and isotropically consolidated undrained triaxial compression tests (CIC) for MC clay is evaluated using data from Jaime, et al. (1988). Table 3.2 shows representative results obtained under three consolidation pressures. The data indicate that the S_u^{CIC}/S_u^{UU} ratio depends on the relation between the consolidation and overburden pressures; S_u^{CIC}/S_u^{UU} ratios near to one correspond to a mean consolidation pressure (p_0') close the in situ overburden effective pressure (σ_{v0}') (Hight, et al., 1987). Fig. 3.9 shows the variation of S_u^{CIC} with consolidation pressure. S_u^{UU} increases with depth and with reductions in water content.

Table 3.2 CIC vs. UU shear strength ratios (Jaime, et al. 1988)

Sample characteristics				S_u^{CIC}			S_u^{UU}	S_u^{CIC}/S_u^{UU}		
Depth	w	σ_{v0}'	σ_{vy}'	p_0', kPa						
m	%	kPa	kPa	20	40	60	kPa			
7.75	456	50	78	27	37	45	22	1.23	1.68	2.05
10.75	377	56	78	27	36	44	42	0.64	0.86	1.05
15.25	269	65	109	58	66	73	70	0.83	0.94	1.04

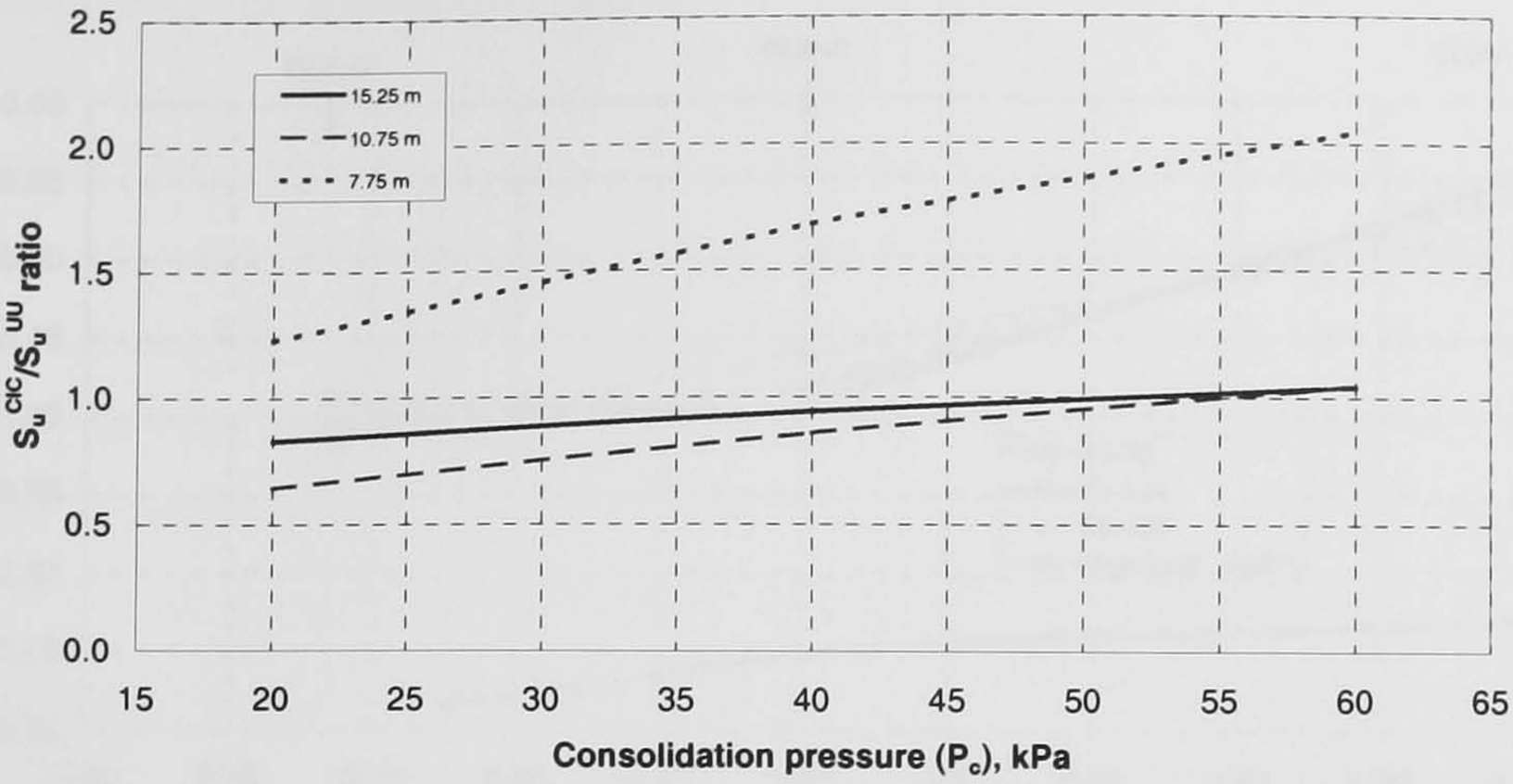


Fig. 3.9 S_u^{CIC} / S_u^{UU} ratio vs. consolidation pressure

3.4.2.2 Overconsolidation effect on S_u

The effects of different levels of overconsolidation on the undrained strength of isotropically consolidated triaxial tests in compression (S_u^{CIC}) are illustrated using data from Giraldo (1996). The tests were consolidated to OCR=1.0 and then tested under compression, or swelled back and tested under compression. Table 3.3 summarises the test conditions and results. (P_p is the mean preconsolidation pressure.)

Table 3.3 indicates a typical trend in which the normalised undrained strengths follow similar relationships with OCR irrespective of their PI's. Figs. 3.10 and 3.11 present these trends, with S_u^{CIC}/p_p' and S_u^{CIC}/p_0' ratios of 0.5 for normally consolidated MC clay. This values are higher than that for Bothkennar clay 0.307 and 0.21 in triaxial compression and extension, respectively (Smith, 1992); or 0.3 and 0.20 suggested by the relationship for normally consolidated clay published by Hight, et al, (1987). Although the MC clay shows high S_u/p_0' ratios, the variation with OCR is the typical for clays (Fig. 3.12).

Table 3.3 Normally consolidated vs. over-consolidated undrained shear strengths (Giraldo, 1996)

	OCR	w, %	p_0', kPa	S_u^{CIC}, kPa	S_{uOC}/S_{uNC}	S_u^{CIC}/p_p	S_u^{CIC}/p_0'
Depth=12.8 m	1	173	170	92	1.00	0.54	0.54
σ_{vy}' = 95 kPa	2	226	127	106	1.15	0.42	0.83
PI=78%	6	233	42	99	1.08	0.39	2.36
Depth=21.6 m	1	266	250	138	1.00	0.55	0.55
σ_{vy}' = 140 kPa	2	253	120	100	0.72	0.42	0.83
PI=154%	6	216	42	103	0.75	0.41	2.45
Depth=33.8 m	1	142	400	208	1.00	0.52	0.52
σ_{vy}' = 160 kPa	2	144	200	176	0.85	0.44	0.86
PI=168%	6	99	67	153	0.74	0.38	2.28

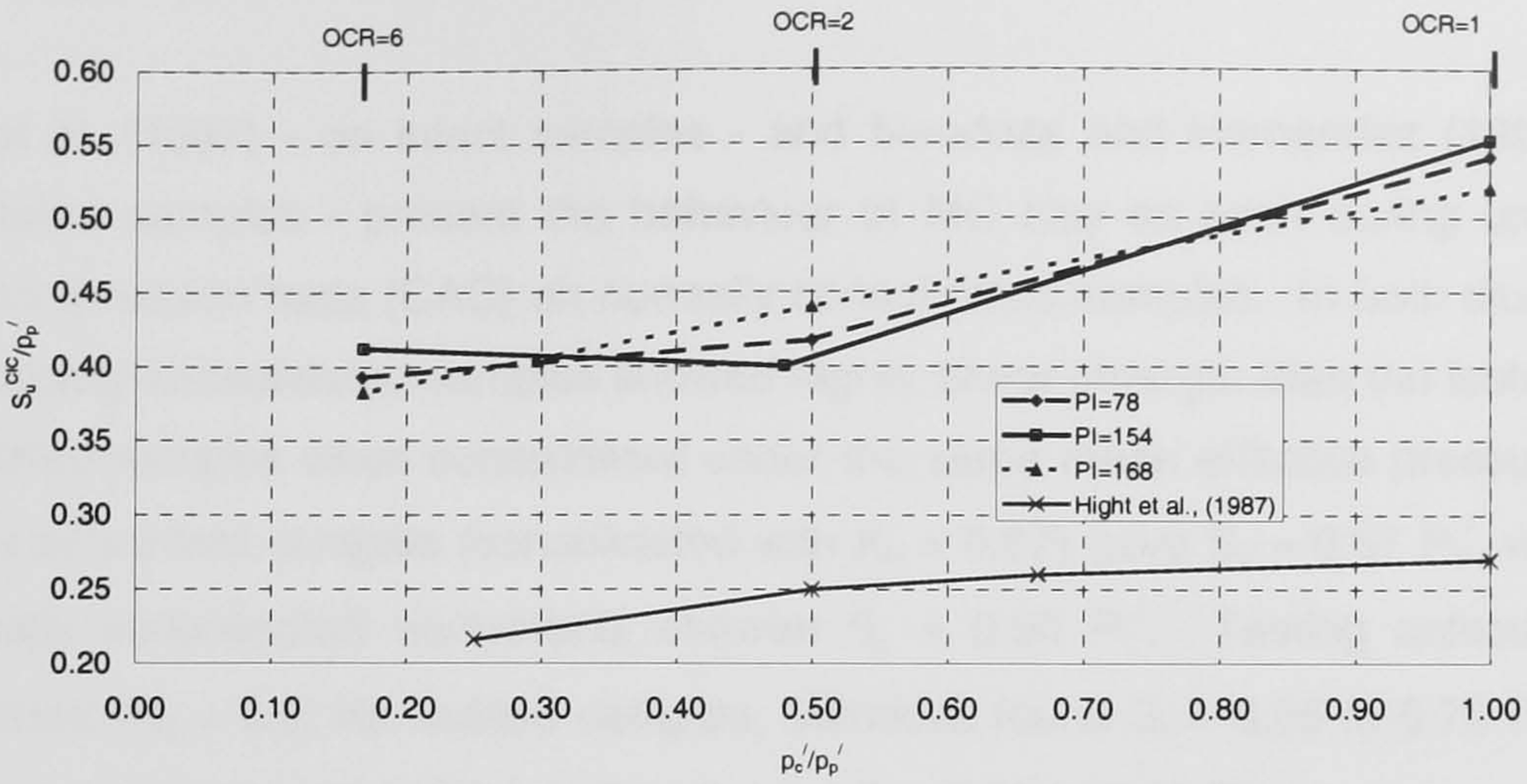


Fig. 3.10 S_u^{CIC} / p_p' vs. normalised consolidation pressure for MC clay

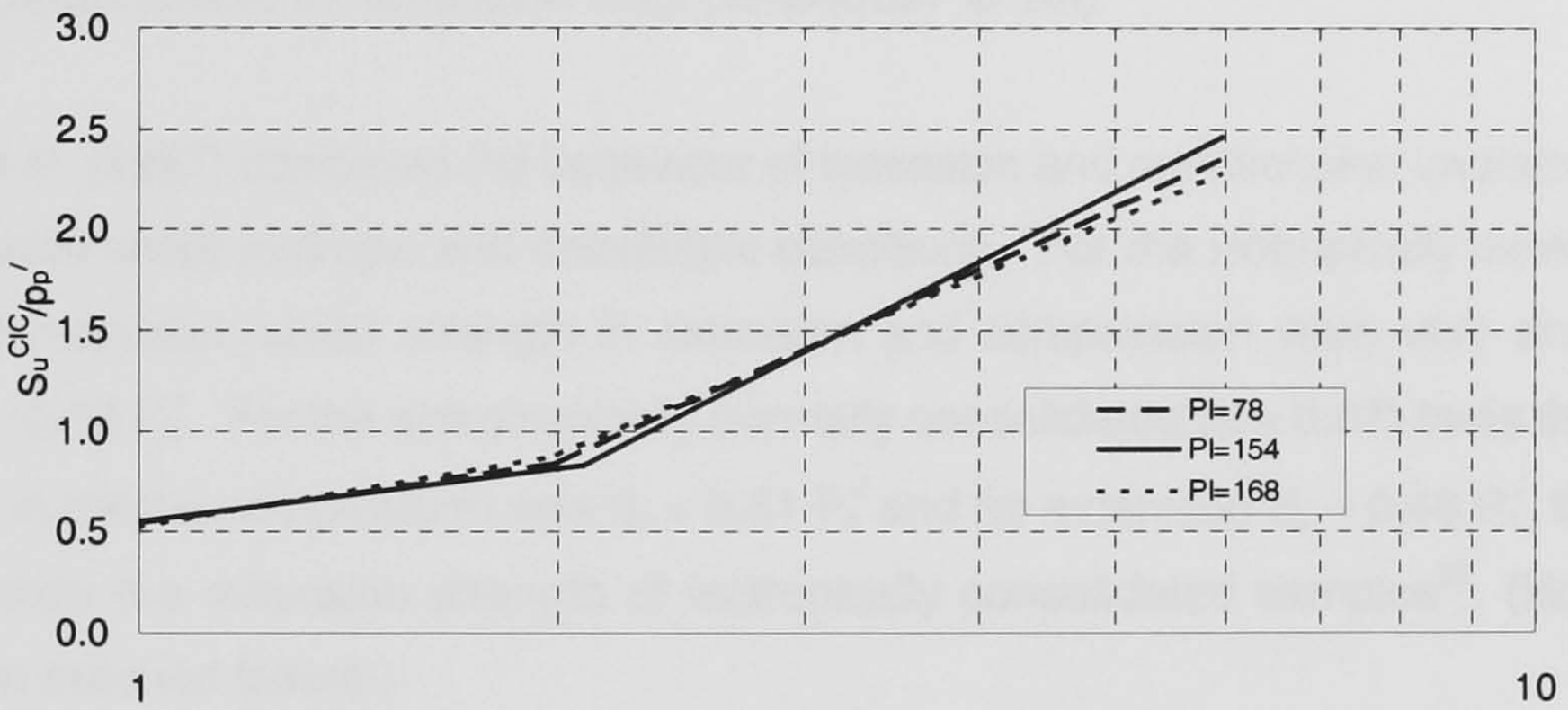


Fig. 3.11 S_u^{CIC} / p_p' vs. OCR for MC clay

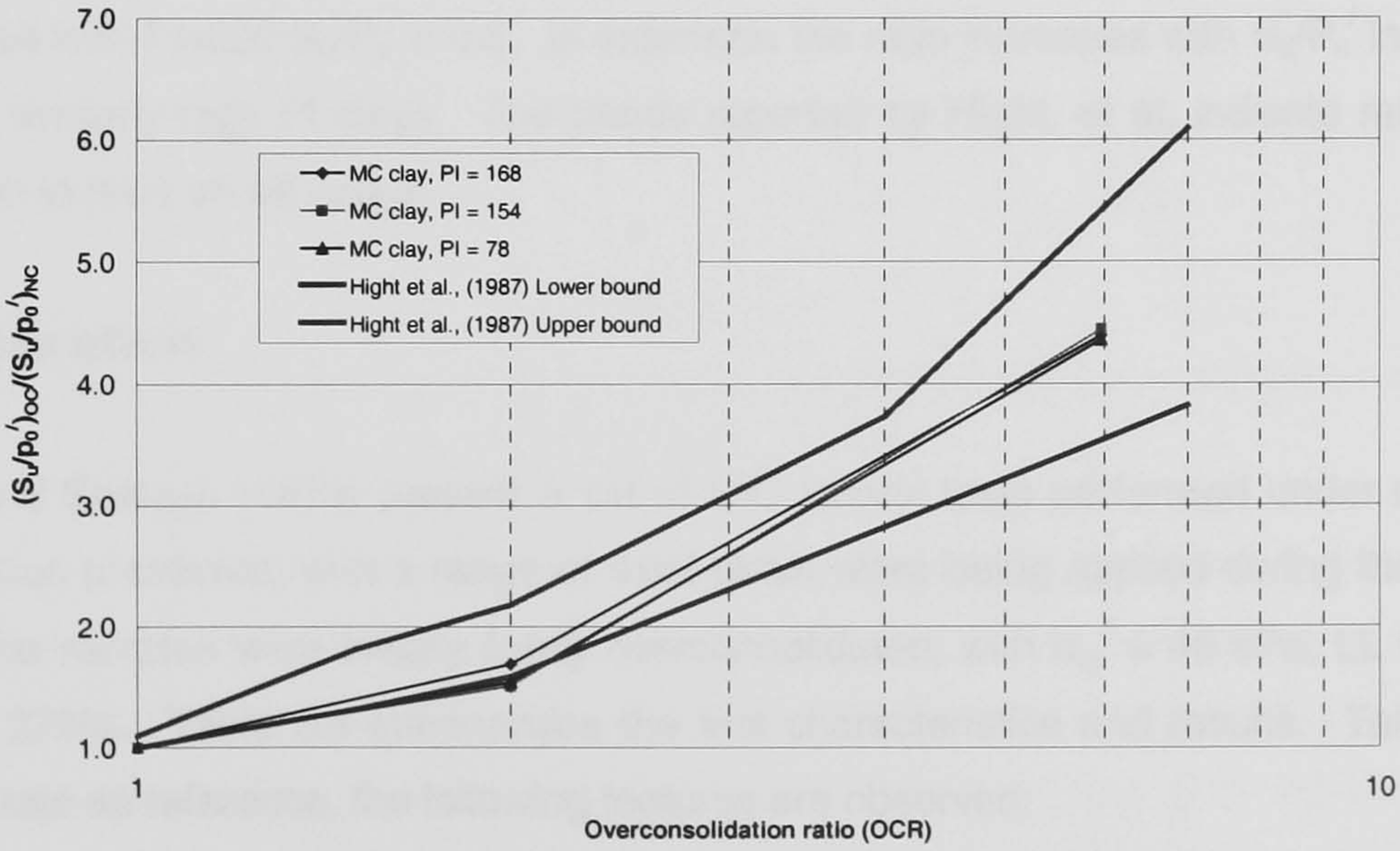


Fig. 3.12 Isotropic $(S_u/p_0')_{OC} / (S_u/p_0')_{NC}$ vs. OCR for MC clay and clays of different plasticity

3.4.2.3. Anisotropic consolidation effect

Rojas, et al. (1987) - on intact samples - and Mendoza and Hernandez (1992) - on reconstituted samples - present the behaviour of MC clay as seen during undrained triaxial compression tests (CAC) on normally consolidated samples. In both studies the anisotropically consolidated samples showed higher shear strength than the isotropically consolidated samples when consolidated under the same mean effective pressure (P_c'). Rojas, et al.'s intact samples (consolidated with $K_0 = 0.67$) gave $S_u \approx 0.57\ P_c'$, while the isotropically consolidated equivalents showed $S_u \approx 0.50\ P_c'$. Testing anisotropically consolidated ($K_0 = 0.5$) remoulded samples, Mendoza found $S_u \approx 0.65$ to $0.70\ P_c'$, while for his isotropically consolidated samples showed $S_u \approx 0.50$ to $0.60\ P_c'$.

3.4.2.4 Compression vs. extension tests (Anisotropy effect)

Rojas, et al. (1987) compared the behaviour of extension and compression undrained tests consolidated under isotropic and anisotropic conditions. For the isotropically consolidated tests the maximum shear strength in extension and compression were very similar, for both $S_u \approx 0.50\ P_c'$. For the anisotropically normally consolidated ($k = 0.67$) tests the shear strength in triaxial compression was $S_u \approx 0.61\ P_c'$ and for extension $S_u \approx 0.46\ P_c'$, the latter falling below the extension strength of isotropically consolidated samples[32]. (No test in extension reached failure.)

Hight, et al. (1987) found that in compression the S_u/P_c' ratio for reconstituted anisotropically consolidated ($K_0 = 0.5$) samples reduces with PI, a trend that predicts that for samples with PI≈200 $S_u/P_c' = 0.3$. In extension the ratio increases with S_u/P_c' indicating 0.225 for similarly high PI clays. The trends reported by Hight, et al. indicate ratios half those seen in tests on MC clays.

3.4.2.5 Rate effects

Alberro and Santoyo (1973) present a set of CIC triaxial tests performed under different consolidation pressures, with a range of axial strain rates being applied during the failure stage. The samples were initially lightly overconsolidated, with $\sigma_{vy}' = 45$ kPa, LL = 343% and PI = 279%. Table 3.4 summarises the test characteristics and results. Taking the 1.88 %/h rate as reference, the following features are observed:

---

[32] Note that triaxial compression after triaxial extension gives approximately the same S_u. This indicates that sampling damage may not be severe.

i) There is a clear trend for S_u to increase with the strain rate - Fig. 3.13 shows the strain rate vs. S_u^{CIC} normalized by the S_u^{CIC} under 1.88 %/hr rate. MC clay agrees with the general criteria that the undrained strength of clay increases between 5 and 15% for a log cycle increment of time to failure (Hight, et al. 1987).
ii) The strain to mobilise peak S_u^{CIC} is hardly affected by the rate of strain.
iii) Stiffness also appears to increase with rate of strain.

Table 3.4 Consolidated undrained triaxial tests at different strain rates during failure stage (Alberro and Santoyo, 1973)

Test No.	w %	P_c kPa	Strain rate (%/hr)	S_u^{CIC} kPa	Time to failure, hr	Strain at failure, %	Rate effect on S_{UU}
1	407	25	94	21	0.034	3.2	1.17
2	407	50	94	32	0.07	6.6	1.19
3	408	100	94	58	0.076	7.1	1.18
4	387	25	1.88	18	1.7	3.2	1.00
5	406	50	1.88	27	3.19	6.0	1.00
6	389	100	1.88	49	3.72	7.0	1.00
7	403	25	0.045	13	75.6	3.4	0.72
8	410	50	0.045	23	124.4	5.6	0.85
9	398	100	0.045	44	175.6	7.9	0.90

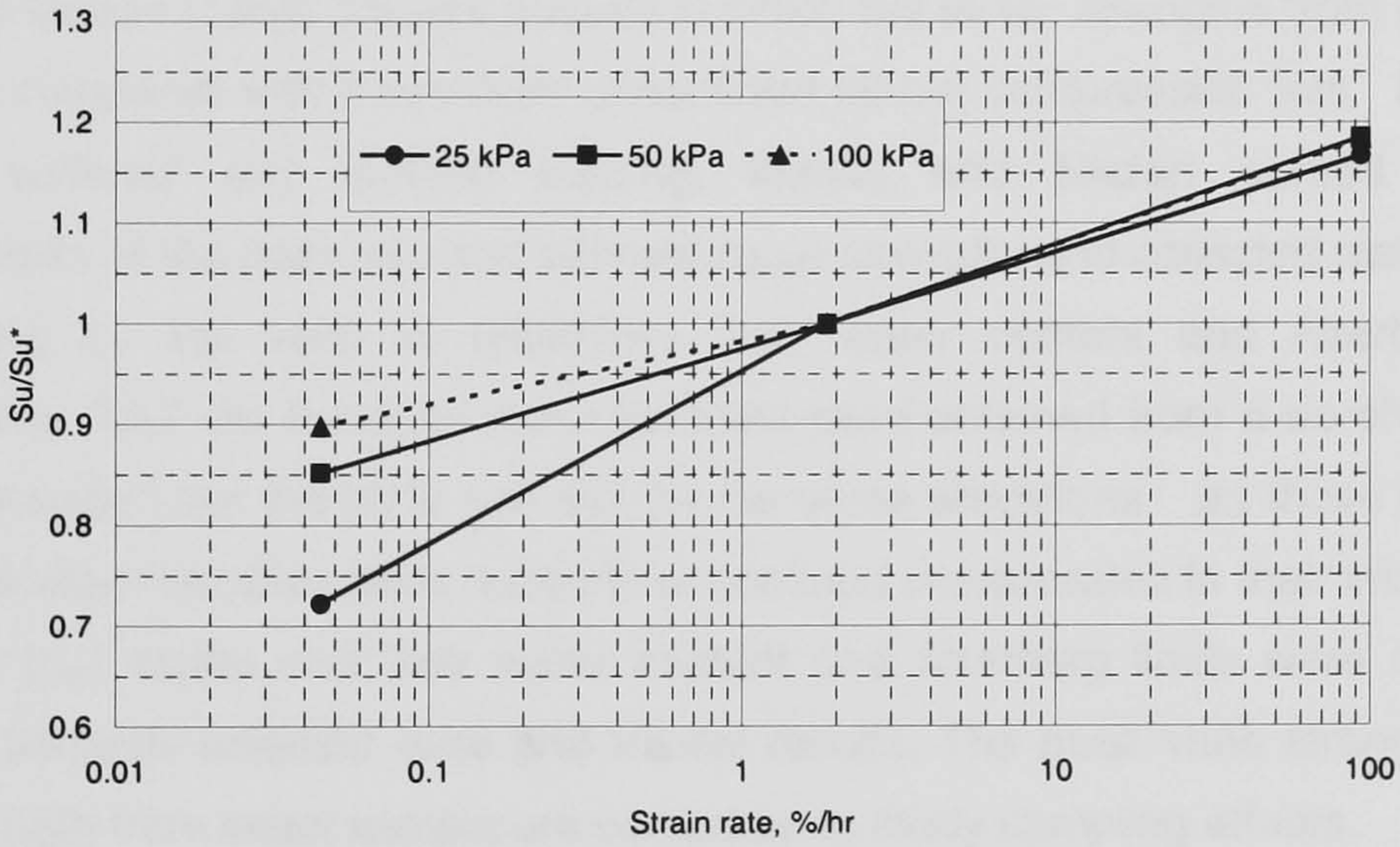


Fig. 3.13 Rate effect on Mexico City clay undrained shear strength (After Alberro and Santoyo, 1973)

According to Mitchell (1976) the rate effect increases as the PI and water content of the clay increase, and its magnitude is typically of the order of 5 to 10% for each order of magnitude of increase in the strain rate – for MC clay it is 10%. Wood (1982) suggested the following explanation: "it seems reasonable that slower cycles give the clay, as a viscous material, more time to follow the applied load and are likely to produce greater strains and greater pore pressures" (Dobry and Vucetic, 1988). Ishihara (1996) pointed out that for cohesive soils the rate effect becomes important for shear strains higher than

10^{-3} %.

3.4.2.6 Cone penetration test vs. S_u^{UU}

The CPT base resistance, q_c, can be correlated to S_u^{UU} by means of the cone factor N_k (= q_c/S_u^{UU}). Santoyo (1989) proposed the following N_k values for each typical stratum in MC: for the surface stratum N_k=14, for stiff clay[33] N_k=24, and for soft clay N_k=13. These factors must be modified to take into account the sample OCR, its disturbed condition and the drying during transport and preparation of the laboratory tests.

A typical S_u^{UU} profile, as determined in quick triaxial tests, in MC Upper Clay Formation is shown in Fig. 3.7. The profile shows the effects of surface drying and consolidation of the layer adjacent to the sandy stratum - through which water is extracted. The linear increment with depth originates from the lightly overconsolidated state of MC clay.

3.4.3 Comparison with in situ vane tests (sampling effects)

Marsal and Mazari (1962) present a study in which the shear strengths from in situ vane tests were compared with those from unconfined triaxial compression test. In a site that had not suffered any surface loading, Marsal and Mazari carried out vane measurements of the peak (q_v) and ultimate (q_{vult}) strength, and collected material of the soil affected by the vane to determine their water content and Atterberg limits. Subsequently, 12.7 cm diameter intact samples were obtained from a borehole located two meters away from the vane test site (at the same elevations as those of the vane tests). The intact samples were tested in unconfined compression in their intact (q_u) and remoulded (q_{ur}) states and their water content and Atterberg limits were determined. Table 3.5 presents selected vane and triaxial results. The peak vane strength and the triaxial strength from intact sample are compared to study sampling effects.

The average water content for all the samples studied by Marsal and Mazari was 294.5% for the in situ vane tests and 285.4% for the unconfined tests; the liquid limits were 306% y 307%, and the plasticity indexes 212% and 215%, respectively. Marsal and Mazari pointed out:

i) The strengths from unconfined tests are almost without exception lower than those

---

[33] Stiff clay q_c>100 kPa. Soft clay 50<q_c<100 kPa

determined from in situ vane tests, with a ratio q_u/q_{uv} equal to 0.74. Furthermore, the ultimate vane resistance is for most of the cases higher than the shear strength obtained from unconfined tests on remoulded samples.

ii) The variation of q_u is erratic with average 54 kPa while the q_{uv} shows a uniform distribution with an average of 86 kPa.

Table 3.5 Vane test vs. undrained triaxial test shear strengths (Marsal and Mazari, 1962)

	Triaxial tests						Vane tests					
Depth,	w	LL	PL	q_u,	q_{ur}, kPa	St	w	LL	PL	q_v,	q_{vult}, kPa	S_t
4.37	90	101	55	159	15	10.6	102	73	73	210	78	2.7
5.12		96	51		11		118	98	58	142	34	4.2
6.67		198	556		5		201	190	58	62	20	3.1
7.47		529	112		7		450	541	137	52	14	3.7
8.73		511	117		7		444	520	149	54	6	9
9.63	537	551	152	35	5	7	412	475	111	52	14	3.7
10.67		399	102		6		405	442	116	48	14	3.4
11.93	451	472	116	37	6	6.2	384	279	92	106	20	5.3
12.27		197	79.	45	5	9	216	176	70	52	4	13
13.53		-	-	74	9	8.2	192	135	46	-	-	-
14.80		-	-	64	6	10.7	-	-	-	84	20	4.2
15.08		-	-	68	5	13.6	-	-	-	70	20	3.5

An important drawback for the previous comparison is that vane and undisturbed strength are not directly comparable. Vane and triaxial tests differ because of influence of tube sampling disturbance, anisotropy, rate of loading, progressive failure and vane installation effects.

The magnitude of sampling effects is determined by the plasticity of the soil, the initial level of structure and the quality of the tube sampler, in particular its geometry. In high plasticity clays (like MC clay) it may be true that the strains associated with sampling do not cause significant damage, even with the standard 100 mm Shelby tube[34]. This needs to be checked following procedures such as those used for the Bothkennar study in the UK.

One method that has been proposed for assessing whether or not any damage has occurred to counter the effects of soil cementing or ageing is to compare shear wave velocities measured on the material in situ and on samples in the laboratory. In making this comparison, there should be similarities between the sample in the laboratory and in situ, in terms of stress state, wave propagation and polarization directions and wave length (Hight, et al., 1997). Romo (1995) points out that "the differences between the in situ and laboratory measurements of G_{max} for MC clay are less significant than those reported by other authors" (on different materials). According with Hight (1993) this is an indication

---

[34] Shelby tube of 100 mm diameter is usually used in Mexico City

that extensive sampling damage does not take place on MC clay.

3.4.4 Triaxial effective stress path tests

This review is based on a set of triaxial tests on 36-mm diameter specimens presented by Rojas, et al. (1987). Despite the large strains developed, none of the extension test samples reached a clear peak in its shear strength.

3.4.4.1 Isotropically consolidated monotonic tests

Fig. 3.14 shows a typical response of MC clay when tested after isotropic normal consolidation. Tests No. 20 and 21 are axial compression tests (under different total stress paths), and tests 17 and 18 are axial extension test (under different total stress path).

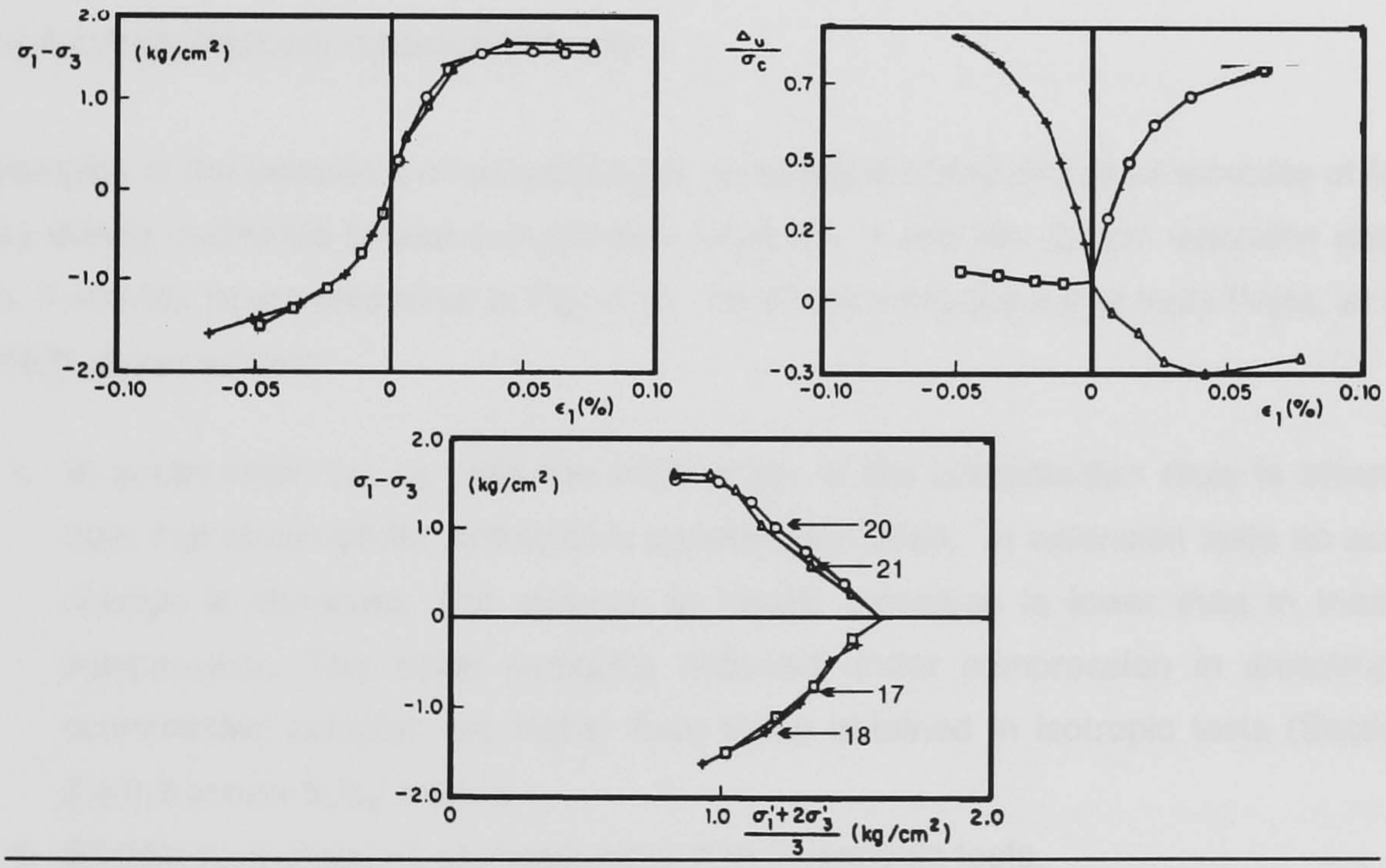


Fig. 3.14 Comparison of isotropically normally consolidated triaxial tests (Rojas, et al. 1987).

Among the characteristics to notice are:

i) The stress-strain (ε_1, q) plots show ductile behaviour. Rojas, et al. pointed out that the initial stiffness and the maximum deviator stress increase with p_0'.
ii) The response is contractant.
iii) The set of tests in compression by Rojas, et al. defined a failure envelope in the p-q

axes with an average ϕ' of 44.8°. Tests in tension did not reach any peak, but the final ϕ' at the end of the extension tests averaged 61.6°. Tests that were failed in compression after tension shown an increment in rigidity after the change in load direction and fail in compression at an average ϕ =49.5°[35]. The corresponding S_u/p_0' ratios are reported in section 3.4.2.4.

iv) The extension and compression tests show similar responses in terms of (ε_1, q), and (p, q) graphs. The $\Delta u/p_0'$ graphs vary between the tests because $\Delta p/\Delta q$ has different values in the two test styles.

In general, the isotropically normally consolidated MC clay responds to shearing in undrained extension or compression in a broadly similar manner (irrespective of whether the shearing is induced by axial or radial stress changes), developing comparable values of S_u/p_0'. The most significant differences observed are that extension leads to higher ϕ' and larger strains to failure.

3.4.4.2 Anisotropically consolidated tests

Examples of the behaviour of anisotropically consolidated (K=0.67) intact samples of MC clay during undrained triaxial compression (tests No. 4 and No. 5) and extension (tests No. 7 and No. 8) are presented in Fig. 3.15. From the complete set of tests Rojas, et al. (1987) observed that:

i. In stress-strain (ε_1, q) plots the initial slope of the compression tests is steeper than that observed for isotropically consolidated tests; in extension tests no such change is observed. The strength in triaxial extension is lower than in triaxial compression. The shear strengths obtained under compression in anisotropic consolidated samples are higher than those obtained in isotropic tests (Section 3.4.2.3 shows S_u/p_0' ratios).
ii. Smaller pore pressure changes apply than in isotropic tests.
iii. The effective stress paths show higher q/p' ratios at failure in compression than the normally consolidated samples. In compression the ϕ' values at failure averaged 50.30°, while the tests at tension did not reach failure despite tension stresses were applied in some cases – tension tests in Fig. 3.15 show ϕ' = 43° when the tests were

---

[35] When a change of load direction is applied the initial elastic modulus increases after the direction change whatever the initial direction. On the other hand, the proportion of reduction of this modulus with the axial deformation is approximately the same that it was observed for one-way loading, resulting in an increase in the maximum deviator stress for two cycle tests.

stopped.

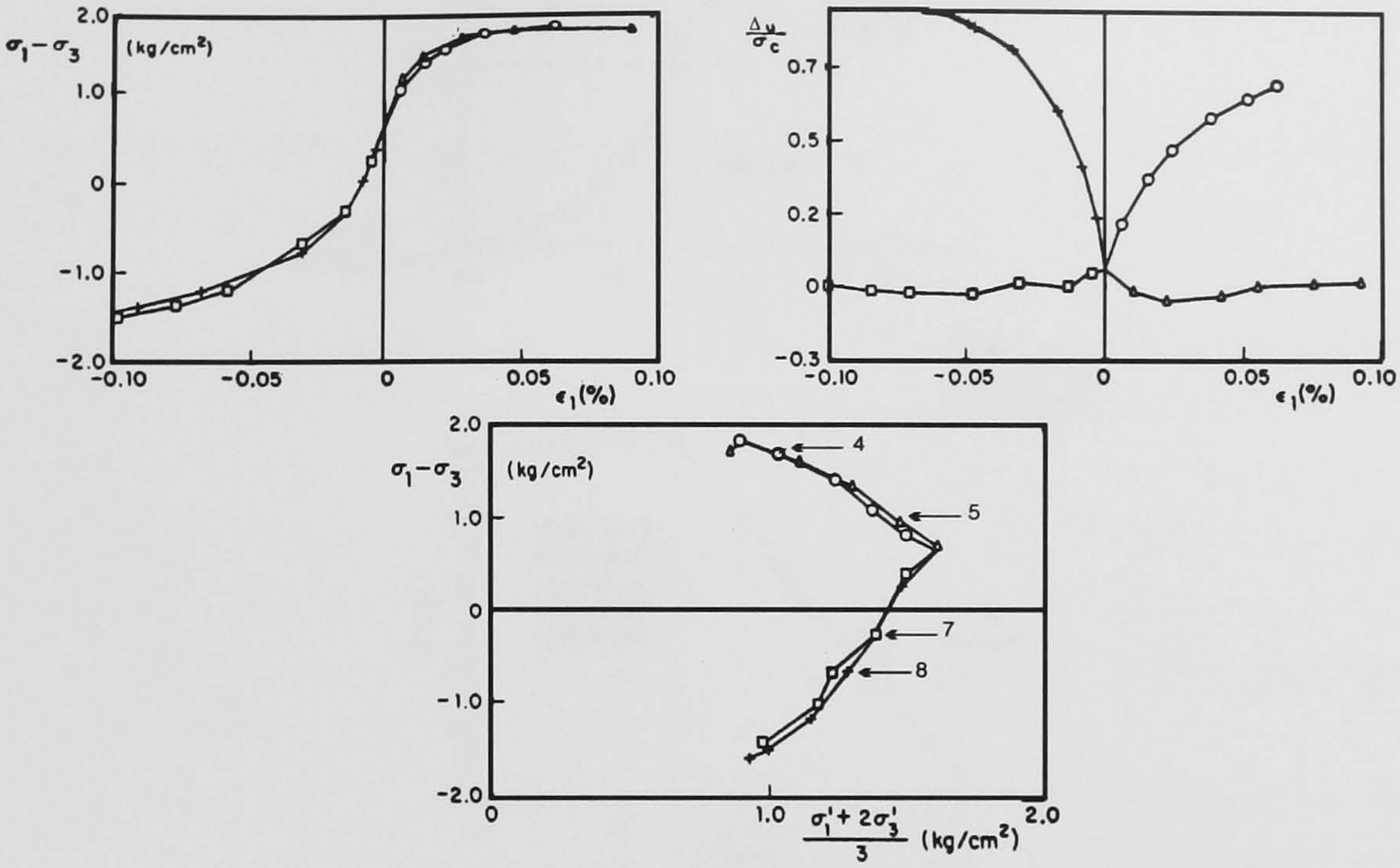


Fig. 3.15 Comparison of anisotropically normally consolidated triaxial tests (Rojas, et al., 1987).

3.4.4.3 Drained tests

Rojas, et al. (1987) carried out two triaxial drained tests, one in extension[36] and another in compression, both were isotropically consolidated at $p_c^{/}$=160 kPa (Fig. 3.16). Main features to observe are:

i. The (σ_1/σ_3, ε_1) plots tend to constant slopes after 4% - 5% of axial deformation.
ii. The volumetric strains under drained compression are just higher than ε_1 indicating that the radial deformation $\varepsilon_r=\varepsilon_2$ is practically nil, suggesting that the pseudo Poisson's ratio is to close to zero. The volumetric deformation (ε_v) seen in drained extension is small compared to ε_1 implying a pseudo-ν near to 0.5. These observations confirm the anisotropic nature of the k_0 consolidated material.

[36] No information regarding the total stress path followed in the extension test was obtained

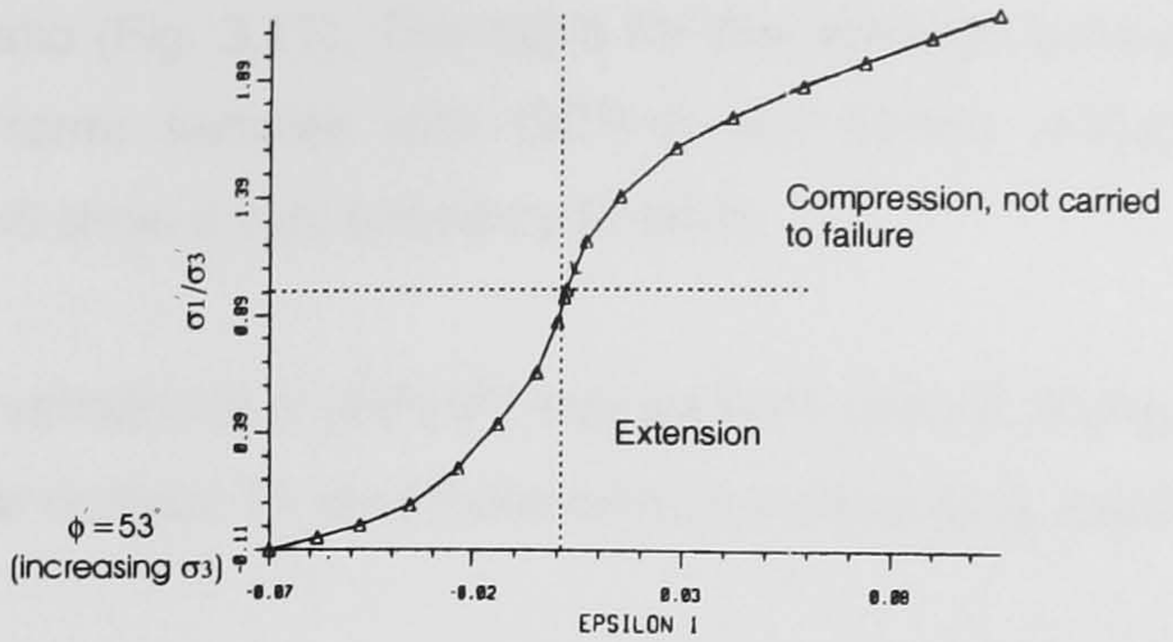


Fig. 3.16 Extension and compression drained tests (Rojas, et al., 1987)

3.4.4.5 Overconsolidated tests

The effects of overconsolidation on MC clay were examined by Giraldo (1996). Intact samples were isotropically consolidated to a mean effective stress slightly higher than the yield stress and then loaded in undrained compression, or swelled back and then loaded.

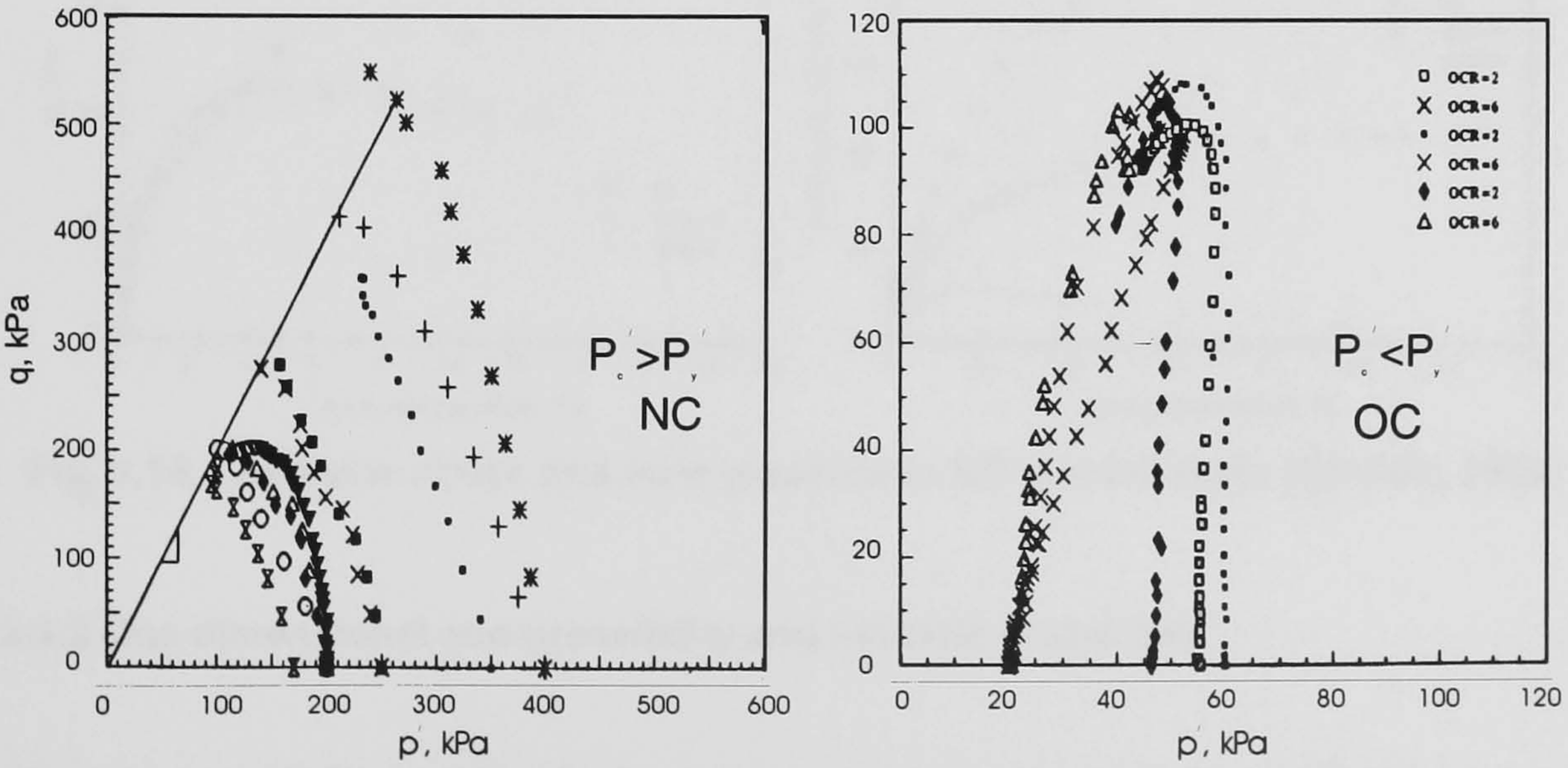


Fig. 3.17 Stress paths for NC and OC tests on MC clay samples (Giraldo, 1996)

The effective stress paths (esp) followed by Giraldo tests show a distinctive shape for each

overconsolidation ratio (Fig. 3.17). The esp's for the normally consolidated tests have an contractive elliptic form; samples with OCR=2 are almost vertical (p' constant); and samples with OCR=6 show a light tendency to dilate.

The observed wide variation in ϕ' ($46^{o}\pm9^{o}$) may be the result of differences in sample depth and with this in water content, PI, and material components (e.g. diatoms content).

The pore pressure and deviator stress responses observed in undrained tests conducted at OCR=1, 2 and 6 are shown in Fig. 3.18. The following features can be seen:

i) Normally consolidated samples reach their peak undrained strength after axial strains in the order of 6%, from this point the strength becomes almost constant. A similar pattern is appreciated in the pore pressure response. The S_u/p_c' and S_u/p_p' ratios are shown in section 3.4.2.2.
ii) Overconsolidated samples reach peak strength at an axial strain of 5% for OCR=2 and 4% for OCR=6. After peak both samples undergo strength reductions in the order of 10%. This means that with an increase in OCR the undrained brittleness increases and the strain to mobilise peak strength reduces.
iii) The pore pressure in OC samples reduces after peak. Dilative behaviour increases with OCR but it does not reach a negative value over the range considered.

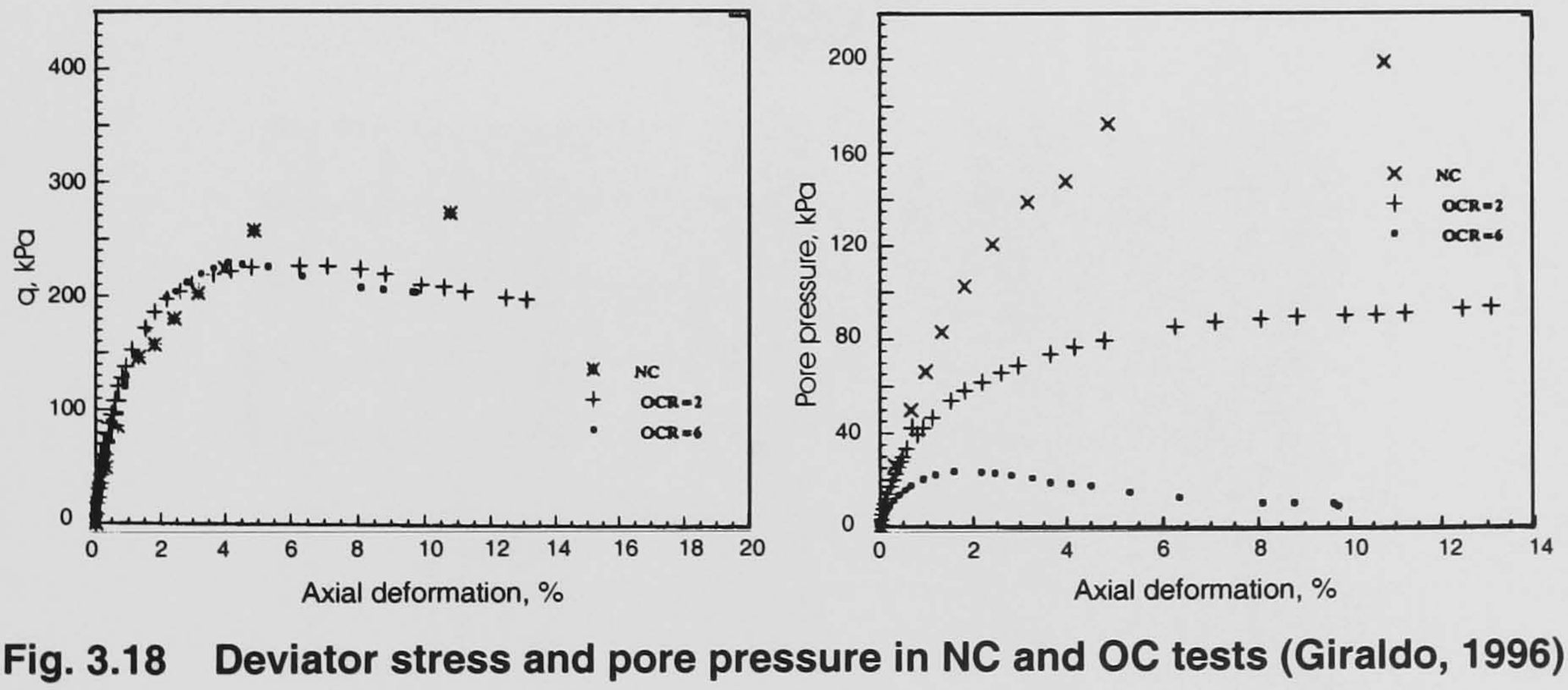


Fig. 3.18 Deviator stress and pore pressure in NC and OC tests (Giraldo, 1996)

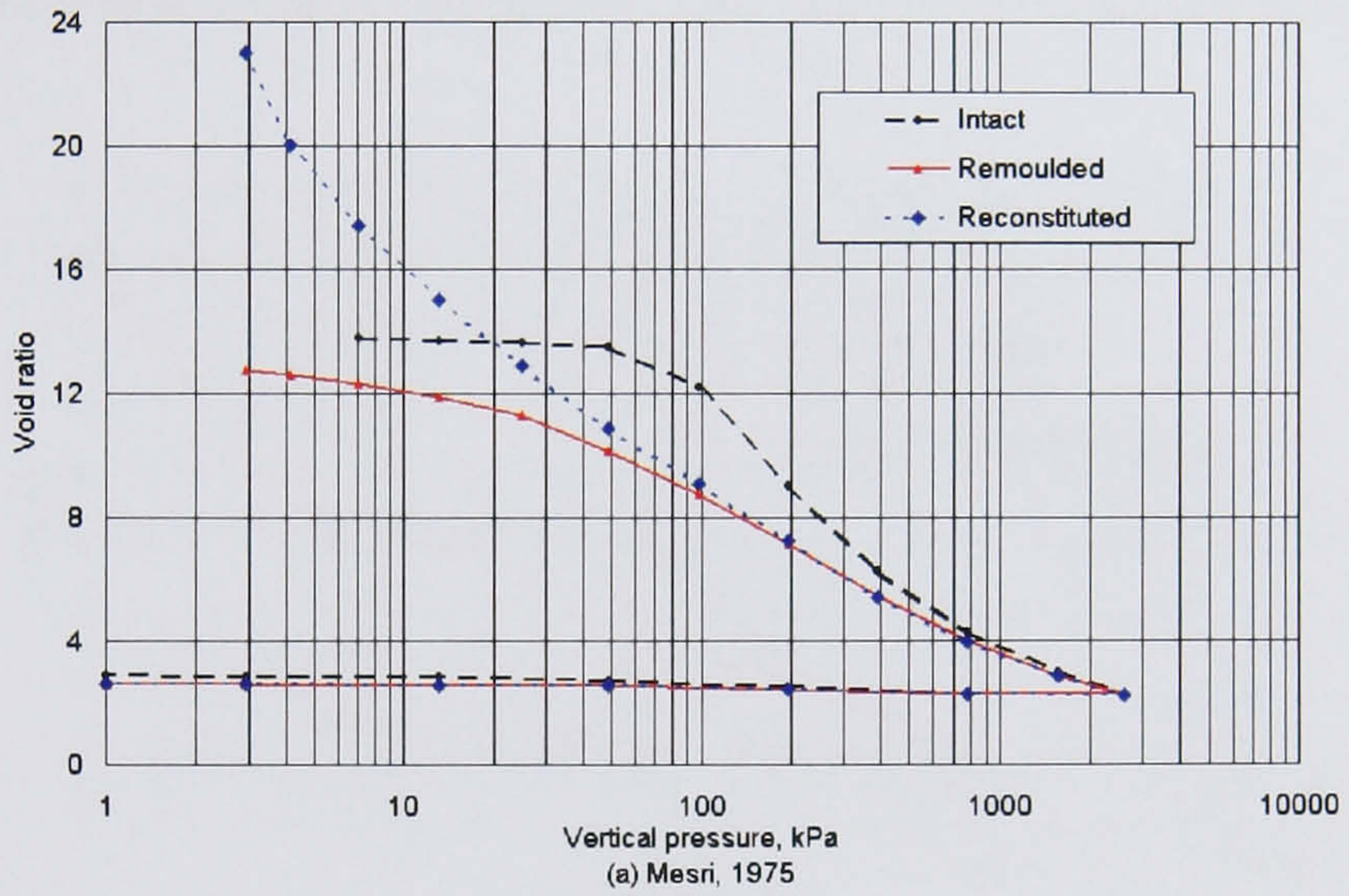
3.4.5 One dimensional compressibility and intrinsic properties

Since compressibility is probably the most remarkable characteristic of MC clay a large number of oedometer tests have been reported in the literature, most of them on intact and remoulded samples. However, tests on reconstituted material (necessary to determine

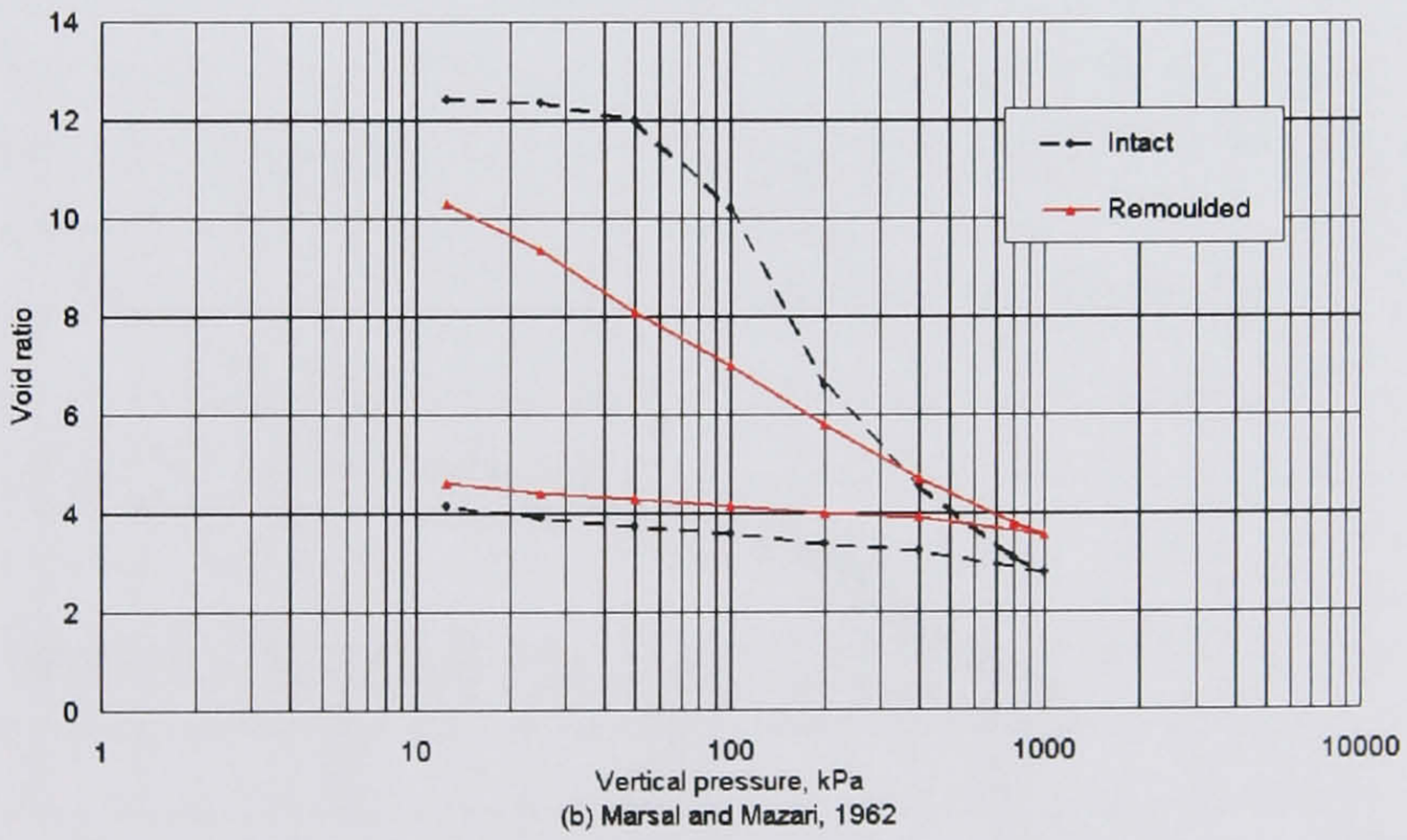
intrinsic properties) are limited. A study on the intrinsic properties has been carried out by the Author, including oedometer tests on samples remoulded at their liquid limits.

3.4.5.1 Oedometer test

The assessment of the in situ state of natural clays and the effects of soil structure (fabric and bonding) in the one-dimensional compression of soils can be carried out by comparing the response on oedometer tests of intact and reconstituted samples (Burland, 1990). Figs. 3.19a and b show the usual behaviour of MC clay when tested in intact, remoulded and reconstituted states, as assessed by Mesri, et al. (1975) and Marsal and Mazari (1962).



(a) Mesri, 1975



(b) Marsal and Mazari, 1962

Fig. 3.19a Intact, remoulded and reconstituted compressibility curve for MC clay

The following features can be observed:

i) A very large variation in the initial void ratios of the intact samples (from 4 to 14), which is related to differences in their depth and location. The initial void ratios of the

intact samples were smaller than for the normally consolidated reconstituted samples, and greater than the void ratios of the remoulded samples.

ii) After compression past their yield stresses, σ'_{vy}, the intact samples showed compressibilities (C_c) that increased and exceed those of the reconstituted and remoulded samples. After this structural collapse the intact samples gradually approached the curves from the remoulded or reconstituted tests.

iii) The post yield maximum C_c values shown by intact material are between 1.5 and 2.5 times those developed by reconstituted or remoulded samples at the same stress level.

iv) The post yield compressibilities (C_c) of the intact materials shown in Figs. 3.19 range from 8.6 to 2.1. The intact swelling index C_s is around 10 times smaller falling between 0.8 and 0.3 for a YSR of ten[37], with much lower values at low OCRs.

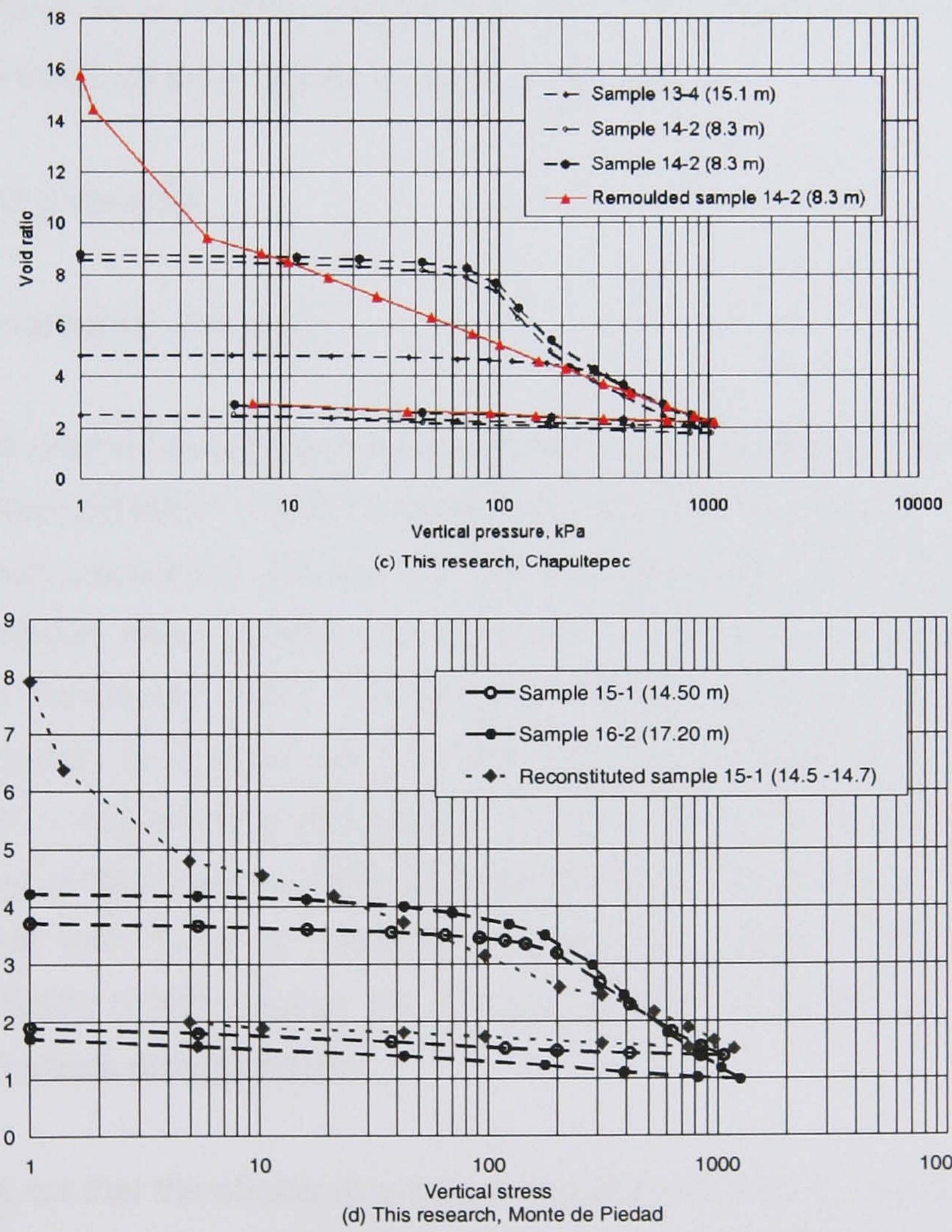


Fig. 3.19b Intact, remoulded and reconstituted compressibility curve for MC clay

The coefficient of volume compressibility (m_v) for overconsolidated intact samples is

---

[37] The expansibility of the clay is non-linear, C_s increases with YSR and PI.

typically between 0.1 and 1.0 m^2/MN, and for normally consolidated samples between 1 and 5 m^2/MN. The coefficient of consolidation (c_v) for normally consolidated intact samples is typically 0.03 to 1.6 m^2/year, while for overconsolidated samples usually lies between 3 and 30 m^2/year (Zeevaert, 1983)[38]. For comparison, the normally consolidated c_v value for Bothkennar clay is typically close to 1m^2/yr, while those for the London clay Canons Park and Cowden sites can fall to 0.5 m^2/yr.

Due to its very high void ratio Mexico City's is a relatively high permeability clay - its typical permeability in laboratory tests is $1x10^{-9}$ m/s. In the field the mean permeability increases due to the presence of thin lenses of igneous glass, sand and fissures in the soil.

MC clay shows high coefficients of secondary consolidation. $c_{\alpha\varepsilon}$[39] has typical values ranging from 0.1 to 0.01, that vary with stress level (the higher the stress the higher the coefficient). Mesri, et al. (1975) suggest that the $c_{\alpha\varepsilon}/C_c$ ratios of MC clay samples lie between 0.03–0.035, which is typical for clays: $c_{\alpha\varepsilon}$ is high.

3.4.5.2 Intrinsic properties

a. Intrinsic compression line (ICL)

Burland (1990) refers to the properties obtained from a sample that has been reconstituted at a water content between 1.0 and 1.5 times its LL as intrinsic properties. Few oedometer tests have been prepared in this way for MC clay, although tests do exist on samples whose reconstitution water content was more than 2.5 times its LL (Mesri, et al., 1975; Mendoza and Hernandez, 1992; for liquidity index (I_L) of 8 and 2 respectively) and samples remoulded at a water content near their LL. As part of this research one reconstituted (I_L = 4.6) and one remoulded at natural water content oedometer tests were carried out. Fig. 3.19a indicates that remoulded samples show compressibility curves that almost coincide with those of reconstituted samples between 100 and 1000 kPa. Following Burland's (1990) notation the intrinsic properties are indicated by an asterisk; e.g. C_c^* is the intrinsic compressibility.

Burland points out that the effects of soil type may be removed by resolving the individual intrinsic compression curves from different clays to a single Intrinsic Compression Line (ICL). This is achieved by replacing void ratio (e) by the void index (I_v), which is defined as:

---

[38] m_v and C_v vary with the stress level

[39] Defined as the slope of the final straight part of the time-deformation curve

$$I_v = \frac{\left(e - e^*_{100}\right)}{C^*_c} \tag{3.2}$$

where e_{100}^* is the intrinsic void ratio at σ'_v=100 kPa, and C_c^* is the intrinsic compressibility between σ'_v=100 and 1000 kPa.

Test data from different clays allowed Burland to give the following equation for the ICL:

$$I_v^* = 2.45 - 1.285 \log \sigma'_v + 0.015 \left(\log \sigma'_v\right)^3 \tag{3.3}$$

Fig. 3.20 compares the ICL expected from Burland's expression with those obtained for this research database. In this figure it is possible to observe:

i) There exist good general agreement between the ICL's between 100 and 1000 kPa, however at pressures lower than 100 kPa the experimental ICLs differ from Burland's ICL.
ii) The ICL obtained from reconstituted materials lie above Burland's ICL and are convex, on the other hand ICL's from remoulded material lie below Burland's ICL and are concave, which point out the importance of following Burland's procedure for the determination of intrinsic properties. This response is probably due to the different initial liquidity indices.

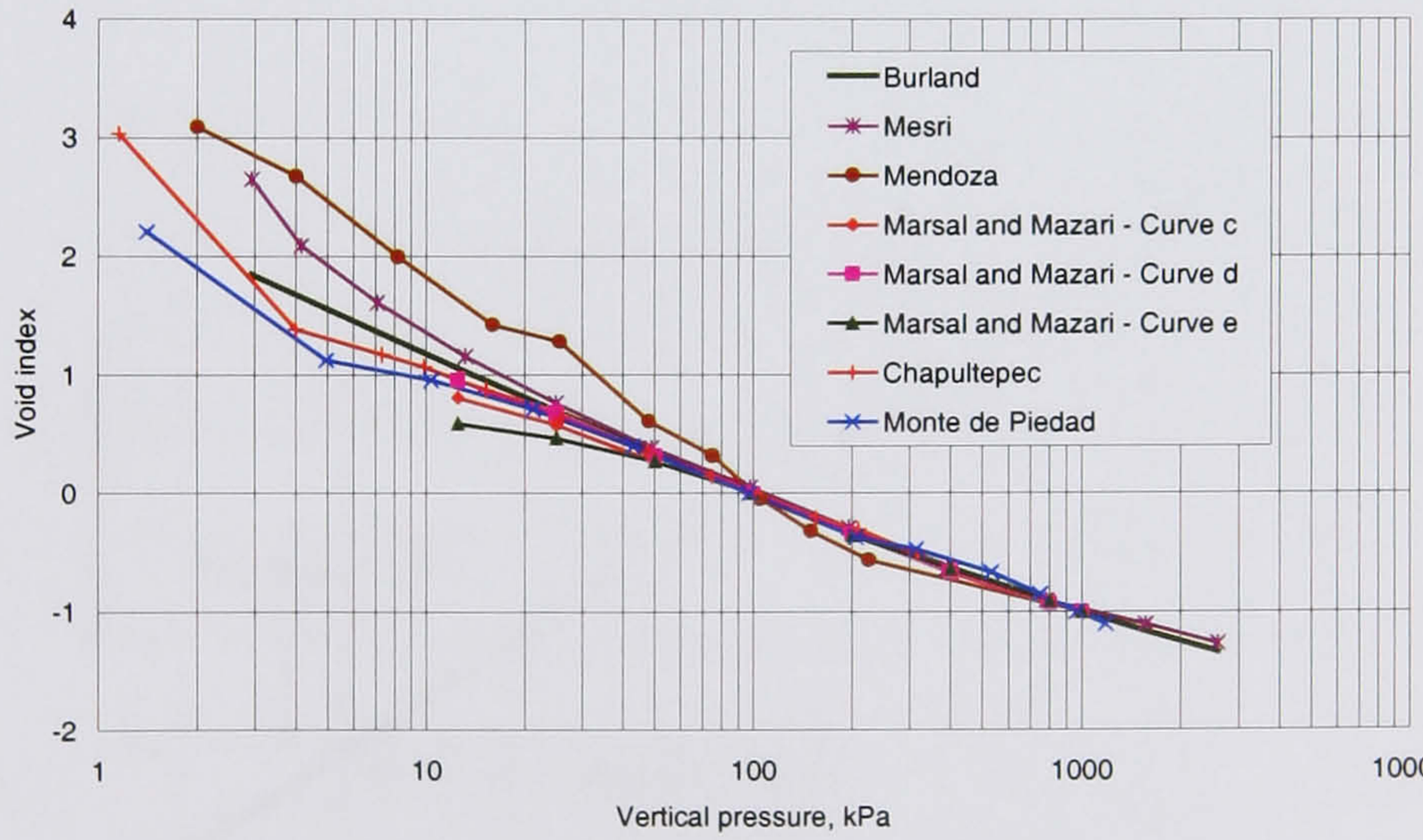


Fig. 3.20 Intrinsic Compression Lines for MC clay

The data collected by Burland allowed him to develop correlations for e^*_{100} and C^*_c based on the void ratio at LL (e_{LL}). But, his correlations were developed for clays with entirely different index properties to those of MC clay, and when they are applied to MC clay e^*_{100} is

not well predicted (Fig. 3.21). Using the few points on reconstituted and remoulded samples available for this research, it was found that the expressions proposed by Nagaraj, et al. (1986) for determining e and C_c in fine grain uncemented normally consolidated soils have better correlation with the measured MC clay intrinsic properties. For 100 kPa, the Nagaraj, et al. expressions becomes:

$$e^*_{100} = 0.6534 e_{LL} \tag{3.4}$$

$$C^*_c = 0.2343 e_{LL} \tag{3.5}$$

The variables were defined before. (The intrinsic symbol * does not appear in Nagaraj equations.) Fig. 3.21 shows the comparison between Burland (1990) and Nagaraj et al. (1986) expressions and the MC clay experimental results. Nagaraj, et al. expressions are used for the assessment of sensitivity in the pile validations presented in Chapter 5.

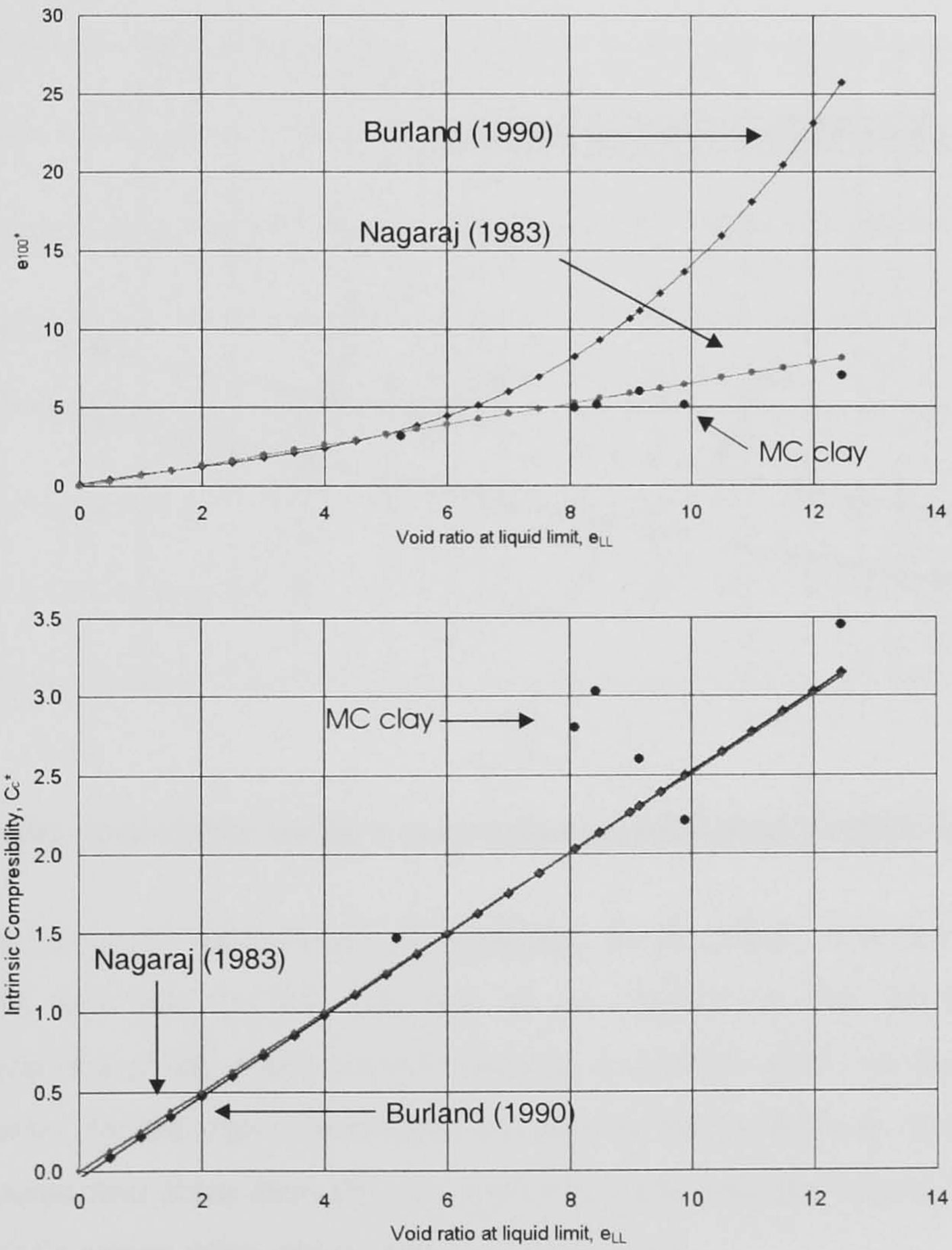


Fig. 3.21 Burland (1990) and Nagaraj, et al. (1986) intrinsic property correlations vs. MC clay measured intrinsic properties

b. In situ void index

The in situ void index of the intact material is defined as $I_{v0} = [e_0 - e^*_{100}]/C^*_c$, where e_0 is the in situ void ratio. The I_{v0} values calculated by the Author using the above correlations for two MC profiles (Marsal and Mazari, 1962) are shown in Fig. 3.22. In these profiles a drying crust is found near the surface, affecting soil down to 10 m depth, while the clay below 30 m has probably been affected by ground water extraction. In between these depths the clay exists in an aged, normally consolidated state. The data shown in Fig. 3.22 generally lie above the ICL and Burland's Sedimentation Compression Line (SCL). The vertical distance between I_{v0} and the ICL ($\Delta I_{v0}=I_{v0}-I_{v0}^*$) appears to depend on the conditions of sedimentation with slow deposition in still water leading to a more open fabric and higher void indices (Smith, 1992). The more porous and open soil fabrics were located between 15 and 25 m in these profiles, and the more compact structures between 0 and 10 m, reflecting the clays' recent consolidation history.

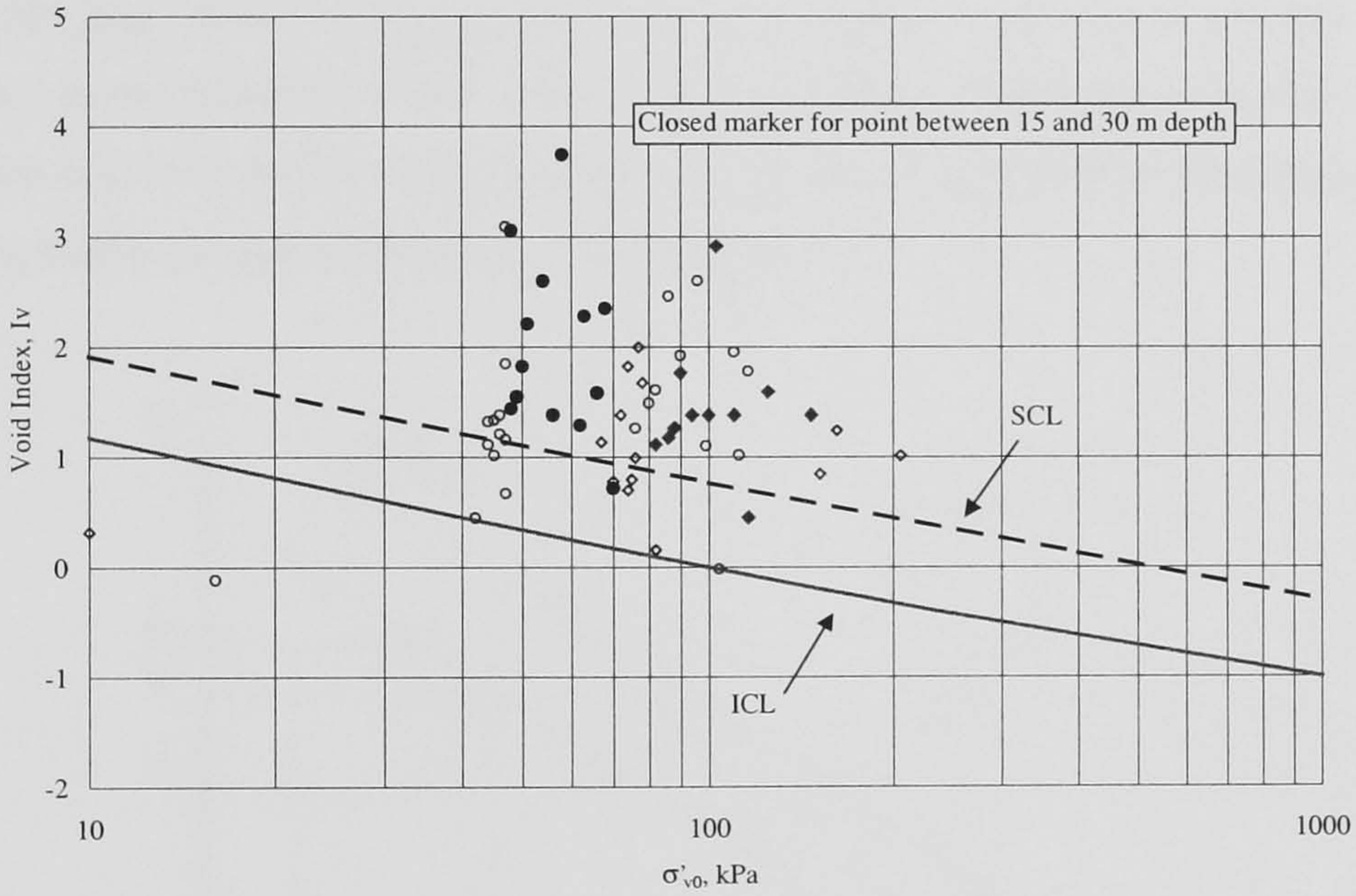


Fig. 3.22 In situ void index for two normally consolidated profiles in Mexico City

These results are in good agreement with Nagaraj, et al. (1986) who terms soils whose state lies above the ICL (which Nagaraj, et al. define as the normally saturated uncemented state line of the soils) as the naturally cemented state. As the natural bonds inhibit compression, for the same overburden pressure the equilibrium void ratio is higher for a naturally cemented state than that for a normally consolidated state[40]. This definition confirms Zeevaert's observation presented in section 3.4.1.

---

[40] It can also be the population of larger pore spaces, and structural reason.

3.4.5.3 Clay sensitivity from oedometer tests

Clay sensitivity (S_t) is usually defined as:

$$S_t = \frac{S_u^{UU}}{S_{ur}^{UU}}$$

i.e. the ratio of intact to remoulded undrained shear strengths, the latter being free from the effects of structure. On the other hand, ΔI_{v0} reflects clay sensitivity when compression of a normally consolidated clay causes "collapse" of the natural fabric and reduction in void index towards the intrinsic condition (Fig. 3.23). However, this condition is affected by overconsolidation which reduces e_0 and I_{v0} in comparison with e_0^* and I_{v0}^* and at sufficiently large OCR's ΔI_{v0} may become negative – the effects of overconsolidation mask those of clay deposition and fabric.

Smith (1992) and Chow (1997) pointed out that a clearer indication of sensitivity can be obtained if it is evaluated from the void ratio at K_0 yielding. At this point the clay fabric and bonding are such that the vertical effective yield stress (σ'_{vy}) is greater than that sustained by a reconstituted sample at the same void ratio (σ'^{*}_{vy}).

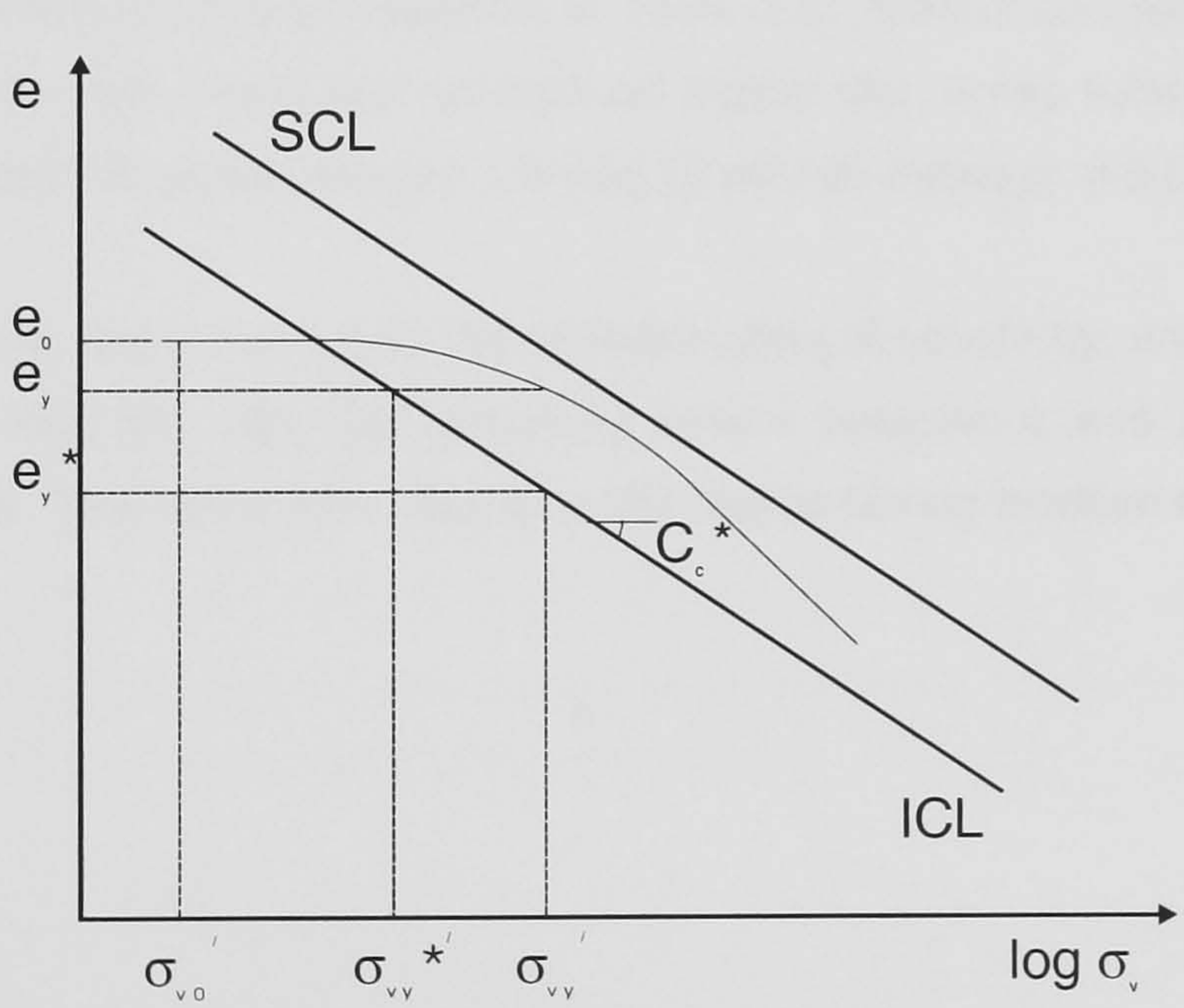


Fig. 3.23 Sensitivity from oedometer test

The compressibility curves of overconsolidated samples cross the ICL and approach the SCL, before yielding and descending back towards the ICL (Fig. 3.23). Smith (1992) suggested measuring sensitivity by comparing soil behaviour with that of the reconstituted material at the same water content. If the ratios of (S_u/σ'_{vy}) and (S_{ur}/σ'^{*}_{vy}) are equal then:

$$S_t = \frac{\left(\frac{S_u}{\sigma'_{vy}}\right)\sigma'_{vy}}{\left(\frac{S_{ur}}{\sigma'^{*}_{vy}}\right)\sigma'^{*}_{vy}} = \frac{\sigma'_{vy}}{\sigma'^{*}_{vy}} \tag{3.6}$$

Alternatively, the difference between intact and intrinsic void indices at the same stress level is equivalent to the logarithm of sensitivity (see Fig. 3.23):

$$\log S_t = \log (\sigma'_{vy}/\sigma'^{*}_{vy})$$

$$\log S_t = \log \sigma'_{vy} - \log \sigma'^{*}_{vy}$$

$$= (e_y - e_y^{*})/C_c^{*}$$

$$\log S_t = \Delta I_{vy} = I_{vy} - I_{vy}^{*} \tag{3.7}$$

Thus, sensitivity can be evaluated by comparing oedometer test data on intact and reconstituted samples. This procedure is applied when using IC Pile Design Method presented in Chapter 5.

Marsal and Mazari (1962) carried out studies of the MC clay sensitivity using unconfined triaxial tests (some results are presented in Table 3.5). Marsal and Mazari pointed out that the sensitivity determined with unconfined triaxial test varies between 3.8 and 17, and using vane tests it varies between 1.9 and 15 with an average of 5.5.

Marsal and Mazari, using more than 700 determinations of sensitivity, produced Fig. 3.24 which indicates that MC clay has sensitivity values between 2 and 20 with a mean between 5 and 8. This information classified MC clay as having medium sensitivity.

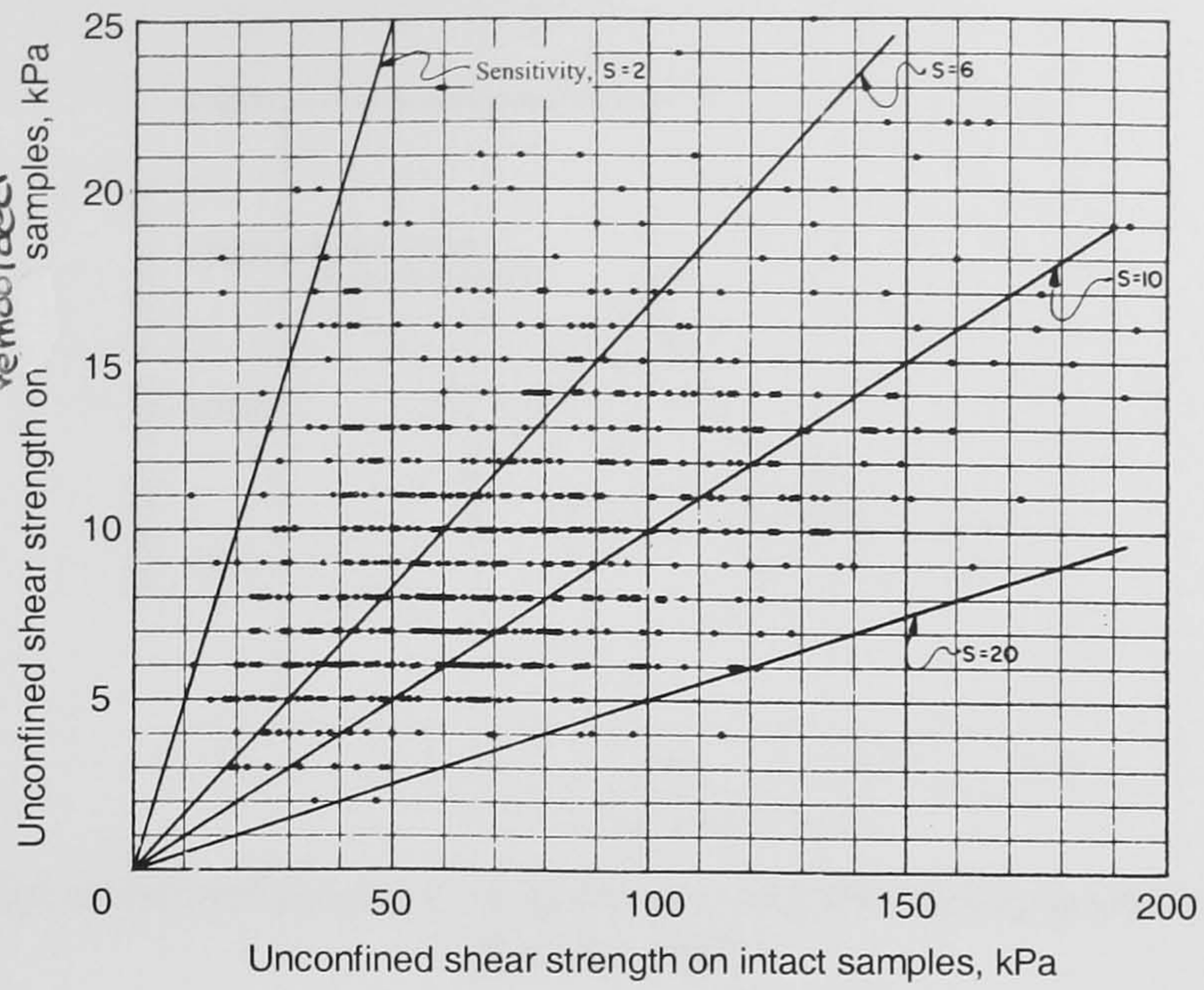


Fig. 3.24 Sensitivity of Mexico City clay (Marsal and Mazari, 1962)

3.5 Dynamical properties

3.5.1 Low-strain shear modulus (G_{max})

The non-linear[41] hysteretic stress-strain behaviour of cyclically loaded soils is often approximated by equivalent linear soil properties. The equivalent linear shear modulus, G, is generally taken as a secant shear modulus determined from the extreme endpoints of a hysteretic loop. G_{max} correspond to the low strain shear modulus.

Fig. 3.25 from Romo (1995) presents G_{max} values determined with resonant column tests on normally or slightly overconsolidated clay samples retrieved from different sites and depths in MC. The figure shows the influence of the p_c', PI, and I_L on G_{max}[42].

---

[41] Nonlinearity of soil stress-strain behaviour means that the shear modulus of the soil is constantly changing with strain. Note that the true elastic range in soils is tiny, soil response is usually non-linear, non-elastic.

[42] Using this data, Romo and Ovando (1994) proposed the following expression to compute G_{max} for MC clay:

$$G_{\max} = 122Pa\left(\frac{1}{PI - I_L}\right)^{PI-I_L}\left(\frac{\sigma_c'}{Pa}\right)^{0.82}$$

where Pa is a constant to define the G_{max} units (e.g. 100 kPa, atmospheric pressure) and ($PI-I_L$) is restricted to positive values.

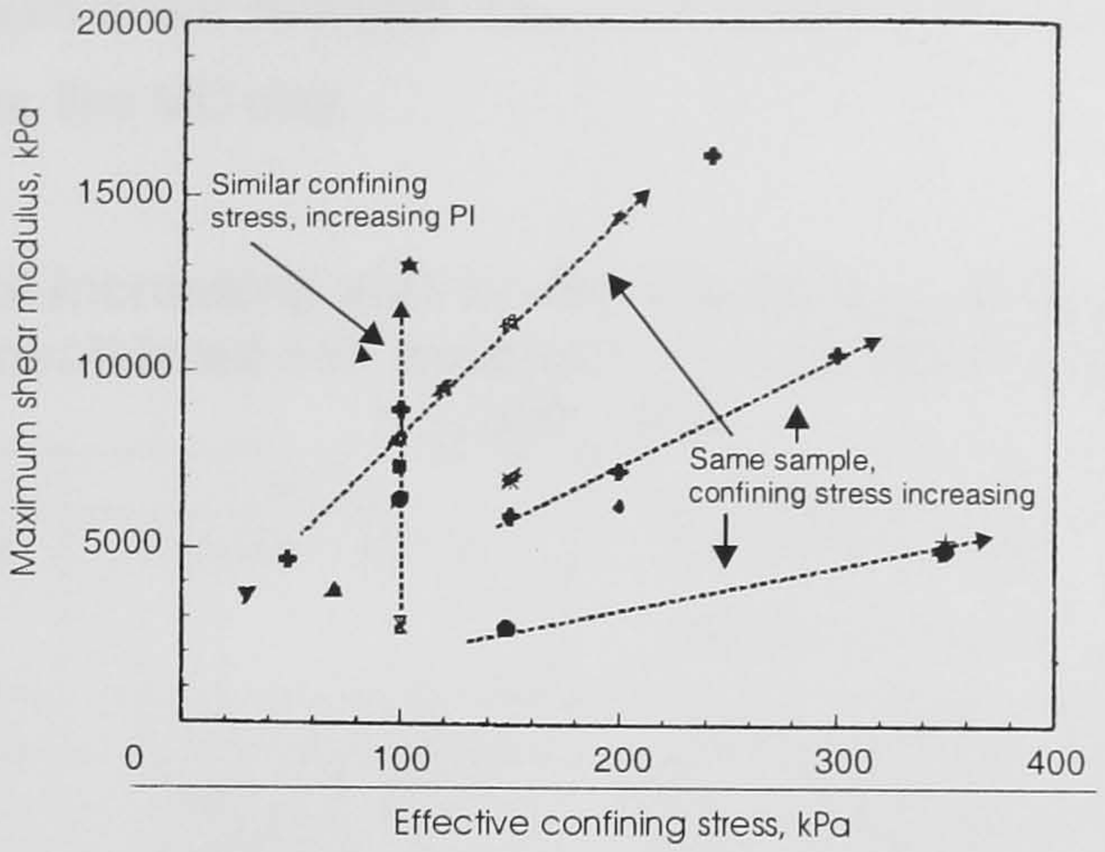


Fig. 3.25 Effect of effective confining stress and Plasticity index on MC clay G_{max} (Romo, 1995)

A reliable value of G_{max} can be obtained from the in situ determination of the shear wave propagation velocity (v_s) and the expression:

$$G=\rho\, v_s^2 \qquad (3.8)$$

where ρ is the soil density (unit weight divided by the acceleration of gravity).

Mean values of shear wave propagation velocities for the Lake zones are presented in Tables 3.6 and 3.7. (These velocities were obtained using suspended probe and down-hole techniques.)

Table 3.6 v_s at Overconsolidated and Virgin (NC) Texcoco lake (Jaime, 1987)

Stratum[43]	No. of data		Mean v_s, (m/s)		G, MPa	
	OC	NC	OC	NC	OC	NC
Superficial layer	8	8	118	113	19.5	17.8
Upper clay formation	128	133	64	54	5.1	3.7
First hard layer	10	8	267	192	123.5	63.9
Lower clay formation	7	12	180	134	56.1	31.1
Deep deposits	22	15	506	358	443.7	222.1

Table 3.7 v_s at Xochimilco Chalco lake zone (NC) - Tlahuac Deportivo site (Jaime, 1987)

Stratum[42]	Depth, m	No. of data	Mean v_s, m/s	G, MPa
Superficial stratum	5 – 6	2	56	3.8
Soft clay	6 – 10	3	145	37.5
	10 – 40	30	81	8.0
Stiff sand	40 – 42	1	317	179.3
Clay with sandy lenses	42 – 48	6	154	42.3
Stiff clay with sand lenses	48 – 57	9	284	143.9
	58 – 66	8	158	44.5

[43] See section 2.2 for Texcoco and Xochimilco-Chalco lakes typical profiles

Table 3.8, from Dobry and Vucetic (1988), summarizes the influence of a number of factors on the maximum shear modulus (G_{max}) for normally consolidated and moderately overconsolidated clays, like MC clay.

Table 3.8 Effects of increasing various factors on G_{max}, G/G_{max} and damping ratio (ζ) for normally consolidated and moderately overconsolidated clays (Dobry and Vucetic, 1988)

FACTOR	G_{max}	G/G_{max}	ζ
Confining pressure σ_0' *(or* σ_{vc}'*)*	Increases with σ_0'	Stays constant or increases with σ_0'	Stays constant or decreases with σ_0'
Void ratio, e	Decreases with *e*	Increases with *e*	Decreases with *e*
Geologic Age, t	Increases with *t*	May increase with *t*	Decreases with t
Cementation, c	Increases with *c*	May increase with *c*	May decrease with *c*
Overconsolidation,OCR	Increases with OCR	Not affected	Not affected
Plasticity index, PI	-Increases with PI if OCR>1 -Stays about constant if OCR=1	Increases with PI (see Fig. 3.23)	Decreases with PI
Cyclic Strain, γ_c	-------	Decreases with γ_c	Increases with γ_c
Strain Rate (frequency of cyclic loading)	Increases with strain rate	*G/G_{max} probably not affected if G and Gmax are measured at the same strain rate	Stays constant or may increases with strain rate
Number of loading Cycles, N	Decreases after N cycles of large γ_c but recovers later with time	Decreases after N cycles of large γ_c (G_{max} measured before N cycles)	Not significant for moderate γ_c and N

Suspended probe tests carried out in the basaltic lava at Garden UNAM Engineering Institute (Hill zone) defined the following shear wave velocities: 220 m/s from 4 to 15 m, 830 m/s between 16 and 17 m and 570 m/s from 18 to 31 m. The shear wave velocity of the deep deposits in the Texcoco lake is near the Hill zone velocities.

3.5.2 Large-strain shear modulus

The equivalent secant shear modulus and damping ratio show curvilinear relationships with the shear strain level over which the hysteretic loop is determined. Secant shear modulus decreases with strain while the damping ratio increases. These relationships play important roles in the response of the soil layer since nonlinearity may offset 'elastic' seismic motion amplification.

Fig. 3.26 shows the typical effects of shear strains, γ, and confining effective stresses, p_c' (σ_c' in the graph), on shear modulus for isotropically normally consolidated MC clay. It is observed that MC clay does not suffer significant shear modulus reductions up to shear strains values that vary from about 0.02 to 0.05% (depending on PI) and then sustain a significant softening in the range of 0.3 to 1.0% (Romo, 1995). Jaime (1988) pointed out that the overall behaviour of the clay from the three Lake subzones is similar, although small differences may be appreciated on the threshold strain where shear modulus starts decreasing.

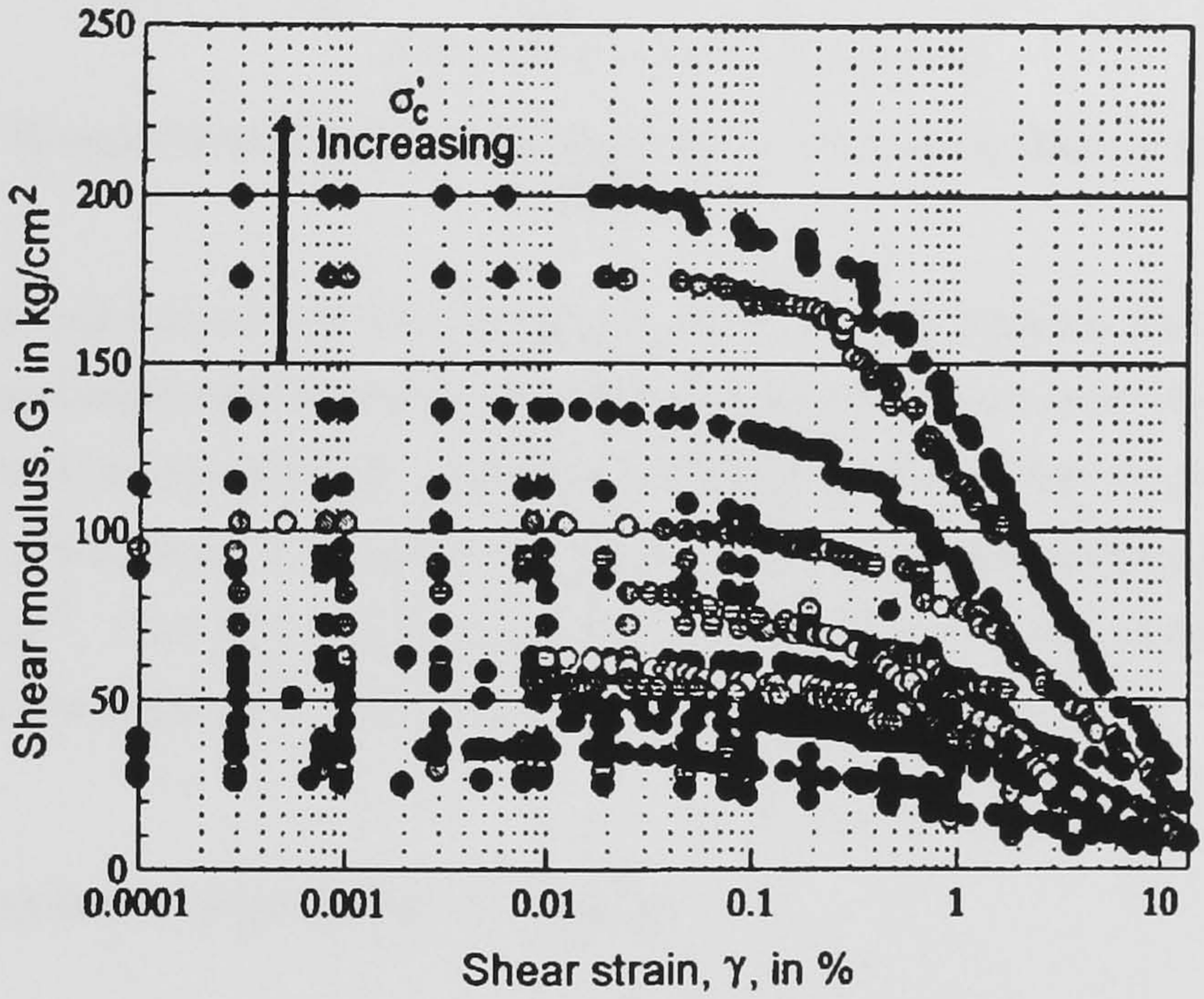


Fig. 3.26 G vs. γ for MC clay (Romo, 1995)

The relationship between G modulus and shear strain amplitude can be characterized by means of a modulus reduction curve. The nature of this curve, which has an ordinate of modulus ratio (G/G_{max}) and an abscissa of log γ, has been well established for many soils. Fig. 3.27 presents modulus reduction curves measured in the laboratory on many different clays, and the curve for MC clay reported by Leon, et al. (1974) and Romo and Jaime (1986). It is observed that MC clay has the most linear stress-strain behaviour among all the represented clays.

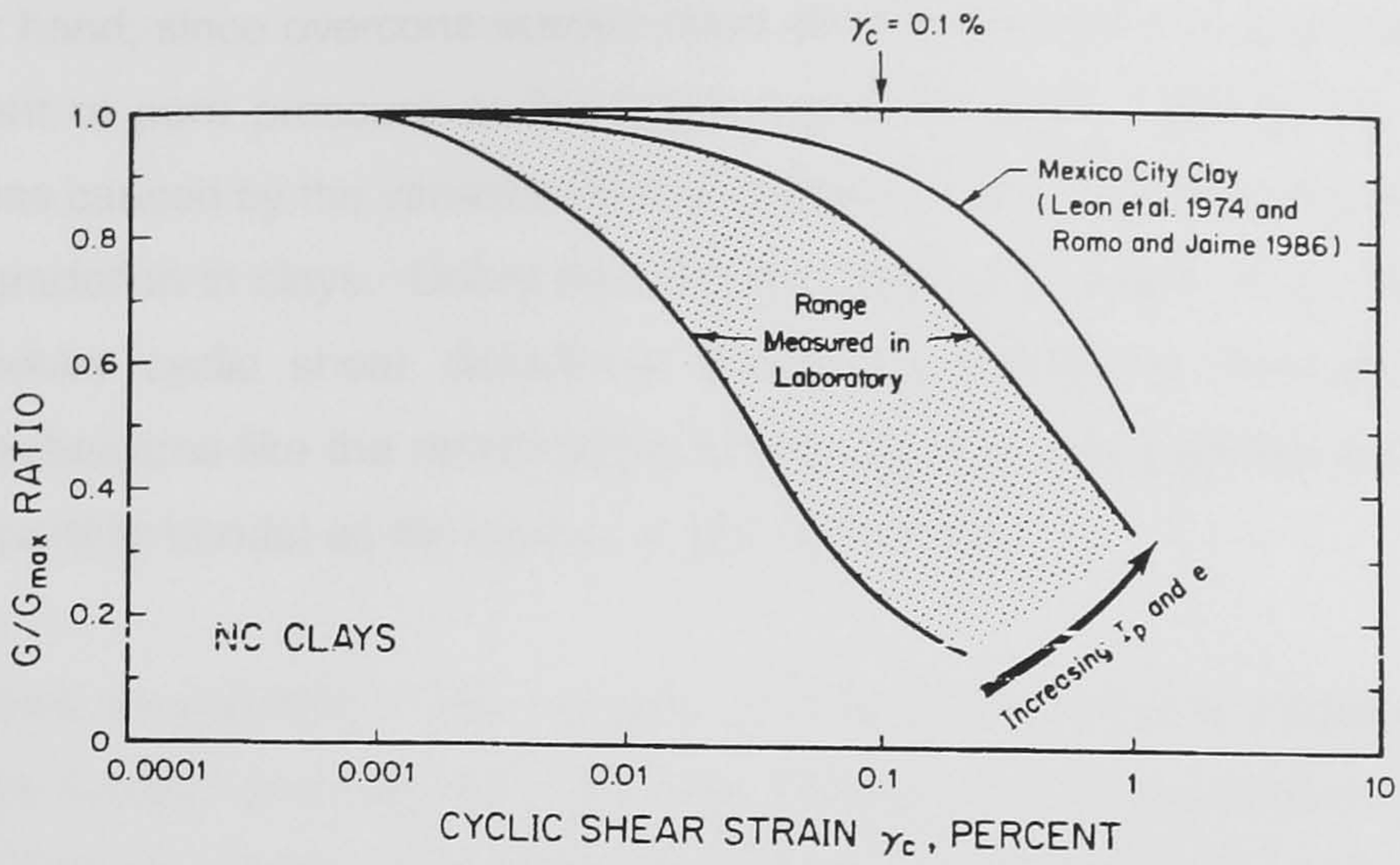


Fig. 3.27 G reduction measured in clays in the laboratory (Dobry and Vucetic, 1988)

Ishihara (1996) pointed out that the changing feature of shear modulus and damping with strain is not significantly influenced by whether the soils have been normally consolidated, overconsolidated, or subjected to long-term confining pressure after the end of primary consolidation (Table 3.8). Consequently, these curves can be developed using G vs. γ curve and G_{max}[44]. (The above is applicable to resonant column under isotropic condition and not for K_0 consolidated triaxial conditions.)

3.5.3 Shear modulus degradation by fatigue

In general, the build up of pore pressure during cyclic loading is considered as the main cause of soil stiffness degradation. If this is true, it could be considered that for soils whose dynamic pore water pressures is negligible the fatigue phenomenon is of little importance - except when the cyclic shear stress plus the sustained shear stress is similar to the soil undrained shear strength.

---

[44] Romo (1990) proposed to represent MC clay shear modulus degradation under shear strain with the expression:

$$G = G_{max}(1\text{-}H(\gamma))$$

$$H(\gamma) = \left[\frac{(\gamma/\gamma_r)^{2B}}{(1+\gamma/\gamma_r)^{2B}} \right]^{A'}$$

$$A' = A + I_L.$$

where I_L is the liquidity index, γ_r is a reference strain and A and B are soil parameters that are plasticity index dependent.

On the other hand, since overconsolidated clays show cyclic stiffness degradation despite the decrement of pore pressure at the beginning of the cyclic loading, the changes in effective stress caused by the variation of pore pressure can not be the only reason for the modulus degradation in clays. Dobry and Vucetic (1988) and Hight, et al. (1997) pointed out simultaneous cyclic shear distortions caused by loading at microstructural level (including mechanisms like the reorientation and bending of clay particles and associated breakage of particle bonds) as the reason of this behaviour.

Fig. 3.28 shows an example of the variation of G modulus with the magnitude of cyclic stress and the number of cycles for a MC clay sample. The importance of the modulus degradation depends on the type of soil, the effective confining stresses, the stress path followed in consolidation, OCR (degradation decreases with increasing OCR), and the magnitude and number of the shear stress cycles (the tests in the figure are under cyclic compression). The rate and form of loading are also important since rapidly applied reversals of stress directions, as in the resonant column tests, result in a reduced rate of degradation of stiffness with strain compared with monotonically applied shear (Hight, et al. 1997).

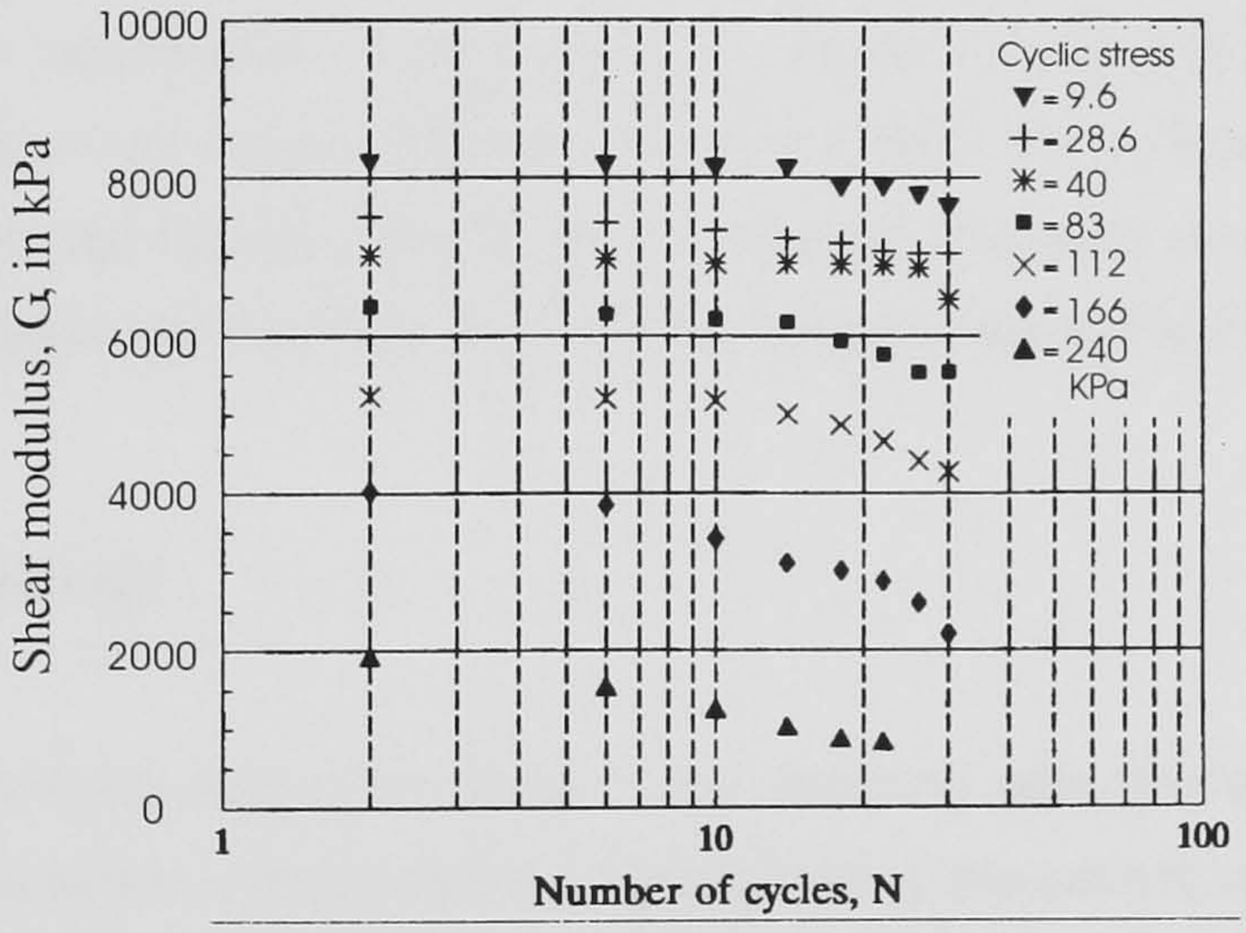


Fig. 3.28 G modulus degradation for MC clay from cyclic triaxial tests (Romo, 1995)

The effect of cyclic degradation, under strain-controlled conditions, can be expressed quantitatively in terms of the degradation index (δ_t) proposed by Idriss, et al. (1978). This index, in terms of shear mode of deformation, can be defined as:

$$\delta_t = G_N/G_1 = N^{-t} \tag{3.9}$$

where G_1 and G_N denote the secant shear modulus in the first and N^{th} cycles and *t* is the

degradation parameter which depends on the cyclic strain amplitude. Since the degradation index δ_t, for a specific shear strain, tends to decrease linearly with the number of cycles when plotted on a log-log scale, *t* is determined from a G vs. N log-log plot by taking the slopes of the straight lines for each strain amplitude.

For the normally consolidated clays found in the Texcoco Lake, resonant column tests show that the parameter *t* varies with cyclic shear strain amplitude according to the following approximate rule (Romo, 1995):

$$t = (2/ (1+\nu))*0.0299\ \gamma \qquad (3.10)$$

for anisotropic consolidation and $\gamma<2\%$; and:

$$t = (2/ (1+\nu))*0.0122\ \gamma \qquad (3.11)$$

for isotropic consolidation and $\gamma<6\%$, where ν is the Poisson ratio.

The above indicates that in resonant column tests anisotropically consolidated soil samples are less susceptible to degradation. Romo (1995) mentioned that this is understandable since the shear stresses induced during the anisotropic consolidation stage modify more significantly (than isotropic stresses) the microstructure, leading to a somewhat more stable soil structure, as shown in the compression test S_u values.

3.5.4 Damping ratio (ζ)

The equivalent damping ratio (ζ) is equal to the damping ratio that would be computed based on the area within a hysteresis loop (considering the secant shear modulus, and the maximum shear strain). The relationship between this equivalent damping ratio and shear strain is characterized by means of a damping curve. The nature of this curve, which has damping ratio as ordinate and log of shear strain as abscissa, has been well established for many soils.

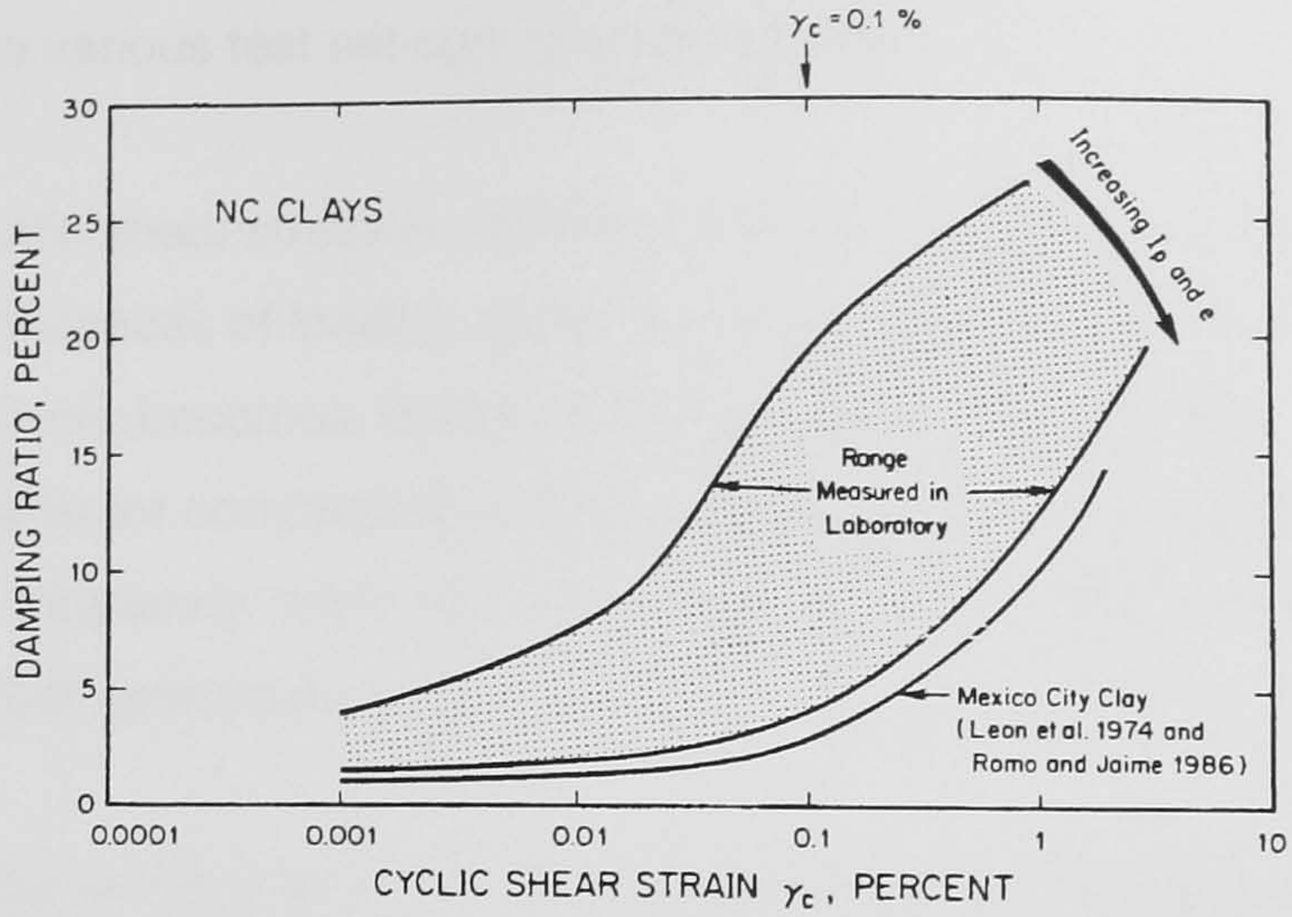


Fig. 3.29 ζ range measured in clays in the laboratory (Dobry and Vucetic, 1988)

Fig. 3.29 includes the damping curve trends associated with the stiffness curve trends plotted in Fig. 3.27 and the curve for MC clay, the latter located below the range for all other clays[45]. The general relationships between ζ, γ, e and PI are consistently opposite to those discussed for G/G_{max}: as e and PI increase and the clays become more linear, G/G_{max} increases and ζ decreases for a given γ, indicating less energy dissipation during cyclic loading (Table 3.8).

Dobry and Vucetic (1988) point out that the large amplification of ground shaking experienced in MC during the 1985 Michoacan earthquake was conditioned by the large pseudo 'elastic' range of the VM clays and their tendency to accumulate, rather than dissipate, energy during shaking.

3.5.5 Stress-strain behaviour

A variety of procedures have been developed to determine the dynamic strength of soils. One procedure consists of a initial phase of static monotonic shear stress application (representing a sustained static pre-earthquake state of stress) followed by a sequence of cyclic stresses until failure occurs (simulating the cyclic shear stress application during an earthquake) (Ishihara, 1996). The soil response depends upon the magnitude of the initial shear stress relative to the cyclic shear stress, the loading rate, number of cycles, consolidation conditions, among others. In the following, some well-known characteristics

---

[45] Romo (1995), following Hardin and Drnevich (1972) who related the damping ratio, ζ, to the shear modulus by the equation $\zeta=\zeta_{max}(1-(G/G_{max}))$, proposed to represent the MC clay variation of ζ with shear strains with the expression $\zeta=(\zeta_{max}-\zeta_{min})(H(\gamma))+\zeta_{min}$. Where $H(\gamma)$ is taken from footnote 15 and ζ_{min} and ζ_{max} are 0.5% and 13% respectively.

of clay response to various test set-ups are summarised.

When the initial static shear stress is relatively large as compared to the amplitude of cyclic shear stress the influences of loading speed and load repetition are weak and the shape of the stress-strain curve becomes similar to that obtained in static tests. Fig. 3.30 shows representative results for compacted partially saturated cohesive clay (Ishihara, 1996). (In this plot the 1 Hz frequency cyclic strength is defined as the static plus cyclic axial stress causing failure in test specimens.)

Fig. 3.30 shows that under cyclic one-way loading the cyclic strength gradually decreases and the initially higher strength (caused by loading rate effects) tends to fade out as the number of cycles increases. Load repetition produces strength deterioration within the test specimen and in this case the final cyclic strength is equal to, or less than, the static strength. For two-way loading the cyclic strength shows entirely different features, the detrimental effect being more severe.

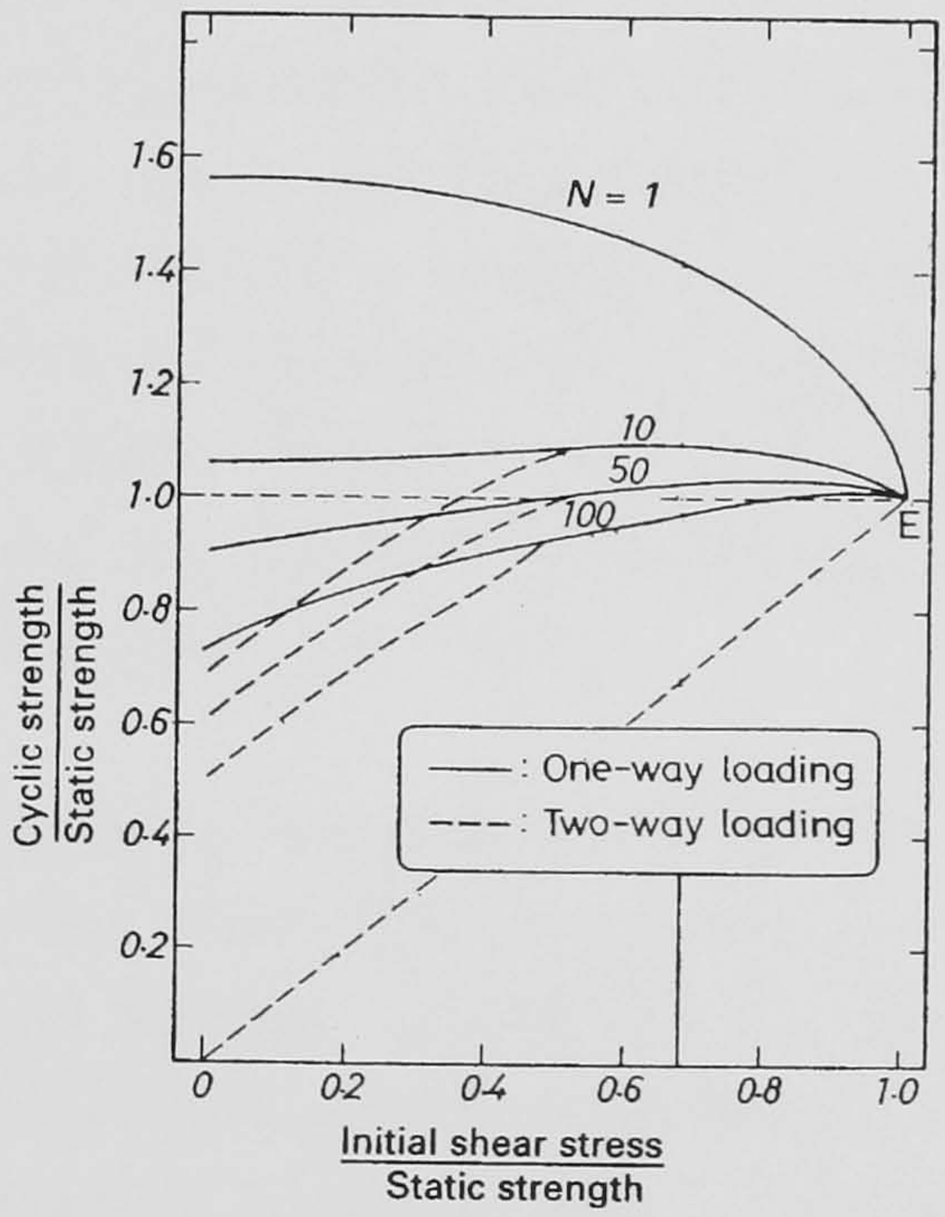


Fig. 3.30 Initial shear stress and cyclic one- and two- way loading effects on volcanic clay (Ishihara, 1996)

The degree of increase of the dynamic strength over the static strength decreases when the confining stress increases. Fig. 3.31 shows the average stress-residual strain curves for tests on specimens that were consolidated under a specified confining stress, subjected to a initial shear stress equal to 70% of the static strength and then loaded under an irregular loading simulating an earthquake condition. Also indicated are the stress-strain curves that would have been obtained if the loading had been continued further

under static conditions. It can be seen that the effect of the dynamic phase of loading increases the stiffness as well as the ultimate strength of the soil, and that the degree of increase of the dynamic strength over the static strength decreases when the confining stress increases (Ishihara, 1996).

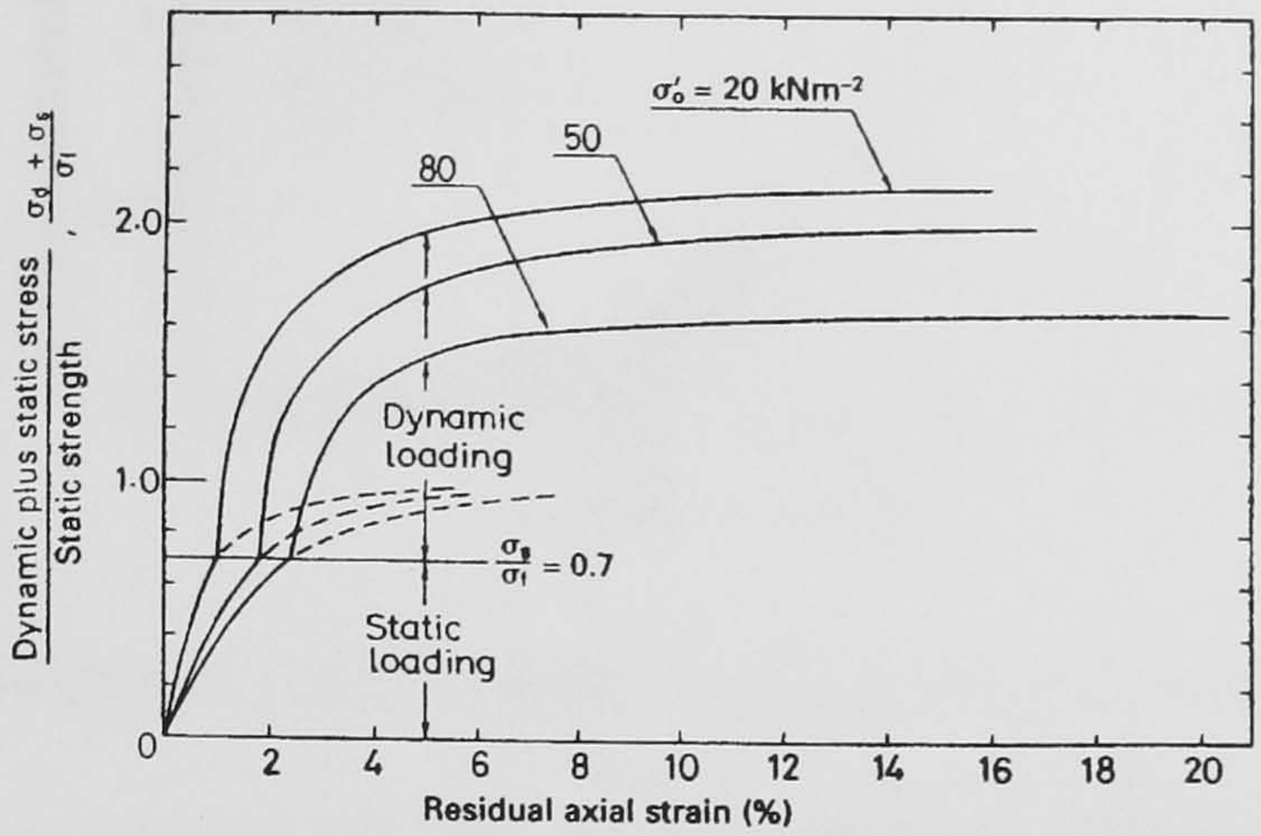


Fig. 3.31 Effects of confining stress on the dynamic strength of a volcanic clay (Ishihara, 1996)

Two threshold strains are used to characterize dynamic soil behaviour: the threshold shear strain, differentiating between linearity and non-linearity (stiffness reduction), and the volumetric threshold shear strain, separating conditions in which degradation and permanent deformations can or can not occur (similar to Jardine's Y_1 and Y_2 boundaries). For a given soil, they both depend on the cyclic stress magnitude, number of cycles, stress path and principal stress direction. Evidence of volumetric threshold are: development of pore pressures, reductions in G_{max}, and the development of permanent strains after unload – reload loops in triaxial tests (Hight, et al., 1997).

Fig. 3.32 shows a cyclic triaxial test[46] result carried out by Romo (1995) in a typical sample (PI=250%) of MC clay. These curves show a strain value where the rate of accumulation of permanent deformations increases indicating the volumetric threshold cyclic strain. According to Fig. 3.32 the critical volumetric (Y_2) axial strain for MC clay is about 3%, corresponding to a shear strain γ= 0.75 (3%) = 2.25%. This threshold strain is around 30 times higher than the critical strain for the Y_1 boundary between linear and non-linear clay behaviour. This implies that in the case of highly plastic clays (like Mexico City's) permanent deformations will develop significantly only when the soil is close to failure under dynamic loading[47]. (MC clay undoubtedly has high strain thresholds, however the very high thresholds presented by Romo suggest that his data may require re-evaluation.)

---

[46] No information on the rate or frequency were found.

[47] The volumetric threshold increases with plasticity.

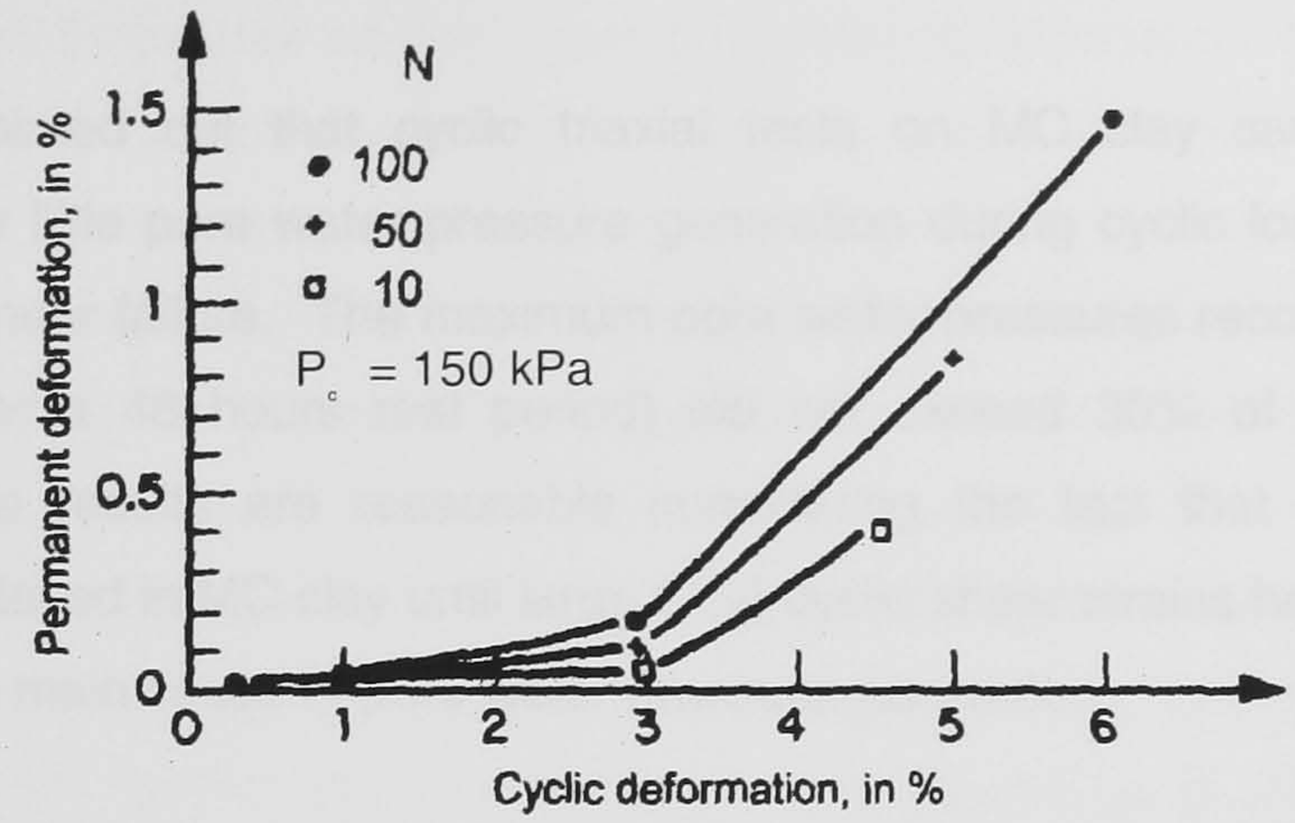


Fig. 3.32 Effect of cyclic triaxial loading on permanent deformation (Romo, 1995)

Such behaviour is manifested in Fig. 3.33 where a total stress vs permanent strain plot for MC clay is shown. The plot shows that permanent deformations (axial deformations) accumulate only when the total stress (cyclic plus static) exceeds the strength of the clay. It also points out the fact that the dynamic strength is higher than the static strength (S_u). In the case of the saturated clays of MC the dynamic strength may be about 60% higher than S_u (Romo, 1995).

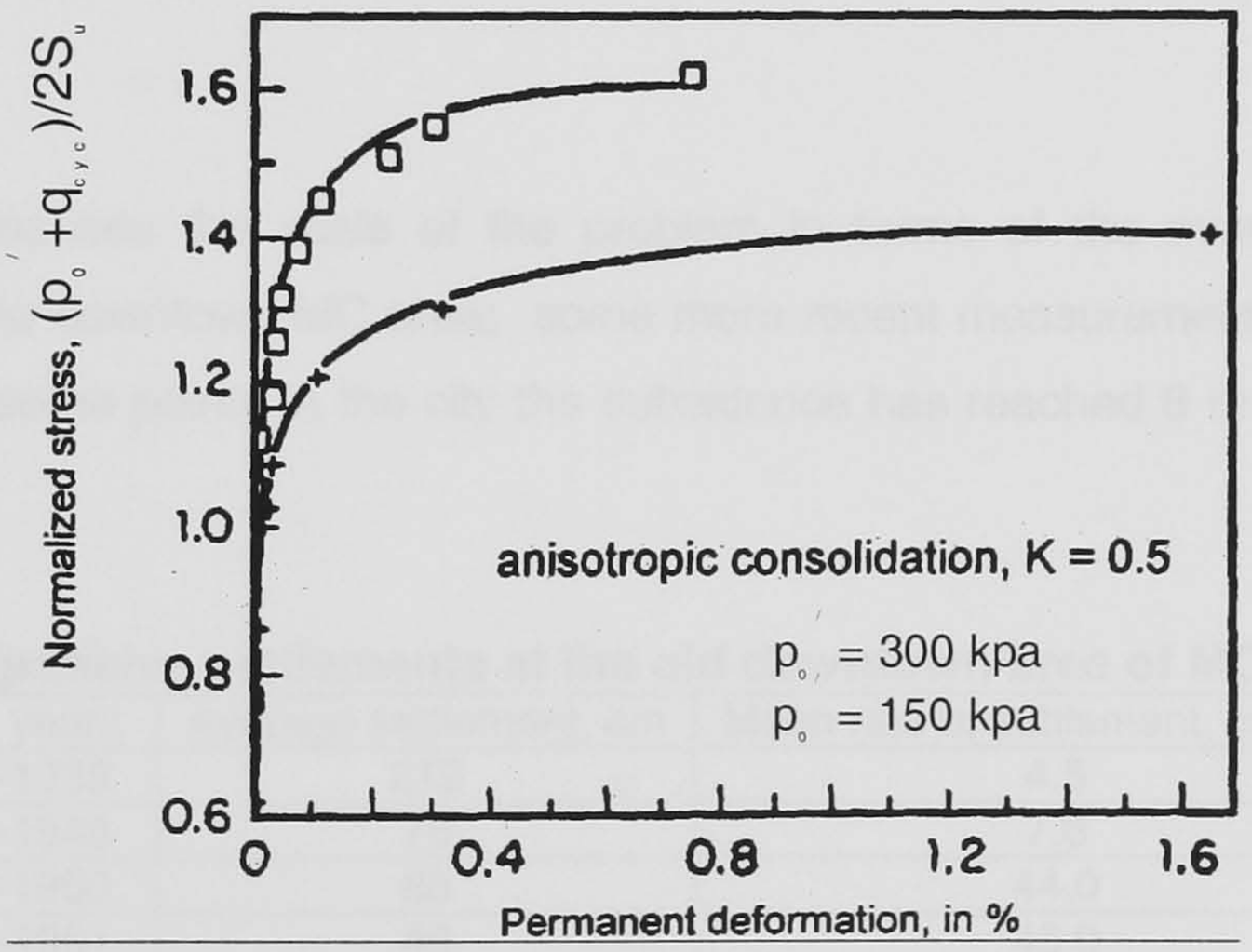


Fig. 3.33 Dynamic stress vs. plastic deformation relationship for triaxial tests on MC clay (Romo, 1995)

3.5.6 Pore water pressure

Pore pressure build-up, or reduction in mean stress p', may result under undrained cycling from plastic straining that damages the soil structure (Hight, et al. 1997). The degree to which this occurs with a given clay depends on its composition, and tends to decrease with

PI.

Romo (1995) pointed out that cyclic triaxial tests on MC clay samples (PI>250%) consistently show little pore water pressure generation during cyclic loading, even when the samples are near failure. The maximum pore water pressures recorded during cyclic loading (and after a 48 hours rest period) did not exceed 30% of the consolidation pressure. These results are reasonable considering the fact that significant plastic deformation is delayed in MC clay until large (2%) cyclic shear strains have been induced, and these are the main cause of pore water pressure generation.

3.6 Regional subsidence

Hydraulic works carried out to prevent flooding, and the extraction of water from underground aquifers, have contributed to the almost complete desiccation of the lakes in the Valley of Mexico and have induced appreciable piezometric head losses within the clay layers. The resultant increment in effective stress in the soil deposits has prompted extensive consolidation in the clay strata and a high rate of regional subsidence in MC. Carillo (1948) established the relationship between the regional settlement and water pumping.

Table 3.9 summarises the scale of the problem in terms of the average progressive settlements in the downtown MC area; some more recent measurements are included in Table 3.10. At some points in the city the subsidence has reached 8 m from the start of the 20th century.

Table 3.9 Progressive settlements at the old downtown area of MC (Jaime, 1987)

Time, years	Average settlement, cm	Mean rate of settlement, cm/year
1891-1938	212	4.5
1938-1948	76	7.6
1948-1950	88	44.0
1950-1951	46	46.0
1951-1952	15	15.0
1952-1953	26	26.0
1953-1957	68	17.0

Table 3.10 Rate of settlement at various zones of MC, 1970-1977 (Jaime, 1987)

Site	Mean rate of settlement,
Calz. De Guadalupe and Rio Consulado	5.3
Calz. De Tlalpan and Av. Baja California	7.5
P.E. Calles and Rio Churubusco	11.3
Calz. De Tlalpan and Taxqueña	2.7
Av. Revolucion and Puente de la Morena	7.0

The regional subsidence has an important influence on foundation behaviour. Thus, even with partially or fully compensated foundations, the draw down of the pore-water pressure induces an increase of the effective pressure that often shifts the current effective stresses on to the virgin part of the compressibility curve, resulting in a dramatic increase in the vertical deformations. Other phenomena occur for the foundations relying on piles. The reduction of pore pressure acting on base slabs transfers load to the piles, which usually develop extra shaft loads. For the case of point-bearing piles supported by the first hard stratum or by the deep deposits, the base loads are increased by negative skin friction, which appreciably decrease the load carrying capacity of the piles.

CHAPTER 4

SHEAR STRENGTH OF MEXICO CITY CLAY ON RING SHEAR

Large strain soil-to-soil and soil-to-interface shearing resistance is relevant to several geotechnical engineering problems, among them: slope stability, friction piles, retaining walls, earth reinforcement, and submarine pipelines. Large strain shearing resistance depends on the soil grain size distribution, mineral composition and shape of the soil particles, clay content[48], water content, interface material and roughness, stress history, magnitude of the normal stress, and rate of shear displacement (Lemos and Vaughan, 2000; Tika, 1991; Lemos, 1986).

The importance to piled foundations of large strain shear strength determination by ring shear testing is apparent from laboratory and field studies of pile skin friction by Martins (1983), Jardine (1985), Bond (1989), and Lehane (1992). Their research points out that laboratory tests carried out on clay soils in the ring shear apparatus predicts reasonably accurately the soil-steel interface friction angles (δ') measured in the field with instrumented piles, provided the test procedure models the rates of shearing experienced during the pile installation and the normal effective stress levels developed before and after pile installation.

This chapter presents the Author ring shear tests on Mexico City (MC) clay, to the Author's knowledge there are no information about the same type of tests in the literature. The results of this study are applied later in a validation exercise involving the Imperial College (IC) pile design method's application to MC conditions (Chapter 5). The ring shear test behaviour of MC clay is extensively described using the framework developed by Lupini, et al. (1981).

Enrique Santoyo and Rene Contreras of TGC Geotecnia provided the soil samples tested. The results of the tests presented here are summarized in Appendix A, where each soil is identified, and details are given of the test characteristics and key results.

---

[48] Clay content is defined as the proportion of clay minerals present in the soil irrespective of particle size.

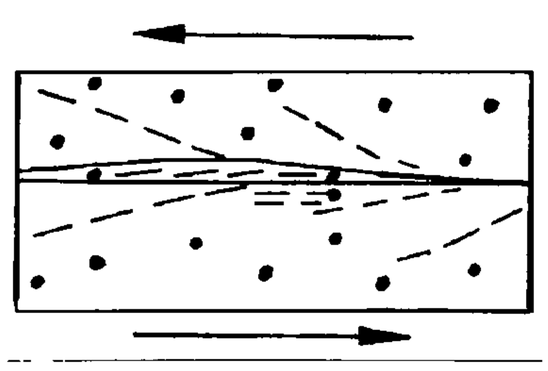
4.1 Shearing modes

4.1.1 Clay-to-clay shearing

Lupini, et al. (1981), using data from soil-to-soil tests on clays of varying plasticity, showed that the large strain shearing mechanism of soils changed with the ratio of platy (low friction) clay particles to rotund particles. They established that the residual[49] strength measured at slow (drained) rates of shearing resulted from three different modes of shearing. These are:

a. A sliding mode

Sliding shear is produced when platy, low-friction particles form the bulk of the soil. The clay particles, being plate-like, rotate as the slip zone develops and eventually become aligned parallel to the direction of shear strain. Nowatzki (1966) and Taylor (1971) observed similar realignment in direct shear and cyclic triaxial tests. These orientated[50] particles deform predominantly by sliding over each other on a thin polished continuous shear surface (Fig. 4.1). This shear surface, which is a permanent feature of the soil, will show residual strength characteristics that are not improved by any subsequent stress history, apart from complete remoulding. The main feature of the sliding shear mode is its initial brittleness[51] which results in low residual friction angles (ϕ_R') typically in the range 5° to 20° – these values depend primarily on mineralogy of the platy particles, pore water chemistry, and the coefficient of inter-particle friction.



Intensely orientated and planar shear surface. Specimen separated on shear surface, with clay in either side showing partial orientation

Fig. 4.1 Lupini, et al. (1981) interpretation of sliding shearing in London clay (48% clay fraction)

---

[49] Residual strength τ_R is the shear stress operating after shear to the residual state. The residual friction angle $\phi_R' = \tau_R/\sigma_n'$. σ_N' is the normal effective stress operating at the failure surface.

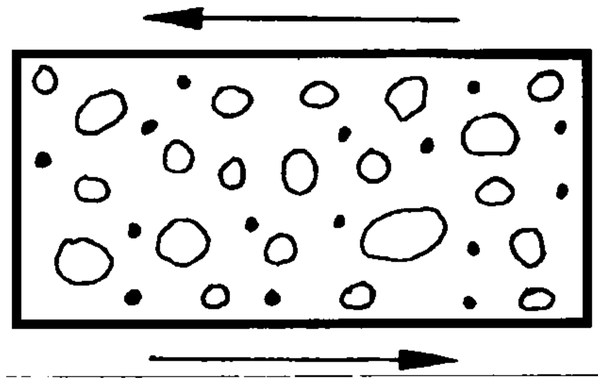
[50] Particle orientation is defined as a function of particle shape and not of particle contacts. Thus random orientation in terms of shape of the particles does not imply isotropy of the contacts (Lupini, 1981).

[51] Brittleness is the post-peak drop in strength produced by dilatancy, particle re-orientation or breaking particle bonds.

When the sliding mode dominates a decrease in shear strength with increasing normal stress is observed - this dependency decreases with stress level. This response can be explained by a net attraction between clay particles; or by an increment in the degree of orientation of the platy particles with the increment of the normal effective stress. If a specimen is unloaded and re-sheared in overconsolidated condition, it will again fail on the same previously formed shear surface and non-brittle failure will occur. (Thus peak strength can only be determined from the first loading stage at one normal stress.)

b. A turbulent mode

Soils that contain a high proportion of rotund granular particles or, possibly, soils dominated by platy particles, whose coefficient of interparticle friction is very high, develop turbulent shear mode at large strains. Their ultimate shearing mechanism involves rotation of the rotund particles, predominantly at constant volume, and is not controlled by particle orientation - interference between rotund particles prevents the formation of a shear zone of oriented clay (Fig. 4.2). The residual shearing angle is high (typically ϕ_R' greater than 25°), is reached at relatively small shear displacements, and depends primarily on the shape and packing of the rotund particles. A shear zone, once formed, has a different porosity (or different water content) to the matrix material and its behaviour can be considerably modified by subsequent stress history.



No separation on shear zone and no preferred orientation of the clay matrix. Relatively dense and interlocking packing of the sand grains, which can be coated in clay particles.

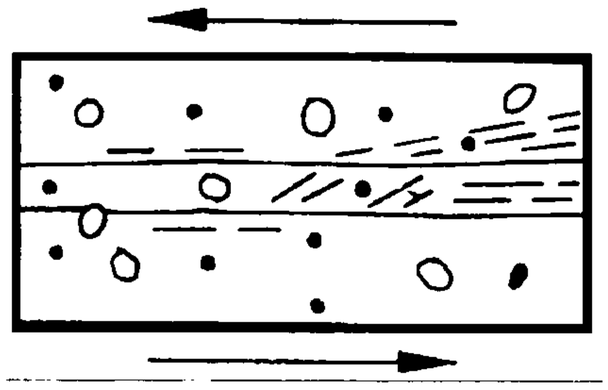
Fig. 4.2 Lupini, et al. (1981) interpretation of turbulent shearing, material with 27% clay fraction

The influence of the normal effective stress level on the residual friction angle for soils that shear in a turbulent way should be small. Compression under increasing normal stress will bring the granular fraction of any mixture into a closer packing, and so promote interference and interlocking between the rotund particles. A slight negative effect could be observed, however, when the massive minerals are separated at their contacts by pockets of clay minerals (Lupini, 1981). If this type of soil is unloaded (i.e. overconsolidated) after residual conditions have been attained, the specimen should dilate during shear and a renewed peak, above residual strength, should be observed on re-shearing - the water content in the shear zone previously formed will have been

modified by overconsolidation. Post peak, the strength should drop to a residual value, reached when dilation is complete, that should be equivalent to the non-brittle strength of a specimen normally consolidated and sheared to large strains at the same normal stress.

c. A transitional mode

Elements of both types of shear could occur where no dominant particle shape stands out within a thick shear zone (Fig. 4.3). In this mode the residual shearing angle is sensitive to small changes in grading of the soil.



Well orientated shear surface that passes round an interfering sand grain. Specimen separated on heavily striated (slickensided) shear surface. Two continuous shear surfaces undulating in the direction of shear with clay particles between them orientated 0-45°.

Fig. 4.3 Lupini, et al. (1981) interpretation of transitional shearing, material with 40% clay fraction

In the transitional shear mode, where turbulent and sliding shear both play a part, the effects of increasing the normal effective stress will be to reduce the residual shearing angle in sliding and, at the same time, to cause a denser packing of the round particles and more interference between them. The overall effect of increasing σ_n on ϕ_r' angle will depend on the two effects described before, which are in opposition and may partly cancel out. Under overconsolidated conditions the transitional shearing shows brittleness (Lemos and Vaughan, 2000).

The zones in which these types of mechanism typically occurs, as a function of residual strength and clay content, are illustrated in Fig. 4.4. In the figure Lupini, et al. (1981) used the packing parameter, the granular void ratio[52] (e_g), to quantify grading. Lemos and Vaughan (2000) included clay fraction[53] in the graph since it is more readily recognized. Clay fraction is adopted as the key variable in the analysis of MC clay results that follows.

---

[52] Granular void ratio for a saturated soil is defined as the volume of platy particles and water divided by the volume of rotund high-friction particles.

[53] The clay fraction is the percentage by weight of particles smaller than 2μm mean particle diameter, as determined by sedimentation.

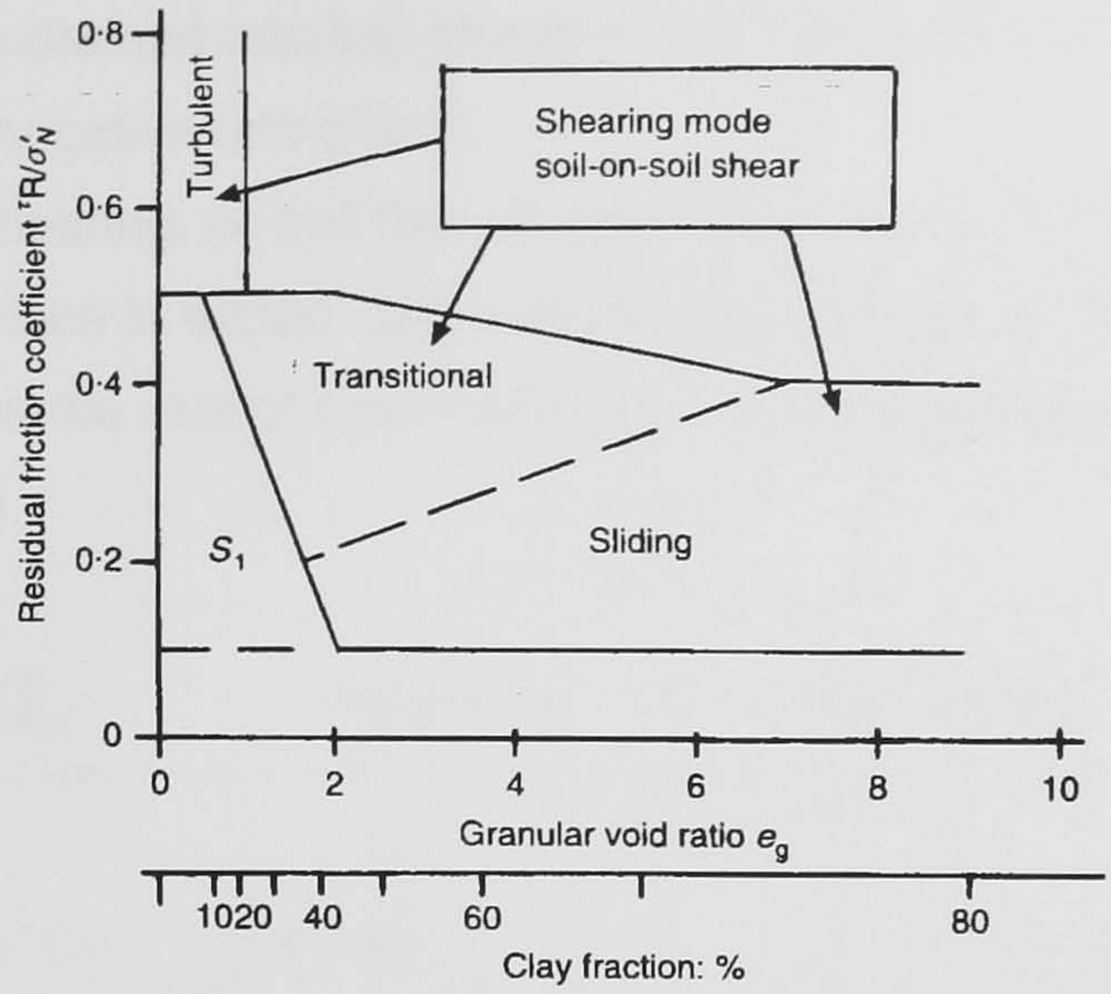


Fig. 4.4 Residual shear mechanism as a function of particle packing and clay fraction. S1 area represent possible sliding shear when soil is failed against a smooth interface (Lemos and Vaughan, 2000 after Lupini, et al., 1981)[54]

4.1.2 Effects of displacement rate on shearing modes

Parathiras (1994) and Tika, et al. (1996) present extensive literature reviews on the influence of the rate of shearing on the residual shear strength of granular and cohesive soils tested in the ring shear apparatus (both Bromhead and Bishop), shear box and viscometer apparatuses. Lupini (1981), Martins (1983), Lemos (1986) and Tika (1989) analyzed fast rate shearing ring shear results adopting the residual shearing modes introduced by Lupini, et al. (1981).

Lemos, et al. (1985) showed that if a shear surface is formed by slow drained shearing to large displacement and then tested at a fast rate, the following features are typically observed (Fig. 4.5):

i) A threshold strength is first mobilized, at which the sample starts to deform more readily after having shown a very stiff initial response. The threshold strength is a function of the rate of displacement and is higher than the slow drained residual strength.
ii) A higher fast peak strength that is mobilized after the threshold strength. This peak strength is a function of the rate of displacement.
iii) A fast residual strength obtained when the strength drops to a minimum value

---

[54] Note $\tau_r/\sigma_n' = \tan\phi_r'$.

with further fast displacement. The fast residual strength usually remains higher than the slow drained residual strength, but it may drop to a lower value in soils that show a "negative rate effect".

iv) If after fast shearing, of soil that shows transitional and sliding shear behaviour, the shear surface is tested slowly an initial slow peak strength is developed that is greater than the slow drained residual. Fast pre-shearing leaves a disordered shear surface.

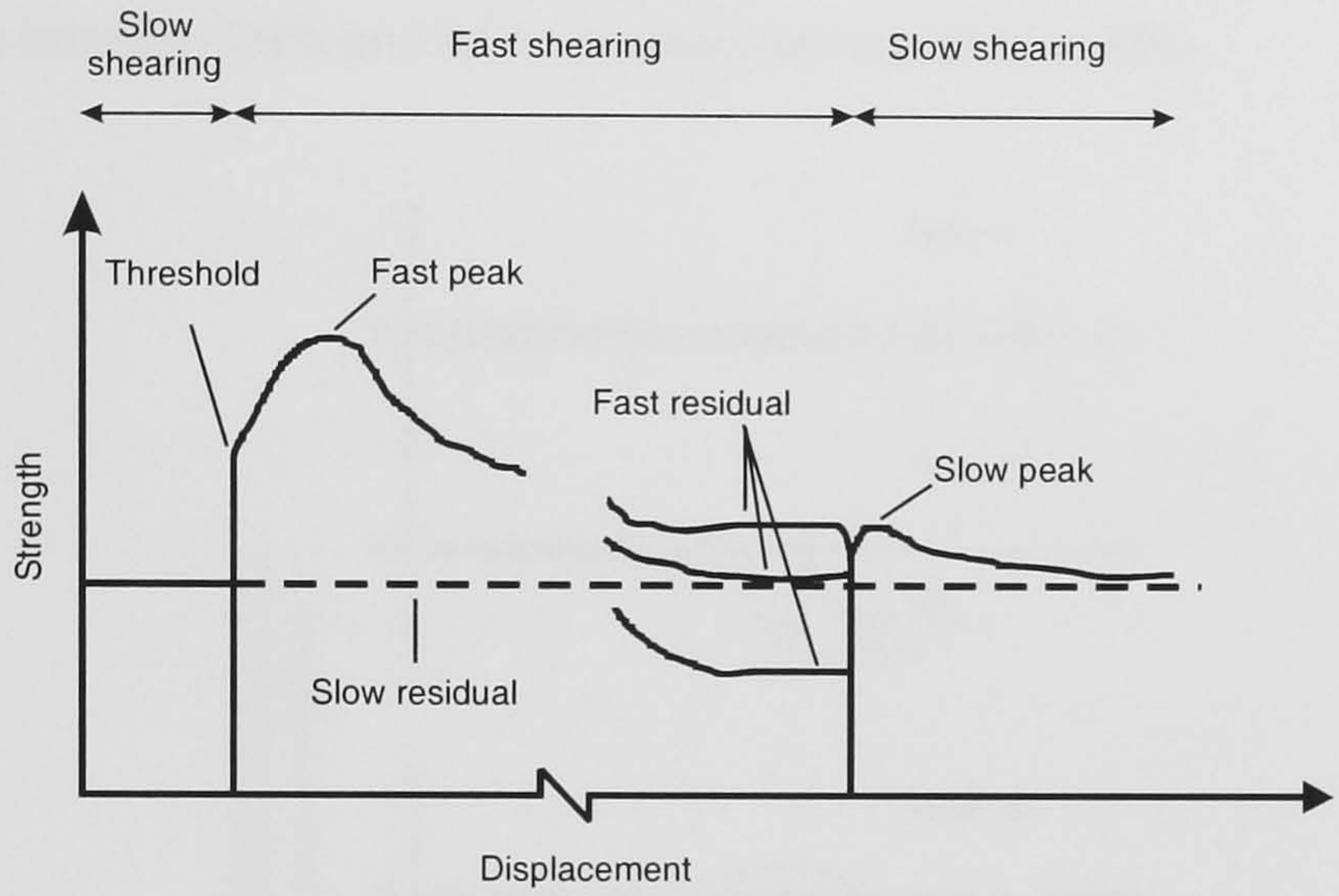


Fig. 4.5 Summary of the observed rate-dependet phenomena for residual strength (Tika, et al., 1996)

Tika (1989) identified five types of variation of the residual strength upon increasing rates of displacement, these are (Fig. 4.6):

- Type I involves insignificant changes of the residual strength with increasing rate of displacement and is characteristic of soils with a turbulent shear mode, PI usually less than 9%, sand content higher than 20%, and clay content lower than 10%.
- Type II involves an insignificant, or moderate, increase or decrease of the residual strength with increasing rates of displacement followed by a substantial decrease in strength as the rates increase further. This develops in soils that exhibit either transitional or turbulent shearing behaviour, and PI typically between 9% and 21%. Deviations from this behaviour have been observed at high normal stresses. Tika, et al. (1996) show that for turbulent shearing an increase in σ_n' can change the soil respond from negative to neutral.
- Type III involves a decrease of the residual strength with increasing rates of displacement followed by an increase and a substantial drop of strength below its slow residual value as the rate of displacement increases further. This behaviour is characteristic of silty clays with transitional or sliding shear mode, and PI usually

between 24% and 26%.

- Type IV involves a decrease of the residual strength with increasing rates of displacement below its slow residual level, followed by an increase above the former as the rate of displacement increases further. To this category belong clays with turbulent or transitional shear mode and PI typically between 10% and 21%, and silty clays with transitional to sliding shear mode and PI typically between 26% and 36%.
- Type V involves an increase of the residual strength with increasing rates of displacement and is characteristic of clays with sliding shear mode, the usual PI range falls between 36% and 51%, and clay content above 48%.

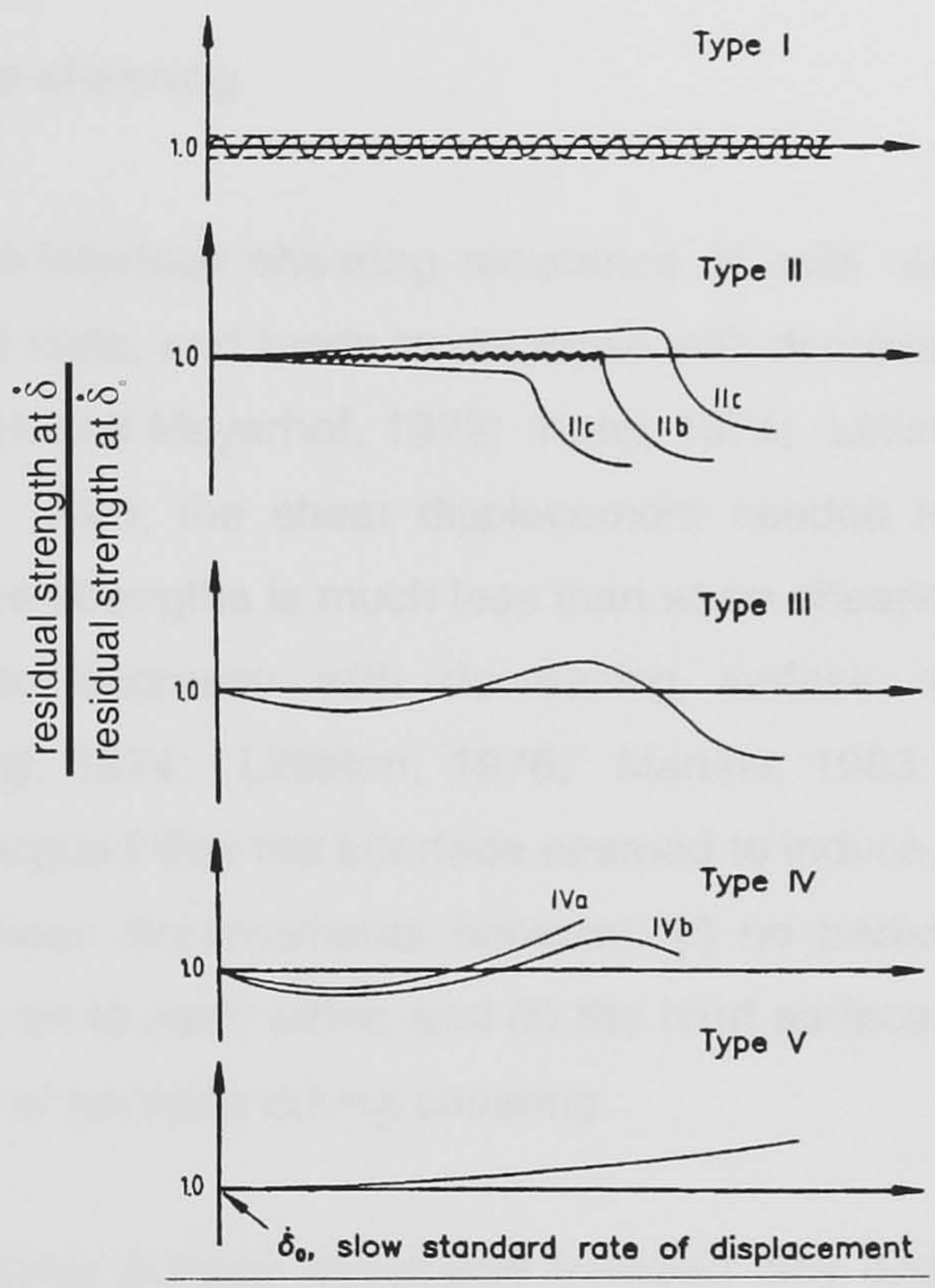


Fig. 4.6 Variation of fast residual strength with an increasing rate of displacement (Tika, 1989)

Tika, et al. (1996) associate the peak during fast shearing to volume changes within the shear zone and the disordering of the structure of the shear zone formed at the slow residual state.

Decay in residual strength with rate can be related to pore pressure generation, loss of soil through the confining rings gap, and water in the water bath. Tika (1989) points out that just the later contributes significantly, and proposed the following explanation for the reduction of shear strength: "*Fast shearing involves dilation of massive particles to permit them to pass over one another. This results in an increase in the void ratio and*

therefore the water content of the shear zone when free water is available. The low strength reached during shearing at a rate of displacement greater than the critical is a steady state without significant excess pore water pressure due to contractive behaviour or heating. It is caused by the increase in the water content of the shear zone, and thus an increase in the ability of soil to flow. Whenever the fast shearing is stopped or slowed down, the shear zone attempts to contract and excess pore water pressure is generated. The low strength in the shear zone, while it results from fast shearing, is not significantly dependent on it. It persists even during slow shearing following a fast stage until the excess pore water pressure dissipates".

4.1.3 Clay-to-interface shearing

The large strain soil-to-interface shearing resistance of soils normally falls below that mobilised in soil-to-soil tests, and tends to decrease with decreasing surface roughness (Potyondy, 1961; Clark and Meyerhof, 1972; Kanji, 1974; Littleton, 1976; and Lemos and Vaughan, 2000). Also, the shear displacement needed to attain the peak and residual soil-to-interface strengths is much less than when shearing clay-to-clay, and the displacement tends to decrease with decreasing surface roughness (Clark and Meyerhof, 1972; Kanji, 1974; Littleton, 1976; Martins, 1983; and Ramsey, et al., 1998). Lupini (1981) argued that the interface seemed to induce orientation of the platy particles at smaller shear displacements because: (i) no particles project across the shear plane and catch on to each other; and (ii) the hard surface provides a fixed plane to guide the alignment of particles during shearing.

Observations of the shear surface developed between clay and steel interfaces have shown that the mechanism often involves clay-to-clay shear. Tsubakihara and Kishida (1993) postulated that there is a critical steel roughness of approximately 10μm; when a steel surface is smoother than the critical roughness, interface sliding occurs at the peak strength; when a steel roughness exceeds the critical value, there is shear failure within the clay specimen. Lemos and Vaughan (2000) considered that interface's influence on shear strength ceased to be significant when the roughness became equivalent to the sand sizes in their sandy clays.

Lupini, et al. (1981) postulated that the presence of an interface could be particularly important in tests on soils of low clay content. Shearing might be encouraged at the interface if the flat interface could prevent interference between massive minerals, allowing an oriented shear zone to form and promoting a sliding-like mechanism (zone 1

on Fig. 4.4).

Lemos and Vaughan (2000) concluded from their tests on sandy-clay soils, that any trend for shearing resistance to increase during large shear displacements is caused by the ploughing action of accumulated degraded interface material near the interface and not from changes in roughness. A clay rich interface sliding surface can be formed initially, but later disrupted by massive rotund particles.

The effect of normal effective stress level on shearing resistance in soil-to-interface tests was found to be similar to that observed in soil-to-soil shear (Lemos and Vaughan, 2000).

4.2 Apparatus and testing procedure

4.2.1 Ring shear principle

The Bishop ring shear (Bishop et al., 1971) and the Bromhead ring shear (Bromhead, 1979) apparatuses were used for the Author's tests on MC clay and other soils. Both apparatuses are displacement-controlled and allow the measurement of the peak and residual strength of a shear zone formed either at mid-height of the soil specimen or between the specimen and an interface.

During ring shear testing an annular specimen is ruptured on a plane of relative rotatory motion while confined laterally and subjected to a constant gross normal stress. The lower half of the sample is carried on a rotating table, while the upper half reacts through a torque arm against a pair of fixed proving rings or load cells that measure the tangential load. The rotation of the table is measured manually.

In the standard test the samples are sheared at a rate to ensure 95% consolidation of the specimen after a shearing displacement of 1-2 mm. The torque, displacement and change in sample thickness are monitored continuously during each test. In the Bishop apparatus (BiA) the torque and changes in sample thickness are measured with load cells and displacement transducers; whilst the Bromhead apparatus (BrA) uses proving rings and dial gauges. The BiA allows for the side friction developed in the upper ring to be measured.

The standard sample set up starts with the remoulding of the material before it is kneaded with the thumb into the apparatus container, trying to avoid trapped air. (The residual friction angle is unaffected by the initial structure of the soil; Lupini, 1981). To reduce consolidation settlement the soil can be placed at a low water content, although the MC clay samples were remoulded at their natural water content to avoid changing their organic content. The samples are then consolidated to the desired pressure, usually in stages, and shearing is commenced.

For interface tests, the interface plate replaces the lower half of the sample for the BiA; for the BrA the upper porous stone is replaced by the interface. Two Bishop and one Bromhead apparatus were used for the test programme.

4.2.2 Bishop ring shear apparatus

Bishop, et al. (1971) and Garga (1970) give a complete description of the apparatus' design, principles of operation and testing procedure. BiA (Fig. 4.7) was preferred to study MC clay response to fast shearing, normal stress, OCR, and reversal of shearing.

The dimensions of the specimen are: outer diameter 152.4 mm, inner diameter 101.6 mm and initial thickness of 19 mm or 12.5 mm, for soil-to-soil and soil-to-interface tests, respectively. Once the soil has been kneaded into the rings the aligned upper platen, with a porous stone, and the torque arm are placed; then the spherical seating and nut are set. The lever arm counterweight is then balanced, the nut tightened and four guide pins inserted. After the load cell was zeroed to balance the weight of the linking yoke, the crosshead is mounted on the rigid columns and the eight fastening screws and two guide pins are inserted. The dial gauge bridge, holding the displacement transducer, is then mounted and the zero readings taken.

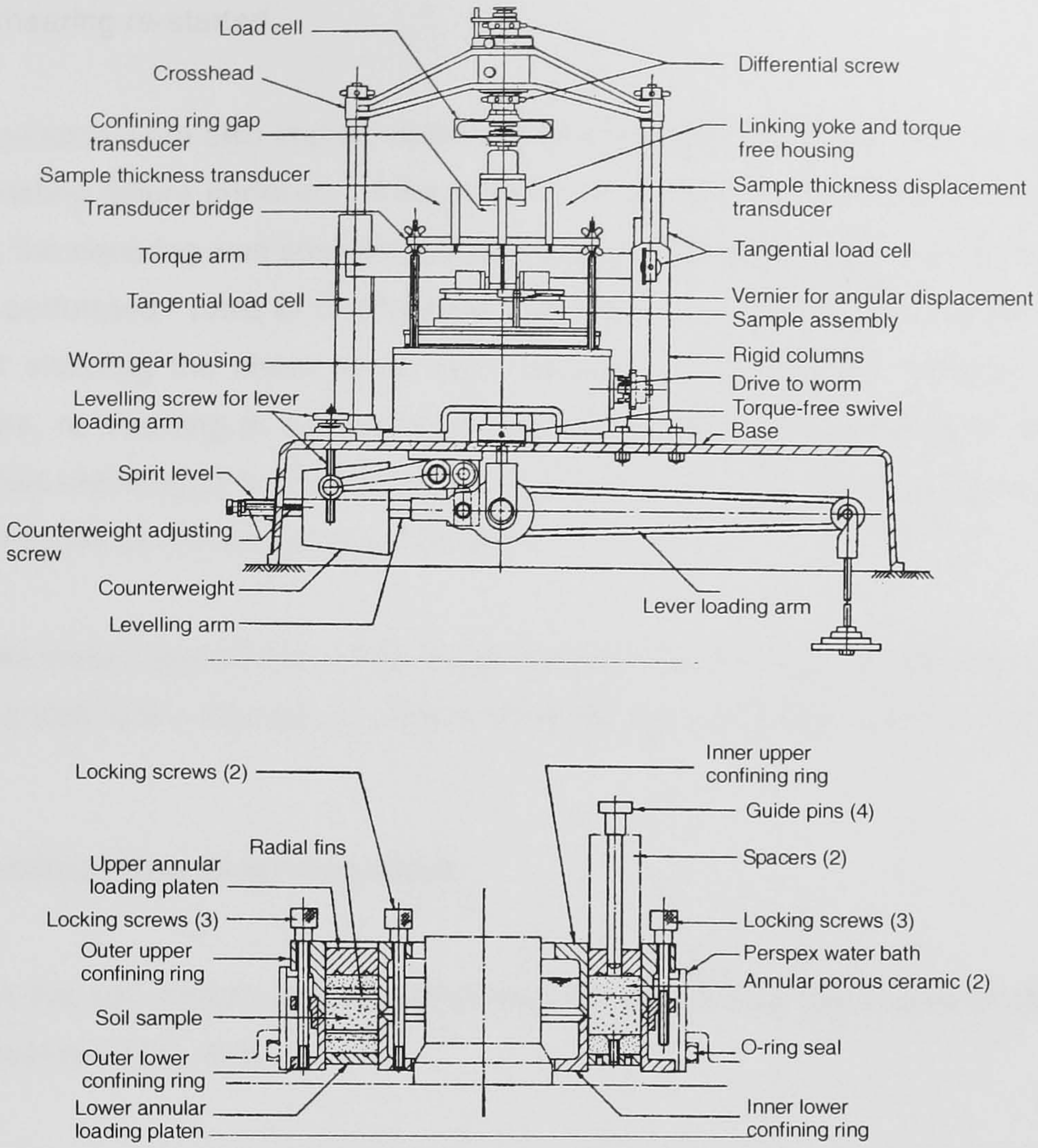


Fig. 4.7 General layout and details of sample assembly for the Bishop ring shear apparatus (Bishop, et al. 1971)

Weights are then applied on the lever arm, the water bath filled and the sample allowed to consolidate. When the vertical displacement readings are stabilised, the locking screws are removed and the upper confining rings retracted. Up to this stage the confining rings were closed to restrict the soil loss between the gap; the loss could be large, particularly at high stress levels. The gross normal load on the specimen is maintained constant during shearing and the net normal load is obtained at any stage of the test by subtracting the measured side-friction force from the gross normal load.

A drained rate of shearing was calculated. The sample was sheared at a constant rate of displacement until a steady state was reached. The shearing was then stopped, and the peak and residual shear strength computed.

Multi-stage tests were carried out to determine the frictional resistance at different normal stress (from 100 kPa to 400 kPa) and OCR's. After the first slow rate shearing finished, the upper ring lowered, the axial stress changed, the consolidation allowed, and

drained shearing re-started.

Multi-stage tests were also implemented to investigate the effects of the rate of shearing on pre-existing failure surfaces. After a shear zone was formed by initial slow drained shearing, the shearing was stopped, the tangential load reduced to a minimum, and fast shearing performed - rates of displacement between 3.5 and 540 mm/min were applied. After fast shearing the shear force was removed completely, the sample allowed to consolidate, re-shearing at the standard drained rate to the residual state was carried out, and fast shearing at a different rate was performed again. The procedure continued for 4 cycles without changing the axial stress.

Some tests were subjected to a first stage of fast shearing, then consolidated, and then tested at a slow rate – this was in order to simulate pile installation (Jardine, 1985).

4.2.3 Bromhead ring shear apparatus

In the BrA the soil sample is 5 mm thick with inner and outer diameters of 70 and 100 mm, respectively (Fig. 4.8).

The testing method adopted for the BrA was based on the procedure of Stark and Vettel (1992). After the soil was moulded into the base plate and the top cap positioned, dead weights were added, zero readings taken and the water bath filled. Stark and Vettel emphasise that one of the problems with the apparatus is that as soil is extruded during shearing, the top platen and the container might come into contact creating frictional resistance. As it is not possible to measure this friction it is necessary to minimise the vertical displacement and hence this error - Stark and Vettel recommend that the vertical displacement is limited to 0.75 mm. Thus, if after consolidation the vertical settlement was greater than 0.75 mm the top platen was removed, more soil was added to the mould, and further consolidation allowed. The samples were then sheared under drained condition.

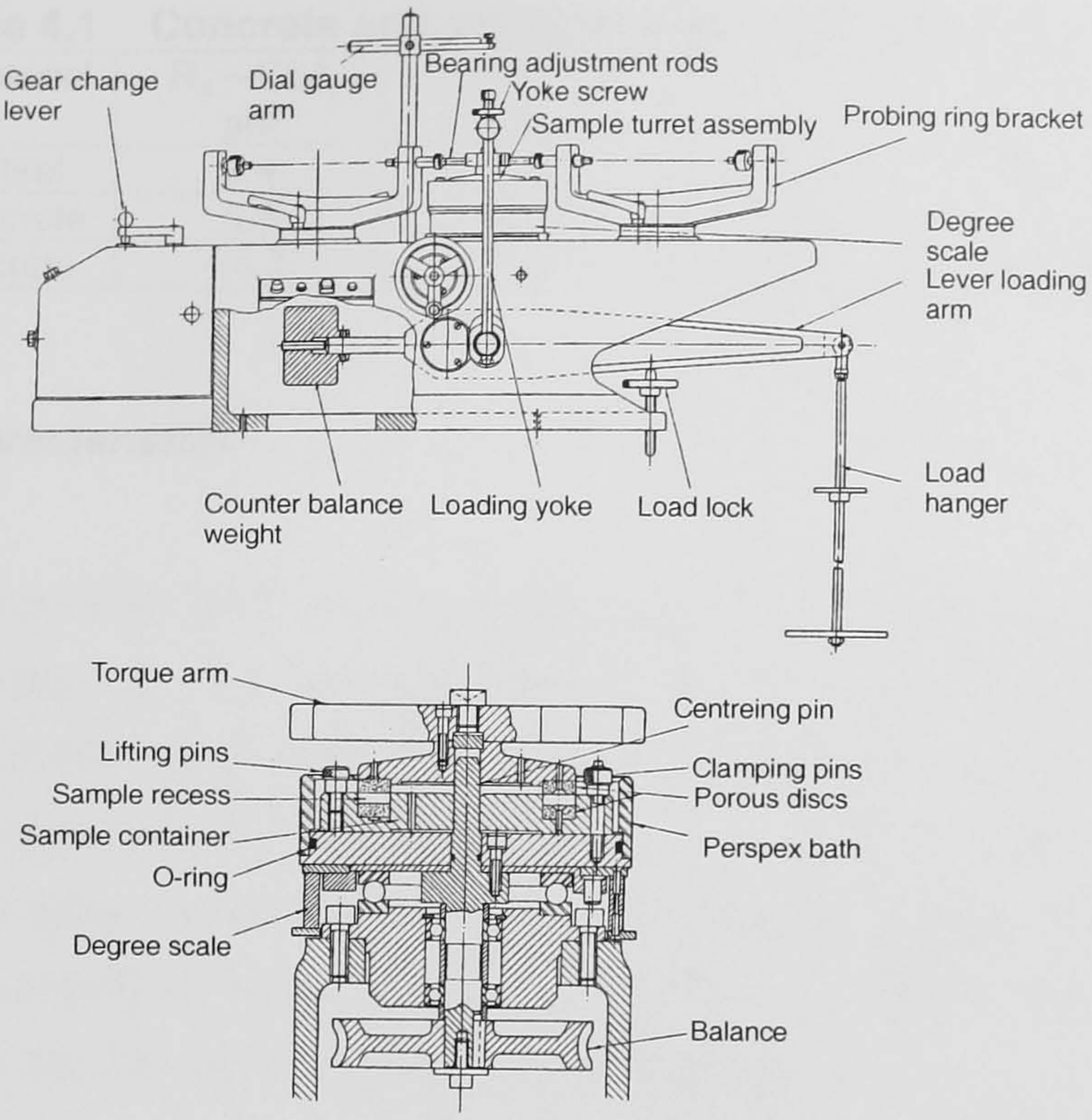


Fig. 4.8 Side view and section through sample turret for Bromhead ring shear apparatus (Wykeham and Farrance Handbook)

In practice, it was found that the settlement limit was exceeded during shearing, especially during fast shearing. As a result fast shearing couldn't be carried out on MC samples, for which the BrA does not seem particularly suitable.

4.2.3 Interface characteristics

The interfaces tested were made from either cast concrete or sand blasted stainless steel. The roughness of the interfaces were measured mechanically by a Form Talysurf Series 2 profilometer manufactured by Taylor Hobson.

The roughness description is based on the standard (in tribology) centre line average (CLA or R_a) roughness parameter. The assessment length was a transverse section of 20 mm, and the cut-off length was 2.5 mm. The surface details are summarized in Table 4.1, where: R_a is the arithmetic mean of the absolute departures of the roughness profile from the mean line; W_a is the corresponding parameter from the waviness, which was adopted since the concrete surface is not as plain as the stainless steel interface; and R_t is the maximum peak to valley height of the profile in the assessment length (Taylor Hobson).

Table 4.1 Concrete and stainless steel interface description

Interface material	R_a – CLA μm	W_a μm	R_t μm	Observation
Stainless steel	6.4	5.9	57.8	Sand blasted
Smooth concrete	5.5	19.9	109.7	Surface with leakage
Rough concrete	14.3	31.5	137.4	Sand at surface

4.3 Sample characteristics

The origin, composition and main mechanical properties of typical MC clay were discussed in Chapter 3. The samples adopted for the ring shear tests are from two typical locations in MC; the Piedad site at the city center, and Chapultepec site located in the area where building damage usually occurs during earthquakes (Fig. 6.14). The profiles for these sites, indicating the depth of the samples, are shown in Fig. 4.9. The relevant sample properties are summarised in Table 4.2[55]. These samples correspond to those used for the intrinsic property study in Chapter 3.

Chapter 3 established that the three main components that combine to give MC clay its physical properties are: organic matter (5-10%); silt sized siliceous microfossils, mostly diatoms (55 to 65%); and clay sized active mineral particles (20 to 30%). The overall surface configuration of MC clay was described as amorphous.

Table 4.2 Characteristics of samples used in ring shear tests

Site	Piedad		Chapultepec	
Sample No.	M15-1	M16-2	C13-4	C14-2
Depth, m	14.50	17.20	15.10	8.30
w, %	215	201	270	360
LL, %	224	201	257	355
PI, %	160	150	181	243
Clay fraction, %	53	45	28	N/A

[55] w is the water content at the start of the tests.

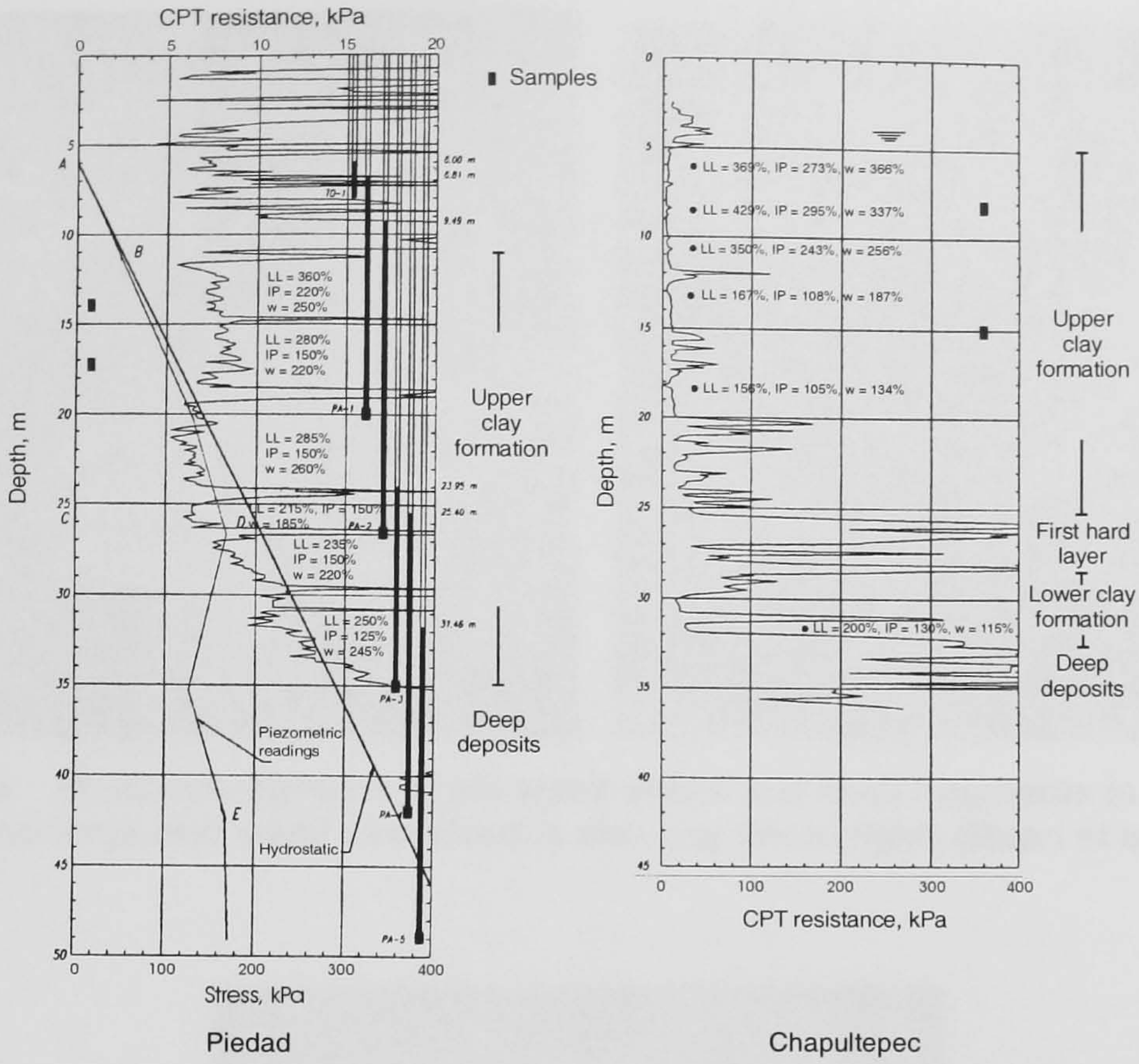


Fig. 4.9 CPT profiles for Piedad and Chapultepec sites (TGC, Geotecnia)

The microfossils, mostly siliceous shells and shell fragments of diatoms, comprise various shapes of highly poriferous skeletal fragments. The textures of the diatom surfaces are the result of a vast number of minute cavities, canals, holes or chambers in the siliceous wall. The siliceous shells display circular or len-shaped forms and contain dots, grooves, ridges and depressions (Fig. 4.10) (Mesri, et al. 1975).

The photomicrographs of the clay-sized fraction appear to show extremely thin, crinkled films (Fig. 4.11). The individual particles are fuzzy and unresolved suggesting a very small ultimate size (Mesri, et al., 1975).

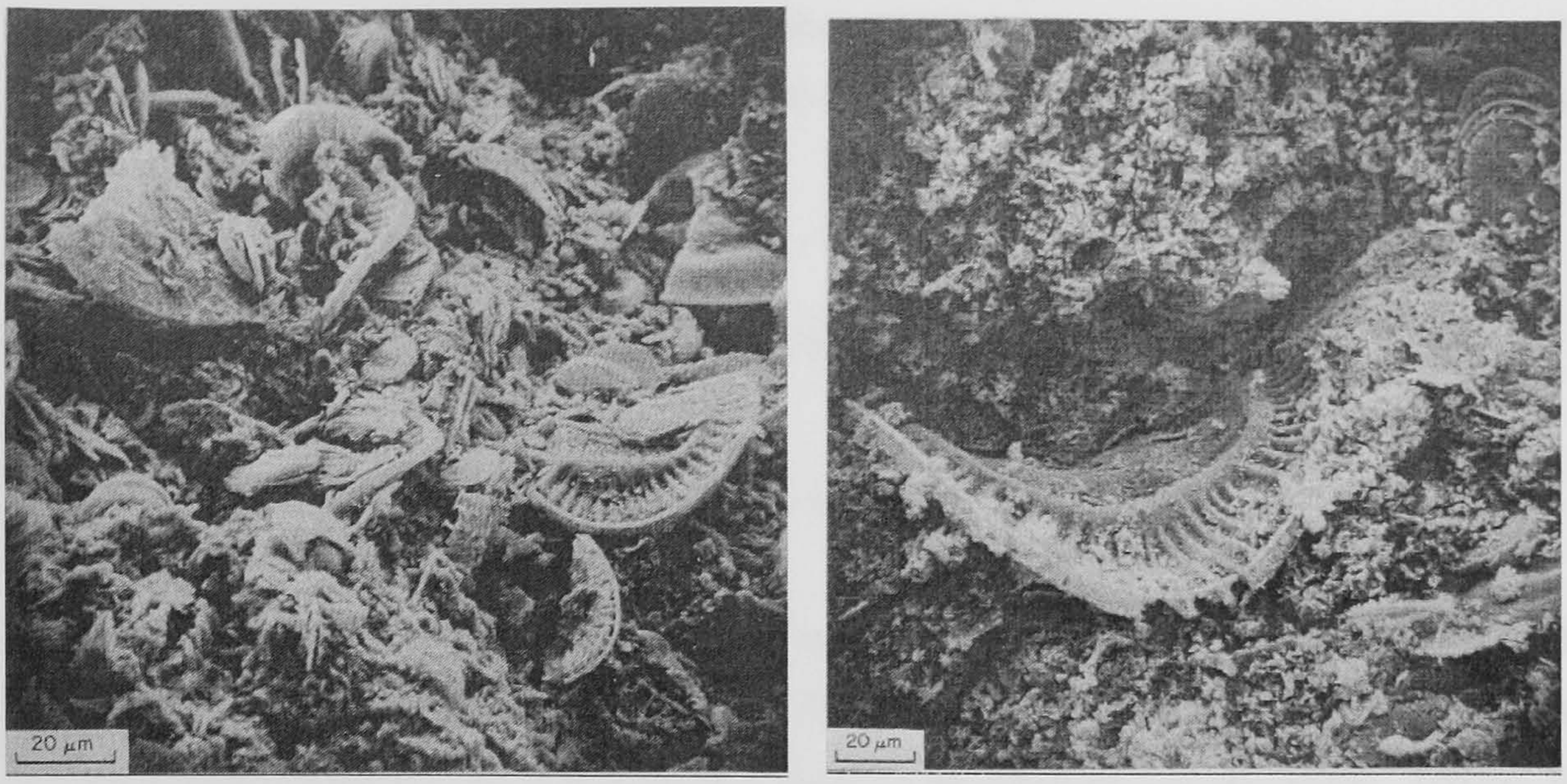


Fig. 4.10 Photomicrographs of silt sized shells and shell fragments in MC clay (left), and large and small microfossils and clay flocs (right) (Mesri et al., 1975)

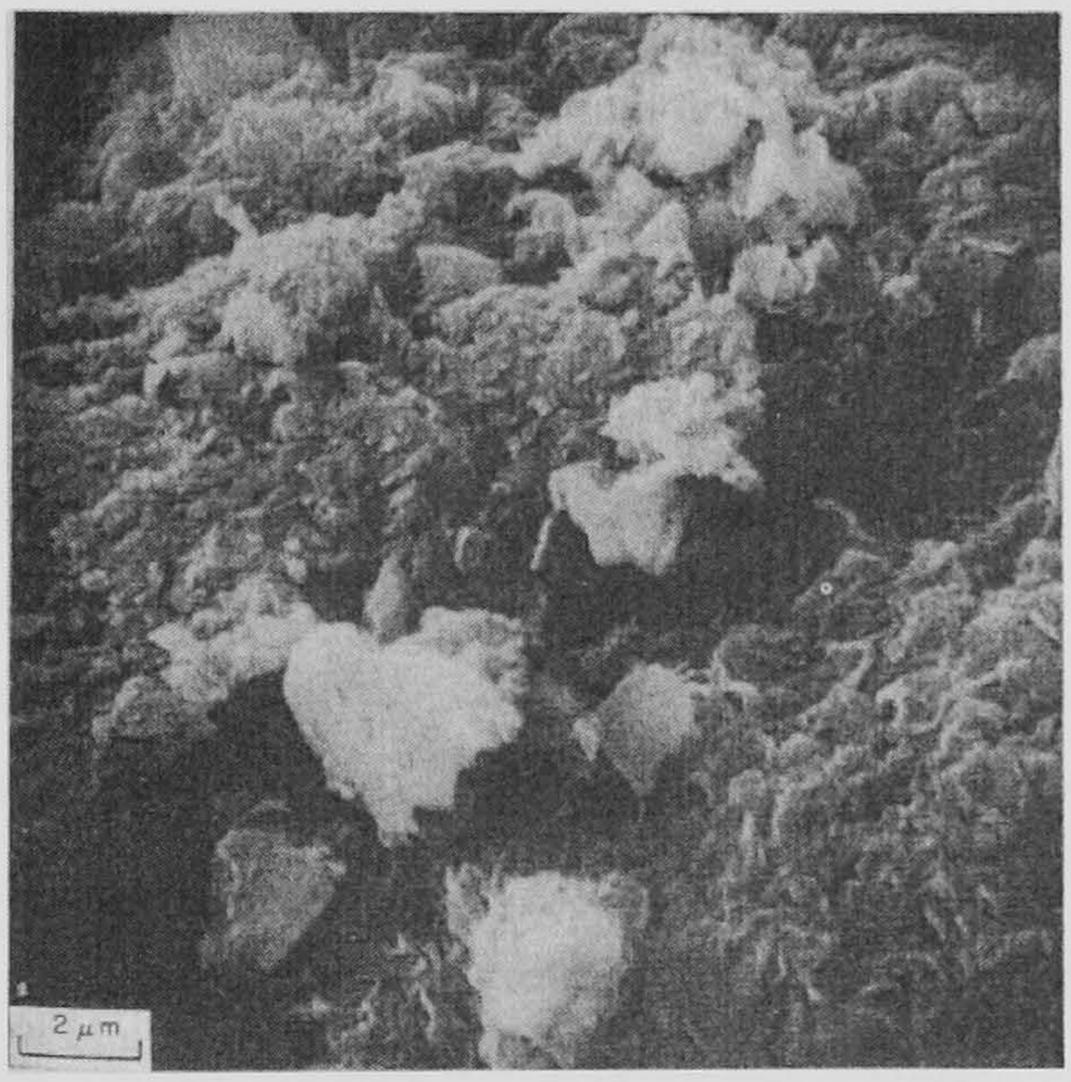


Fig. 4.11 Photomicrograph of clay-sized fraction of MC clay showing film clay mineral particles (lower right) and fine fragments of micro-organisms (Mesri, et al., 1975)

4.4 Mexico City clay response to ring shear testing

The main reason to carry out ring shear tests on MC clay was to determine its clay-to-concrete shearing resistance. Since the latter is applied in the validation study of the IC pile design method, some tests included the pile installation simulation procedure suggested by Ramsey, et al. (1998)[56]. In addition, the following aspects were studied:

---

[56] In this procedure, after consolidation at a total normal stress representative of the in situ

(i) relative reliability of the Bishop and Bromhead ring shear apparatus; (ii) influence of the sample and interface characteristics; (iii) influence of fast rate of shearing; and (iv) influence of the normal stress level.

4.4.1 Apparatuses and Interface material effects

a. Comparison of Bishop and Bromhead ring shear apparatuses

A limited number of Bishop ring shear apparatus (BiA) exist, and these are mainly used for research. The Bromhead equipments (BrA) is mainly used in practice due to its commercial advantages (simpler, robust, inexpensive) (Ramsey, et al. 1998). Hence, it is convenient to carry out a study into the relative reliability of the two types of apparatuses – study on which little research have been carried out. Fearon (1998), testing a plastic Italian clay, and Ramsey, et al. (1998), on soils of various plasticities, found good agreement for residual soil-to-soil and soil-to-steel shear strength, respectively. Ramsey, et al. showed that the clay-to-steel angle of friction (δ) is not extremely sensitive to the choice of apparatus, with comparative test results obtained with both apparatuses agreeing generally to within ±10%.

In order to compare the data obtained with Bishop and Bromhead apparatuses four sets of soil-to-soil, soil-to-steel, and soil-to-concrete ring shear tests, on four different MC clay samples, were carried out. The results cover peak and residual angles of shearing under first time shearing at a drained rate (0.024 mm/min for Bromhead and 0.01 for Bishop) at axial stresses between 100 and 150 kPa. (Only the Bishop tests involving concrete interface on samples 14-2, 15-1 and 16-2 include an initial fast shearing stage.) Figs. 4.12 and 4.13 and Tables 4.3 and 4.4 present the results.

The Author's tests on MC indicate that the peak angle in BiA is higher than in BrA for 9 out of 11 comparative tests (with average difference between comparative tests of 2.5° or 7%, Fig. 4.12). For the residual strength there is no clear trend: BiA angles are higher in 6 out of 11 tests (Fig. 4.13). The BiA reaches peak and residual at larger displacements, probably as a result of its greater sample thickness (Tables 4.3 and 4.4).

---

horizontal effective stress in the ground, the specimen is subjected to a series of fast shearing pulses in order to simulate the displacement history of soil elements adjacent to a pile during driving. (5 pulses of 200 mm at 500 mm/min, with pauses of 3 min in Bromhead apparatus and 10 min in Bishop apparatus.) Previous to drained shearing, the sample is allowed to consolidate under a vertical stress representative of the equalised effective radial stress acting on the pile wall.

Table 4.3 Peak angles and associated displacements for comparative Bromhead and Bishop tests[57]

	Sample C13-4		Sample C14-2		Sample M15-1		Sample M16-2	
	mm	degrees	mm	degrees	mm	degrees	mm	degrees
Soil-to-soil								
Bromhead	3.02	31.9	6.31	33.8	7.90	32.5	12.20	33.5
Bishop	10.08	35.3	22.19	37.6	13.70	35.4	10.09	35.7
Soil-to-concrete								
Bromhead	2.66	32.9	4.95	36.3	2.67	33.0	4.50	32.4
Bishop	2.74	32.1	2.40	38.0	1.40	37.5	3.45	36.7
Soil-to-steel								
Bromhead	2.35	33.1	9.37	33.9	7.90	32.3	10.80	32.7
Bishop	3.60	31.5	N/A	N/A	9.66	36.6	27.18	35.8

Table 4.4 Residual angles and associated displacements for comparative Bromhead and Bishop tests[57]

	Sample C13-4		Sample C14-2		Sample M15-1		Sample M16-2	
	mm	degrees	mm	degrees	mm	degrees	mm	degrees
Soil-to-soil								
Bromhead	5.28	31.4	8.55	33.8	7.90	32.5	12.20	33.2
Bishop	92.60	19	22.19	37.5	20.62	35.0	13.7	35.8
Soil-to-concrete								
Bromhead	2.66	32.9	26.92	35.5	6.65	32.9	33.75	29.4
Bishop	15.81	28.7	16.10	35.3	17.38	31.2	6.08	36.4
Soil-to-steel								
Bromhead	5.99	31.6	9.87	33.9	7.90	32.3	10.80	32.5
Bishop	19.33	29.0			15.12	36.1	39.12	37.1

The soil-to-soil tests on BrA show no or little brittleness, while the tests on BiA show a degree of brittleness (maximum loss in ϕ' of 6.3° or 16%) - except for Bishop tests on sample C13-4 whose angle dropped by 16°. The average ϕ'_p-ϕ'_r for the database is 3.0° and 0.5° for Bishop and Bromhead apparatus, respectively. Ramsey, et al. (1998) observed similar ductile trend in their BrA tests; whose ϕ'_p values should be regarded as less reliable.

---

[57] Soil-to-concrete Bishop tests for samples C14-2, M15-1 and M16-2 include an initial fast shearing stage.

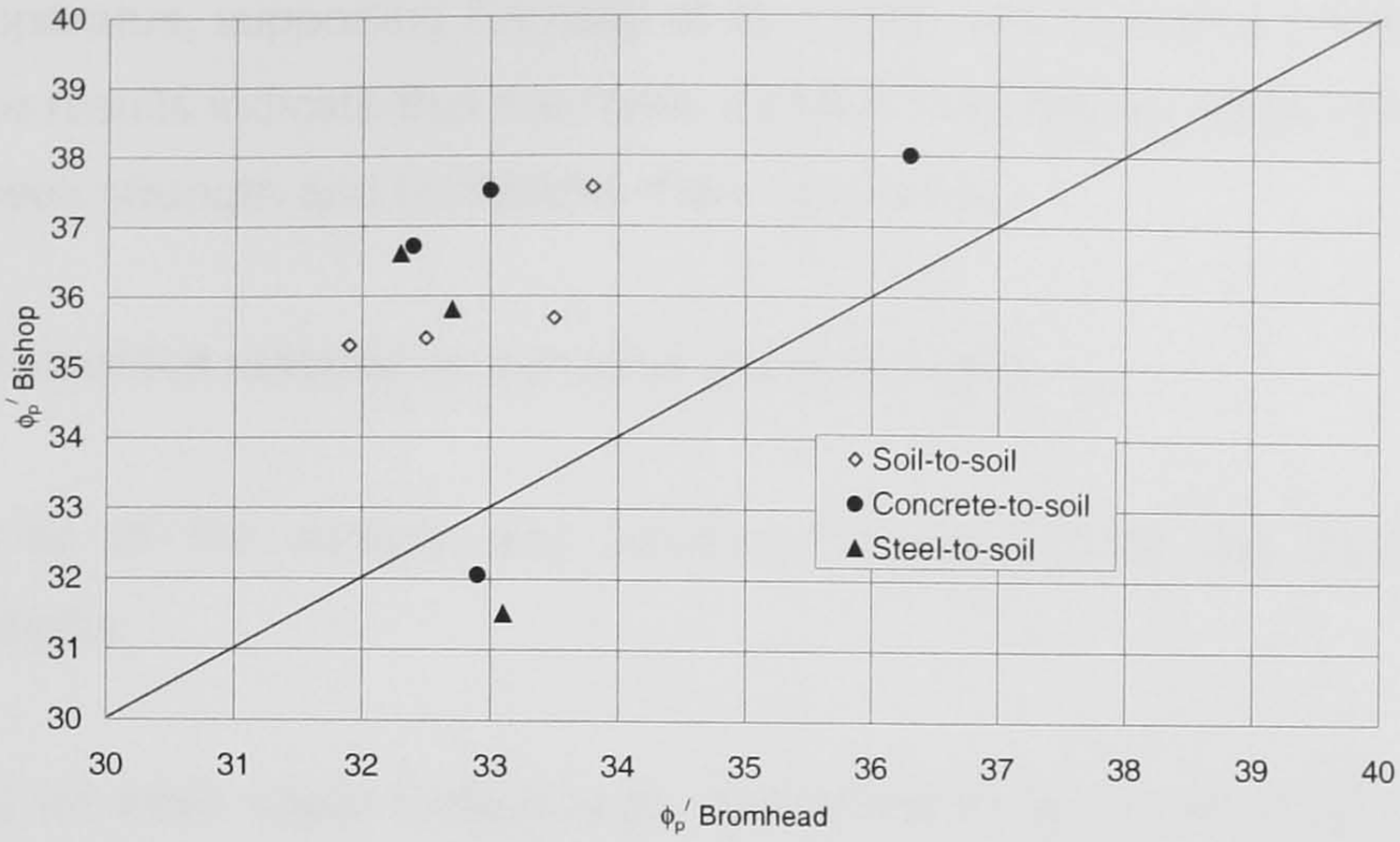


Fig. 4.12 Comparison of peak angles of shearing from Bromhead and Bishop apparatus

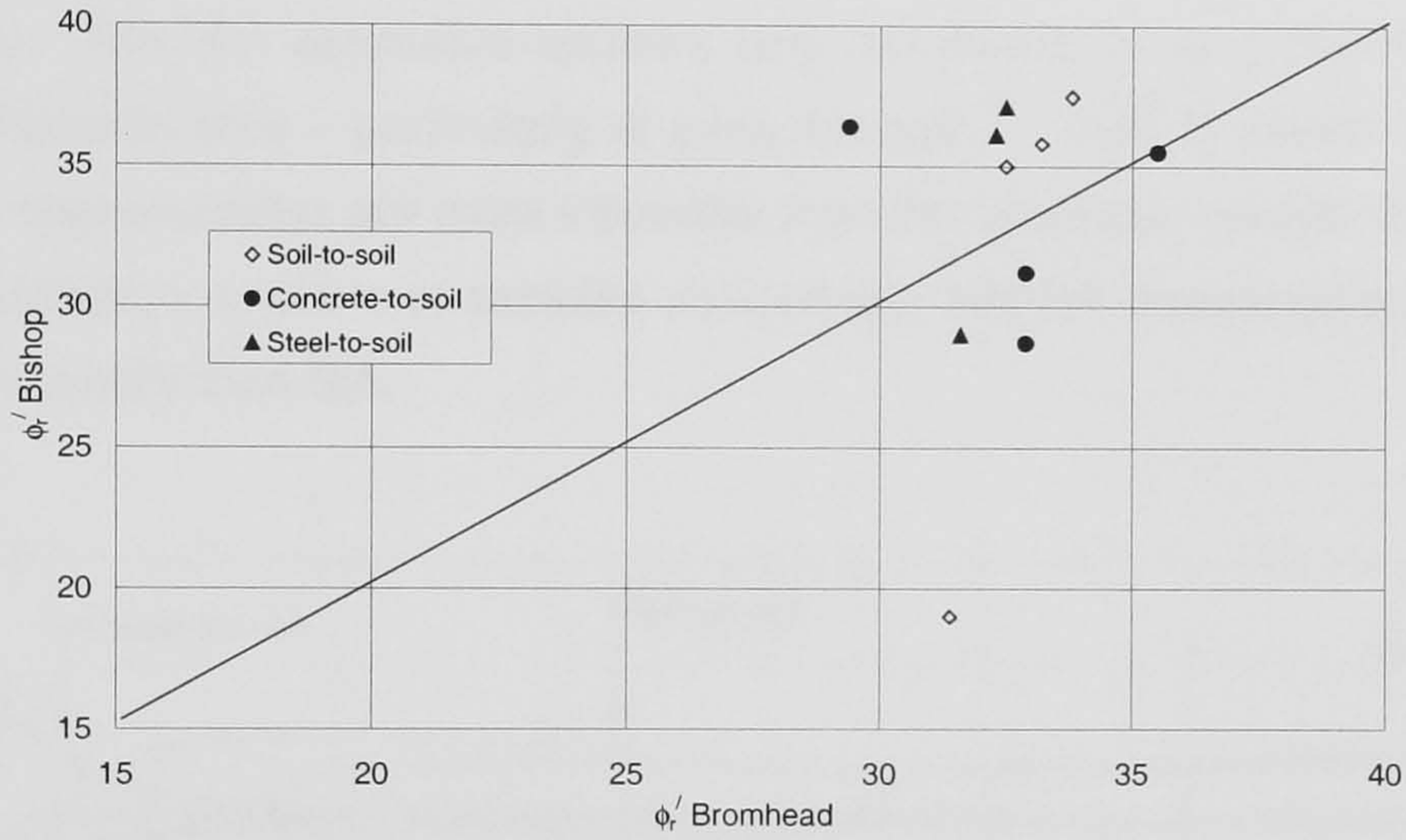


Fig. 4.13 Comparison of residual angles of shearing from Bromhead and Bishop apparatus

The differences in brittleness shown by Bishop and Bromhead apparatus could be the result of the following:

i) Friction between the top cap and sample container in BrA may have led to higher residual shear strengths. Although shearing started with vertical displacements lower than the recommended 0.75 mm minimum, this limit was exceeded during shearing.
ii) Differences in the displacements applied to reach residual strength in each test.
iii) The manual recording of displacements and forces in the available BrA might have impeded the registration of peak strengths.

The results indicate that the residual shear strength is not extremely sensitive to the

choice of apparatus, supporting Ramsey et al. (1998) and Fearon's (1998) conclusions. However, the results indicate that the more sophisticated Bishop apparatus is capable of identifying peak strength and brittleness more accurately.

b. Effects of interface material on available shear strength

The influences of the sample and interface characteristics are considered in the following analysis.

Mean values for peak shear friction angle developed in BrA tests differed by less than 0.7° (2%) between the three interfaces tested, and by less than 2° (6%) between the four soil samples. The respective ranges for the residual values are 0.14° (0.4%) and 2.7° (8%). The BiA tests gave differences of 1.4° (4%), 4.8° (13%), 2.3° (7%) and 11° (32%), respectively. The BrA apparatus appears less influenced by changes in sample and interface characteristics – particularly at peak strength[58]. Also, it seems that with MC, the sample characteristics are more influential than the interface material (Figs. 4.14 and 4.15). In addition, inspection of samples showed that the BrA developed soil-to-interface failure more readily than BiA.

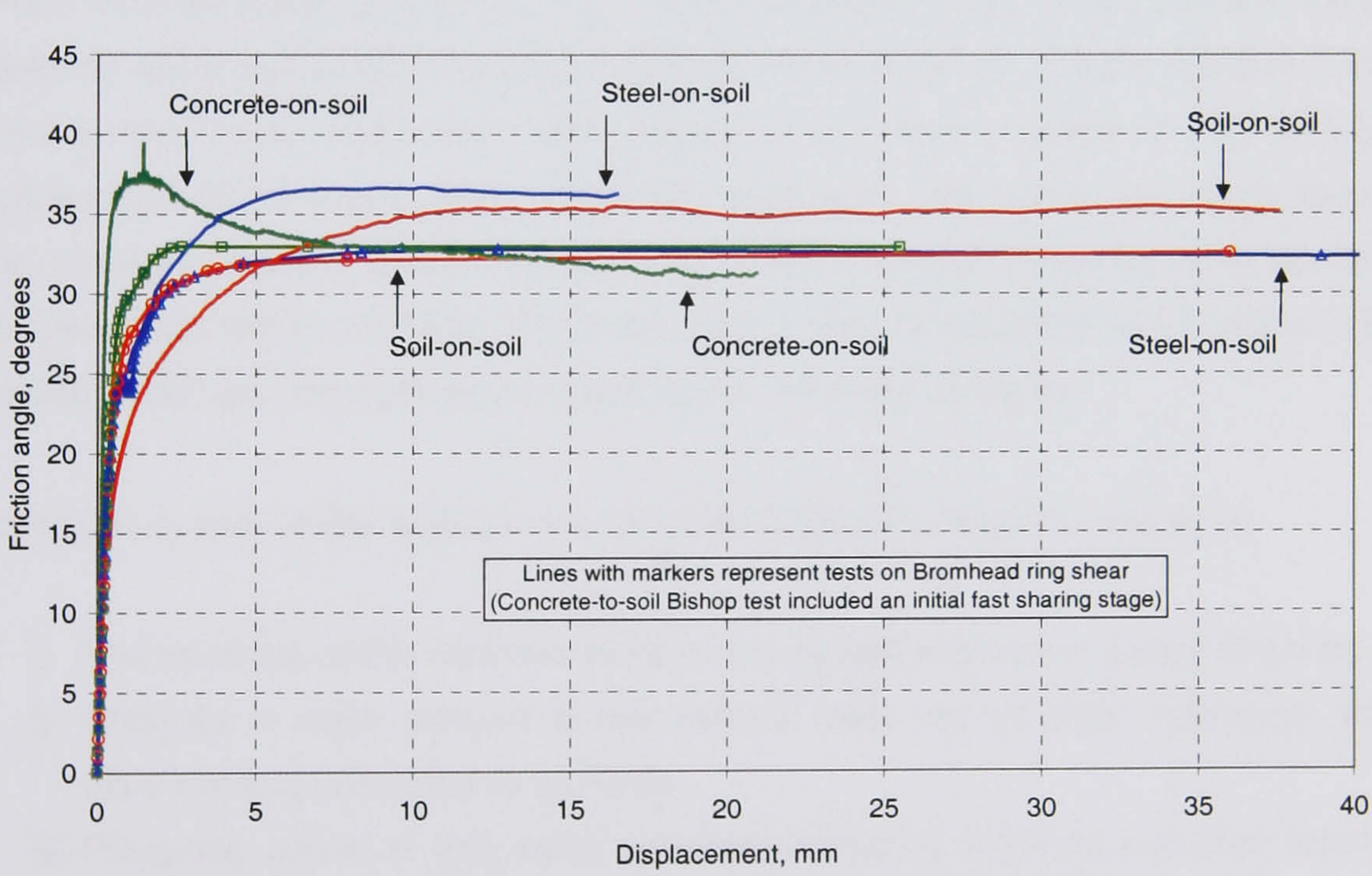


Fig. 4.14 Comparison of Bromhead and Bishop ring shear test results for sample M15-1

[58] Based on smaller differences in mean values and smaller standard deviations.

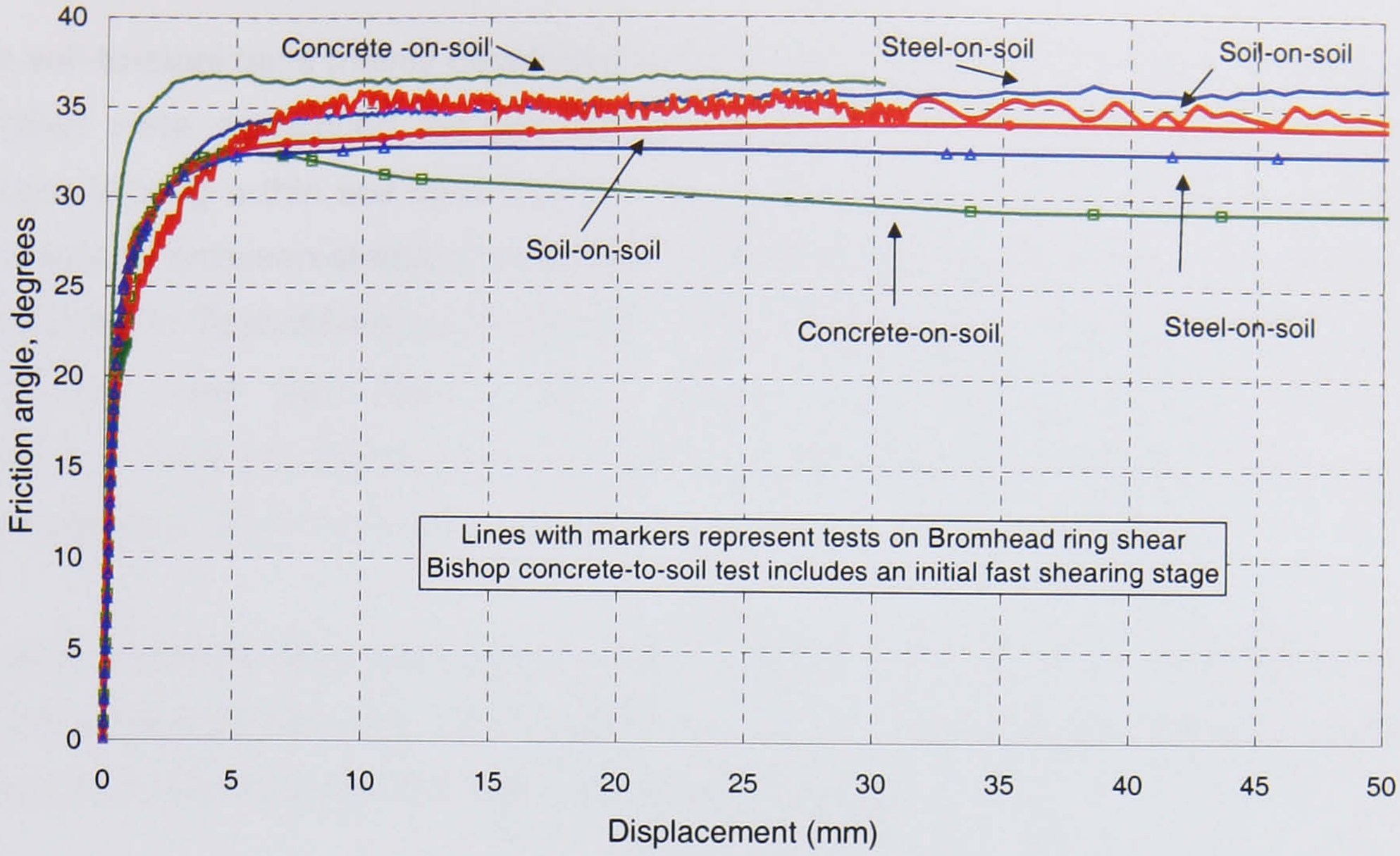


Fig. 4.15 Comparison of Bromhead and Bishop ring shear test results for sample M16-2

Soil-to-concrete interfaces produce the highest peak interface friction angles (δ_p) in 5 out of the 8 comparative tests. (However, the results for different interfaces under similar sample and apparatus are located in a 10% interval, Table 4.3). The marginally lower δ_p values for soil-to-soil and soil-to-steel are similar to each other. For the residual δ_r there is not a clear trend. Potyondy (1961) compared the shear strength of clay and sand sheared against concrete, steel, wood and soil-to-soil. He found that shear strength from concrete interface tests is consistently higher than that of all the other interfaces but lower than soil-to-soil tests. Potyondy (1961) and Tsubakihara and Kishida (1993) consider soil-to-soil strength as the upper bound for shear strength.

The higher δ_p seen in the Author's concrete interface tests might be related to:

i) The waviness of the concrete surface that causes extra-work during shearing
ii) Changes in water content of the material near the concrete interfaces, which were not saturated prior to the tests
iii) Ploughing action of any sand particles protruding from the concrete interface (Lemos and Vaughan, 2000).

The latter was observed in some tests which showed channels produced in the clay by protuberances in the concrete interface. For some soil-to-concrete tests partial concrete-soil and soil-soil interface shearing occurred.

The soil-to-steel tests mainly developed a soil-to-soil failure mode. In general, when the samples were dismantled the soil did not separate at the interface, but on a shear surface leaving a thin soil layer stuck to the steel interface. This observation explains the similarity between strength from the soil-to-steel and soil-to-soil tests. However, this is opposite to Tsubakihara and Kishida's (1993) criterion who established that for steel roughness lower than 10μm interface sliding occurs (while for higher values of roughness the shear failure is located within the clay specimen). Not rust was observed in the stainless steel interface.

No clear evidence of a relationship between displacement at peak or residual and the interface material was observed (Tables 4.3 and 4.4). In general, the interface material does not modify the large strain MC clay shearing modes.

It is important to recall that minor random variations inevitably exist between the tests and specimens, so small non-systematic differences maybe expected.

4.4.2 Normal effective stress and overconsolidation ratio effects

a. Normal effective stress effects

Lupini, et al. (1981), Kenney (1967) and other authors have noticed an increase in the residual friction angle at low effective stresses, implying that the failure envelope is curved. Several investigators have found that for most cohesive soils the ϕ_r' and the displacement necessary to establish it is dependent on the level of the normal effective stress when $\sigma_n' < 200$ kPa (Lupini, 1981). The evidence of this behaviour, which is typically greater for the sliding shearing mode, is not conclusive. Contradictory cases exist and no general conclusions have been accepted.

The influence of the normal effective stress on the friction angle for MC clay is examined by comparing two normally consolidated shearing stages in Figs. 4.16 and 4.17. The graphs indicate that the increasing of the normal effective stress from 100 kPa to 400 kPa reduces the peak and residual δ' by 2.5° (6.8%) and 3.9° (11%), respectively. The brittleness appears to increase and the stiffness to reduce, which could be related to the presence of clay minerals in between the contact of silt size particles - as suggested by Lupini (1981) for turbulent shearing mode.

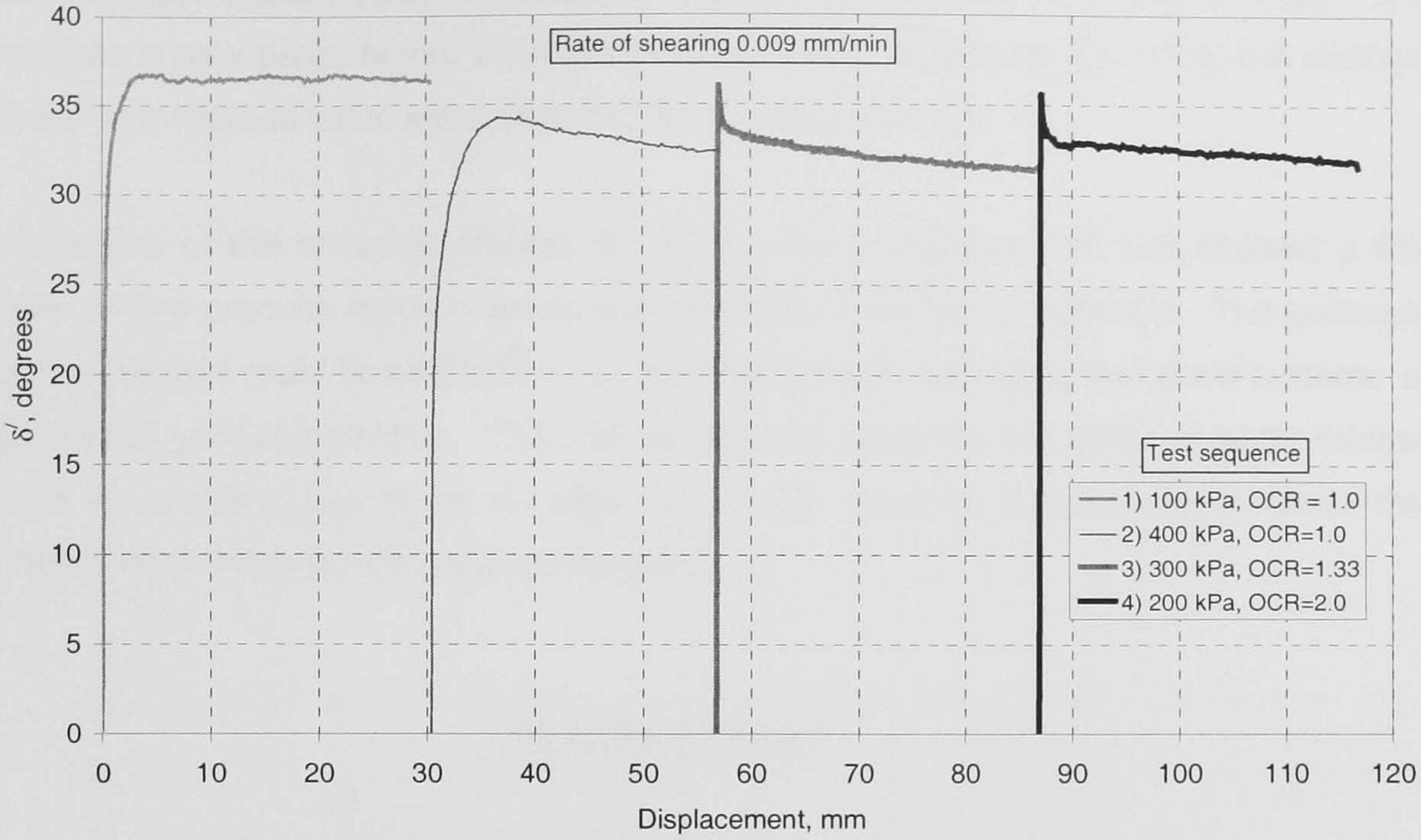


Fig. 4.16 Normal effective stress and overconsolidation effects on Sample M16-2. Soil-to-concrete test with fast pre-shearing, four stages

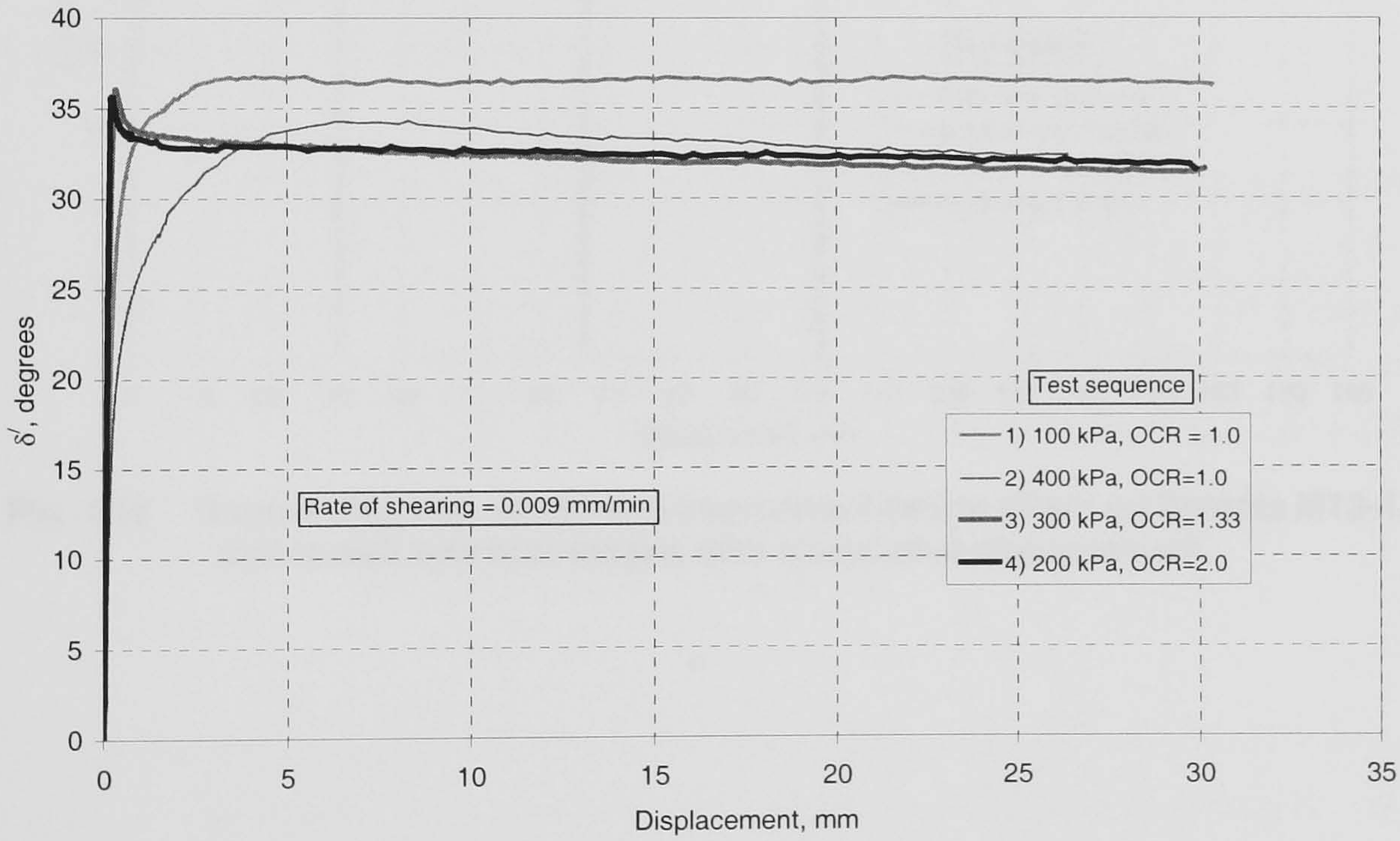


Fig. 4.17 Normal effective stress and overconsolidation effects on Sample M16-2. Soil-to-concrete test with fast pre-shearing, four individual stages

b. Overconsolidation effects

Fig. 4.16 to 4.19 show examples of the behaviour of MC clay under overconsolidated conditions – a failure surface was previously created at OCR=1. As shown in Fig. 4.17 normally consolidated (NC) MC clay develops little or no brittleness. When unloaded to

an overconsolidated (OC) condition the specimen response is stiffer, it dilates and reaches a new peak, higher than the previous peak. Following from this, the strength drops to a residual value lower than the NC residual strength.

Inspection of the shearing surface for M16-2 soil-to-concrete OC test showed a thin layer of fine granular loose material in a wet state close to the interface. The presence of the material could be explained by: (i) migration of soil particles to the shear surface; or (ii) diatom particle crushing. The wet appearance could be the result of water release from the diatoms due to the crushing, or by the reduction in total normal stress that makes water migrate to the failure surface[59].

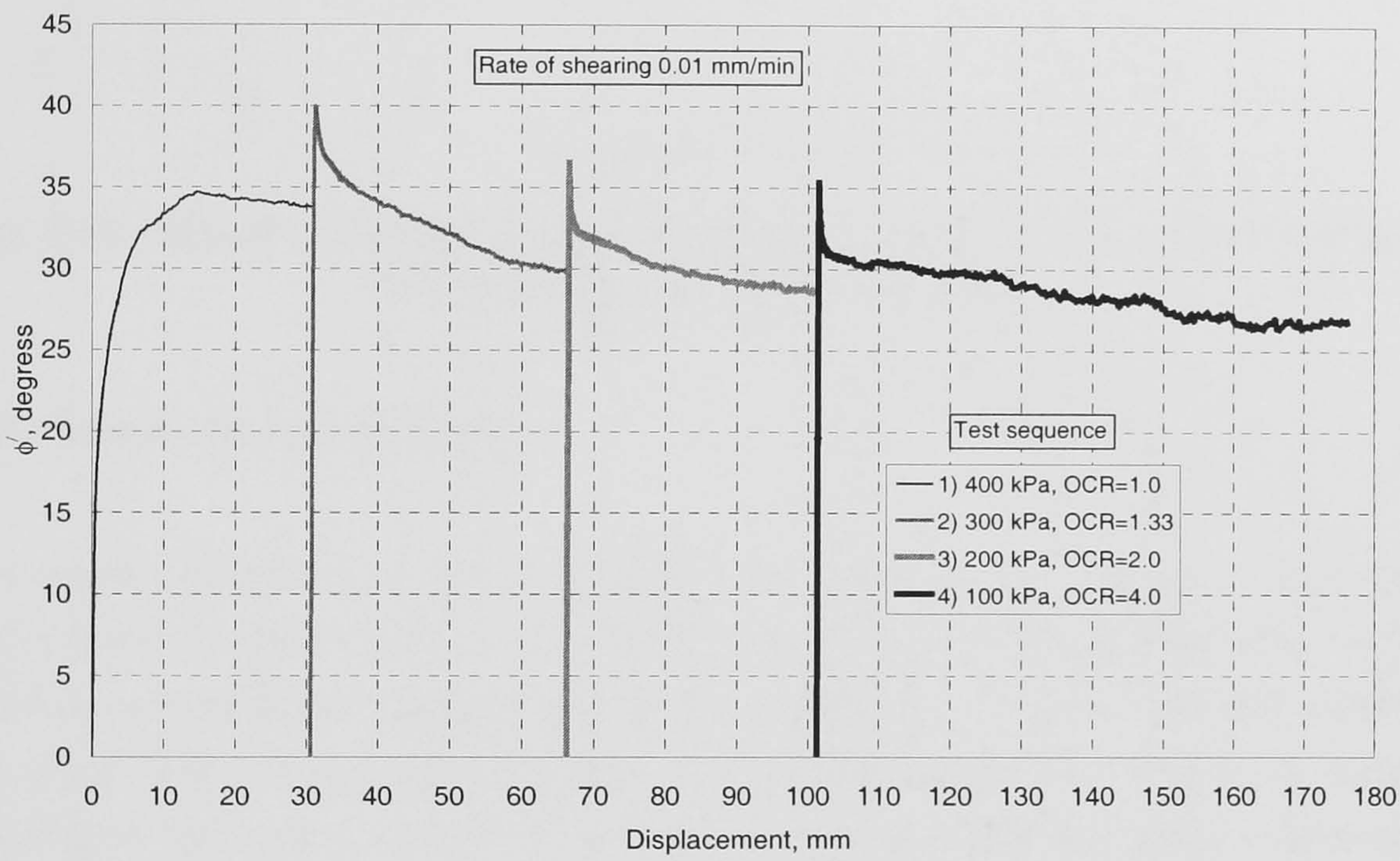


Fig. 4.18 Normal effective stress and overconsolidation effect on Sample M13-4. Soil-to-soil test four stages with cumulative displacement

---

[59] Bishop, et al. (1971) report a clay that shows turbulent behaviour in normally consolidated and overconsolidated states, with brittleness appearing a little with overconsolidation. This response is consistent with turbulent behaviour, with perhaps slight indications of transitional behaviour. The material had 58% of platy particles (38% clay fraction) and according to Bishop, et al. it showed that in soils a high salt content could lead to unusually high residual strengths due to interparticle friction. MC clay shows similar response (see Figs. 4.16 to 4.19).

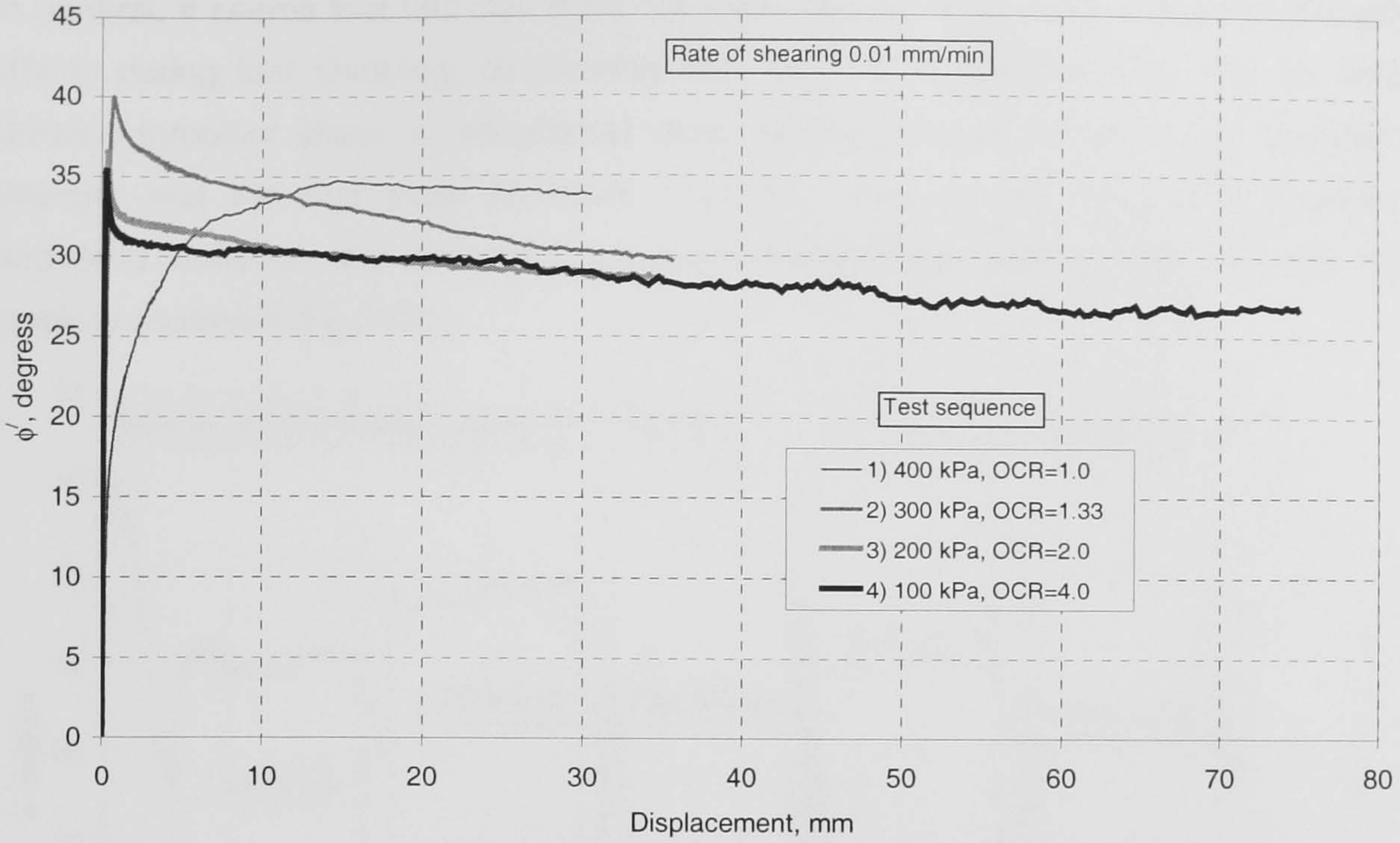


Fig. 4.19 Normal effective stress and overconsolidation effect on Sample M13-4. Soil-to-soil test four individual stages

4.4.3 Rate of displacement effects

The section explores MC clay response to rate of shearing. Multi-stage tests were implemented in which after a shear zone was formed by initial slow drained shearing, the shearing was continued at a fast rate between 3.5 and 540 mm/min. After fast shearing, the shear force was removed completely, the sample allowed to consolidate, a drained shearing to the residual carried out, and fast shearing at a different rate was performed again.

a. Peak strength

Due to recording frequency limitation (the smallest time interval for recording was 0.7 sec.) peak and threshold strengths were not recorded for rates of shearing higher than 50 mm/min.

Threshold strengths were observed just in 2 fast shearing stages, these were for soil-to-soil test on sample C13-4 (Fig. 4.20). This and the increment of shear strength with increasing rate during the two first fast shearing stages on Fig. 4.20, further confirm that sample C13-4 shows transitional-sliding characteristics.

In general, it seems that MC clay does not show clear and separate threshold strength effects during fast shearing, conforming with Tika, et al.'s (1996) view that for soils showing turbulent shear, or transitional shear tending towards turbulent, the threshold strength and the fast peak strengths coincide. Due to the mentioned recording frequency limitation, the increment on peak strength with rate of shearing was not properly observed (Fig. 4.21).

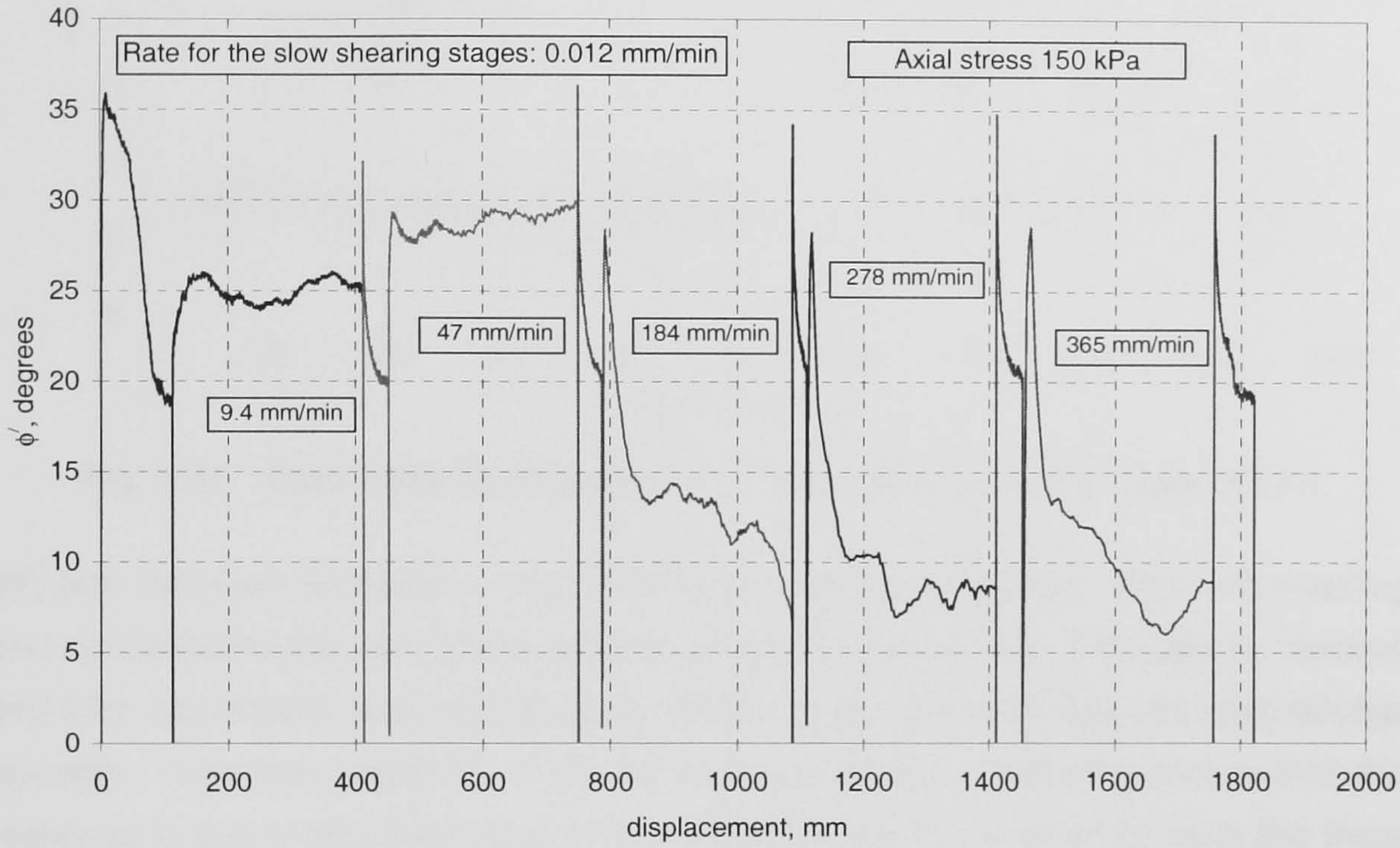


Fig. 4.20 Fast shearing response on soil-to-soil test of sample C13-4

b. Slow shearing peak strength after fast shearing

Tika, et al. (1996), pointed out that soils showing the transitional and the sliding shear modes show peak strengths above their slow drained residual in re-tests followed fast pre-shearing. Tika relates this response to the disordering of the clay particles orientated in the shear zone during fast rates of displacement. No such increases were identified in soils showing the turbulent shear mode.

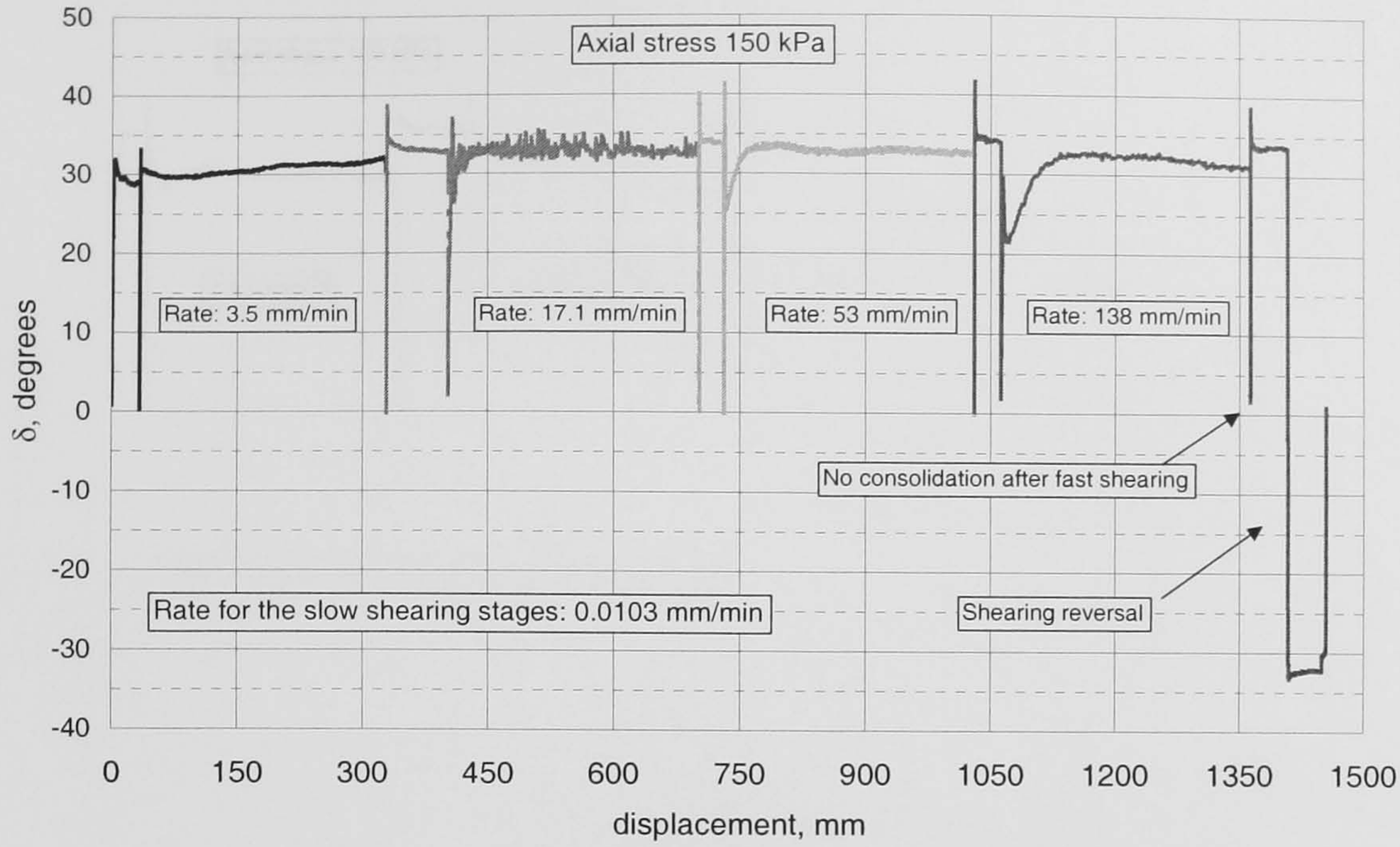


Fig. 4.21 Fast shearing response on soil-to-steel test of samples C13-4

MC clay behaviour conforms to the transitional behaviour described. After fast shearing and consolidation the slow shearing peak strength is higher than the previous residual, and then drops back to a residual value similar to the previous slow shearing residual strength. This was observed in all the samples tested. Further evidence that this response is due to structural (and not consolidation) effects is given by tests like those shown in Fig. 4.21 and 4.22, in which slow shearing was started immediately after completing fast shearing without allowing any time for pore pressure dissipation. These tests showed the same peak and residual values although the peak is reached at a larger displacement than when consolidation is allowed; this behaviour does not depend on interface material (Figs. 4.21 and 4.22).

Samples C13-4 and M15-1 were subjected to reversal shearing stages without intermediate pause for consolidation. These tests showed peak shear strengths close to the preceding residual, indicating that particle re-orientation may not be important. Also, the rate of strength reduction (brittleness) increased.

Tika, et al., (1996) noted a critical rate of pre-shearing above which subsequent slow shearing strengths are affected by the earlier fast shearing. No such limit was observed in the MC clay tests; the shearing response was independent of pre-shearing over the rates investigated (3.5 to 500 mm/min).

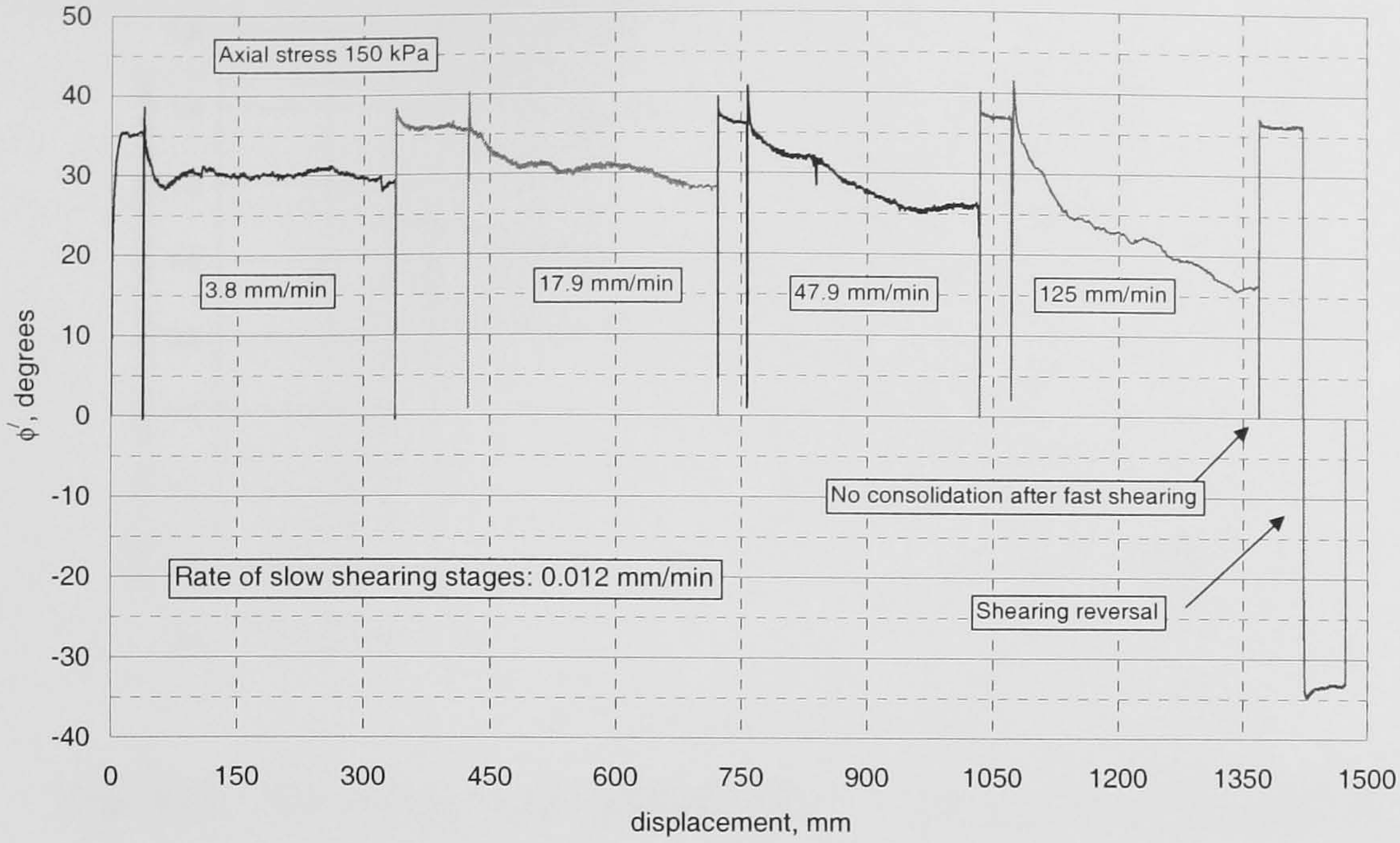


Fig. 4.22 Fast shearing response on soil-to-soil test of samples M15-1

c. Fast residual strength

Ratios of the total stress fast residual friction angle[60] to the corresponding effective stress slow residual friction angle are plotted against rate of displacement in Fig. 4.23. It appears that the resistances available at rates exceeding 200 mm/min are 60% lower than the drained slow residual strength. The features seen at intermediate rates are more dependent on the sample and testing conditions.

Sample M15-1 shows classical turbulent shearing behaviour independently of the interface (Tika's Type II), with Fig. 4.23 reporting ratios lower than 1. Sample C13-4 shows slightly higher resistances than the slow residual, until the rates exceed 50 mm/min[61]. Fig. 4.24 gives more details of the test on sample M15-1 sheared against a steel interface, including the last slow shearing stage in which negative rate effects were observed when increasing the shearing rate from 0.09 to 0.9 mm/min and back down to 0.012 mm/min. This points out that structural effects are responsible for the behaviour of sample M15-1. Similar results were found with sample M16-2 during soil-to-soil and soil-to-steel testing.

---

[60] Note that this is in terms of total stress, pore pressure is not measured.

[61] The critical rate of displacement decreases with increasing clay fraction, palsticity index or granular void ratio (e_g).

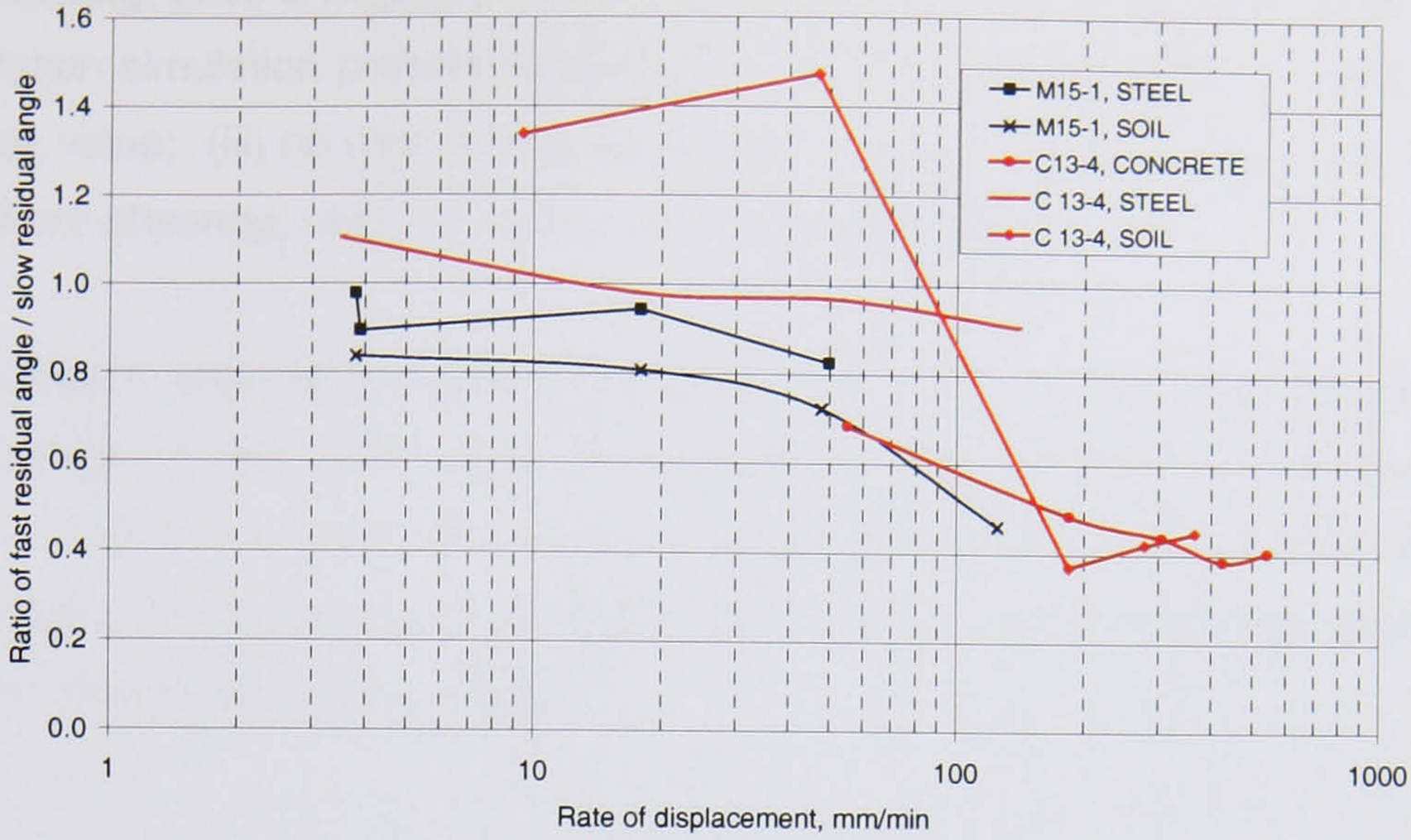


Fig. 4.23 Variation of fast residual / slow residual with rate of shearing

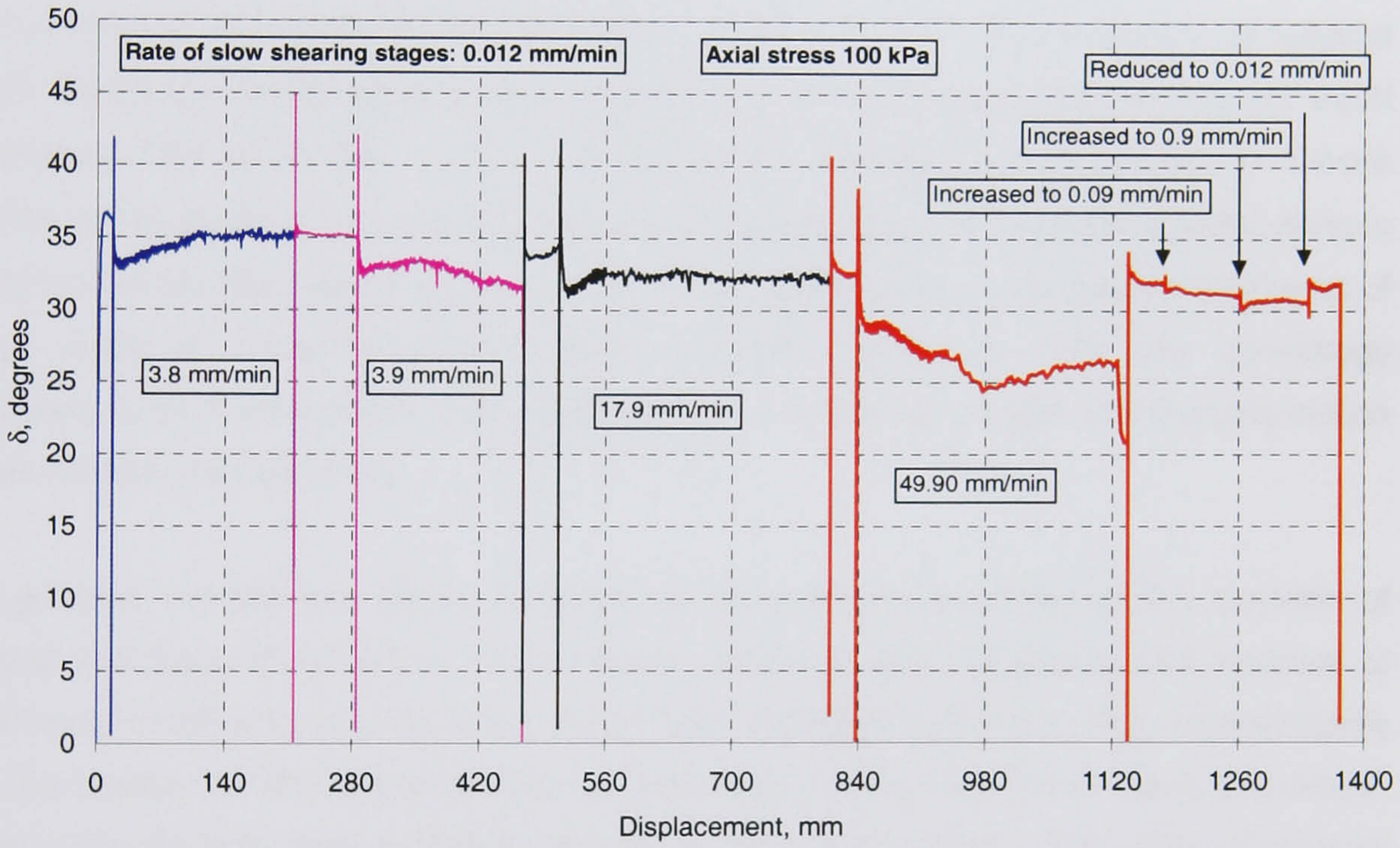


Fig. 4.24 Soil-to-steel fast shearing response of sample M15-1

Sample C13-4 shows also a Type II shearing mode, however soil-to-concrete and soil-to-soil tests show lower residual than soil-to-steel tests (Fig. 4.20 and 4.21). The different behaviour of sample C13-4 during soil-to-steel test could originate from the alignment of clay particles produced by the interface. Sample C13-4 has shown the highest sliding tendency of all the MC clay samples tested, indicating higher content of platy particles.

Fast shearing at 500 mm/min, carried out without previously creating a failure surface by

drained shearing, gave a negative rate effect. The application of Ramsey, et al. (1998) pile installation simulation procedure results in: (i) a shorter displacement to peak; (ii) higher peak value; (iii) no clear effect on residual strength, it seems this is not affected by the fast pre-shearing; and (iv) more pronounced brittleness.

For the validation exercise presented in Chapter 5 a mean δ value of 36° was selected, as the average of the peak values developed in Bishop tests on soil-to-concrete interface – 3 of the 4 tests considered included fast pre-shearing. Note that this interface angle, which applies to a highly plastic clay, is higher than that available to silica sands (Jardine and Chow, 1996).

4.4.4 Characterisation of MC clay in the ring shear

All of the test data indicate that large strain shearing of MC clay involves a transitional (with tendency to turbulent) mode of behaviour, which is dominated by the silt sized particles. One of the four samples (sample C13-4) showed a tendency towards a more brittle sliding shear mode, giving a minimum residual angle ≈20° even though the sample had the lowest clay fraction. This is interpreted as being due to an ordered alignment of high angle of interparticle friction platy particles developing. MC clay mineralogy appears to be dominated by illites and kaolinites – which have higher interparticle friction than montmorillonitic soils.

In general, the MC clay shear surfaces are striated and orientated in the direction of shear, but they did not shine. At the failure surface it was common to find residues of fine sand or silt size material, which could have migrated during shearing, independently of the location of the failure surface (at soil mass or interface) and testing procedure. For steel interface tests in Bishop apparatus there was usually a thin layer of material attached to the interface covering at least 70% of the surface. The more irregular concrete interface produces bigger irregularities at soil interface, with material attached to it but in less area than the steel interface.

The MC clay response to shearing shows aspects of the three shearing modes, which results from the diverse components of natural soil samples. This observation indicates the uncertainties related to the use of correlations based on clay fraction or plasticity index to classify soil response to shearing.

Consider for example the default curves offered by Jardine and Chow (1996) for peak

and residual δ' of clays (Figs. 4.25 and 4.26) – here updated by the Author's own tests on samples from different offshore region[62] (Table 4.5). Also included in the figures are the peak and residual friction angles for the MC clay M15-1 sample obtained during soil-to-steel interface test under Ramsey, et al. (1998) test procedure.

In the figures it is clear that MC clay has an extraordinarily high δ' despite its high PI, putting it off the scale of any PI correlation chart.

The limitation of correlating ϕ with PI is that the latter does not adequately describe the key factors that control the shearing response of soils, such as the mineralogy, grading of the granular phase, shape of the clay and rotund particles, and relative size of rotund and platy particles. Classifications based on PI are not useful to predict the shearing mechanism of MC clay; criteria based on shape and size of components predict it better.

Table 4.5 Samples used to expand IC ring shear database

Site	Region	Problem	Type of test
Italy	Offshore Italy	Pile design	Soil-to-steel
Norway	Offshore North sea	Slope stability	Soil-to-soil
Venezuela	Offshore Caribbean	Pile design	Soil-to-steel
Gulf of Mexico	Offshore WD 58A	Pile test validation	Soil-to-steel

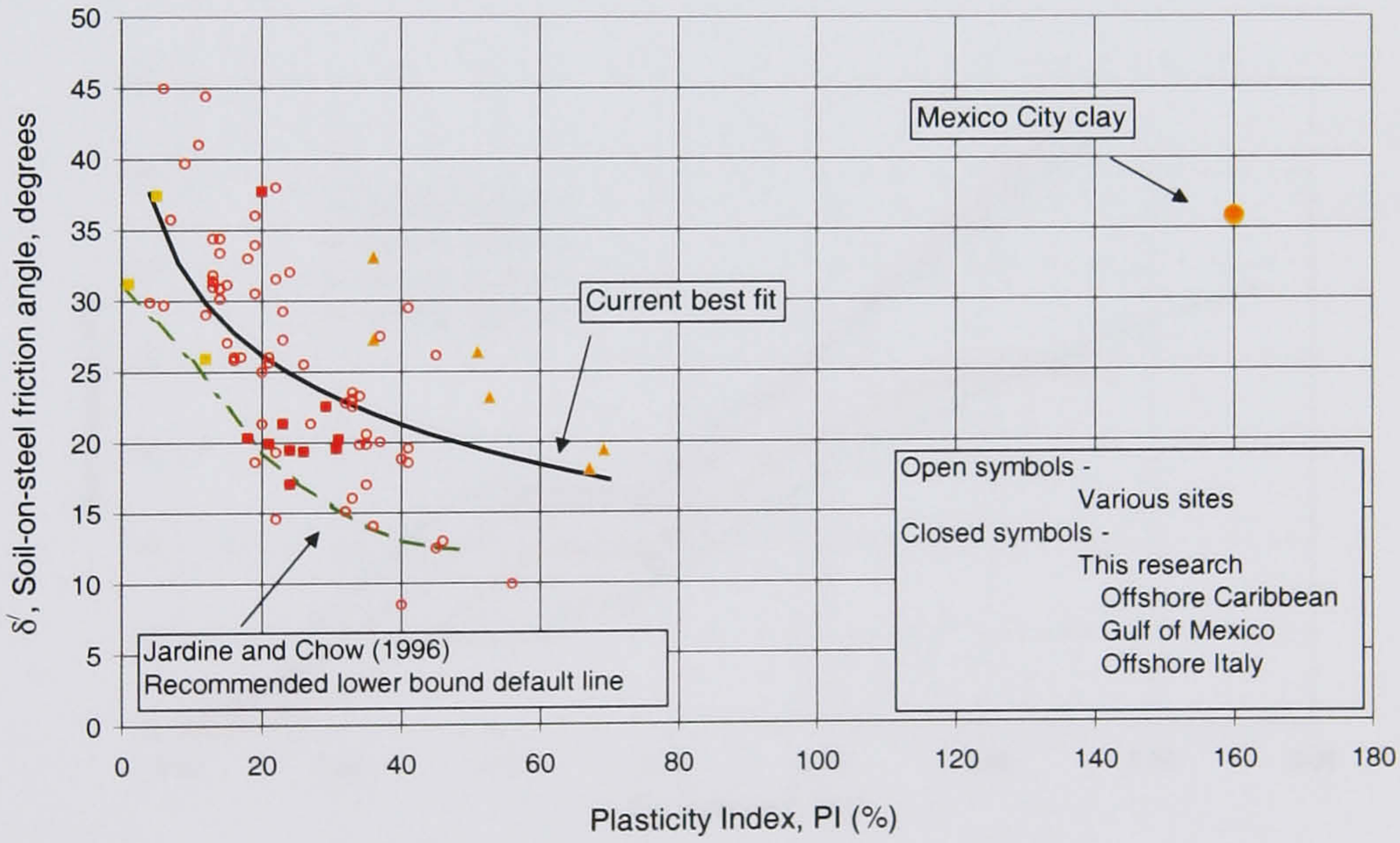


Fig. 4.25 Database of peak interface soil-to-steel friction angles, tests include fast shearing pulses, extended from Ramsey, et al. (1998)

---

[62] The tests were carried out for different geotechnical studies, therefore they differ in axial stress and rates of shearing (see Table 4.5). All the tests were executed according to the procedure established by Ramsey, et al. (1998).

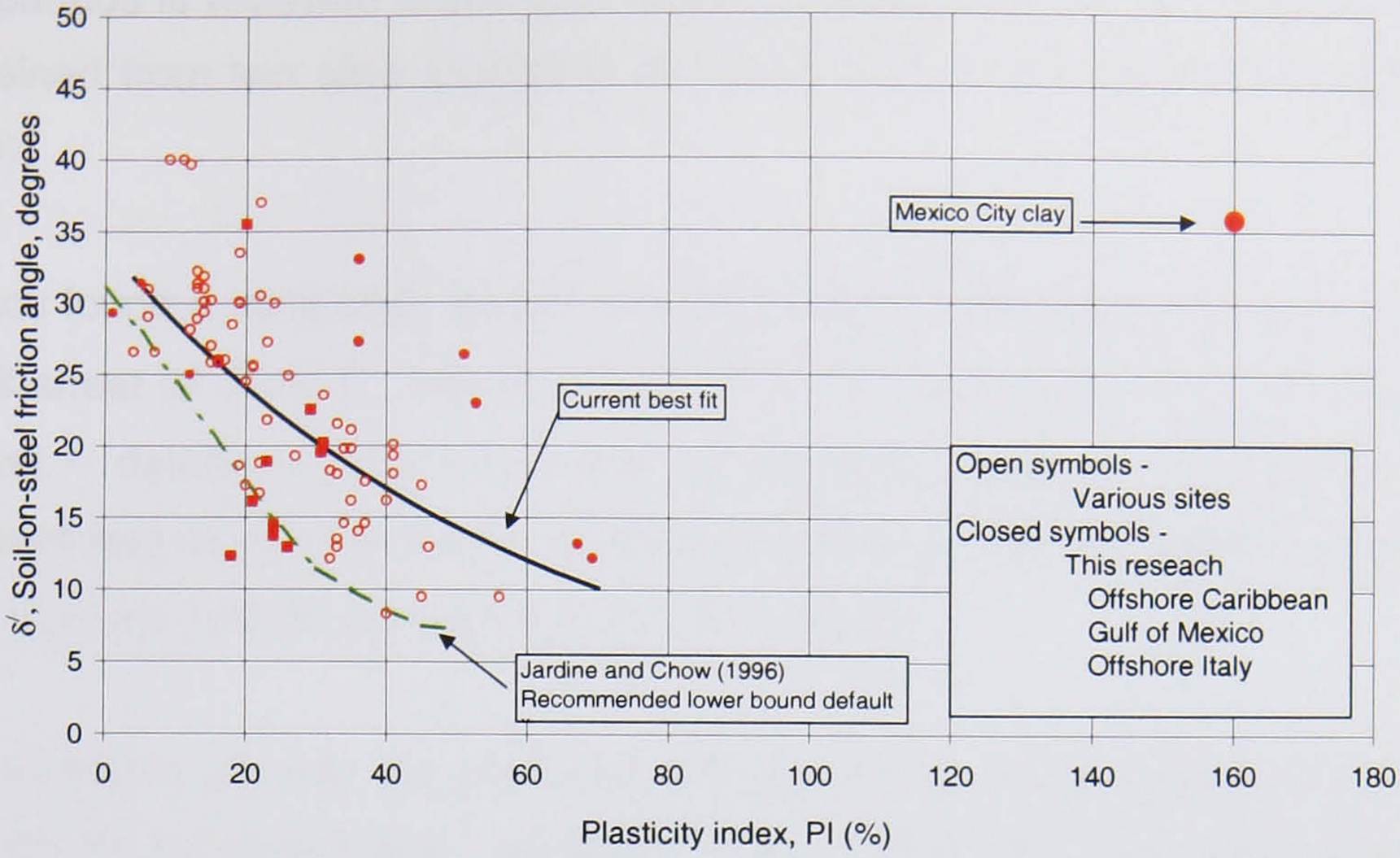


Fig. 4.26 Database of residual interface soil-to-steel friction angles, tests include fast shearing pulses, extended from Ramsey, et al. (1998)

Most of the drained tests (see Appendix A) show a "plateau" at small displacement and low shear strength, independently of the interface or apparatus but depending on stress history (Fig. 4.27). This response could be associated with the sample preparation, apparatus response, or different shearing mechanisms on the soil components. The ϕ' corresponding to those plateaus are 17°, 13°, 8°, and 3° for 100, 200, 300 and 400 kPa.

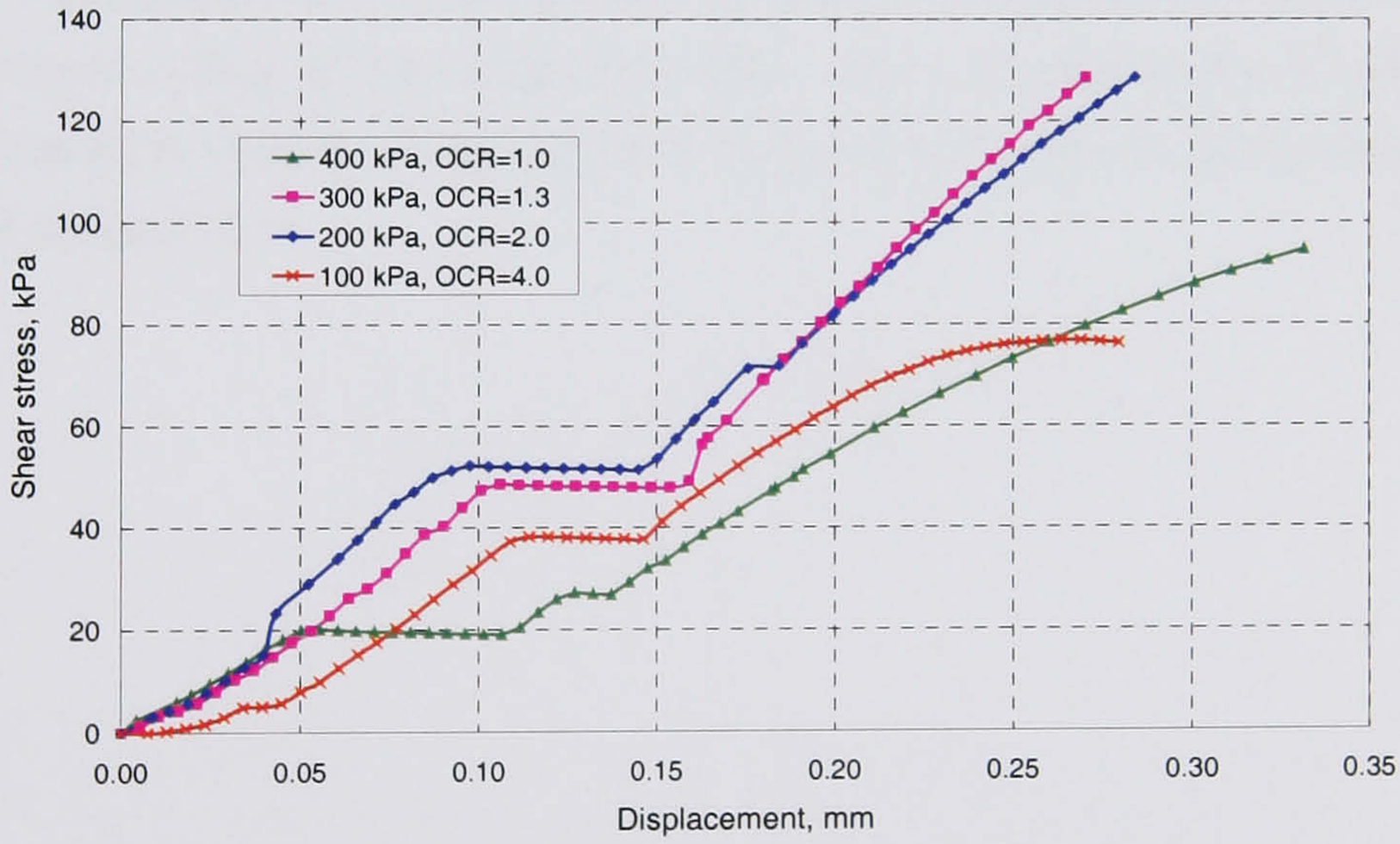


Fig. 4.27 Detail of initial plateau for ring shear tests in MC clay sample 13-4 soil-to-soil Bishop apparatus test

4.5 Direct shear tests

The response of MC clay to soil-to-soil and soil-to-interface testing in conventional direct

shear apparatus is reviewed drawing on work by Castellanos (1998). His soil samples were obtained from two sites located in the Lake zone, in the vicinity of Chapultepec (Fig. 6.14).

Castellanos found a completely ductile response with an average undisturbed peak ϕ' in soil-to-soil shear of $\phi'=52.7^{\circ}$, falling to $\delta'=40.3^{\circ}$ for soil-to-concrete, and to $\delta'=29.8^{\circ}$ for soil-to-steel – details of interfaces were not reported, the tests were performed at displacement rate of ≈0.14 mm/min. Castellanos' results show the highest friction angle for soil-to-soil test, and the lowest for soil-to-steel tests[63].

Castellanos points out that the peak strength appears at a displacement between 1.5 and 2.0 mm for soil-to-soil tests, between 1.0 and 1.8 mm for concrete interface, and between 0.5 and 1.0 mm for steel interface. The bigger brittleness observed was 15% of the peak strength for a displacement of 21 mm.

The angles of shearing resistance reported by Castellanos are much higher than those determined from this research. The differences could be related to the difference in apparatus and sample characteristics. However, the main reason for these differences is attributed to the low axial effective stresses applied by Castellanos, between 33 and 60 kPa - in the region where the shearing resistance is highly affected by axial stress. Castellanos suggested that the low stresses he applied resembled the horizontal stress effective stresses acting on pile surfaces in MC. The validation of the IC pile design method presented in Chapter 5 indicated that that range of pressure acts in the pile shaft at a depth of around 10 m.

---

[63] Ovando, et al. (1993) found the same trend for MC clay.

CHAPTER 5

VALIDATION OF THE IC PILE DESIGN METHOD FOR MEXICO CITY

A statistical analysis, based on 78 pile load tests performed in the southern states of the USA, by Briaud and Tucker (1988) indicated that none of 13 popular driven pile design methods was able to predict axial capacity reliably[64]. Conventional pile design approaches are generally unreliable. Given this and the unusual characteristics of Mexico City (MC) clay, the design of friction piles MC has been the subject of extensive research. Among the more significant contributions are: Mendoza, et al. (1996); Jaime, et al, (1988); Hjort and Carrillo (1985); Zeevaert (1982); Resendiz and Auvinet (1973); Rosenblueth (1965); Resendiz (1964); and Marsal and Masari (1962). Hjort and Carrillo (1985) assembled a large database of pile tests and showed that the existing methods for predicting pile axial capacity in MC are also relatively unreliable. This chapter considers whether the Imperial College Pile Design Method (ICPDM: Jardine and Chow, 1996) is more suitable for computing the static capacity of friction piles in MC. If so, the new approach could be used to compute the static capacity of the friction piles considered in the dynamic case histories studied in the following chapters.

The chapter describes the database assembled for this purpose, and the validation calculations and results. The effects of cross sectional shape and pre-boring on pile behaviour are discussed, and factors are introduced to account for their influence on pile capacity.

5.1 Description of the database

A database of full-scale pile tests was assembled to assess the reliability of the ICPDM for predicting medium term (fully equalized), first time loading single pile capacity in the conditions of MC. The database comprised 26 load tests from different locations around the Lake Zone (see Chapter 3). Only one test had the base and shaft capacities accurately separated.

---

[64] Briaud and Tucker deal with predictions of the response to monotonic axial loading of single piles in various soil conditions.

The database comprises concrete, circular and square cross-section, closed-ended piles. Installation for all the piles was by driving, some of them with pre-boring (Tables 5.1 and 5.2).

All the tests are load-controlled type where load increments are applied until a determined strain rate threshold is reached. For the Linea 4 pile tests, which constitute the majority of the database, 20 ton load increments were applied when the displacement for a 2 hours interval is less that 5% the total displacement for that specific load increment. Load testing was carried out at least 15 days after installation. Fig. 5.1 shows a typical test result for the Linea 4 pile tests (test G-29).

Table 5.1 Summary of the pile test database

Number of piles tests	26
Tension tests	1
Compression tests	26
Average embedded length, m	24
Range of lengths, m	10-35
Average size (square piles), m	0.45
Range of size (square piles), m	0.30 – 0.50
Average equivalent radius, m	0.26
Range of equivalent radius, m	0.17 – 0.28
Average YSR	1.61
Range YSR	1.21 – 7.36
Average sensitivity	13.1
Range of sensitivity	3 – 22

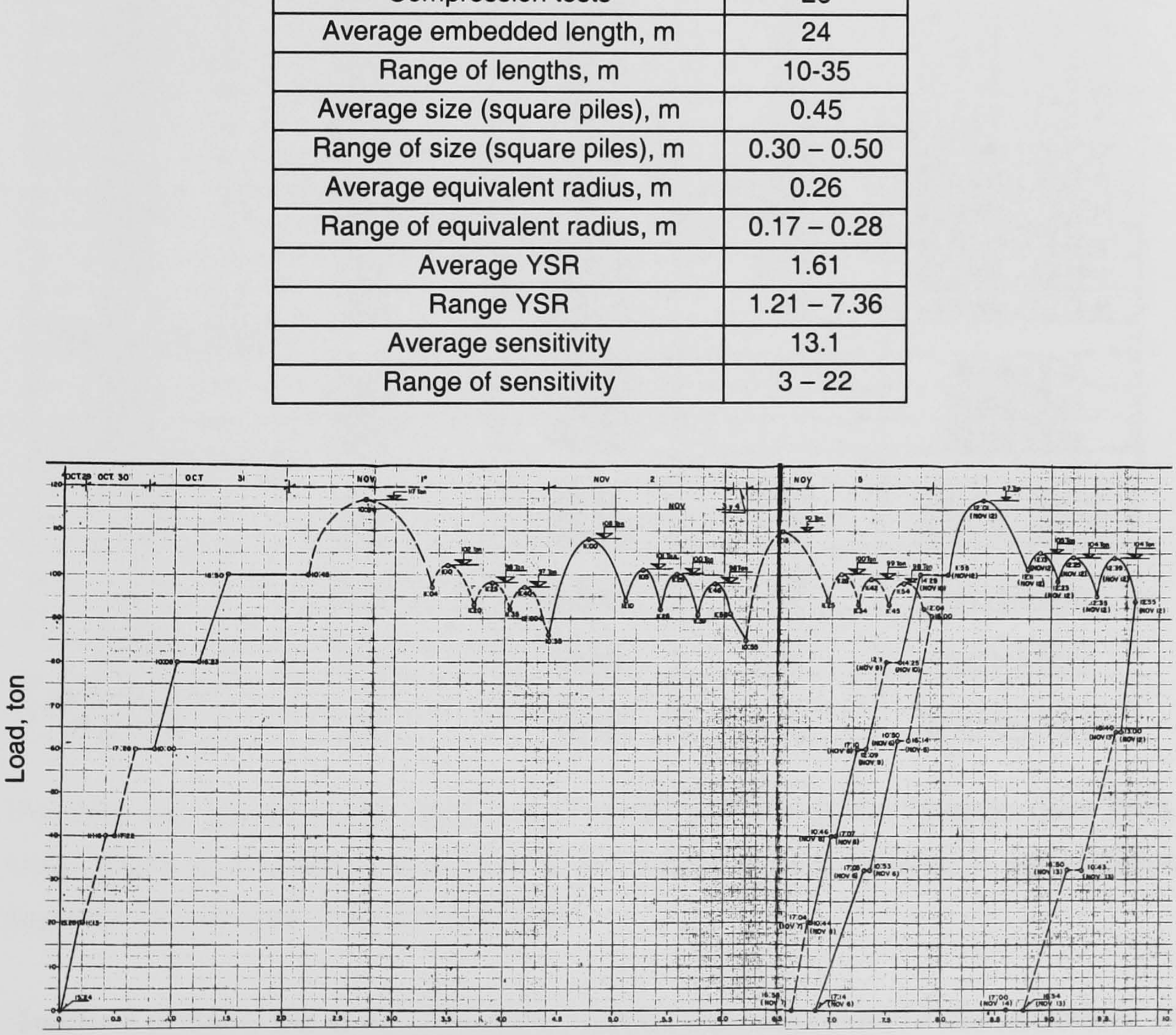


Fig. 5.1 Typical test result for Linea 4 pile tests

The information on the pile tests and soil conditions was obtained from geotechnical

consultants, mainly TGC Geotecnia, through Mr. Enrique Santoyo and Mr. Rene Contreras, and Ingenieros Civiles Asociados (ICA) through Mr. Roberto Ayala and Mr. Benjamin Silva. Mr. Luis Bernardo Rodriguez provided the details on pre-driving boreholes for the Linea 4 tests. Note that they are nearly all pre-bored, allowance was made for this.

Table 5.2 Details of the database pile tests

Name/Site	Embedded length (m)	Dimension (cm)	Equalisation (days)	Pre-boring Diam/length
Metro Line 4 (ICA)				
BC2	22.0	50x50	> 15	47.5 cm / 14.5 m
BC12	22.0	50x50	> 15	47.5 cm / 14.5 m
BC23	22.5	50x50	35	47.5 cm / 15.0 m
BC26	23.0	50x50	> 15	47.5 cm / 15.0 m
CC20	23.5	50x50	94	47.5 cm / 16.0 m
CC27	23.0	50x50	57	47.5 cm / 15.0 m
CC32	24.0	50x50	> 125	47.5 cm / 16.0 m
CF27	26.0	50x50	113	47.5 cm / 17.0 m
CM8	25.0	50x50	38	47.5 cm / 17.0 m
CM17	26.0	50x50	15	47.5 cm / 16.5 m
CM25	25.5	50x50	15	47.5 cm / 17.0 m
FJ11	26.0	50x50	> 15	47.5 cm / 17.0 m
GT17	20.5	50x50	> 15	47.5 cm / 13.5 m
GT29	20.5	50x50	> 157	47.5 cm / 13.5 m
GT38	19.5	50x50	268	47.5 cm / 13.0 m
MC1	25.5	50x50	> 15	47.5 cm / 17.0 m
TB8	18.5	50x50	> 15	47.5 cm / 12.3 m
TB13	20.0	50x50	> 15	47.5 cm / 13.0 m
Metro Line 9 (TGC)				
ML91	35.0	30x30	-	10 cm / 9 m
ML92	35.0	30x30	-	10 cm / 9 m
ML93	29.0	50x50	-	30 cm / 9 m
CT Iztacalco (TGC)				
CTI 16	32.0	50x50	> 40	45.0 cm / 25.0 m
CTI68	32.0	50x50	> 40	45.0 cm / 25.0 m
CNT				
CNT	24.3	35 diam.	59	No pre-boring
CUPJ				
CUPJ	10.0	30x30	191	15.0 cm / 8 m
Viaducto (TGC)				
Viaducto1	24.0	35x35	> 15	28.0 cm / 1.5 m

The piles are located in the Upper Clay Formation (FAS) of the Texcoco Lake Zone. Inter-layered sand strata of more than 50 cm thickness were included in the validation analyses (see Chapter 3 for typical profile).

Chapter 3 presents the study of the more relevant parameters used in the validation. In cases where the report on the pile test did not include the appropriate information, the parameters were determined using the nearest available study.

The YSR values were determined using oedometer tests and in situ piezometric

measurements. The calculated YSR were checked against the clay's geological history.

Sensitivity (S_t) was determined using oedometer compression curves and Burland's equation for the Intrinsic Compression Line; the intrinsic properties were determined using Nagaraj's expressions (Chapter 3). The S_t values from this procedure were judged against Marsal and Mazari's database and a specially developed w/LL vs. S_t database.

The interface friction angle was obtained from the soil-on-concrete ring shear tests presented in Chapter 4. Clay fraction was not available for all the sites where the pile tests were carried out and correlations of δ with PI are unreliable. Thus, $\delta = 36^{\circ}$ was considered as a representative peak value and it was used in all the validation calculations.

The pile capacities were calculated using a spreadsheet procedure that divided the embedded pile length into at least 20 sections. Pile cross section effect on pile capacity was included using Cowley (1998), pre-boring effects were included following Jaime, et al. (1991); these approaches are introduced in the following sections.

5.2 Modification of the ICPDM for square cross section piles

Currently most of the piles used in MC foundations are square cross section piles, although in the past triangular cross section piles were common practice. The ICPDM was developed for tubular closed and open-ended piles. The following section deals with the effects of cross sectional geometry on pile capacity, covering the extension to the ICPDM developed by Cowley (1998).

5.2.1 Effects of cross section geometry on pile behaviour

To the Author's knowledge, little research has been undertaken into the effects of pile cross section on subsequent capacity. Among the identified publications are Chellis (1961), Jaime, et al. (1991), Aubeny (1992), and Stuckrath (1992)[65].

Jaime, et al. (1991), using reconstituted MC clay, carried out 1-g model tests on circular,

---

[65] Stuckrath conducted model pile tests in clay and sand but proposed no conclusion from his test with different cross section shape piles.

square, equilateral triangular, hexagonal, and rectangular[66] micro-concrete piles to examine the influence of different cross sections on pile capacity (Fig. 5.2)[67]. They concluded:

i. Everything else being equal, the peak and residual capacity is highly dependent on the shape of the section. The pile capacity increases with the number of sides, circular piles have the greatest capacity (considered as having an infinite number of sides), with triangular and rectangular shapes the least.
ii. Stress concentrations at the pile vertices affect the radial effective stresses around the pile. This directly influences the shaft capacity.
iii. It is possible to establish a relationship between the pile capacity and the interior angle between the pile sides. The relationship is expressed as a shape factor that takes account of the pile geometry and it is defined as $\gamma=0.5(1+\beta/\ 180^{o})$, where β is the internal angle in degrees formed by two sides of the section. The value of the parameter γ should be unity for a circular pile and progressively reduces as the number of sides of the section of the pile increases – for square cross section the shape factor is 0.75.

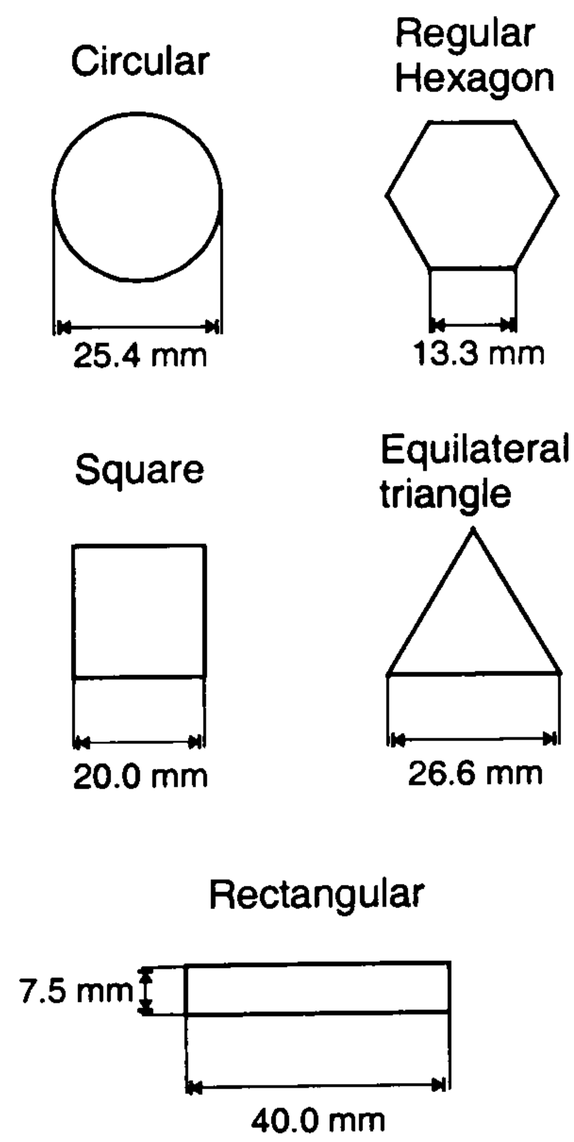


Fig. 5.2 Shapes and dimensions of Jaime et al's model piles (Jaime, et al., 1991)

---

[66] The shorter side of the rectangular pile had an aluminium surface, so that the perimeter of micro-concrete was 80 mm.

[67] All piles were 780 mm long with an effective embedded length of 710 mm.

Chellis (1961) stated that the geometry of the pile cross section influences the shaft friction resistance with respect to circular and square piles. Chellis pointed out that for square piles where the diameter of the round pile equals the side dimension of the square piles the ratio is approximately 4 to 3 – the same ratio specified by Jaime, et al. (1991).

Jaime, et al. (1991) also studied the effects of pre-boring on pile capacity. They concluded that both peak and residual pile capacities reduce when a pile is installed in this manner, the loss being greater for the square and triangular sections than for the circular section. Jaime, et al. analysed their laboratory results by plotting the ratio of the capacity obtained with and without pre-boring (P_u and P_{us}, respectively) against the ratio between cross sectional areas of the pre-driven borehole and the pile (A_{pp} and A_{tp} respectively). Fig. 5.3 shows this plot which indicates that the effect of pre-boring is independent of the pile cross-section and that the capacity depends upon the volume of soil displaced – Aubeny (1992) supports this conclusion. (Fig. 5.3 is used to determine the reduction in pile capacity for the piles in the database that were driven using pre-boring.)

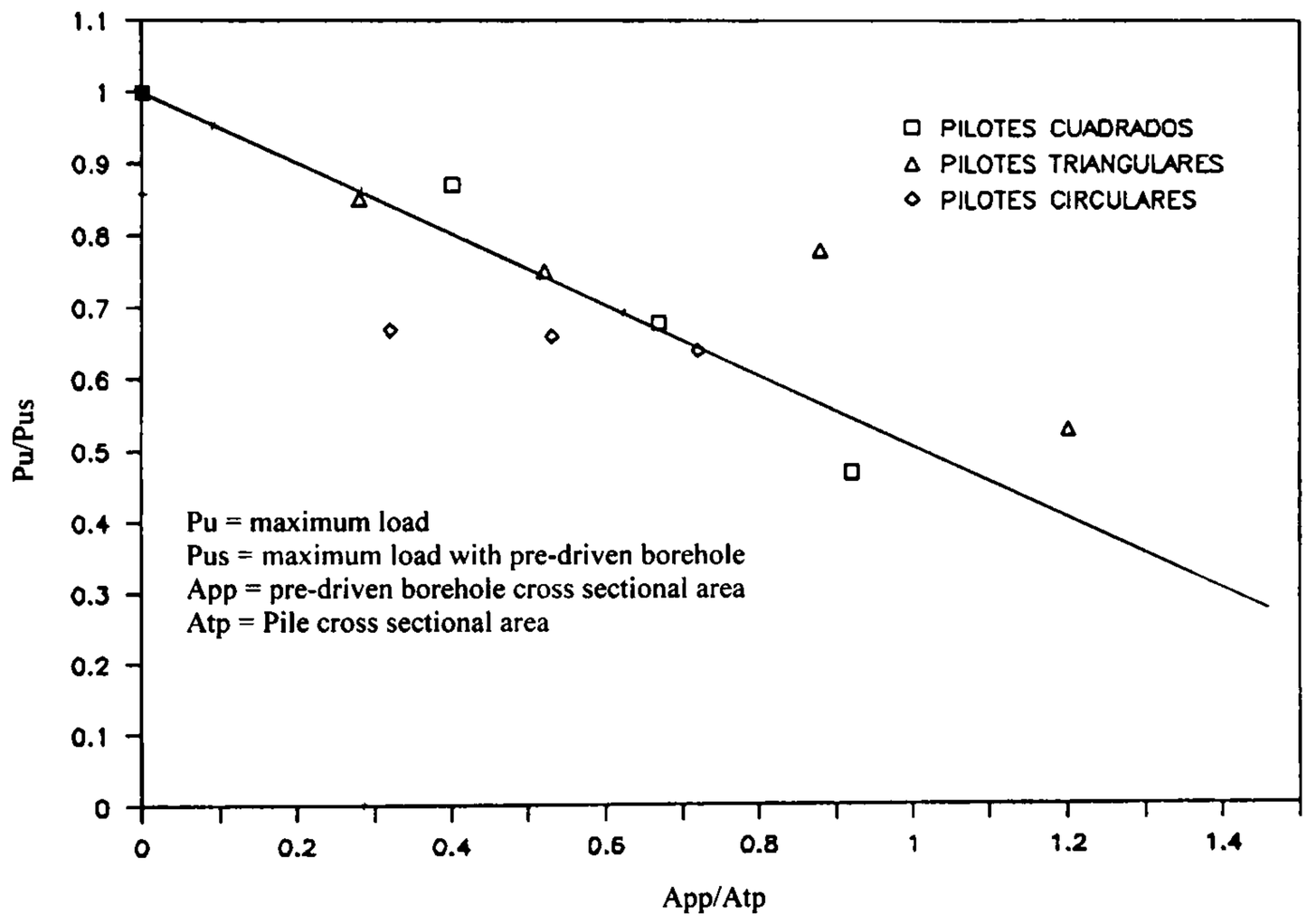


Fig. 5.3 Normalised pile capacity vs. pile/borehole area ratio (Jaime, et al. 1991)

Aubeny's (1992, cited by Cowley, 1998) Strain Path Method (SPM) analyses on the possible influence of different penetrometer geometry are related to the process of installation of non-circular piles. Cowley points out that Aubeny observed that the radial effective stresses and pore pressures, for both a simple circular pile and the Marchetti

(1980) dilatometer[68] (modelled as a flat plate), were very similar when normalised by an equivalent radius (R_{eq}). Fig. 5.4 shows Aubeny's comparisons for excess pore pressures along the centre line and far above the plate boundary for both geometries. Cowley indicates that Aubeny concluded that: (i) the penetrometer geometry has a relatively minor influence on pore pressure and stress distributions and that these are more dependent on the volume of soil displaced than the geometry of the displacing object; and (ii) the pile geometry effects are removed if an appropriate normalising radius is included within a design approach.

The insights gained from Aubeny's SPM and Jaime, et al.'s results on model tests allowed Cowley to conclude that the application of the ICPDM to different pile geometries can be reduced to establish an R_{eq}, the appropriate shaft perimeter, and the base area for the geometry in question. These values can then be substituted into the appropriate equations for calculating the shaft and base capacities. The structure of the ICPDM is well suited for including this modification.

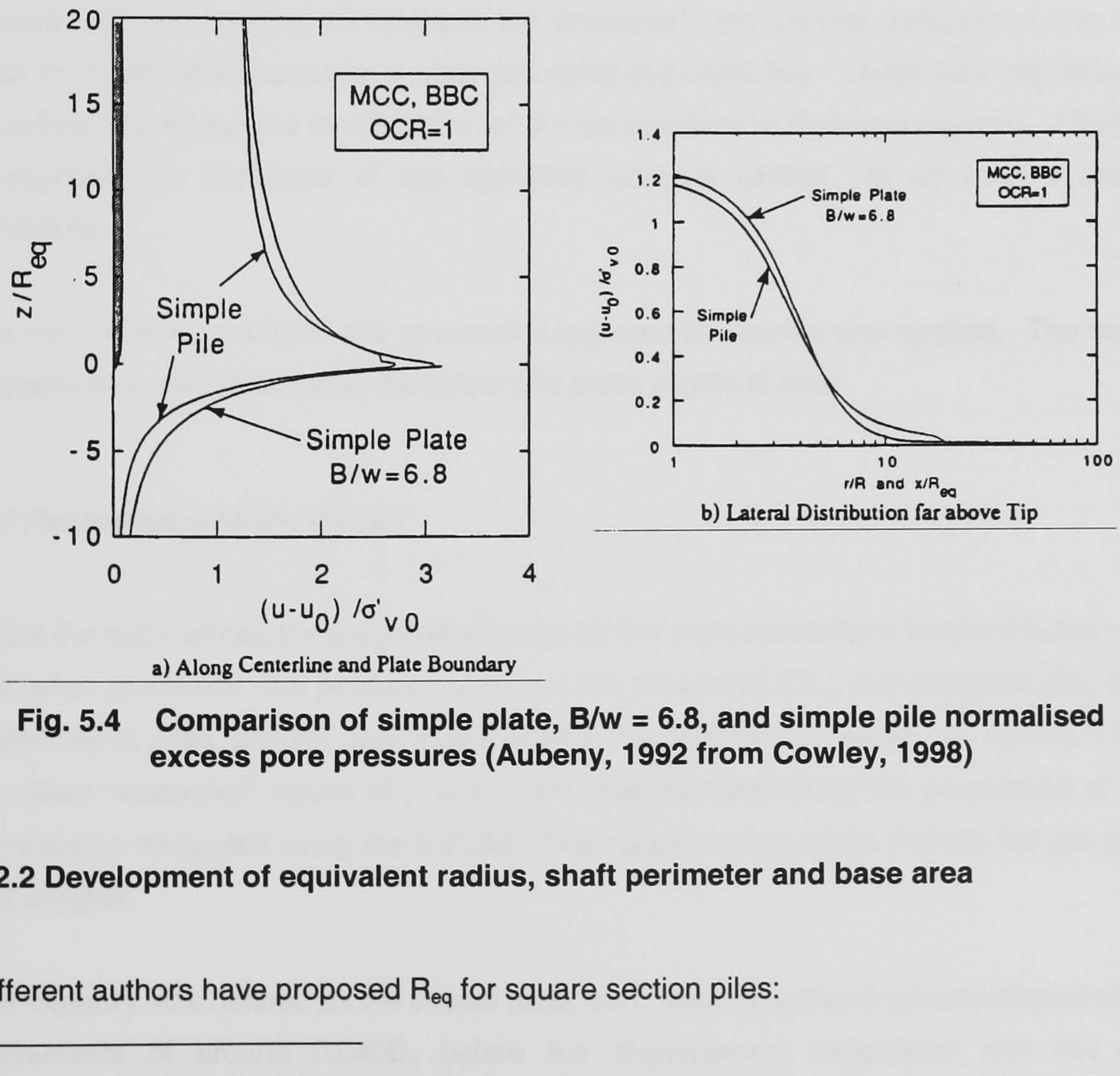


Fig. 5.4 Comparison of simple plate, B/w = 6.8, and simple pile normalised excess pore pressures (Aubeny, 1992 from Cowley, 1998)

5.2.2 Development of equivalent radius, shaft perimeter and base area

Different authors have proposed R_{eq} for square section piles:

---

[68] The Marchetti dilatometer consists of a blade with overall thickness of 14 mm, width of 95 mm and a cutting edge with apex angle of 18 to 20 degrees.

i) Chow (1997) assumed that the side length of the square pile is equal to R_{eq}.

ii) Chellis (1961) assumed that the side length of a square pile is equivalent to the diameter of a round pile.

iii) Aubeny (1992) assumed that R_{eq} is found from the base area of the square section.

iv) A further approach bases the R_{eq} computation on the shaft perimeter of a square pile. Table 5.3 summarises these approaches.

Table 5.3 Approaches analysed by Cowley for the R_{eq} of square piles

Approach	R_{eq}	Shaft perimeter
(i)	d	4d
(ii)	d	πd
(iii)	$d/(\pi^{1/2})$	4d
(iv)	$2d/\pi$	4d

Cowley applied these expressions to a database of 11 tests on square piles in clay (from Mexico City and San Francisco bay in the US). From the inspection of the statistical results obtained with the ICPDM and the equivalent radii Cowley established that the best fit for the shaft capacity is obtained using approach (iii). There was not enough evidence to propose the modification for the computation of the base capacity. Cowley recognised the limitations of this statistical analysis carried out on such a small database.

For the following validation the approach suggested by Cowley was applied. The base capacity was calculated using the actual pile cross sectional area.

5.3 Performance of the ICPDM

Table 5.4 summarizes the weighted average for the main parameters involved in the pile validation procedure, the predicted stresses, the measured (Q_m) and predicted (Q_c) pile capacities at peak, and the parameters used in the analyses of results. In Table 5.4 the so-called "measured" values of β and α are inferred considering the percentage of tip contribution computed using the ICPDM. The measured capacities include the pile and soil weights.

Pile capacity was defined as the overall peak load, which in general was developed after settlements of around 0.045D, before the displacement associated with pile tip contribution (0.1D) is reached. (D is two times R_{eq}.)

Table 5.4 Summary of results from the validation of the ICPDM for Mexico City conditions

Pile Test	L (m)	D (cm)	L/D	Eq. (days)	YSR	S_t	S_u (kPa)	σ_o (kPa)	S_u/σ_o	Q_m (kN)	Disp. (mm)	Q_c (kN)	Q_c/Q_m	τ_{rzc} (kPa)	β_c	α_c	α_m	β_m
BC2	22.0	50x50	39	15	1.7	11.6	25.4	68.3	0.37	1274	27.0	1266	0.99	31.0	0.45	1.22	1.04	0.39
BC12	22.0	50x50	39	15	2.0	11.9	25.4	48.4	0.52	1048	23.8	1013	0.97	24.4	0.50	0.96	0.83	0.44
BC23	22.5	50x50	40	35	2.1	10.0	29.3	46.0	0.64	993	37.5	1046	1.05	25.5	0.55	0.87	0.69	0.44
BC26	23.0	50x50	41	15	2.0	9.7	29.3	46.8	0.63	1231	32.2	1140	0.93	25.9	0.55	0.88	0.81	0.51
CC21	23.5	50x50	42	94	1.8	9.0	20.6	47.9	0.43	1104	28.4	1153	1.04	26.1	0.55	1.27	1.02	0.44
CC27	23.0	50x50	41	57	1.7	7.3	23.7	49.7	0.48	1040	30.8	1124	1.08	26.1	0.53	1.10	0.85	0.40
CC32	24.0	50x50	43	125	1.6	5.6	25.8	54.4	0.47	1162	27.0	1293	1.11	29.4	0.54	1.14	0.85	0.40
CM8	25.0	50x50	44	38	1.9	8.4	27.2	45.3	0.60	1048	24.8	1185	1.13	25.7	0.57	0.95	0.69	0.41
CM17	26.0	50x50	46	15	1.8	8.4	27.4	48.6	0.56	1049	24.8	1326	1.26	27.2	0.56	1.00	0.67	0.38
CM25	25.5	50x50	45	15	2.0	9.1	27.4	47.7	0.57	1058	23.6	1262	1.19	26.4	0.55	0.96	0.68	0.39
CNT	24.3	35	69	59	1.4	7.7	37.7	82.4	0.46	1316	29.8	1015	0.77	38.2	0.46	1.01	1.01	0.46
CTI16	32.0	50x50	57	40	2.3	13.5	43.4	73.5	0.59	1858	18.9	1783	0.96	29.9	0.41	0.69	0.59	0.35
CTI68	32.0	50x50	57	40	2.3	13.5	43.4	73.5	0.59	1843	17.4	1803	0.98	29.9	0.41	0.69	0.59	0.35
CF 27	26.0	50x50	46	113	1.7	9.9	30.9	66.0	0.47	1255	21.4	1360	1.08	29.1	0.44	0.94	0.72	0.33
CUPJ	10.0	30x30	30	191	1.6	8.4	34.6	55.0	0.63	540	22.0	370	0.69	30.9	0.56	0.89	1.23	0.77
CUPJ	10.0	30x30	30	191	1.6	8.4	34.6	55.0	0.63	448	34.0	349	0.78	30.9	0.56	0.89	1.08	0.68
FJ11	26.0	50x50	46	15	1.5	10.2	30.9	69.0	0.45	1035	16.7	1358	1.31	29.9	0.43	0.97	0.61	0.27
GT17	20.5	50x50	36	15	1.2	8.5	25.8	90.5	0.29	1433	19.6	1527	1.07	41.7	0.46	1.62	1.25	0.36
GT29	20.5	50x50	36	157	1.5	7.0	43.2	73.7	0.59	1207	27.4	1447	1.20	39.3	0.53	0.91	0.62	0.36
GT38	19.5	50x50	35	261	1.3	8.1	64.4	86.9	0.74	1233	15.0	1445	1.17	42.4	0.49	0.66	0.46	0.34
MC1	25.5	50x50	45	15	1.3	9.6	27.4	60.4	0.45	1135	30.6	1268	1.12	28.1	0.47	1.03	0.77	0.35
ML91	35.0	30x30	104	100	1.1	9.2	19.2	63.0	0.30	865	16.2	1110	1.28	25.9	0.41	1.35	1.04	0.32
ML92	35.0	30x30	104	100	1.6	17.0	22.8	62.5	0.36	864	19.5	840	0.97	19.5	0.31	0.86	0.87	0.32
ML93	29.0	50x50	51	100	1.7	16.4	22.8	55.0	0.41	1151	19.5	1154	1.00	19.5	0.35	0.86	0.82	0.34
TB8	18.5	50x50	33	15	1.2	6.4	64.4	80.2	0.80	1093	22.0	1359	1.24	41.4	0.52	0.64	0.43	0.34
TB13	20.0	50x50	35	15	1.3	6.1	25.2	64.8	0.39	943		1196	1.27	32.9	0.51	1.30	0.87	0.34
VIA	24.0	35X35	61	32	1.6	8.2	35.3	62.0	0.57	1163	19.1	1162	1.00	34.0	0.55	0.96	0.93	0.53

Fig. 5.5 shows the Q_c vs. Q_m comparison, which provides the clearest indication of the IC method's performance. An statistical evaluation of the (Q_c/Q_m) ratios was carried out using the mean (μ) for accuracy[69], the standard deviation (s) for precision[70], the coefficient of variation (COV=s/μ) and the ranking index (RI) - defined as RI = $|\mu[\ln(Q_c/Q_m)]| + s[\ln(Q_c/Q_m)]$. RI, COV and s should be as low as possible (Briaud and Tucker, 1988). Table 5.5 shows the statistical results for the collected database.

Table 5.5 Statistical results of the validation

μ	1.06
s	0.16
COV	0.15
RI	0.14

[69] Ability to predict the measured ultimate load.

[70] Scatter around mean.

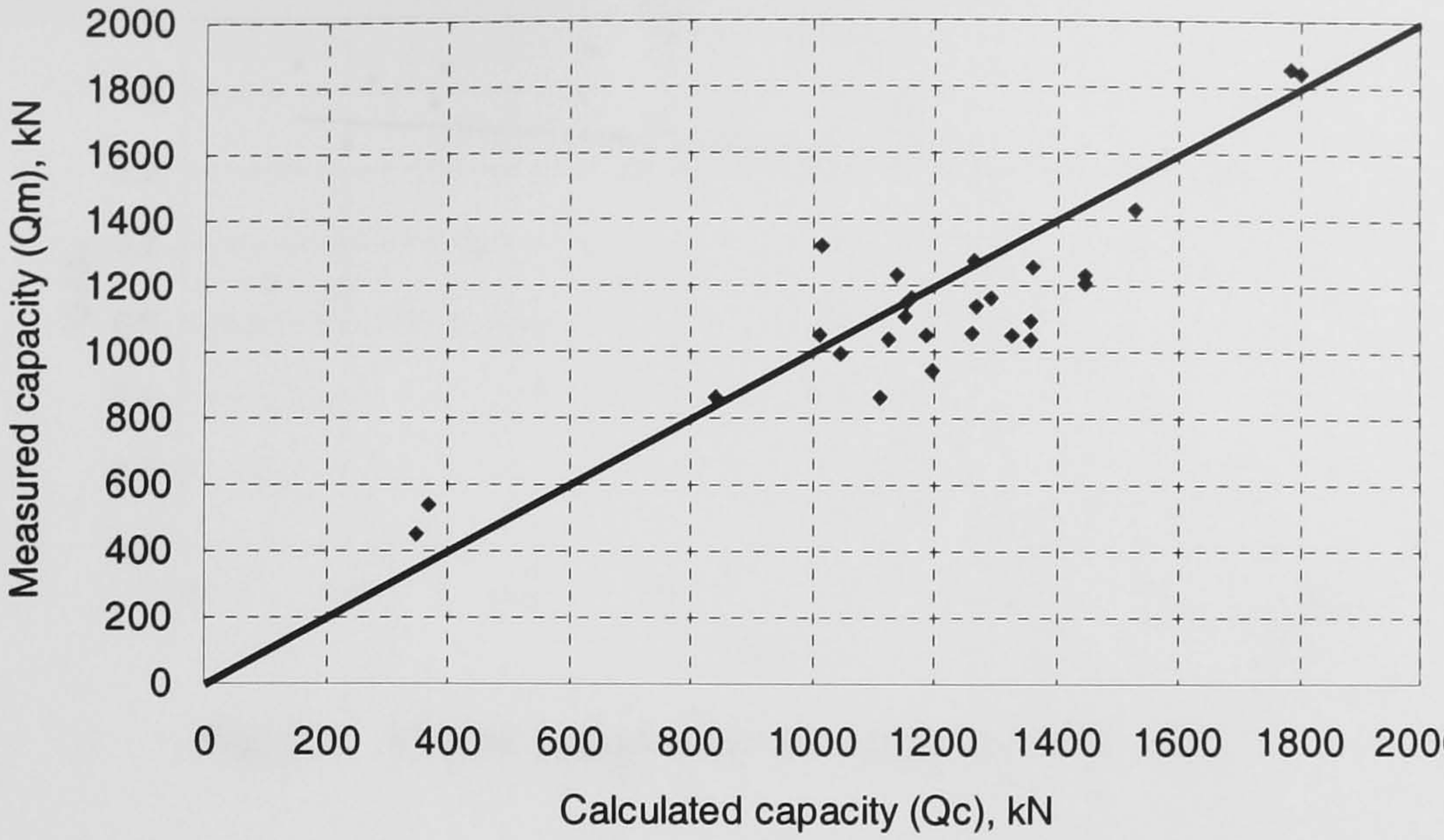


Fig. 5.5 IC design method prediction vs. measured piles capacities

The statistic analysis shows satisfactory results for the design method, in general the method shows a (slightly) tendency to overpredict by 6%, with a standard deviation of ±16%. Note that the load test database is totally independent from the research used to develop the IC method or the full-scale database assembled by Chow (1997) to test the method's practical applicability. This comparison represents an independent evaluation of the method.

The IC pile design method predictions are examined for bias with respect to key parameters on figures 5.6 to 5.8. The method shows no clear skew with the pile length-equivalent radius ratio (L/R) (Fig. 5.6). On the other hand, the method shows a marginal trend of overpredicting slightly with reducing S_t and YSR (Figs. 5.7 and 5.8).

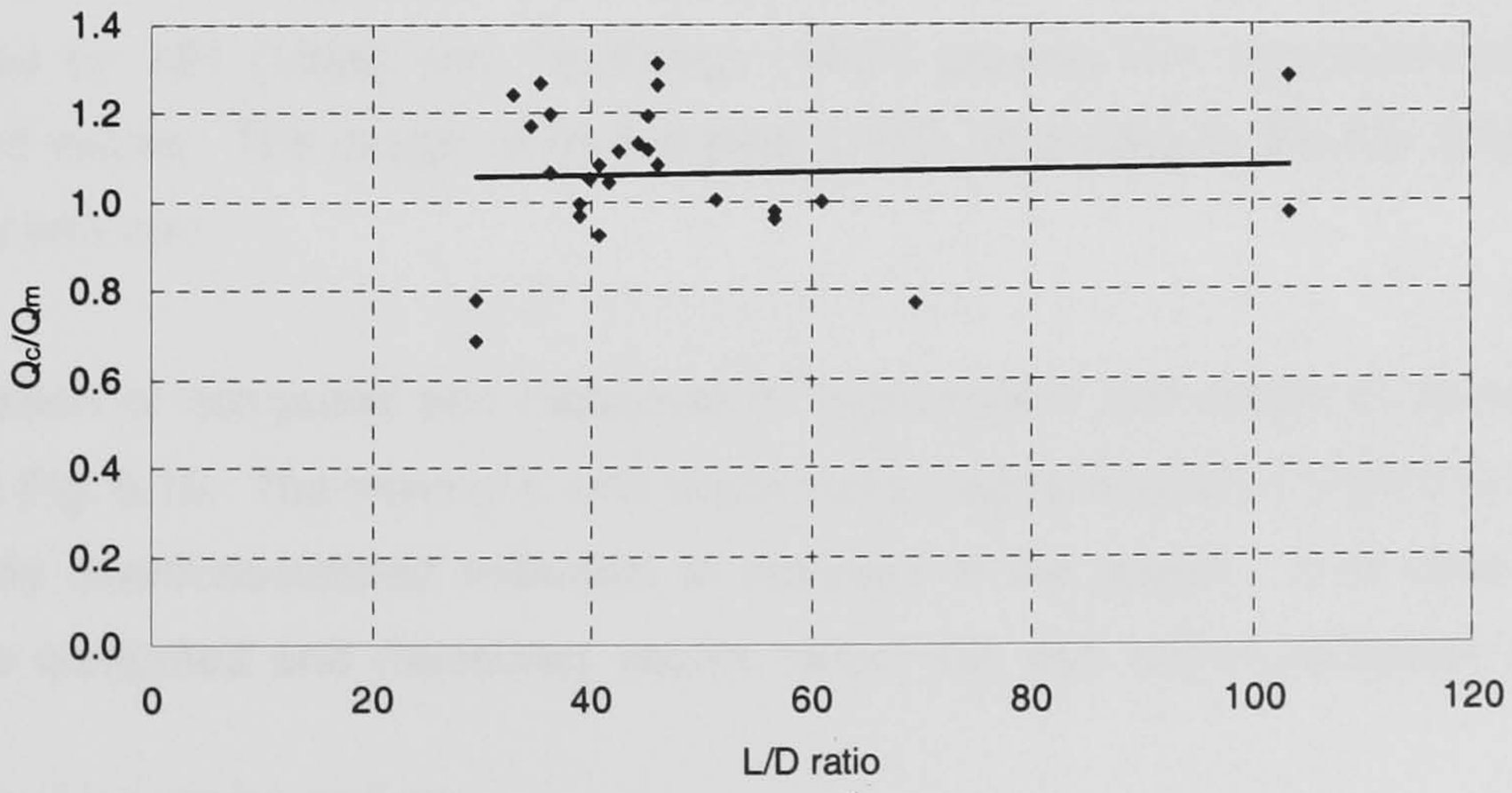


Fig. 5.6 IC pile design method response with L/D ratio

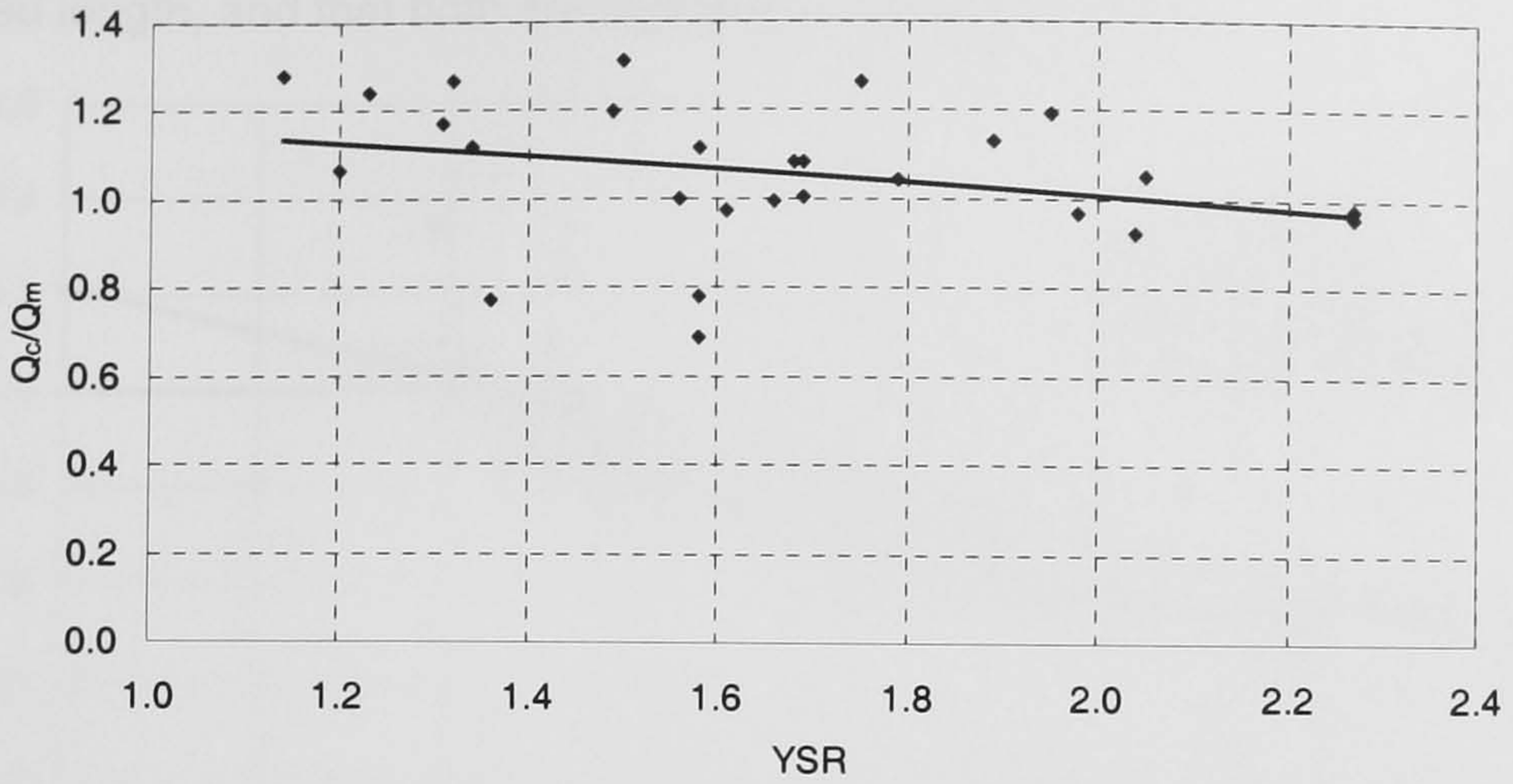


Fig. 5.7 IC pile design method response with YSR

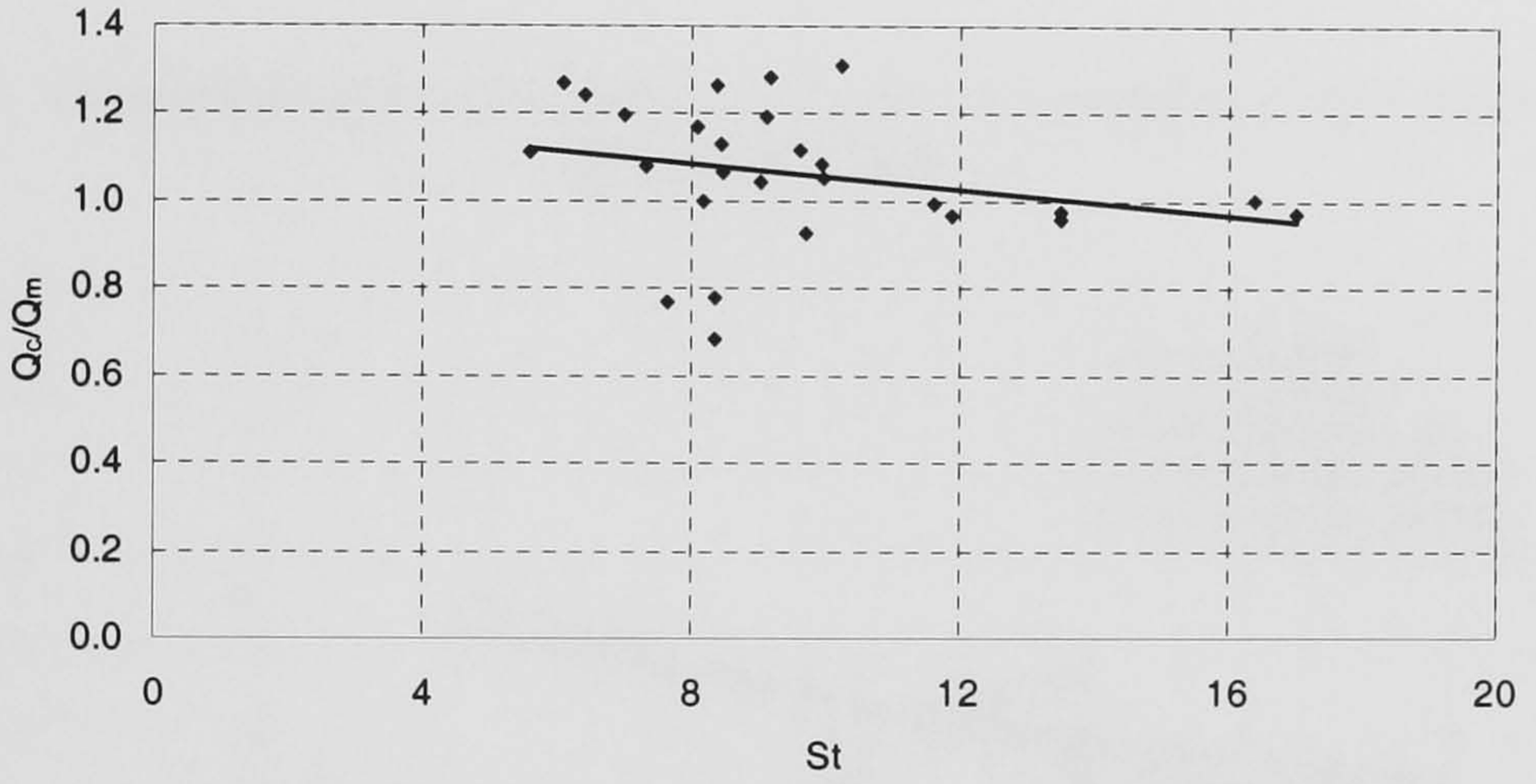


Fig. 5.8 IC pile design method response with S_t

Further analyses were carried out to evaluate known pile response characteristics. Fig. 5.9 shows the known trend of α reduction with increasing S_u - the figure also shows that the database measured values are in general lower than the computed. The α values suggested by API (1986) and Tomlinson (1957) provide fair approximations to the measured values. The design of friction piles in MC, according to the city design code, is carried with α=1.

The variation of computed and measured β[71] parameters with depth of penetration is shown in Fig. 5.10. The trend of β with depth computed by Meyerhof (1976) for normally and lightly overconsolidated materials is included in the graph. It is clear that the database computed and measured values reflect the well known reduction of β with

---

[71] Measured shaft capacities are computed considering the percentage of shaft capacity computed using the IC pile design method.

embedded length, and that both are higher than Meyerhof values.

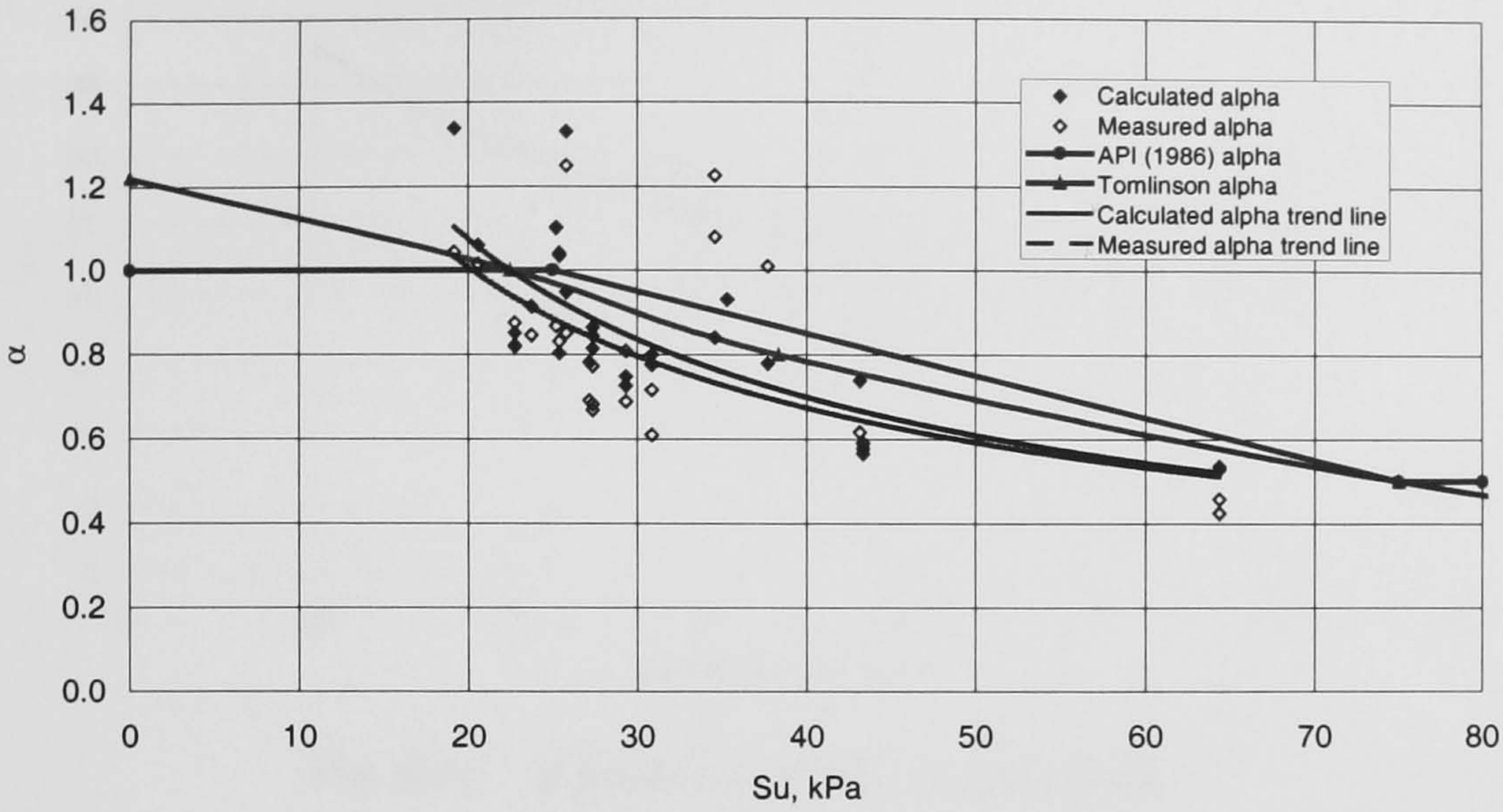


Fig. 5.9 Computed and measured α vs. S_u and API (1986) and Tomlinson (1957) suggested values

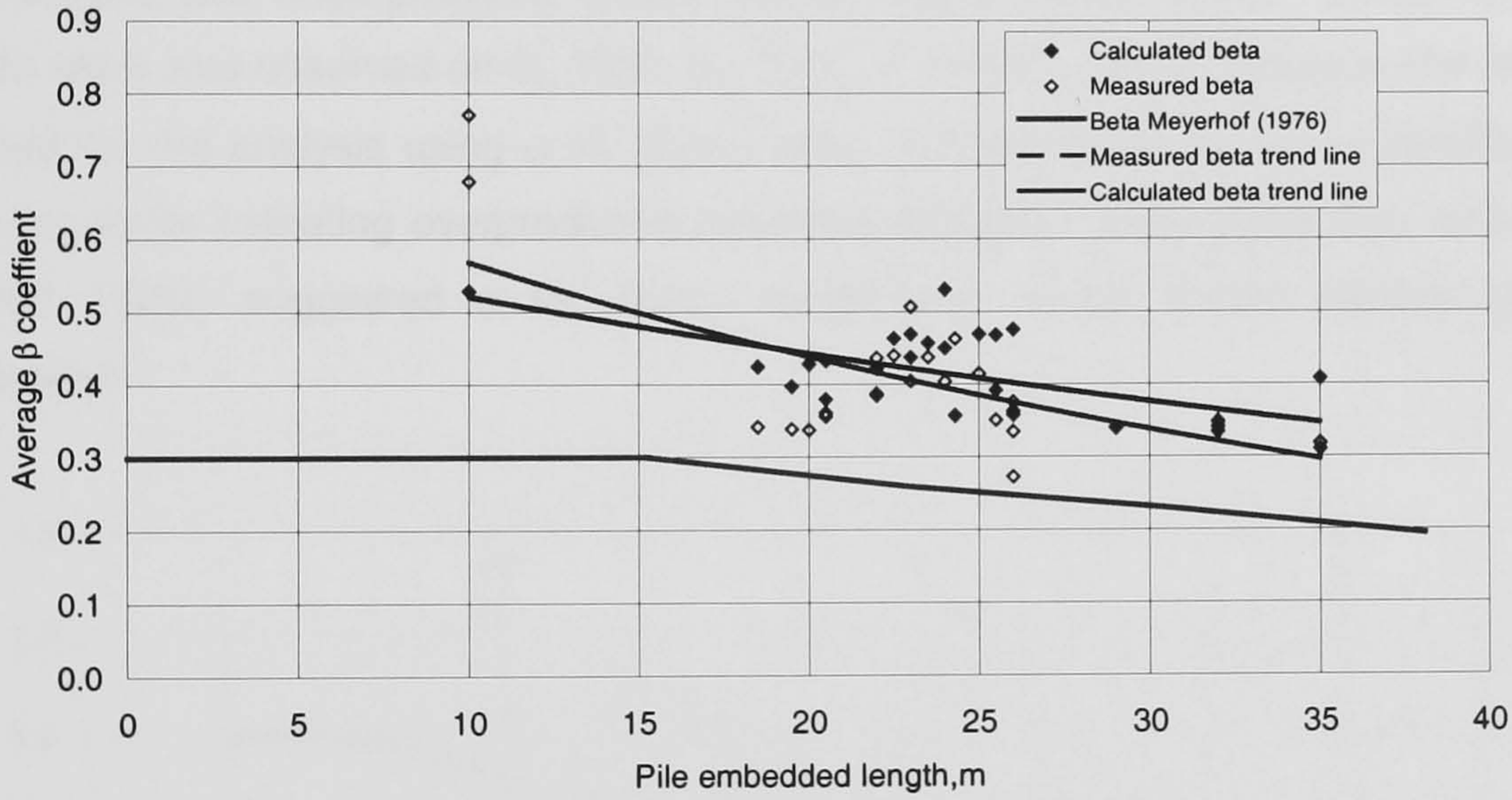


Fig. 5.10 β vs. depth of penetration for computed and measured capacities and Meyerhof (1976) suggested values

Fig. 5.11 shows the reduction of inferred (from measured capacity) average shear strength τ_{rz} with pile embedded length. This trend is observed in the computed τ_{rz}, and the computed and inferred of both α, and β factors.

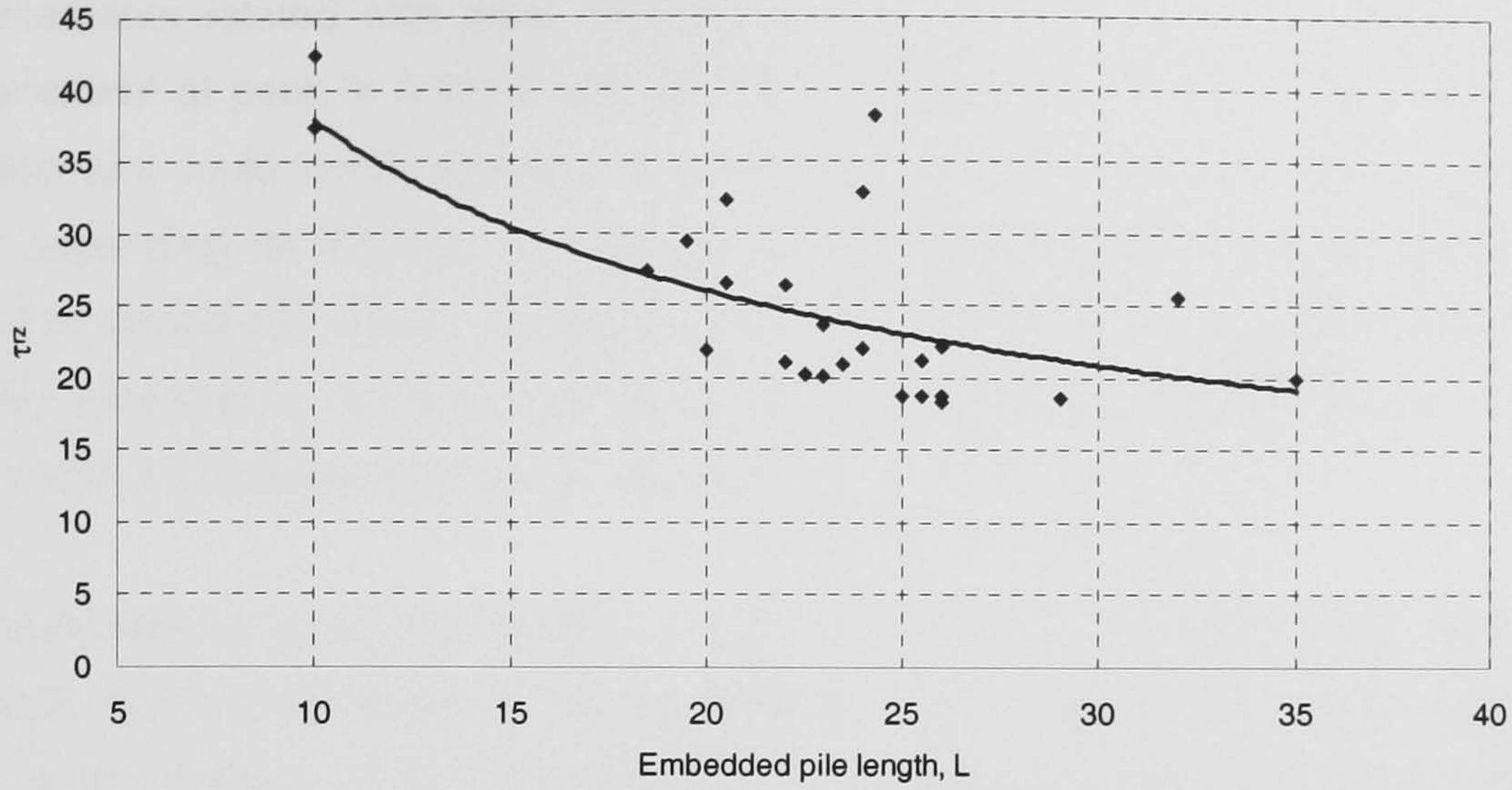


Fig. 5.11 Inferred τ_{rz} values vs. pile length

Additional analyses were carried out to identify the possible reason of the IC design method overall overprediction. This was carried out through the comparison of overpredicted and underpredicted cases against relevant parameters. However, no specific skew was observed on S_t, YSR, S_u, S_u/σ_{vo}', L or L/D. Fig. 5.12 shows the result obtained for the analysis using α vs. S_u/σ_{vo}' ratio, in which there is not an identifiable trend for points indicating overprediction or underprediction. (This graph also includes the API (1991) suggested α vs. S_u/σ_{vo}' relationship, which shows general good agreement).

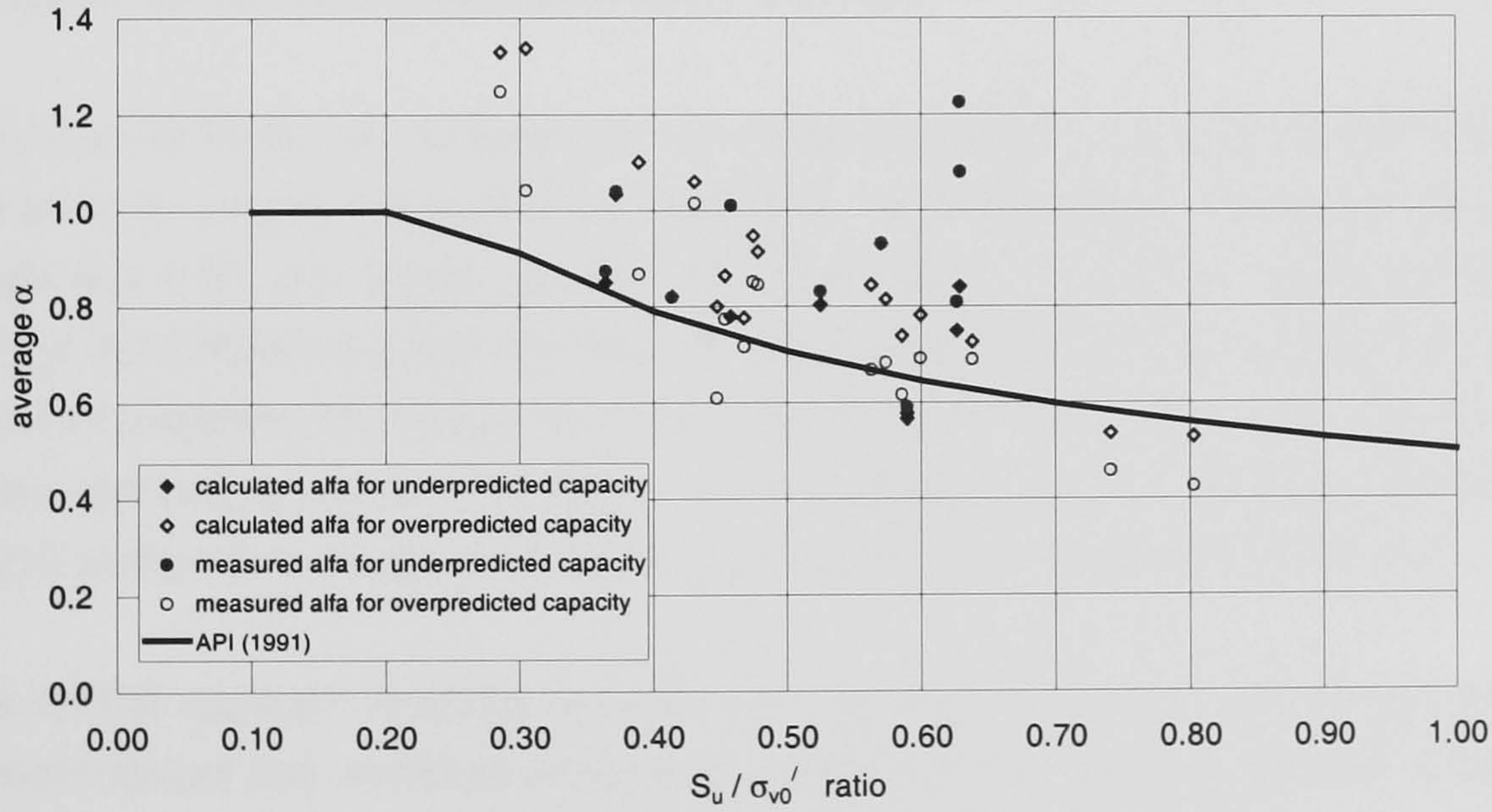


Fig. 5.12 Calculated and inferred a vs. S_u/σ_{v0}' ratio, with identified overpredicted and underpredicted tests

The origin for the slight ICPDM overprediction could be related to the rather large

displacements related with peak capacity in most of the pile tests, whose average displacement at peak is 0.045D with extreme values of 0.07D and 0.03D. This large displacement could locally reduce δ to an ultimate value (reductions of up to 15% can occur depending on the clay composition (Chapter 4)), while the predictions consider peak δ for all the pile length. While the large displacement to peak could increase the pile tip's contribution, the shaft contributes with at least 70% of the pile capacity and so shaft brittleness is likely to be more important.

Measurements of base contribution to pile capacity in MC by Resendiz (1964) and Mendoza, et al. (1996) show that this is 22% (for a pile length of 26.3 m) and 25% (for 29.5 m pile length) of the total capacity. The average calculated base capacity contribution for the database was 9%. From geometrical considerations, this contribution decreases with increasing pile slenderness ratio (L/D).

5.4 Comparison of the ICPDM vs. Mexico City traditional design method

The Author's database has been used to assess the relative reliability of the MC pile design code (presented in section 2.3.4) and the Jardine and Chow (1996) approach. No allowance was made in applying the MC (α=1) approach for the different cross sectional shapes or pre-boring. Table 5.6 summarizes the Q_c/Q_m ratios found in individual cases for the IC method and the traditional procedure in MC, while Table 5.7 compares the statistical parameters for both methods.

The mean for Q_c/Q_m ratio indicates that the traditional method in general overpredicts by around 21%, but can overpredict for up to 56%. This trend slightly increases with pile length and YSR, and slightly reduces with increasing S_t. The closer mean and lower COV of the ICPDM show that the latter has advantages over the traditional method used in MC for predicting the medium term capacities of single piles in clays. The IC effective stress approach provides what appear to be unbiased and more reliable predictions. The IC method was marginally (6%) non-conservative, for the database considered.

The ICPDM approach implicitly addresses the changes in the piles' stress regimes at different stages and, therefore, it has the possibility of implementing rationally different load and soil conditions. The advantage of the α method is its simplicity.

A further validation of the ICPDM that the Author carried out for an offshore Gulf of Mexico installation is given in Appendix B. The Gulf of Mexico is a region of intensive

offshore petroleum production, where most of the fixed platforms are founded on driven piles.

Table 5.6 ICPDM vs. Total stress method for Mexico City conditions

Pile Name	ICPDM	ICPDM Q_c/Q_m	$\alpha = 1$	$\alpha = 1$ Q_{calf}/Q_m
BC2	1266	0.99	1118	0.88
BC12	1013	0.97	1118	1.07
BC23	1046	1.05	1320	1.33
BC26	1140	0.93	1349	1.10
CC21	1153	1.04	968	0.88
CC27	1124	1.08	1092	1.05
CC32	1293	1.11	1238	1.07
CM8	1185	1.13	1359	1.30
CM17	1326	1.26	1423	1.36
CM25	1262	1.19	1396	1.32
CNT	1015	0.77	1008	0.77
CTI16	1783	0.96	2775	1.49
CTI68	1803	0.98	2775	1.51
CF 27	1360	1.08	1604	1.28
CUPJC	370	0.69	466	0.86
CUPJT	349	0.78	415	0.93
FJ11	1358	1.31	1604	1.55
GT17	1527	1.07	1058	0.74
GT29	1447	1.20	1770	1.47
GT38	1445	1.17	2510	2.04
MC1	1268	1.12	1396	1.23
ML91	1110	1.28	805	0.93
ML92	840	0.97	956	1.11
ML93	1154	1.00	1320	1.15
TB8	1359	1.24	2381	2.18
TB13	1196	1.27	1008	1.07
VIA	1162	1.00	1187	1.02

Table 5.7 Statistical results for ICPDM and total stress α=1.

Parameter	ICPDM	α =1
μ	1.06	1.21
S	0.16	0.35
COV	0.15	0.29
RI	0.14	0.34

CHAPTER 6

BASE REACTIONS ON CASE HISTORIES

A fundamental goal of the research is to compare the seismic and static capacities of friction piles in Mexico City (MC). For that purpose, a key part of the work is the determination of the seismic axial loads developed on piles during strong earthquake shaking. The means chosen to find these loads are: (i) analyses through a dynamic structural mechanics program; and (ii) acceleration records obtained from the basement of instrumented buildings. The acceleration records, which are from buildings in MC, are used as input motions in the structural analysis. The piles themselves are not included in the building models; instead the reactions computed at the base are used to determine the forces developed on the pile head (Chapter 10). Subsequently, the seismic loads are compared with the pile static capacity determined using the Imperial College pile design method in order to assess whether any systematic bias can be recognized between the best estimates of the static pile capacity and the forces mobilized during shaking in the field (Chapter 11).

The September 19 1985 Michoacan earthquake in MC constitutes an important event to study the behaviour of pile founded structures under seismic loads. During this event 13.5% of the 6 to 12 storey high buildings in the downtown area – most of them supported on friction piles – were reported damaged, ranging from large settlements (up to one meter) and marked tilting, to complete collapse due to overturning (Mendoza, 1990). Since no suitable buildings had been instrumented prior to 1985, the proposed methodology cannot be directly applied to the 1985 earthquake. However, strong motion records from buildings instrumented after 1985 are used to extrapolate the 1985 building earthquake loading conditions on the basis of the well-established 1985 ground acceleration records.

This chapter describes the background ideas, the methodologies and the structural program used to carry out the dynamic back-analyses.

6.1 Principles of the proposed seismic structural analysis

6.1.1 Proposed methodology of analysis

In the seismic analysis of a structure founded on rigid rock, the motion experienced by the base is identical to that occurring in the same point before the structure is built. In this situation the seismic response of a structure depends only on its own properties.

In the case of a structure founded on a soft stratum that lies on rock two important changes occur in response to the same incident seismic waves. First, the free-field motion at the site is affected. Second, the structure will interact with the surrounding soil, leading to further changes in the amplitude and frequency content of the seismic motion at the structure base. These modifications constitute the dynamic soil-structure interaction (SSI), which, in general, results in a more flexible soil-structure system with a fundamental frequency below that applicable for the fixed-base structure.

Conventional soil-structure interaction analysis for seismic excitation implicitly assumes the law of superposition to be valid. The total solution equals the sum of the responses of the free field and of the interaction part when the structure is inserted into the seismic environment of the free field. This means that a linear system is actually calculated. For the building in Fig. 6.1a the dynamic interaction of the soil-structure system (and the analysis of the forces at the piles) would include an input motion at some point in the free field or rock base, and the more relevant soil, foundation, building and seismic environment characteristics.

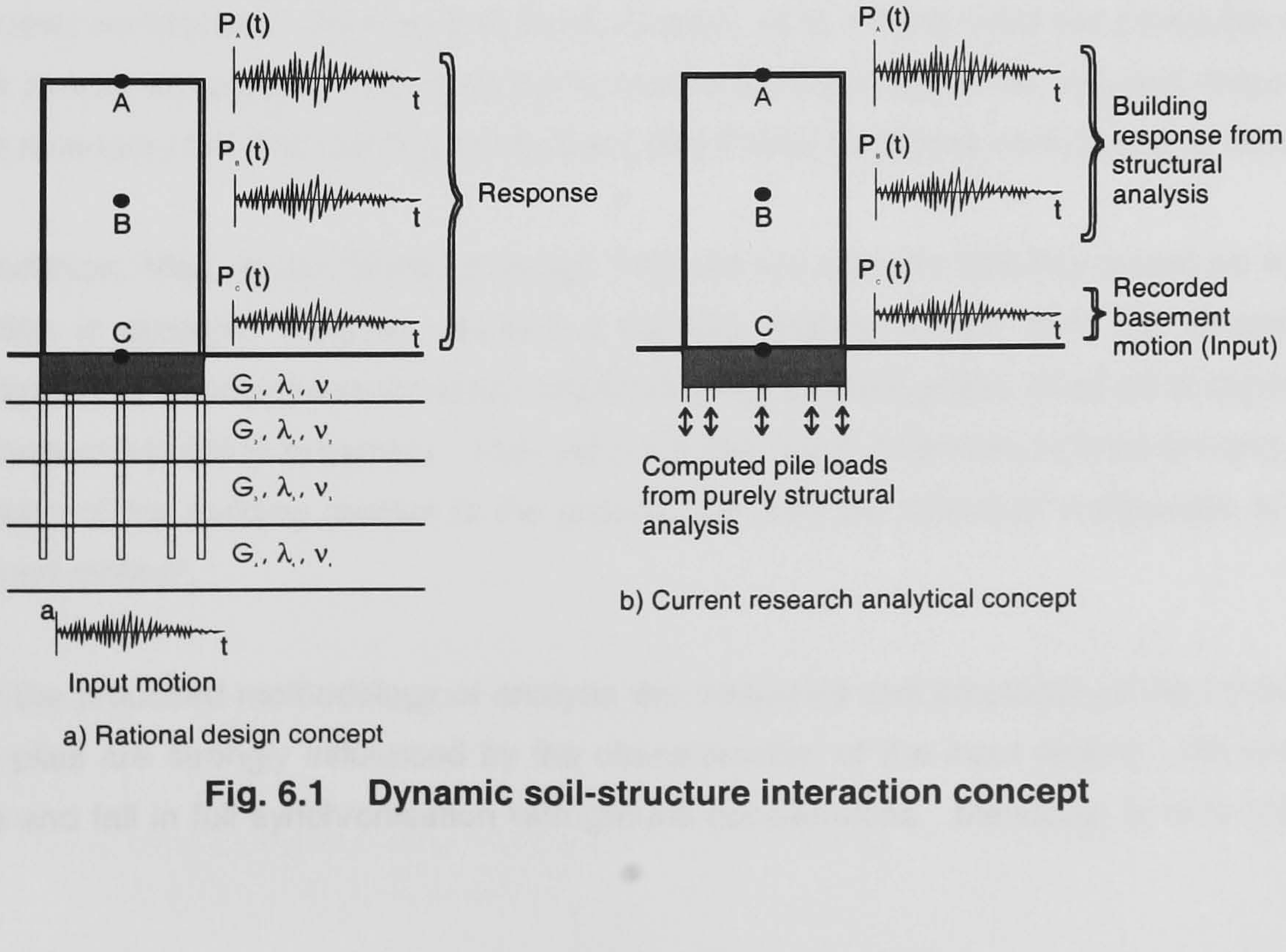


Fig. 6.1 Dynamic soil-structure interaction concept

On the other hand, if the de-coupling technique (section 6.1.2) is considered valid, and acceleration records from the base of instrumented buildings are available, the seismic forces at pile head level in a soil-structure system can be computed by analyzing only the structure as a sub-system under that recorded motion. This motion contains the kinematic and inertial effects of SSI (including the influence of the piles), and the influence of the structure sub-system (section 6.1.3). Thus, in this thesis proposed methodology to determine pile forces (Fig. 6.1b) neither the soil stratum nor the piles are included, and the analysis consists only of the structure subjected to a motion recorded at its base (point C in the figure). This motion already includes the pile-soil effect plus the structural effect.

There exists a wide literature on dynamic SSI theory and its effects on pile founded structures. Various state-of-the art presentations and reviews can be found in the published literature (e.g. Veletsos, 1977; Roesset, 1980; Luco, 1980; Gazetas, 1983; Novak, 1991). More relevant for this research are the works of Papageorgiou, et al. (1989) and Durrani, et al. (1994) who carried out dynamic analyses of structures using building records obtained at foundation level as input motions.

Papageorgiou, et al. (1989) stated that "the translational components of motion of the foundation were recorded and considered as input motions in the identification analysis, the inferred parameters reflect not only the characteristics of the superstructure but also the characteristics of the foundation and of the underlying soil...". Papageorgiou, et al. analyzes the recorded earthquake response to extract the modal properties of the 14-storey, reinforced concrete Hollywood Storage building shaken during the 1987 Whittier Narrows earthquake. On the other hand, Durrani, et al. (1994) used two horizontal and one vertical acceleration record as input motions for the study of the dynamic response of a nine-story flat-slab building during the Loma Prieta, California earthquake of 1989.

In addition, Meli, et al. (1998), although they did not use the building record as input motion in dynamic analyses, derived a building rocking motion from the difference between the vertical displacements computed using accelerograms obtained at opposite corners of a building basement. They point out that "such difference reflects not only the rocking of the building relative to the ground, but also the rotational component of the ground motion".

For the proposed methodology of analysis the frequency and amplitude of the forces at the piles are strongly influenced by the characteristics of the input record - pile forces rise and fall in full synchronisation with ground accelerations. Mendoza, et al.'s (1997)

comparison of the Fourier spectra of seismic records of geotechnical variables[72] and of accelerations at the base of the foundation box supports this observation (sections 10.1.2 and 10.1.3 present a complete description of Mendoza, et al.'s research). They conclude that the dominant frequencies of the soil-structure system and the geotechnical variables are very similar and move in phase. Fig. 6.2 shows Mendoza et al.'s Fourier spectra for forces in two instrumented piles and for the acceleration record obtained at the base of the structure.

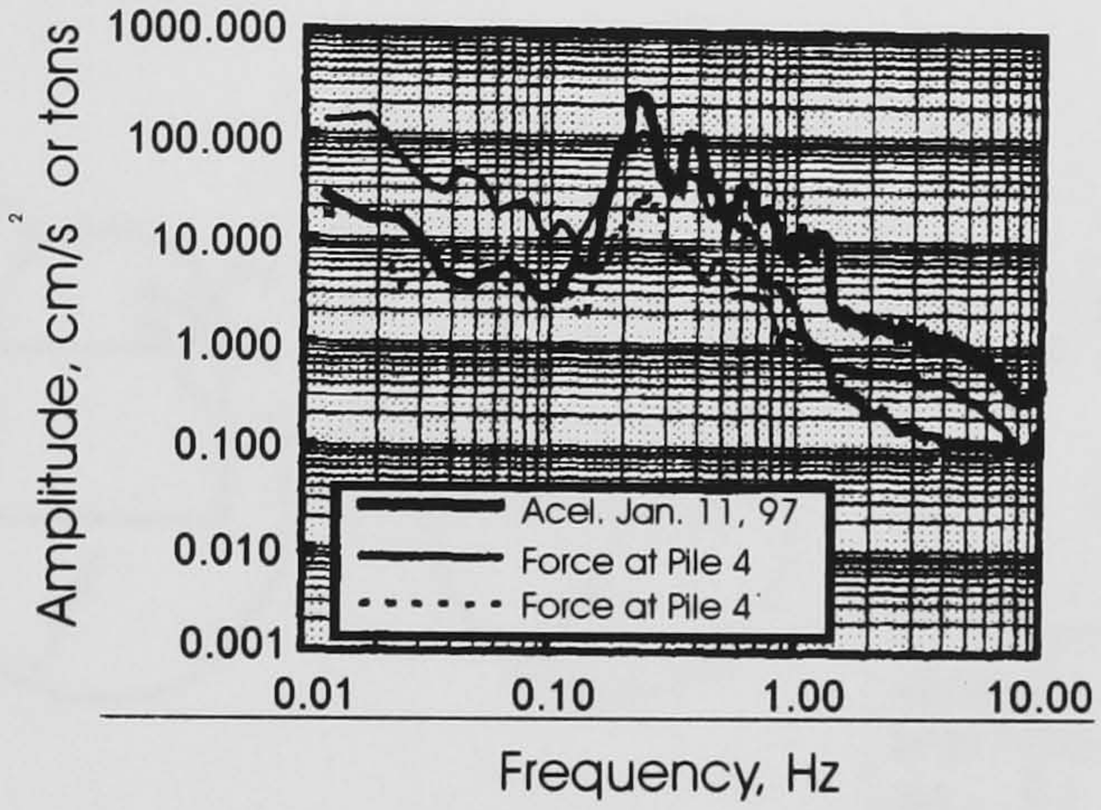


Fig. 6.2 Fourier spectra of basement acceleration and pile forces (Mendoza, et al. 1998)

The seismic reactions obtained from the proposed analysis are located at the base of the idealised foundation. The forces at the piles will be computed from the seismic reactions taking into account the contribution of the foundation raft, and the pile group effect.

In the following section, the two basic assumptions for the above introduced methodology (decoupling of the SSI system and the presence of interaction effects in building recorded motions) are explained.

6.1.2 De-coupling of SSI subsystems

A subsystem with a mass can be de-coupled from a dynamic model. The response (u_c) of a subsystem with a stiffness matrix [k_c], a mass matrix [M_c], and a damping ratio (ζ_c) under a dynamic load (e.g. an earthquake excitation specified at the surface of the free field (u_f)) can be determined by studying subsystems as follows (Fig. 6.3). In the first step, the dynamic model without the de-coupled subsystem is analyzed. The acceleration or displacement time history (u_s) at the location where the subsystem is in

---

[72] Forces at piles, pressure at raft-soil contact, and pore pressures.

reality connected to the structure is calculated. This motion - called in-structure response - will be influenced just by the dynamic characteristics of the model of this first step. In the second step, this calculated motion is applied to the support of the de-coupled subsystem, resulting in its response (u_c). In this procedure the two systems are assumed to behave independently of one another with no feedback from the subsystem to the dynamic model of the first step – for the proposed methodology the feedback is included in the input motion.

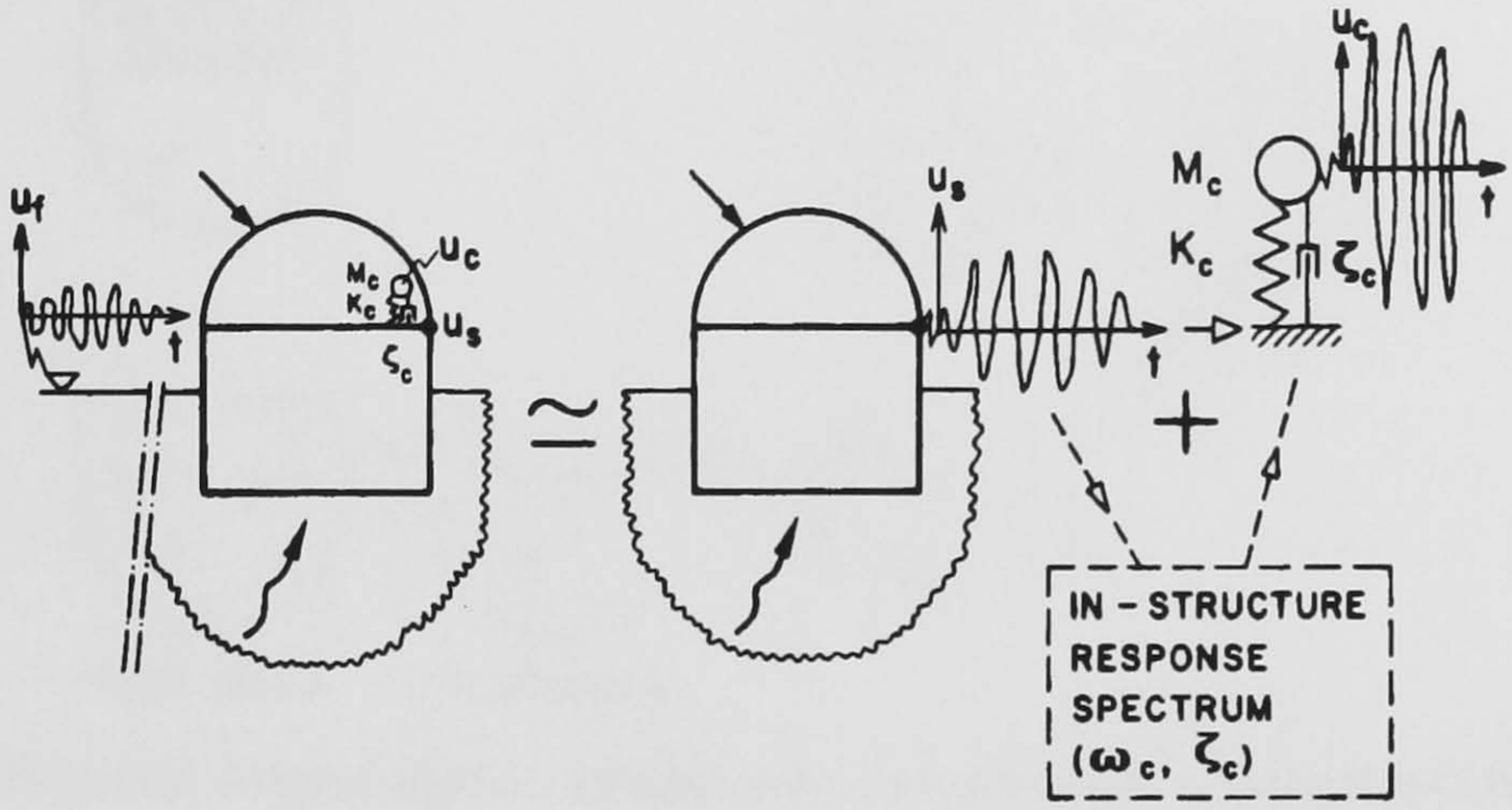


Fig. 6.3 De-coupling of subsystems (Wolf, 1985)

6.1.3 Characteristics included in motions recorded at the basement of buildings

The sub-structure concept is used here to explain the interaction effects included in a motion recorded in an instrumented building.

The Substructure method is often used for routine elastic analysis of dynamic SSI. This method is based on the law of superposition that allows the complicated soil-structure system to be broken down into more manageable parts – inertial and kinematic interactions.

By means of the substructure method, the stiffness and damping constants of a pile foundation can be defined separately and then introduced into the governing equations of the structure. Once the impedances[73] of the pile foundation are determined, the

---

[73] The impedance functions (complex dynamic stiffness) are defined as amplitudes of harmonic forces (or moments) that have to be applied to the pile head in order to generate a harmonic motion with a unit amplitude in the specified direction (Novak, 1991). For piles, they express stiffness and energy dissipation (viscous damping) characteristics of the overall pile-soil system or of individual parts of that system. These functions depend on the frequency of the force, material, length and radius of the pile, shear stiffness and hysteretic damping of the soil, and the mode of

procedure of seismic analysis is the same as that for the structure rested on shallow foundation. Fig. 6.4 shows a discretized system of the SSI consisting of the structure and, in the embedded region, of the difference of the structure and the soil supported on a generalized spring[74] (Wolf, 1985).

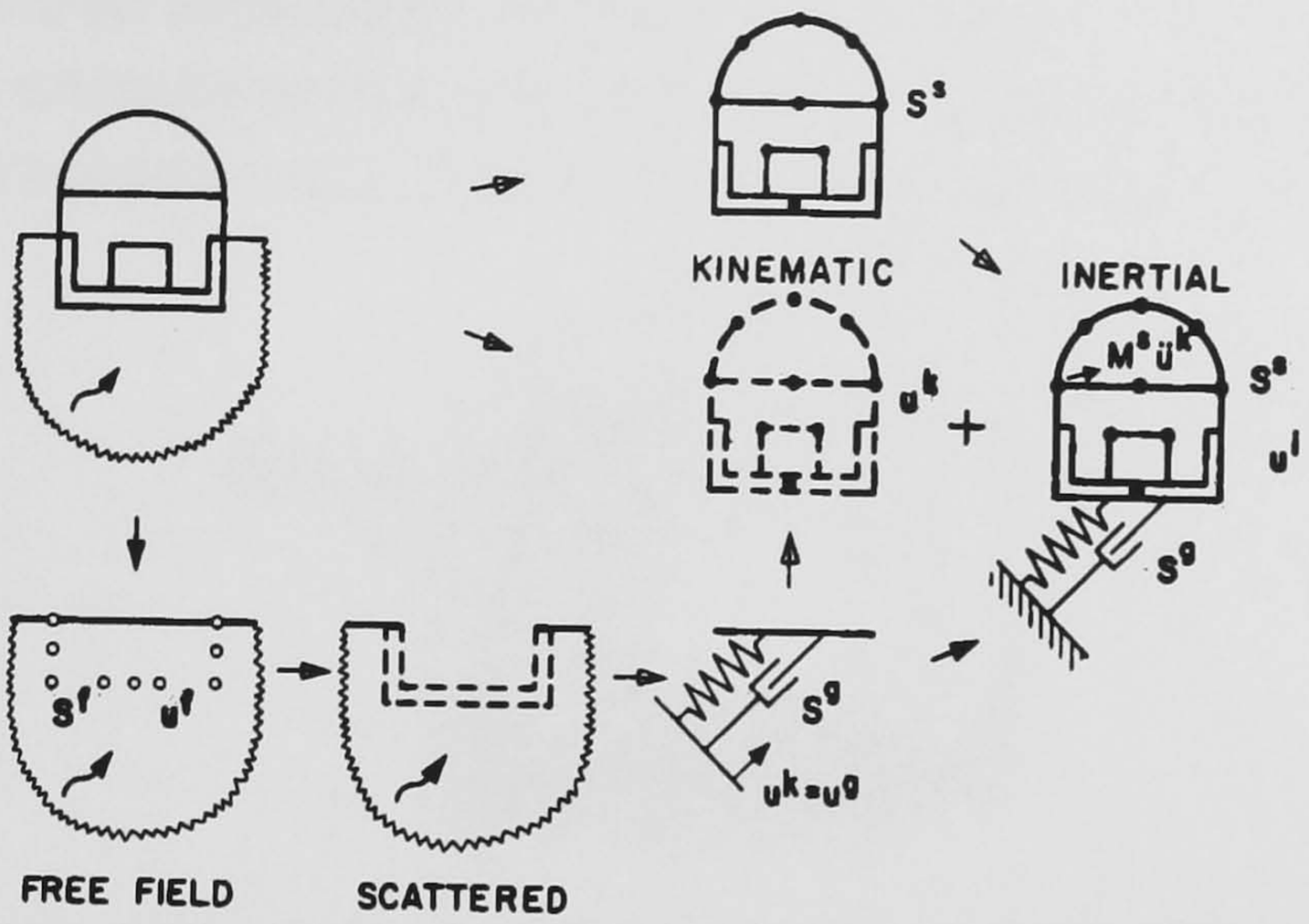


Fig. 6.4 Physical interpretation of kinematic and inertial interaction (Wolf, 1985)

For the system shown in Fig. 6.4, a substructure analysis of SSI consists of the following stages (Wolf, 1985):

i) From the knowledge of the free-field response (u_f)[75], the motion of the kinematic interaction (u^k) and the foundation impedances $[S^g]$ are calculated.

ii) Using rigid body kinematics and the displacements and impedances from step 1, the inertia loading to be applied throughout the structure in the inertial-interaction part of the analysis is determined. The local inertia forces are calculated in all nodes of the structure as the product of the mass of that part of the structure and the corresponding local inertia loading from the kinematic interaction.

iii) The motions of the inertial interaction (u^I) are computed by applying the inertial forces from step 2 to the structure supported on the generalized spring without applying support motion.

---

vibration.

[74] If a structure supported on the surface of a layer of soil resting on rigid rock is considered, the generalized spring would represent the stiffness and damping of the layer built in at its base at the top of the bedrock.

[75] (u) vector of displacements, [S] stiffnes matrix.

Thus, the total displacements resulting from the interaction effects are divided into displacements caused by the kinematic and inertial interactions. The kinematic interaction originates from the incompatibility of the seismic free-field displacements with the rigid body displacement of a mass-less foundation. On the other hand, the inertia interaction is a direct consequence of inertia forces developing in the structure during its vibration. Fig. 6.5 shows the motions originated from the kinematic interaction (u_s^k, u_0^k)[76] and the inertial interaction (u_s^i, u_0^i) as components of the total motion (u_s^t, u_0^t).

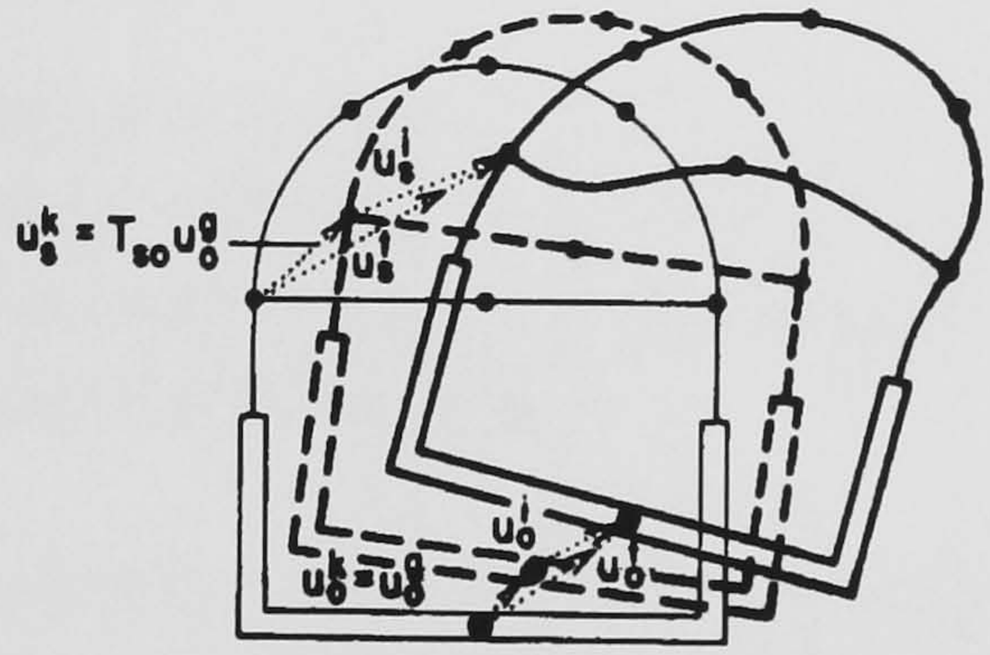


Fig. 6.5 Kinematic and inertial interaction motions (Wolf, 1985)

From the above elastic analysis it can be seen that the motions recorded at the base of a building include the effects of both kinematic and inertial interactions.

The above conclusion has been drawn based on linear soil structure behaviour and as such applies strictly to minor and moderate seismic loadings. Under strong earthquake shaking however, both the structure and soil are likely to experience non-linear deformations. Under such conditions one cannot strictly use the kinematic- and inertial-interaction notions, but these concepts can still be employed to visualize the mechanism of force development in the piles and the SSI concepts (Kayna and Mahzooni, 1996).

In the de-coupling and substructure methods it is possible to analyze the sub-systems with different levels of detail. However, the results from the crude structural model of a structural-soil system are, in general, not sufficient to design the structure directly. As a result, in order to determine the detailed structural response, it is necessary to analyze a separate and more precise structural model using certain results from the crude total system - e.g. the motion at the base of the structure of the crude total model (Wolf 1985).

---

[76] (u_s) and (u_0) are the vector of motions in the structure and at the foundation base, respectively.

6.2 Characteristics of the program of structural analysis

The structural analytical work was carried out using the computer code ADAPTIC, a finite element program developed at Imperial College (Izzuddin, 1991). This program is capable of predicting the large displacement behaviour of steel and reinforced concrete plane and space frames under static or dynamic loading, taking into account both geometric and material non-linear behaviour.

Non-linear behaviour refers to the condition of a structure where the response to realistic loading can not be linearly extrapolated from the response to small loads without incurring on significant inaccuracies. In general, engineering structures exhibit nonlinear behaviour due to material and geometric effects.

Material non-linearities can form a major contribution to the global structural non-linear behaviour, depending on the level of loading and the type of material under consideration. Mild steel, for example, exhibits an almost linear response up to the point of yield, and hence its non-linear effects are only detected under relatively high loads. On the contrary, the concrete is inherently nonlinear even under small strains and induces non-linearities on the structural level at low loads.

On the other hand, geometric non-linearities are developed in structures composed of all materials when changes in geometry occur due to load application and the resulting overall structural response. In general, geometric non-linearities are caused by large displacements.

In summary, ADAPTIC was selected due the following reasons:

i) First, and above all, the program accepts independent asynchronous dynamic support motion as excitation.
ii) The program is capable of analyzing concrete and steel frames taking into account the geometric and material non-linearities.
iii) The cross sections, type of elements, and materials available in the libraries make it possible to include concrete and masonry walls.
iv) As an IC developed program the availability of advice would not be a problem.

A general description of ADAPTIC characteristics is given in the following sections.

6.2.1 Material models

a. Constitutive models for steel: Two cyclic models for mild steel were originally implemented within an elasto-plastic cubic formulation in ADAPTIC. The first is the bilinear model with kinematic hardening, which is relatively simple to implement, computationally efficient, and with easily identifiable parameters. In this model, shown in Fig. 6.6, the elastic range remains constant throughout the various loading stages, and the kinematic hardening rule for the yield surface is assumed to be a linear function of the increment of plastic strain.

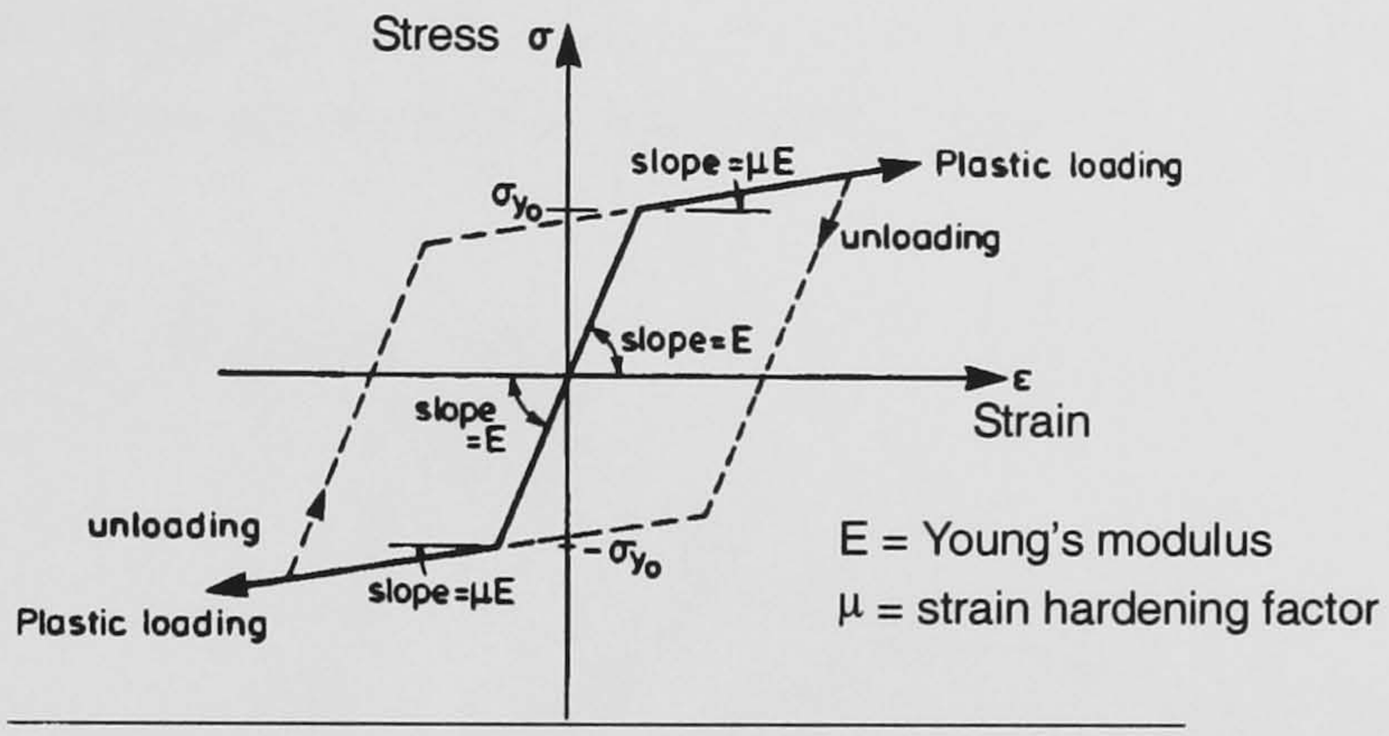


Fig. 6.6 Loading and unloading paths of bilinear kinematic model (Izzuddin, 1991)

The second model is the uniaxial case of a multi-surface model. This more complex constitutive relationship captures the three dimensional behaviour of mild steel under variable amplitude more realistically. In this model, a number of yield surfaces encircle the initial elastic yield surface, each of which is associated with a value for the increment of plastic strain (Fig. 6.7). The expansion/contraction (isotropic hardening) and translation (kinematic hardening) of these surfaces are governed by pre-specified hardening rules (Elnashai and Izzuddin, 1993).

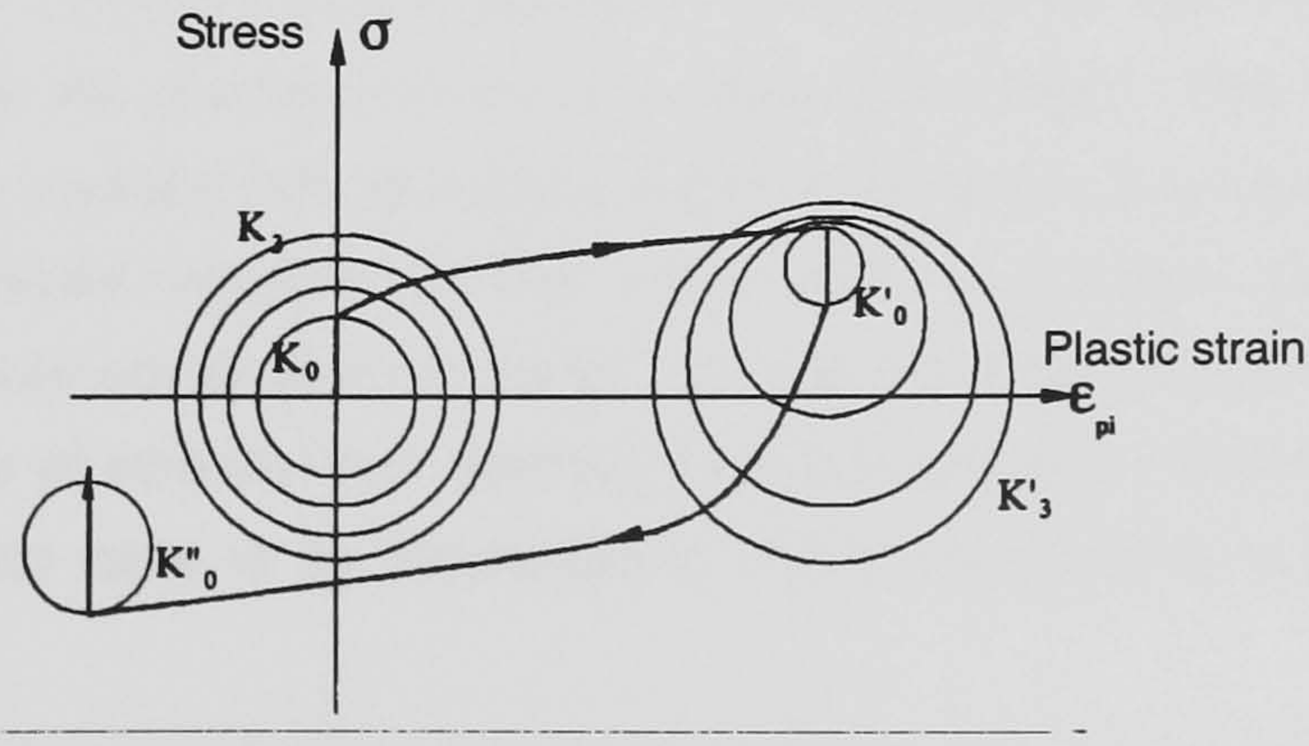


Fig. 6.7 Loading surfaces for multi-surface plasticity model (Elnashai and Izzuddin, 1993)

b. Constitutive model for concrete: Most available uniaxial concrete models consider the stress-strain relationship under compressive cyclic load history to possess an envelope curve, which is unique and identical to the stress-strain curve obtained under constantly increasing load. If the stress is decreased, an unloading curve will be traced. Increasing the stress again forces the material along a reloading curve. In these relationships, one or more of the significant three-dimensional effects that influence the principal axial direction of loading may be represented. These include the effect of triaxial confinement on the peak stress, the peak strain and the inclination of the post-peak stress-strain curve. The constitutive relationship model used in ADAPTIC is a uniaxial variable confinement model capable of predicting the degradation of strength and stiffness, as shown schematically in Fig. 6.8 (Martinez-Rueda, 1997).

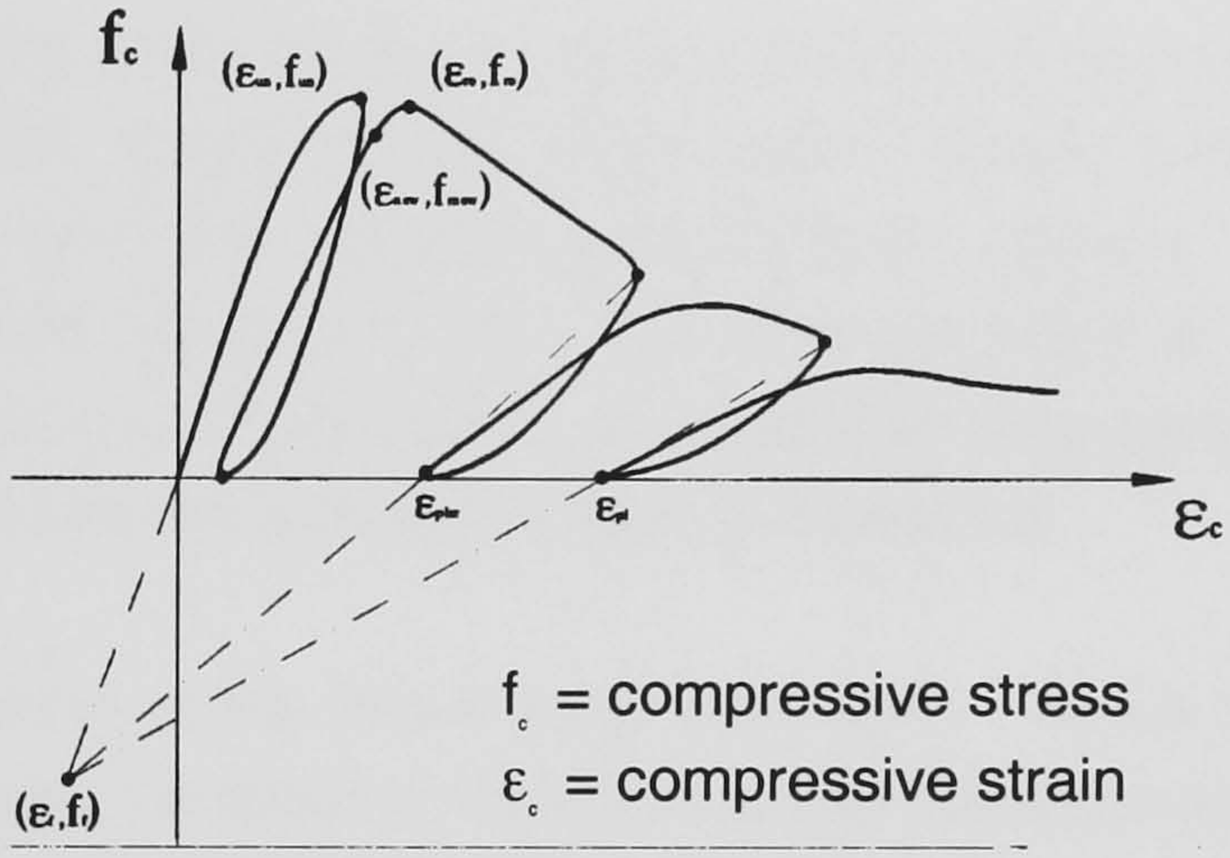


Fig. 6.8 Uniaxial stress-strain relationship for concrete (Martinez-Rueda, 1997)

Regarding the modelling of confinement provided by lateral reinforcement, two options are implemented in ADAPTIC. For the active confinement method a constant confining pressure is assumed taking into account the maximum transverse pressure from confining steel. This is introduced on the model through a constant confinement factor, used to scale up the stress-strain relationship throughout the entire strain range (Fig. 6.9). Alternatively, the passive confinement model is available. This model calculates and continuously updates the transverse confinement stress for a given applied axial strain of a reinforced concrete member under cyclic or transient loading. Thus, in addition to concrete compressive strength, the characteristics of confinement detailing such as diameter of stirrups, their spacing and yield strength, confined core area and Poisson ratio, also have to be introduced to define the material model (Madas and Elnashai, 1992).

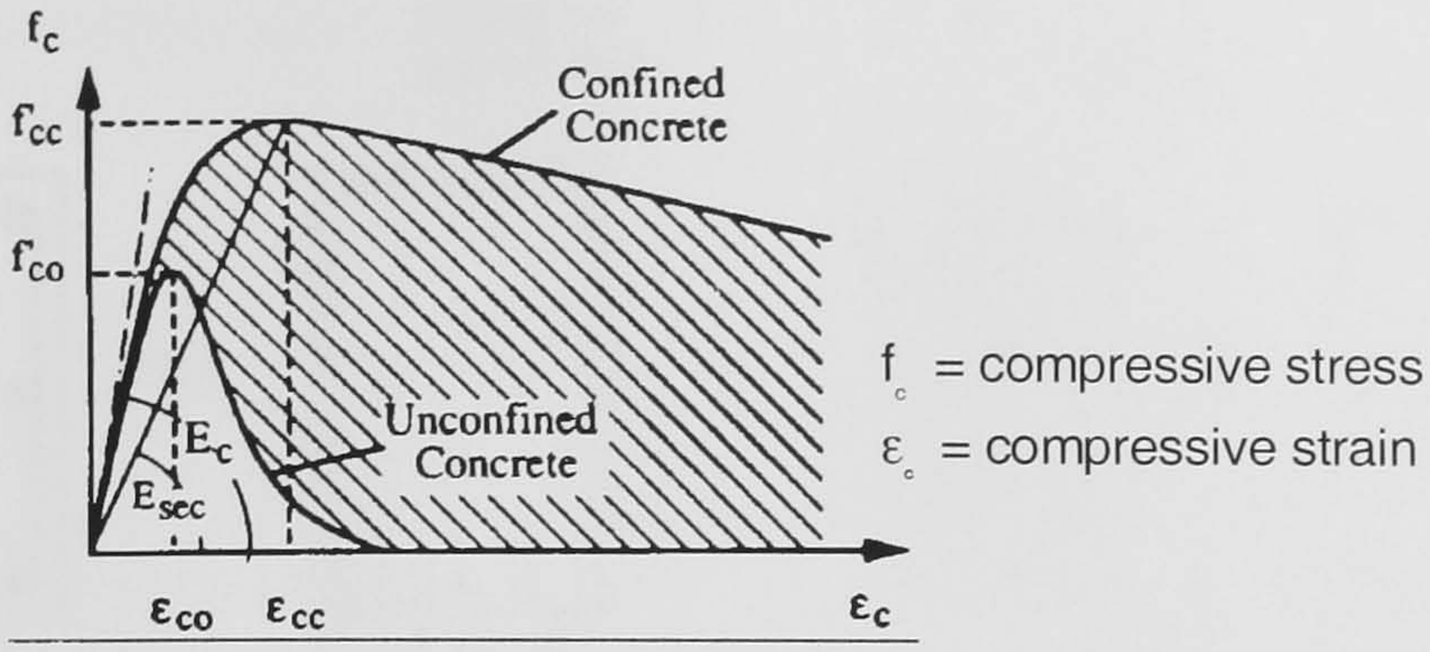


Fig. 6.9 Uniaxial stress-strain relationship with active confinement (Mander, et al., 1988)

6.2.2 Geometric non-linearity (Changes in stiffness due to deformations)

Three main modelling philosophies are available to represent geometric nonlinearity in ADAPTIC. The first makes uses of elastic quartic element formulation, whereby beam/column members are modelled using a single element. Elastic material formulations, however, cannot provide a good representation of the behaviour of structures, which can only be obtained if material plasticity is accounted for. Therefore, two other more elaborate alternatives are available in ADAPTIC.

The second alternative is the Plastic hinge formulation. In this formulation, rigid-perfectly plastic hinges are added to the elastic quartic formulation to provide a simple method for analysis involving material plasticity (Izzuddin, 1991).

The third alternative is an elasto-plastic cubic formulation, which represents accurately the spread of inelasticity in the highly nonlinear range (such as heavy cracking and/or crushing of concrete). This formulation is intended to represent the inelastic cyclic response of short lengths of reinforced concrete members. It is implemented through a layered approach where the response of element cross-sections is assembled from the response of individual layers for which the constitutive material relationships described above are employed. The discretisation of a typical reinforced concrete column cross-section into layers is depicted in Fig. 6.10.

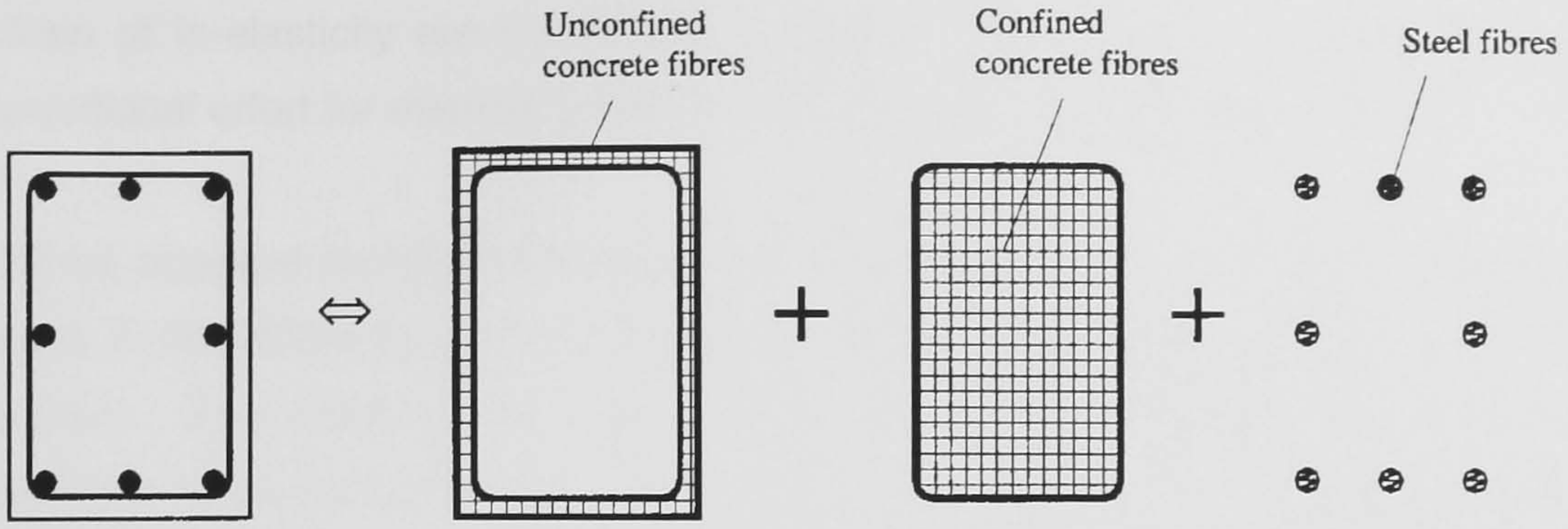


Fig. 6.10 Discretisation of RC sections (Pinho, 2000)

All the element formulations described above have been developed with both 2D and 3D versions for application in either plane or space analysis, respectively. Moreover, other elements are incorporated into the program enabling representation of a variety of structural features. These include different types of joint, mass and damping elements. To define the element cross-section, as required by the elasto-plastic cubic formulation, a large selection of pre-defined sections is also available in the program library. These extend from single-material solid sections to more complex reinforced concrete and composite sections such as the structural wall shown in Fig. 6.11. The sections are defined explicitly in the program thus allowing for independent modelling of confined core concrete and unconfined cover concrete (Pinho, 2000).

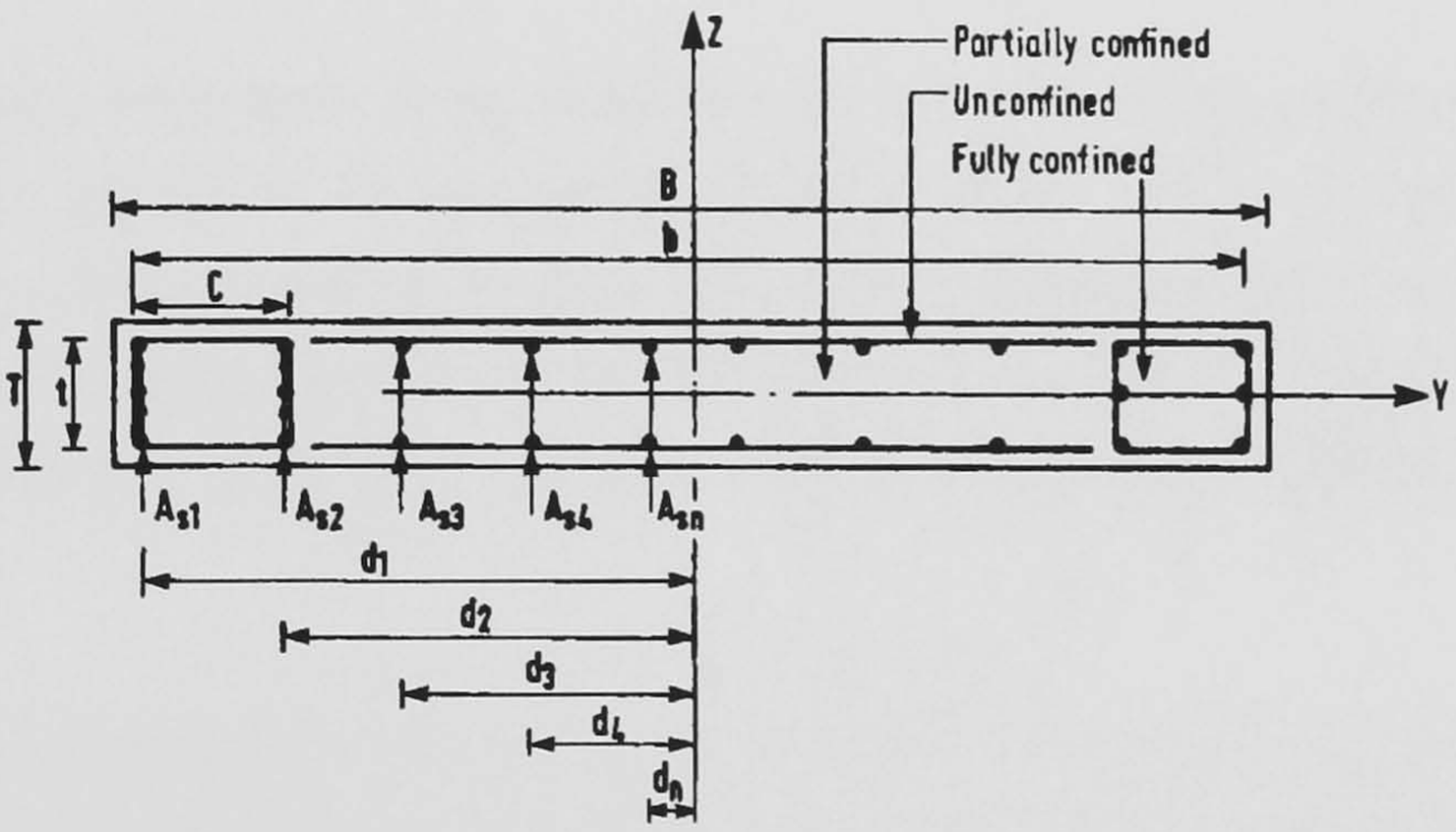


Fig. 6.11 Flexural wall section (Izzuddin and Elnashai, 1993)

6.2.3 Solution procedure

As described above, the inelastic cubic formulation is capable of representing the spread of inelasticity within the member cross section and along the member length. However, in a conventional approach for the nonlinear analysis of reinforced concrete frames, this would require a very fine mesh of cubic elements throughout the structure since the

locations of in-elasticity are not known a priori. This results in unnecessary wasted computational effort for members that remain elastic during load application.

Therefore, adaptive techniques based on the concept of automatic mesh refinement are included in ADAPTIC to optimize nonlinear analysis procedure in terms of computer resources. This involves the use of an elastic formulation capable of accurately modelling a whole member with one element and the automatic refinement of elastic elements into inelastic elements after detection of material inelasticity (Pinho, 2000).

Regarding the modelling of external loading, the program accepts static proportional/non-proportional loading (forces or displacements) as well as dynamic action. In the latter, independent asynchronous support motion is possible, using displacement, velocity or acceleration input. A solution is obtained following an iterative procedure consisting of either full or modified Newton-Raphson methodology. In addition, for the case of dynamic loading, direct integration of the equations of motion can be accomplished using the Hilber-Hughes-Taylor numerical algorithm, with automatic time-step adjustment for optimum accuracy and efficiency (Pinho, 2000).

6.2.4 Post-processing of results

Upon successful completion of an ADAPTIC run, an output file is produced containing the numerical results at all requested load/time steps. This includes the nodal displacements, member internal forces, and section stresses at each time-step. Results obtained from the output file can be used to create an extensive collection of plots and tables to illustrate the variation of a number of structural response parameters during the analysis.

A more convenient approach is to use the ADAPTIC post-processing application that enables the user to see the results on screen. Two post-processing options can be accessed, Line Graph for plotting X-Y graphs, and Deflected Shapes for plotting the deflected shapes of the structure.

6.3 Characteristics of the structural models

The structural models developed for the Author's studies included as many details regarding the material and structural characteristics as the program's capabilities and

the site data allowed. A high level of modelling can be used to compensate for the lack of knowledge of the dynamic characteristics of a structure - more complex analyses gave better results. The structural analyses showed that both the structural inelasticity and the structural modelling have a significant influence on the overall structural response, and on the forces at the building base.

The frames analysed included three-dimensional elements and inelastic material in all the different types of elements in the structure (i.e. columns, beams, masonry and concrete walls, among others). Elastic eigenvalue analyses were also carried out to determine the model elastic fundamental periods.

The coupling of the building base with the boundary condition was a fundamental concern in the analyses. The main aspect was the definition of which input motions and which motion components to specify at the supports to obtain the closest response to the real foundation movement. Two main conditions were evaluated: (i) only horizontal components as input motions (fixed base), or (ii) horizontal and vertical motions in order to include the flexibility of the soil into the models.

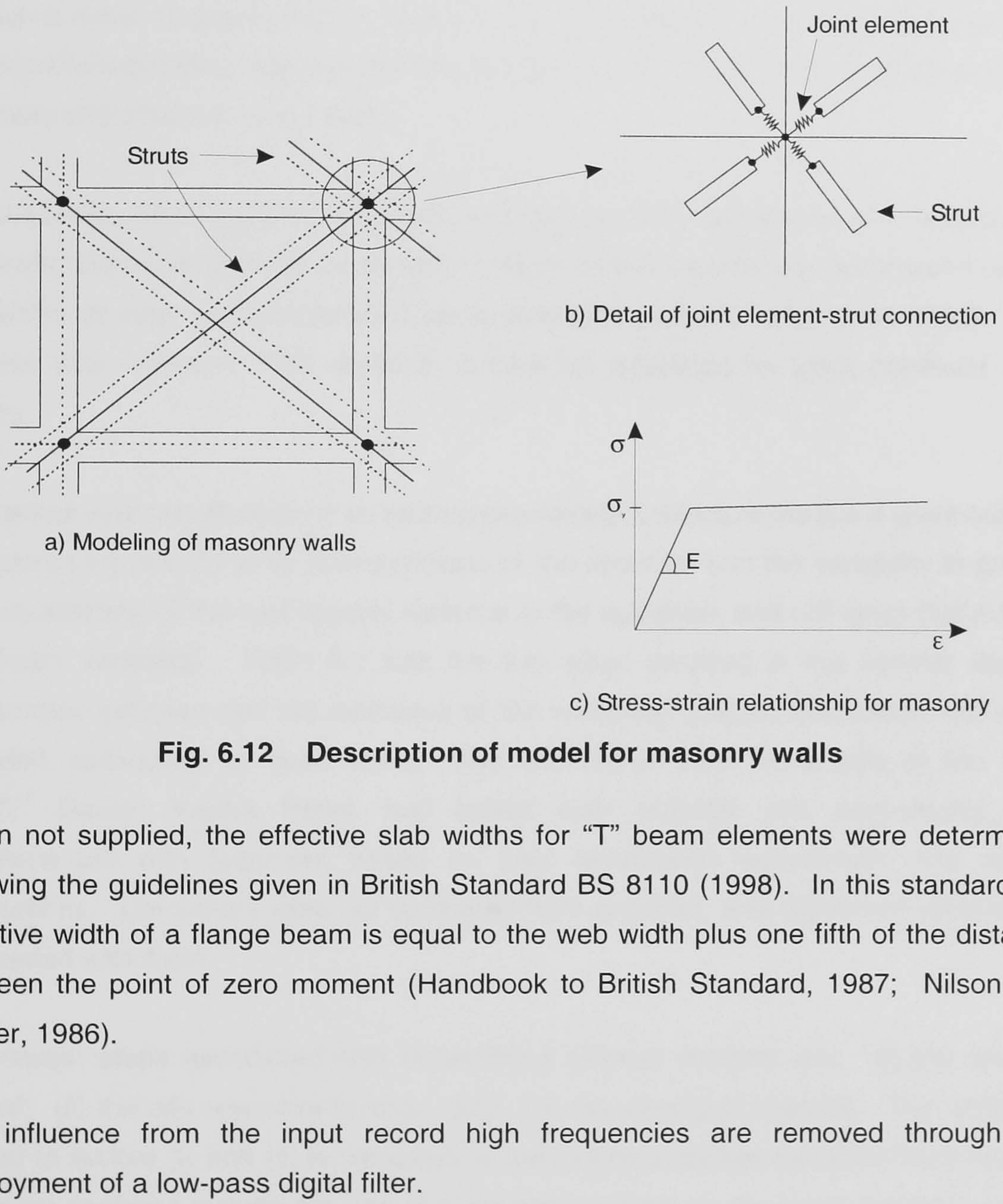
After several trials, it was established that the best approximation was obtained by making use of all the available records and all of their components of motion; both parallel to the frame and the vertical components. For the horizontal direction only one common motion is used for all the supports because the basement stiffness along its axis makes the horizontal acceleration components very similar.

In the structure models all connections are assumed to be rigid and to be fully fixed for all the out of plane degrees of freedom. Vertical initial loads are applied at nodes whilst inertial masses are placed at the beam-column joints. Hysteretic damping is included in the material properties, and equivalent viscous Rayleigh damping is introduced through discrete dashpot elements, the latter placed at each column and beam element. The Rayleigh damping aims to represent the small fraction of damping that might be introduced by sources other than the inelastic deformations.

As mentioned earlier, a uniaxial constant confinement model was used to represent concrete. As for the reinforcement bars, the bilinear elastoplastic constitutive relationship with kinematic strain hardening was adopted.

All member sections are represented explicitly. Columns, beams and concrete walls are modeled using a cubic elasto-plastic 3D-beam column element. The cross sections are

represented with reinforced concrete column, reinforced concrete "T" beam and flexural wall sections, respectively. Since detailed inelasticity study is not required, the column and beam elements are discretized using one and two elements per member, respectively. Masonry infill walls are introduced as a pair of diagonal idealised struts (Fig. 6.12a). The struts are modelled using Rectangular Solid sections with masonry properties and equivalent width of 25% of the strut length (Tomazevic, 1999). Joint elements are used to unite the struts to the concrete frames at both strut extremes (Fig. 6.12b). The joint elements are not able to take load at tension and under compression show the behaviour observed in Fig. 6.12c.



a) Modeling of masonry walls

b) Detail of joint element-strut connection

c) Stress-strain relationship for masonry

Fig. 6.12 Description of model for masonry walls

When not supplied, the effective slab widths for "T" beam elements were determined following the guidelines given in British Standard BS 8110 (1998). In this standard the effective width of a flange beam is equal to the web width plus one fifth of the distance between the point of zero moment (Handbook to British Standard, 1987; Nilson and Winter, 1986).

Any influence from the input record high frequencies are removed through the employment of a low-pass digital filter.

The study of the structural response of a given structure under a given earthquake or static load must be determined based on the structure geometry and material properties, along with certain simplifying modelling assumptions. Assumptions regarding the

analytical model, current state of the structure, effect of time on material properties, magnitude and distribution of floor loads, all add to uncertainty of the predicted response. This uncertainty is further compounded in reinforced concrete buildings where an accurate estimate of the extent and distribution of flexural and shear cracks is hard to make on a rational basis. Furthermore, the stiffness of the building changes with the amplitude of the imposed ground motion and a linear elastic analysis is unlikely to be strictly valid. Thus, it is common practice in dynamic analysis to vary some of the key assumptions on mass distribution and stiffness in a parametric fashion until the most plausible results are obtained. The validity of such parametric studies is ascertained through a direct comparison of the results of the analysis with any recorded or identified building characteristics, such as the vibration frequencies, deflection mode shapes, and interstory drift (Durrani, et al. 1994).

Consequently, when trying to reproduce the response of case histories it is necessary to "calibrate" the model through parametric changes in the material and structural member properties, or even the elimination of some structural elements (Meli, et al. 1998). This process was applied in this research, as will be described for each particular case history.

The design and construction of an earthquake-resistant structure involve a great number of factors (e.g. the dynamic characteristics of the structure and the variability in ground motion, intensity of the earthquake, distance to the epicenter, and soil type) that include significant variability. Table 6.1 lists the key steps involved in the seismic design-construction process and the estimates of the variability typically associated with each provided, calculated, or used value. The variabilities were developed by the 1994 BSSC[77] Design Values Panel, and reflect both scientific and engineering data supplemented with judgment based on past earthquake experiences and design applications. The values were not computed from statistics, and significant variability is associated with them.

The design steps associated with determining seismic demand are: (i) the seismic hazard; (ii) the site response factors; and (iii) the structural analysis. The variability related to factors (i) and (ii) is cancelled in the Author's studies because the proposed structural analyses include the use of a recorded motion as the input excitation at the base of the structural models.

---

[77] Building Seismic Safety Council of the USA.

Factor (iii) involves the prediction of the structure seismic response, which is affected by all the factors in Table 6.1. The development of an uncertainty factor for the Author's structural analyses is out of the scope of this thesis, as indicated by discussions with colleague researches in the engineering seismology section at IC. The difficulty of developing this uncertainty factor is indicated in FEMA (1995), which pointed out that "although the study of their combined effects is desirable, a specific value or percentage is difficult to determine". Ang and Newmark (1977; cited by FEMA, 1995) performed simplified studies that suggested that the total variability for the prediction of structural response could be from 0 to 60%. It is considered that the calibration of the Author's structural models against measured responses reduces such uncertainty to no more than 50%.

Table 6.1 Variability in main analysis and design input parameters during a structural seismic study (FEMA, 1995)

Design Stage	Parameters	Approximate Variability
Seismic Hazard	Source zones Recurrence rates Maximum magnitudes Ground-motion attenuation	± 100%
Site Response Factors	Soil/rock impedance Soil depths Soil properties Strain levels	± 40%
Structural Analysis	Material properties Damping Elastic moduli Weights Modelling of structure Modelling of foundation Combination of modal responses Combination of directions R factors/ductility	0 - 20% 0 - 50% 0 - 50% ± 15% ± 15% 0 – 50% 0 – 50% 0 – 50% 0 – 50%
Structural design	Seismic hazard exposure group Selection of seismic resistance system Redundancy Story drift determination Detailing requirements P-delta effects Load combinations Material strength properties	±40%
Quality assurance and control procedures	Application of the procedures Review of the calculations and plans Material tests	±100%
Construction Practices	Use of proper materials Proper placement and erection of materials and components Inspection	± 25%

The design steps associated with seismic capacity are structural design data, quality assurance and control procedures, and construction practices.

6.4 Procedure to upgrade records to 1985 Michoacan earthquake characteristics

6.4.1 Description of the procedure

As mentioned above, the importance of analyzing the building response under the 1985 earthquake conditions relies upon the fact that this event produced a widespread failure on friction piles founded buildings. The forces assessed as acting during the 19 September 1985 Michoacan event are considered as landmark. In the analysis presented in the following chapters the post 1985 basement records will be upgraded to the conditions of the Michoacan event.

The reference accelerograms for the Michoacan event are those obtained at the SCT site – which is 3.5 km away from the location of the case histories buildings. The SCT records were the only records obtained in the region that concentrated most of the earthquake damaged buildings.

The study of the site response in MC shows extreme sensibility to small changes in soil shear wave velocity, clay stratum thickness, and earthquake characteristics[78]. This section presents the proposed procedure to obtain the best possible estimation when upgrading an earthquake record to match Michoacan earthquake characteristics. The very clear fundamental frequency of 2 seconds developed in most of the MC's Lake zone reduces some uncertainties.

Consider the cross section of the MC Lake zone shown in Fig. 6.13. The figure indicates two sites in the clay zone and one further site at a rock outcrop, each with a key indication of record availability. Let us then consider how to scale the acceleration records obtained in a magnitude 7.5 event at the JAL building site in 1995 to the accelerations developed at the same site in 1985.

---

[78] Earthquake characteristics include focal mechanism, directivity, path, and depth of energy release.

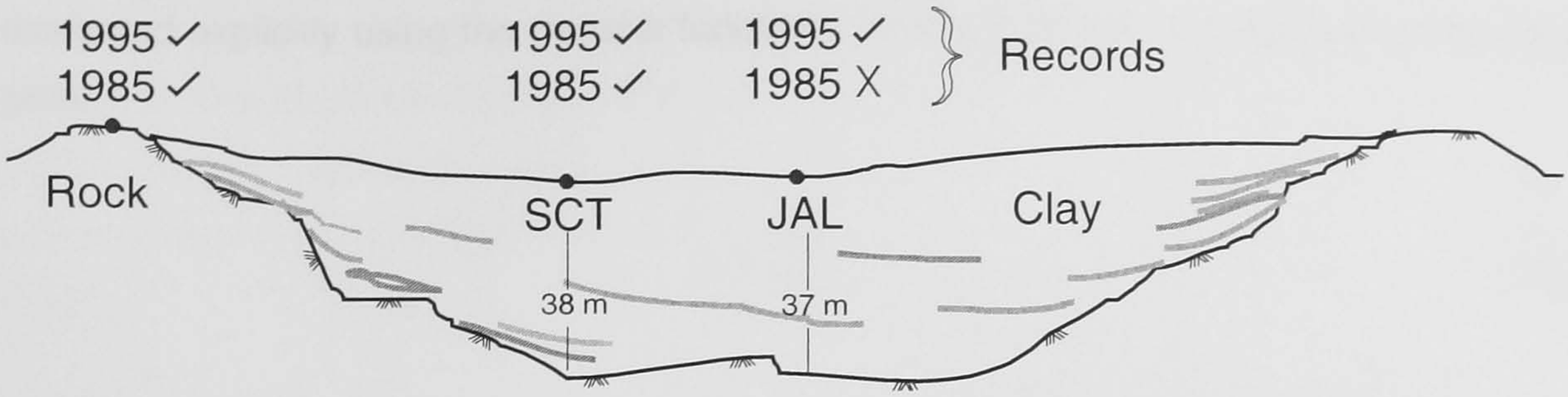


Fig. 6.13 Analysis of record upgrading to 1985 conditions

Consider the transfer functions A1 to A4 which represent the relationships between records obtained in the 1995 Copala and 1985 Michoacan earthquakes at the three mentioned locations:

$$A1 = \frac{95SCT}{95Rock}, \qquad A2 = \frac{95JAL}{95Rock}$$

$$A3 = \frac{85SCT}{85Rock}, \qquad A4 = \frac{85JAL}{85Rock} \tag{6.1}$$

These ratios can be evaluated using a range of variables, such as peak acceleration, spectral accelerations, Aria's intensities, etc….

The global effects of the clay layers on the ground accelerations could be different between the 1985 and 1995 events due to different non-linear response produced by different amplitude of rock motions. Any difference between 1985 and 1995 may be quantified by a parameter ρ, and the following relationship can be considered:

$$\frac{A4}{A2} = \rho$$

$$85JAL = A2\ 85Rock\ \rho$$

$$85JAL = 95JAL\left(\frac{85Rock}{95Rock}\right)\rho \tag{6.2}$$

Setting ρ=1 means the clay layers modified the rock motion in the same way during the two events. Under this condition the 85JAL records can be obtained by multiplying the 95JAL record by the ratio between the 85 and 95 rock motions. According with this assumption, the 95JAL records obtained from this expression includes (although partially) the amplification characteristics at the JAL site. On the other hand, ρ[79] can be

[79] The differences in profile response related to different rock motion

evaluated explicitly using the transfer functions for the SCT site. Consider the following ratio:

$$\rho = \frac{A3}{A1} \tag{6.3}$$

Where ρ reflects the amplification of the motion at SCT taking into account the non-linear profile response and without the amplifying contribution from the input records. Consequently, by applying (6.3) in (6.2) the non-linear response of the profile is included, resulting in:

$$85JAL = 95JAL \left(\frac{85SCT}{95SCT} \right) \tag{6.4}$$

terming 85SCT/95SCT ratio as λ, we obtaining:

$$85JAL = 95JAL \cdot \lambda \tag{6.5}$$

The record for the 1985 event at JAL is equal to the 1995 JAL record multiplied by the ratio between the records at SCT for those dates (factor termed λ). Values of λ will be specified for each site under study in the following chapters. As mentioned above, λ can be evaluated for several record parameters.

6.4.2 Upgrading of 1995 Copala records to 1985 Michoacan earthquake characteristics

The calibration of the structural models is carried out using the 1995 Copala event which is the strongest earthquake recorded in each building. Then, the building 1995 Copala records will be upgraded using the ratios of the 1985 Michoacan and 1995 Copala SCT records.

a. 1985 Michoacan earthquake characteristics and comparison against 1995 Copala earthquake

The earthquake of 19 September 1985 ruptured a region known as the Michoacan seismic gap and was the second largest earthquake of the 20th century in Mexico (Singh and Suarez, 1986). The 8.1 Richter magnitude earthquake shocked MC – located 400 km to the east – at 7:19 a.m. and had a major 7.5 Richter magnitude after-shock the

following day. The main movement occurred in two actions spaced about 26 seconds (Cassaro and Martinez-Romero, 1986) and it contained at least 20 major damaging cycles with a dominant period of about two seconds. Table 6.2 compares the characteristics of the 1995 Copala and 1985 Michoacan earthquakes (data from SMIS, 1997).

Table 6.2 Characteristics of the Copala 1995 and Michoacan 1985 earthquakes

	1995 Copala	1985 Michoacan
Max. ground acceleration, g's	0.027	0.05 – 0.17
Period, sec.	1.5 – 3	1.5 – 5
Duration, sec.	160	180
Max. rock acceleration, g's	0.013 – 0.014	0.03 – 0.04
Epicentral location	16.81 Lat N; 98.65 Long W	18.14° Lat N, 102.71° Long W
Epicentral distance, km	298	400
Depth, km	22	15
Richter magnitude (Ms)	7.2	8.1

b. Amplification factor (λ)

The factor λ, as mentioned above, can be obtained using several record and earthquake characteristics, all having their justification but none including all the relevant factors involved in the problem. The choice of λ will be reviewed here using peak acceleration, maximum spectral accelerations from Fourier and Response spectra, and an intensity scale based on the Housner Intensity (but using the acceleration response spectra, instead of the velocity response spectra[80]; Newmark and Rosenblueth, 1971).

Table 6.3 shows the summary of the peak ground accelerations and maximum spectral accelerations for the 1985SCT and 1995SCT records, and the 1985SCT/1995SCT ratios. The table includes the average and running average for the response spectra ratio, and the modified intensities.

Table 6.3 Summary of JAL records amplification analysis

Variable	SCT 85 (B1)			SCT 95 (B2)			λ		
	Vert.	N90E	N00E	Vert.	N90E	N00E	Vert	N90E	N00E
Time-history	-35.8	161.6	93.8	13.4	32.2	26.4	2.7	5.0	3.5
Response spectra	122.1	931.1	568.0	71.1	152.3	152.1	1.7	6.1	3.7
R. S. Average							3.4	5.7	4.2
R. S. running average							3.6	6.0	4.1
Fourier spectra	1.0	7.1		0.4	1.5	1.3	2.5	4.7	
Intensity	179.2	1087.0	634.0	54.5	195.3	171.7	3.3	5.6	3.7

As expected, Table 6.3 shows scatter in the results depending on the variable used to

---

[80] The Housner intensity is defined as $S = \int_{0.1}^{2.5} V_\zeta dT$, where T is period and ζ damping.

define λ. However, the mean values of 2.9, 5.5 and 3.8 for the vertical, N90E and N00E components are considered as representative values.

6.5 Case histories

The seismic instrumentation of buildings in Mexico began in 1950 with the installation in the Torre Latinoamericana of displacement transducers and accelerographs (Zeevaert, 1960 and 1963). The analysis of the records obtained was used as reference for establishing the seismic coefficients proposed in the construction code of that time. Unfortunately, this did not result in the instrumentation of more buildings and when the 1985 earthquake struck no building in the country had active instruments (Muria, 1997). The widespread building damage produced by the 1985 earthquake in MC led to a wide program of building instrumentation.

In the Author's search for instrumented building information several research centres were consulted, among them Centre of Scientific Research and Postgraduate Studies of Ensenada (CICESE), National Centre for Disaster Prevention (CENAPRED), Engineering Institute (II) UNAM and Federal Commission for Electricity (CFE). Nowadays there are 12 instrumented buildings in MC, 3 of which are on friction pile foundations (Table 6.4). The locations of these instrumented buildings, and of others with different types of foundation are shown in Fig. 6.14.

Table 6.4 Database of instrumented buildings on friction piles

Name	No. of histories	Earthquake settlements	Source of information
JAL	14	Settlements in 1994-95	II-Structures
PC	17	No settlements	II-Instrumentation
PCC	6	Settlements 1985	CICESE

The institutions responsible for the buildings kindly provided the Author with detailed building structural and foundation characteristics, geotechnical site information, and information related to the buildings' seismic behaviours before, during and after earthquakes.

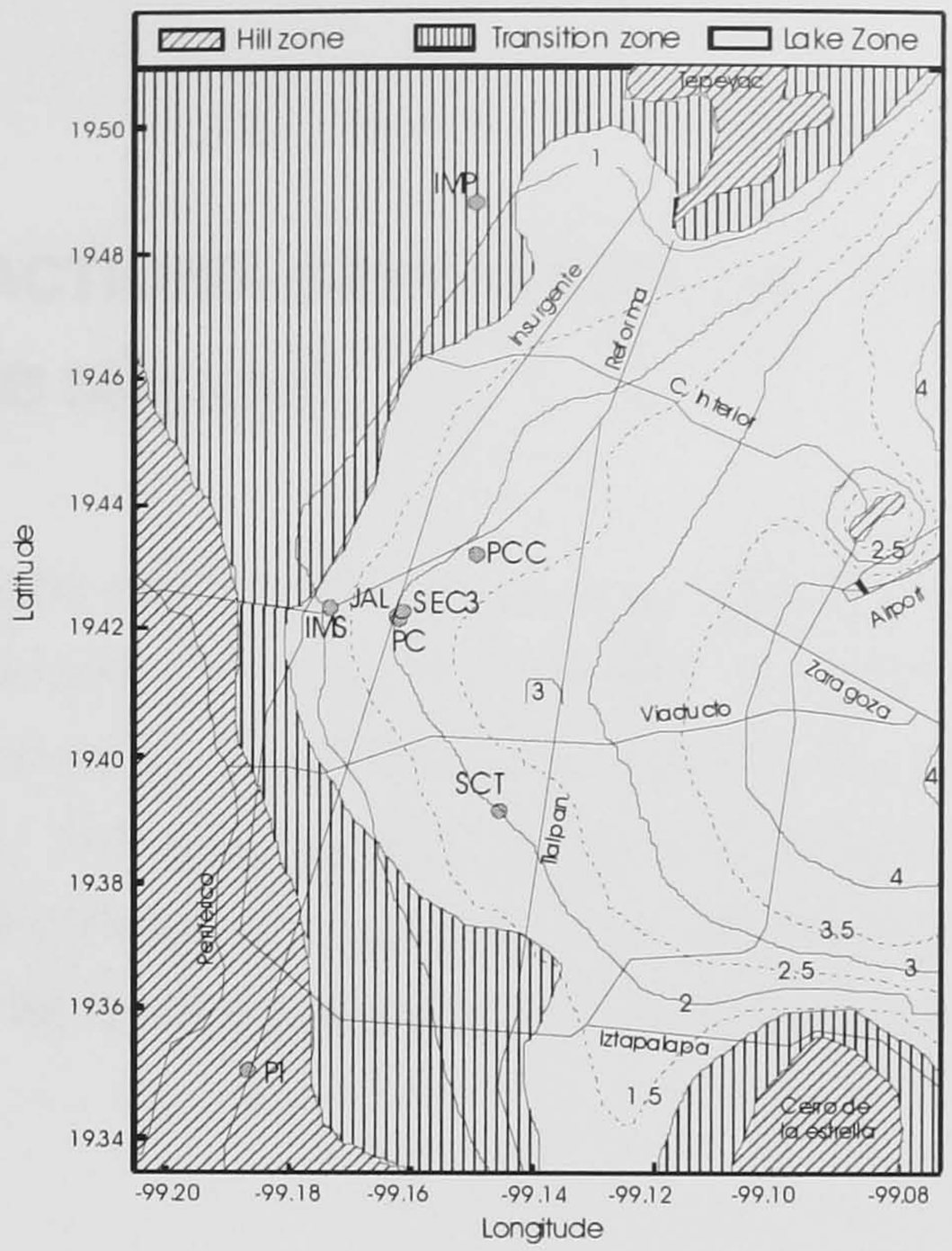


Fig. 6.14 Location of the studied buildings in a iso-period plan (After Muria, 1997)

Eigenvalue and dynamic analyses were carried out. For each time-history analysis, the Fourier spectrum of the response of the building was computed and the inelastic period of vibration of the structure identified. The time histories of the reactions at every specified support and its Fourier spectra were computed as well. Additionally, the computed and recorded acceleration time histories at the roof level, and the transfer functions between the roofs and the basements were compared to asses and improve the performance of the numerical models in reproducing the observed response of the building.

A more detailed comparison between the measured and computed response was also carried out through the evaluation of drifts (relative displacements) between the storeys where the instruments are placed.

The application of the methodology of analysis described in this chapter to the three case histories is fully presented in the following chapters.

CHAPTER 7

THE BASE REACTIONS DEVELOPED ON THE JAL BUILDING DURING SEISMIC SHAKING

This chapter presents the Author's own seismic analyses of a frame of the JAL building. The analyses were performed with the code ADAPTIC in such a way that the dynamic base reactions could be isolated and considered as inputs to a foundation loading study (Chapters 10 and 11). The analyses were carried out using structural information and accelerometer records provided by Dr. David Muria Vila and Mr. Luis Fuentes from the Structures Division of the Engineering Institute of the National Autonomous University of Mexico (UNAM).

7.1 A general description of the JAL Building

The JAL building consists of a 14-storey tower united to a 3-storey lower section through the basement. It is a reinforced concrete structure with a regular shape, both in plan and elevation (Fig. 7.1). It was built in 1970 and currently is used as offices except for the first three stories that are used as parking.

Extensive studies on the building's behaviour under static and seismic loads have been presented by Meli, et al. (1998), Muria and Del Toro (1998), Gamboa and Muria (1996), and Paolucci (1993).

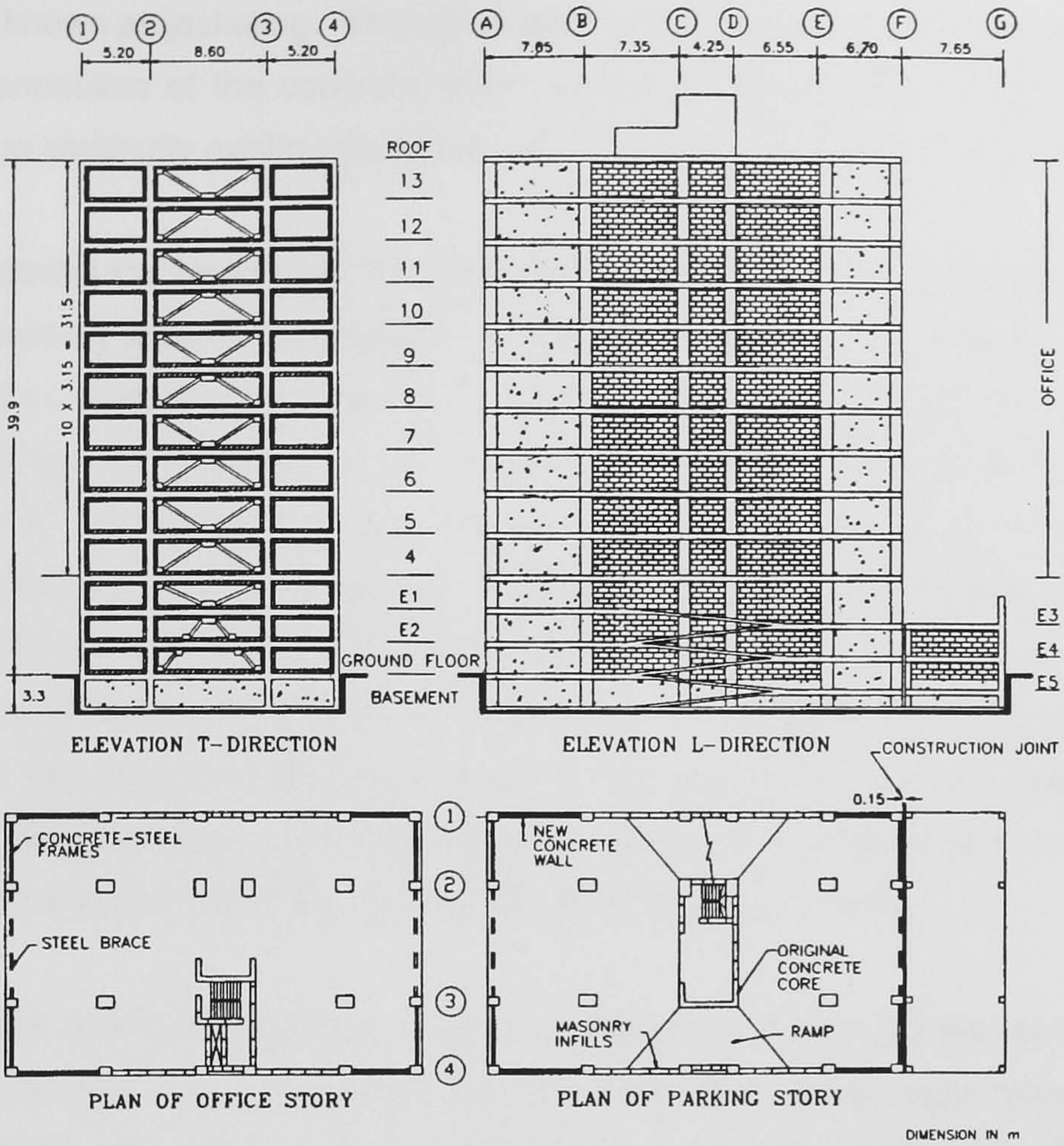


Fig. 7.1 Elevation and plan views of the JAL building (Muria and Del Toro, 1998)

7.2 Structural configuration and material characteristics

Originally, the structure consisted of waffle slabs[81] supported on relatively slender rectangular columns, masonry infill in the end frames of the longitudinal direction, and a core of concrete shear walls around the shaft for staircases and elevator (Fig. 7.1) (Muria and Del Toro, 1998). However, since 1985 the building has undergone two major reinforcements due to structural and non-structural damage sustained under seismic events.

First, for the September 19 1985 Michoacan earthquake, the damage consisted of shear cracking in many columns and in most of the masonry infill walls, mainly above the seventh story. Widespread cracking of the ribs of the waffle slab was also evident and no appreciable settlement of the foundation was observed. As a result of this damage, additional reinforced concrete shear walls were placed in the external longitudinal frames (Fig. 7.1), and the section of some internal columns was increased using a

---

[81] 450 mm thick flat plate.

procedure known as jacketing. Through a later review of the structure it was determined that the connection of the concrete shear walls was only effective through the upper slab, with no continuity existing along the bottom slab and the sides of the wall.

Secondly, during the December 10, 1994 earthquake the damage consisted of cracking in all the masonry walls of the structure and in the columns of the transversal axes E and F. In addition, several cracks appeared in the first two parking levels due to settlement of the structure in the area of the attached section (no information regarding the magnitude of the settlements was found). For the September 14, 1995 Copala earthquake the non-structural damage increased, some suspended ceiling elements fell down and the settlements and the widths of cracks in the columns increased. As a result of this additional damage further structural rehabilitation was started at the end of 1995. On this occasion structural braces were attached to exterior frames in the transverse direction (Fig. 7.1), and the larger cracks in the walls and columns were repaired with the injection of epoxy resin (Muria and Del Toro, 1998).

Regarding the structural materials, the actual properties of the concrete were assessed using core samples, rebound hammer and ultrasonic tests. These tests showed that the concrete quality was rather uniform throughout the structure. Below the 7th storey the average compressive strength and the Young's modulus of elasticity were 28 MPa and 19 000 MPa, respectively. Above the 7th storey, the compressive strength was around 25 MPa and the Young's modulus of elasticity was typically 18 000 MPa (Meli, et al., 1998).

No information on the properties of the reinforcing steel bars was found. The Author's analyses were carried out assuming a yield strength of 420 MPa and a Young's modulus of 195 800 MPa – which are considered standard values in Mexico.

7.3 Foundation configuration

The foundation of the JAL building is typical of the Mexico City (MC) clay zone. It consists of a reinforced concrete box resting (at 3.3 m. depth) on 54 friction piles that overlapped 10 end-bearing piles. As shown in Fig. 7.2, the friction piles are driven into the clay soil without reaching the firm layer and are fixed to the foundation slab. The end bearing piles are driven down to the firm layer, but are separated from the foundation. The weight of the building is carried by the friction piles, and partially transferred through shear to the end-bearing piles, allowing the building to sink following

the regional subsidence.

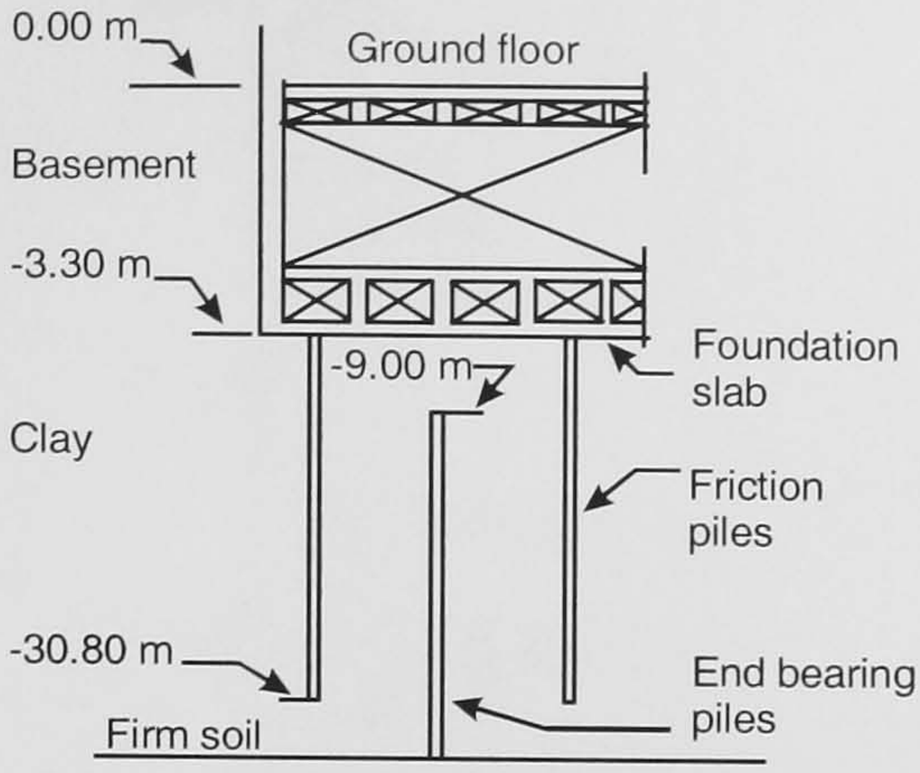


Fig. 7.2 JAL Building pile foundation solution

The friction piles are 28 m long, 60 cm side length triangular cross section piles, whereas the end-bearing piles are 28 m long, 40 cm side rectangular cross section piles. The foundation plan is shown in Fig. 7.3.

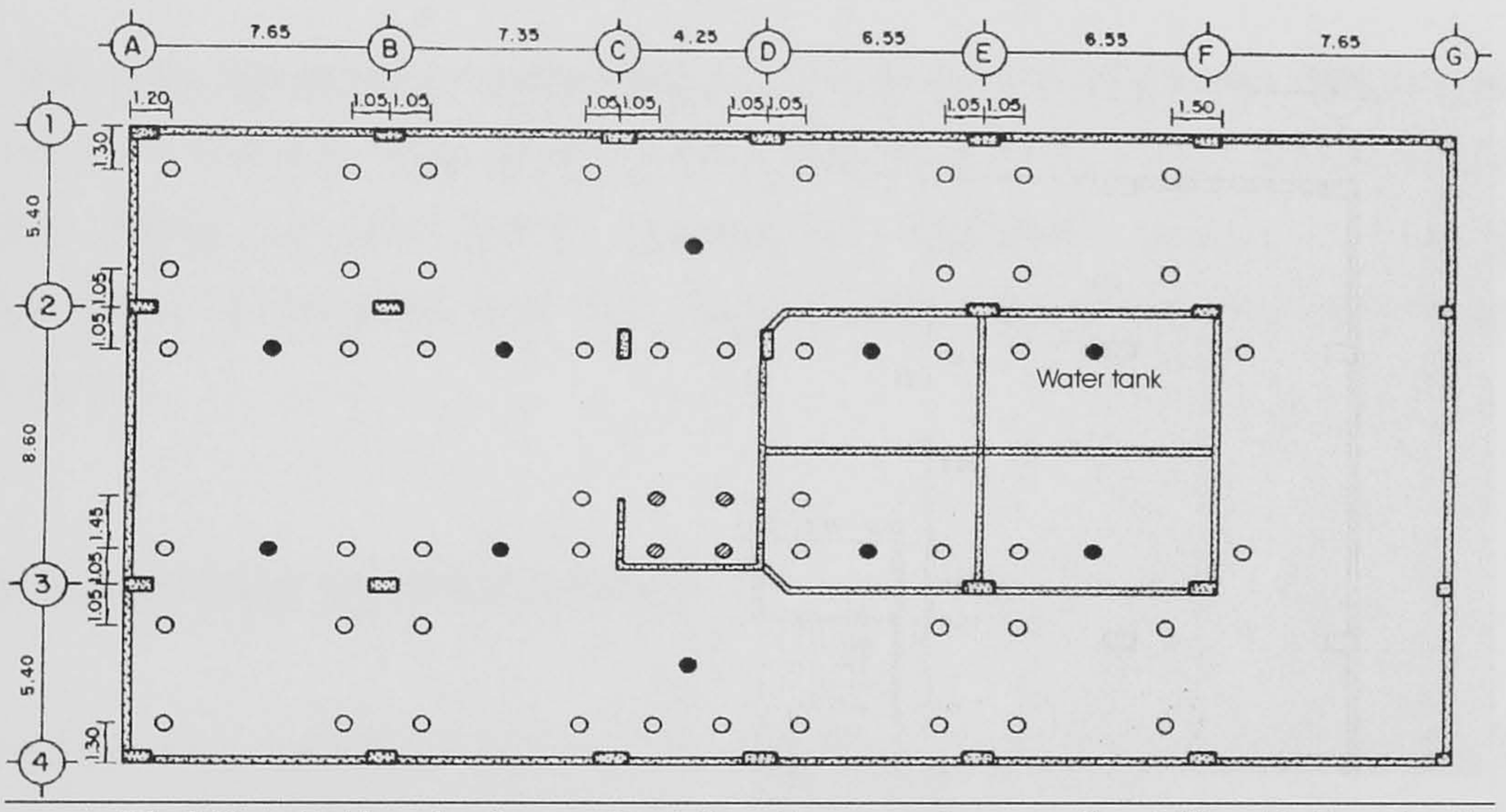


Fig. 7.3 Plan of JAL Building foundation (Provided by Dr. D. Muria)

The soil profile at the building site is typical of the lakebed area of MC. Beneath a superficial crust of about 5 m, the upper soft clay deposits extend to a depth of 29.5 m followed by a 3 m thick intermediate firm layer. The lower clay formation extends from 32.5 m to 38.5 m depth, followed by the so-called deep firm deposits. These strata and the shear wave velocity profile proven at the near by SCT site are shown in Fig. 7.4 (Meli, et al., 1998). Considering an average shear wave velocity of 68 m/s and a clay stratum thickness of 38 m, the fundamental frequency for the site is 0.45 Hz.

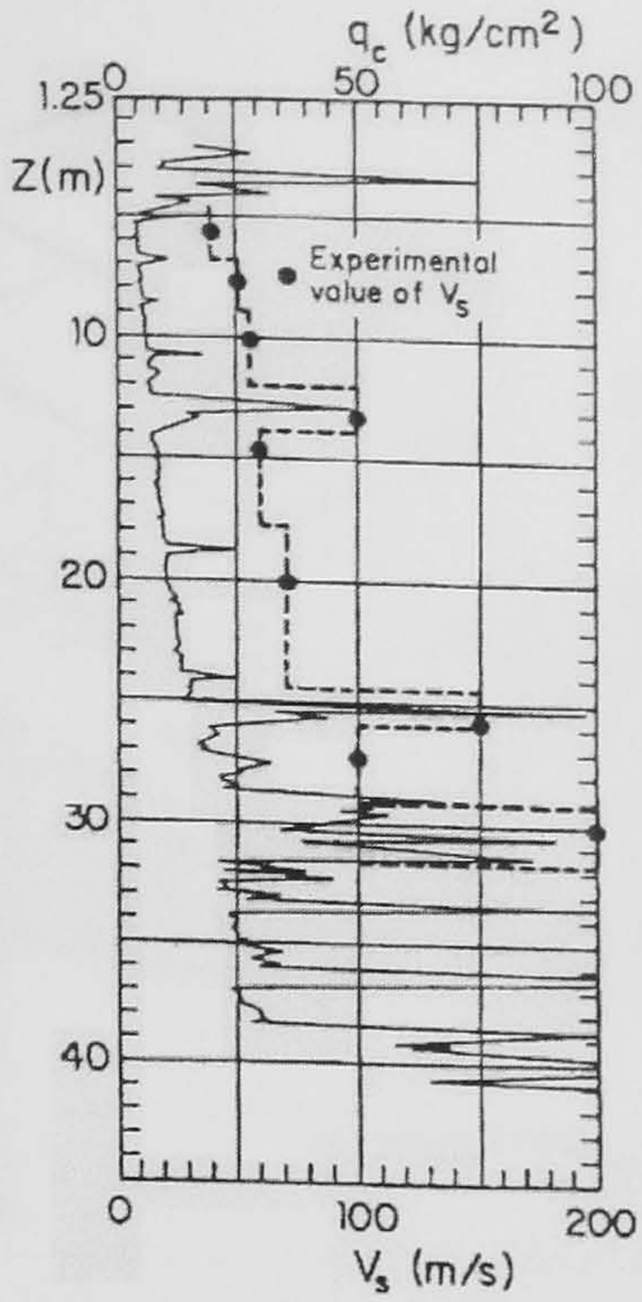


Fig. 7.4 Shear wave velocity (V_s) profile and cone penetration resistance (q_c) at SCT site (Meli, et al., 1998)

The friction pile capacity computed applying the Imperial College pile design method is 1835 kN (187.1 tons). The effect of the triangular cross section was allowed for by adopting Jaime, et al's (1991) geometrical correction factors. The general characteristics of the piles and the capacity computation process are reported in Appendix C.

7.4 Instrumentation and input motions

The seismic instrumentation for the JAL building was designed to provide a detailed description of the building's response to earthquakes. Consequently, a total of 14 triaxial accelerographs were allocated as follows (Fig. 7.5): two borehole instruments at 20 m and 45 m depth underneath the building; one instrument at a "free field" location 50 m away from the building; and eleven instruments at different levels of the structure, including 4 at the basement and 3 at the roof (Paolucci, 1993).

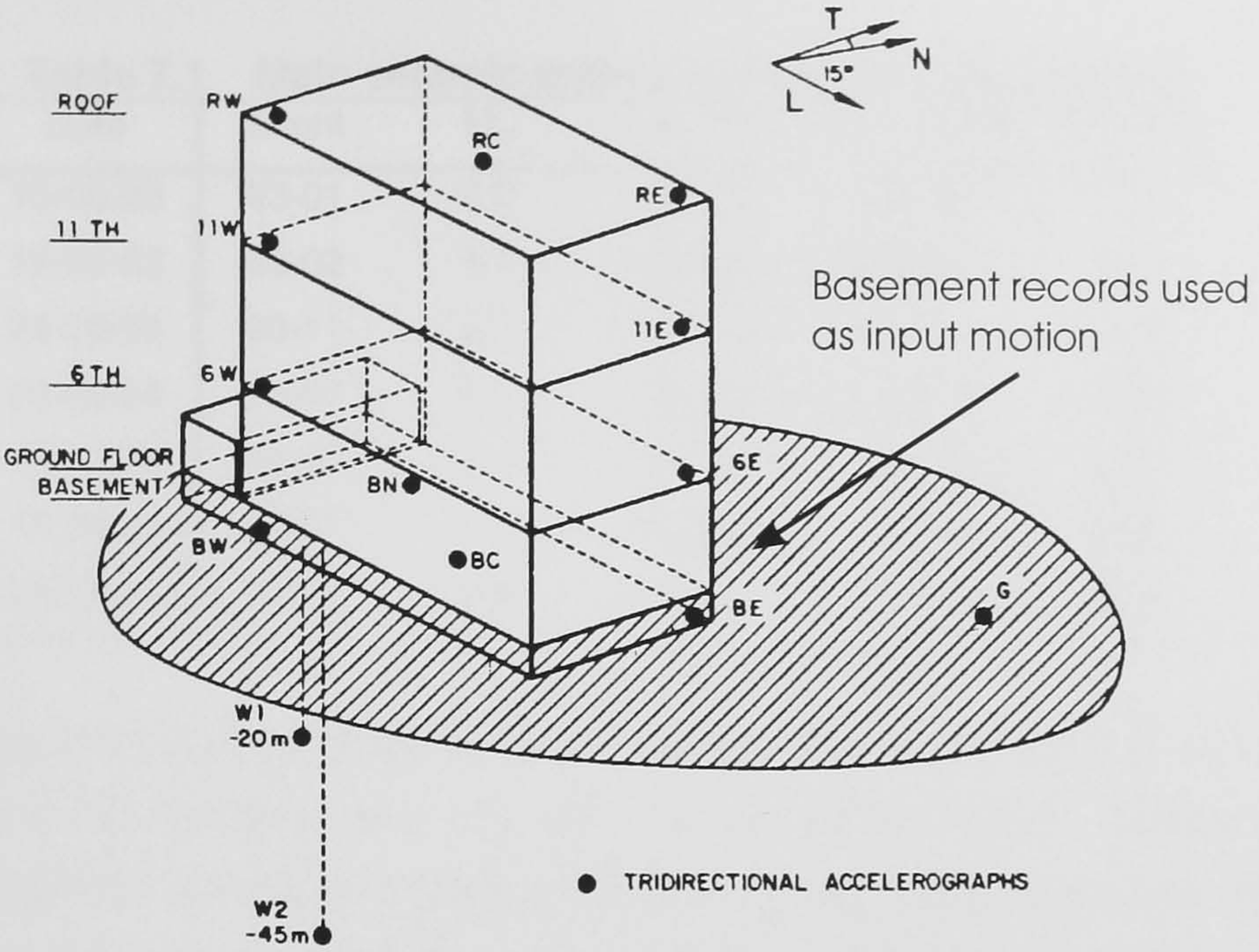


Fig. 7.5 Overview of the building instrumentation (Meli et al. 1998)

All instruments are tri-dimensional solid state Terra Technology DCA-333R digital accelerographs interconnected in a master-slave configuration to allow for a simultaneous trigger when the threshold of the master instruments is reached - all the instruments had a common time reference. Since 1997 the system has included a remote trigger based on a seismological station located half way between MC and the Guerrero Coast, allowing the recording of the events to initiate about 30 seconds before the arrival of the seismic waves at the building site (Meli, et al., 1998).

The operation of the array started in November 1992 under a project sponsored by the Commission of European Communities, involving the Engineering Institute UNAM, and the Technical University (Politecnico) of Milan, Italy (Paolucci, 1993). The instruments were first triggered on May 15, 1993 and since then several earthquakes have been recorded - Table 7.1 shows the characteristics of the considered seven more important earthquakes. (In the table EP is the epicentral distance, and the latitude and longitude are for the epicenter.)

The goal of the present study is to determine the pile forces under the 1985 earthquake conditions. The 95-1 “Copala” earthquake has produced more damage and bigger amplitudes of accelerations and displacements in the building than any other recorded event. The Copala records are 160 sec long which, with a frequency of acquisition of 100 Hz (Δt=0.01s), results in a file with 16000 values. Important to remark is that the Copala event was recorded before the second structural reinforcement.

Table 7.1 Main seismic events recorded at JAL building

Date	Event	M_w	Lat. (°N)	Long. (°O)	EP (km)
15-05-93	93-01	6.0	16.673	98.417	318
15-05-93	93-02	6.1	16.698	98.395	315
24-10-93	93-11	6.7	16.755	98.717	303
23-05-94	94-01	6.3	18.165	100.527	206
10-12-94	94-03	6.5	18.136	101.384	280
14-09-95	95-01	7.5	16.808	98.648	298
09-10-95	95-02	7.9	19.245	104.4188	532

Fig. 7.6 shows the recorded longitudinal components at the W2, W1, G, BC, 6W, 6O, 11W, 11E and RC locations (see Fig. 7.5) for the Copala event. Before using the records in ADAPTIC, they were filtered in the time domain using a low pass digital filter, with 0.2 Hz and 20 Hz as the pass and stop bands, respectively. Sensitivity studies were carried out to ensure that the choice of filtering parameters did not affect the time history records.

The input motions for the analysis are the Basement Center (BC), Basement East (BE) and Basement North (BN) in the vertical component, and the longitudinal BC for the horizontal component. These records show a very clear fundamental frequency of 0.5 Hz, except for the vertical component of the BC record which first fundamental frequency is 0.35 Hz and the second is 0.5 Hz.

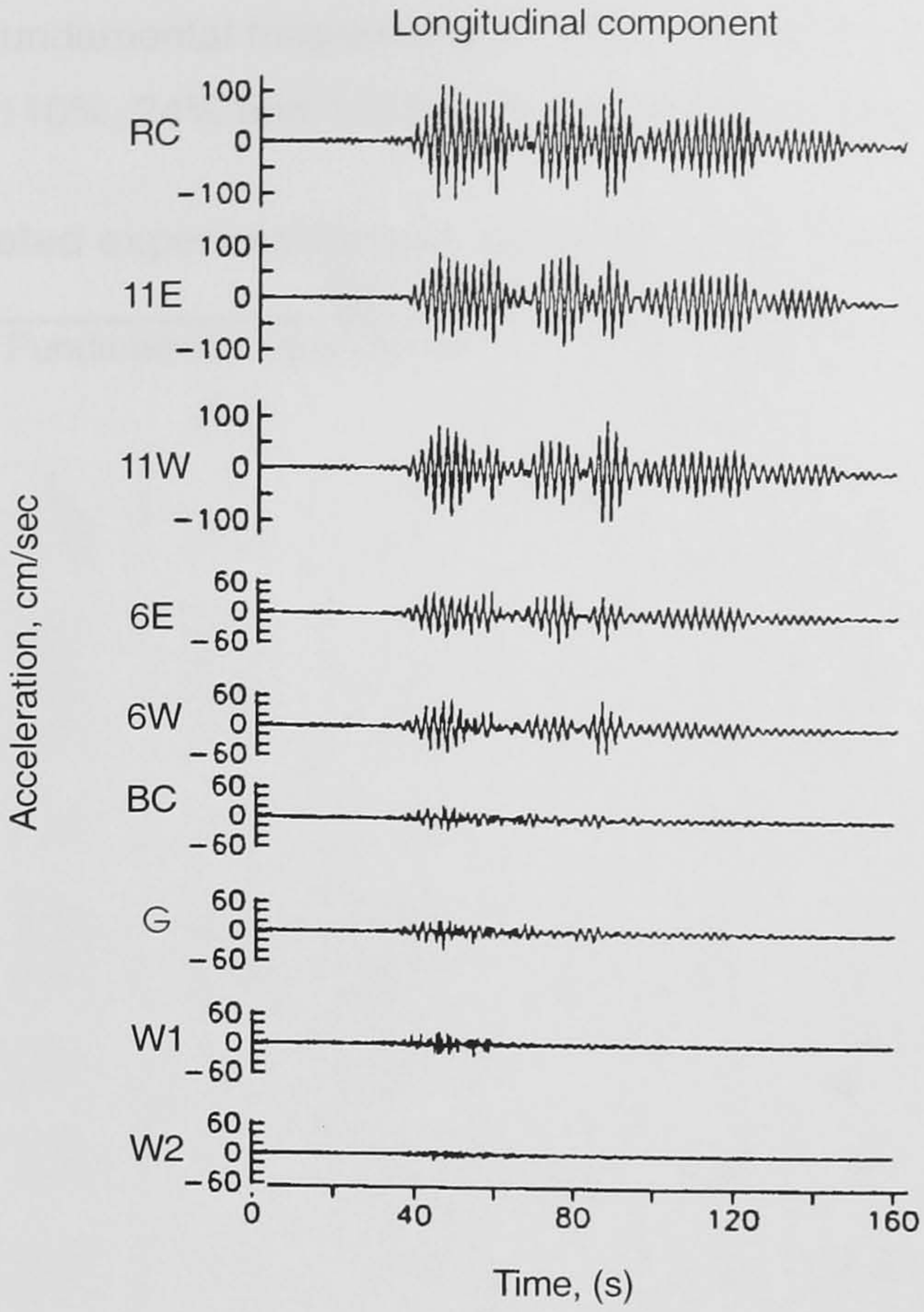


Fig. 7.6 Records from the 1995 Copala earthquake (Gamboa and Muria, 1996)

7.5 Behaviour of the building during earthquakes

Meli, et al. (1998) and Muria and Del Toro (1998) pointed out that the most important feature in the response of the JAL building is its nonlinear behaviour. According to them, this behaviour is characterised by a high sensitivity to the amplitude of the imposed ground motion and by structural stiffness degradation during earthquake loading. Since non-linear response is relevant for modelling the building response[82], a summary of its origin and effects follows.

Muria and Del Toro identified the stiffness degradation during earthquake events by carrying out spectral analyses of the building's recorded accelerations. Table 7.2 indicates that the reductions in building fundamental vibration frequencies between the 93-3 and 95-2 events were 24%, 31% and 8% in transversal (T), longitudinal (L) and torsion (R) directions, respectively. The same effect was found even for low and moderate intensity earthquakes, and was especially clear for the 94-3 and 95-1 events. The change in building stiffness was also observed after the 1995 rehabilitation had

---

[82] Similar nonlinear responses are observed for the PC and PCC buildings.

finished, when the fundamental frequencies for the T, L and R components for the 97-1 event increased by 110%, 24% and 146% with respect to the 95-2 event (Table 7.2).

Table 7.2 Estimated experimental parameters for JAL Building (After Muria and Del Toro, 1998)

Event	Date	Fundamental frequencies (Hz)			Max. Acc. (cm/s^2)			Max. Drift[83] ($x10^{-3}$)	
		L	T	R	Soil	L	T	L	T
AV	23-09-92	0.73	0.44	0.83		<0.1	<0.1		
93-3	15-05-93	0.65	0.37	0.50	4	10	11	0.21	0.46
93-4	15-05-93	0.61	0.35	0.51	11	27	24	0.61	0.97
93-11	24-10-93	0.57	0.35	0.50	13	56	35	1.42	1.32
AV	25-11-93	0.70	0.44	0.68		<0.1	<0.1		
94-1	23-05-94	0.55	0.37	0.51	7	19	19	0.44	0.45
94-3	10-12-94	0.42	0.29	0.43	17	124	49	3.45	2.40
AV	04-02-95	0.64	0.44	0.65		<0.1	<0.1		
95-1	14-09-95	0.45	0.28	0.43	37	130	116	3.76	4.71
AV	23-09-95	0.66	0.42	0.64		<0.1	<0.1		
95-2	09-10-95	0.45	0.28	0.46	12	72	32	2.56	1.68
96-1	15-07-96	0.48	0.32	0.46	9	35	22	0.92	0.77
97-1	11-01-97	0.56	0.59	1.13	16	54	55	1.08	1.13

The sensitivity of the seismic response of the structure to the amplitude of the imposed ground motion is evident in Table 7.2, where the natural frequencies of vibration derived from the seismic records are significantly smaller than those obtained from the ambient vibration (AV) tests.

Meli, et al. (1998) obtained further evidences of non-linear response through computing the temporal variation of natural frequencies of the building within a specific event. Meli, et al. found that after the strongest phase of motion the estimated natural frequency reduces up to 20% – 25% in either the L- or T- directions (Fig. 7.7). (Similar results are presented by Durrani, et al. (1994) for a 9-storey building in California USA that did not show structural damaged during shaking.)

The non-linear building behaviour described above could be attributed to several structural features and to soil-structure interaction effects; among the former are (Meli, et al., 1998; and Muria and Del Toro, 1998):

---

[83] Drift is the relative lateral displacement between two stories.

i) Discontinuities between the reinforced concrete walls added after the 1985 earthquake and the structural frames. Inspections of the building after the 94-3 and 95-1 earthquakes indicated that sliding occurred along three sides of the wall.

ii) Reduction in lateral stiffness of the building due to the level of damage in the masonry infill walls. These walls maintain a certain continuity with the structure through the renewed plaster, but a small shaking is enough to separate them from the structure.

iii) Cracking of the floor system, and the degradation effects on the structural and non-structural elements under several seismic motions.

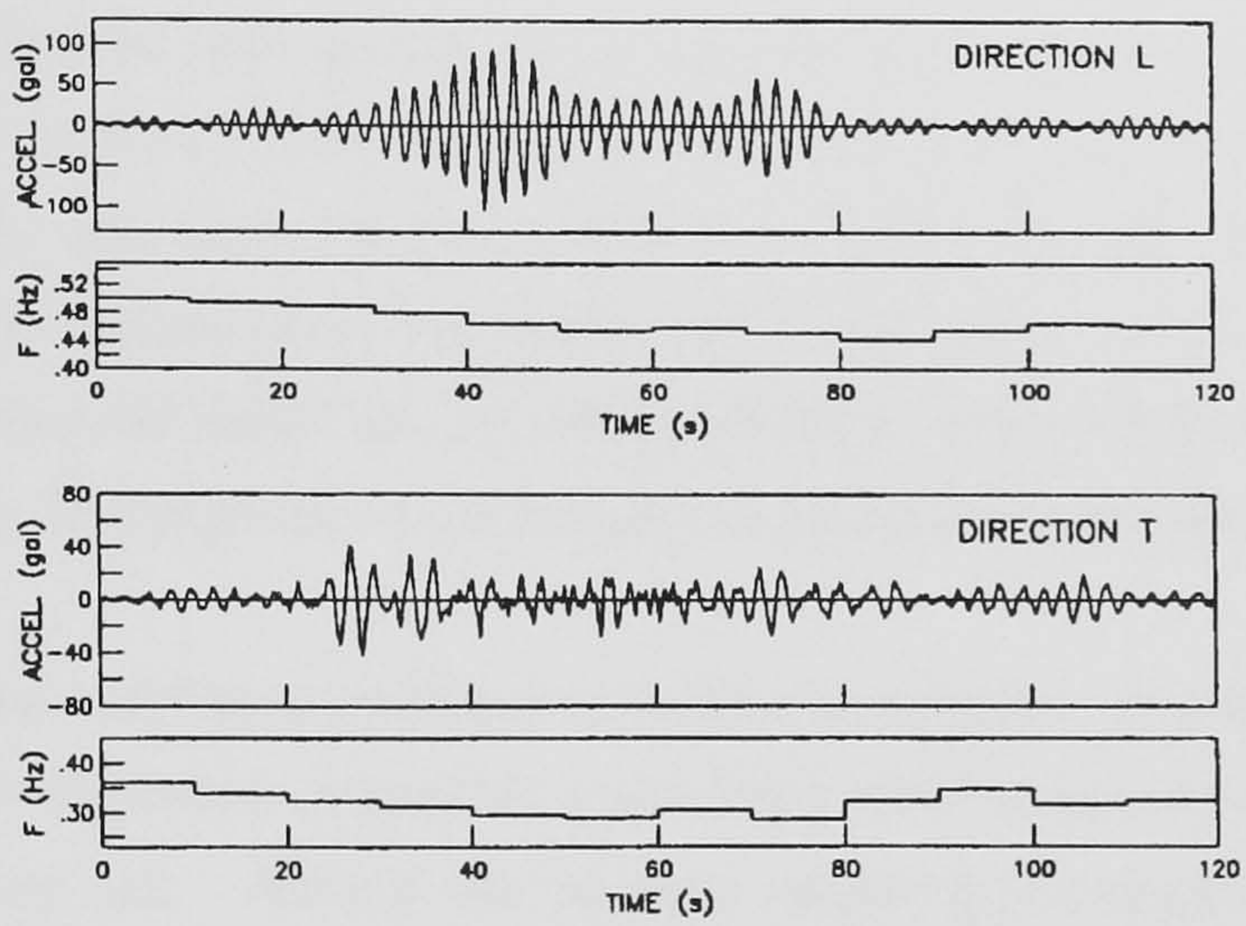


Fig. 7.7 Accelerogram at roof center for the 94-3 event, and the corresponding time evolution of the natural frequencies in the L and T directions (Meli, et al., 1998)

Muria and Del Toro (1998) suggest that Soil-Structure Interaction (SSI) does not contribute very significantly to the non-linear behaviour of the structure. They establish that due to the strong similarity between the motions recorded in the basement of the building and in the free field no significant discontinuities between the foundation-soil interface occur. Meli, et al., (1998) support the statement by establishing that due to the high flexibility of the building on both horizontal directions, the deformations due to SSI are not significant and only moderate inertial SSI effects take place. According to Meli, et al., the reductions of the fundamental frequencies of the building due to SSI vary from 10% for the transverse direction up to 25% for the longitudinal (stiffer) direction.

The dominant frequency of the site is very close to the fundamental frequencies of the T, L and R components of the building. As it is shown in Table 7.2, the flexible characteristics of the frame resulted in fundamental period of vibration (obtained from recorded motions) that falls near the resonance frequency.

7.6 Modelling

7.6.1 JAL building model description

The Author's approach to developing a structural model for the JAL building was set out in Section 6.3.

The bare longitudinal frame model of the JAL building consists of 189 nodes, and 230 tri-dimensional elements represented by 15 column and 18 beam sections. 5 flexural wall sections, 15 masonry infill walls and damping elements are used to develop alternative models. Mr. Luis Fuentes provided the effective slab widths. The vertical loads consist of the self-weight of the slabs, transverse beams, columns and infill walls and the quasi-permanent static load, as indicated in the 1987 MC building code (Garcia-Ranz, et al. 1988). The analyses were carried out for 155 seconds with 0.01 sec steps.

The response of the building to earthquake loading is complex. In order to reproduce its behaviour a model calibration procedure, exploring a wide number of modelling aspects, needed to be carry out. Among the aspects requiring investigation are the beam equivalent widths, the unusual contact condition of reinforced concrete wall, and the cracked structural and non-structural elements. However, in order to explore such conditions special structural elements would have to be developed, which falls outside of the scope of this thesis.

Nonetheless, Meli, et al. (1998) established that the behaviour of the wall elements controls the JAL building response and that analytical precision in modelling other members is beneficial but not essential. Consequently, the Author's calibration procedure targeted the location and properties of the existing wall elements, including the following configurations: bare frame (without walls), frame with masonry walls, and frame with reinforced concrete walls.

The non-linear dynamic analyses of the mentioned configurations are described in the following sections. Although several structural models were used to study various aspects of the seismic response of the building, in the following only the studies aimed at reproducing the observed structural response are presented. The results are shown concisely, and only the peak values of the most relevant parameters are given.

Nevertheless, qualitative comments regarding the structural assessment of each frame are made based on all the information collected.

7.6.2 Bare frame

In this section, a 3D model of an external longitudinal frame (axis No. 1) with reinforced concrete walls at the basement level - termed the "Bare" frame – is analysed (Fig. 7.8). All member dimensions and reinforcement characteristics are based on the known building information. Rayleigh damping elements were used to simulate extra sources of damping. This extra damping (e.g. that produced by friction during movement) usually accounts for 1% or 2% of the total damping experienced during a dynamic event.

Eigenvalue analyses were undertaken to provide a first insight into the response of the structure. They serve as a means of checking the modelling of the building and the validity of the inelastic time-history analyses. The computed elastic eigenvalue fundamental frequency was 0.24 Hz, which is a low frequency for a 14-storey RC building and would correspond to a very flexible structure.



Fig. 7.8 JAL Building, Bare frame configuration

The friction piles are located below the columns (nodes 1, 33, 67, 99, 143, and 175). The reactions obtained at those nodes are considered for the pile analysis in Chapter 10

and 11.

Using the Copala 95-1 event, the dynamic response of the structural model was evaluated comparing the recorded and predicted accelerations at roof level (Figs. 7.9 and 7.10). The acceleration time histories of Fig. 7.9 show that the model slightly under-predicts the acceleration amplitudes during the intervals of maximum acceleration and fails to reproduce the low acceleration amplitude intervals. This figure also shows differences in the acceleration periods that are confirmed by the Fourier spectra shown in Fig. 7.10. Indeed, while the recorded response shows a clear fundamental frequency of 0.5 Hz – which coincides with the site fundamental frequency - the predicted acceleration shows a softer response with a shorter fundamental frequency of 0.36 Hz - plus clear second and third mode frequencies. These indications of lack of stiffness in the model were further supported through the comparison of predicted and estimated roof-basement transfer functions.

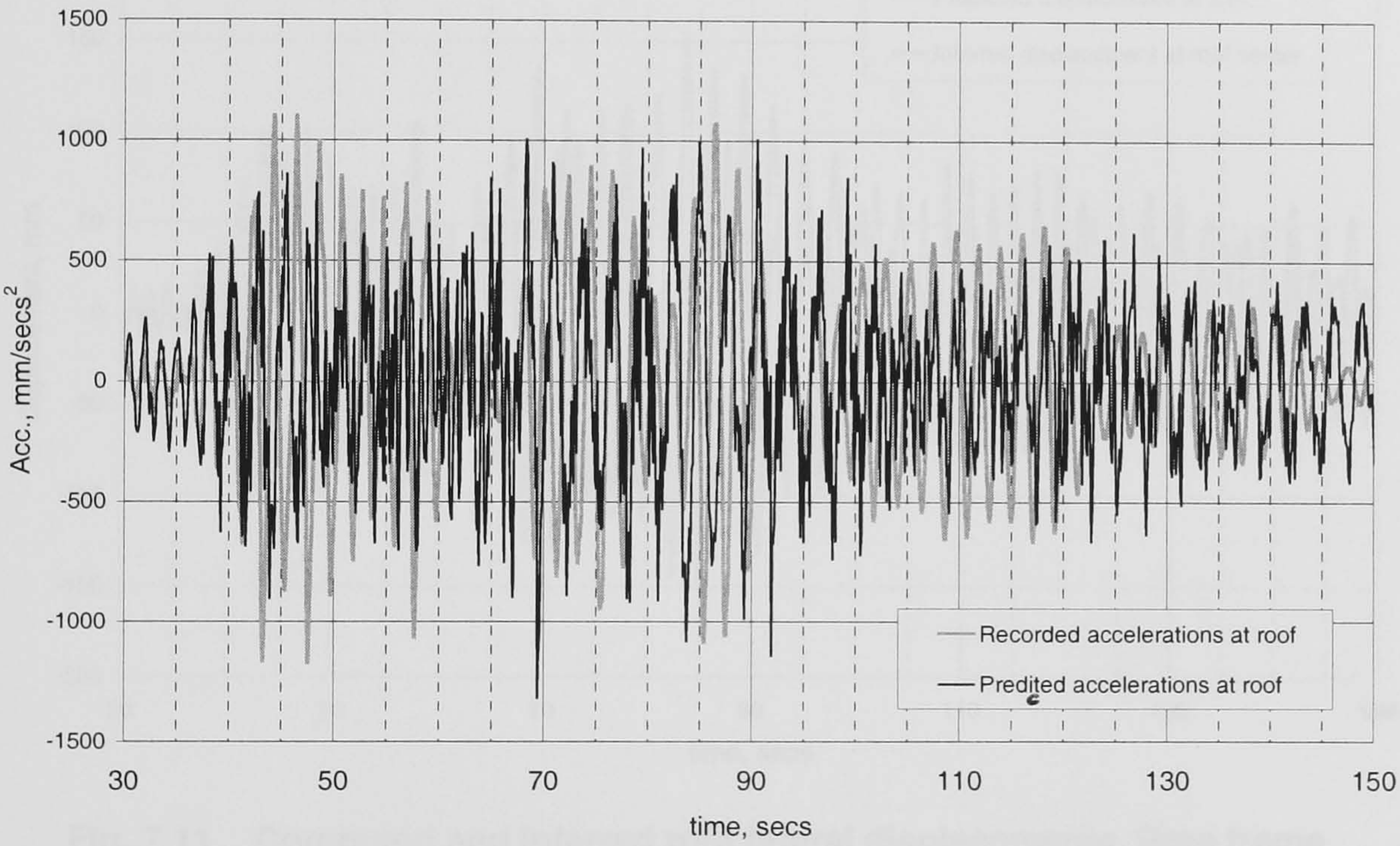


Fig. 7.9 Recorded and predicted roof acceleration, Bare frame

Table 7.3 Predicted and inferred absolute maximum lateral displacements and drifts, Bare frame under Copala event

Lateral displacement (mm)			Drift index		
	Predicted	Inferred		Predicted	Inferred
Level 6 (L6)	64.70	40.90	Basement-L6	0.0044	0.0019
Roof	154.30	112.20	L6-Roof	0.0044	0.0030
Frequency (Hz)	0.36	0.49			

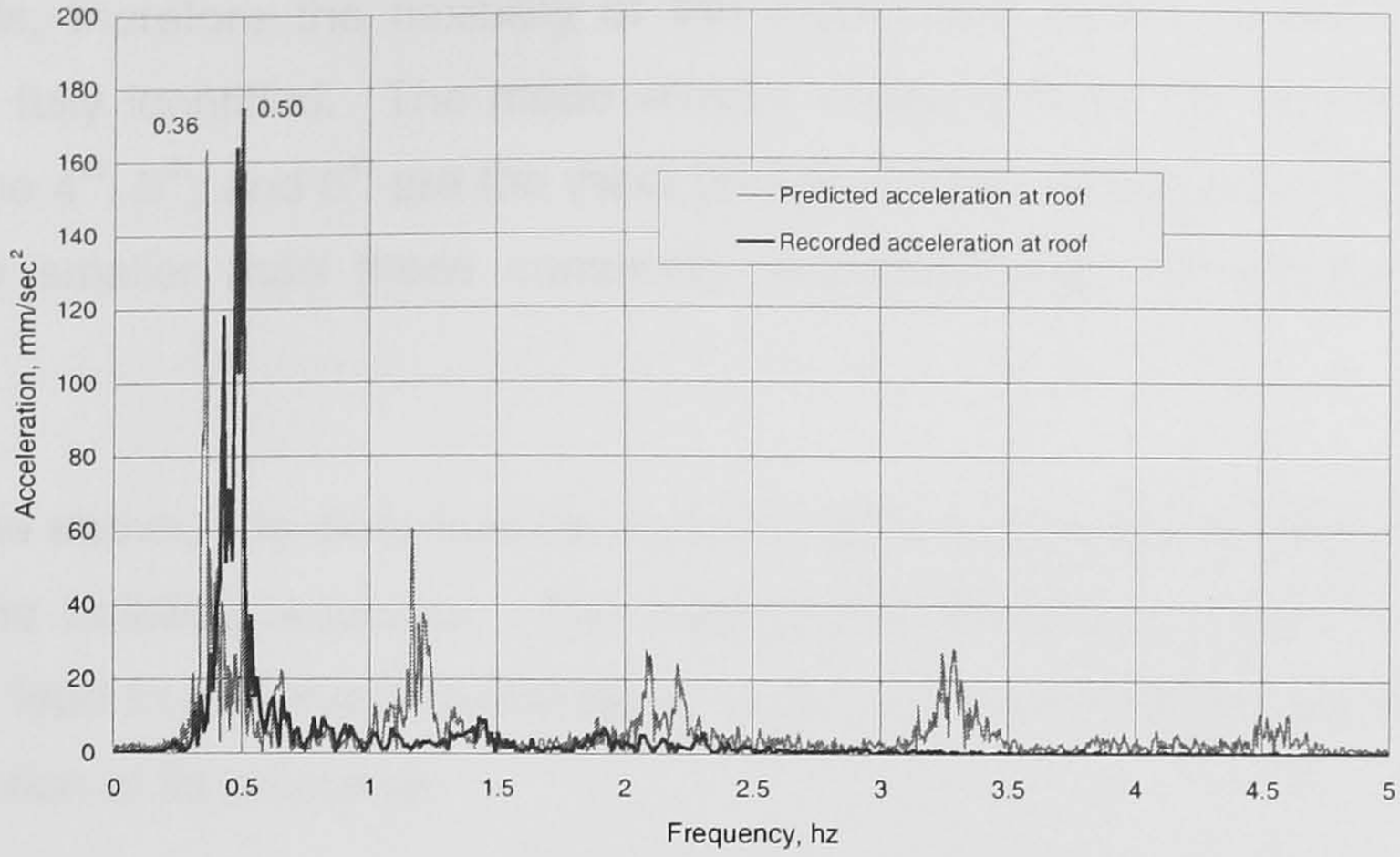


Fig. 7.10 Fourier spectra of recorded and predicted roof acceleration, Bare frame

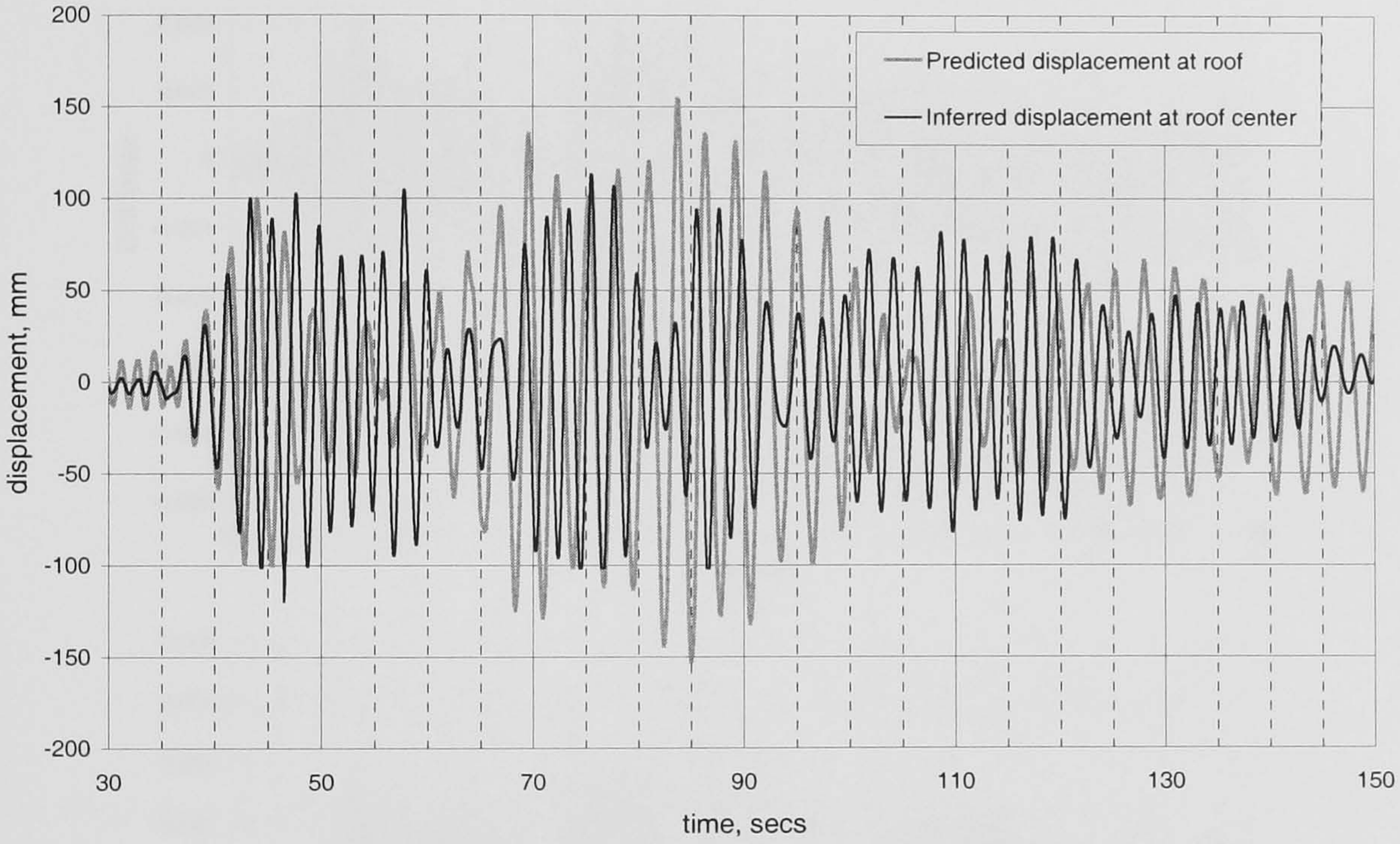


Fig. 7.11 Computed and inferred roof lateral displacements, Bare frame

A further assessment of the model behaviour was carried out using the storey lateral displacements and drift indexes[84], the latter derived between instrumented storeys[85]. Figs. 7.11 and 7.12 show the predicted and inferred time histories for both variables and Table 7.3 shows their maximum values and fundamental frequencies.

In general the predicted displacement and drift indexes are bigger than those inferred

---

[84] Drift index is the drift between two storeys divided by the distance between them.

[85] Displacements and drift indexes computed from recorded accelerations are denominated "inferred" displacement or "inferred" drift indexes.

from records, therefore the flexibility of the model due to the absence of any wall elements is fully identified. The mode shapes obtained from the eigenvalue analysis show that the 4th, 5th, and 6th are the most flexible storeys. In general, the inferred drift indexes are smaller than those commonly associated with the onset of structural damage.

In view of the above, it is clear that the model required increases in stiffness in order to represent the building response. The inclusion of the shear walls to the model is expected to lead to a better representation of the structure real configuration and to a better prediction of its response.

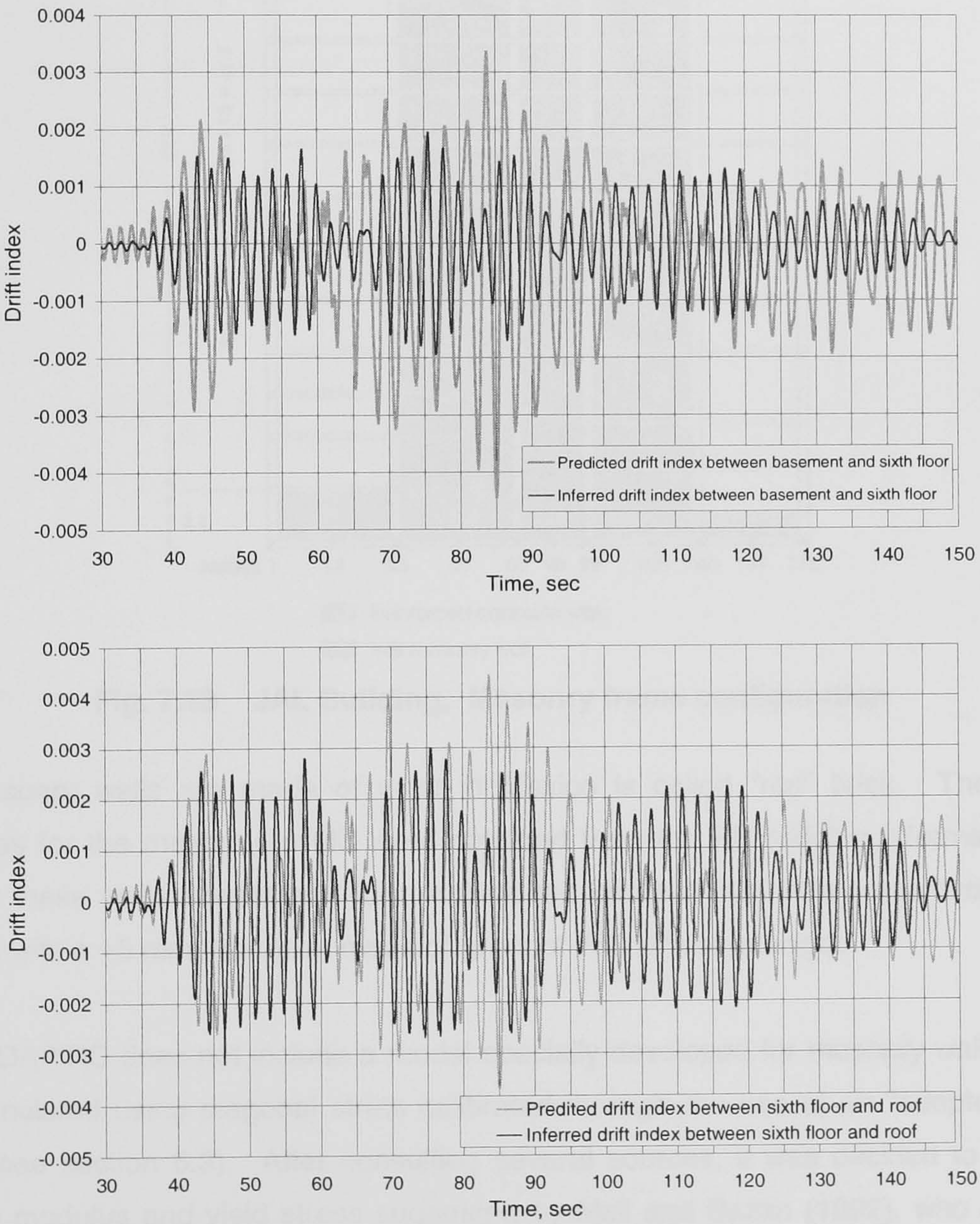


Fig. 7.12 Computed and inferred drift indexes, Bare frame

7.6.3 Frame with masonry walls

In the following analyses masonry walls were added to the Bare frame covering the three central bays from the base to the roof (Fig. 7.13). This is the frame configuration that sustained the 1985 earthquakes. The model is termed "Masonry" frame.



Fig. 7.13 JAL Building, Masonry frame configuration

The masonry walls are made of what in Mexico is called "red" brick. The typical properties for the masonry in MC were obtained from the PC building information. In general, these walls consist of 140 mm thick red bricks of 400 kPa compressive axial strength with a 15 mm thick joint made of grout of 750 kPa of strength.

Since ADAPTIC does not include a model specially developed for masonry walls, these were simulated using diagonal struts calibrated through the use of an "adapted" steel model (see section 6.3). After consulting several sources, it was decided to use the Young's modulus and yield stress suggested by Meli and Bazan (1992), who consider the masonry characteristics and construction practice found in MC. Thus, the analyses were carried out using a Young's modulus of 588 MPa and a yield stress of 1.47 MPa. The Masonry model also includes Rayleigh elements to provide extra sources of

damping, as explaining in 7.6.2.

The predicted elastic eigenvalue fundamental frequency of 0.30 Hz (25% higher than that for the Bare frame) reflects the increment in stiffness produced by the masonry walls, although the model is still in the low frequency region.

The comparison of the recorded and predicted acceleration-time histories at roof level in Fig. 7.14 shows good agreement in amplitude and frequency - including when the amplitude changes significantly (e.g. between 60 and 70 sec). The Fourier spectra shown in Fig. 7.15 show a clear fundamental frequency of 0.5 Hz for the recorded response, while the predicted acceleration shows a stiffer response with a fundamental frequency of 0.6 Hz and a second mode frequency of 0.5 Hz. The maximum computed value for the basement-roof transfer function appeared also at 0.6 Hz.

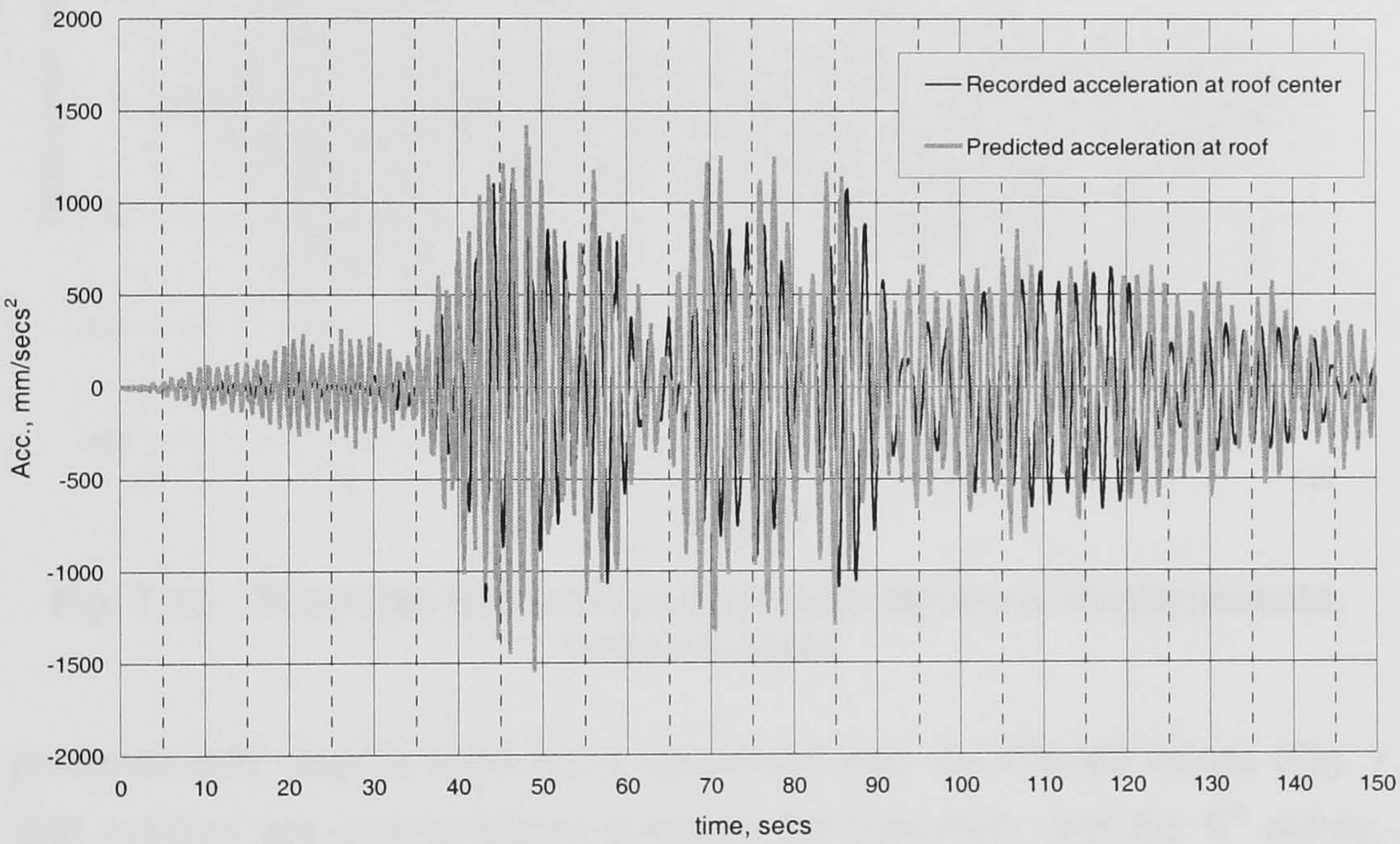


Fig. 7.14 Recorded and predicted roof acceleration, Masonry frame

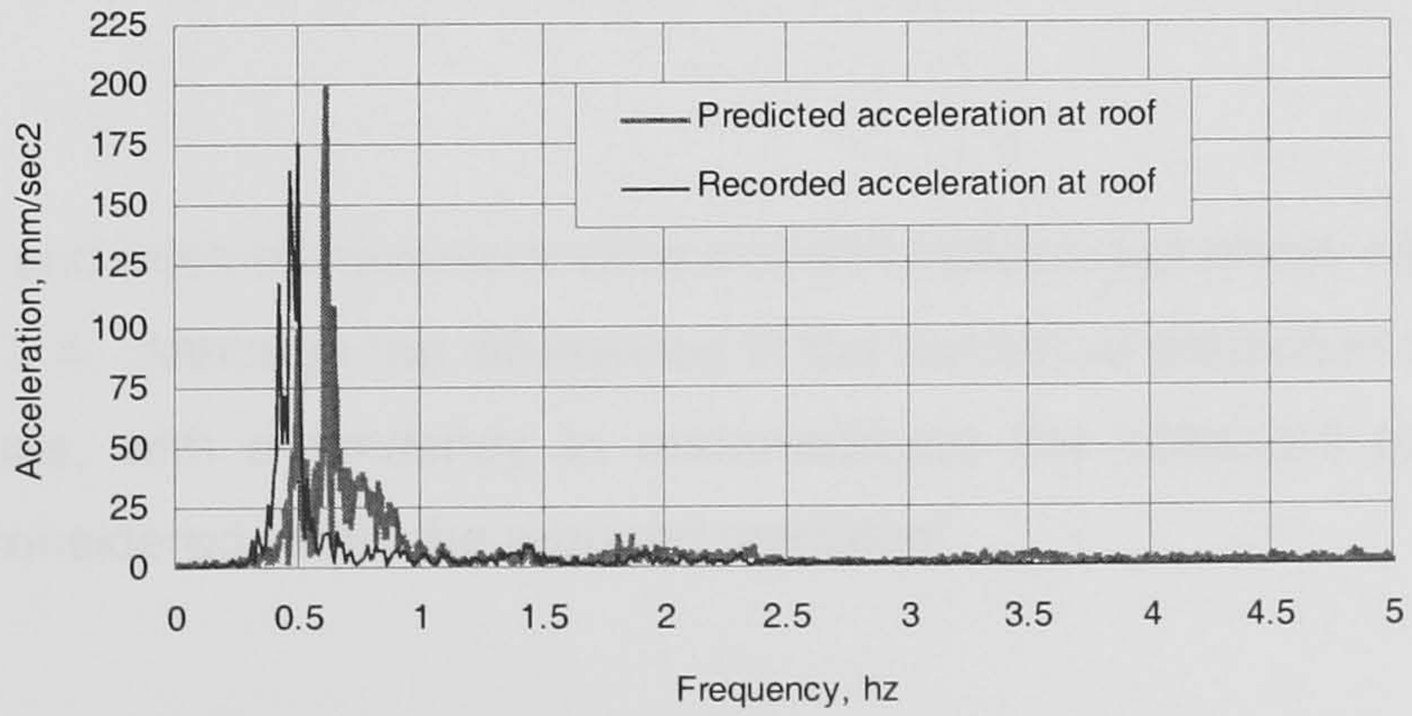


Fig. 7.15 Fourier spectra of recorded and predicted roof acceleration, Masonry frame

Figs. 7.16 and 7.17 show the time histories of lateral displacements and drift indexes obtained from the prediction and from the acceleration records. Table 7.4 shows their maximum values and fundamental frequencies.

The predicted displacements during the intervals of higher amplitude show, in general, amplitudes 10% smaller than those inferred (Fig. 7.16), however, after 100 sec differences of 20% are common. Similarly to the acceleration, the predicted roof displacement fundamental frequency is 0.6 Hz.

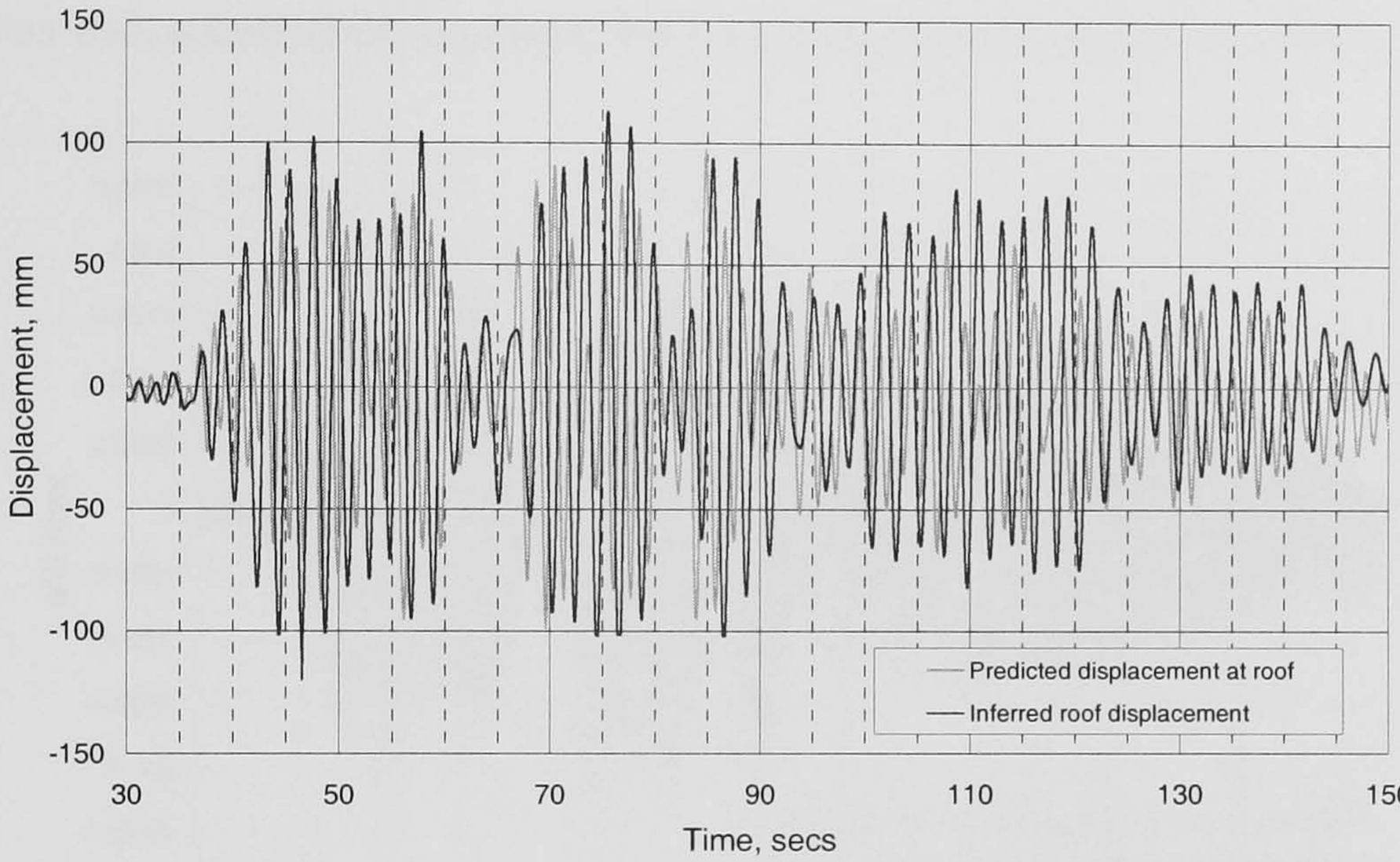


Fig. 7.16 Predicted and inferred from records lateral displacements, Masonry frame

The predicted drift indexes show good agreement with the inferred values (Fig. 7.17). The drift indexes are over-predicted between the basement and the 6th storey, and under-predicted between the 6th floor and the roof, the differences are in the order of 20%. Compared to the Bare frame, it is evident an increment in the stiffness of the model.

The computed and inferred maximum values of drift indices and storey displacement are given in Table 7.4. Although the differences in the numerical prediction are appreciable in several cases, with a tendency to underestimate the observed roof values, the agreement is considered within the required precision.

Table 7.4 Predicted and inferred maximum absolute lateral displacements and drift indexes, Masonry frame under Copala event

Lateral displacement (mm)			Drift index		
	Predicted	Inferred		Predicted	Inferred
Level 6 (L6)	57.0	40.9	Basement-L6	0.0024	0.0019
Roof	98.44	112.2	L6-Roof	0.0022	0.0030
Frequency (Hz)	0. 6	0.50			

The fundamental frequencies obtained from the masonry model are in reasonable agreement with those obtained from the 93-3, 93-4, and 93-11 events (Table 7.2).

The results of the analysis point out that the Masonry frame model predicts the key variables well, substantially improving the results obtained from the Bare frame.

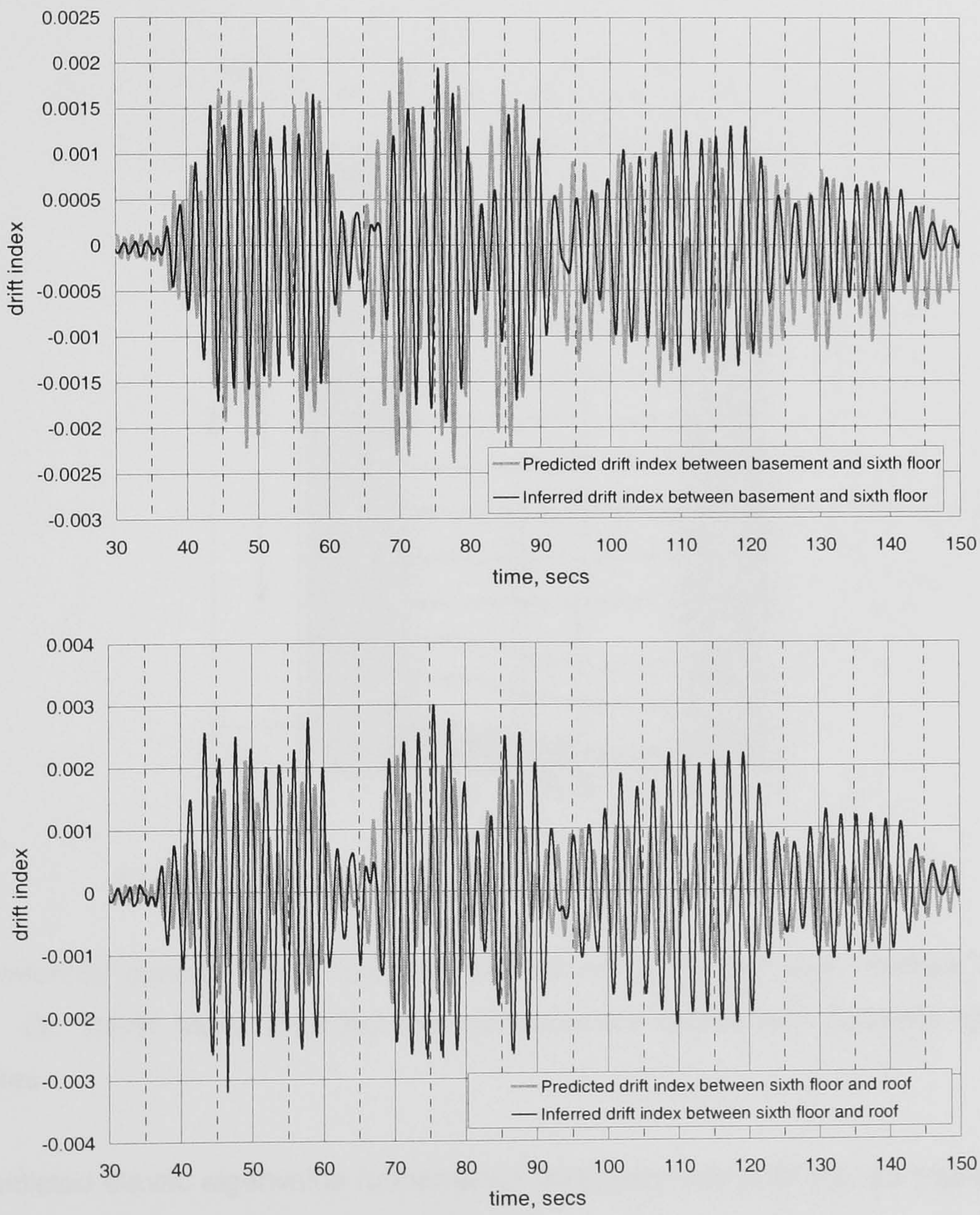


Fig. 7.17 Predicted and inferred drift indexes, Masonry frame

Additional modifications to the model using the capabilities available in ADAPTIC[86] did not produce significant improvements to the predictions.

7.6.4 Frame with concrete walls

The third frame configuration analysed consists of the bare frame plus reinforced concrete walls at the extreme bays – which were built after the 1985 earthquake (Fig. 7.18). This configuration, which is termed as "RC Wall" frame, represent the case that would apply if the reinforced walls had been implemented perfectly. However, as noted earlier, the RC walls seem to be largely ineffective due to non-adequate contact between the walls and the frame.

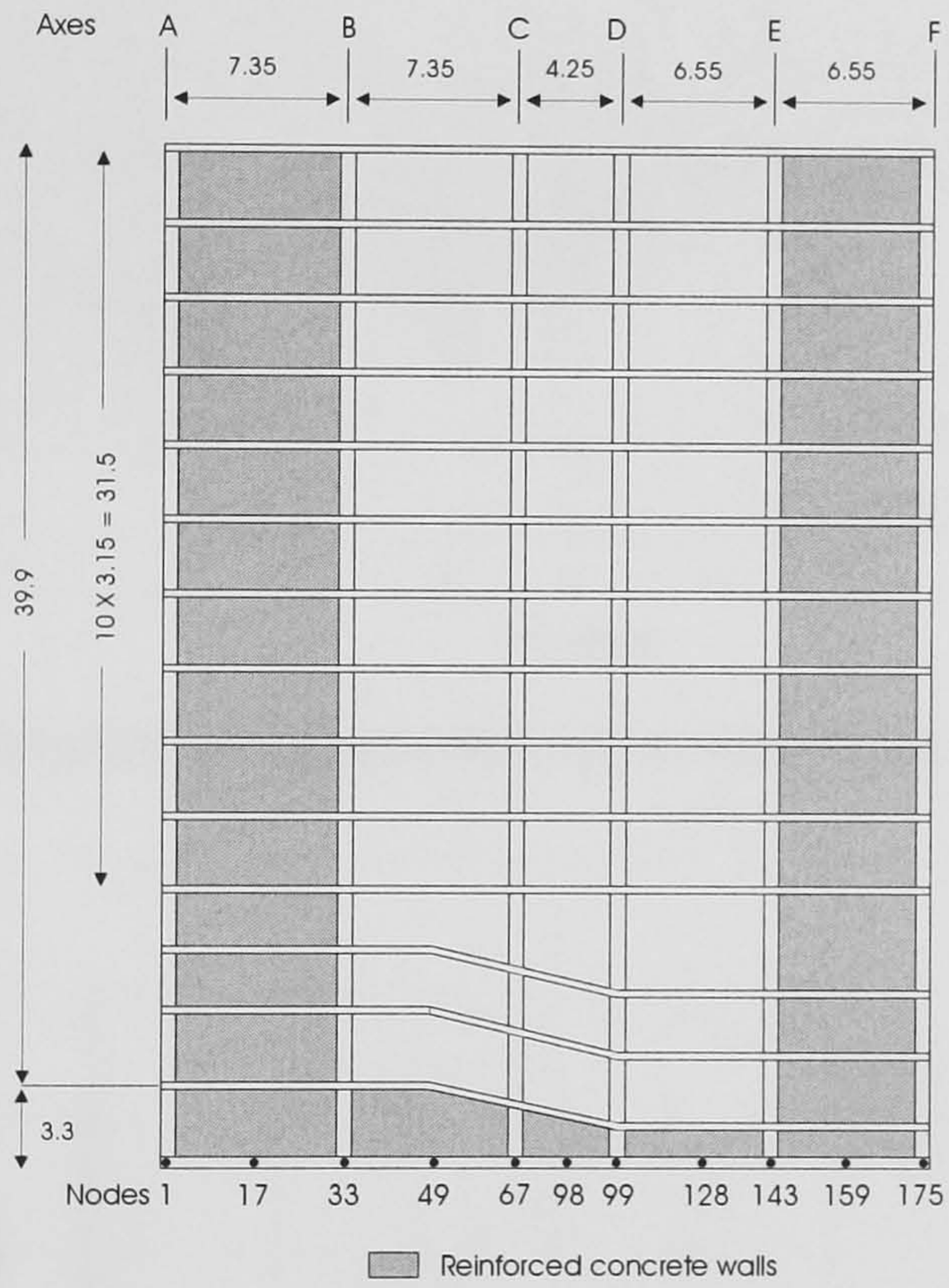


Fig. 7.18 JAL Building, RC Wall frame configuration

The reinforced concrete walls are represented using Flexural wall sections (section 6.2.2). Dr. David Muria provided the reinforcement details and concrete and steel properties.

The predicted elastic eigenvalue fundamental frequency was 0.43 Hz, as expected this is the highest for the configurations under study.

---

[86] Mainly changing the distribution and properties of the masonry walls.

The comparison of predicted and measured acceleration-time histories shown in Fig. 7.19 indicates that the model over amplifies the acceleration amplitude by up to 100%, indicating a model stiffness much higher than that of the actual structure. This is confirmed in Fig. 7.20 which presents a predicted inelastic fundamental frequency of 0.8 Hz – compare to 0.5 Hz for the recorded acceleration. The basement-roof transfer function also shows 0.8 Hz as fundamental frequency.

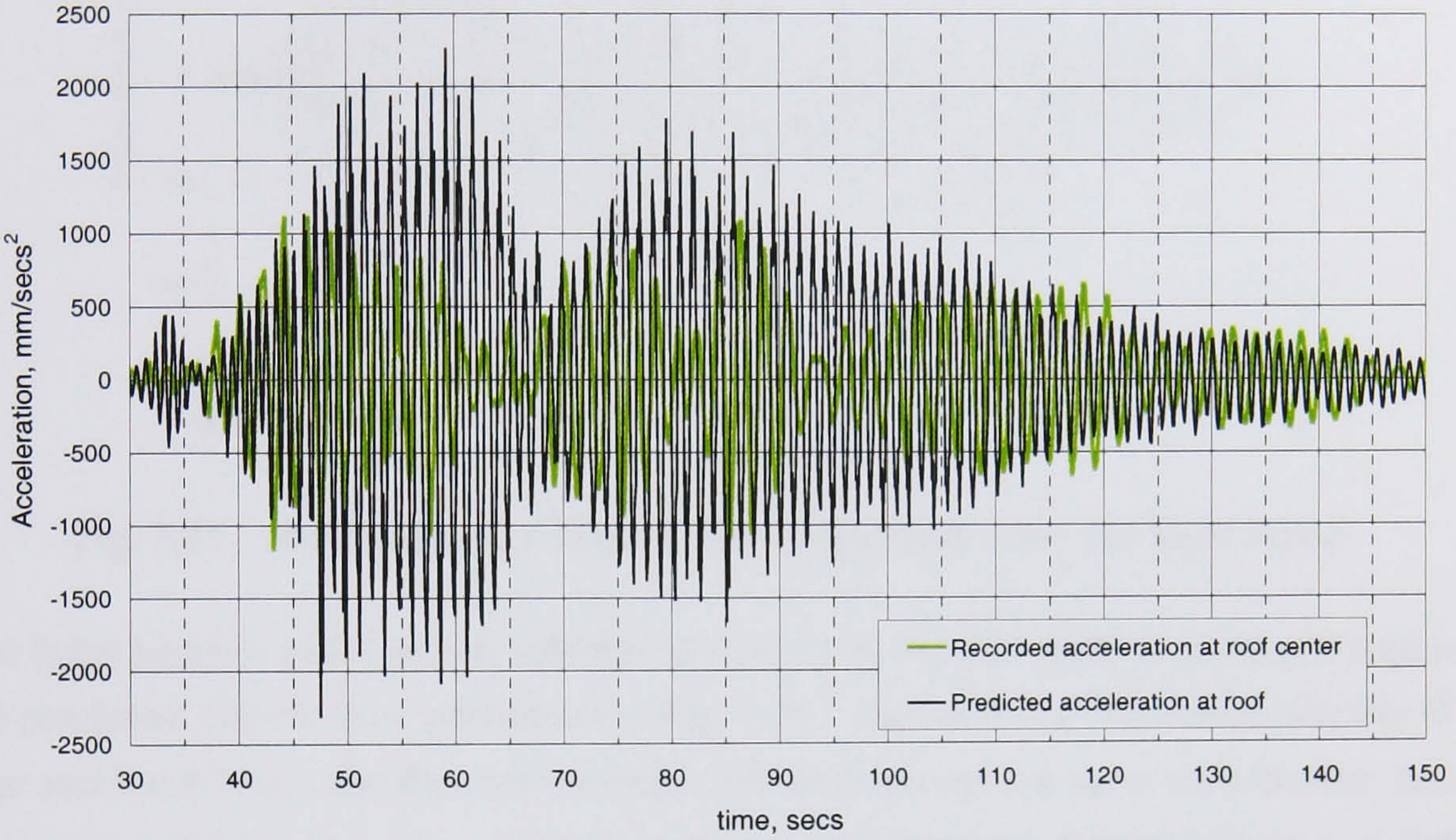


Fig. 7.19 Recorded and predicted roof accelerations, RC Wall frame

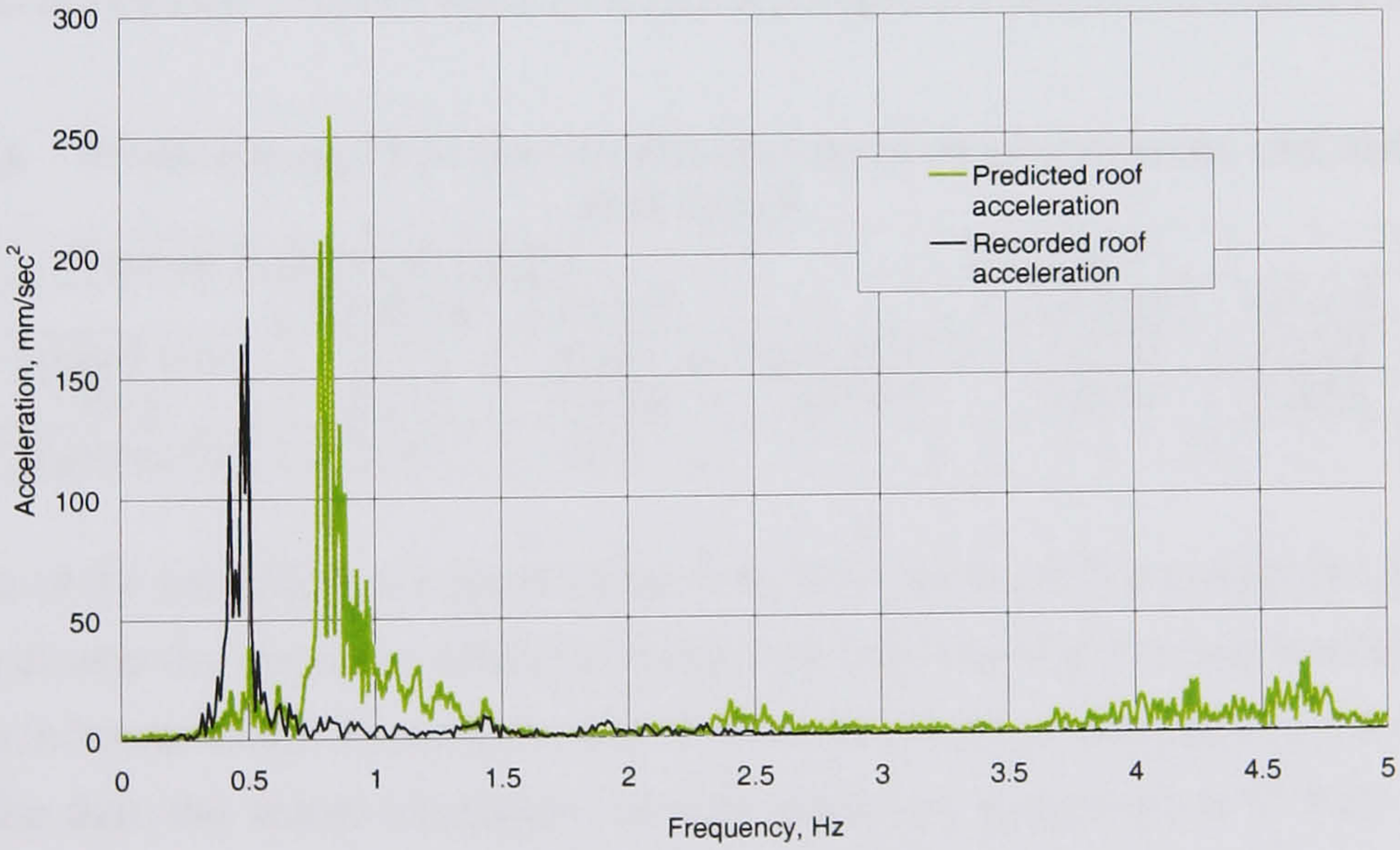


Fig. 7.20 Fourier spectra of recorded and predicted roof accelerations, RC Wall frame

The comparison between the predicted and inferred lateral displacement time histories

presented in Fig. 7.21 shows that the predicted displacements are in general 50% smaller than those inferred. The predicted roof displacement fundamental frequency is 0.8 Hz – similar to that of the acceleration data.

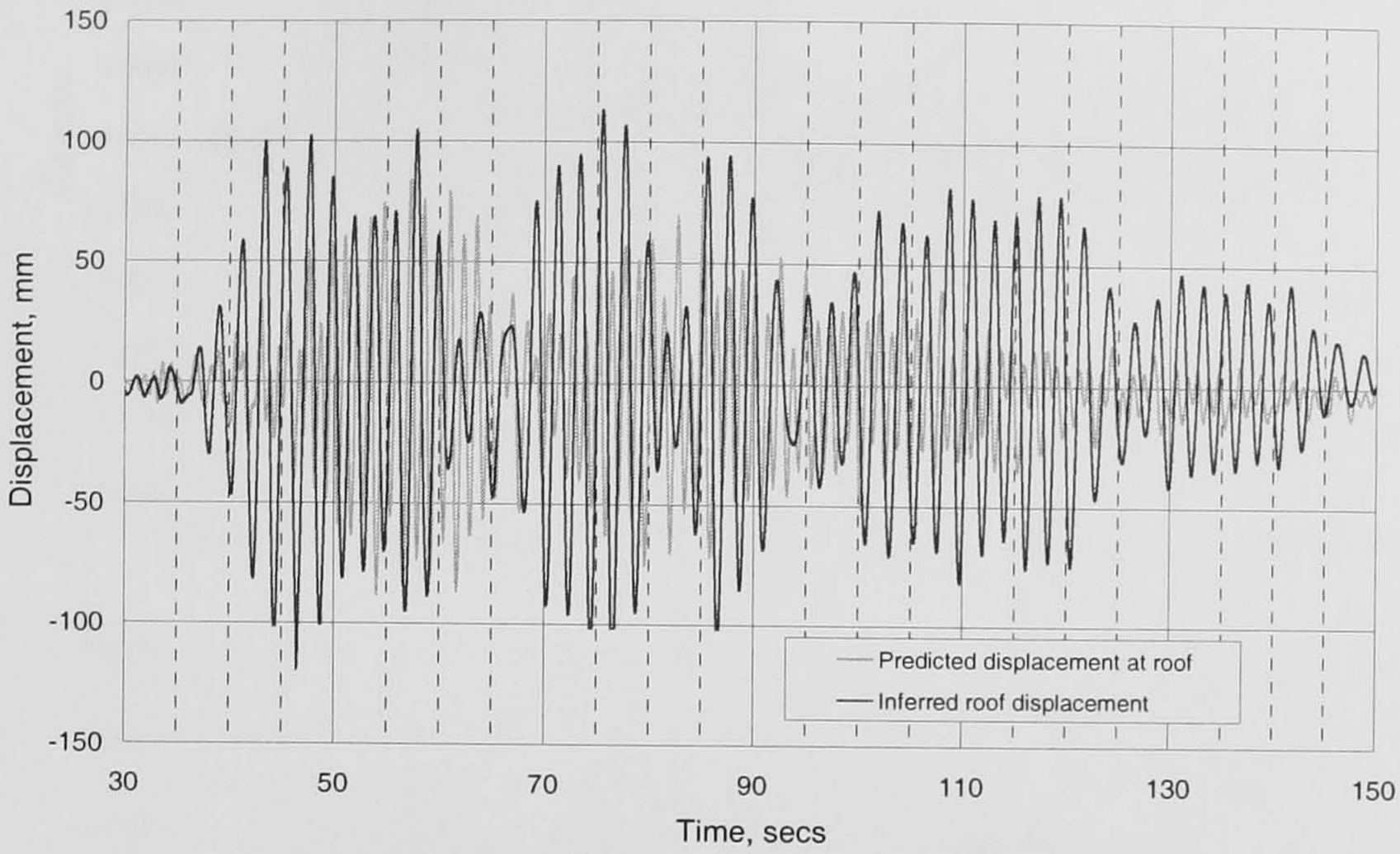


Fig. 7.21 Predicted and inferred lateral displacement, RC Wall frame

The large positive increment in stiffness produced by the RC walls is observed also in the predicted drift indexes presented in Fig. 7.22. Between the basement and the 6th floor and the 6th floor and the roof the predicted drift indexes are up to 50% smaller than those inferred from records. Table 7.5 shows the maximum displacements and drift indexes and their fundamental frequencies, the latter are even higher (30%) than those from ambient vibration – where elastic structural behaviour is expected (Table 7.2).

Table 7.5 Predicted and inferred maximum lateral displacements and drifts, RC Wall frame

Lateral displacement (mm)			Drift index		
	Predicted	Inferred		Predicted	Inferred
Level 6 (L6)	37.12	40.90	Basement-L6	0.0015	0.0019
Roof	88.12	112.20	L6-Roof	0.0022	0.0030
Frequency (Hz)	0. 80	0.50			

The errors of the prediction are appreciable in several cases, with a systematic tendency to underestimate the observed displacements, and overestimate the accelerations. The difference in fundamental frequencies and drift indexes further indicates that the model is much stiffer than the actual structure – for both sections, basement to 6th floor, and 6th floor to roof. It is concluded from the analysis that this configuration does not provide good predictions for the building under any of the recorded events. This result may be due to the problem of continuity between the frame and the reinforced concrete walls that exists in the actual frame and that allows slippage between them to occur – which

results in a more flexible structure.

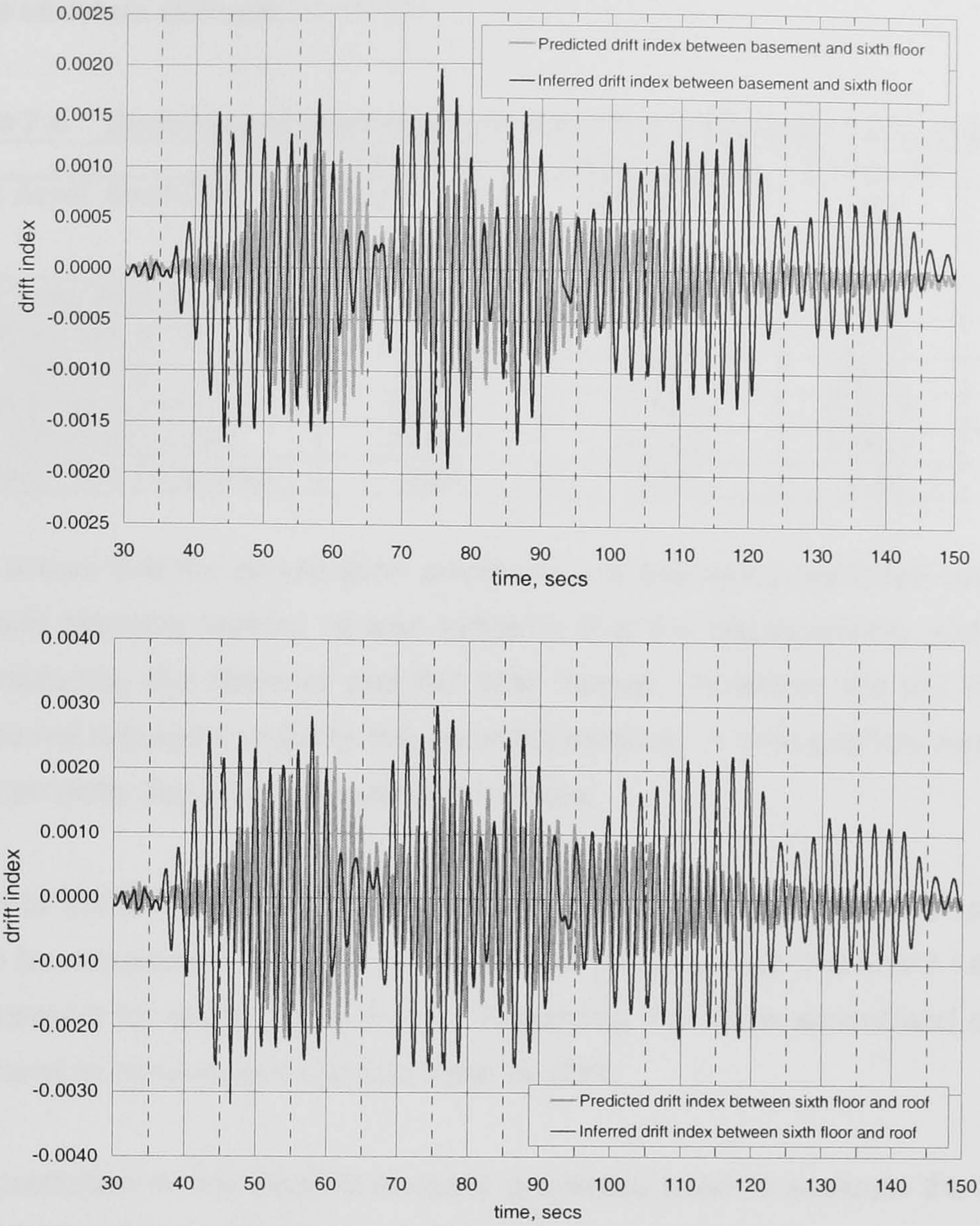


Fig. 7.22 Predicted and inferred drift indexes, RC Wall frame

7.6.5 Analysis

The structural response at the roof of a longitudinal frame from the JAL building was adequately predicted under the Copala event using inelastic models and a calibration procedure. The calibration consisted mainly of modifying the location of structural wall elements (whose influence could have been eradicated or their performance modified by damage sustained during previous earthquakes) in order to obtain the actual response of the building. Although this calibration procedure differs from the conventional analysis its purpose was to reduce the uncertainties involved in the study of a damaged building.

Table 7.6 shows a summary of the main results used to evaluate the performance of the studied models. This information allows an evaluation of the influence of the reinforced

concrete and masonry walls on the inelastic and eigenvalue fundamental frequencies and on the structure stiffness.

Table 7.6 Summary of predicted and recorded response of JAL building

	Bare frame	Masonry frame	Wall frame	Recorded
Roof Accel. Amplitude	Slightly under-predicts	Slightly over-predicts	Over-predicts	
Fund. Freq. Roof Accel.	0.36	0.60	0.80	0.49
Max. displacement 6th floor (L6)	64.70	57.00	37.12	40.90
Max. displacement roof	154.30	98.44	88.12	112.20
Max. drift index basement-L6	0.0044	0.0024	0.0015	0.0019
Max. drift index L6-roof	0.0044	0.0022	0.0022	0.0030
Eigenvalue Fund. Frequency	0.24	0.30	0.43	-

Table 7.6 shows that the acceleration amplitude and frequency are better predicted by the Bare and Masonry frames. It also indicates that the displacements and drifts are better predicted by the Masonry and RC Wall frames. However, the RC Wall frame model does not represent properly the recorded motions; it over-predicts accelerations and under-predicts displacements and drift indexes.

In the case of the Bare frame, although the margin of error in the predicted acceleration appears to be comparable with that for the Masonry frame, Figs. 7.9 and 7.14 indicates better agreement for the Masonry frame. Regarding the displacement and drift index, the Bare frame in general over-predicts them by 50%.

The best prediction of the inferred dynamic properties used to evaluate the models is obtained with the Masonry frame model. The lateral displacements and accelerations at roof, drift indexes and fundamental frequency are predicted within around ±20%. This result supports the findings of Meli, et al., (1998) and Muria and Del Toro (1998) who point out that because the concrete walls are partially separated from frames and the masonry walls cracked, their contribution is relatively ineffective during an earthquake event.

Some explanation for differences between recorded and predicted motions are: (i) the low number of elements used to represent the frame elements, which put limits to the capacity of the program to reproduce inelastic behaviour; (ii) neglecting other sources of inelasticity (e.g. cracks in structural elements, change of material properties with time, and special conditions in the reinforced concrete wall-frame joint); and (iii) the fact that we try to represent a tri-dimensional structure with a frame (although tri-dimensional) model.

Both the computed and inferred drift indexes for the three configurations under study were smaller than those commonly associated with the onset of structural damage. Meli et al. (1998) consider this observation as further indication that the cause of the observed non-linear behaviour of the building lies in the inadequate repair of previous damage. Inelasticity under this condition can be achieved by producing a frame model for every earthquake magnitude. On the other hand, low values of predicted drift indexes indicate that the program computes low inelastic behaviour in the models.

Meli, et al.'s (1998) analyses of the JAL building followed similar calibration procedure but including cracked structural elements and concrete walls with just one side in continuity with the frame. Meli, et al. found that the model that included only the reinforced concrete walls gave fundamental frequencies closer to the 93-11 and 94-1 events. For the strongest events of 94-3 and 95-1 Meli, et al. obtained a better agreement using a model with masonry and reinforced concrete walls – the latter connected only at the top, and with reduced stiffness.

7.7 Base reaction under the 1995 Copala earthquake

Although the Masonry frame model is considered the base for future analyses of the base reactions, some comments on the reactions obtained from the Bare and RC frames are included in the following sections. The purpose is to show the influence that the super-structure has on the magnitudes and frequencies of the reactions developed at the model's base during a seismic event.

7.7.1 Static reactions

The static distribution of load at each node at the base of the three model configurations under study is shown in Table 7.7 and Fig. 7.23[87]. Table 7.7 shows that nodes 49 and 128 sustain tension forces, which corresponds to two-way loading; this is not significant since these are points of low initial load and low cyclic force.

The total reaction at the base of each model frame (weight of each model configuration) is the same since for this study only the structural contribution is removed; the structural elements contribute to the total weight even when their structural contribution is removed. The total reaction at base is 11776.9 kN.

---

[87] The pile distribution below the longitudinal external frame can be observed in Fig. 7.3.

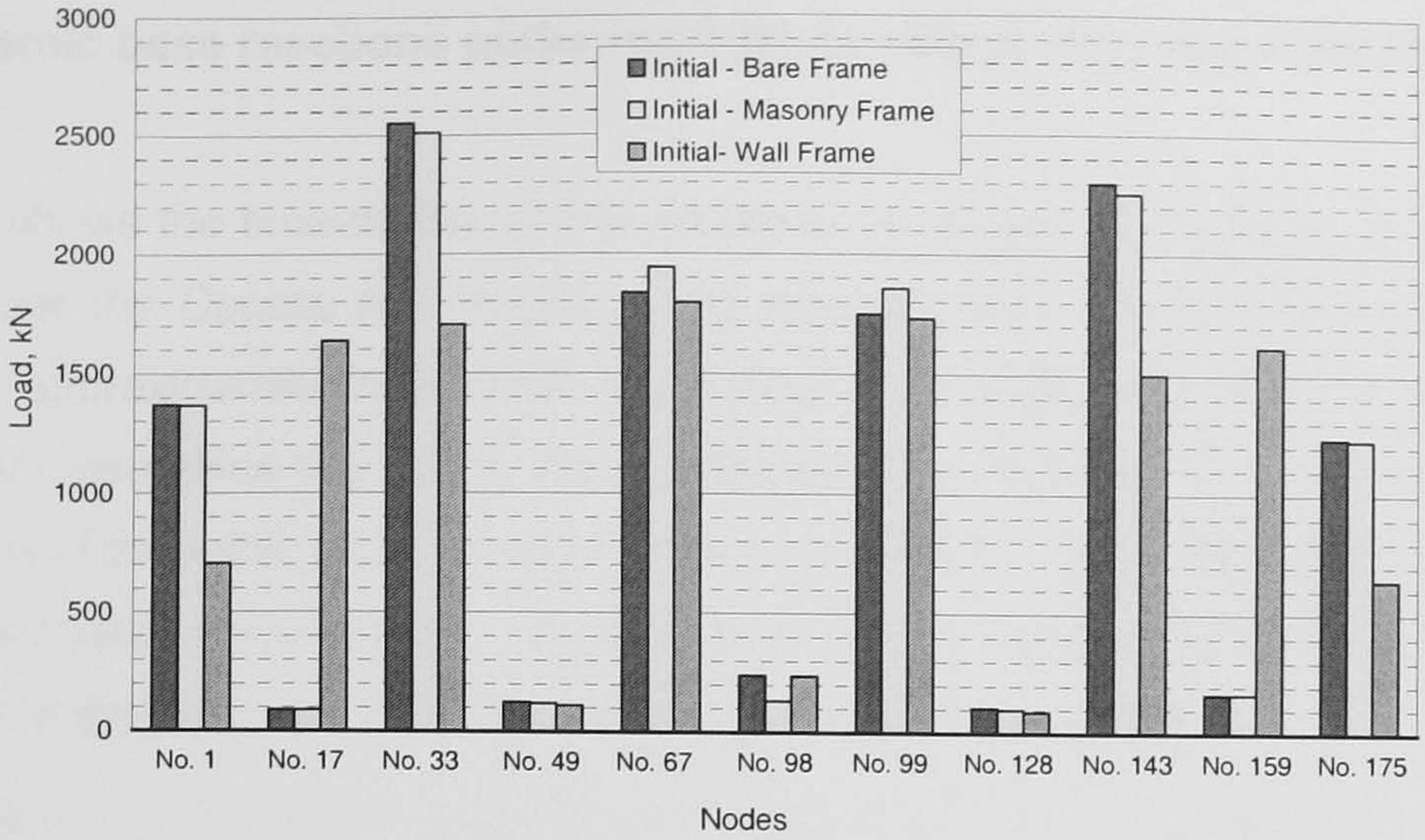


Fig. 7.23 Initial static load distribution at the base of the studied configurations

Table 7.7 Initial forces on each model configuration and maximum and minimum seismic forces during the Copala earthquake expressed as percentage of initial static forces[88]

Node	Bare frame, kN			Masonry frame, kN			RC Wall frame, kN		
	Initial	Max, %	Min, %	Initial	Max, %	Min, %	Initial	Max, %	Min, %
1	1367.6	131	70	1365.6	131	67	703.9	211.8	6
17	90.5	110	57	90.1	122	63	1636.0	100.0	74
33	2553.8	114	91	2511.8	137	68	1701.4	145.3	72
49	126.3	230	-89	119.9	252	-113	112.1	270.6	-114
67	1835.5	136	68	1942.8	136	67	1797.0	127.0	76
98	241.3	109	55	134.3	145	16	239.0	122.6	82
99	1751.4	126	72	1858.0	129	62	1733.6	128.2	72
128	107.6	394	-229	101.8	425	-324	92.5	443.2	-263
143	2300.2	127	79	2256.3	144	57	1502.2	171.3	41
159	167.3	140	64	166.7	148	46	1615.1	100.5	71
175	1235.4	140	59	1229.5	152	51	644.1	234.0	-21

The static load distribution for the Bare and Masonry frames are practically equal because the simulation of the masonry walls does not allow them to take load under static conditions (their contribution appears when the models are submitted to lateral loading). On the contrary, the static load distribution for the RC Wall frame shows that the intermediate nodes 17 and 159 contribute to the load carrying, producing a re-distribution of load. These intermediate nodes are located where the reinforced concrete walls were added, indicating, as expected, that these walls are load-bearing elements. The loads at nodes where there are not reinforced concrete walls are similar to those of the Bare and Masonry frames (Fig. 7.23).

[88] Tension forces happens in nodes with low initial static loads.

7.7.2 Seismic base reactions under the 1995 Copala earthquake – Masonry model

Fig. 7.24 shows the time-history of the reactions developed at the base of the Masonry frame under the Copala earthquake. Two intervals with maximum amplitudes, each lasting for approximately 20 seconds or 10 cycles, are easily identified (the layout of the time-history resembles that of the input motions). The maximum and minimum loads as percentage of the initial static load are shown in Table 7.7, Fig. 7.25 presents the lowest and highest loads at each node. (The maximum and minimum loads presented in Fig. 7.25 are the absolute values, which could occur at different cycles.)

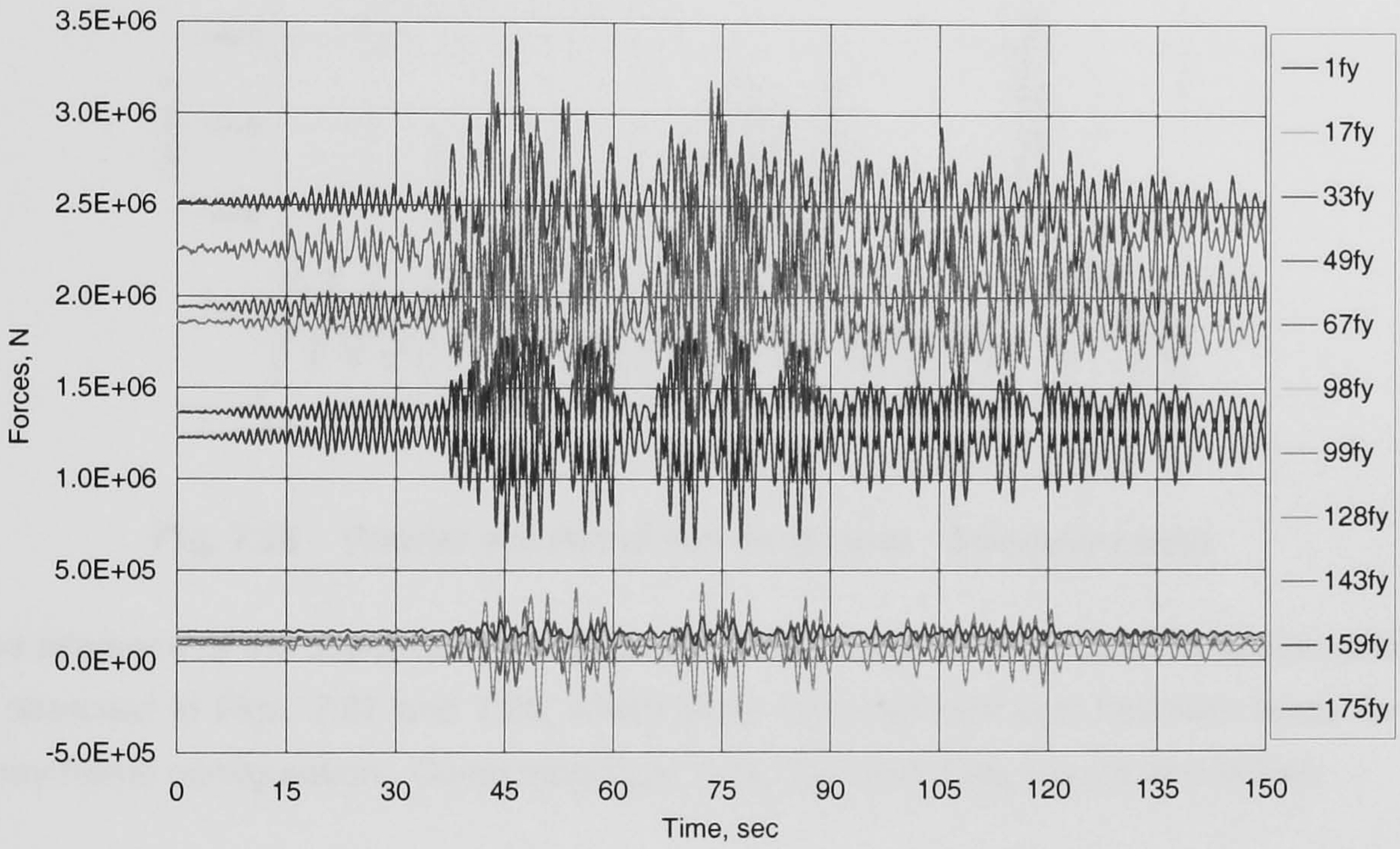


Fig. 7.24 Time-history of calculated forces at the base of the Masonry frame

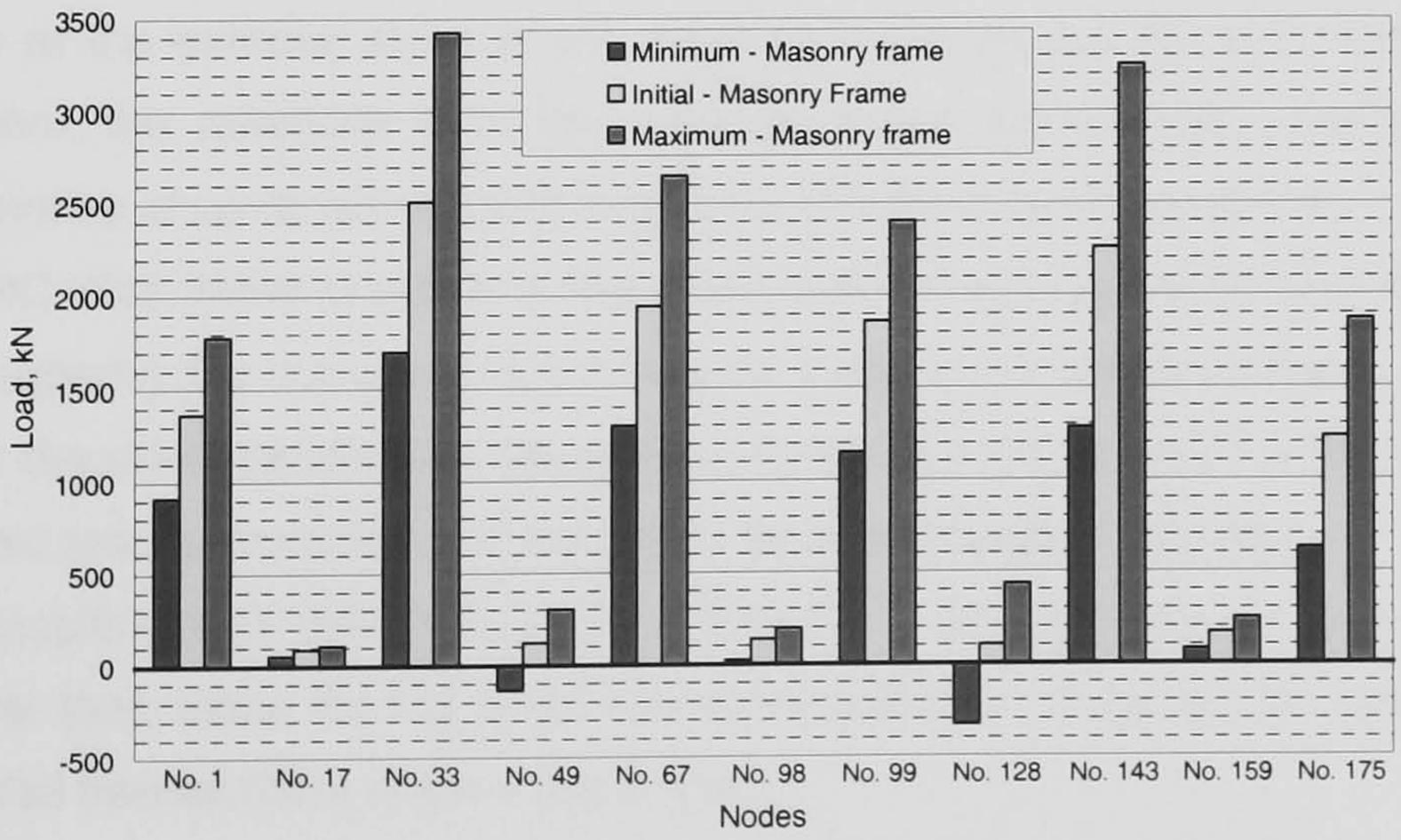


Fig. 7.25 Maximum and minimum load under the Copala event – Masonry frame

The Fourier spectra for the forces at the base of the Masonry model show the highest amplitudes for two frequencies, 0.5 and 0.6 Hz (Fig. 7.26[89]). The 0.5 Hz frequency corresponds to the fundamental frequency of the input motion (the amplitudes for this frequency in any of the frame configurations vary between ±10%), while the 0.6 Hz frequency corresponds to the Masonry frame model fundamental frequency (section 7.6.3). This combination of input motion and model fundamental frequencies appears also in the results for the RC Wall and Bare frame configurations.

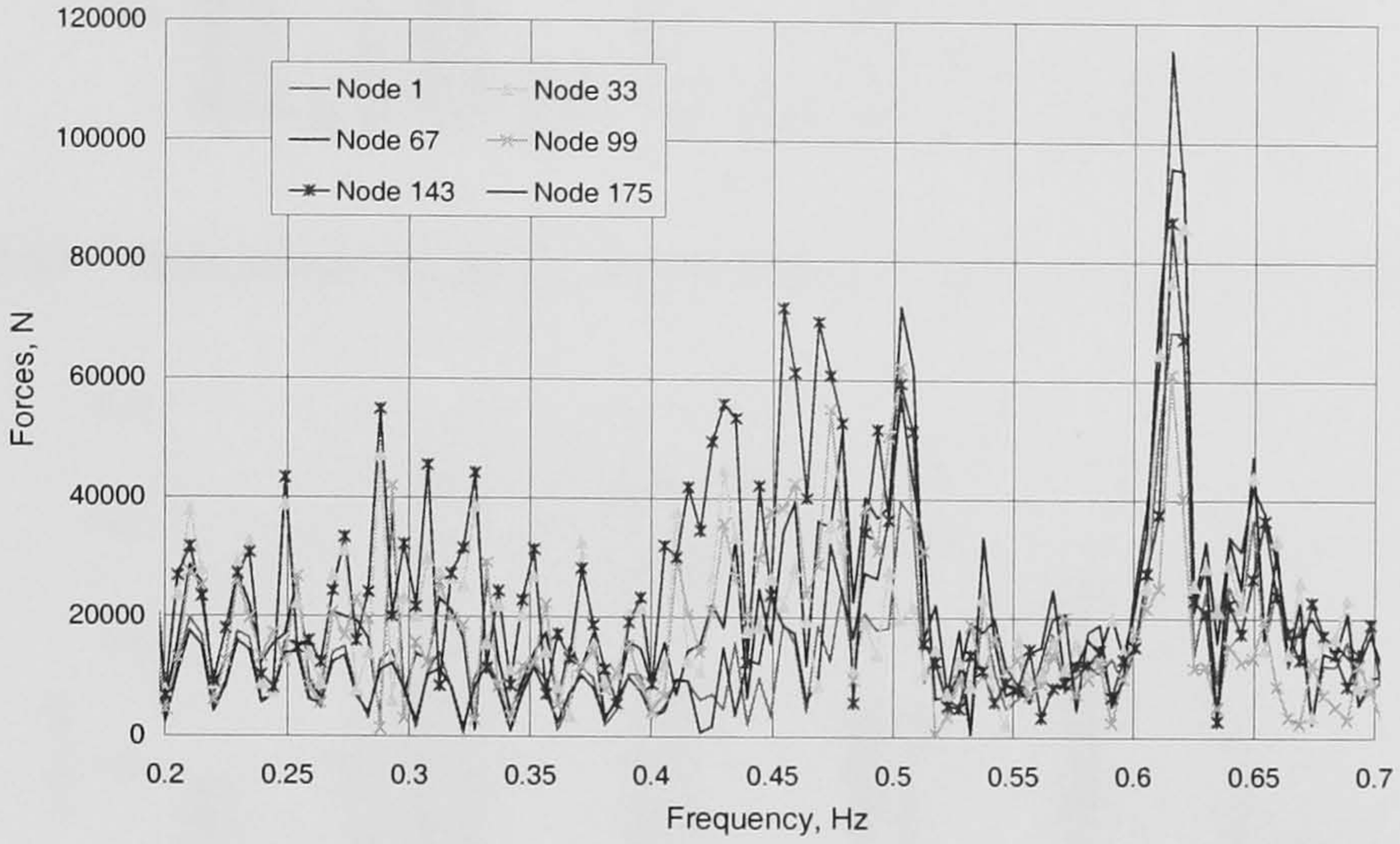


Fig. 7.26 Fourier spectra of forces at base – Masonry frame

The influence of the super-structure on the seismic reactions at the base of the models is observed in Figs. 7.27 and 7.28, which show the maximum and minimum loads for every frame configuration. Comparing Figs. 7.23, 7.27 and 7.28, it is observed that:

i) Between the Bare frame and the Masonry frame, which start with very similar static loads, the maximum and minimum reactions are similar at all nodes except those at the external sides of the masonry walls (nodes 33 and 143). At both locations the reactions from the Masonry frame have larger amplitudes, with differences of up to 600 kN with respect to the Bare frame reactions.
ii) The RC Wall frame presents a significantly different initial static load distribution, consequently the comparison of the cyclic loads is not straightforward. However, as for the static distribution, the nodes located at the bays with no RC walls show seismic reactions similar to those of the Bare and Masonry frames.
iii) The amplitudes of the base cyclic reactions for the Bare frame are consistently smaller than those for the other two configurations. Between the Masonry and RC Wall frames there is not a clear trend.

---

[89] The Fourier spectra of the nodes located between columns are not presented since they carry small load.

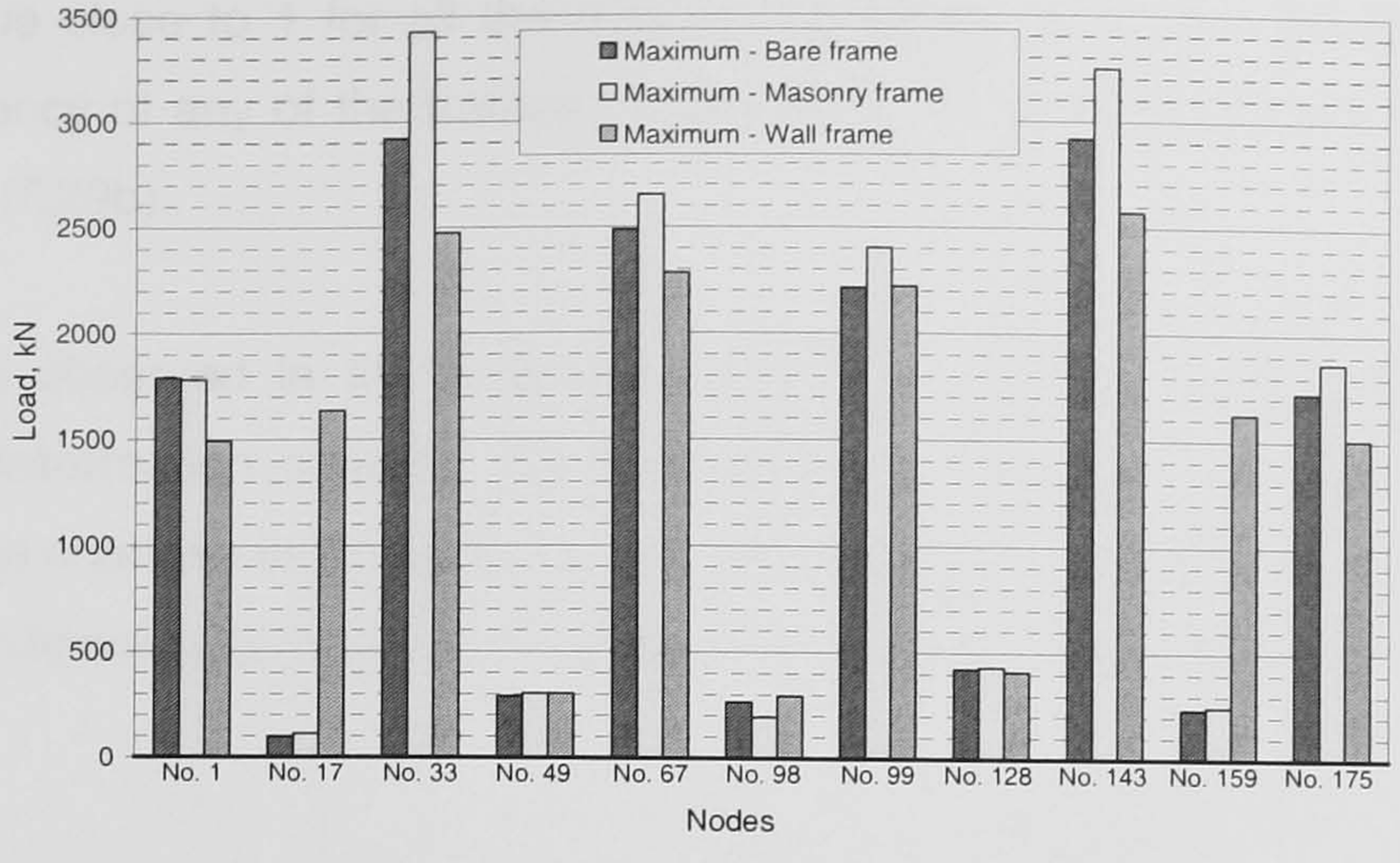


Fig. 7.27 Maximum loads for the three configurations of the under study

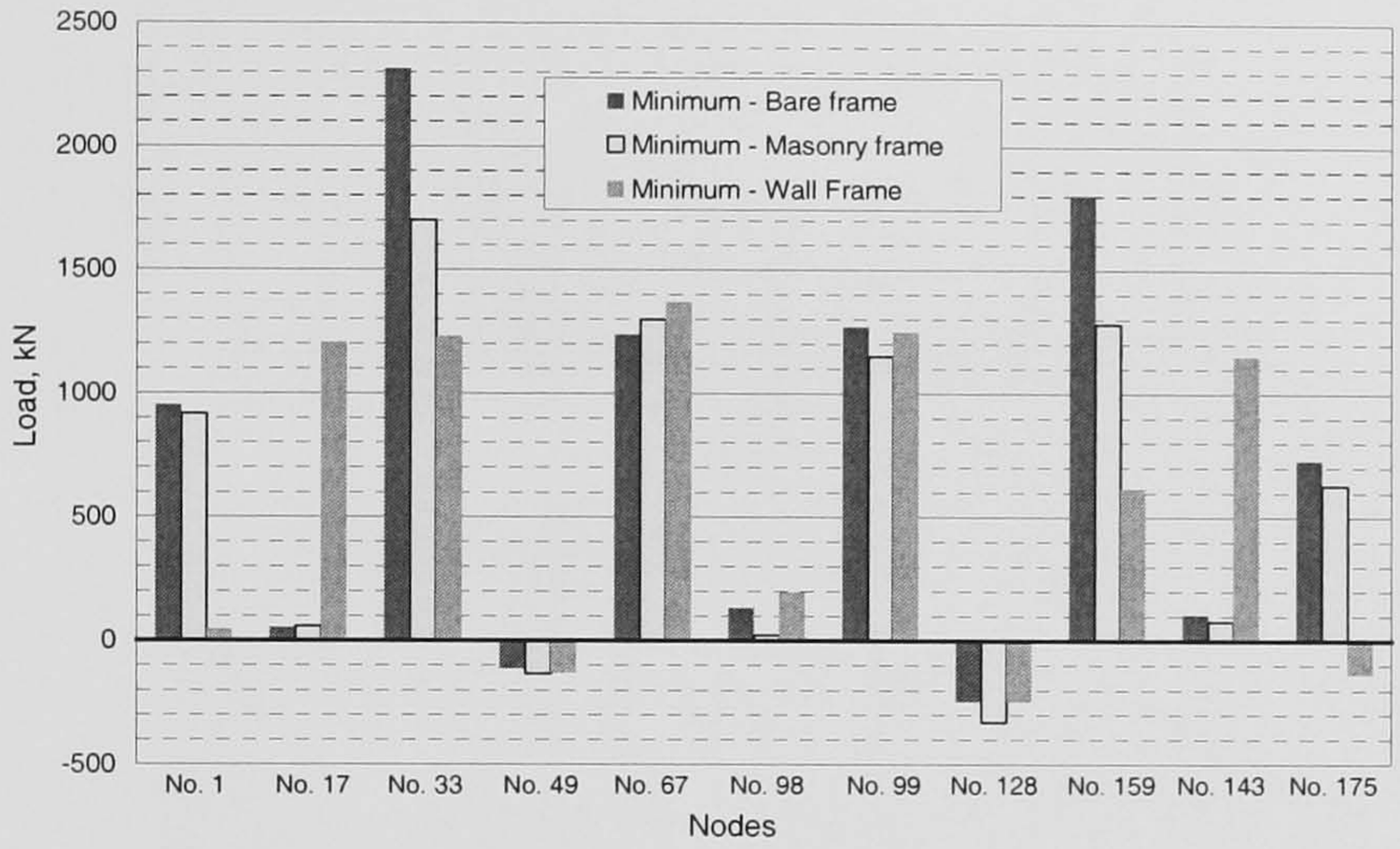


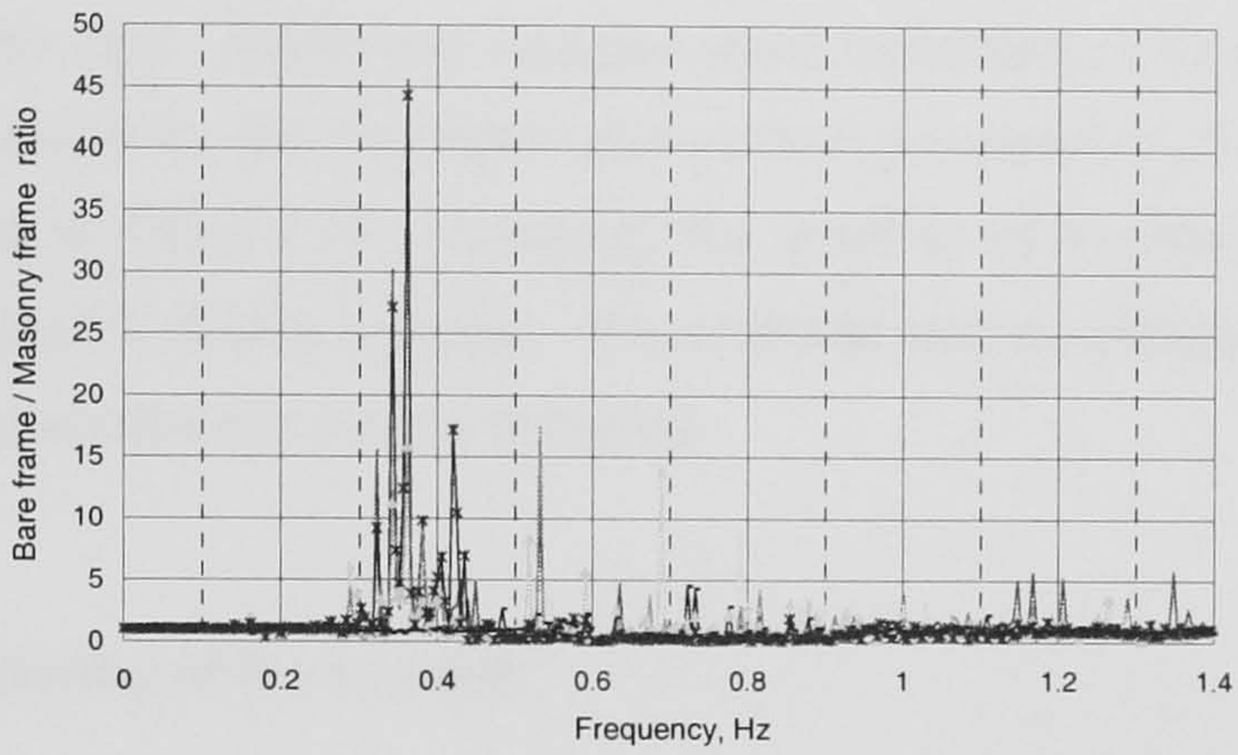
Fig. 7.28 Minimum load for the three configurations under study

In order to show the shift in the base reactions' fundamental frequencies for the RC Wall and Bare frame models (with respect to the Masonry model), the Fourier spectra of their base reactions were divided by the Fourier spectra of the base reactions from the Masonry frame (Fig. 7.29, for the sake of simplicity the signal names were omitted). (This procedure is favoured because the influence of the fundamental frequency from the input motion is partially removed.) Among the features observed in Fig 7.29 are:

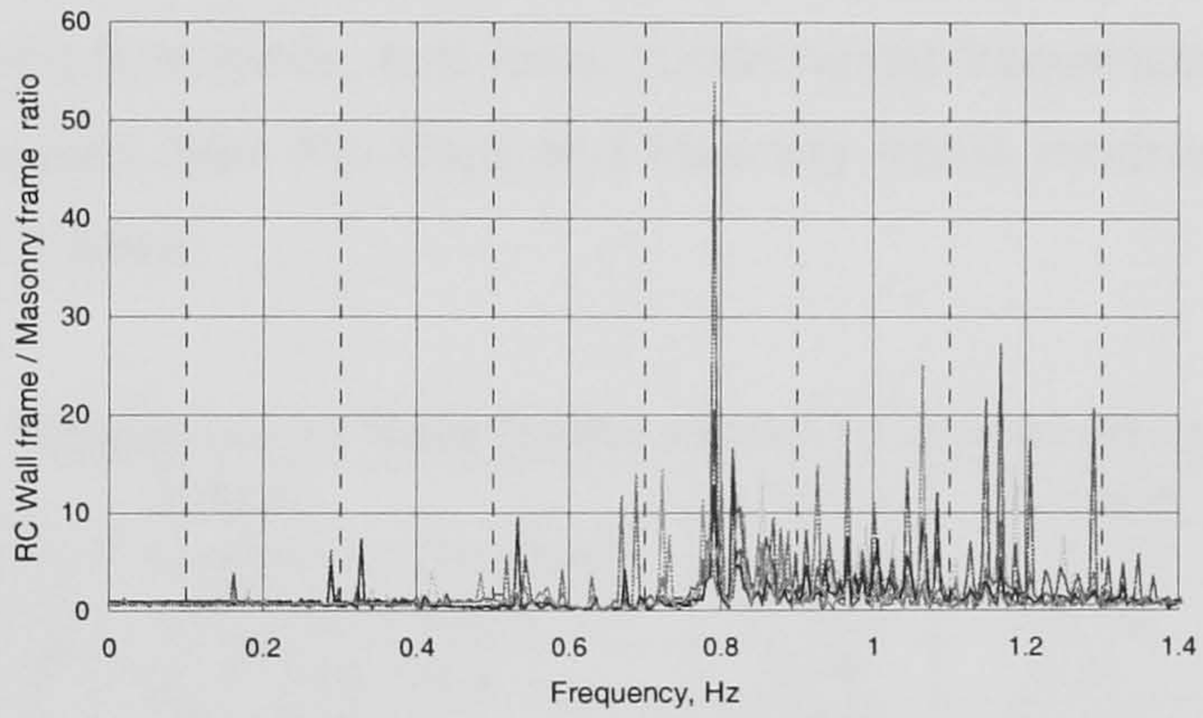
i) An ordinate value close to 1 for all the frequencies smaller than the lowest fundamental frequency of any of the frames involved (0.36 Hz for graph 7.29a and 0.5 Hz for graph 7.29b).
ii) A high ordinate for the fundamental frequency of the normalised Fourier spectra (0.36 Hz in graph 7.29a, and 0.8 Hz in graph 7.29b).
iii) A ratio smaller than 1 for the fundamental frequency of the Masonry frame (0.6 Hz).

iv) A value close to 1 for all the frequencies bigger than the highest fundamental frequency of any of the frames involved (0.6 Hz for graph 7.29a, and 0.8 Hz for graph 7.29b).

The changes observed in the reactions at the base of the models result from the changes in deformation capacity, shear strength, and dynamic characteristics of the structure. The changes in the magnitude of reactions due to structural modifications are an important aspect to consider when designing foundations under seismic loads.



a. Bare frame / Masonry frame ratio



b. RC Wall frame / Masonry frame ratio

Fig. 7.29 Ratios of the base reaction Fourier spectra for the three frame configurations under study

As part of the study of the response of the JAL building a purely elastic analysis was conducted in the calibrated Masonry model. The response produced a totally different response of the building with concentration of forces and deformations at the first few storeys, bad prediction of the recorded accelerations, and seismic reactions at the base up to 98% bigger that for the analysis including inelasticity.

7.8 Base reactions under the 1985 Michoacan earthquake

The amplification factor λ chosen to upgrade the 1995 JAL records to the September 19 1985 conditions is 5 - the amplification ratio determined from the peak acceleration (section 6.4.2). (An average SCT85/JAL95 ratio of 6 was computed by comparing the longitudinal component of the free field on JAL site and the N90E component of the 1985 SCT record.)

The Bare and Masonry frames described above were subjected to the Copala event multiplied by a factor of 5. Additional analyses were undertaken using a factor of 3 and a combination of factors for the horizontal and vertical components, 5 and 3 respectively (following the ratios in Table 6.3). However, the analysis of the Masonry model under λ=5 and λ=3 indicated building collapse; the analysis was successful under λ=2. The following sections describe the results obtained.

7.8.1 General response of the models

The response of the models to the amplified motions shows greater predicted accelerations and displacements, and lower fundamental frequencies. Tables 7.8 and 7.9 compare key results from the Bare and Masonry frame models under the original and upgraded input motion.

Table 7.8 Response of Bare frame model to amplified input motion

Variable	Copala	3*Copala	5*Copala
Hor. Max. roof acceleration (mm/sec^2)	1317.28	3189.50	3672.26
Hor. Max. roof displacement	154.30	356.00	480.26
Roof Displ. 1st frequency	0.36	0.31	0.31
Max. drift (L6-Roof)	0.0044	0.0104	0.0148

Table 7.9 Response of Masonry frame model to amplified input motion

Variable	Copala	2*Copala
Hor. Max. roof acceleration (mm/sec^2)	-1539.88	-3146.95
Hor. Maximum roof displacement	-98.48	-248.22
Roof Displ. 1st fundamental frequency	0.60	0.50
Maximum drift (L6-Roof)	0.0024	0.0048

7.8.2 Forces under upgraded motions

When a model is subjected to an amplified input motion the result is an amplification of the computed reactions at its base, however the important matter is to determine the percentage of amplification. Fig. 7.30 shows the overall maximum and minimum

reactions computed for the Bare model when it is subjected to 3 and 5 times upgraded motion. Fig. 7.31 shows the results for the Masonry frame subjected to twice the original input motion. The figures illustrate the variation in amplitude with the upgrading of the input motion[90].

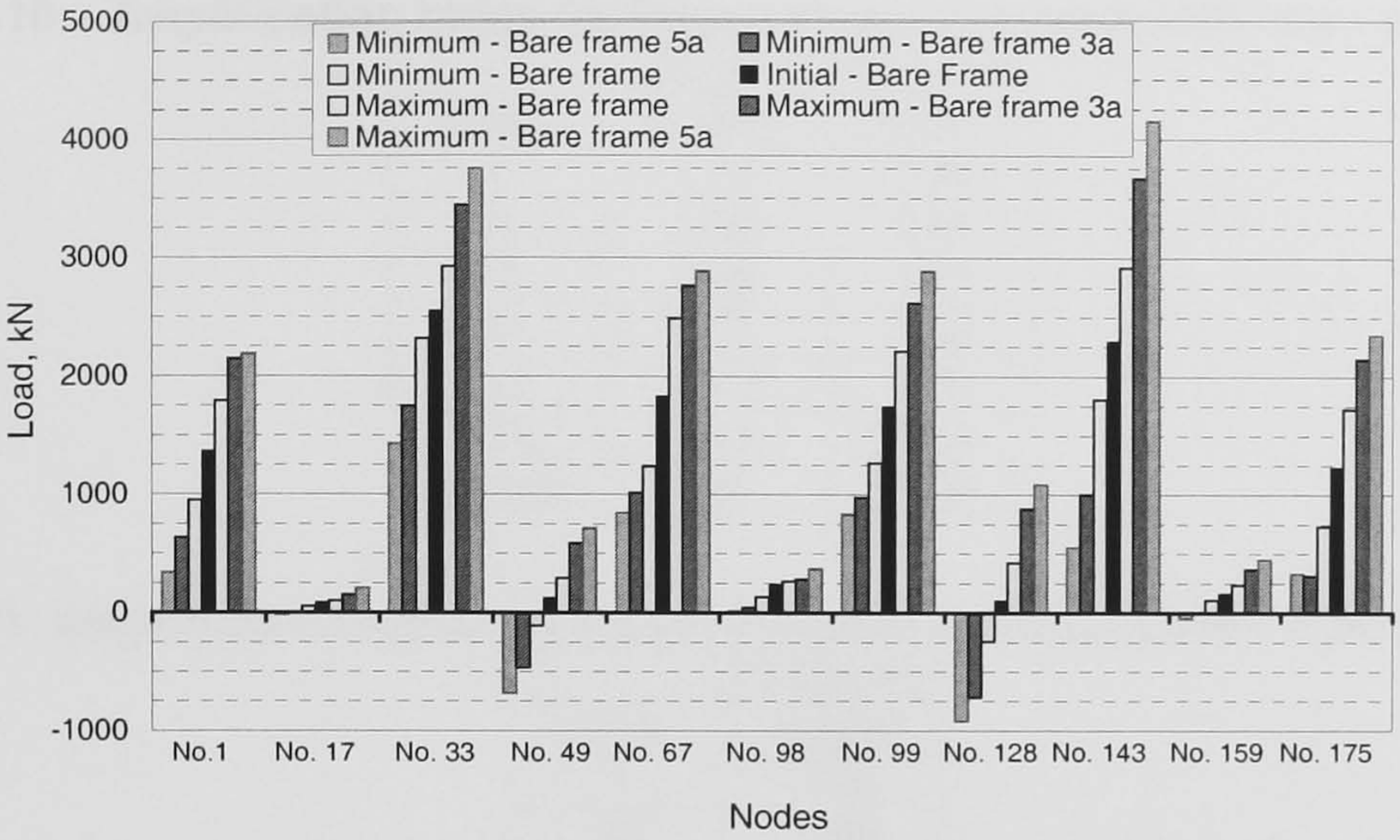


Fig. 7.30 Maximum and minimum reactions for Bare frame under amplified motions

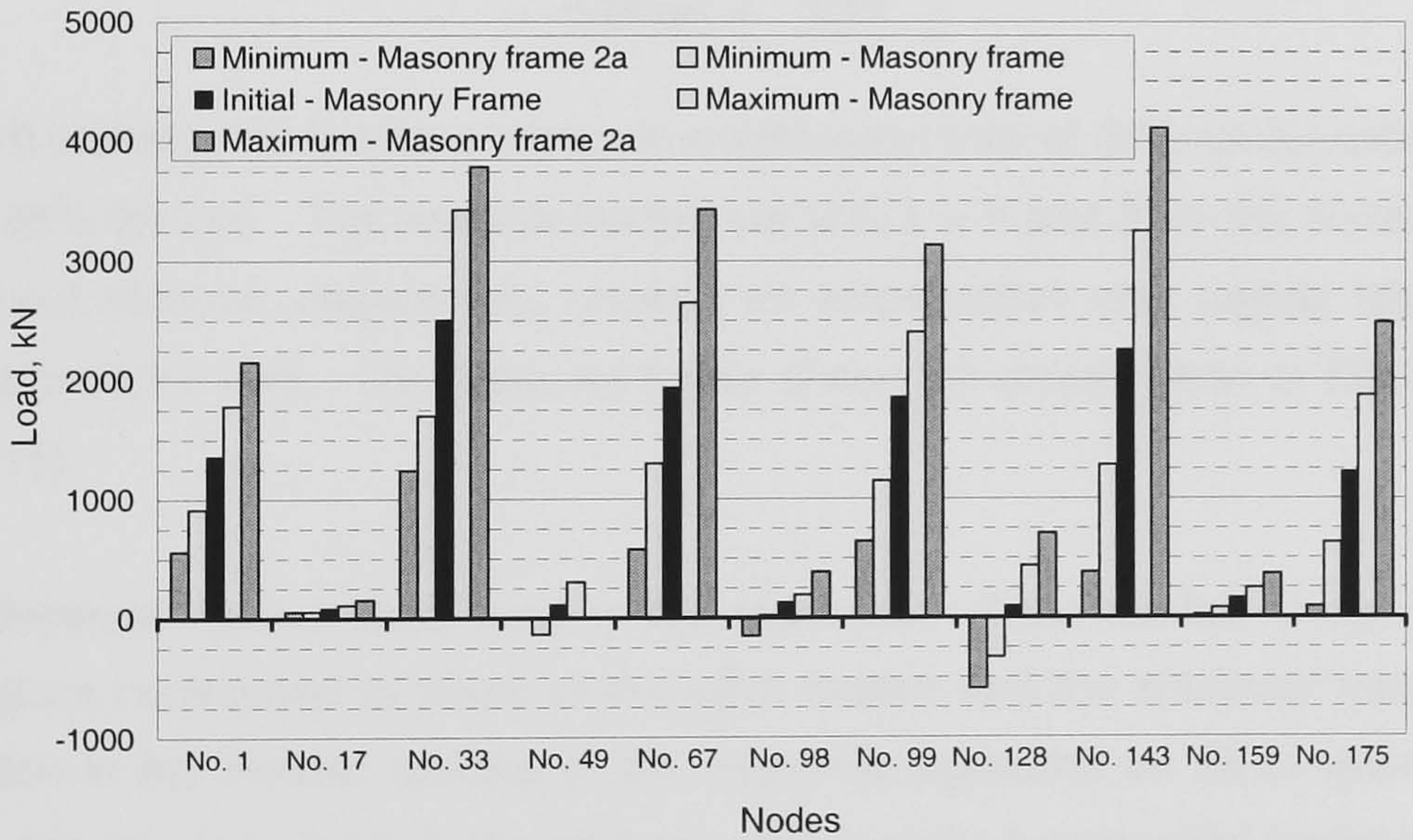


Fig. 7.31 Maximum and minimum reactions - Masonry frame under amplified motions

Figs. 7.30 and 7.31 show that the largest seismic amplitudes are located at the nodes 33 and 143, although their ratios respect to the initial static loads are slightly smaller than those for nodes 1 and 175.

---

[90] The values included in the figures are absolute values. Absolute values are those maximum or minimum values for the complete time history, which does not necessarily belong to the same cycle.

An indication of the amplification of the reactions can be obtained from the spectral ordinate of the fundamental frequencies in Fourier spectra. Tables 7.10 and 7.11 show the results of these analyses for the nodes where columns are located.

Table 7.10 Amplification ratios for Bare frame under upgraded input motions

	3*Copala	5*Copala
Node	Fourier	Fourier
1	1.19	1.20
33	1.86	2.40
67	0.89	1.00
99	0.92	1.20
143	2.10	2.80
175	1.14	1.20
Average	1.35	1.65

Table 7.11 Amplification ratios for Masonry frame under upgraded input motions

	2*Copala
Node	Fourier
1	1.23
33	1.48
67	1.72
99	2.06
143	1.43
175	1.08
Average	1.50

Table 7.10 indicates for the Bare frame an amplification ratio of 35% for the analysis with λ=3 and 65% for λ=5. The analysis carried out with λ = 5 and 3 for the horizontal and vertical input motions, respectively, showed an amplification ratio slightly higher than those obtained for λ=3. The Masonry frame shows an amplification of 50% for λ=2 (Table 7.11).

The fundamental frequencies found in the responses of the models under amplified input motions correspond to those of the input motion and the structural model. The modification in the Fourier spectra of the response appeared as increments in peak spectral ordinates (see Table 7.10 and 7.11), mainly at the fundamental frequency of the input motion. Another modification of the upgraded input motion was a reduction in the frame model fundamental frequency, which for the Bare frame passed from 0.36 Hz to 0.31 Hz, (the latter for the analyses under λ=3 and 5). The fundamental frequency for the Masonry model did not show such a reduction, maybe due to the smaller amplification for the input motion. The reduction in frame fundamental frequency could be the result of a wider non-linear response of the model when subjected to a stronger motion.

A complete analysis of the axial base reactions and axial pile forces is presented in Chapters 10 and 11.

CHAPTER 8

THE BASE REACTIONS DEVELOPED ON THE PC BUILDING DURING SEISMIC SHAKING

This chapter reports the Author's analysis to determine the seismic reactions at the base of a transversal frame of the PC Building. Reactions obtained from both the Copala 1995, which is used to calibrate the building structural model, and a simulated 1985 event are included. For the calibration procedure several frame structural configurations were proposed, analyzed in ADAPTIC, and evaluated against the recorded response. The results from the original configuration of the frame and the optimum calibrated model are shown.

The calibration procedure is mostly concentrated in the location of the reinforced concrete walls that were added after the 1985 event, and whose location and performance are not known. The results of the analyses indicate that the reinforced concrete walls, if they were placed along the complete building tower height, could be damaged or detached from the building frames.

It is important to remember that due to the non-linear response of buildings a calibrated model is strictly valid only for the event under which it is calibrated.

8.1 A general description of the PC Building

The PC building is located in the Colonia Roma in an area that usually sustains high accelerations during earthquakes (Fig. 6.14). It is a 17-storey reinforced concrete structure that includes a basement with a perimeter of reinforced concrete walls, ground floor, mezzanine, eight alternated parking levels joined by ramps, and a 12-storey tower, the plan dimension of which reduces with height. The inter-storey height is 3.15 m and the total height of the building is 51.4 m. As observed in plan and elevation in Fig. 8.1, the building has an irregular shape.

Mr. Marcos Macias[91] made available the structural drawings (containing the building

---

[91] Seismic Instrumentation Division of the Engineering Institute of the National Autonomous University of Mexico (UNAM)

geometry and the dimensions and reinforcement characteristics of the structural elements) and the accelerometer records required for the Author's seismic analyses. Muria-Vila (1997) and Alcantara, et al. (1999) have presented studies of the building's response to static and seismic loading.

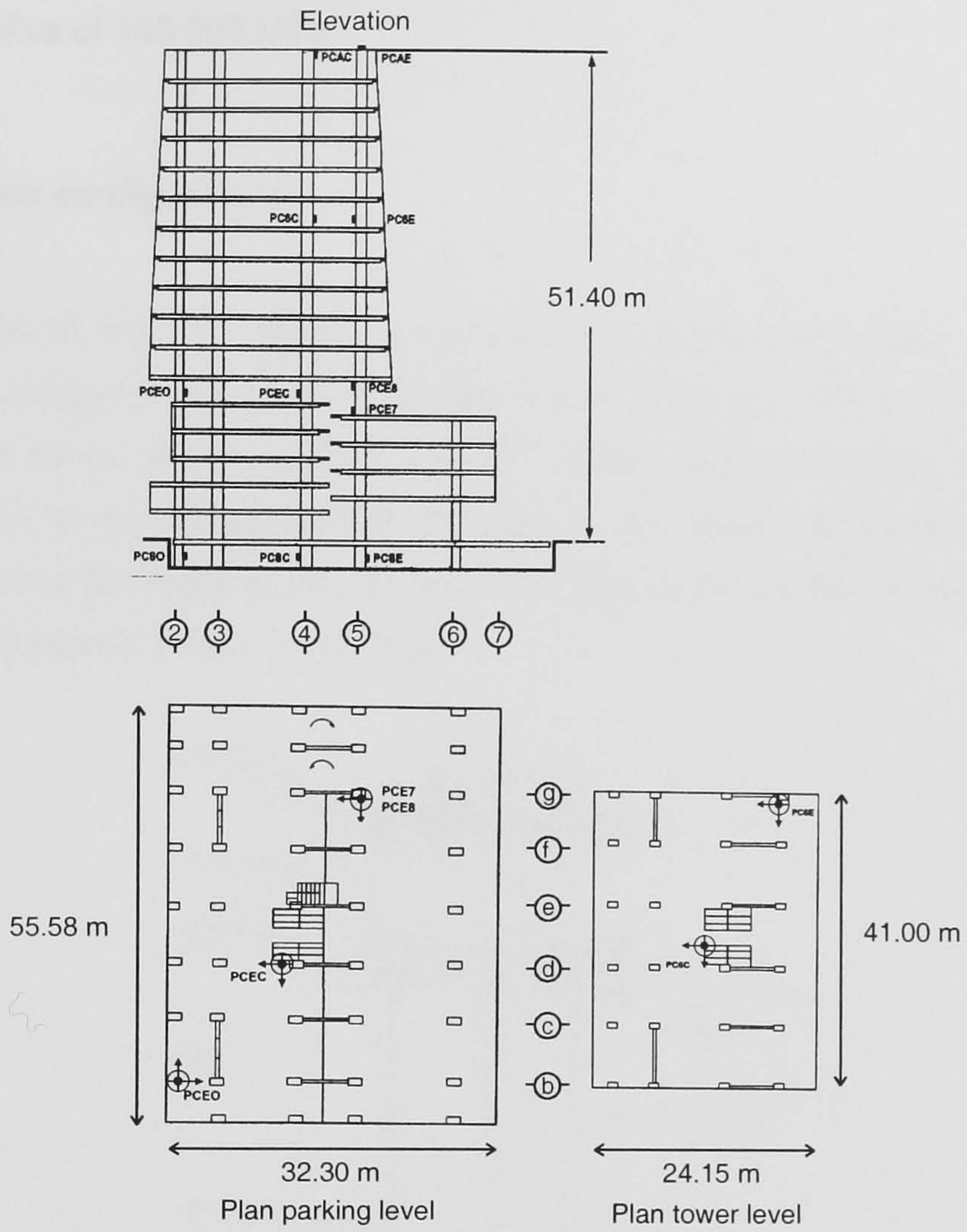


Fig. 8.1 Elevation and plan views of PC building (after Alcantara, et al. , 1999)

8.2 Structural configuration and material characteristics

Originally, the structure consisted of waffle[92] slabs supported on rectangular columns (Fig. 8.7), masonry infill and a core of concrete shear walls around the shaft for staircases and elevator (Fig. 8.1). It is known that the building sustained light damage during the 1985 earthquake which was repaired by placing reinforced concrete walls in some frames and substituting masonry walls for reinforced concrete walls. Unfortunately there is no specification regarding the location of the new concrete walls since a complete survey of the structural state of the building has not been carried out.

---

[92] 450-500 mm thick flat plate.

The material properties for the analysis are those specified in the structural drawings provided by Mr. Marco Macias. From the basement to the fifth floor, the concrete compressive strength is 30 MPa, and from the sixth floor to the roof, the compressive strength is 25 MPa. The reinforcement bars' axial yield stress is 412 MPa with a Young's modulus of 195 800 MPa.

8.3 Foundation configuration

The foundation of the PC building is typical of the Mexico City (MC) Lake zone. It consists of a reinforced concrete box resting at a depth of 3.30 m on 266 triangular friction piles of 65 cm side and 27 m length[93]. In this configuration the piles carry most of the weight of the building and since the piles do not reach the firm stratum (Fig. 8.2), in ideal conditions the building would sink at the same rate as the regional subsidence. The foundation plan is shown in Fig. 8.3.

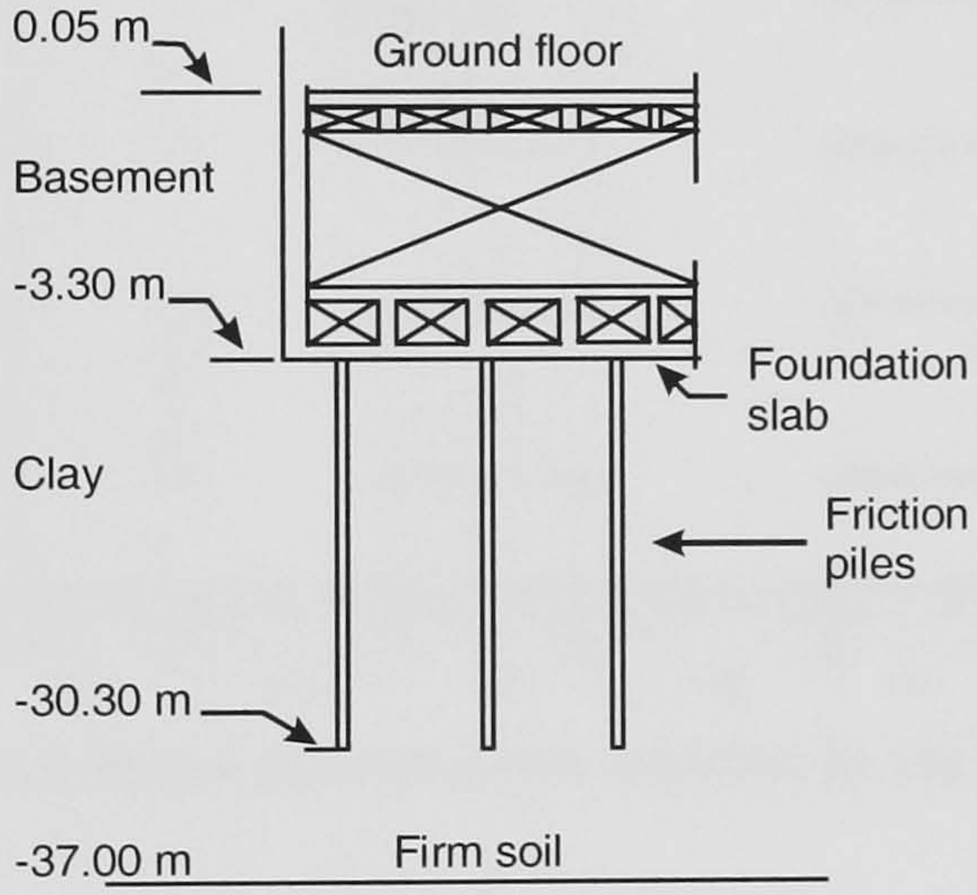


Fig. 8.2 PC Building pile foundation solution

The construction procedure for the foundation was as follows: (i) a 1.55 m deep excavation was carried out in the basement area; (ii) a 7.5 cm diameter 20 m deep pre-boring was carried out just before the piles were installed; (iii) the reinforced concrete piles were driven; (iv) the excavation was continued until a depth of 3.20 m; and (v) the pile heads were demolished to enable them to be fixed to the foundation slab.

No geotechnical profile was available for the PC site. However, a good data set was established for the JAL building (approximately 300 m from the PC building), and this

---

[93] The piles consist of 2 or 3 pre-cast sections united by welding.

profile was adopted to characterize the PC building site (see section 7.3). The building is located in a region with a fundamental period of 2 seconds (Fig. 6.14 and Table 8.2).

The friction pile capacity computed applying the Imperial College pile design method is 1866 kN (190.2 tons). The effects of the triangular cross-section and pre-boring were allowed for by adopting Jaime, et al.'s (1991) correction factors. The general characteristics of the piles and the static capacity computation process are shown in Appendix C.

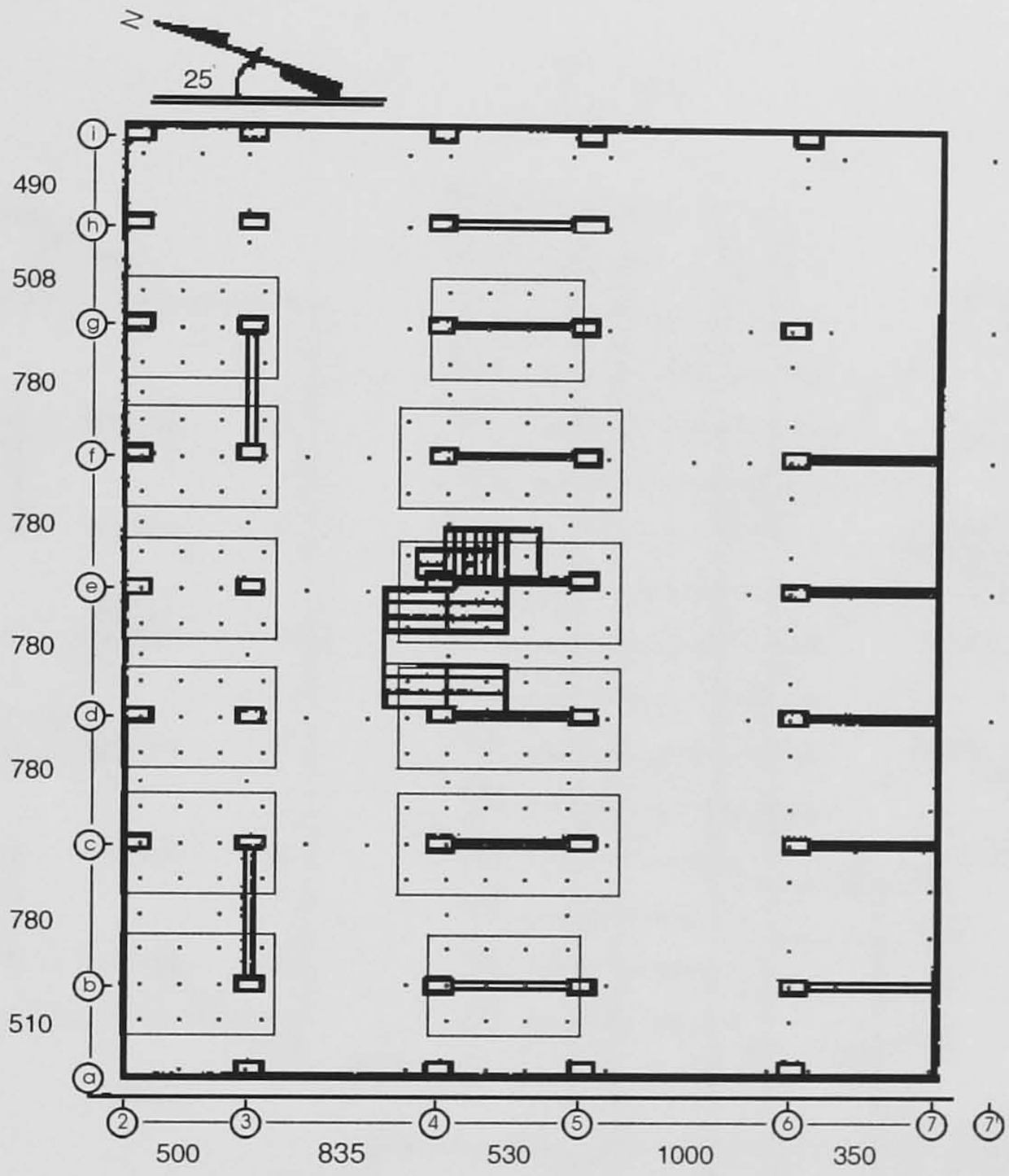


Fig. 8.3 Foundation plan and pile location in the PC Building

8.4 Instrumentation and input motions

The number and location of instruments installed in the PC building were designed based on its structural characteristics. Eleven accelerometers were installed in 1990, including: three instruments at the basement, two of them at the extreme columns and a third at the center; four instruments at the 4th level; two at the 10th level; and two instruments at the roof. Two additional instruments were installed in 1999, one at the Garden (free field) and another at the south side of the basement (Muria-Vila, et al., 2000).

Instruments PCSE, PCE7, PCE8 and PCAE are located along a vertical axis that starts in the basement and finishes at the roof. The same is true for instruments PCSC,

PCEC, PC6C and PCAC. Fig. 8.4 shows the location of the instruments in plan and elevation and their components positive directions.

All instruments are triaxial digital accelerometer interconnected in a master-slave configuration under the same time record. When the pre-established acceleration threshold is passed in the master instrument, this sends a signal to all the others instruments to start recording. In addition, each instrument can work independently with its own memory and threshold (Muria Vila, 1997).

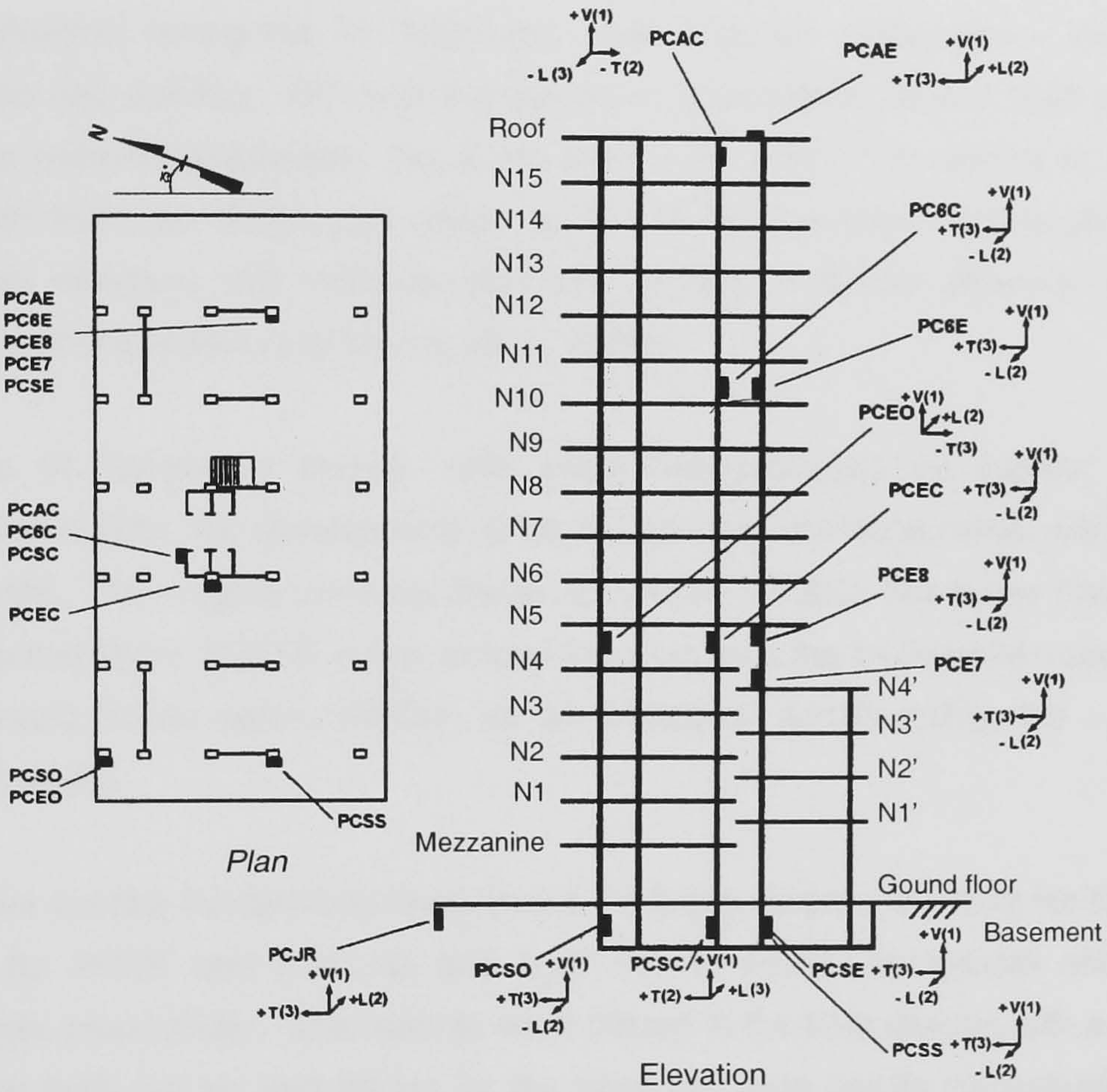


Fig. 8.4 Overview of the building instrumentation (Alcantara, et al. 1999)

The array recorded for the first time on May 11, 1990 and since then all the major earthquakes affecting MC have been recorded. Table 8.1 shows details of the considered more important earthquakes and their maximum recorded accelerations. (In Table 8.1, EP is the epicentral distance, km.; * Magnitude M_s; $^{+}$ Magnitude M_E.)

Table 8.1 Maximum registered accelerations at PC building, cm/s^2 (Alcantara, et al., 1999)

Date	Mw	EP	Depth	PCSE	PCE8	PC6E	PCAE
11-05-90	5.3	317	12	-3.65	-6.39	10.56	-19.72
31-05-90	5.8	315	16	-7.10	-14.32	-21.30	-35.45
01-04-91	5.5	382	26	-3.29	-5.87	11.07	15.57
15-05-93	5.8	334	20	10.85	-12.78	39.72	53.46
24-10-93	6.2	319	19	-15.10	23.79	59.42	-89.89
10-12-94	6.5	280	20	-17.28	-32.18	115.85	-169.34
14-09-95	6.4	298	22	-34.38	-46.88	-140.45	-195.27
11-01-97	6.8	417	17	18.08	40.24	-88.62	-164.78
15-06-99	6.7$^+$	223	92	-26.11	40.00	-95.80	166.69

The maximum acceleration recorded is 195 cm/s^2 for the transversal component of the PCAE instrument during the 14 September 1995 "Copala" earthquake – same event as for the JAL building. Although the maximum acceleration for the 1999 event was also in the transversal direction, this is not always the case. The events of 1997 and 1994 (both from the Michoacan coast) produced the maximum acceleration in the longitudinal direction, this indicates that the building response depends upon the earthquake characteristics (Alcantara, et al., 1999).

Since the 14 September Copala 1995 event has produced the highest recorded acceleration to date, the development of the PC building structural model will be based on this event. The records used are Basement Center (PCSC), Basement East (PCSE) and Basement West (PCSO) in the vertical direction, and the transversal component of the Basement Center record (PCSC) for the horizontal direction (Fig. 8.5 – note the change of scale).

The Fourier spectra fundamental frequencies for these records are 0.42 Hz for PCSO, 0.46 Hz for PCSE and 0.46 Hz and 0.32 Hz for PCSC transversal and vertical components, respectively. The records were filtered in the time domain with a low pass digital filter (with 0.2 Hz and 20 Hz as the pass and stop bands respectively) before using them in ADAPTIC.

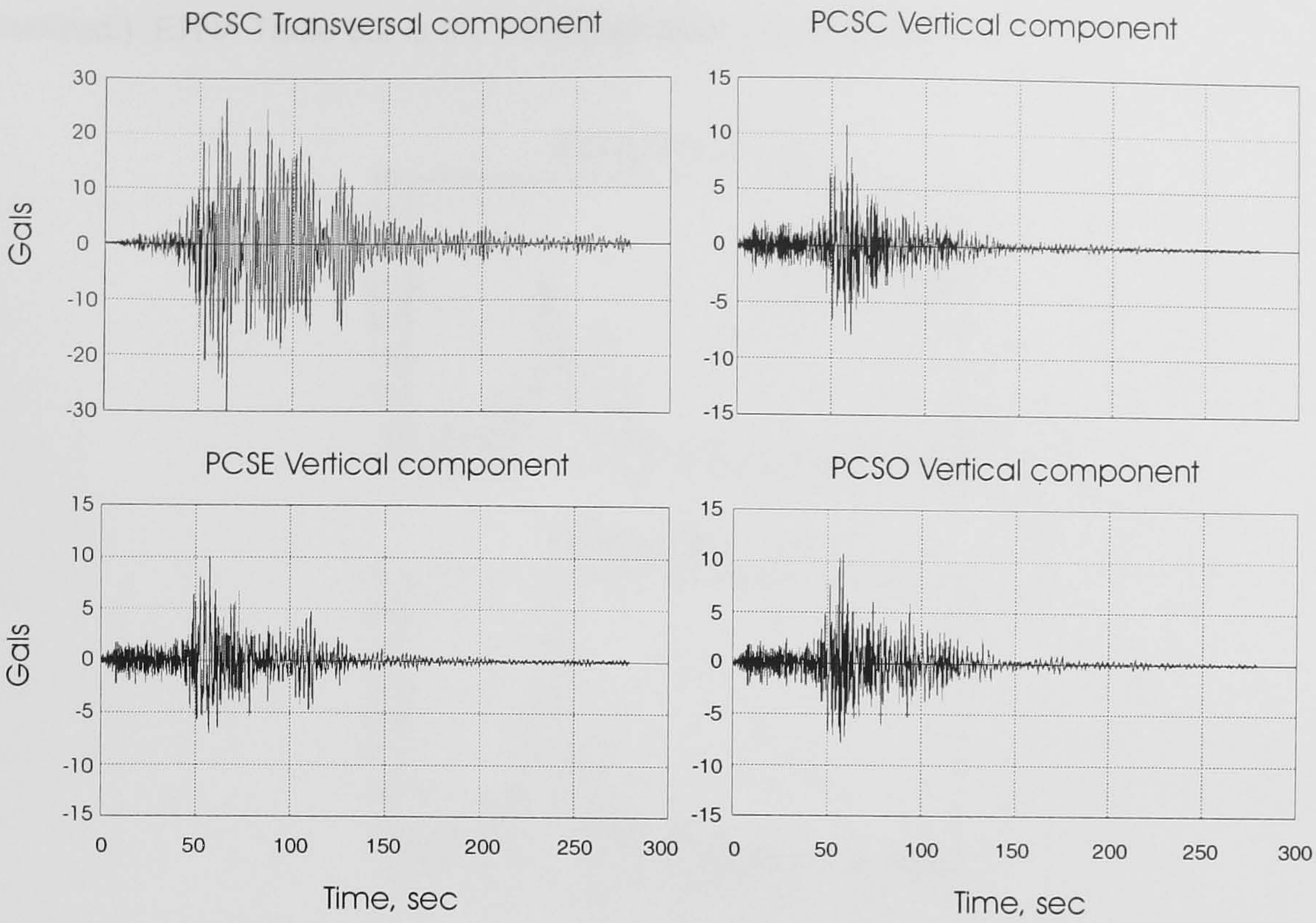


Fig. 8.5 Input records for PC dynamic analysis (19-09-1995 event)

8.5 Behaviour of the building during earthquakes

Muria-Vila (1997) presented a study of the characteristics of the PC structural system through the spectral analysis of its recorded response. The study consisted of computing the Fourier transfer and several spectral ratios in order to obtain the fundamental frequencies associated with the soil structure system.

The spectral ratios between roof and basement (PCAC/PCSC) obtained by Muria Vila (1997) for the longitudinal and transversal components of four events are shown in Fig. 8.6. Considering that in the case of a linear system the fundamental frequencies for each of the events would be the same, the figure shows that the building undergoes non-linear behaviour.

Table 8.2 compares the fundamental frequencies identified for the four events in Fig. 8.6. The table indicates that, as for the JAL building and many others (Durrani, et al., 1994; Foutch, 1978), the fundamental frequencies of vibration depend upon the amplitude of excitation. Furthermore, the soil-structure system's fundamental frequencies show a clear decay due to the accumulated effects of successive earthquakes – mainly for the longitudinal (L) and torsional (R) components. (This reduction in frequencies is reported to occur even when structural damage is not

involved.) ER in Table 8.2 is the maximum spectral acceleration.

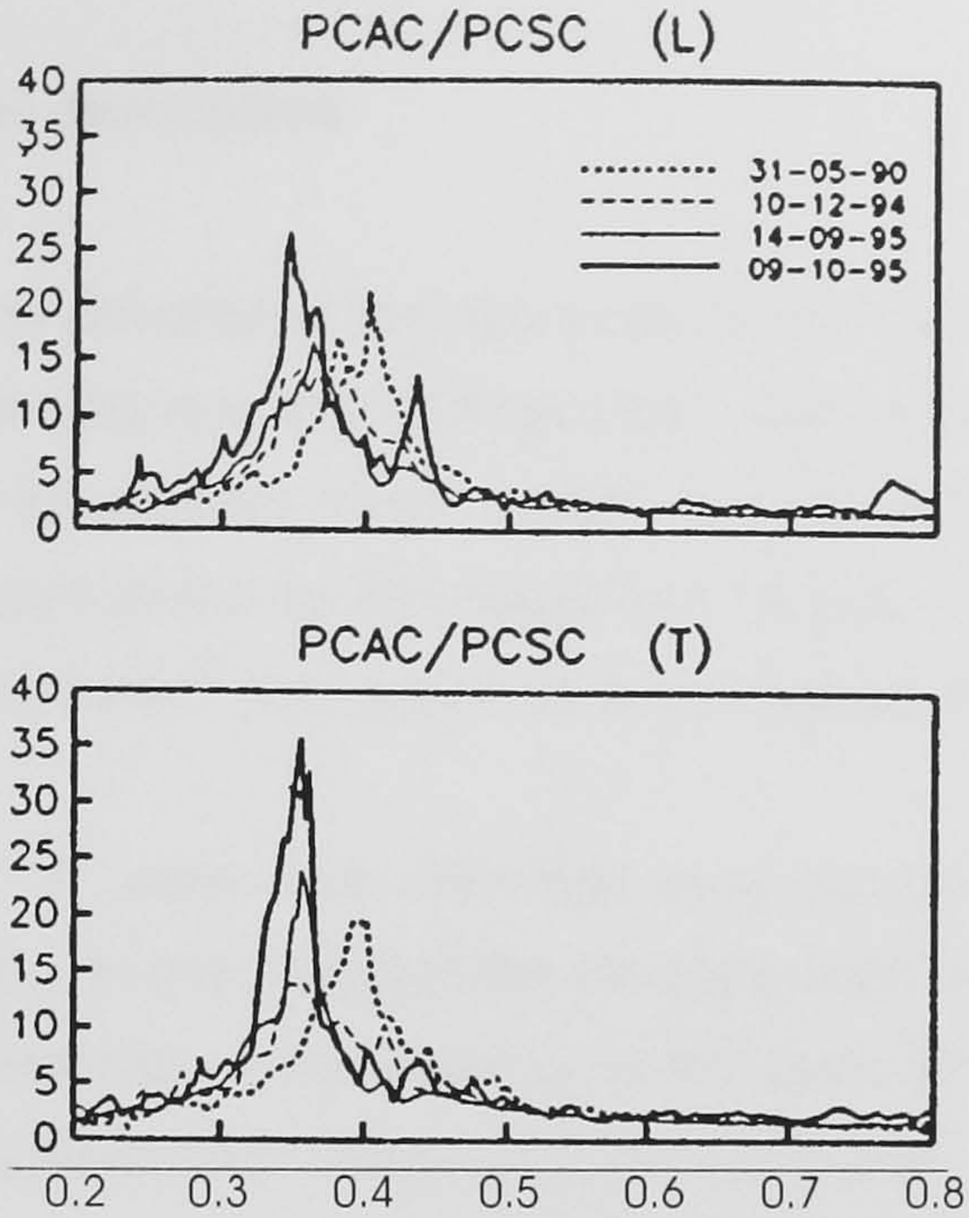


Fig. 8.6 Roof (PCAC) vs. basement (PCSC) spectral ratios for PC building

Table 8.2 Recorded response of the PC Building (Muria Vila, 1997)

Date	Frequency (Hz)				Acceleration (gal)				ER (gal)
	Ground	Building			Building				
					Base		Roof		
		L	T	R	L	T	L	T	
31-05-90	0.45	0.40	0.38-0.40	0.47-0.57	6	7	35	39	25
10-12-94	0.45	0.34-0.38	0.34-0.36	0.45-0.52	9	15	90	170	99
14-09-95	0.45	0.36	0.36	0.41-0.43	32	30	151	195	139
9-10-95	0.45	0.35	0.34-0.36	0.39-0.42	15	16	72	106	98

As described for the JAL building, the non-linear behaviour could be attributed to several structural features and to soil-structure interaction effects. Among the former are: (i) changes in the elastic modulus of concrete with time; (ii) discontinuities among structural elements; (iii) reduction in lateral stiffness of the building due to damage in the reinforced concrete and masonry infill walls during seismic events; and (iv) cracking of the floor system and degradation on the structural and non-structural elements under several seismic motions.

The strong similarity between the motions recorded at basement of the building and at surface free field suggests no significant discontinuities at the foundation-soil interface, and that the soil-foundation interaction does not contribute to the overall non-linear behaviour of the structure (Muria and Del Toro, 1998).

8.6 Modelling

8.6.1 PC building model description

The Author's approach to developing the structural models was set out in Section 6.1. The model developed corresponds to the transversal external frame of the tower (G axis in Fig. 8.1). The bare longitudinal frame model consists of 162 nodes, and 224 tri-dimensional elements represented by 22 column and 18 beam sections. 4 flexural wall sections and damping elements[94] are used to develop alternative models.

The effective widths of "T" beam slab elements were computed following the British Standard BS 8110 (1998). In this standard the effective width of a flange beam is equal to the web width plus one fifth of the distance to the point of zero moment (Fig. 8.7) (Handbook to British Standard, 1987; Nilson and Winter, 1986).

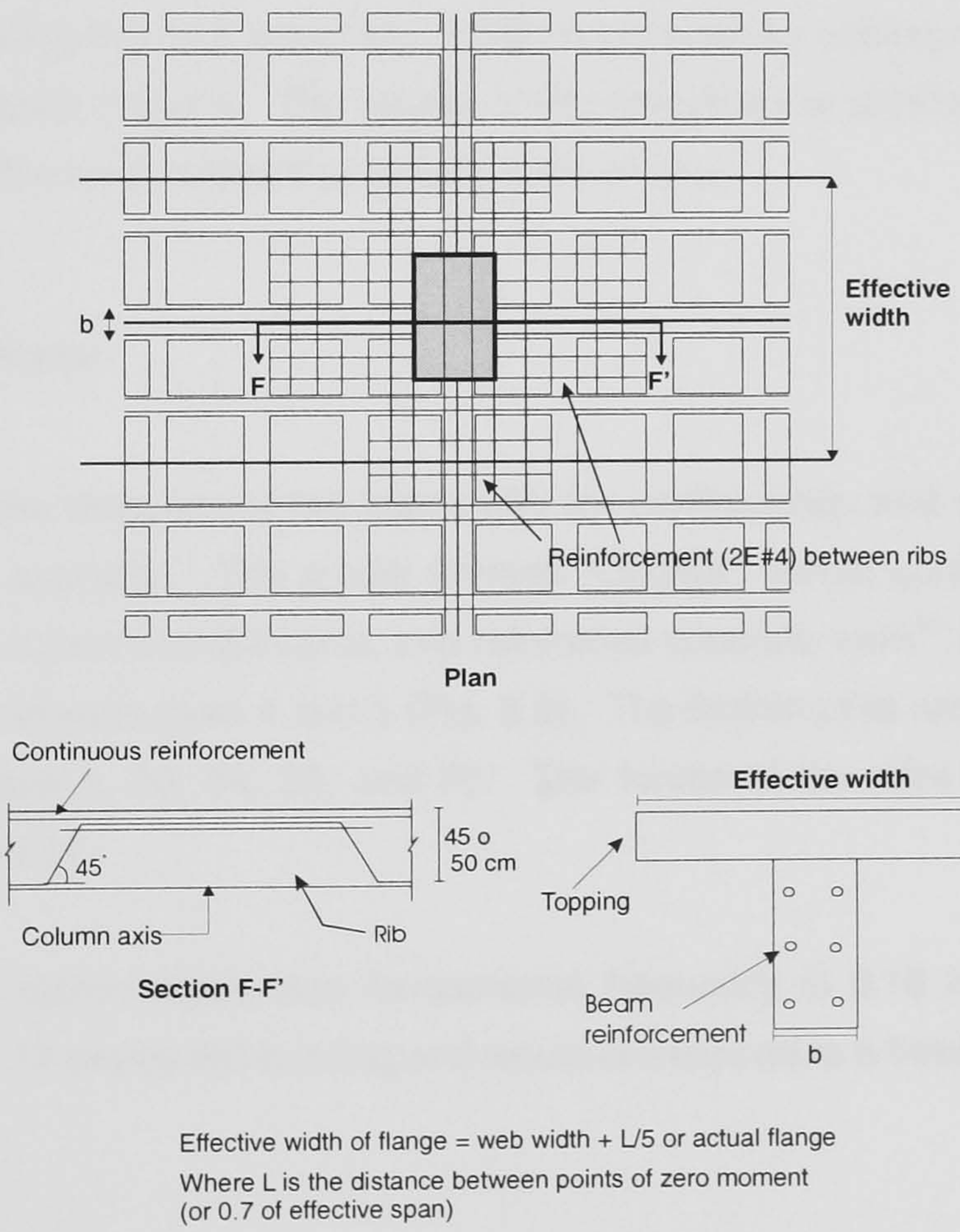


Fig. 8.7 Slab and beam effective width details

---

[94] Rayleigh damping elements are used to simulate extra sources of damping (e.g. produced by friction during dynamic excitation).

The vertical loads consist of the self-weight of the slabs, transverse beams, columns and shear walls and the quasi-permanent static load – the latter according the 1987 MC building code (Garcia-Ranz, et al., 1988). The analyses were carried out for 200 sec at 0.01 sec intervals.

The calibration procedure defined in Chapter 6 and applied in Chapter 7 was adopted to calibrate the structural model so it predicted the PC building behaviour better. Due to the lack of information on the performance of the structural and non-structural elements of the building and the modelling limitations (e.g. impossibility of using cracked elements) the calibration analysis was based on the location and properties of the reinforced concrete walls and on the quantity of damping applied.

Although several structural models were used to study various aspects of the seismic response of the building only the results from two configurations are presented. Those include: (i) the original configuration (obtained from the original structural drawings) consisting of the bare frame plus concrete walls between axes 4 and 5, and; (ii) the configuration giving the best prediction, which is obtained by adding reinforced concrete walls between axes 3 and 4. The results of the analyses are presented concisely, and peak values of the most relevant parameters are shown.

8.6.2 Original frame

In this section the response of the frame with the configuration that sustained the 1985 earthquakes is analyzed. The model (termed "Original" frame) consists of 4 bays, 17 levels made of columns and beams, and reinforced concrete walls[95] from the basement to the 4th floor between axes 4 and 5 (Fig. 8.8). The friction piles are located below the columns at nodes 1, 20, 39, 58, and 76. The forces at the piles are established in Chapters 10 and 11.

The computed elastic eigenvalue fundamental frequency is 0.18 Hz, which is a low frequency for a 17-storey RC building and would correspond to a flexible structure.

---

[95] Represented with flexural walls sections.

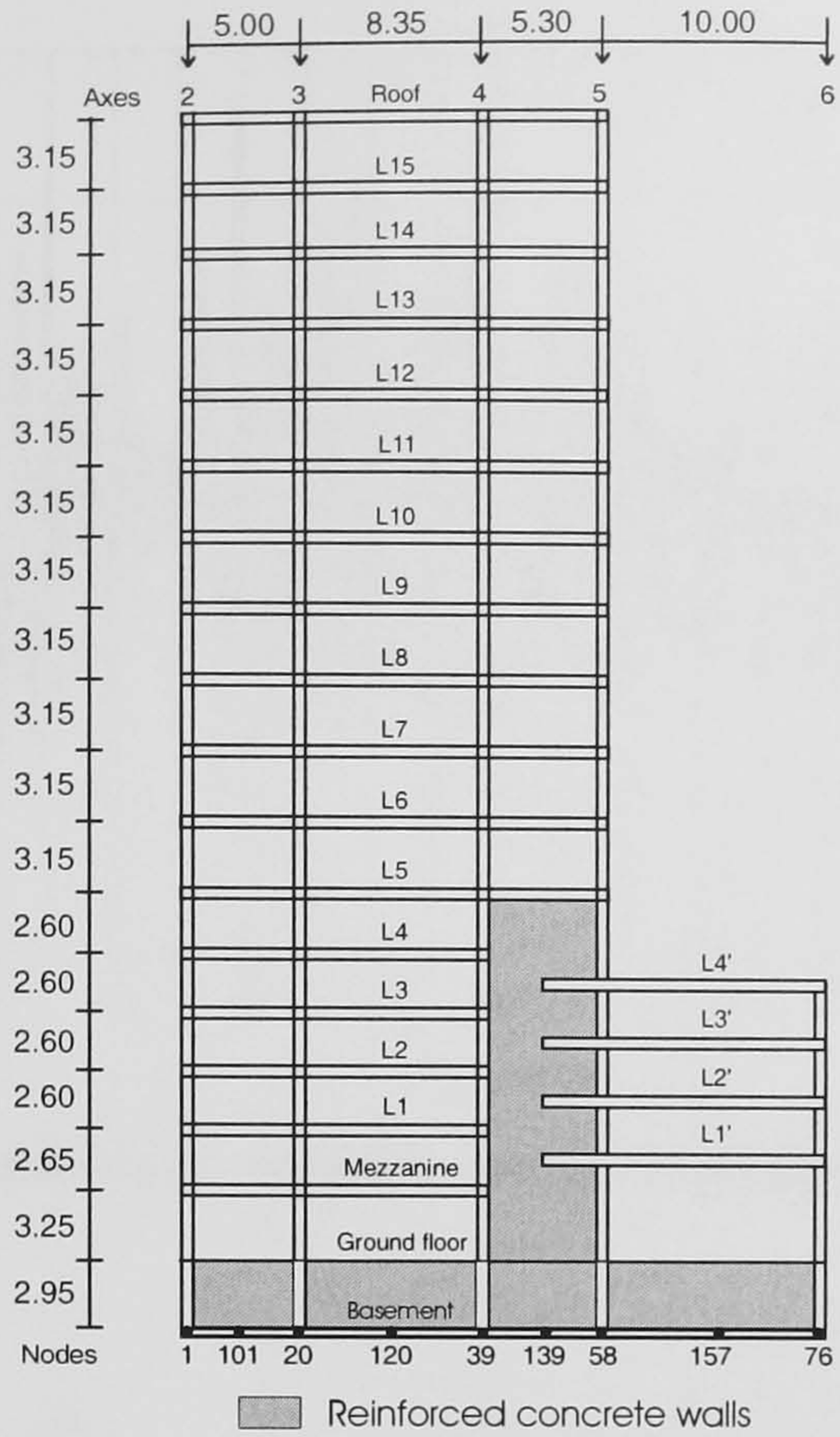


Fig. 8.8 PC Building, Original frame configuration

The behaviour of the Original model under seismic loading was evaluated by comparing recorded and predicted accelerations at roof level for the Copala[96] 1995 event. The acceleration time history in Fig. 8.9 shows that although the model correctly represents the intervals of low and high acceleration amplitude, it under-predicts the maximum accelerations by up to 50%. Fig. 8.9 also shows that the period of the predicted accelerations is longer than the period of the recorded accelerations. Accordingly, the Fourier spectra shown in Fig. 8.10 indicate a fundamental frequency for the recorded accelerations of 0.33 Hz and for the predicted acceleration of 0.29 Hz. Both spectra show a second fundamental frequency at 0.45 Hz, although with bigger amplitude for the recorded acceleration.

[96] The same event than that used for the JAL building.

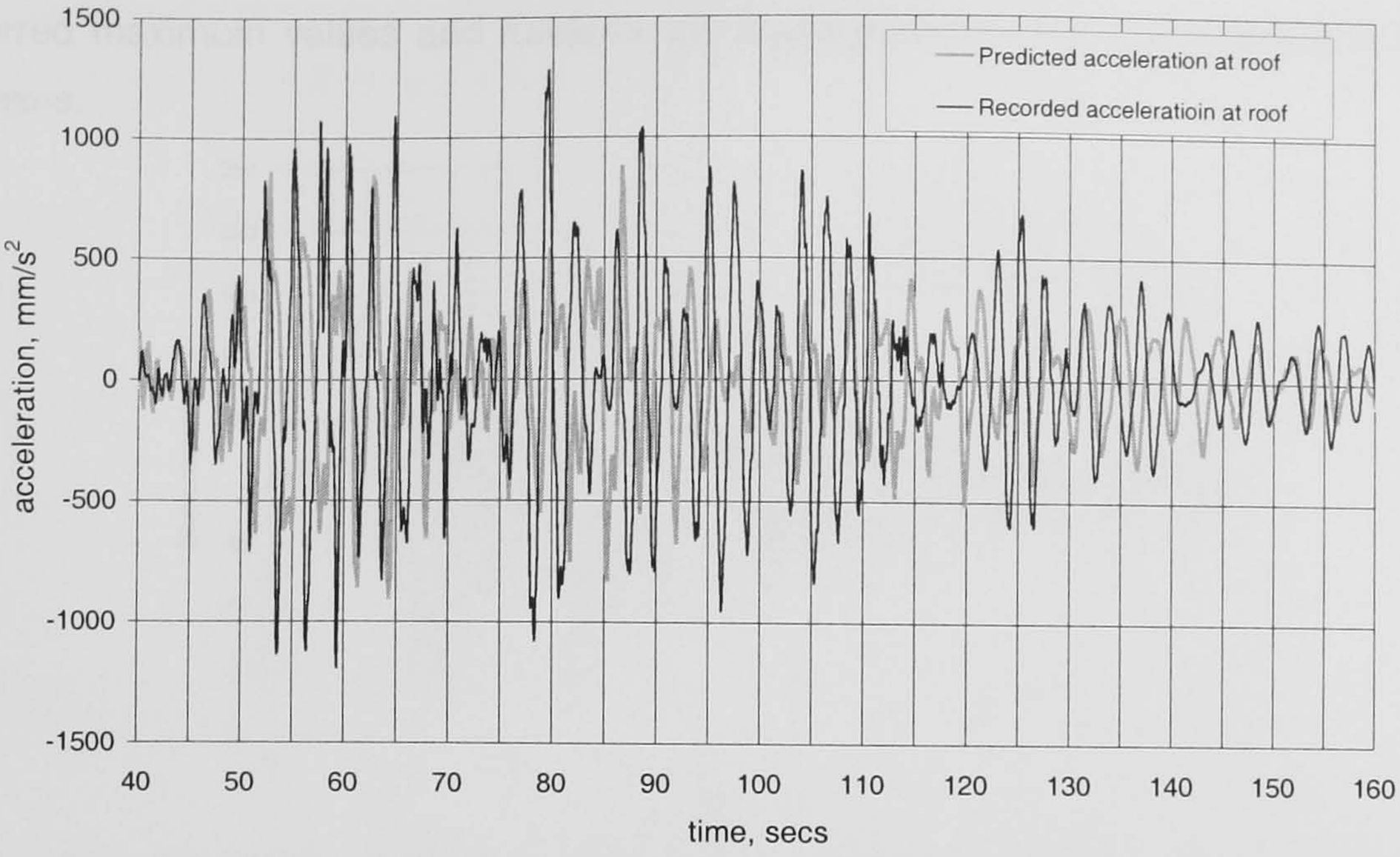


Fig. 8.9 Recorded and predicted roof acceleration, Original frame

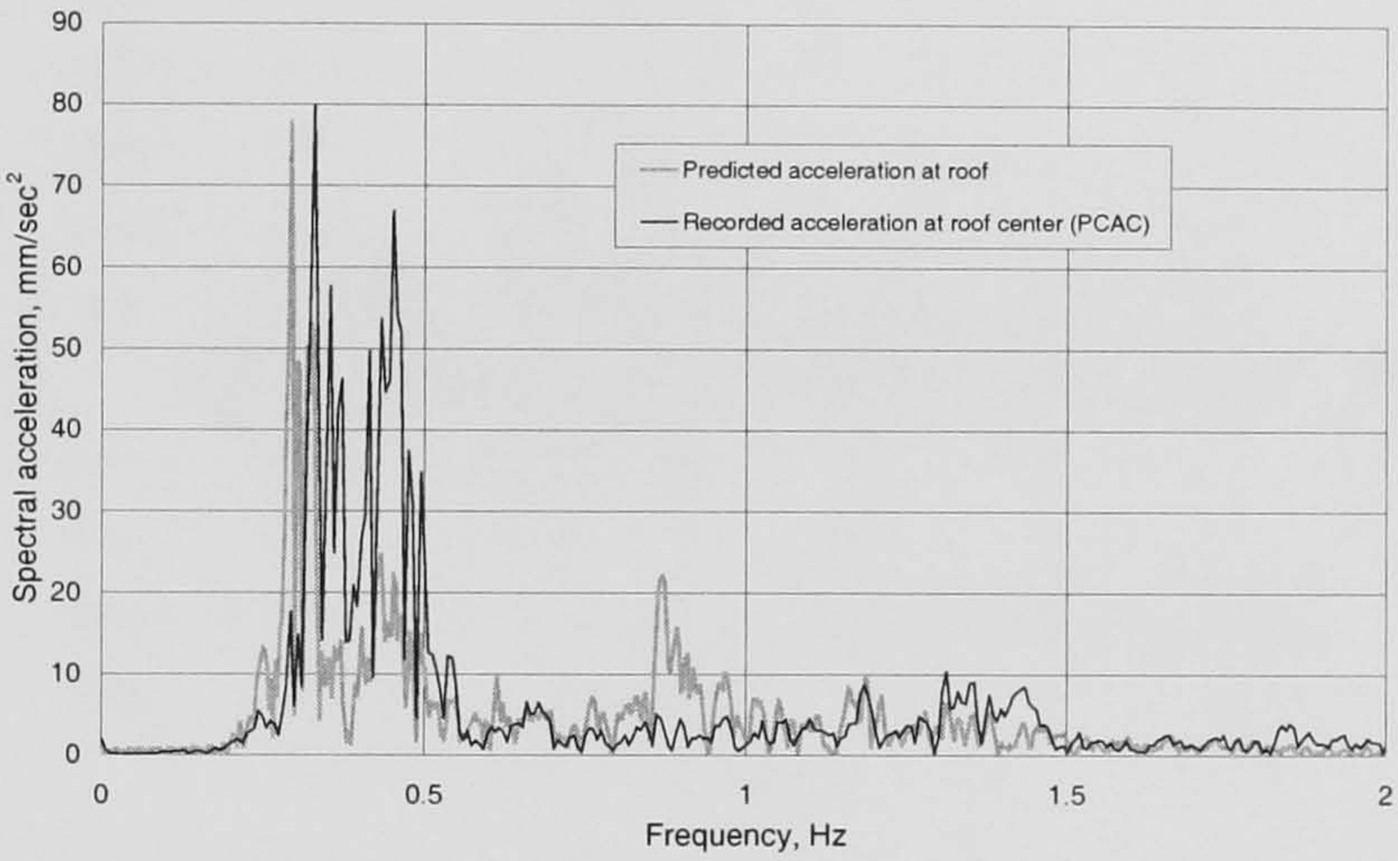


Fig. 8.10 Fourier spectra of recorded and predicted roof accelerations, Original frame

The inferred[97] lateral displacements of the building are slightly under-predicted by the Original frame model (Fig. 8.11). A more detailed description of the model behaviour is obtained from the predicted and inferred drift indexes[98] computed between the basement and the 5th floor and between the 5th floor and the roof (Fig. 8.12). The drift indexes indicate that the model is stiffer than the actual structure at the lower body and softer at the tower; these two responses combine to produce a good prediction of the displacements at roof. The inferred drift indexes are slightly smaller than those associated with the onset of structural damage. Table 8.3 presents the predicted and

---

[97] Displacements and drift indexes computed from recorded accelerations are denominated "inferred" displacement or "inferred" drift indexes.

[98] Drift index is the drift between two storeys divided by the distance between them.

inferred maximum values and fundamental frequencies for the displacement and drift indexes.

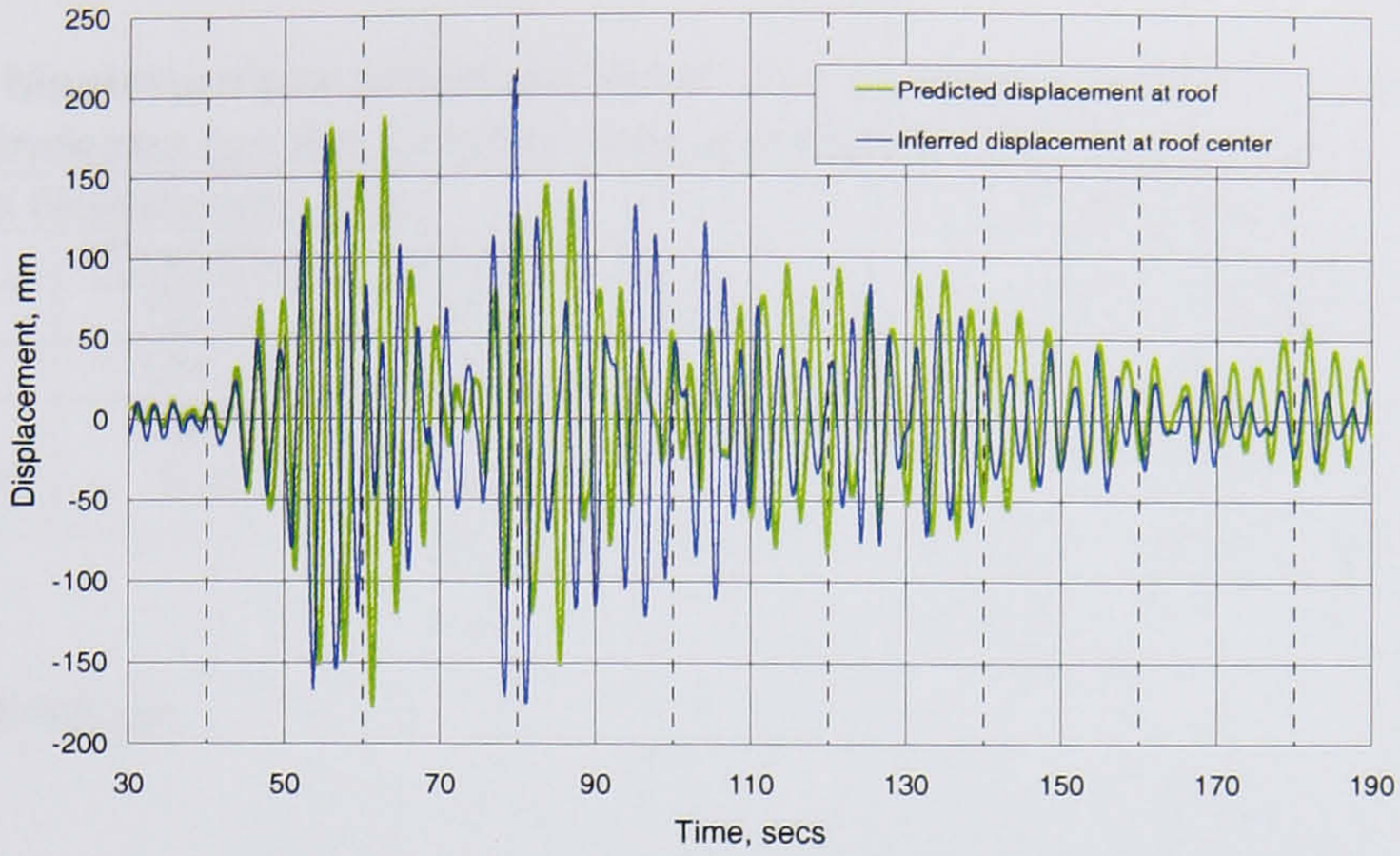


Fig. 8.11 Predicted and inferred horizontal roof displacements, Original frame

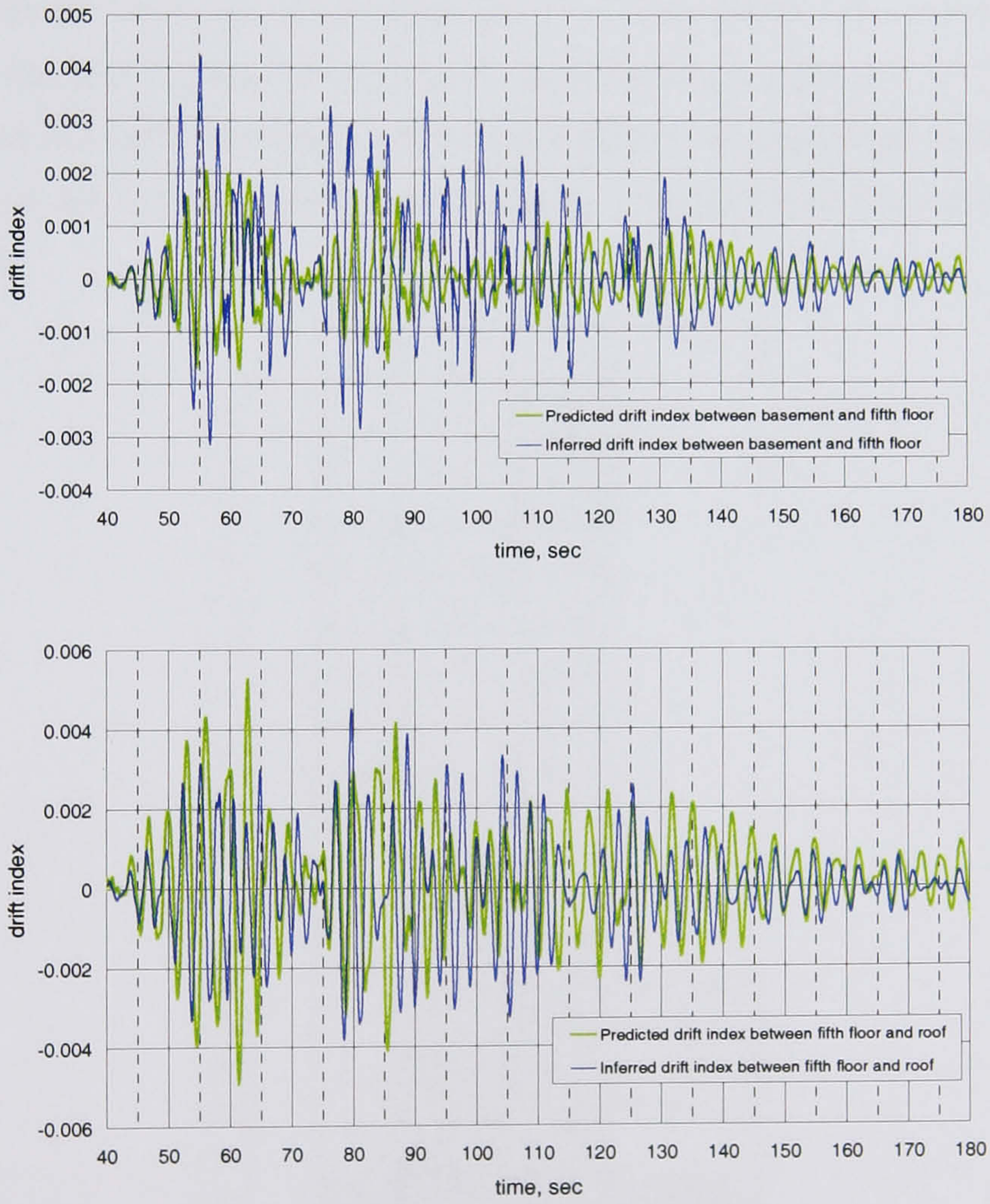


Fig. 8.12 Predicted and inferred drift indexes, Original frame

In general, the Original frame model slightly under-predicts the amplitude and fundamental period of accelerations recorded at roof. The amplitude of the

displacements at the roof is well predicted due to the combination in the model of a stiff lower section and a soft tower – this situation was relevant for the calibration procedure.

Table 8.3 Maximum predicted and inferred horizontal displacements and drift indexes for the Original frame model under Copala event

Lateral displacement (mm)			Drift index		
	Predicted	Inferred		Predicted	Inferred
5th Level	52.12	69.41	Basement - 5th Level	0.0020	0.0042
11th Level	134.76	-149.62	5th – Roof	0.0053	0.0045
Roof	186.38	212.07	Basement - Roof	0.0042	0.0042
Frequency (Hz)	0.29	0.34			

8.6.3 Selected frame

A calibration procedure was followed in which the structural model was "tuned" to improve the prediction of the recorded building response. The model that produced the best overall prediction consists of the Original frame plus reinforced concrete walls up to the 5th level at the bay between axes 3 and 4 (nodes 20 and 39) (Fig. 8.13). The fact that the included RC walls produced a better prediction does not mean that they actually exist or that there are no more walls in the building. The calibrated model is termed the "Selected" frame.

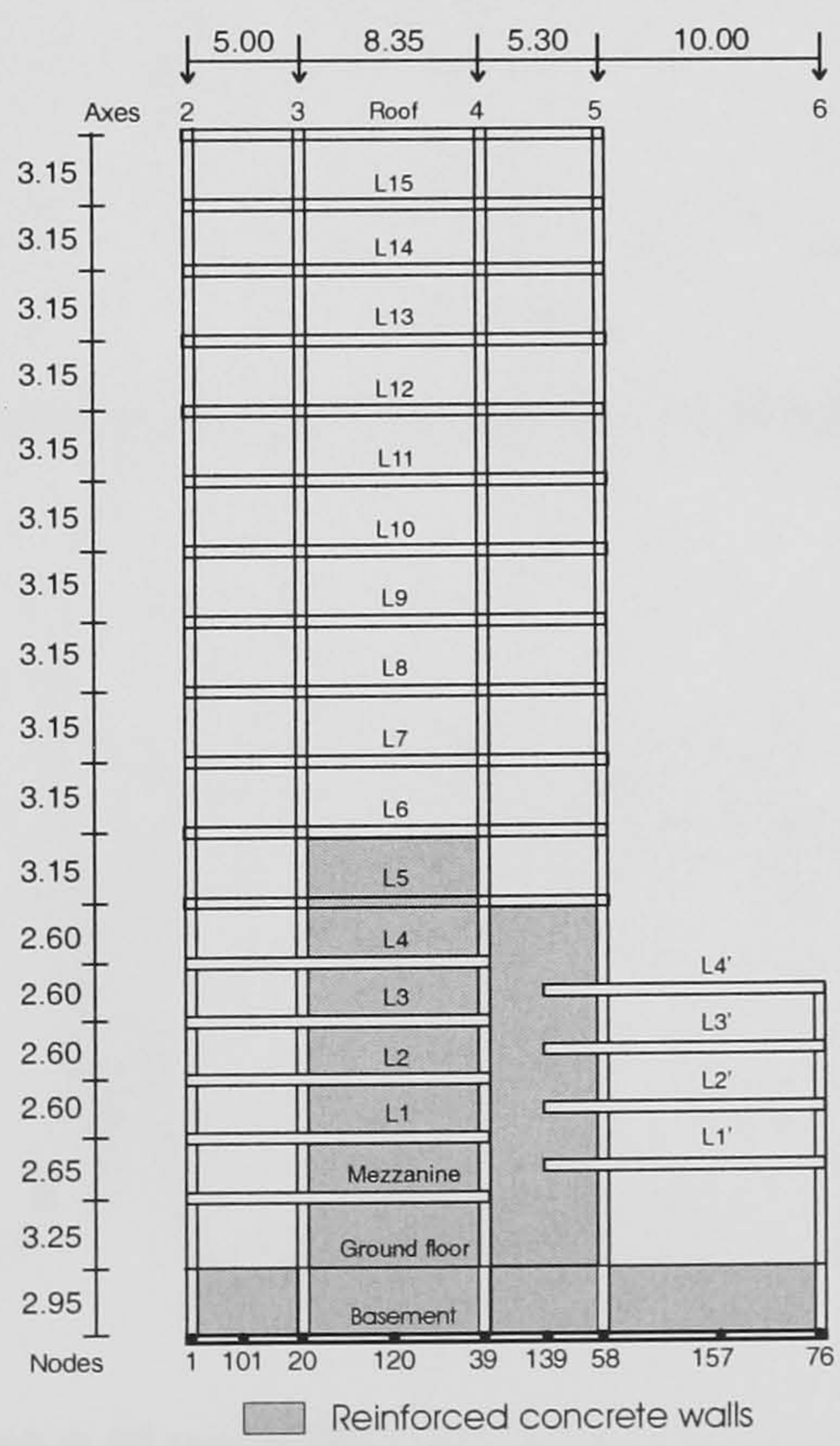


Fig. 8.13 PC Building, Selected frame model configuration

The predicted elastic eigenvalue fundamental frequency of 0.21 Hz (17% higher than

that for the Original frame) reflects the increment in stiffness produced by the included reinforced concrete walls. However, the building model is in the low frequency region.

The comparison between recorded and computed acceleration-time histories at the roof level on Fig. 8.14 shows general good predictions for amplitudes and frequencies. Although the predicted accelerations are slightly lower than the measured accelerations (especially around 110 sec), the former represent adequately the changes between stages of low and high accelerations (e.g. between 70 and 80 sec). Fig. 8.15 indicates a 0.33 Hz fundamental frequency for both the predicted and recorded accelerations; the second fundamental frequency is also well predicted although the computed amplitude is lower than the recorded amplitude.

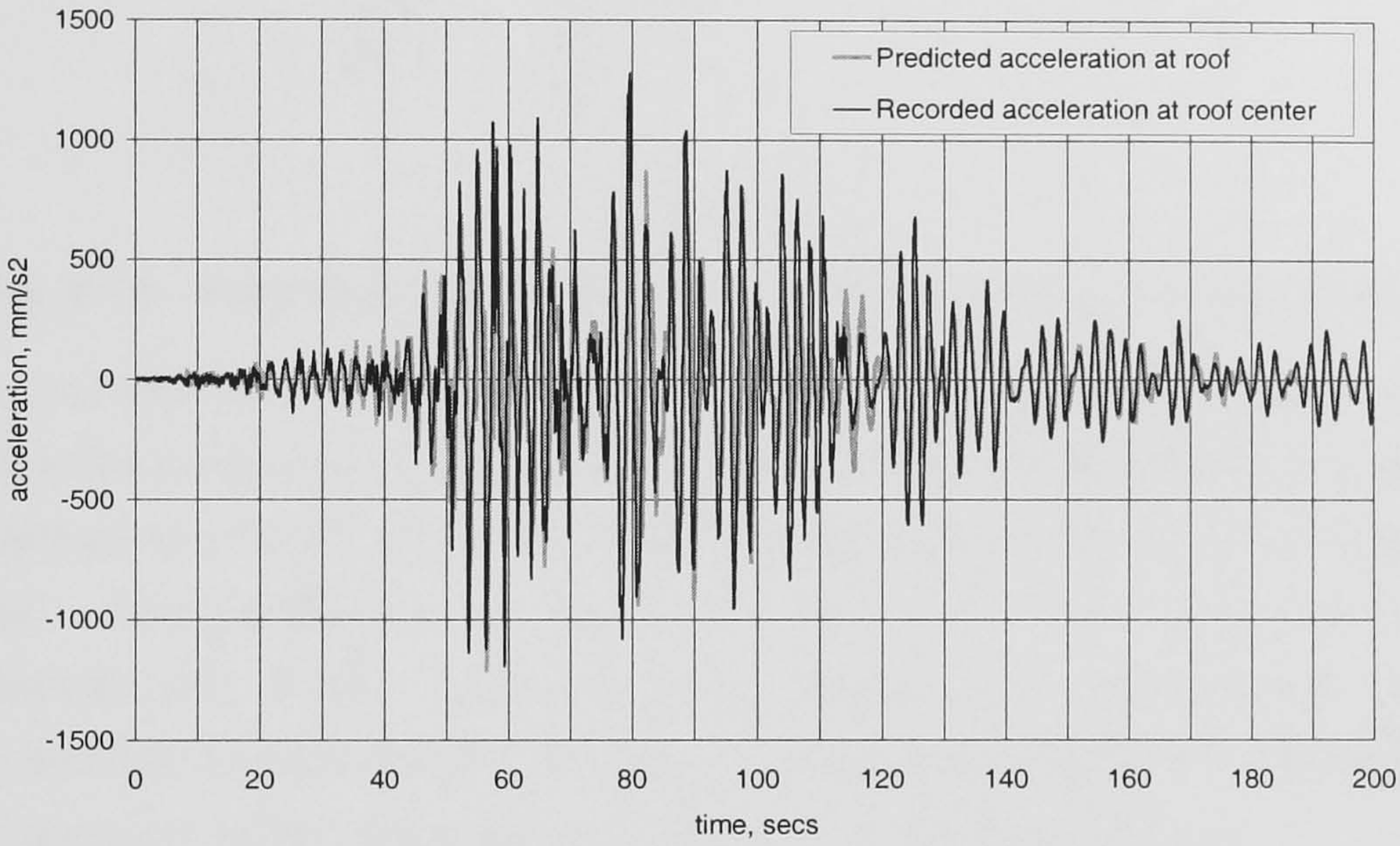


Fig. 8.14 Recorded and predicted acceleration time histories, Selected frame

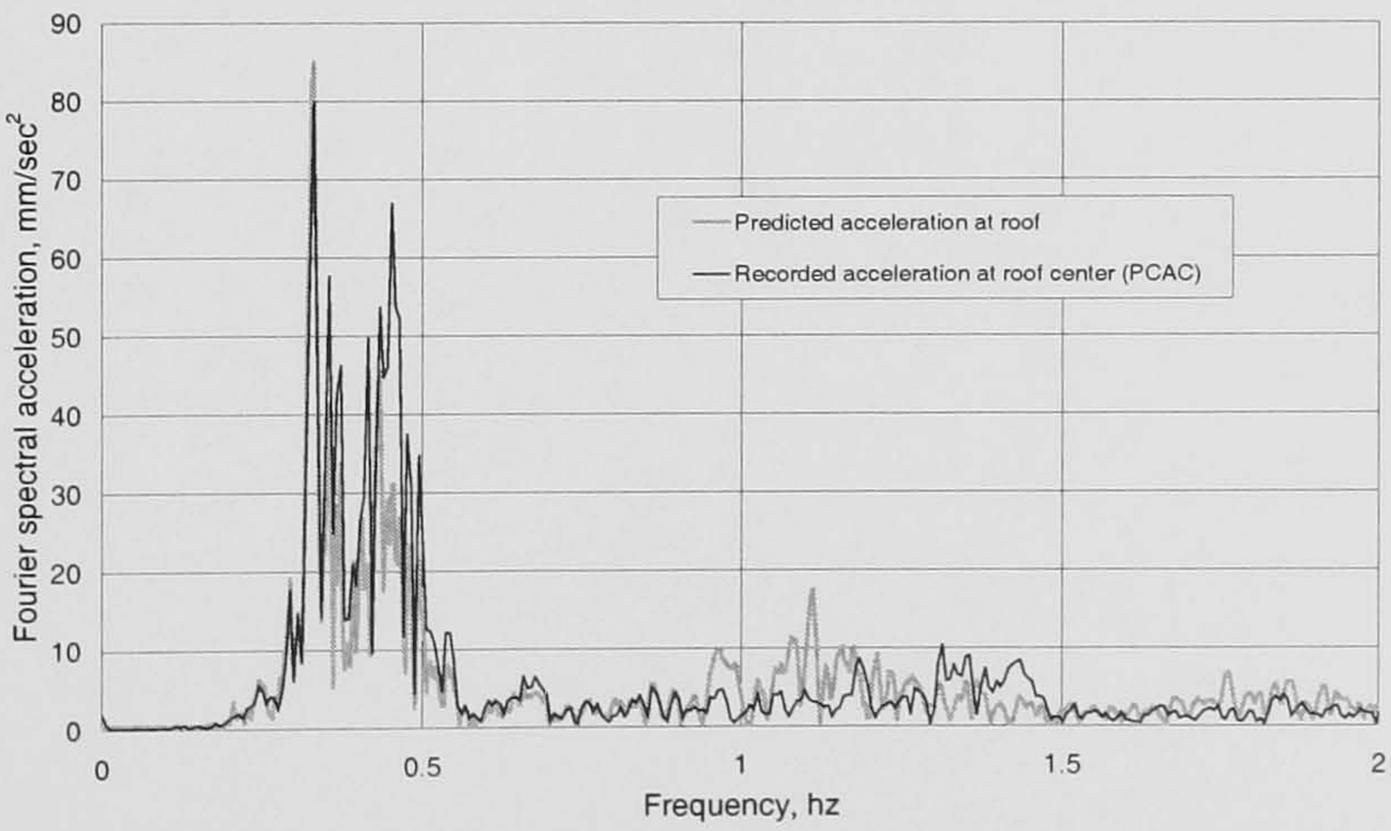


Fig. 8.15 Fourier spectra of recorded and predicted roof acceleration, Selected frame

The comparison of the computed and inferred horizontal displacements at the roof

confirms the good performance of the model both in amplitude and frequency (Fig. 8.16). The biggest discrepancies are for the low amplitude displacements around 110 sec, when the predicted displacements are up to 50% higher than those inferred. The roof displacement fundamental frequency is 0.33 Hz.

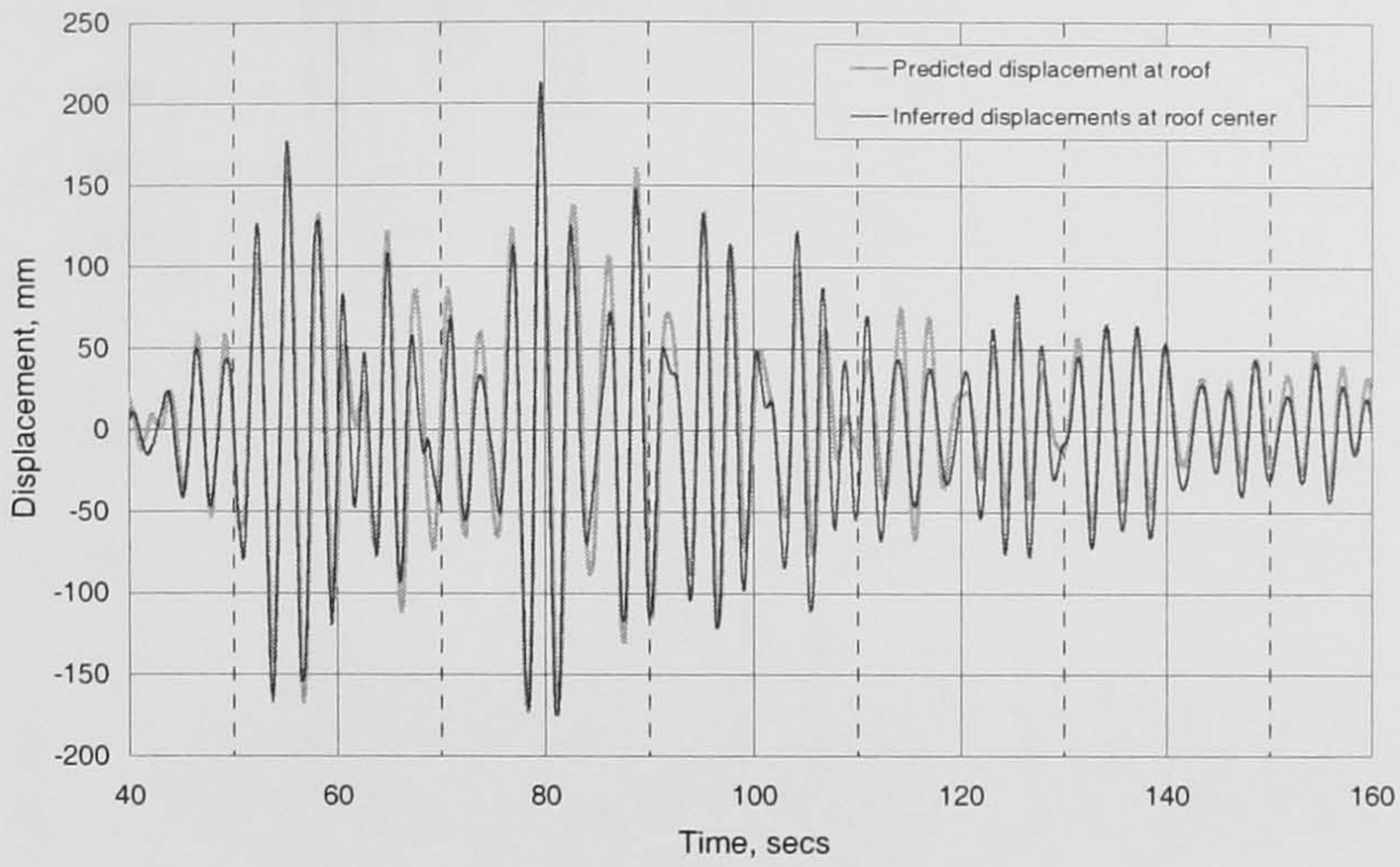


Fig. 8.16 Predicted and inferred lateral displacements, Selected frame

A better understanding of the model performance is obtained through the drift indexes. The drift index comparison shown in Fig. 8.17 indicate strong under-prediction between the basement and the 5th storey and slightly over-prediction between the 5th storey and the roof. The combination of these produces good overall prediction of roof displacements (Fig. 8.16). Table 8.4 shows the maximum displacements and drift indexes and their fundamental frequencies. The computed and inferred drift indexes are close to the lower values associated with the onset of structural damage.

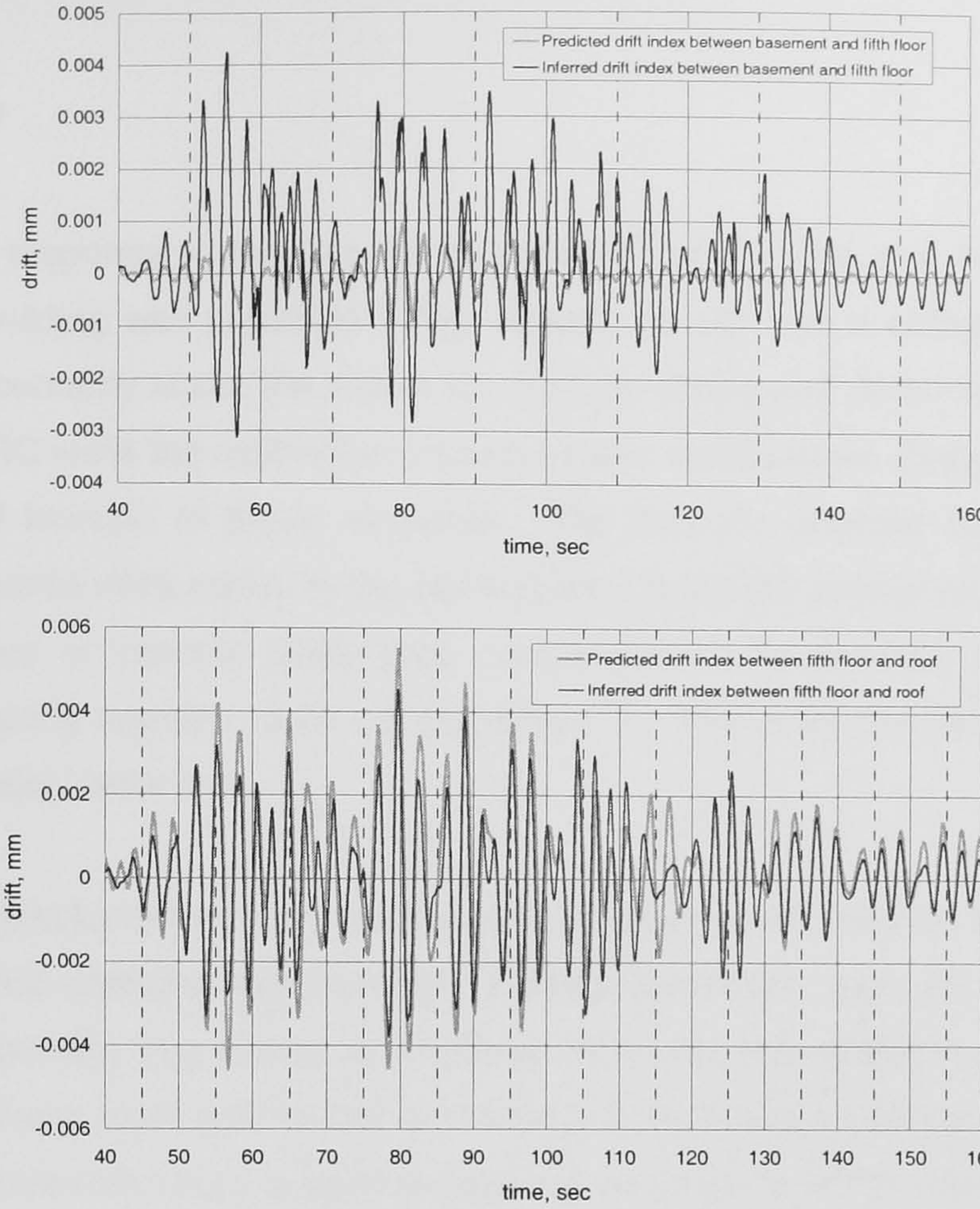


Fig. 8.17 Computed and inferred from records drift indexes, Selected frame

Table 8.4 Maximum lateral displacements and drifts indexes, Selected frame under Copala event

Lateral displacement (mm)			Drift index		
	Predicted	Inferred		Predicted	Inferred
5th Level	-33.79	69.41	Basement – 5th Level	0.001	0.0042
11th Level	129.08	-149.62	5th – Roof	0.0055	0.0045
Roof	206.51	212.07	Basement - Roof	0.0041	0.0042
Frequency (Hz)	0.33	0.34			

The results from the Original frame analysis indicated the need for an increase in the stiffness of the tower. During the calibration exercise, when reinforced concrete walls were included in the complete high of the tower (results are not shown here) the increment in stiffness was such that the roof accelerations were over-predicted. This would indicate that if there are reinforced concrete walls in the tower of the building they are damaged or have become detached from the frames.

The Selected frame model produced the best prediction of the variables used to evaluate the models. The Selected frame, compared against the Original frame, improves the predictions of the roof accelerations and displacements but worsens the drift index prediction between the basement and the 5th storey.

8.6.5 Analysis

The structural response to the Copala earthquake[99] at the roof of a transversal frame from the PC building was predicted using inelastic models and a calibration procedure. Due to the uncertainty about the actual location, condition and performance of the infill masonry and RC walls the calibration procedure was focussed on changing the material properties and location of these elements. The Author's analysis indicated that the reinforced concrete walls added to the building after the 1985 events could be separated from the frames or cracked since their contribution to the building response during earthquake loading appears to be not significant[100]. The extra damping from Rayleigh elements was also calibrated.

The horizontal displacement and accelerations at the roof, drift indexes and fundamental frequencies were predicted satisfactorily. A better prediction could be possible if other sources of inelasticity (e.g. cracks in structural elements, the condition of the reinforced concrete wall-frame joint) and further refinement of the model were included. However, the prediction presented here is good enough for the purpose of the analysis.

It is important to remember that due to the non-linear nature of the building's response a calibrated model is valid only for the event under which it is calibrated.

8.7 Base reaction for the 1995 Copala earthquake

8.7.1 Static reactions

The static distribution of load at each node at the base of the Original and Selected models is shown in Fig. 8.18 and Table 8.5; the latter also gives the percentage of the static reactions against the minimum and maximum forces predicted for the calibration Copala 1995 seismic event. The total reaction at the base of each model (weight of each model configuration) is the same since for the calibration procedure only the structural participation of the walls is removed. The weight of the building including dead

---

[99] The strongest recorded by the PC accelerometer array.

[100] The performance of structural elements is modified by damage sustained during previous earthquakes.

and live loads is 30158.8 kN.

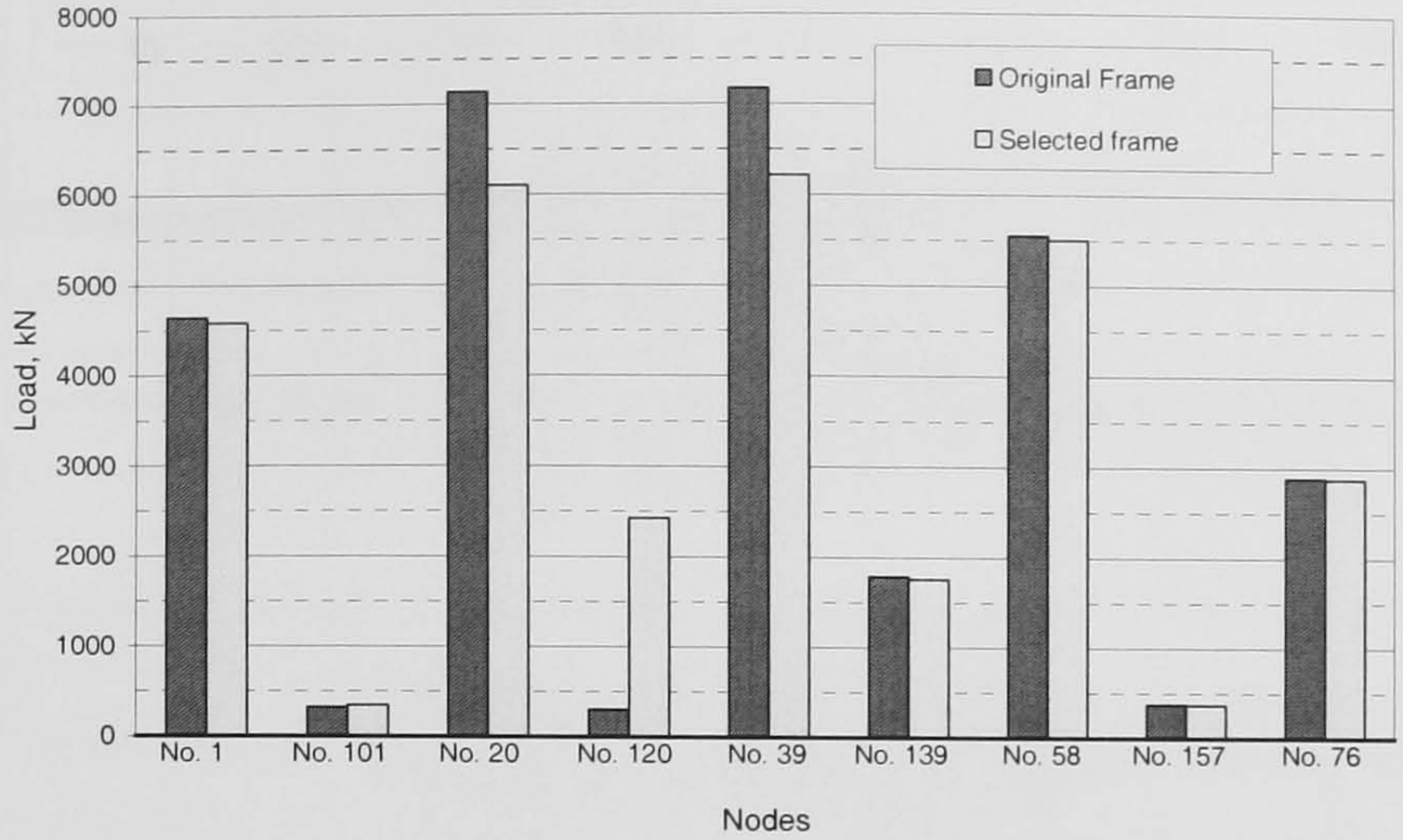


Fig. 8.18 Static load distribution at the frame base[101]

Table 8.5 Ratios of the maximum and minimum seismic loads to the static loads

Node	Original frame, kN			Selected frame, kN		
	Static	Max, %	Min, %	Static	Max, %	Min, %
1	4638.5	134.0	64.9	4580.9	130.8	65.5
101	318.9	102.9	90.7	342.4	102.7	71.4
20	7133.8	113.8	87.4	6100.0	115.7	88.7
120	300.0	117.4	69.1	2425.4	105.9	74.8
39	7173.8	105.7	94.8	6211.9	104.3	98.7
139	1787.0	150.5	34.4	1751.0	150.8	39.9
58	5549.6	132.3	71.4	5504.2	120.1	84.1
157	373.4	119.6	74.9	369.6	122.6	82.7
76	2883.8	107.7	93.7	2873.4	104.4	96.0

The static load distribution shows that the columns take the majority of the load, and the central columns the most. The load distribution for the Selected model (Table 8.5 and Fig. 8.18) shows the redistribution produced by the reinforced concrete walls, node 120 increases its load while the load at nodes 20 and 39 reduces.

8.7.2 Seismic base reactions for the Selected model under 1995 Copala earthquake

Fig. 8.19 shows the time-history of the vertical reactions developed at the base of the Selected frame when it is subjected to the Copala earthquake. The time history contains a long interval of 60 seconds (approximately 24 cycles) of high amplitude loads. The maximum and minimum seismic loads as percentage of the initial static load are given in Table 8.5; Fig. 8.20 shows the lowest and highest loads for each node. (The

---

[101] See node location in Figs. 8.8 and 8.13.

figure presents absolute values, which usually occur at different cycles.)

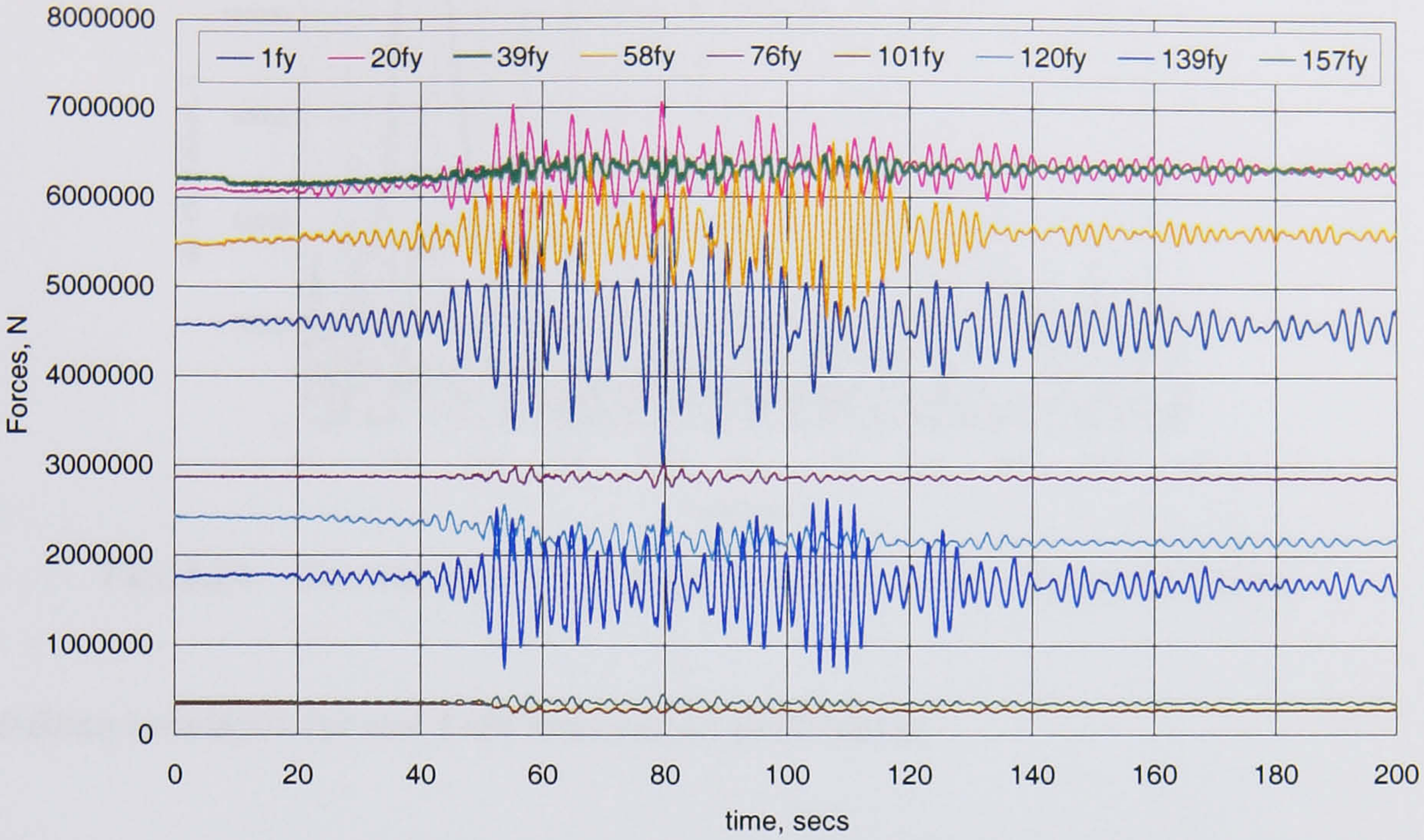


Fig. 8.19 Time-history of calculated reactions at the base of the Selected frame during the Copala 1995 earthquake

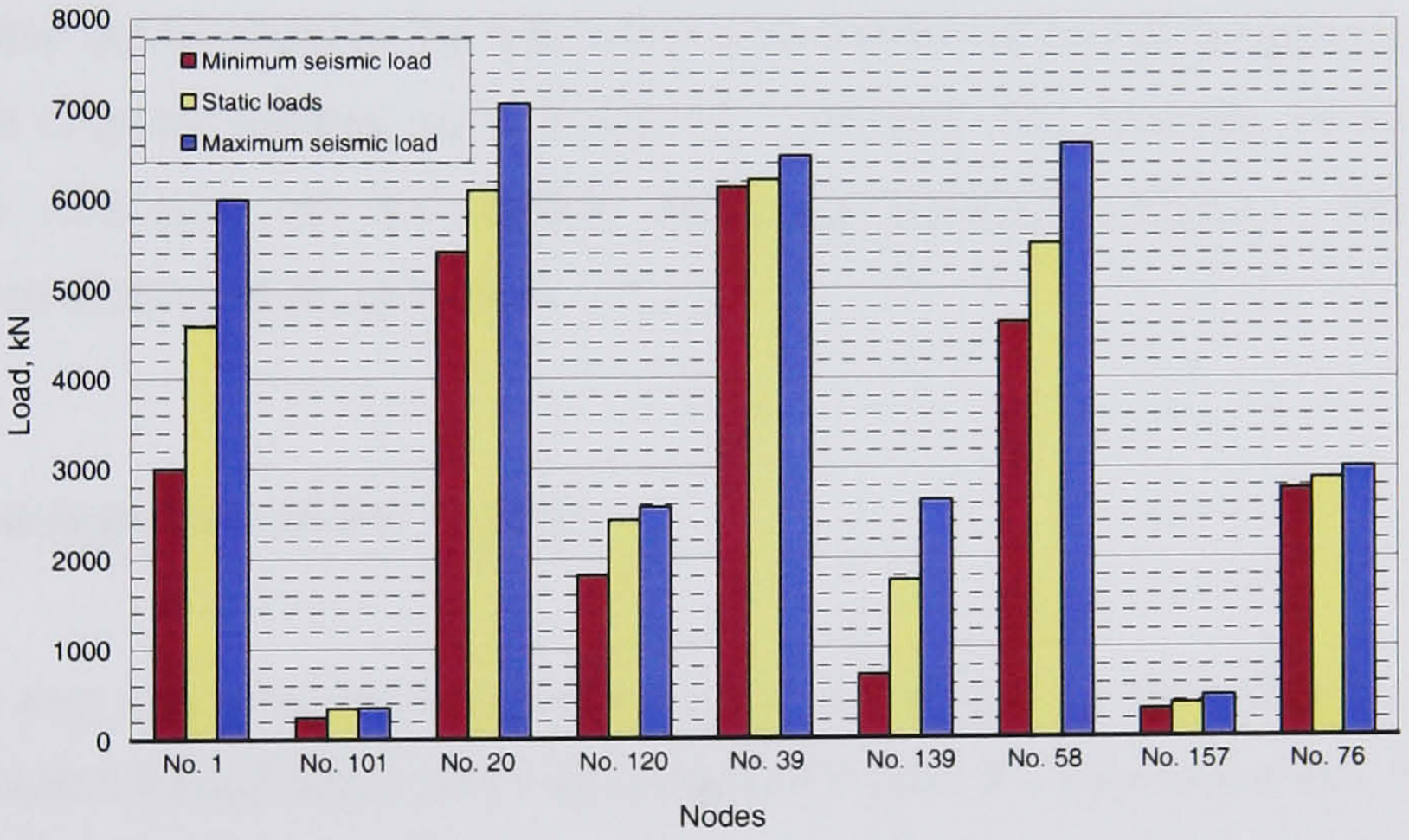


Fig. 8.20 Maximum and minimum load for 1995 Copala event – Selected frame

The slightly different configuration of the Original frame does not produce major changes in the amplitude of the seismic loads. Only node 120, located at the axis of the additional reinforced concrete walls, shows a noteworthy change.

The first and second fundamental frequencies of the reactions at the base correspond to those identified previously for the site (0.45 Hz) and the structure (0.33 Hz) (Fig. 8.21). This combination of site and model fundamental frequencies also appeared in the JAL and PCC buildings.

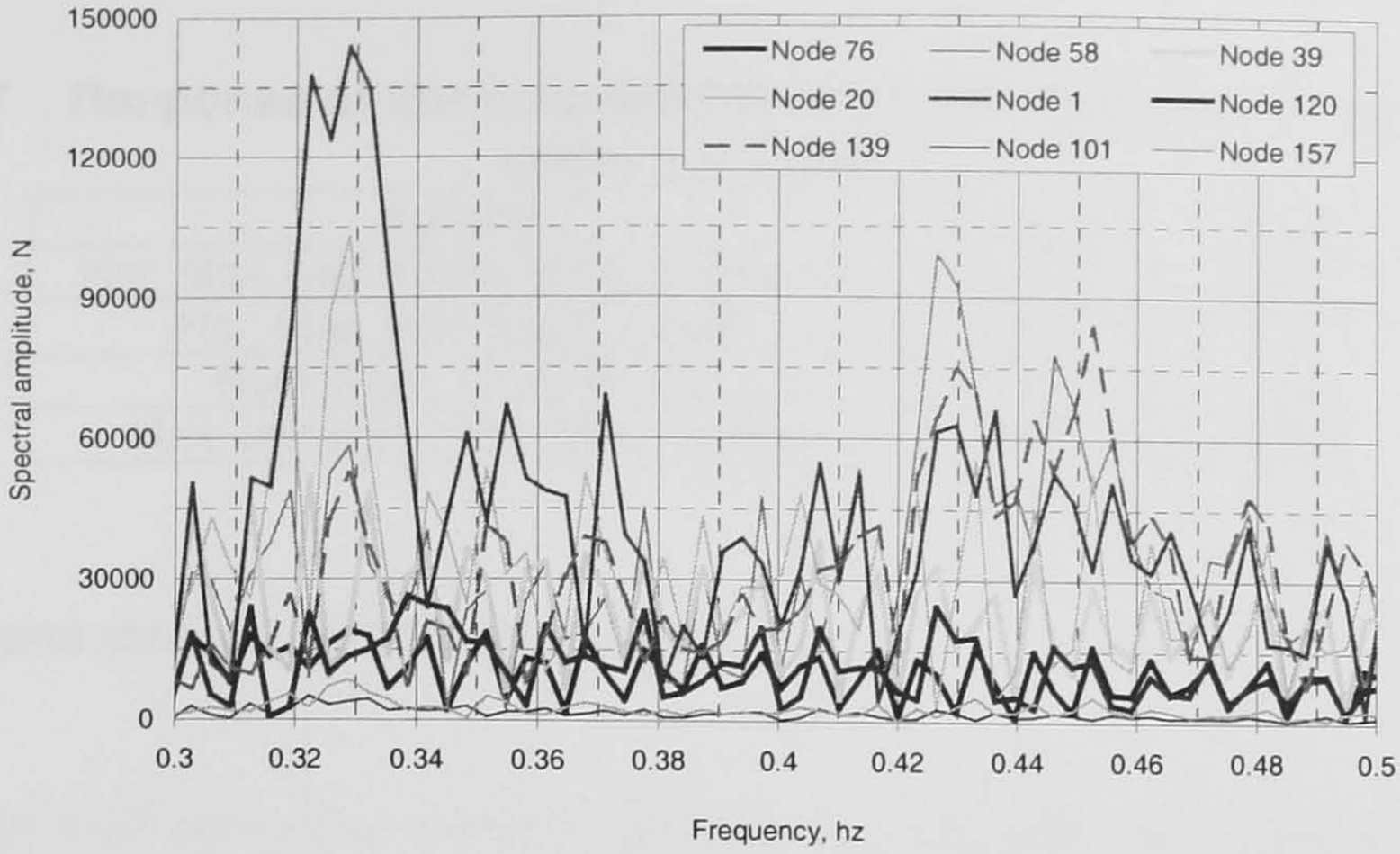


Fig. 8.21 Fourier spectra of base reactions base – Selected frame

8.8 Base reactions for the 1985 Michoacan earthquake

The amplification factor λ[102] required to obtain a 1985-like motion is 5 - the ratio being determined from the peak acceleration. This is the same as for the JAL building frame since the PC building was calibrated for the same event[103]. An additional analysis with λ=3 was carried out to observe the behaviour under different motion amplitude. Both the Selected and Original models were analyzed. However the analysis of the Selected model under λ=5 was not successful, indicating building collapse. The following sections describe the results obtained.

8.8.1 General response of the models

The Original and Selected models show greater accelerations and displacements and lower fundamental frequencies under the amplified motions - Tables 8.6 and 8.7 present a summary of the relevant results.

Table 8.6 Response of the Original model to the calibration Copala motion under λ = 1, 3, and 5[104]

Variable	1*Copala	3*Copala	5*Copala
Hor. Max. roof acceleration (mm/sec^2)	-901.5	-1824.4	-2149.7
Hor. Max. roof displacement (mm)	186.4	321.1	-417.8
Roof Displ. 1st frequency	0.29	0.24	0.23
Max. drift index (Basement-Roof)	0.0042	0.0081	0.0107

[102] Defined in Chapter 6.

[103] The SCT site is 3.5 km away from the PC building.

[104] The calibration Copala motion amplified five times (λ-5) corresponds to a 1985-like motion.

Table 8.7 Response of the Selected model to the calibration Copala motion under λ = 1, and 3

Variable	1*Copala	3*Copala
Hor. Max. roof acceleration (mm/sec^2)	-1170.4	-2550.0
Hor. Max. roof displacement	206.5	414.5
Roof Displ. 1st frequency	0.33	0.30
Max. drift index (Basement-Roof)	0.0041	0.0091

8.8.2 Reactions under amplified motions

Figs. 8.22 and 8.23 show the overall maximum and minimum reactions predicted for the Original and Selected models when subjected to the input motions amplified 3 times (λ=3). The values included in the figures are absolute values[105].

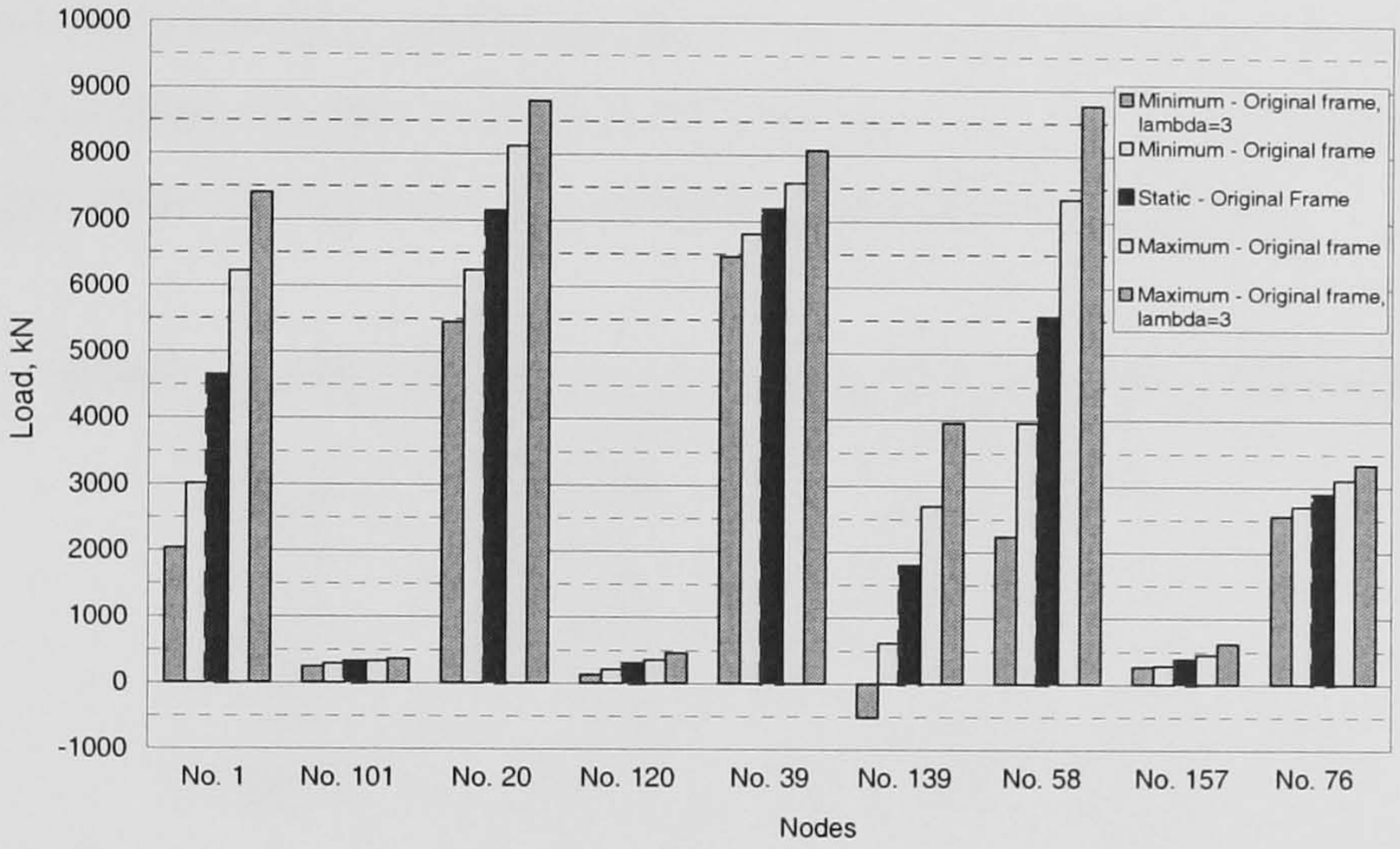


Fig. 8.22 Maximum and minimum seismic reactions in the Original frame for input Copala motion under λ = 1 and 3

Figs. 8.22 and 8.23 show that the biggest seismic load amplitudes are produced at the external columns of the tower, at nodes 1 and 57, and just below the concrete walls at node 139. The absolute values do not give a clear indication of load amplification due to the scalation of the input motions. A clearer indication of the amplification of the reactions can be obtained from comparing the spectral ordinate of the fundamental frequencies in Fourier Spectra. Tables 8.8 and 8.9 show the results for the nodes carrying the highest loads for both Original and Selected frames, respectively.

---

[105] Absolute values are those maximum or minimum values for the complete time history and they do not necessarily belong to the same cycle.

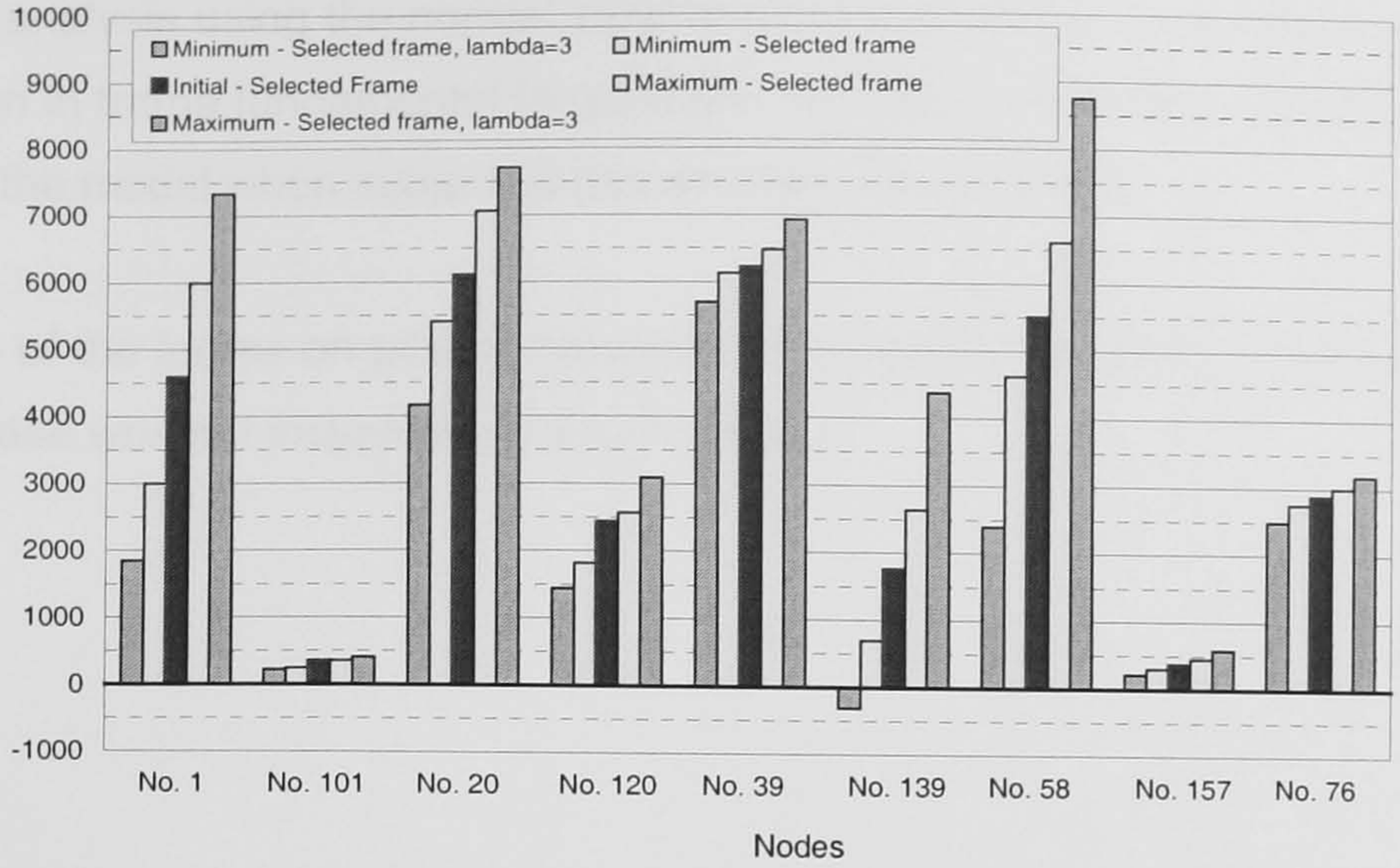


Fig. 8.23 Maximum and minimum seismic reactions in the Selected frame for input Copala motion under λ = 1 and 3

Table 8.8 indicates that the base reactions of the Original frame are amplified by 60% and 85% for the analysis with λ=3 and λ=5, respectively. Table 8.9 indicates that the Selected frame underwent a 104% amplification in base forces for λ=3.

Table 8.8 Spectral ratios of forces for Original frame under amplified motions

	3*Copala/Copala	5*Copala/Copala
Node	Fourier	Fourier
1	1.43	1.52
20	1.32	1.62
139	2.04	2.35
58	1.62	1.93
Average	1.601	1.857

Table 8.9 Spectral ratios of forces for Selected model under amplified motions

	3*Copala/Copala
Node	Fourier
1	1.85
20	1.28
139	2.48
57	2.57
Average	2.042

The fundamental frequencies of the model under amplified input motion include the input motion and building model fundamental frequencies. However, in addition to the increment in peak spectral ordinate, the fundamental frequencies were lower than for the calibration analysis. The fundamental frequency for the Original frame decreased from 0.29 Hz (for analysis using the normal input motions) to 0.24 Hz (for the analysis with λ = 3); the fundamental frequencies for analyses carried out with λ=3 and λ=5 are not significantly different. The fundamental frequency for the Selected model dropped from

0.33 Hz (for analysis using the normal input motion) to 0.30 Hz (for analysis using λ=3). The reduction in frame fundamental frequencies probably results from a wider non-linear response of the model when subjected to a stronger input motion.

The analysis of the forces on piles is presented in Chapter 10 and 11. The lateral shear load at the base was not included in these analyses.

CHAPTER 9

THE BASE REACTIONS DEVELOPED ON THE PCC BUILDING DURING SEISMIC SHAKING

This chapter reports the Author's analyses to determine the seismic reactions at the base of a longitudinal external frame of the PCC Building. A calibration procedure in which several frame structural configurations were proposed, analyzed in ADAPTIC, and evaluated against a recorded response was followed.

The low basement accelerations measured in the available calibration motion (1995 Colima earthquake), resulted in the reactions predicted for the stronger 1995 Copala and 1985 Michoacan events being subject to greater uncertainty than was accepted for the JAL and PC buildings. In mitigate this, an alternative limited calibration was carried out based on a manually reproduced Copala event. After further processing the base reactions (Chapters 10 and 11), it was decided that the uncertainty remained too high and the results for this building are not carried forward for the pile seismic capacity analysis presented in Chapter 11. However, the analyses made of the PCC building are still reported here for the sake of completeness.

9.1 A general description of the PCC Building

The PCC building is located in the Colonia Centro area, in the Lake zone of Mexico City (MC) (Fig. 6.14). It is a 9-storey reinforced concrete structure that includes a rigid basement with a perimeter of reinforced concrete walls, a ground floor, and seven regular shape levels (Fig. 9.1). The inter-storey height is variable and the total height of the building from the ground level is 33.3 m. It is a critical facility housing the control center and power generators for lines 1 to 6 of the MC subway.

Dr. Alfonso Reyes[106] made available some details of the structural information and the building acceleration records for the Colima event. Reyes and Luco, Rodriguez (1991), and Romo and Barcena (1993) have also presented studies of the PCC building's response to static and seismic loading.

---

[106] Center for scientific research and postgraduate studies of Ensenada (CICESE)

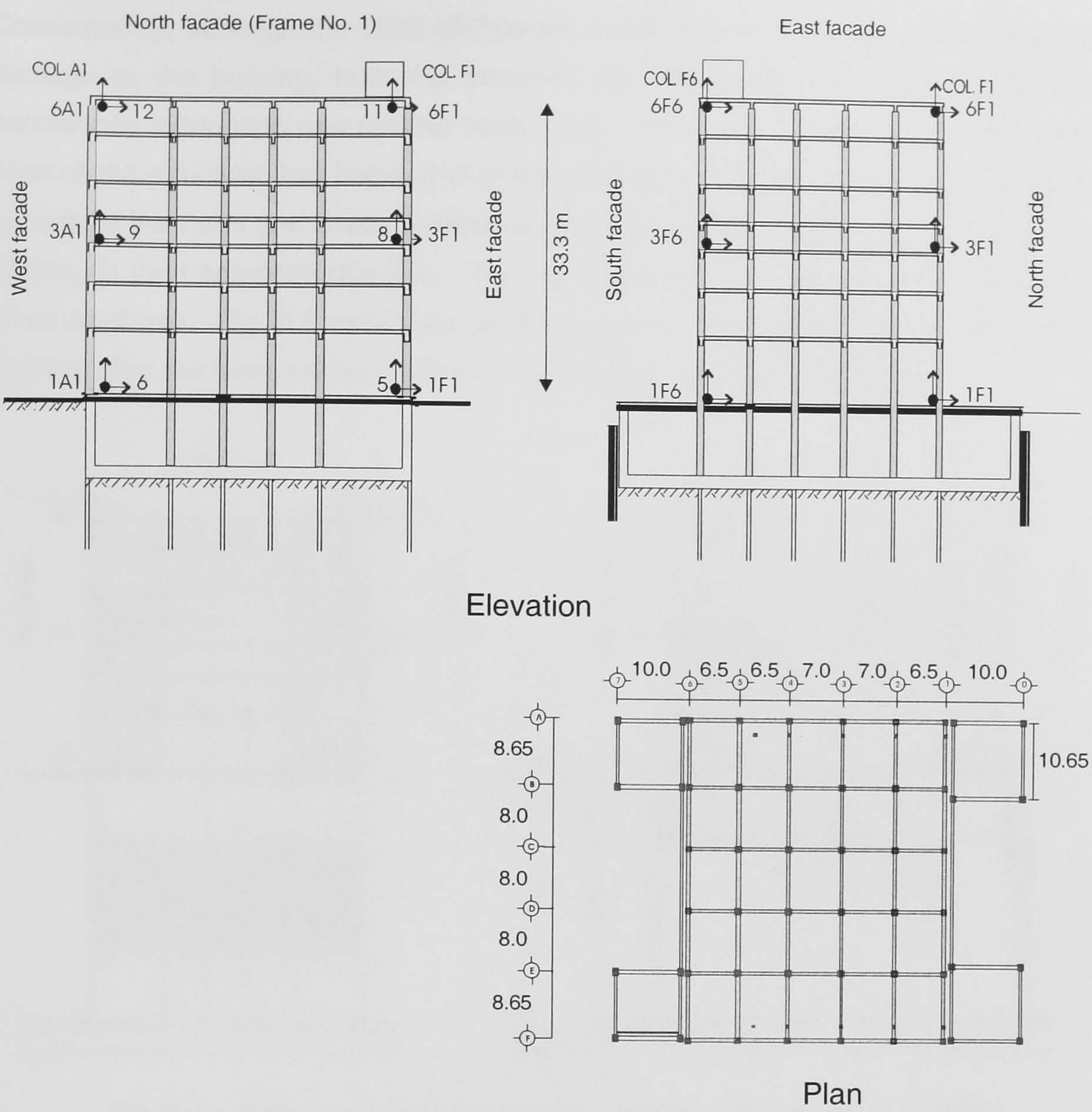


Fig. 9.1 Original elevation and plan views of the PCC building (Reyes, et al., 1995)

9.2 Structural configuration and material characteristics

Originally, the structure consisted of 12-cm thick reinforced concrete (RC) slabs supported on RC frames with rectangular columns, and a core of concrete shear walls around the shaft for staircases and possibly elevator.

The damage sustained by the PCC building during the 1995 earthquake consisted in light cracking in some structural elements at the third floor and cracks in tunnels located at the south side of the building (Rodriguez, 1991). No information regarding foundation settlement was found.

The PCC building is a sensitive element of the underground transport system in MC.

Consequently, although the 1985 Michoacan events did not produce severe structural damage to the building, both the structure and the foundation were reinforced in accordance to the then new seismic coefficients of the 1987 Construction Code. In the case of the structure, two inverted U-shape steel braced frames were attached on the outside of the north and south facades (external transversal frames) to strengthen the building in the transversal direction. The upper slab of the foundation box supports the steel structures. Fig. 9.2 shows the transversal and longitudinal elevation views of the building after the reinforcement works on the structure and the foundation.

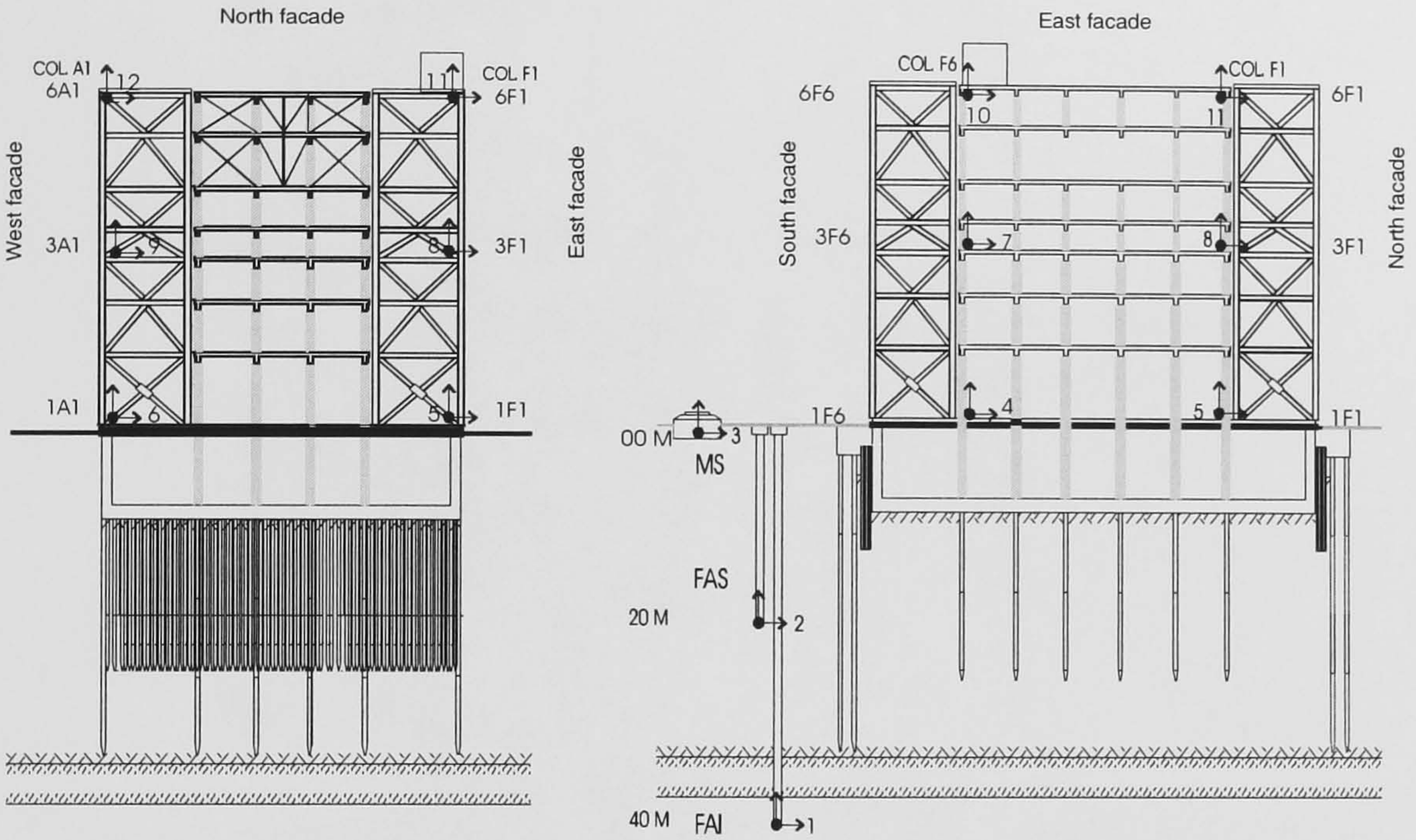


Fig. 9.2 Reinforcement of the PCC building (Reyes, et al., 1995)

Dr. Alfonso Reyes provided the material properties for the analysis. The concrete compressive strength was 23.5 MPa. The steel reinforcement bars' axial yield stress was 421 MPa with a Young's modulus of 195 900 MPa.

9.3 Foundation configuration

The foundation of the PCC building is typical of the MC Lake zone. Originally it consisted of a RC foundation box resting at a depth of 8.25 m on 82 friction piles that extend until 22.4 m depth, without reaching the firm stratum (Fig. 9.2). The pile cross sectional shape was not available to the Author, however triangular piles of 65 cm side were considered. The predicted pile capacity for the friction piles, computed by applying the Imperial College pile design method, was 947 kN (96.3 tons)[107]. Fig. 9.3 shows the

---

[107] The effects of the pile assumed triangular cross-section were allowed for by adopting Jaime, et

distribution of the original piles. After the 1985 Michoacan earthquake, 155 21 m-long end bearing piles were attached to the foundation box (84 in the north side and 71 in the south) in order to reduce rocking of the foundation raft in the transversal direction. Fig. 9.2 shows an elevation of the upgraded foundation, and Fig. 9.4 shows a plan view with the distribution of the new end-bearing piles, which are square cross section of 50 cm side.

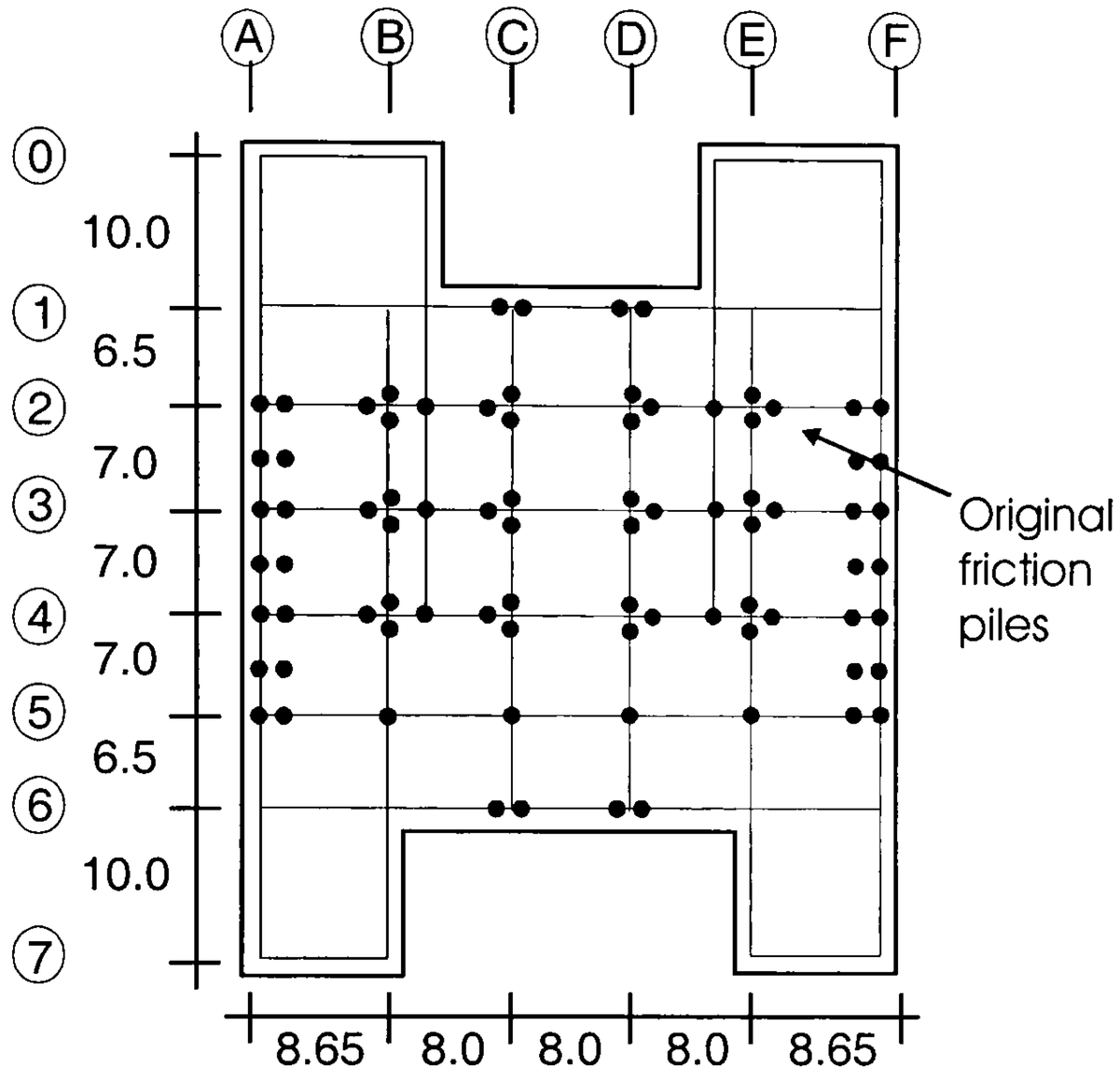


Fig. 9.3 Foundation plan and original friction piles (Rodriguez, 1991)

al.'s (1991) correction factors.

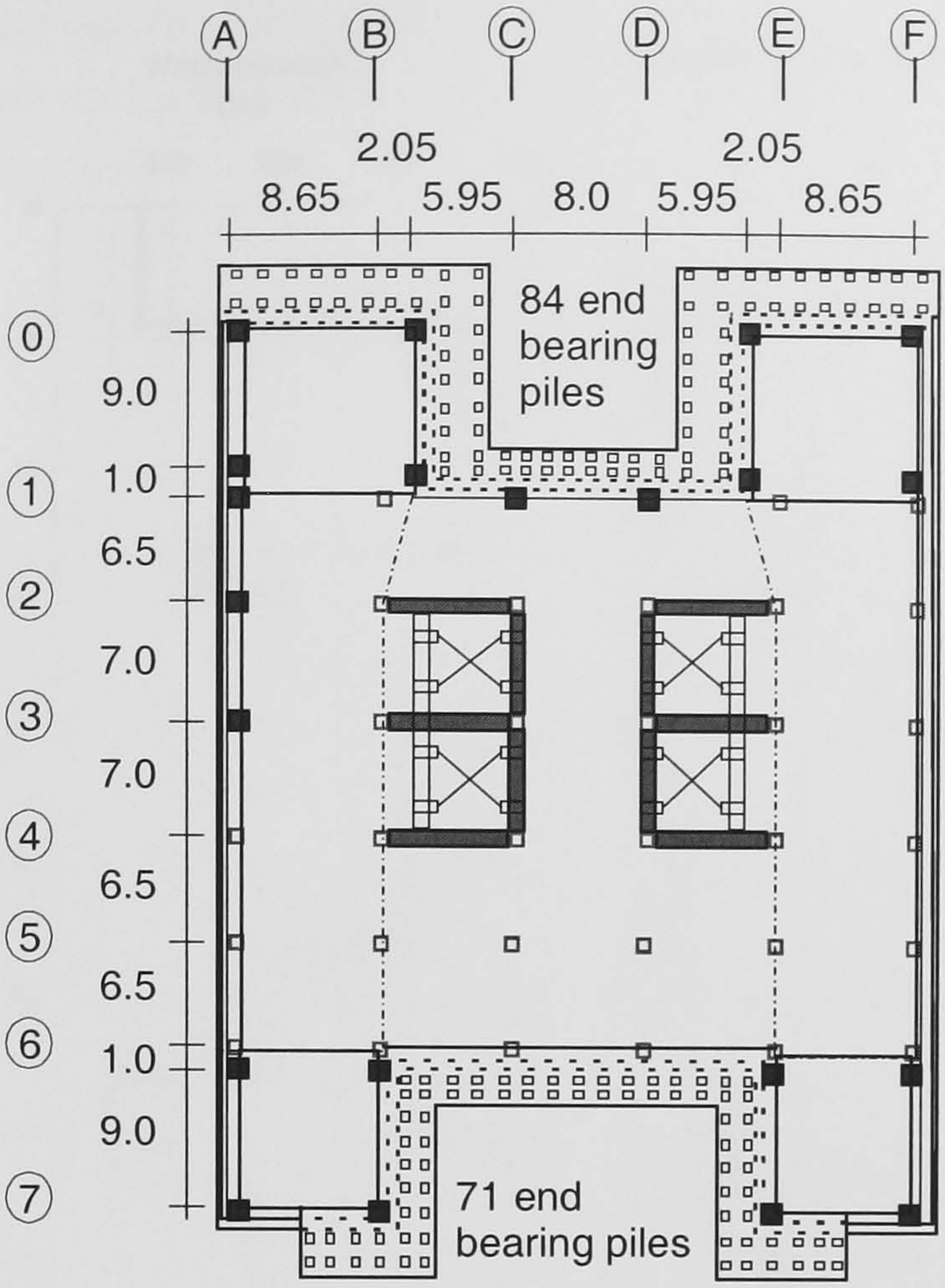


Fig. 9.4 Plant view of the PCC building foundation with the location of new end bearing piles (Rodriguez, 1991)

The foundation box consists of a perimeter of RC walls and a raft that, together with the foundation beams, form a monolithic structure with the base of the building columns and the piles (Fig. 9.1). The depth of the foundation box indicates that the building weight was compensated by the weight of the excavated soil. The actual raft-pile load distribution in this type of foundation solution is a matter of disagreement. The response of the foundation to regional subsidence will depend on the ratio between the weight of the excavated soil and the weight of the building.

The geotechnical profile at the building site consists of 4.5 m of a superficial fill followed by 29.5 m of typical MC clay (with thin layers of sand), 4 m of a first hard layer, and from 37 m downward the second MC clay stratum (Fig. 9.5 and 9.2). The soil properties were obtained from soil mechanics studies in the vicinity of the site. The site fundamental period is between 2.0 and 2.5 seconds (Fig. 6.14).

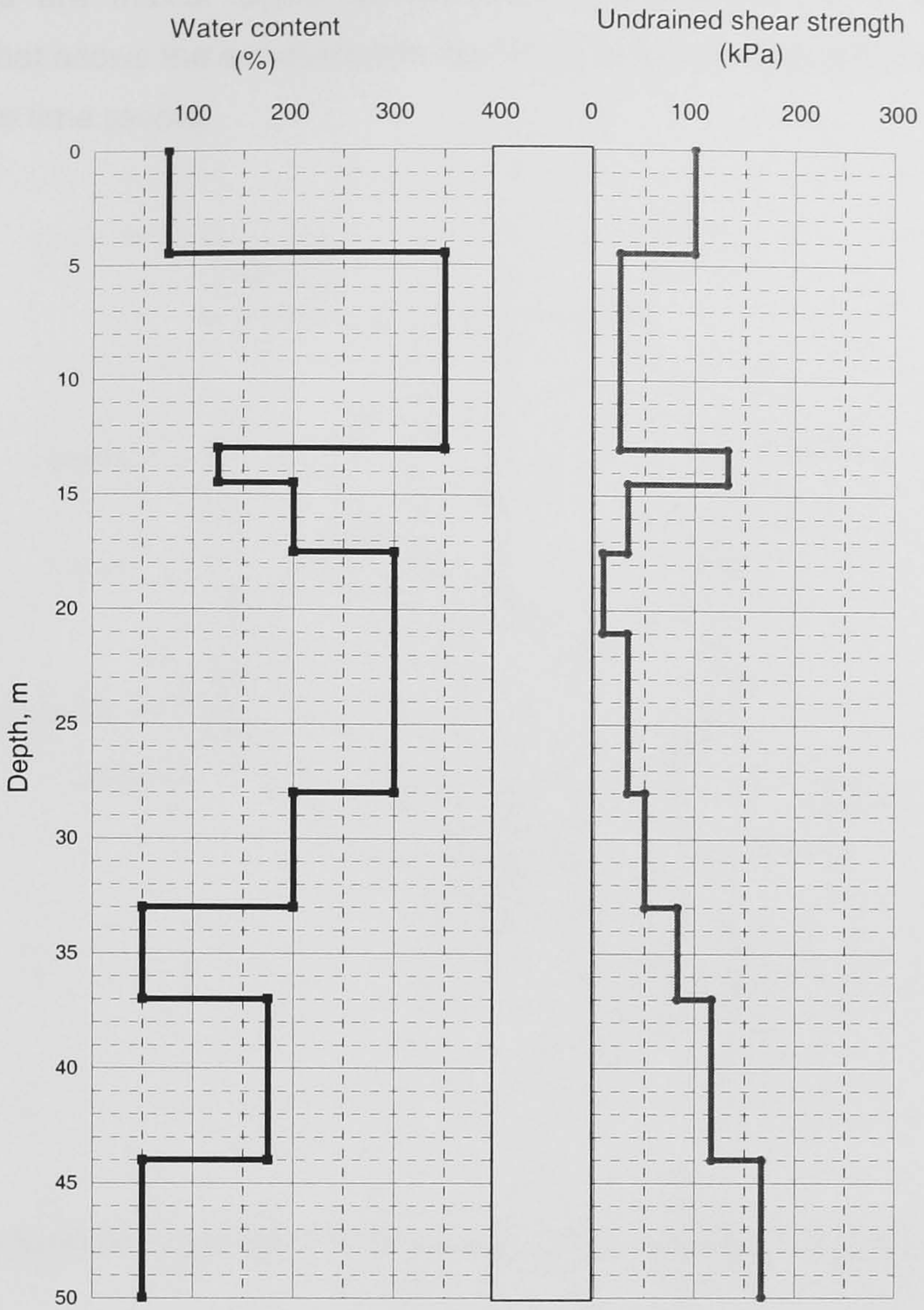


Fig. 9.5 Water content and fast triaxial undrained shear strength from soil profile at PCC building site (Reyes and Luco)

9.4 Instrumentation and input motions

The seismic instrumentation of the PCC building was carried out in two stages. The first stage involved the installation of an array of three accelerometers into the ground, 10 m from the south side of the building. The instruments were installed at ground level, at 20 m depth in the first clay stratum, and at 40 m depth in the second clay stratum.

The second stage was completed in 1993 and covered the installation of three instruments in the ground floor, three in the third floor, and three in the top sixth floor, all located at corner columns (Fig. 9.6). The instruments are located along a vertical axis that starts in the first floor and finished at the top floor (Reyes and Luco).

All instruments are triaxial digital accelerometers interconnected in a master-slave configuration that allows the simultaneous recording of the subsoil and building response under the same time record.

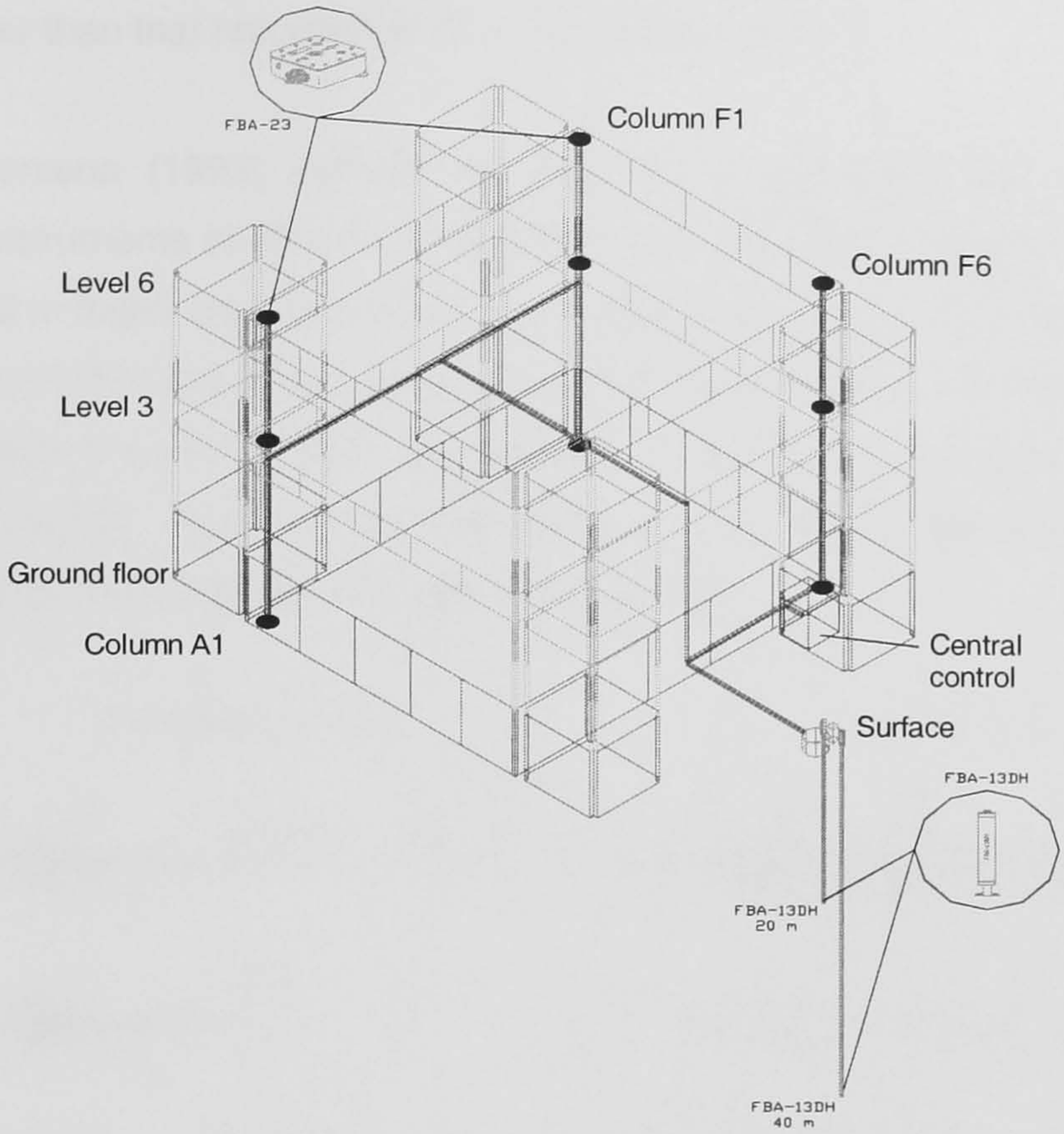


Fig. 9.6 Location of accelerometers at the PCC building (Reyes, et al., 1995)

The complete accelerometer array has recorded 10 earthquakes with magnitudes (M_w) between 4.6 and 7.6. The maximum mean acceleration recorded at 20 m depth ranges between 2 and 26 cm/sec^2, and at the top floor between 4 and 46 cm/sec^2. The database includes the records for the September 14, 1995 "Copala" earthquake (Reyes and Luco). Table 9.1 shows some earthquake characteristics and the maximum longitudinal accelerations for the 1995 Copala and Colima earthquakes. (EP is the epicentral distance)

Table 9.1 Maximum longitudinal accelerations (cm/s^2) at PCC building for the Copala and Colima earthquakes (Reyes, et al., 1997)

	14/09/95 Copala		9/10/95 Colima	
Characteristics	Mw =7.5 EP = 305.6 km Depth = 21 km		Mw = 7.6 EP = 530.5 km Depth = 33 km	
	Accel.	Freq.	Accel.	Freq.
20 m deep	26.24	0.49	5.59	0.44
Soil surface	25.72	0.49	9.07	0.44
Ground floor	25.52	0.49	9.22	0.44
Third level	34.53	0.49	9.99	0.44
Sixth level	45.61	0.49	10.49	0.44

Fig. 9.7 compares the longitudinal accelerations at different levels of the system for the Colima and Copala events. The figure provides examples of motion amplification from underground to the top of the building, the maximum acceleration at the top floor was 1.9 times bigger than that recorded at 20 m below ground level.

Romo and Barcena (1993) pointed out that the acceleration amplitude increased between the instruments at 40 and 20 m depth (as it would be expected for soft soils), but between 20 m depth and the surface the acceleration amplitude reduces. Romo and Barcena indicated that this is caused by the dynamic interaction of the deep foundation box, which affects the acceleration amplitudes to a distance in the order of three times the foundation width. The surface instrument for the PCC building is located at a distance 0.3 times the foundation longitudinal dimension.

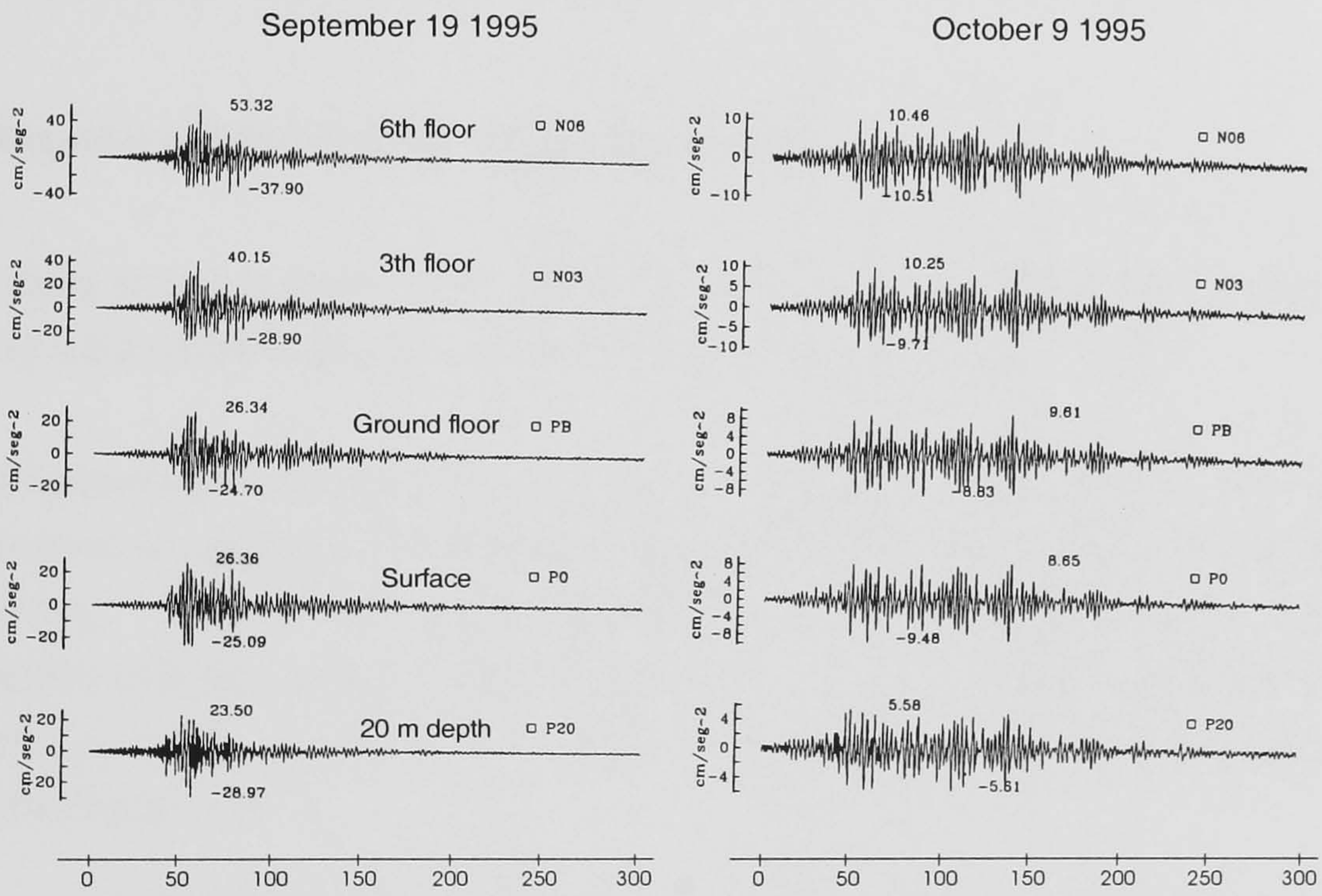


Fig. 9.7 Longitudinal accelerations at F6 location for Copala and Colima events (Reyes, et al., 1997)

As for the JAL and PC buildings, the Copala event has produced the highest accelerations at the PCC building to date, therefore it was the ideal event to carry out the calibration of the Author's frame model. However, the records for the Copala event were not made available for this research and the calibration was carried out with the Colima event, the only available to the Author. The records for the calibration are the vertical and horizontal component of the F6 column and the vertical component of the F1 column, all from the ground floor (Fig. 9.6). The Fourier spectra of these records show a

0.44 Hz fundamental frequency.

Ideally the calibration procedure is carried out using the highest recorded accelerations. The reason is to include some of the building non-linear response when it is subjected to high intensity events – as the September 19 1985 Michoacan event. The low accelerations produced by the October 19 Colima event on the PCC building (Fig. 9.7 and Table 9.1) brings about more uncertainties to the Author's analysis. In an attempt to overcome this difficulty, the horizontal component for ground floor motion of the Copala event was manually reproduced from a time-acceleration graph and implemented as an input motion. The vertical component was considered as a fraction of the horizontal component.

The records were filtered in the time domain with a low pass digital filter (with 0.2 Hz and 20 Hz as the pass and stop bands respectively) before using them in ADAPTIC.

9.5 Behaviour of the building during earthquakes

The study of the response of the PCC structural system to earthquake shaking was carried out through the spectral analysis of its recorded response.

The important reinforcement of the structure resulting from the retrofitting of the building is identified by comparing the ambient vibration (AV) tests performed before and after retrofitting. The AV test results showed that the fundamental frequency of the foundation building system increased 59% (from 1.1 to 1.75 Hz) in the transversal direction, and 36% (from 0.99 to 1.21 Hz) in the longitudinal direction (Fig. 9.8 and Table 9.2) (Rodriguez, 1991).

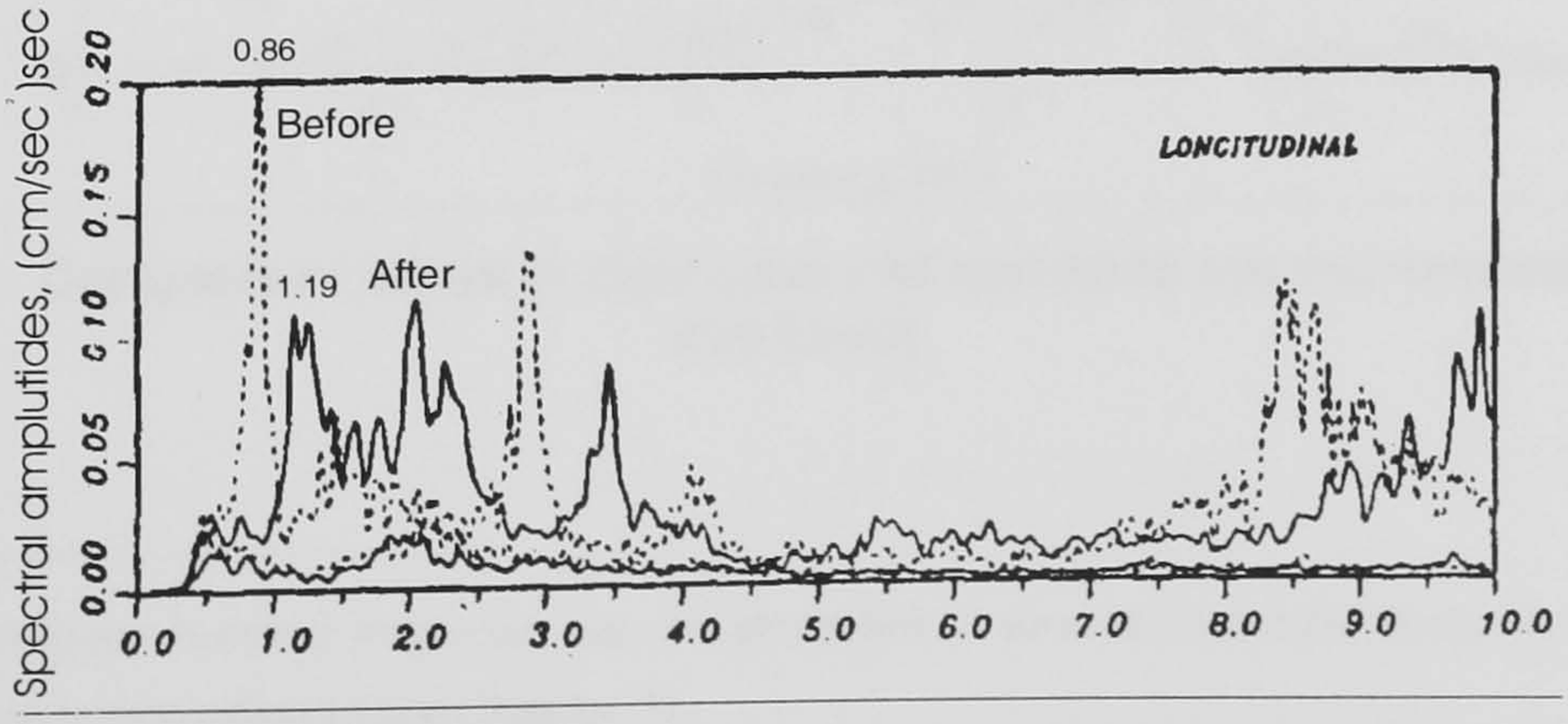


Fig. 9.8 Ambient vibration tests on PCC building (Rodriguez, 1991)

The dependency of the building fundamental frequency on the amplitude of shaking

(non-linear response of the building[108]) is presented in Table 9.2, which shows reductions of at least 60% on fundamental frequency when the response derived from the seismic records of 1995 events are compared to the AV tests.

Table 9.2 Recorded fundamental frequencies for PCC Building (Reyes and Luco)

Test	Date	Longitudinal, Hz	Transversal, Hz
AV	July 1999	0.99	1.1
AV	Nov 1990	1.21	1.75
Copala	14/09/1995	0.49	0.45
Copala	Rigid base	1.3	1.31
Colima	9/10/1995	0.44	0.46
Site		0.49-0.44	0.45-0.46

According to the study of the JAL and PC buildings, the natural frequencies of buildings are expected to decrease between successive events. However, although this appears to happen for the PCC building, there is not conclusive information to support such decrease in fundamental frequencies.

The soil-structure-interaction (SSI) effects on the PCC building were analyzed by Reyes and Luco by comparing the spectra for the total system displacement[109] (UTn) and the spectra for the displacements in rigid base condition (Xn) (Fig. 9.9). As observed, the fundamental frequency of the soil-structure interacting system is smaller than that of the structure alone[110] (Table 9.2). For the very soft soil conditions in MC the fundamental frequency of the soil-structure system is expected to be close to the fundamental frequency of the site (Meli, et al., 1999).

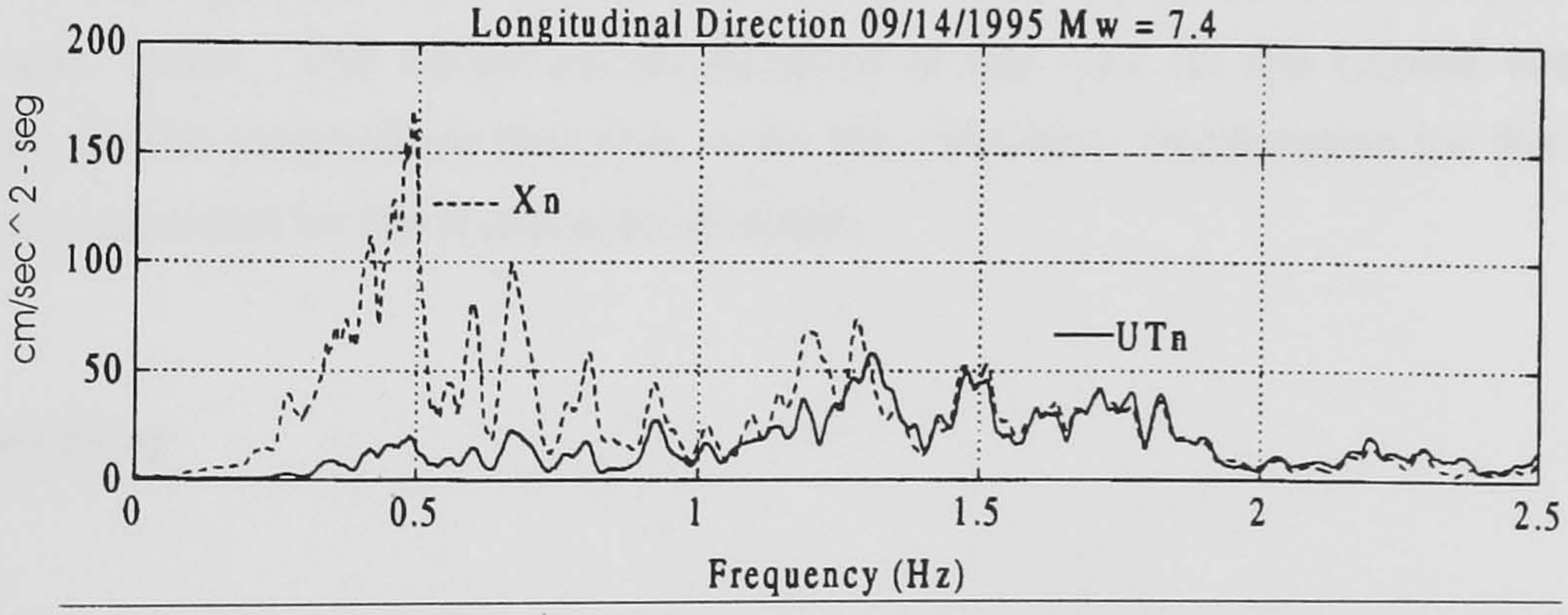


Fig. 9.9 Comparison between rigid base and complete system response (Reyes and Luco)

---

[108] The non-linear building response can be attributed to several structural features and to soil-structure interaction effects (see Chapter 7).

[109] The total system displacement comprises the displacement of the free field, the displacement and rocking of the soil-foundation system, and the displacement of the structure.

[110] The system frequency will depend on the relative stiffness of the soil and the foundation.

Romo (1995) carried out dynamic finite element analyses of the PCC building SSI. Romo showed that the deep box foundation attenuates the building base motion at the natural (and larger) building frequency with respect to that of the free field. Romo pointed out that the attenuation capacity of deep foundation boxes results from: (i) the reduction on motion amplitude with depth (Fig. 9.10), and (ii) the stiffness contrast between the soil and the foundation - the kinematic interaction influence is more important in soft soils.

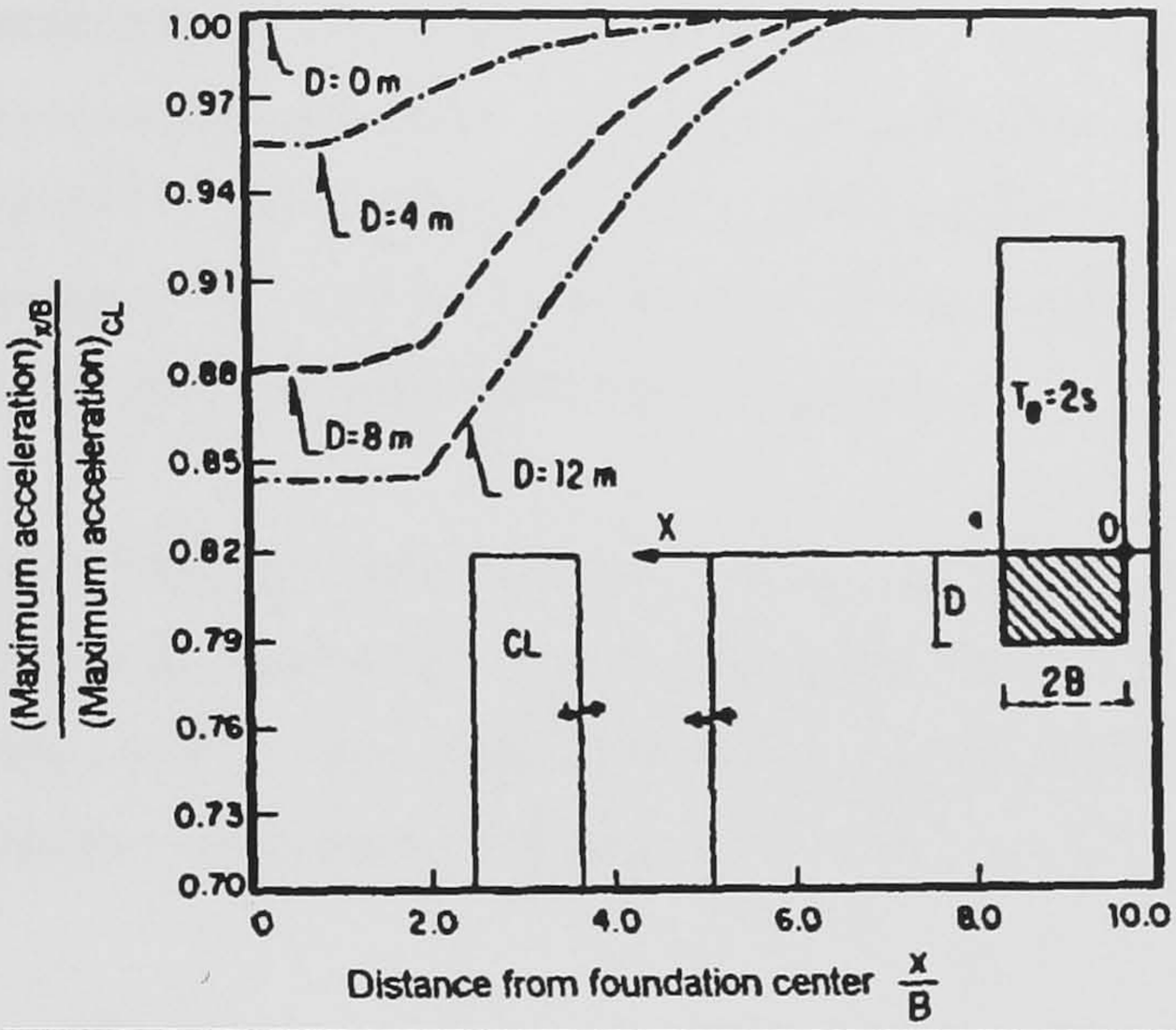


Fig. 9.10 Effect of foundation depth on ground motion (Romo, 1995)

The PCC building response depends upon the earthquake magnitude and location of the earthquake focus. The maximum acceleration at top floor for the Copala event was recorded for the longitudinal direction, while the maximum acceleration for the Colima event was recorded for the transverse direction.

9.6 Modelling

9.6.1 PCC building model description

The developed model corresponded to the longitudinal external frame at the F axis (Fig. 9.1) before retrofitting. The model of the bare longitudinal frame consists of 121 nodes, and 220 tri-dimensional elements represented by 18 column and 9 beam sections. 2 flexural wall sections and damping elements[111] are used to develop alternative models.

[111] Rayleigh damping elements are used to simulate extra sources of damping (e.g. produced by

The vertical loads consist of the self-weight of the slabs, beams, columns, and walls, and the quasi-permanent static load – the latter according to the 1987 MC building code (Garcia-Ranz and Gomez, 1988). The analysis is carried out for 200 sec at 0.02 sec intervals.

The calibration procedure defined in Chapter 6 was adopted to tune the structural model so it predicted the PCC building behaviour. The analyses lacked the following important information: (i) reinforcement of the structural elements; (ii) state of integrity of the structural and non-structural elements; and (iii) adequate input record. This lack of information increased the uncertainties on the predicted reactions and, on the other hand, it allowed freedom to calibrate the model by changing the reinforcement in structural elements, and the effective slab widths for T beams.

Initially the calibration procedure was carried out using the Colima earthquake records. A second model was calibrated using the Copala event, which was obtained manually from a graph. All the records were obtained after the extensive building reinforcement. The frame configuration to validate corresponds to that which sustained the 1985 earthquake.

Although several structural models were used to study the seismic response of the building only the results from two configurations are presented. Those include: (i) the configuration that produce the best prediction for the Colima event; and (ii) the configuration giving the best prediction of the peak acceleration from the Copala event. The results of the analyses are presented concisely, and peak values of the most relevant parameters are shown.

9.6.2 Primary frame under Colima event

This section presents the calibration of the frame configuration using the low intensity 1995 Colima event, which struck when the structure and the foundation had been reinforced. The frame configuration corresponds to that which sustained the 1985 earthquake.

The model is termed “Primary” frame and consists of 5 bays, 9 levels of columns and

---

friction during dynamic excitation).

beams (including basement), and reinforced concrete walls[112] at the basement (Fig. 9.11). The following assumptions were made regarding the input motions: (i) although the base records are located at the ground floor, they were applied at the base of the stiff basement; (ii) the similarities of the horizontal motions allow the use of only one horizontal input motion; and (iii) since the vertical records indicate that the building is not rocking, after studying the influence of one or two vertical input motions, the analysis was carried out using the same vertical input motion for all the base nodes.

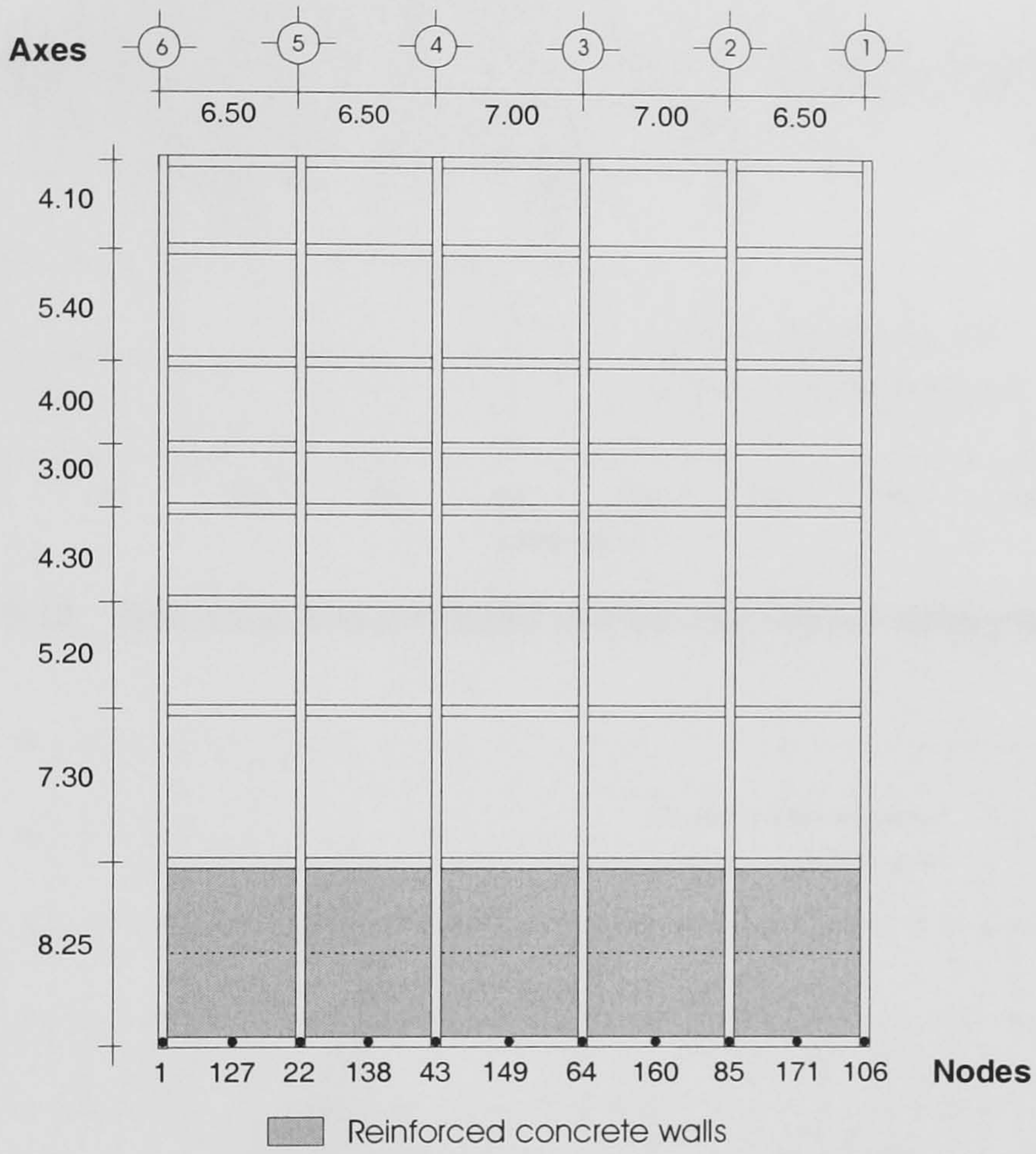


Fig. 9.11 PCC Building, Primary frame configuration

The elastic eigenvalue fundamental frequency for the model was 0.49 Hz, which is a low frequency for a 9-storey RC building and would correspond to a flexible structure.

As for the previous buildings, the behaviour of the model under seismic loads was evaluated by comparing recorded and predicted accelerations at roof level. The acceleration time histories in Fig. 9.12 show that the model correctly represents the amplitude and period of the recorded acceleration. Accordingly, the Fourier spectra shown in Fig. 9.13 indicate that the fundamental frequencies for the recorded acceleration (0.46 Hz) and for the predicted acceleration (0.43 Hz) are very close. Both

---

[112] Represented with flexural walls sections.

spectra show a second fundamental frequency at 1.1 Hz, with bigger amplitude for the predicted acceleration. As for previous analysis, the first two fundamental frequencies correspond to the site and structure frequencies.

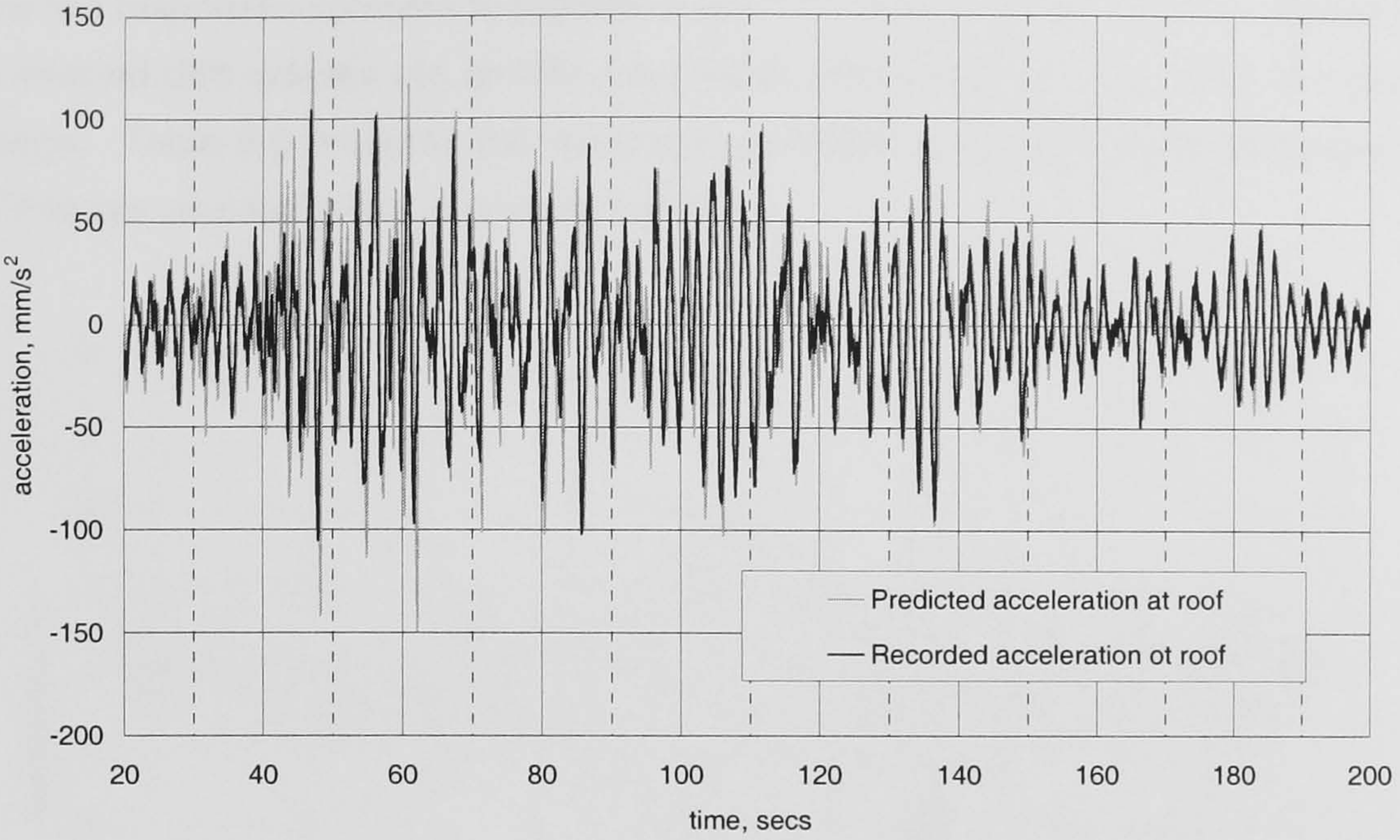


Fig. 9.12 Recorded and predicted roof acceleration, Primary frame

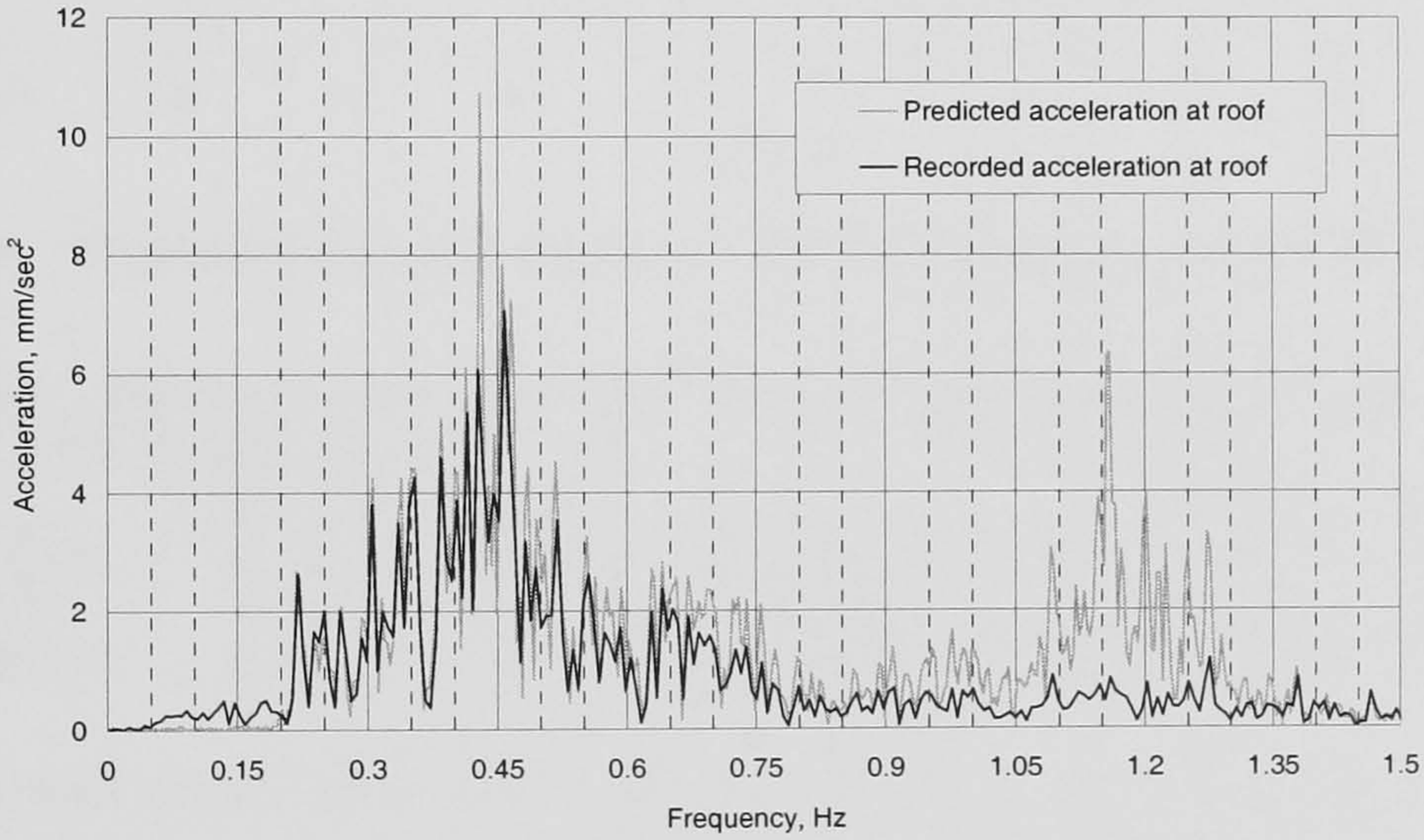


Fig. 9.13 Fourier spectra for the recorded and predicted roof accelerations, Primary frame

The predicted displacements show excellent agreement with the inferred[113] displacements (Fig. 9.14). It is possible that the good predictions arise from the high stiffness of the building and the low intensity of the input motion, which make the model

---

[113] Displacements and drift indexes computed from recorded accelerations are termed "inferred" displacement or "inferred" drift indexes.

and the actual structure follow the base motion. The drift indexes[114] between ground floor and the 3rd floor and between the 3rd floor and the roof indicate that the model is softer than the actual structure at the lower half and stiffer at the upper half (Fig. 9.15); these two responses combine to produce a good prediction of the displacements at roof. The inferred drift indexes are smaller than those associated with the onset of structural damage. Table 9.3 presents the maximum predicted and inferred displacements and drift indexes, and their fundamental frequencies.

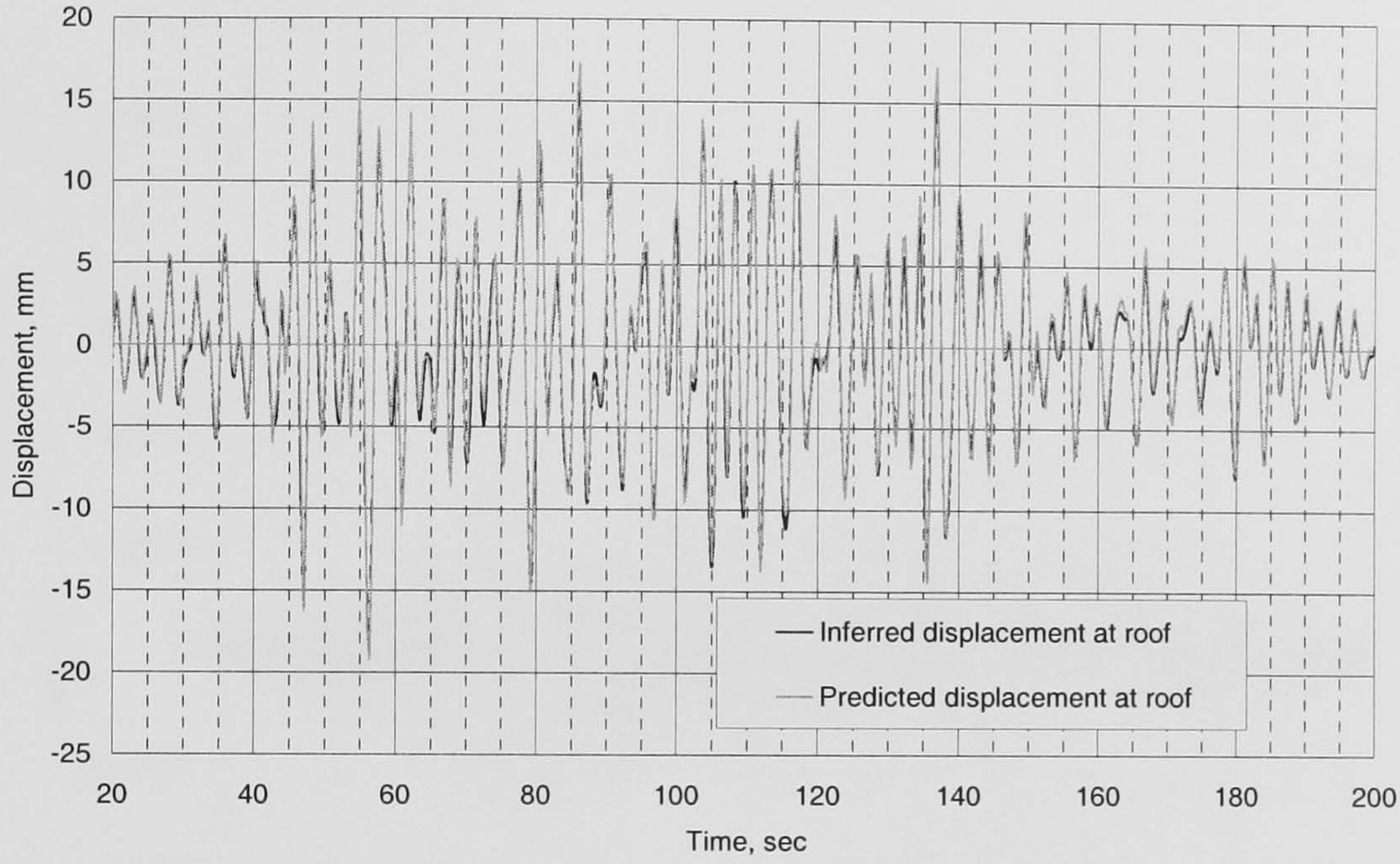


Fig. 9.14 Predicted and inferred horizontal roof displacements, Primary frame

Table 9.3 Maximum computed and inferred displacements and drift indexes

Lateral displacement (mm)			Drift index		
	Predicted	Inferred		Predicted	Inferred
3rd Floor	22.10	-19.79	Ground floor – 3rd Floor	0.00013	0.00007
Roof	-19.92	-19.39	3rd floor – Roof	0.00004	0.0001
Freq. (Hz)	0.43	0.43	Ground floor - Roof	0.00009	0.00005

In general, the Primary frame produced good prediction of the PCC response to the low magnitude Colima event, both in acceleration and displacements. The amplitude of the inferred displacements at the roof is well predicted due to the combination of a soft low section and a stiff upper section.

---

[114] Drift index is the drift between two storeys divided by the distance between them.

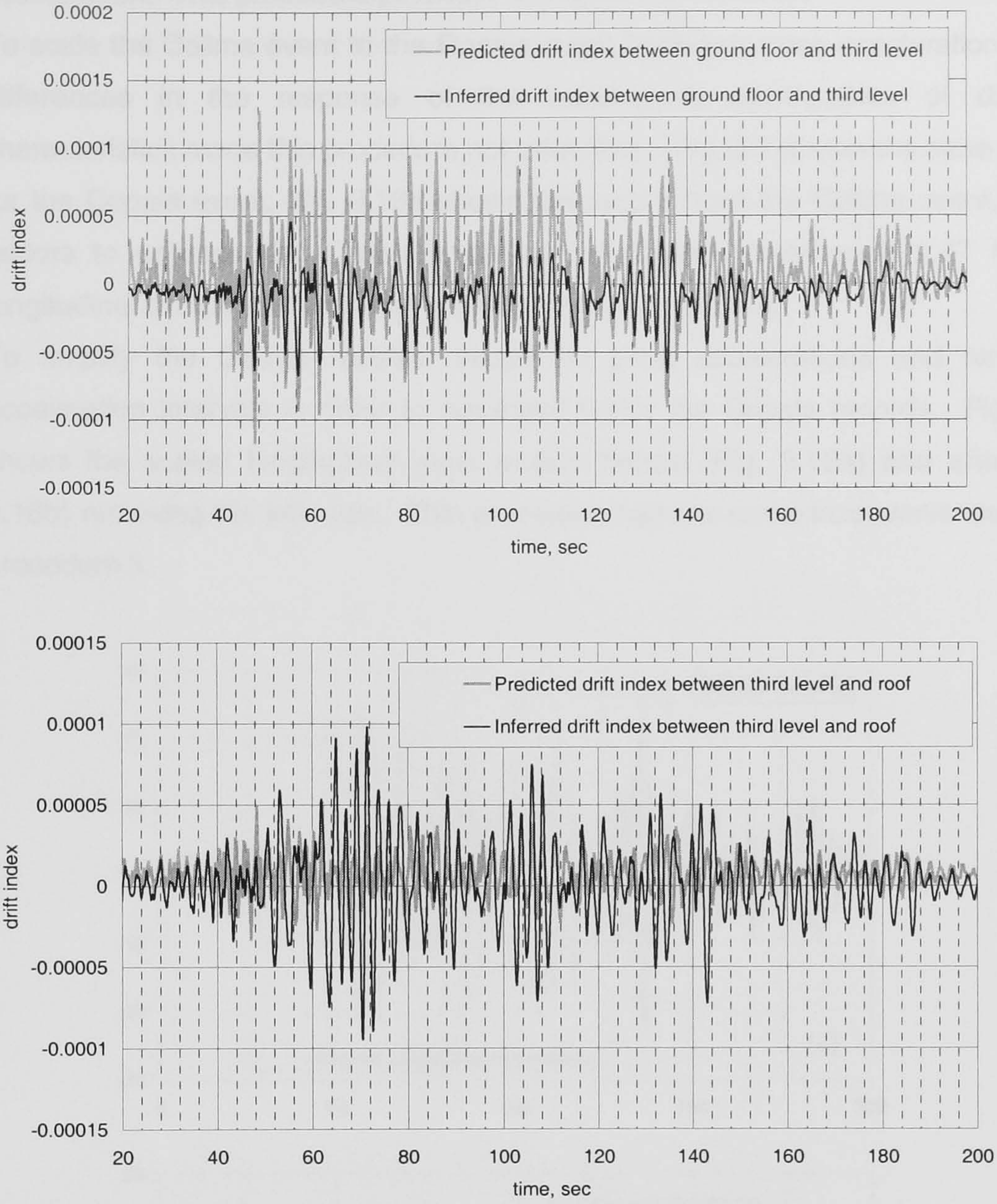


Fig. 9.15 Computed and inferred drift indexes, Primary frame

9.6.3 Structural model of the frame under simulated Copala event

The records available from the Colima event correspond to an earthquake that induced small accelerations on the PCC Building than the Copala event. Therefore, if the Colima event is scaled to the 19 September 1985 Michoacan earthquake more non-linear uncertainties than in the previous buildings, for which the Copala event was amplified, will appear. In order to avoid these uncertainties, several procedures to obtain a simulated PCC Copala event were applied. These were:

i) To obtain the input motion from a graph of the horizontal basement motion of the Copala event. The procedure was applied until after the interval of maximum

acceleration. This procedure produces the lowest uncertainty.

ii) To scale the Colima event to the Copala event based on peak accelerations. The differences in the response of the building to earthquakes of different characteristics made this procedure not attractive. (Fig. 9.7 shows the base record for the Copala event, Fig. 9.16a shows the record from the Colima event.) The factors to upgrade the Colima event to the Copala event were 2.77 for the longitudinal component and 3.94 for the vertical component.

iii) To amplify the Colima motions based on peak accelerations and removing acceleration intervals in order to represent better the Copala records. Fig. 9.16 shows the scaled longitudinal input motion before (Fig. 9.16a) and after (Fig. 9.16b) removing the intervals. This procedure has the same inconveniences as procedure ii.

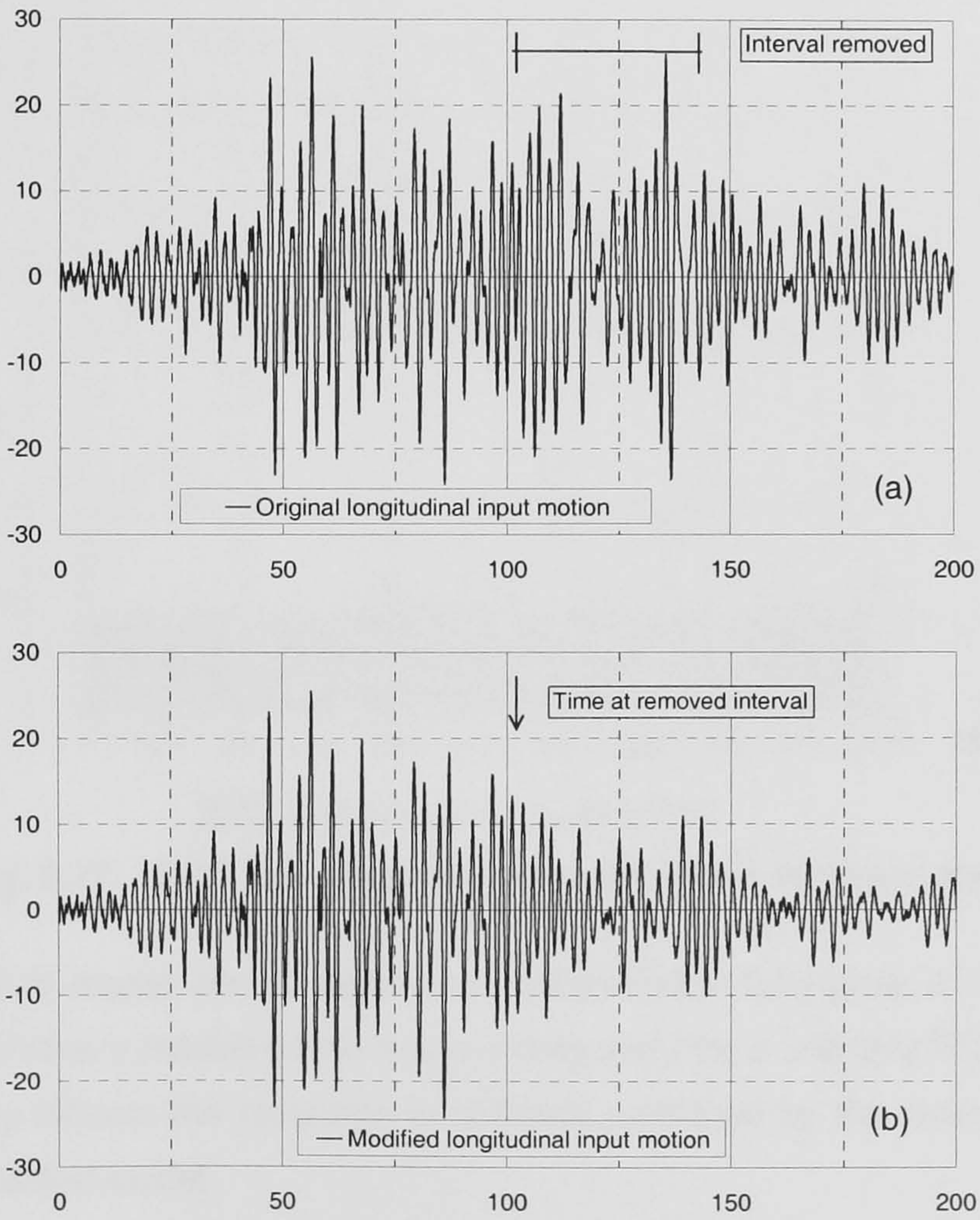


Fig. 9.16 Original and modified longitudinal basement input motion from the Colima event

The evaluation of the model under the Copala motion was based on the prediction of the acceleration amplitude at roof. After several configurations were evaluated, the model giving the best prediction during the Copala earthquake consists of the Primary frame

with the following modifications: (i) the walls at the basement are removed from the top half of the basement; (ii) the structural reinforcement at columns is reduced to a minimum quantity (ρ= 0.01, steel area/concrete area); (iii) the effective width of beams is reduced; and (iv) the Rayleigh damping is reduced from 2% to 1.7%. The model is termed "Implemented" model (Fig. 9.17).

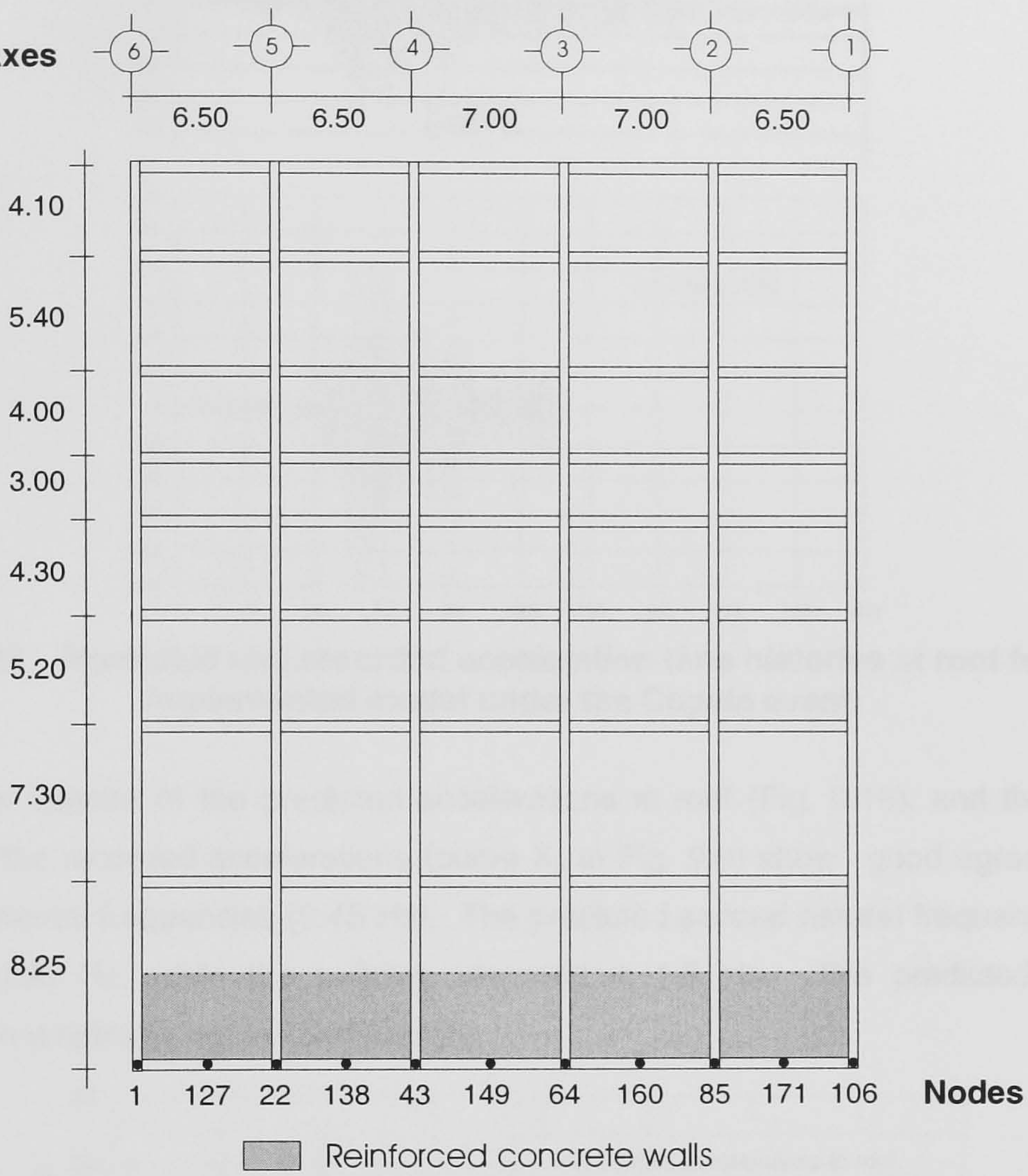


Fig. 9.17 PCC Building, Implemented frame configuration

The Implemented model elastic eigenvalue fundamental frequency of 0.35 Hz (36% lower than the Primary model) which is a low frequency for a 9-storey RC building. The lower frequency reflects the reduction in stiffness produced by the changes applied to get the Implemented model.

Fig. 9.18 shows the recorded and predicted roof acceleration time histories for the Copala event. The predicted accelerations follow the pattern of the measured accelerations, and although the peak maximum acceleration is not predicted, the prediction of the acceleration amplitude is satisfactory – under the conditions of this analysis. The maximum recorded acceleration during the Copala event was 539 mm/s^2,

the structural model predicts 497 mm/s^2, an 8% under-prediction.

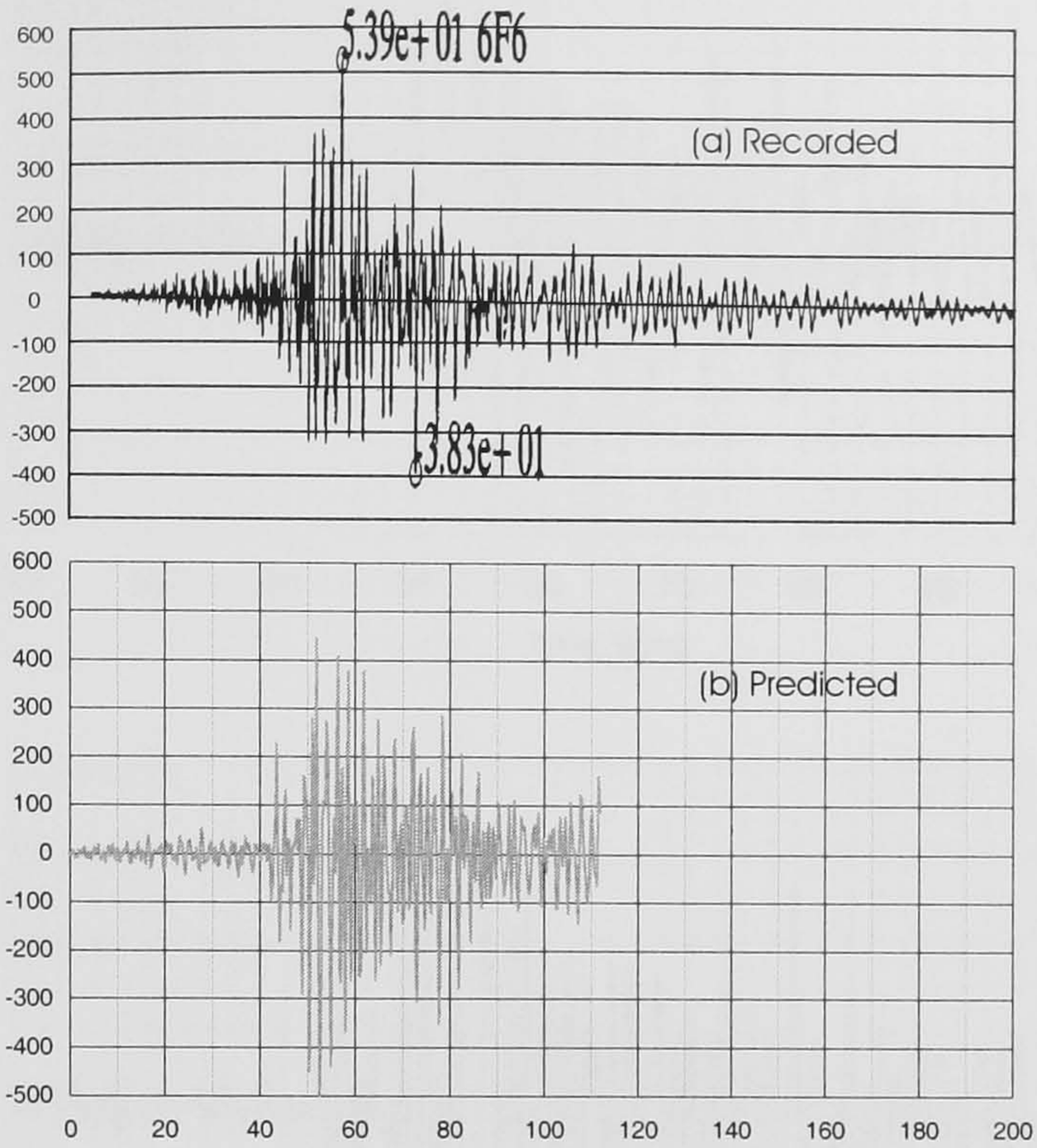


Fig. 9.18 Predicted and recorded acceleration time histories at roof for the Implemented model under the Copala event.

The Fourier spectra of the predicted accelerations at roof (Fig. 9.19), and the Fourier spectra of the recorded accelerations (curve X_n in Fig. 9.9) show good agreement for first fundamental frequencies (0.45 Hz). The predicted second natural frequency for the model is 0.95 Hz, while the building recorded is 1.3 Hz. The predicted spectral acceleration amplitude are not satisfactory.

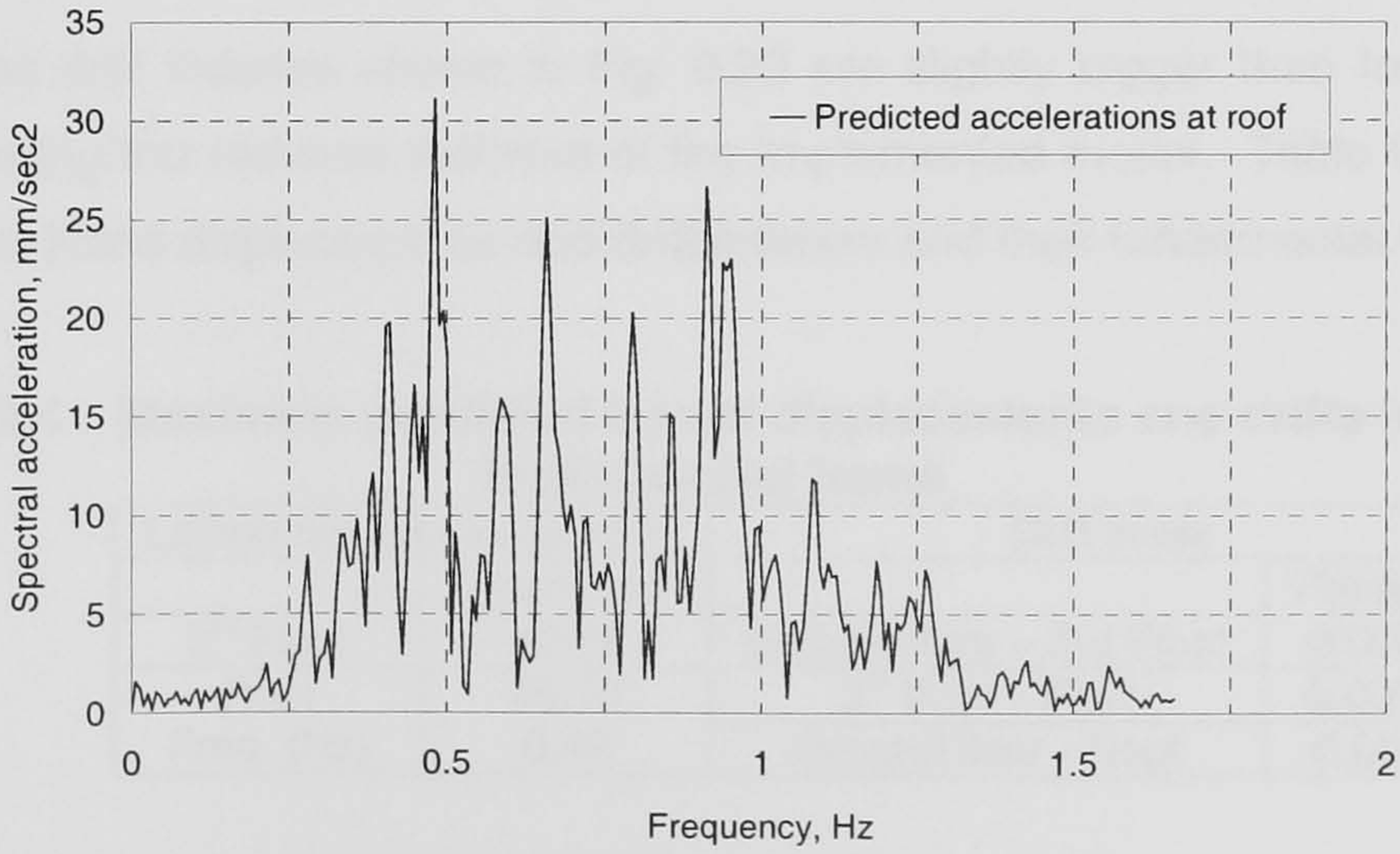
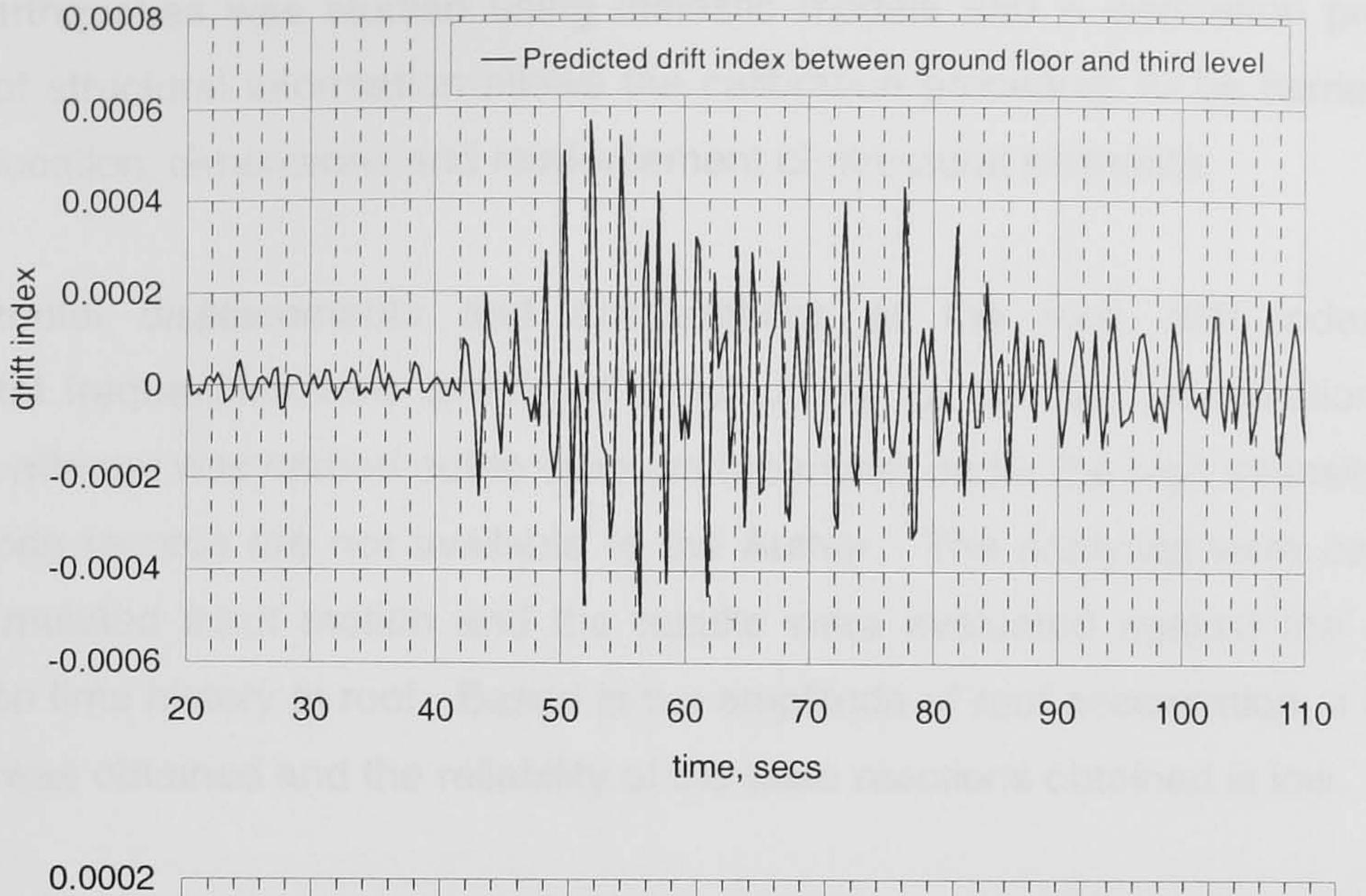


Fig. 9.19 Fourier spectra of predicted roof acceleration, Implemented frame



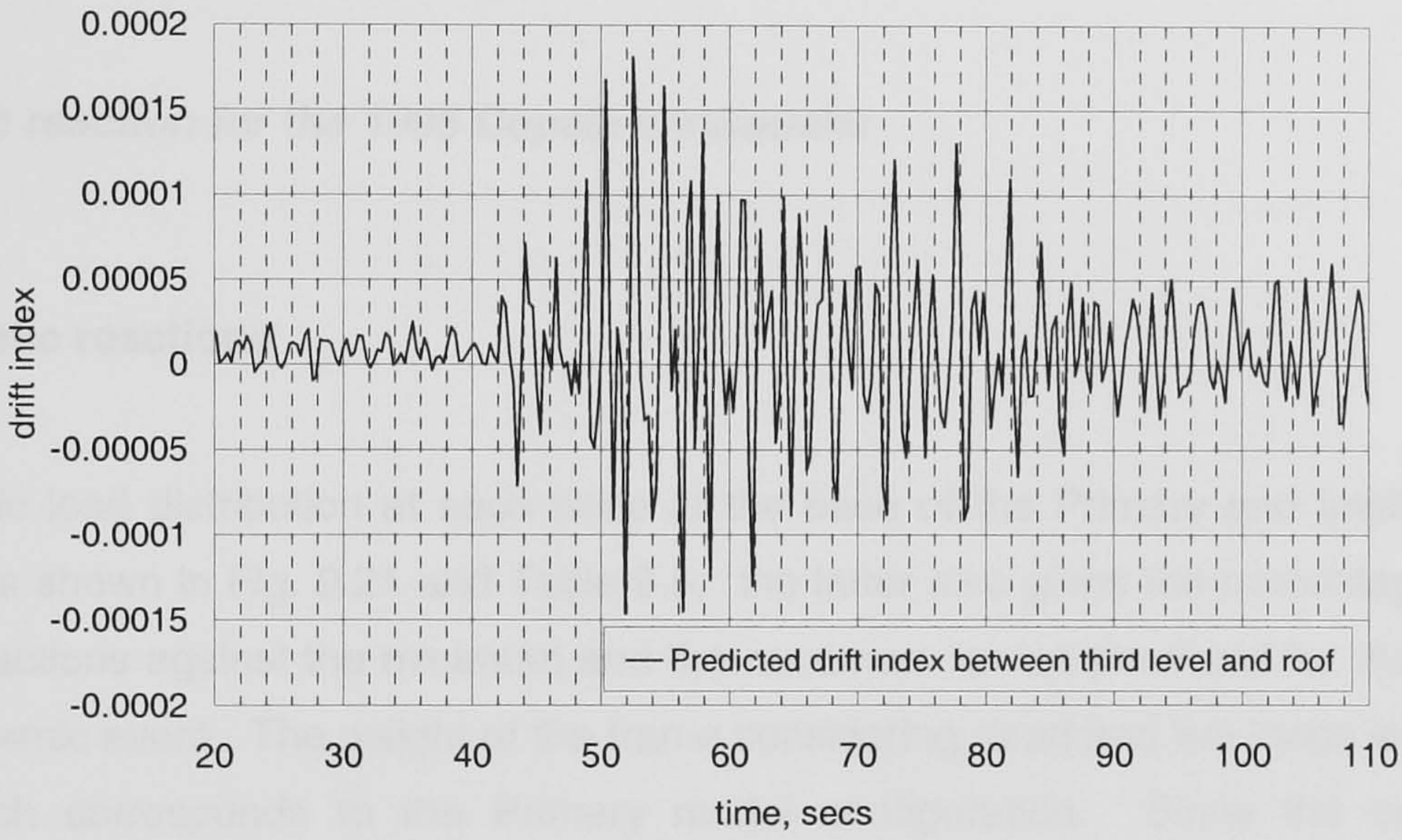


Fig. 9.20 Predicted drift indexes, Implemented frame

The predicted drift indexes shown in Fig. 9.20 are slightly bigger than for the Primary model, indicating the reduced stiffness of the Implemented model. Table 9.4 shows the maximum predicted displacements and drift indexes and their fundamental frequencies.

Table 9.4 Maximum predicted lateral displacements and drifts indexes, Implemented frame

Lateral displacement (mm)		Drift index	
	Predicted		Predicted
3rd Floor	43.99	Ground floor – 3rd Floor	0.00057
Roof	46.70	3rd floor – Roof	0.00019
Freq. (Hz)	0.42	Ground floor - Roof	-0.00039

9.6.4 Analysis

The structural response of a longitudinal frame from the PCC building to the Colima and

Copala earthquakes was studied using inelastic models and a calibration procedure. The lack of structural information allows the calibration procedure to be carried out by changing location, dimensions and reinforcement of structural elements.

The horizontal displacements and accelerations at the roof, drift indexes and fundamental frequencies were predicted satisfactorily for the low acceleration Colima event. An attempt was carried out to calibrate the model under the high intensity Copala event, whose records are not available to the Author. The analyses were carried out using a simulated input motion and the results were evaluated against the graph of acceleration time history at roof. Based in the amplitude of roof acceleration, a not good prediction was obtained and the reliability of the base reactions obtained is low.

9.7 Base reaction for the 1995 Copala earthquake

9.7.1 Static reactions

The static load distribution at each node at the base of the Primary and Implemented models is shown in Fig. 9.21 and Table 9.5; the latter also gives the percentage of the static reactions against the minimum and the maximum forces predicted for the Copala 1995 seismic event. The weight of the frame considering dead and live loads is 11199.1 kN, which corresponds to the Primary model configuration. Since the calibration procedure involves only the removal of the structural participation of the structural elements, the total static reaction for the Implemented model is the same.

The static load distribution shows that the columns take much of the load and the central columns the most. Table 9.5 and Fig. 9.21 also show that the nodes at the base of the RC walls in the Implemented frame carry less load . than for the Primary frame.

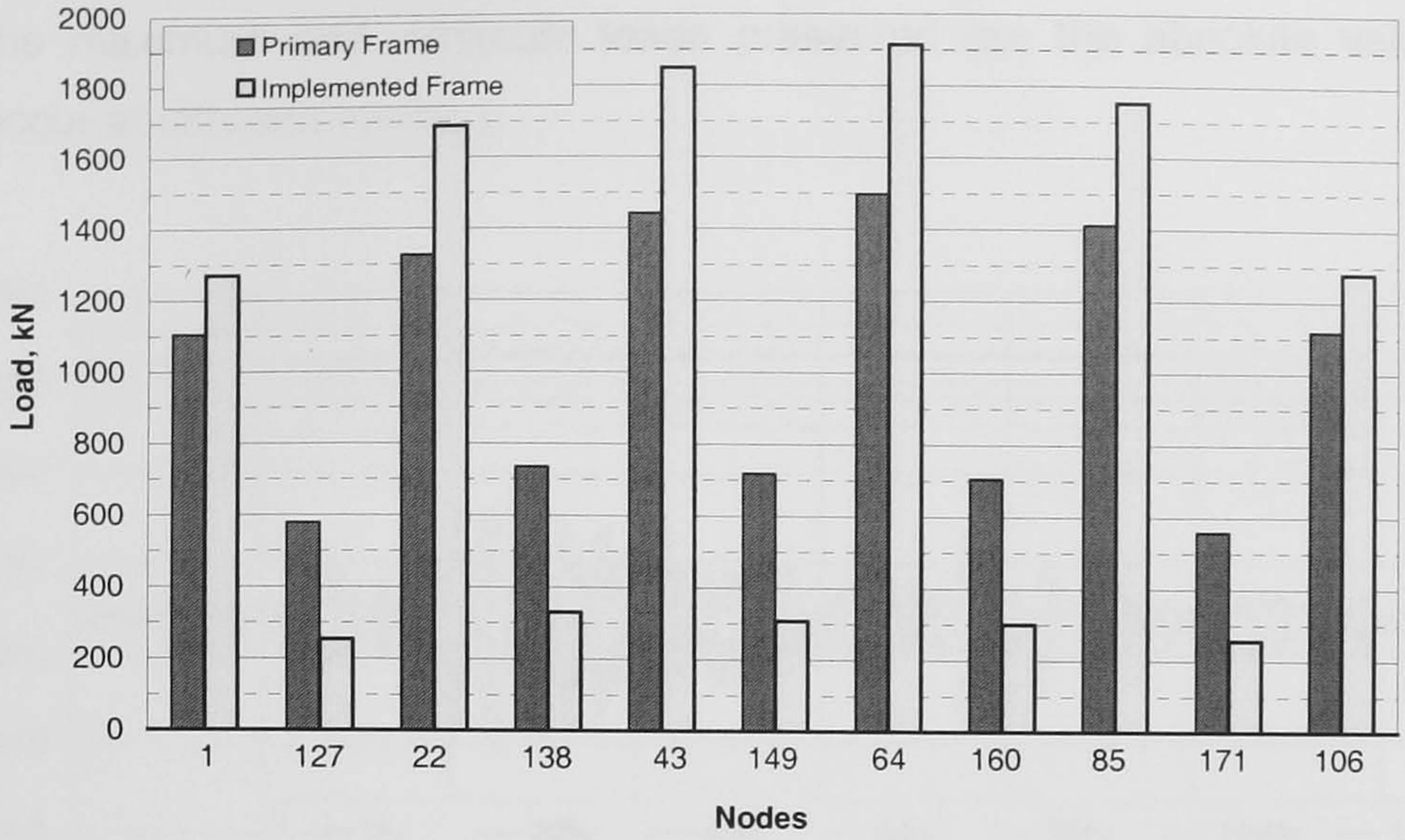


Fig. 9.21 Static load distribution at the base of the Primary and Implemented models

Table 9.5 Ratios of the maximum and minimum seismic loads predicted under the Copala event against the static loads

Node	Primary frame, kN			Implemented frame, kN		
	Initial	Max, %	Min, %	Initial	Max, %	Min, %
1	1104	123	77	1271	120	77
127	579	100	92	253	102	95
22	1326	106	100	1697	102	99
139	736	100	100	330	100	96
43	1442	105	100	1948	102	100
149	719	100	91	307	100	96
64	1499	105	100	1914	102	99
160	706	100	89	301	101	96
85	1413	103	100	1753	102	99
171	559	101	94	255	101	97
106	1117	124	82	1279	120	81

9.7.2 Seismic base reactions under the 1995 Copala earthquake

Fig. 9.22 shows the time-history of vertical reactions developed at the base of the Implemented frame when it is subjected to the Copala earthquake; Fig. 9.23 shows the maximum and minimum loads at each node. The time history contains a 30 seconds interval (with approximately 17 cycles) of high amplitude loads. The reactions show cyclic variations only for the extreme nodes (1 and 106).

The ratios of the maximum and minimum seismic loads to the static load (in percentage) for the Implemented and Primary[115] frames under the Copala event are given in Table

---

[115] The damping had to be increased in the Primary frame to approximately reproduce the acceleration amplitudes recorded at the top of the building during the Copala event.

9.5. (The maximum and minimum loads presented are the absolute values, which usually occur at different cycles.)

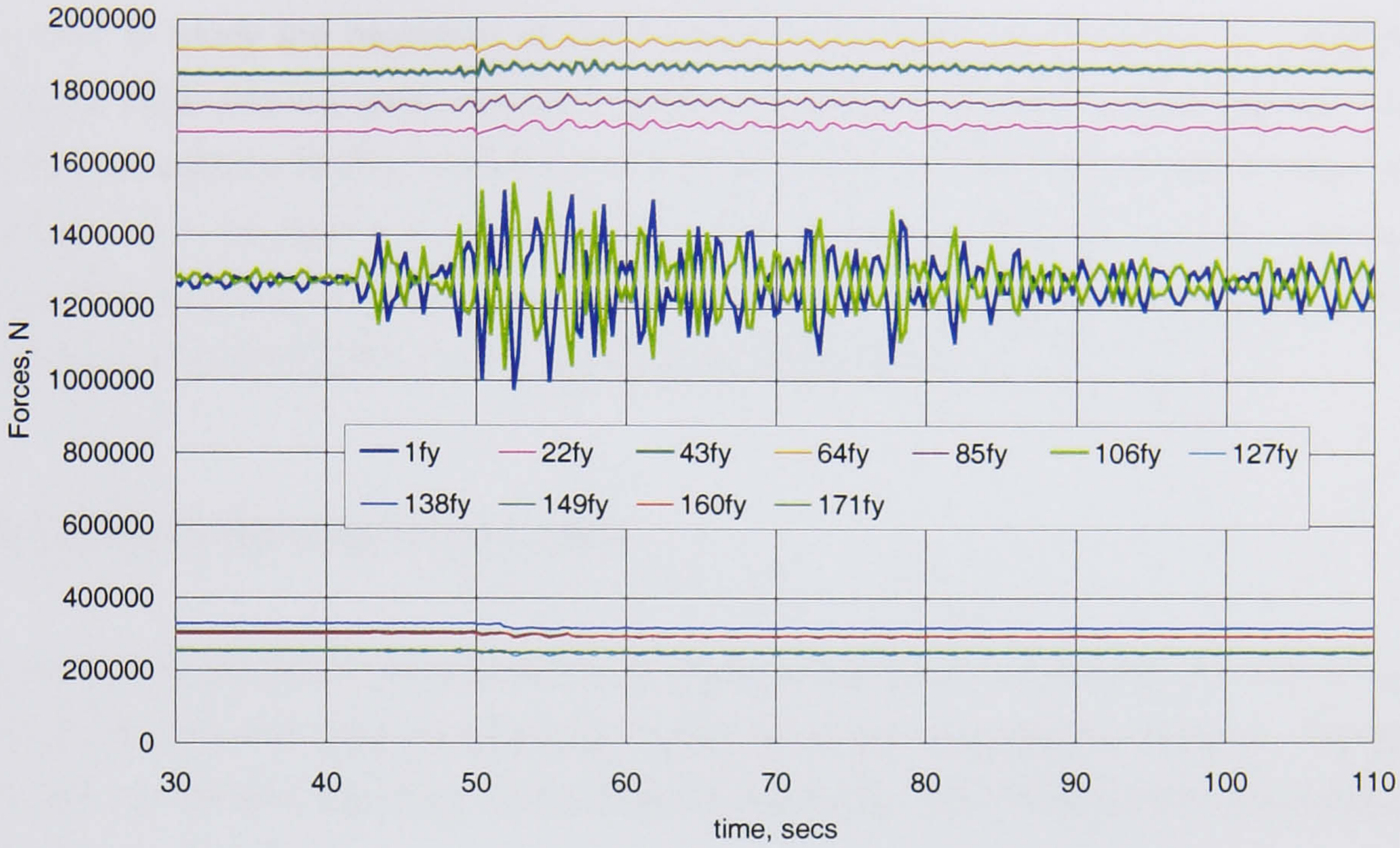


Fig. 9.22 Time-history of predicted base reactions in the Implemented frame under the Copala event

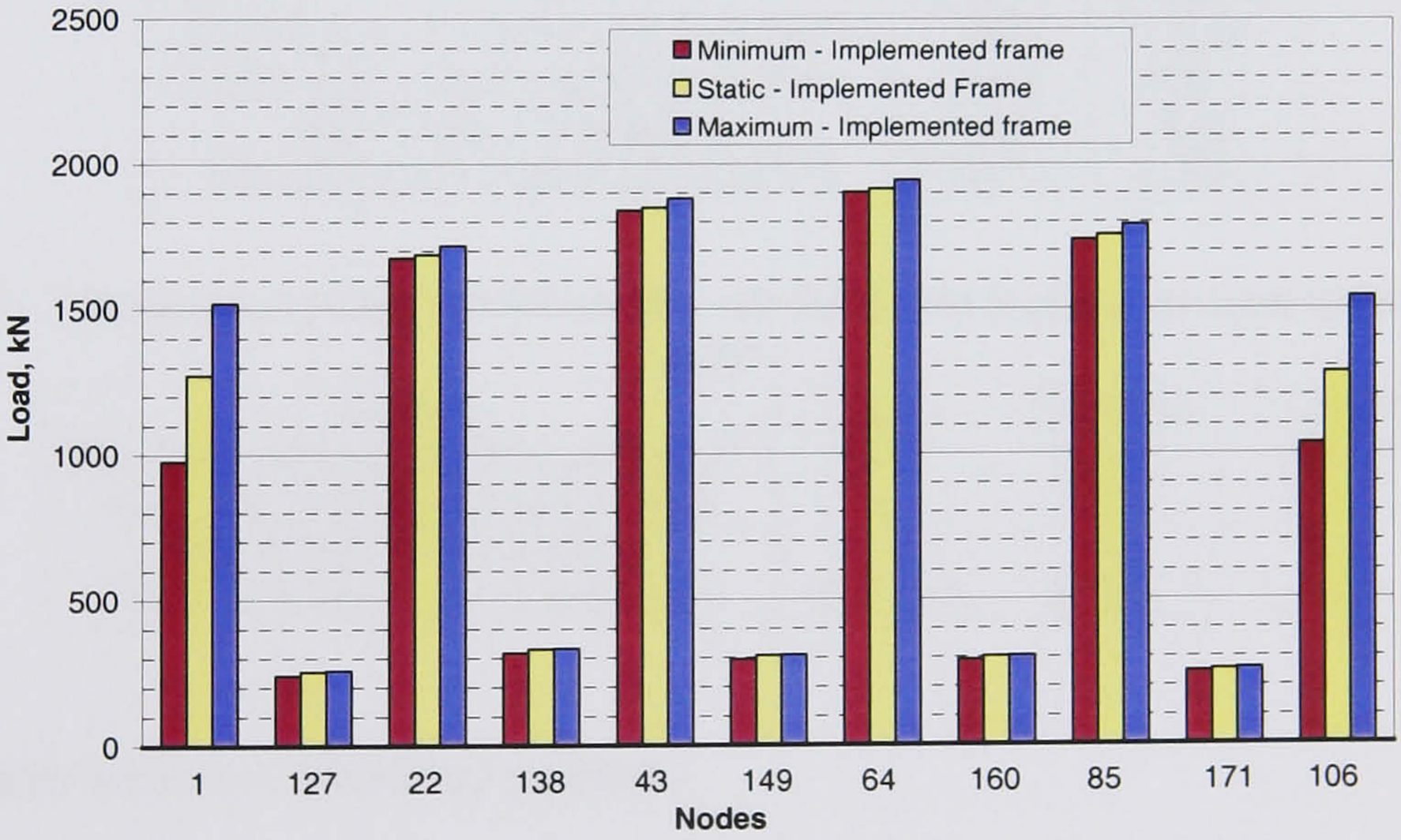


Fig. 9.23 Maximum and minimum reactions at the base of the Implemented frame under the Copala earthquake

The first and second fundamental frequencies of the reactions at the base of both models correspond to those identified previously for the site (0.45 Hz) and the structure (0.66 Hz). This combination of input motion and model fundamental frequencies also appears for the PC and JAL buildings.

9.8 Base reactions for the 1995 Michoacan earthquake

In order to study the response of the Primary and Implemented frames to amplified motions, both frames were analyzed using a 5 times amplified Copala record. An additional analysis of the Implemented frame under λ=3 was carried out in order to compare with previous building analyses. The base reactions for the PCC building under the Michoacan 1985 event correspond to those obtained by analyzing the Implemented model under a λ^{116}=5 amplified Copala motion.

9.8.1 General response of the models

Increments in predicted accelerations and displacements, and reductions in fundamental frequencies characterize the structural model response to upgraded motions. Tables 9.6 and 9.7 show a summary of the relevant results for the Primary and Implemented frames, respectively.

Table 9.6 Response of the Primary model to the Copala motion under λ= 1 and 5

Variable	Copala	5*Copala
Hor. Max. roof acceleration (mm/sec^2)	-149.2	-1950.0
Hor. Max. roof displacement (mm)	-18.92	230.8
Roof Displ. 1st frequency	0.43	0.40
Max. drift index (Ground floor-Roof)	0.00008	0.0023

Table 9.7 Response of the Implemented model to the Copala motion under λ = 1, 3, and 5

Variable	Copala	3*Copala	5*Copala
Hor. Max. roof acceleration (mm/sec^2)	-497.7	1312.5	-2910.7
Hor. Max. roof displacement (mm)	46.7	174.2	373.2
Roof Displ. 1st frequency	0.42	0.48	0.48
Max. drift index (Ground floor-Roof)	-0.00038	0.0023	0.0061

9.8.2 Reactions under amplified motions

Figs. 9.24 and 9.25 show the overall maximum and minimum reactions predicted for the Primary and Implemented models when subjected to the Copala motion amplified 5 times (λ=5). The reactions included in the figures are absolute reactions.

---

[116] Determined from the peak acceleration ratio. The SCT site is around 3.9 km away from the PCC building.

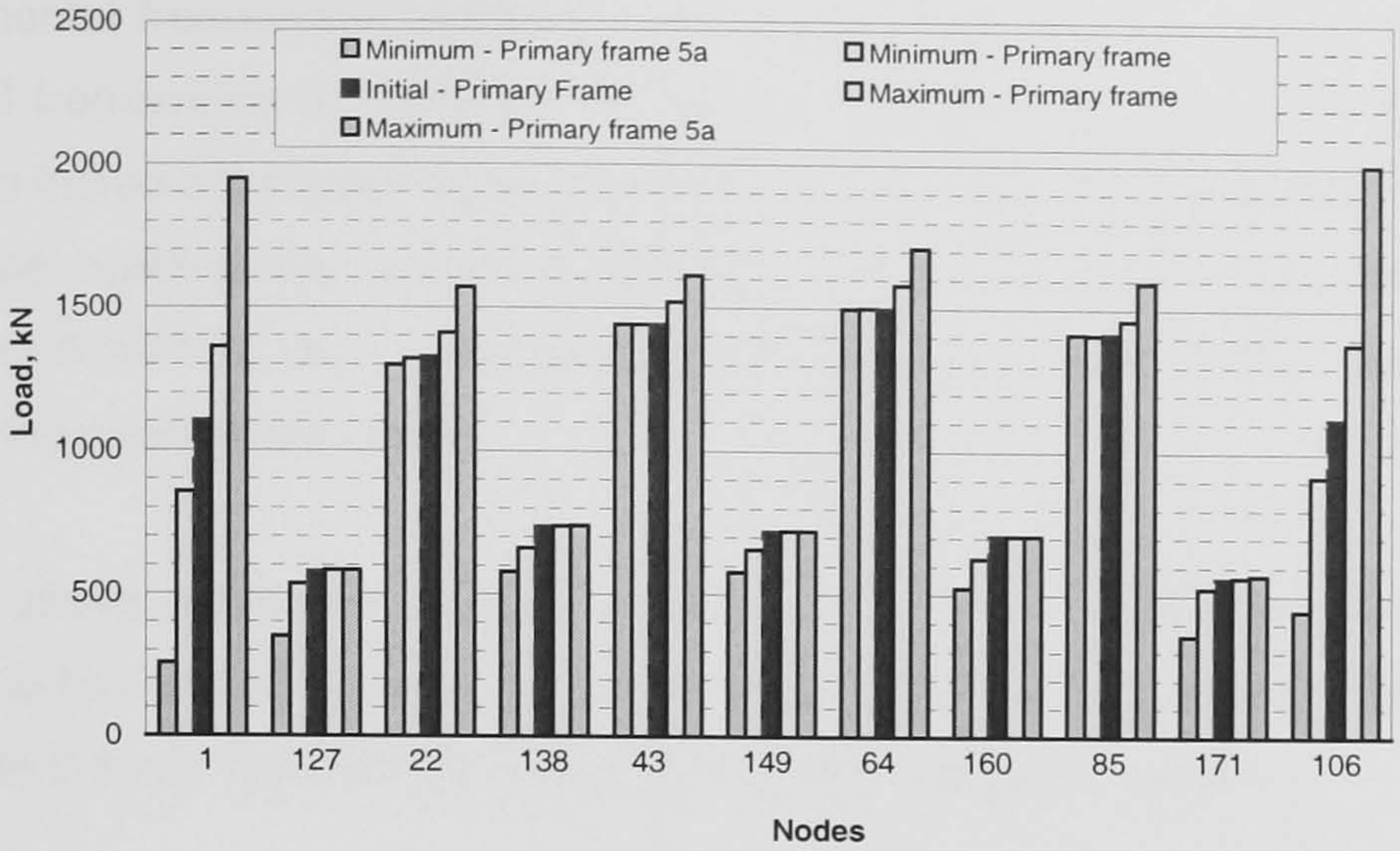


Fig. 9.24 Maximum and minimum seismic reactions in the Primary frame for Copala motion under λ = 1 and 5

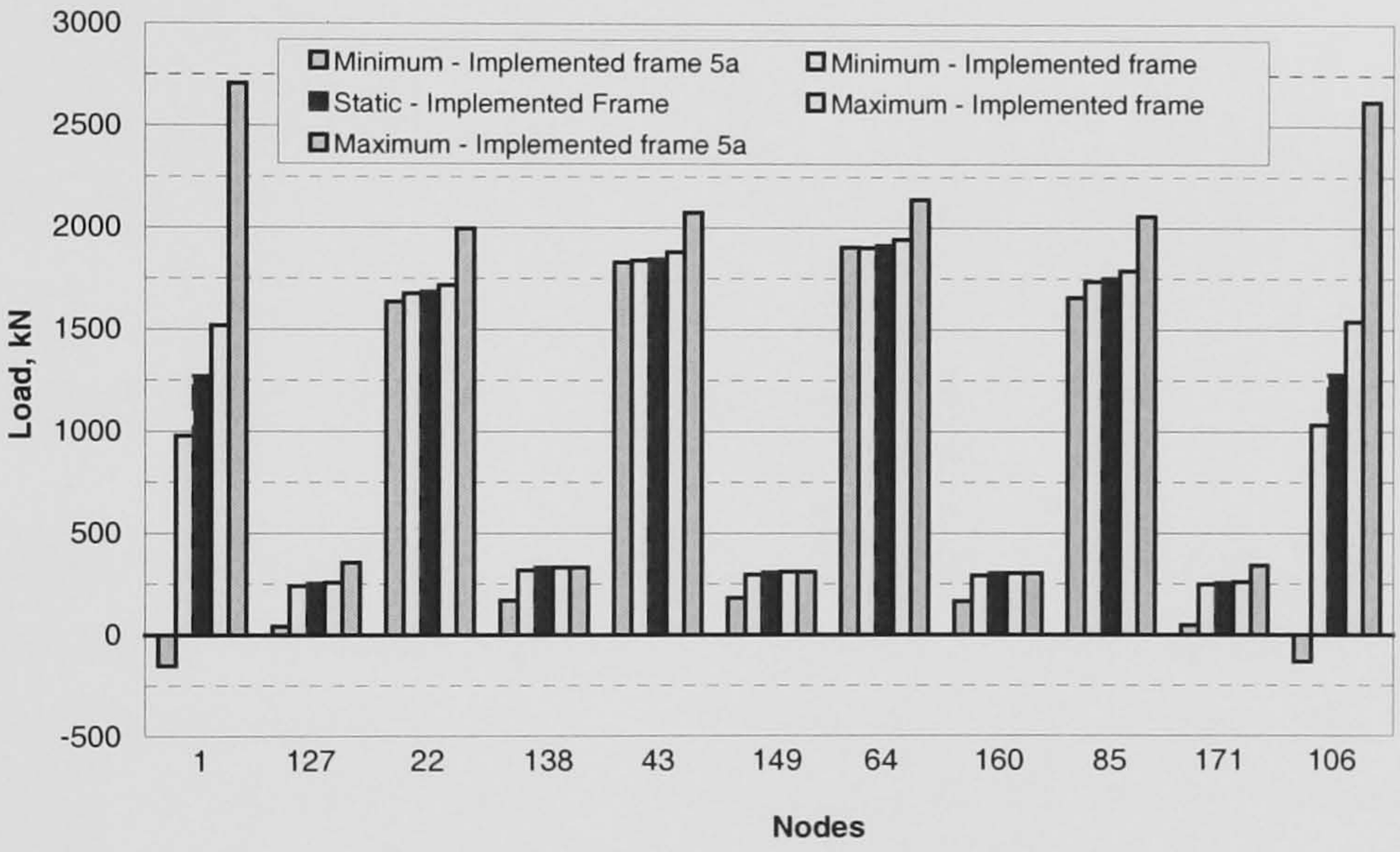


Fig. 9.25 Maximum and minimum seismic reactions in the Implemented frame for Copala motion under λ = 1 and 5

Figs. 9.24 and 9.25 show that the biggest seismic amplitudes occur in the columns located at the extreme sides of the structure, at nodes 1 and 106. The high seismic load amplitudes in these nodes contrast with the small variation in all the other nodes. This unusual load distribution for the intermediate nodes produces low confidence in the results.

The reaction amplification was evaluated through their Fourier spectral amplitudes at the fundamental frequencies. The base reactions of the Implemented frame are amplified by 82% and 213% for the analysis with λ=3 and λ=5, respectively. On the other hand, the Primary frame underwent a 109% amplification in base forces for λ=3.

The fundamental frequencies of the model under amplified input motions included the fundamental frequencies of the input motion and the building model. The results also indicated the increment in peak spectral ordinates. However the results did not show the reductions on building fundamental frequency observed in previous analyses. This indicates that ADAPTIC does not predict inelastic behaviour for the PCC building even under the 5 times amplified motion.

Due to the above mentioned uncertainty, the results from the PCC analyses are not considered to be reliable. After further processing of the base reactions it was decided not to include them in the final analysis of the dynamic capacity of piles.

CHAPTER 10

FACTORS INVOLVED IN THE COMPUTATION OF PILE FORCES ON THE CASE HISTORY BUILDINGS

This chapter describes factors and analytical tools involved in the conversion of basement base nodal reactions[117] into pile loads for the case history buildings. The chapter includes: (i) an elastic methodology to evaluate the static pile-raft load sharing on the case history buildings; (ii) the compensation analysis of the building foundations and the static capacity of the piles determined from the Imperial College Pile design method (ICPDM); (iii) the processing of the base reactions predicted for the case history buildings; (iv) the analysis of the stability of the foundations when subjected to lateral loads; and (v) a brief description of the kinematic interaction forces on the friction piles.

Chapter 11 uses the results from this chapter to compute seismic pile forces and so asses the corresponding seismic capacity of the piles.

10.1 Previous studies on the pile - raft load distribution in Mexico City

The considered piled raft foundations may transmit loads to the soil by way of both pile-soil and raft-soil contacts. This load sharing occurs for two main reasons: (i) the cap of the pile group is cast directly on the ground, even when a foundation has been designed as a pile group; or/and (ii) the piles are designed to reduce settlements in a system that has adequate shallow foundation bearing capacity. Currently few methods of analysis allow explicitly for the load-carrying potential of the raft, and these are either very approximate or of limited applicability[118]. The lack of an adequate method has resulted in a design practice that usually ignores the bearing contribution of the raft, giving conservative estimates of the foundation performance (Clancy and Randolph, 1996; Horikoshi and Randolph, 1996; Poulos, 2001).

---

[117] Base reactions are the loads computed from the structural seismic analyses. When this loads are modified by the effects of compensation, pile group, number of piles at the support, and pile-raft load sharing they are termed pile loads.

[118] According to the Technical Committee TC18 of the International Society of Soil Mechanics and Geotechnical Engineering which studied the concept of piled raft foundations (O'Neill, et al., 1996).

Poulos (2001) indicates the following conditions as being unfavourable for piled rafts: (i) soil profiles containing soft clays or loose sands near the surface; (ii) soil profiles consisting of soft compressible layers at relatively shallow depths; and (iii) soil profiles that are likely to undergo consolidation settlements or swelling movements due to external causes. From the summary presented in Chapter 3, the typical profile for Mexico City (MC) can be classified as unfavourable for piled raft foundations, with the raft contribution being relatively minor compared to other geotechnical scenarios.

The relevant research undertaken on pile-raft load sharing in MC is introduced in the sections below. This review is used to evaluate a proposed methodology of analysis and to understand the general response of piled-raft foundations in MC.

10.1.1 Finite element analysis of La Azteca building in Mexico City

Hain and Lee (1978) presented a finite element (FE) analysis of the compensated raft-friction pile foundation of La Azteca building, which is located in the Lake Zone of MC. Hain and Lee's study[119] was based on the case history presented by Zeevaert (1957). Hain and Lee modelled a high stiffness raft using rectangular finite elements, without including the pile group's reinforcing effect on the soil layer.

The foundation solution for La Azteca building consisted of a 6 m deep excavation and 83 concrete friction piles of 0.4 m side width driven to a depth of 24 m (see pile layout in Fig. 10.1). The total structural load was 79.2 MN that corresponds to an average total vertical pressure of 118 kPa. Allowing for the 6 m of excavated soil reduced the net pressure to 32 kPa, and the potential load in the pile group to 21.5 MN - with an average load per pile of 259 kN. In Hain and Lee's FE analysis the net pressure was applied uniformly to the piled raft.

Hain and Lee's FE analysis of La Azteca building predicted that the raft carries 17% of the 32 kPa net pressure, or 5.4 kPa. Thus, the raft total contribution was the 5.4 kPa predicted plus the 86 kPa "compensated stress" provided by the 6 m excavation. This gives 91.4 kPa or 77% of the total vertical pressure for the raft; the piles taking 23% of the total pressure. It will be shown later that 77% contribution from the raft is high for the soft clay profile in MC. The computed 17% raft participation of the net pressure agrees with other simple analytical solutions.

---

[119] Also presented in Hemsley (2000).

Hain and Lee (1978) predicted pile loads that varied considerably from the average design load of 259 kN; their calculations indicated that 40% of the piles carried a load less than 100 kN, with 8% exceeding the piles ultimate capacity of 690 kN.

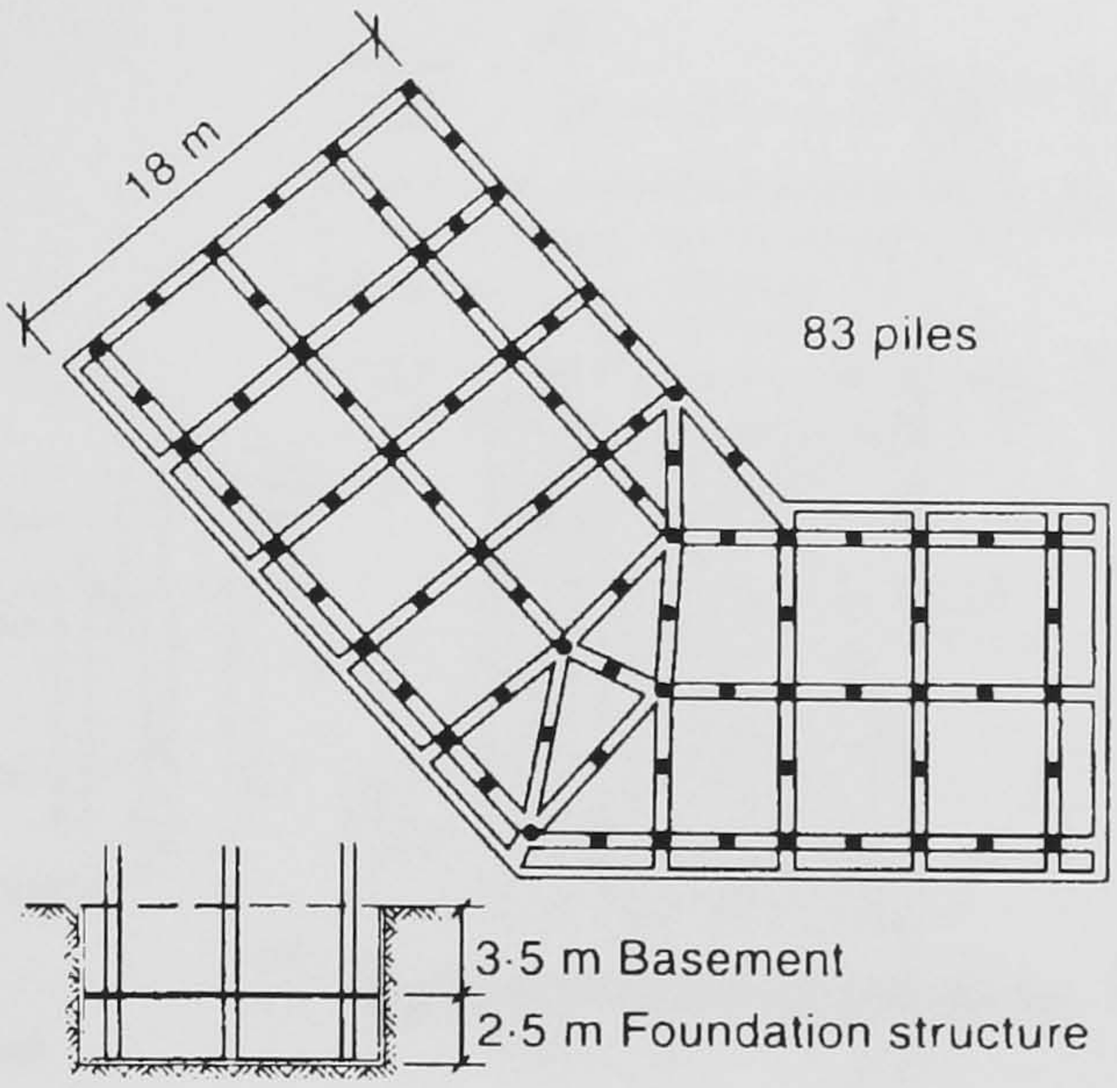


Fig. 10.1 Basement layout for La Azteca building (Hemsley, 2000)

The Author carried out an evaluation of pile-raft load sharing by substituting MC clay properties into the worked examples presented in Randolph (1983), Clancy and Randolph (1993 and 1996), Horikoshi and Randolph (1999), and Poulos (2000) – all of them based on elasticity concepts. In general, in all the examples, the soft MC clay properties led to a raft contribution of less than 30%.

10.1.2 Instrumented piled raft foundation – static response

Mendoza, et al. (1998) have been carrying out research into the pile-raft load sharing response of piled foundations in MC. An extensive review of this research is presented since it is an important antecedent to the Author's studies.

Mendoza, et al.'s research is based on an instrumented friction pile-box foundation that is a central support of an urban bridge (Impulsora bridge, Fig. 10.2). The foundation instrumentation focuses on the load transfer mechanism that develops at the pile-soil and slab-soil interfaces during the bridge construction (1995) and operation, for both static and seismic conditions. To this end, a total of 13 load cells, 8 pressure cells, 6

piezometers and 1 accelerometer[120] were installed during construction. In addition, in 1997, two accelerometers (one free field device located at the surface and one at 60 m depth), and instruments to measure foundation and ground settlements up to 60 m depth, were installed. The upper-structure of the bridge has also been instrumented.

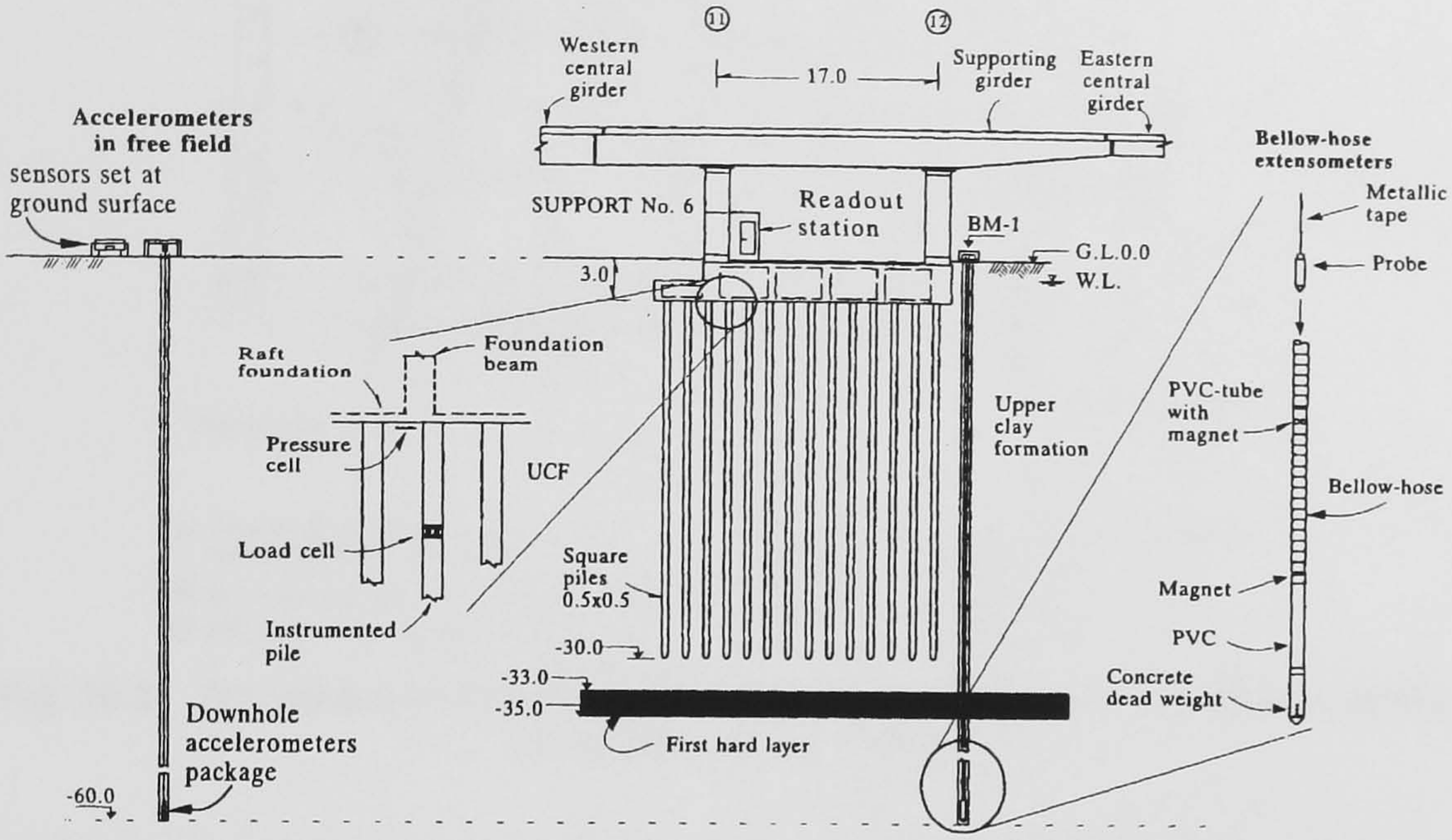


Fig. 10.2 Impulsora bridge instrumented support (Mendoza, et al., 2000b)

The foundation box rests on 77 square (0.5 X 0.5 m) 27.4 m long concrete piles. Seven piles were equipped with load cells located 2.0 m below the raft level. Two of these piles were also instrumented with three additional load cells located at other depths along their length. The layouts of the piles and the transducers are shown in Fig. 10.2 and 10.3.

[120] Located on top of the foundation box.

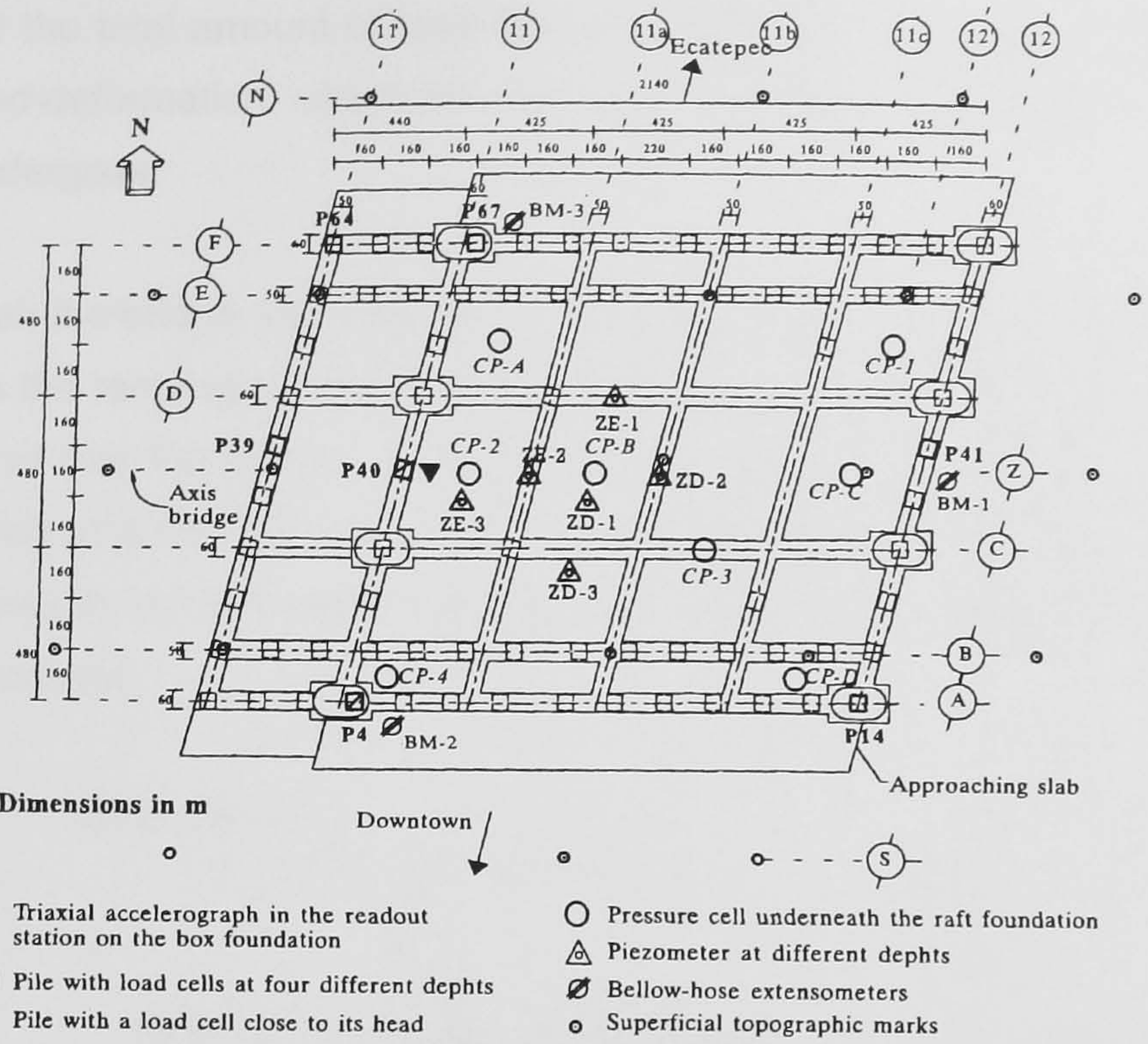


Fig. 10.3 Impulsora bridge foundation plan view and instrumentation layout (Mendoza, et al., 1998)

Some of Mendoza, et al.'s main observations from the foundation static response are:

i) The raft-soil contact pressures increased rapidly as a result of the load applied by the construction of the raft and the foundation beams. When the box foundation was completed and further loads applied the contact pressure kept growing, although the rate reduced as the piles took up load at a faster rate due to the pile group's higher stiffness.

ii) The contact pressures were not uniform throughout the foundation raft. In the early construction stages the maximum to minimum contact pressure ratio was 2.64, towards the end of bridge construction this fell to 2.42, reducing further to 1.93 after 2.5 years of bridge operation, and to 1.70 after 4 years (August 2000). This equalisation of stresses progressed as the foundation settled under load.

iii) The piles located at the corners and in the longitudinal external sides took higher loads than those located in the central section or in the transversal external sides. These differences in load appeared during the construction process and tended to reduce in the long term.

iv) Load transfer can take place under different conditions with either the pile loads increasing, while the raft contact pressures decrease, or the converse. The

percentage of the total amount of load that both piles and slab carry depends on their individual load-deformation characteristics and on the total settlement that the foundation undergoes.

v) When the bridge was opened for vehicular transit, the piles shared 85% of the total load with the remainder carried by the foundation raft (Fig. 10.4). Mendoza, et al. (1998) indicated that the raft-soil contact pressure amounts to 70% of the vertical total stresses existing at grade elevation previous to the soil excavation[121]. That is to say that the ground beneath the basement level remains unloaded by approximately 30% of its overburden pressure.

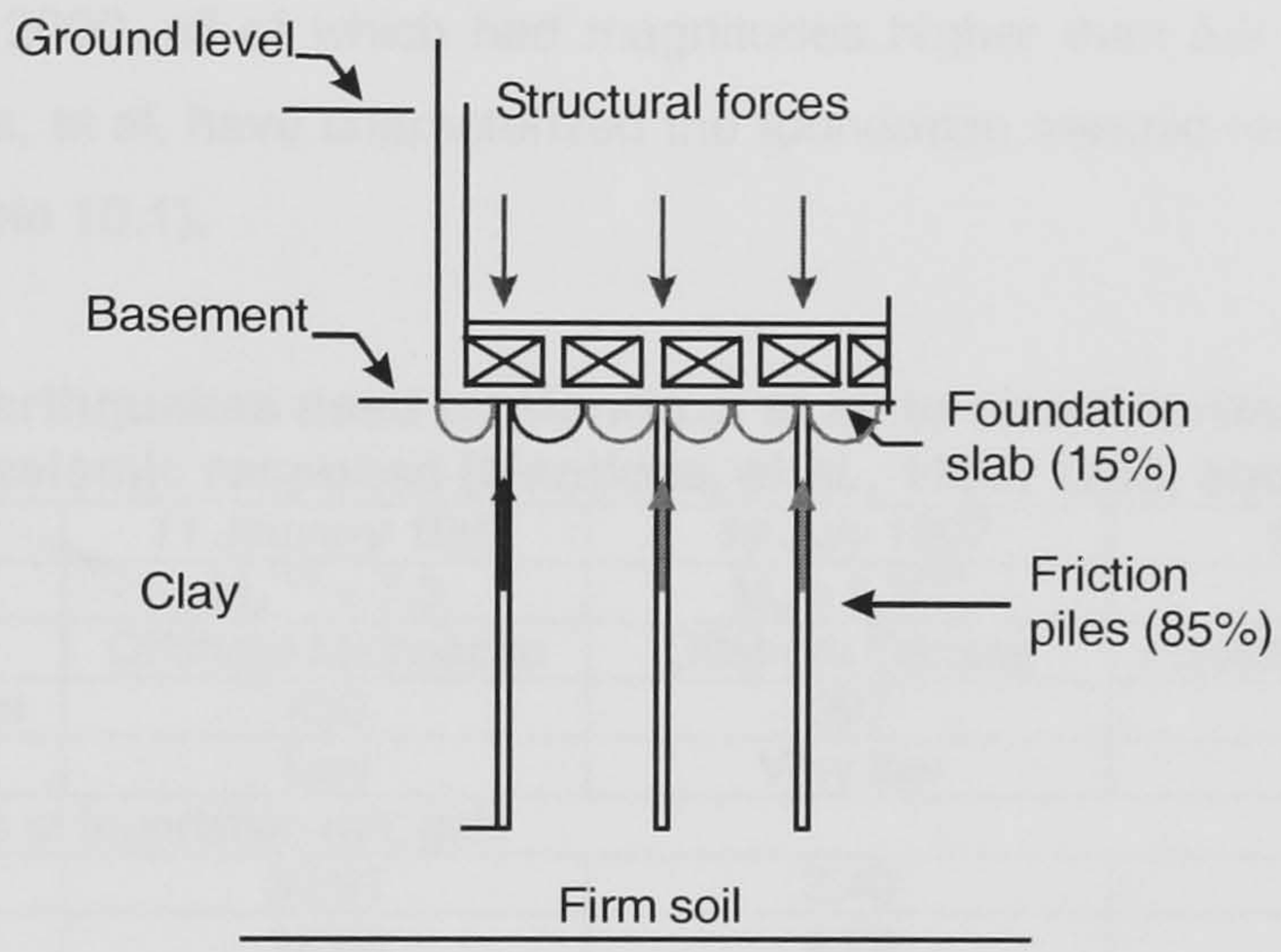


Fig. 10.4 Long term static pile-raft load distribution for Impulsora bridge (Mendoza, 1998)

Nevertheless, Mendoza, et al. (2000b) indicated that towards the end of the construction stage (1996) the foundation developed a settlement of the order of 20 cm, with a differential settlement of 2.4 cm between the columns that support the counter beams (possibly rebound). By February 2000, the total settlement was more than 40 cm on axis 11 (which support the central beams of the larger bridge span) and 36.5 cm on axis 12, resulting in a 3.5 cm differential settlement in the longitudinal direction (the axes are shown in Figs. 10.2 and 10.3).[122]

---

[121] Mendoza, et al. (1998) pointed out that this 70% agrees with the criterion adopted by Hansbo and Jendeby (1983), who established that for normally consolidated clays the raft-soil contact pressure is between 70% and 80% the in situ total stress. (The Author considers that this percentage may depend on the excavation depth and on the site conditions).

[122] This may seem contradictory since it suggests $\sigma_v' > \sigma_{v\,initial}'$, however the settlements could be related to dewatering and regional subsidence.

Hjort and Carrillo (1985), who also installed load cells to measure raft-soil contacts, gave another example of static pile-raft load sharing measurements in MC. They observed that long term regional subsidence eliminated the contribution of the rafts at different times ranging from 30 to 290 days. This may indicate the loss of contact between the raft and the soil, and load increments on the piles.

10.1.3 Instrumented piled raft foundation in Mexico City – seismic response

Mendoza, et al.'s instrumented foundation experienced 8 relevant earthquakes between its construction in 1995 and February 2000. There were two events in 1997, four in 1999 and two in 2000, all of which had magnitudes higher than 5.9 (Mendoza, et al., 2000a). Mendoza, et al. have characterized the foundation seismic response using 3 of those events (Table 10.1).

Table 10.1 Earthquakes used by Mendoza et al. to characterize the Impulsora bridge seismic response (Mendoza, et al., 1997, 1998, and 2000a)

Date	*11 January 1997*	*19 July 1997*	*15 June 1999*
Magnitude	M_e[123] = 7.3	M_a = 6.3[124]	M_w = 6.7
Epicentre	Offshore Michoacan	Offshore Oaxaca	Puebla – Oaxaca border
Epicentral dist., km	450	397	230
Intensity in MC	Low	Very low	Low
Max. accelerations at foundation raft, gals			
Longitudinal	30.91	3.40	28.10
Transversal	12.83	4.29	24.62
Vertical	0.88	0.30	2.15
Duration, sec.	124	54	≈150

Regarding the seismic response of the pile-raft system Mendoza, et al. pointed out:

i) The axial loads on piles, the pressures developed at the soil-raft interface, and the pore pressures recorded show cyclic responses that follow closely the accelerations recorded in the foundation box (see section 6.1). Mendoza, et al. (1998) indicated that the geotechnical cyclic response is influenced very strongly by the high stiffness of the foundation box.

ii) The pressure cells in the soil-raft contact recorded higher cyclic amplitudes near the border of the longitudinal sides due to building rocking. During the January 1997 earthquake the load cell CP3 (Fig. 10.5b), located at the bridge axis, recorded a maximum amplitude of 0.05 t/m^2 (0.45 kPa), while the load cell CP1 (Fig. 10.5a), located

---

[123] M_e, based on energy content.

[124] M_a, based on wave amplitude.

in one corner, recorded a maximum amplitude of 0.25 t/m^2 (2.51 kPa) (Mendoza, et al., 1997). The maximum amplitudes seen during the June 1999 event were 0.08 t/m^2 (0.78 kPa) and 0.25 t/m^2 (2.45 kPa) for the CP2 (located at the bridge axis) and CP1 load cells, respectively (Mendoza, et al., 2000a). See Fig. 10.3 for the location of instruments.

iii) The average raft pressure increased by 3% to 20% during the earthquake, so reducing the forces on the friction piles. The load transferred from the piles to the raft persists for some weeks after the earthquake before reversing. In the long term the piles recovered their capacity and the soil-raft pressure reduced (Figs. 10.5, 10.7 and 10.8) (Mendoza, et al., 1998).

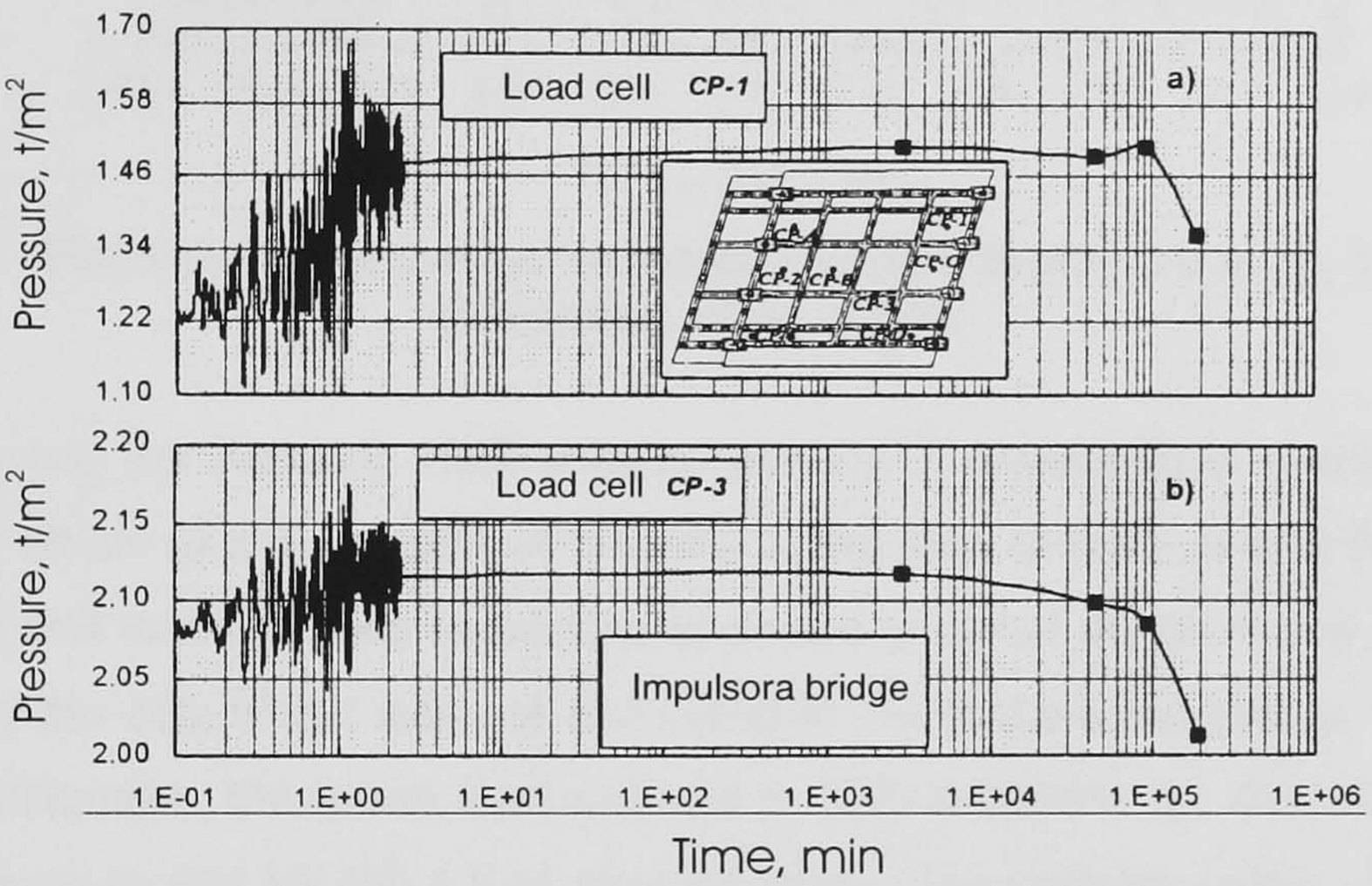


Fig. 10.5 January, 1997 event and long term recorded pressures at the soil-raft contact of the Impulsora bridge (Mendoza, et al., 1998)

Mendoza, et al. monitored the pile seismic response by recording the pile seismic loads at different pile depths. Their main observations are:

i) The head load history at pile P41 during the January 1997 (Fig. 10.6a) showed a maximum seismic amplitude of 24.5 kN (2.5 ton), or 4.6% of the load at the start of the earthquake (54.4 ton). The average static load on pile P41 remained unchanged as a result of both 1997 earthquakes. This implies that the dynamic shear stresses developed at the pile-soil interface did not cause any degradation (Mendoza, et al., 2000b).

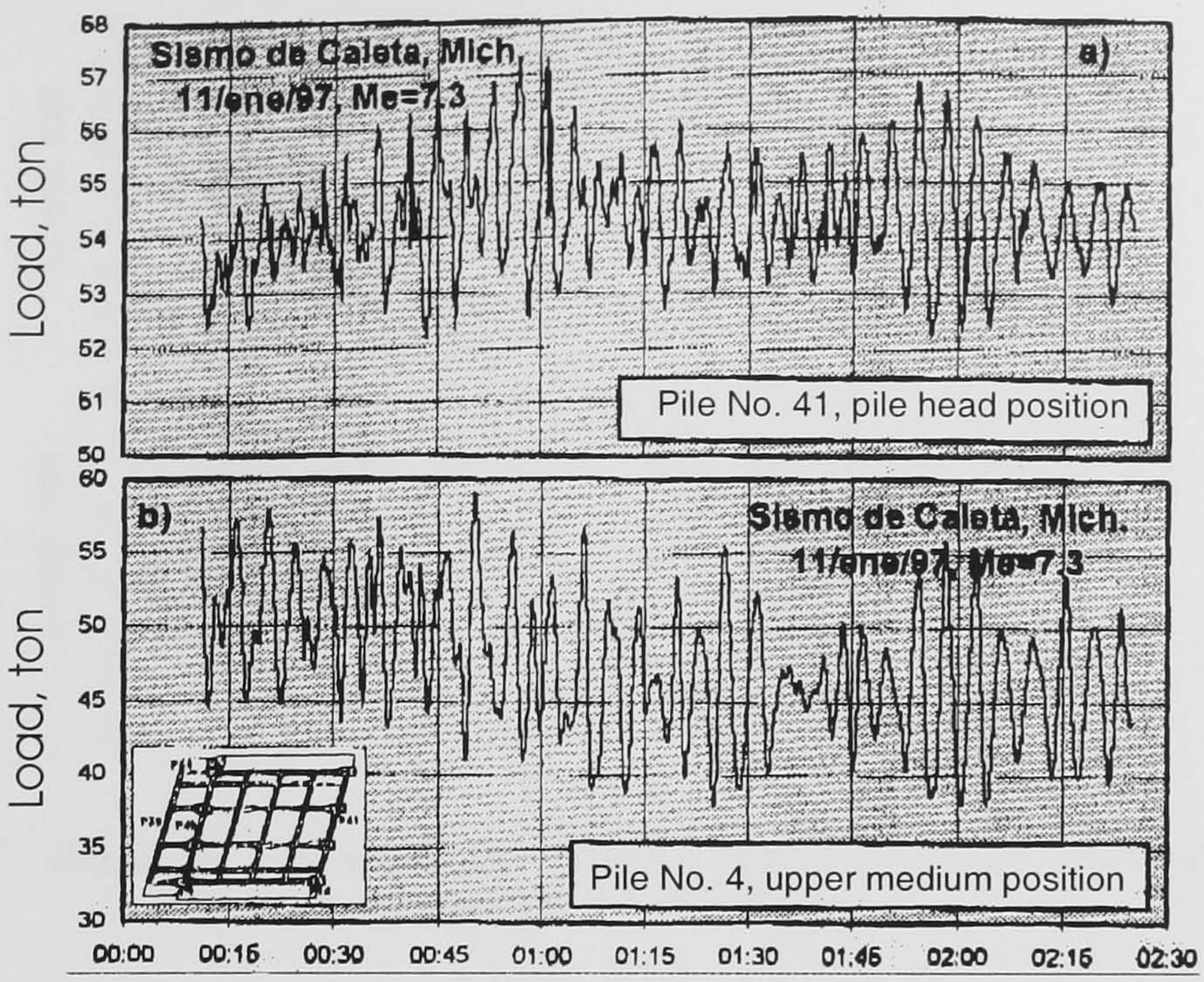


Fig. 10.6 Pile load recorded on Impulsora bridge during January, 1997 event (Mendoza, et al., 1997)

ii) During the January 1997 shaking pile P4[125] developed a maximum seismic amplitude of 88 kN (9 ton), or 16% of the load at the start of the event (= 55.7 ton) (Fig. 10.6b). The first loading pulse induced a decrease of about 40 kN in the average load measured by the cell, which was not recovered in the succeeding cycles. Immediately after the earthquake, the mean load showed a 19% reduction (to 441 kN or 45 ton), which recovered to 494 kN (50.4 ton) after 48 hours, and complete after ≈70 days (Fig. 10.7a). Mendoza, et al. (1997) considered that this recovery results from thixotropic effects at the pile surface.

[125] The cell in pile P4 is located at a depth of 11.35 m below the foundation box slab.

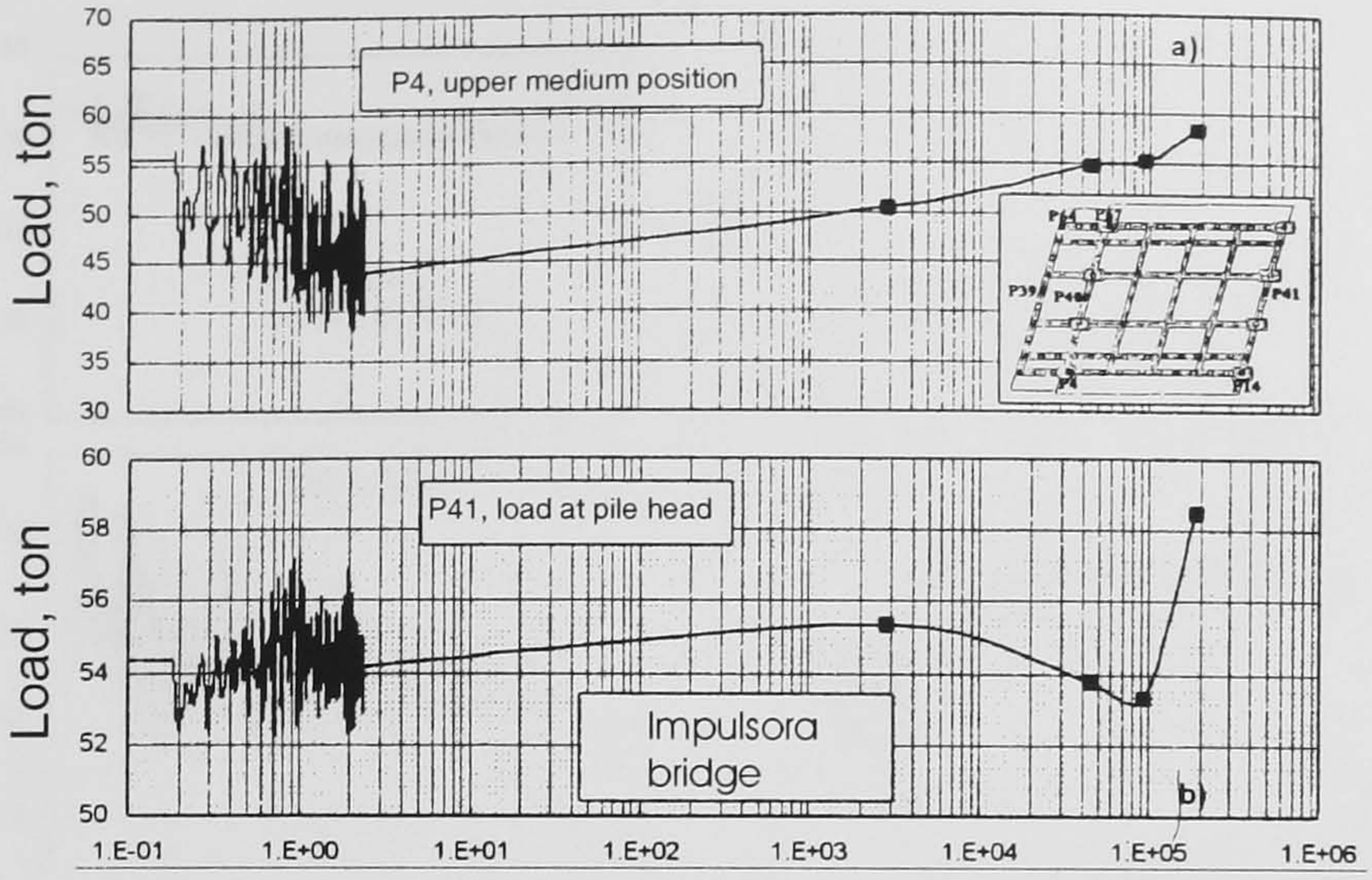


Fig. 10.7 January, 1997 event and long term pile loads on Impulsora bridge (Mendoza, et al., 1998)

iii) For the June 1997 low intensity shaking, the seismic load amplitudes were much lower and the pre-earthquake pile conditions remained unchanged (Mendoza, et al., 2000b).

iv) The recorded time histories of load for piles P14 and P40 and the raft pressures developed on load cells CP1 and CP2 during the June 1999 event are shown in Fig. 10.8. The maximum seismic amplitudes recorded were 3.55 ton (34.8 kN) for pile P4, and 14.10 ton (138.3 kN) for pile P40. As for pile P4 during the January 1997 earthquake, piles P14 and P40 suffered a reduction in capacity towards the end of the event. For pile P14 the recorded load reduced 4.4% from 74.3 ton (728.9 kN) to 71.0 ton (696.5 kN) (Fig. 10.8a). For pile P40 the load reduced 11%, from 63 ton (618.0 kN) to 56 ton (549.4 kN) (Fig. 10.8b) (Mendoza, et al., 2000a).

v) Mendoza, et al. (2000a) pointed out that even though pile P14 is located near to a corner of the raft, it is pile P40 – located on the axis of the foundation – which underwent the highest load increments during the earthquakes. Mendoza, et al. indicated that higher forces developed on piles P40 and P4 because of the concentrated forces applied above them by the bridge beams supported on axis 11 (Fig. 10.2).

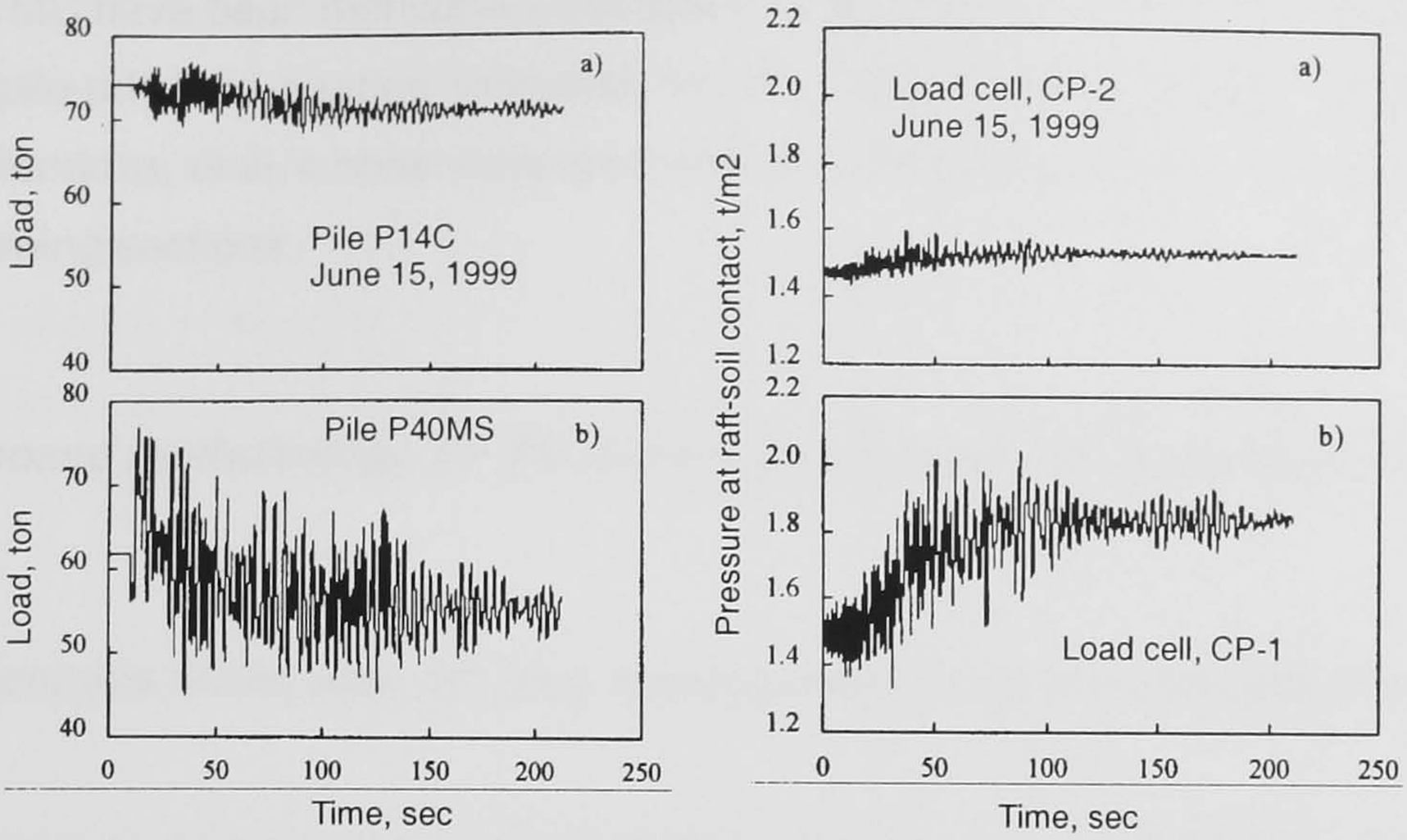


Fig. 10.8 Pile load and cell pressures on the Impulsora bridge foundation during the June 1999 event (Mendoza, et al., 2000a)

The load transfer along the piles cannot be interpreted from Mendoza et al's papers since they do not report records from cells at the head and along the shaft of the same pile. The tendency for static capacity to recover after shaking in all the instrumented piles conforms with the general trends for the effects of time on pile capacity, as reported in Chapter 2.

Finally, the effects of shaking on settlements are illustrated by the data shown in Fig. 10.9 for the June 1999 event. The records for axis 11 showed a step settlement of ≈ 20 mm, but comparing the trends for the period prior to June and over the following months seems to indicate that the settlement rate was increased by the seismic actions (Mendoza, et al., 2000a). Settlement measurements were not available for the 1997 events (Mendoza, et al., 1998).

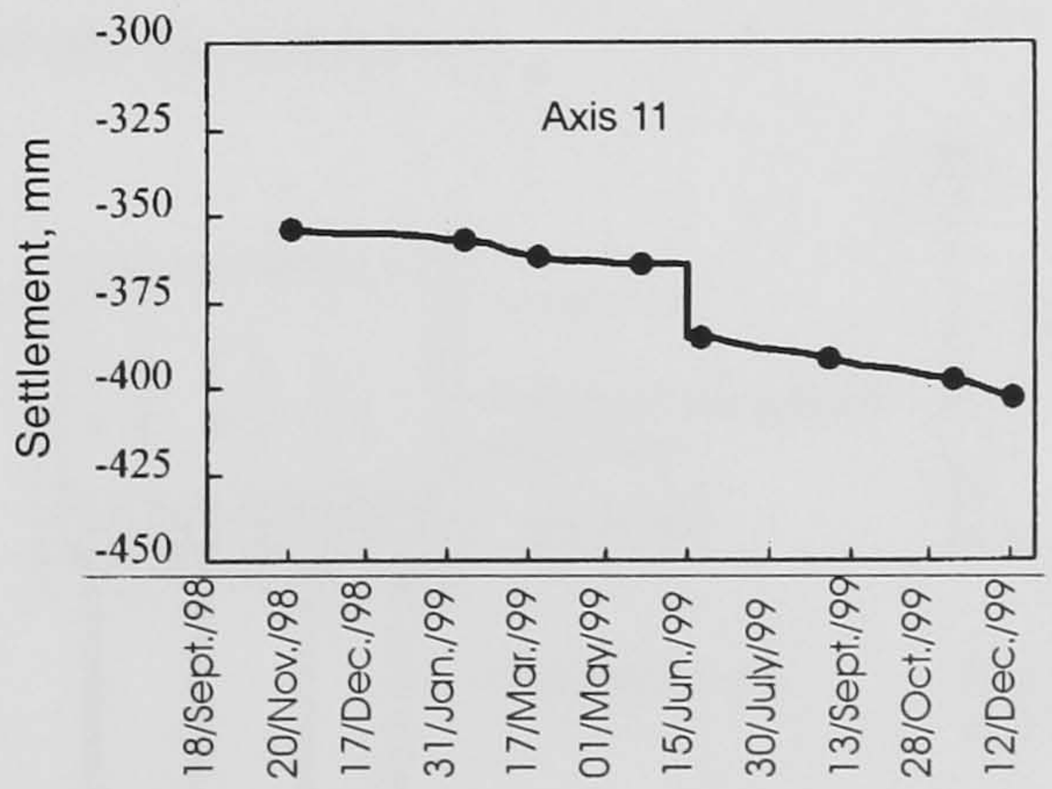


Fig. 10.9 Settlements on the Impulsora Bridge foundation (Mendoza, et al., 2000a)

Once the previous studies and the general piled-raft response to static and seismic

loading in MC have been mentioned, the following sections introduce the methodology to compute pile-raft load sharing response for the case history buildings studied in this Thesis. Mendoza, et al.'s observations constitute a reference for the analyses presented in the following sections.

10.2 Proposed methodology for the analysis of the pile-raft load distribution

10.2.1 Principles of the pile-raft load sharing analysis on the case histories

The assessment of the load sharing between pile group and overlying raft for the MC case histories was performed by the Author following the simple methodology presented by Poulos (2000). The method combines the Equivalent Pier (Poulos and Davis, 1980) and the interaction Flexibility Matrix (Randolph, 1983) approaches. In the subsequent analyses, the pile group stiffness is also computed using single pile stiffness and Group Factors. These concepts are explained in the following sections.

Studies on the accuracy of these simplified methods against more complete and complex analyses are presented in Horikoshi and Randolph (1999) and Poulos, et al. (1997), among others. In these studies linear elastic behaviour is generally assumed up to the point of local failure (or until the initial stress condition at the raft level is reached, Fig. 10.10). This simplification is unlikely to be realistic (Jardine, et al., 1986). Poulos, et al. indicated that the average settlement predicted by these methods is similar provided that the piles are not approaching failure. When the capacity of a significant number of the piles is fully utilised, the differences between simplified and more complete numerical analyses tend to become more pronounced. Simplified non-linear methods tend to overpredict the settlement.

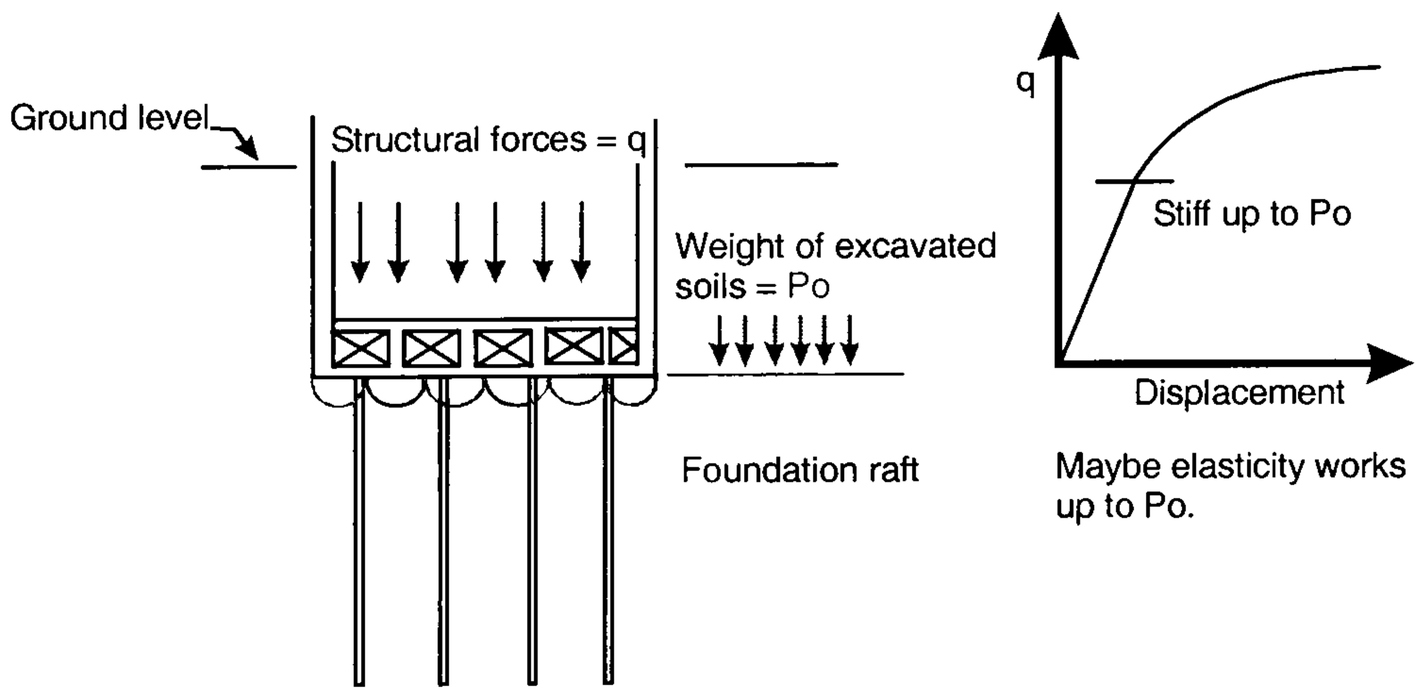


Fig. 10.10 Load displacement response of compensated foundation rafts

Mandolini and Viggiani (1997) and Randolph (1994) indicated that the measured performance of a piled raft foundation can be predicted applying elastic analysis and small strain shear moduli measured by seismic methods. As mentioned earlier, this result is surprising given the highly non-linear behaviour of most soils, even at small to moderate strains. However, MC shows a remarkably extensive linear portion of its shear modulus-strain curve and so substituting the shear moduli obtained from shear-wave velocity measurements may not lead to large errors.

10.2.2 Flexibility Matrix approach

The stiffness of the piled raft foundations and the load sharing between the rafts (rigid) and the pile groups are estimated using Randolph (1983)'s approximate linear method[126]. This method, based on the principle of superposition, tends to underpredict the load carried by the piles, thus overestimating long term raft loads.

From an analytical study of a single pile-raft unit, Randolph derived the overall stiffness (i.e. the load displacement response) of the piled raft foundation (K_{pr}) - the definition of the pile problem considered by Randolph is shown in Fig. 10.11. For cases where the soil stiffness varies with depth K_{pr} is given by:

$$K_{pr} = \frac{(P_p + P_r)}{w_{pr}} = \frac{K_p + K_r(1-2\alpha_{cp})}{1-(K_r / K_p)\alpha_{cp}^2} \qquad (10.1)$$

And the proportion of the total applied load carried by the raft is given by:

$$\frac{P_r}{P_t} = \frac{K_r(1-\alpha_{rp})}{K_p + K_r(1-2\alpha_{rp})} \qquad (10.2)$$

where:

K_p = stiffness of the pile group

K_r = stiffness of the raft alone

w_{pr} = average settlement of the pile raft

P_p, P_r and P_t = the loads carried by the piles, the raft and the total applied load, respectively

α_{cp} = raft-pile interaction factor, which allows for interactions between the

---

[126] The real response of a foundation is complex. Strictly, the analysis needs to consider, among others, the full sequence of construction, and the water pressures in the long term.

stiffnesses of the pile group and the raft.

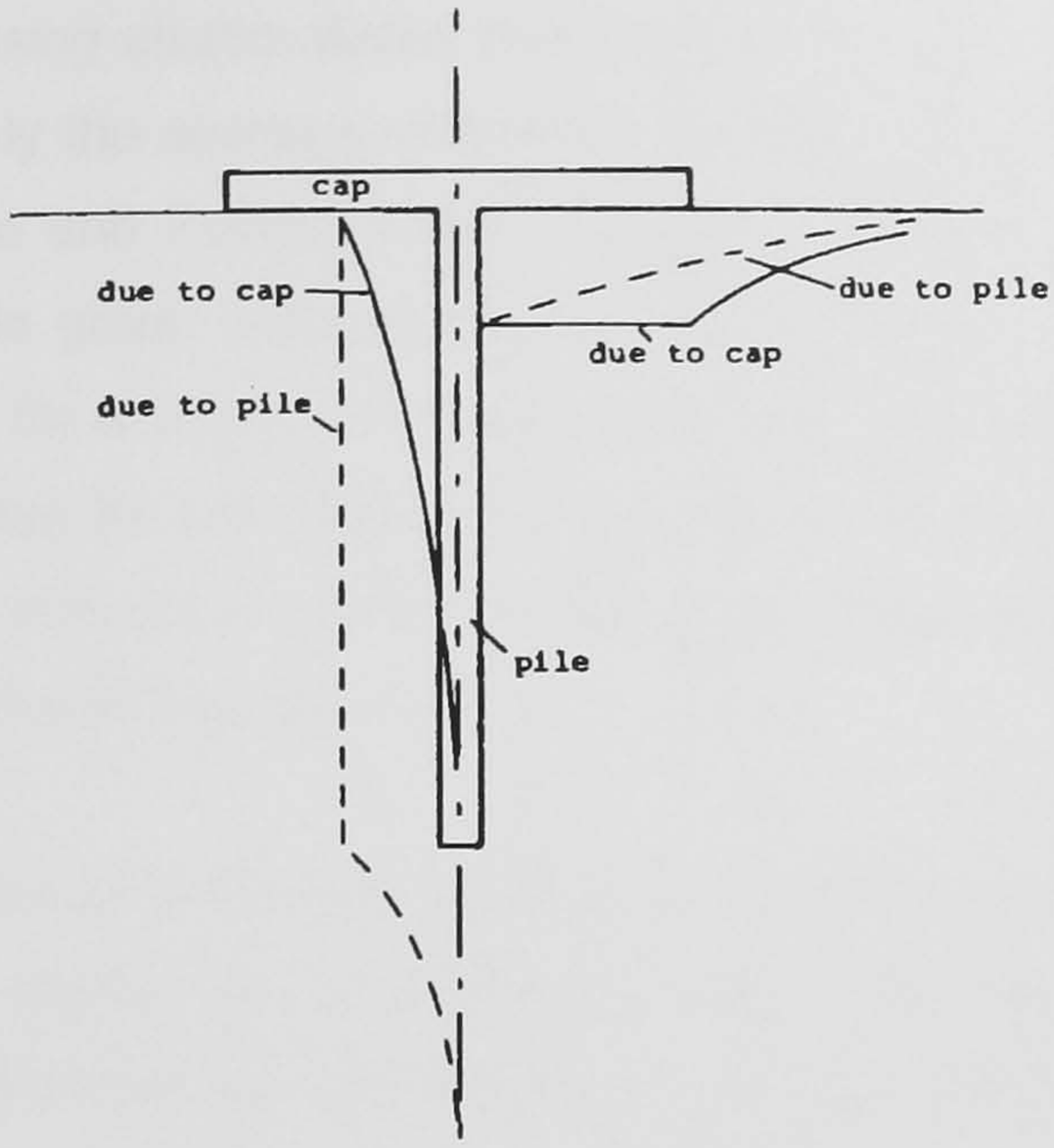


Fig. 10.11 Settlement interactions between single pile and cap (Randolph, 1983)

For single piles with circular caps of radius r_r, Randolph (1983) showed that the interaction factor, α_{rp}, can be approximated by:

$$\alpha_{rp} = 1 - \frac{\ln(r_r / r_p)}{\zeta} \tag{10.3}$$

where:

r_r = average radius of the raft (corresponding to an area equal to the raft area divided by number of piles)

r_p = radius of pile

$\zeta = \ln(r_m/r_p)$; the maximum radius of influence of an individual pile

$r_m = 0.25+\xi[2.5\rho(1-\nu)-0.25]\ L$

$\xi = E_{sl} / E_{sb}$

$\rho = E_{sav} / E_{sl}$

ν = Poisson's ratio of soil

L = pile length

E_{sl} = soil Young's modulus at level of pile tip

E_{sb} = soil Young's modulus of bearing stratum below pile tip

E_{sav} = average soil Young's modulus along pile shaft (Poulos, 2001).

Clancy and Randolph (1993) concluded that α_{rp} approaches a value of approximately 0.8 as the size of the pile group is increased, independently of the pile spacing, slenderness

ratio, pile stiffness and raft-soil stiffness ratio.

K_r can be estimated using elastic closed-form analytical solutions and assuming a fully rigid raft or alternatively the average settlement beneath a fully flexible raft (e.g. using the solutions of Mayne and Poulos, 1999; Fraser and Wardle, 1976; or Poulos and Davis, 1974). The pile group stiffness, K_p, can be calculated from elastic theory in a manner similar to that for a single pile but including pile to pile interaction effects. The pile to pile interaction can be included using: the equivalent pier approach; or the single pile stiffness together with group factors or pile group efficiency charts (such as those published by Butterfield and Douglas, 1981).

The pile cap has a relatively small effect on the overall stiffness of the foundation. For a pile cap that extends beyond the outer piles by 20% of the foundation dimension, the combined stiffness of the piled raft will be 10% greater than that of the pile group.

10.2.3 Stiffness of a single pile

K_p can be computed using the stiffness of a single pile and pile group efficiency charts or Group factors. Randolph and Wroth (1978) presented an approximate elastic solution to compute the stiffness of a compressible single pile based on separate treatment of the pile shaft and the pile base. The solution allows for a linear increase of shear modulus with depth using an average value of shear modulus. The head stiffness response of a single pile installed in a deep soil deposit is given by the following equation:

$$\frac{P_t}{G_l r_p w_t} = \frac{\dfrac{4\eta}{(1-\nu)\xi} + \rho\dfrac{2\pi}{\zeta}\dfrac{\tanh \mu L_p}{\mu L_p}\dfrac{L_p}{r_p}}{1+\dfrac{1}{\pi\lambda}\dfrac{4\eta}{(1-\nu)\xi}\dfrac{\tanh \mu L_p}{\mu L_p}\dfrac{L_p}{r_p}} \qquad (10.4)$$

where:

P_t = pile head load

G_l = shear modulus at pile length depth

r_p = pile radius

w_t = pile head settlement

L_p = pile length

$\eta = r_b/r_p$ = ratio of under-ream for underreamed piles

r_b = radius of pile base

ν_{soil} = Poisson's ratio of soil

$\xi = G_l/G_b$ = ratio of end bearing for end bearing piles

G_b = shear modulus of soil below the level of pile base

$\rho = G_{ave}/G_l$ = variation of soil modulus with depth

G_{ave} = average shear modulus of soil along pile length

$\mu L_p = \sqrt{(2/\zeta\lambda)}L_p / r_p$ = a measure of pile compressibility

$\lambda = E_p/G_l$ = pile-soil stiffness ratio

$\zeta = \ln(r_m/r_p)$ = measure of radius of influence of pile

r_m = maximum radius of influence

Although designed for piles of slenderness ratio (L_p/r_p) in excess of about 20, the above solution remains accurate for even shorter piles (Randolph, 1994). The variation of soil modulus with depth can be taken into account in terms of the factor ρ. Randolph and Wroth (1978), and Fleming, et al. (1992) suggested the following relationships of ζ for slender piles:

$$\zeta = \ln[2.5\rho(1-\nu_s)L_p / r_p] \text{ } (\xi=1, \text{ for friction piles}) \tag{10.5}$$

$$\zeta = \ln\{[0.25 + (2.5\rho(1-\nu_s) - 0.25)\xi]L_p / r_p\} \text{ } (\xi<1, \text{ for end-bearing piles}) \tag{10.6}$$

Randolph and Wroth (1978) showed that equations 10.4 and 10.5 are not suitable for long compressible piles such as $(L_p/r_p)^2/\lambda>20$, or for piles of very low slenderness ratio. Randolph (1994) indicated that for relatively stubby piers ($L_p/r_p \leq 5$) in deep homogeneous soil the maximum radius of influence, r_m, should be increased. He gave a revised equation for ζ:

$$\zeta = \ln[A + 2.5(1-\nu_s)L_p / r_p] \tag{10.7}$$

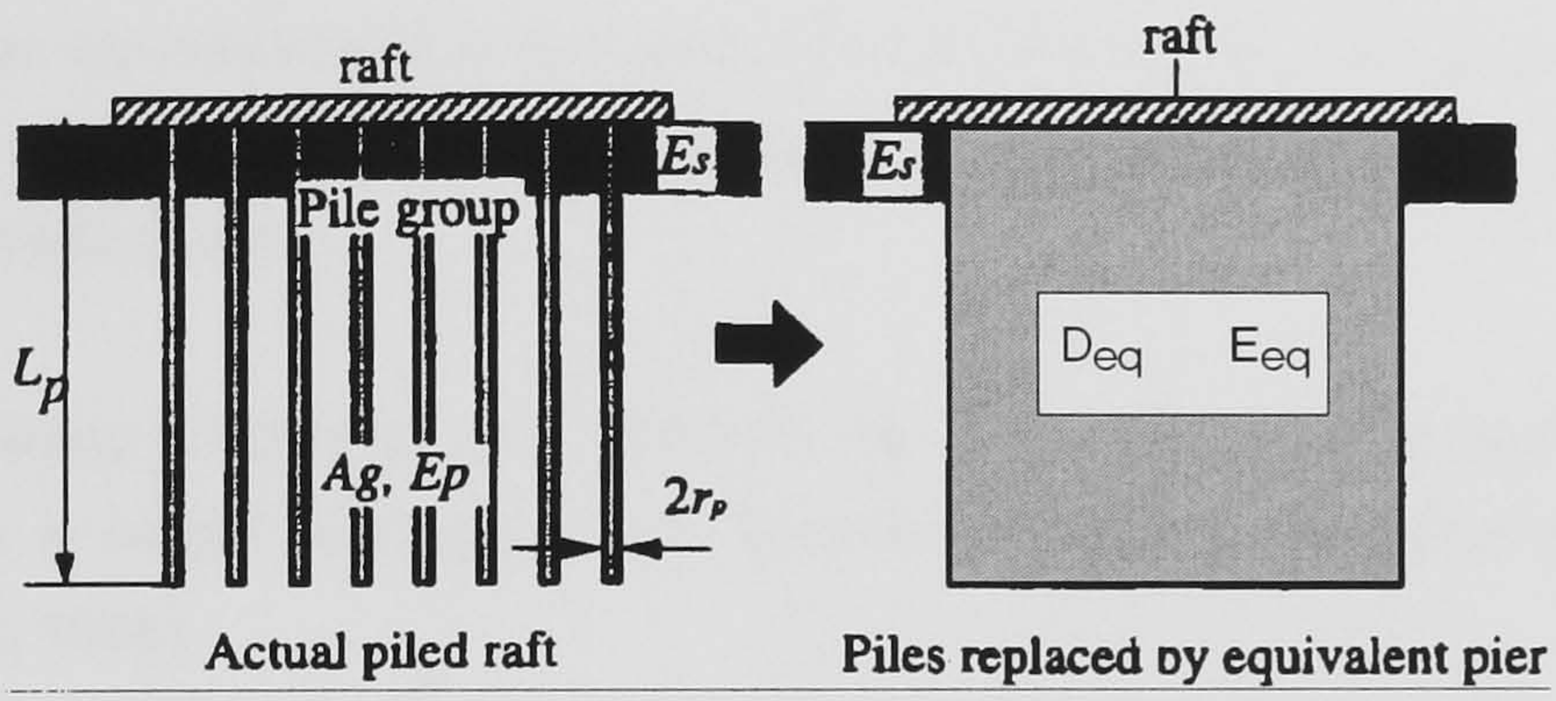
(A=5, for small L_p/r_p). Horikoshi and Randolph (1999) proposed the following equation for piles in deep non-homogenous soils where the soil modulus increases linearly with depth:

$$\zeta = \ln\{5 + [0.25 + (2.5\rho(1-\nu_s) - 0.25)\xi]L_p / r_p\} \tag{10.8}$$

(for small L_p/r_p). Where ξ is G_l/G_b', and G_b' is the soil modulus at a depth of $L_p+d^*d_{eq}$ (d^* is a depth factor, $d^*=1$ is appropriate).

10.2.4 Pile group stiffness using the Equivalent Pier approach

Poulos and Davies (1980) proposed the Equivalent Pier method that enables a simple hand-calculation of the stiffness of a pile group. In this procedure, the overall behaviour of a pile group is modelled by replacing it by a single "equivalent pier" of composite pile-soil material (Fig. 10.12) (Horikoshi and Randolph, 1999). Once the pile group has been replaced by a "stubby" pier, its stiffness can be computed applying the elastic solution for a single compressible pile (using for example Randolph and Wroth, 1978; section 10.2.3).



Lp = pile length
Es, Ep and Eeq = Young's modulus of the soil, pile and equivalent pier, respectively
Deq = diameter of the equivalent pier
Ag = plan area of the pile group as a block

Fig. 10.12 Concept of equivalent pier method (Horikoshi and Randolph, 1999)

Horikoshi and Randolph (1999) proposed the following parameter to categorize pile groups:

$$R = \sqrt{ns/L_p} \tag{10.9}$$

where n is the number of piles and s is the pile spacing. The Equivalent Pier approach is suitable for values of R smaller than 4.

Randolph (1994) suggested that the diameter of the equivalent pier, d_{eq}, might be approximated as:

$$d_{eq} = \frac{2}{\sqrt{\pi}}\sqrt{A_g} \tag{10.10}$$

for both friction and end-bearing piles. The length of the equivalent pier is the same as that of the piles in the group. The Young's modulus of the equivalent pier, E_{eq}, is calculated as:

$$E_{eq} = E_s + \left(E_p - E_s\right)\frac{A_{tp}}{A_g} \tag{10.11}$$

where A_{tp} is the total cross-sectional area of the piles in the group, and A_g is the plan area of the pile group as a block. For a non-homogeneous soil, the averaged soil modulus along the pile length can be used.

For large L_p/h (h is the stratum thickness) conditions, the equivalent pier analyses produce increasingly overestimated overall stiffness. According to Poulos and Davies (1980) if an equivalent pier of the same circumscribed area as the group is assumed, an accurate stiffness estimation must assume an equivalent pier length which is shorter than the original pile.

The modelling of several piers beneath the raft (rather than replacing the complete group by a single pier) allows an estimate of differential settlement (Clancy and Randolph, 1996).

10.3 Prediction of the pile-raft load sharing in the case history buildings

This section deals with the application of the pile-raft load sharing elastic analyses to the foundations of the case history buildings. The section includes the summary of the predicted static pile capacities, and the analysis of the foundation box compensation conditions.

10.3.1 Static capacity of the case history piles

The static capacity of the piles of the case history buildings was computed using the ICPDM. In each case the pile was subdivided into 20 to 33 subsections with the local shaft capacity being assessed in each layer and the overall capacity being found by summation. As described in Chapter 5, a validation exercise indicated that for the assumed global δ value this method marginally over-predicts (by 6%) axial pile static capacity in MC conditions, with a relatively low standard deviation of 16%. Table 10.2 provides a summary of the application of the ICPDM to the piles of the case history buildings, while appendix C gives the computation details. (The cross section of the PCC piles was assumed to be triangular with 65 cm sides).

Table 10.2 Computed pile capacity for the piles of the case history buildings

	JAL	*PC*	*PCC*
Pile length (m)	27.5	26.15	14.2
Cross section	Triangular	Triangular	Assumed triangular
Cross section dimensions (cm)	60	65	Assumed 65
Average S_t	8.07	7.77	9.6
Average YSR	1.20	1.20	1.35
Average τ_{rz} (kPa)	54.5	54.1	44.0
Pile capacity (kN)	1835	1866	847
Base capacity (%)	10	10	18

10.3.2 Compensation analyses

The static and seismic performance of a piled foundation in Mexico City's Lake zone is closely related to any compensation of weight through excavation (Mendoza and Auvinet, 1988). Table 10.3 summarizes the Author's analysis of the compensation on the foundations of the case history buildings. The analysis is based on the total stresses at the pile raft level.

Table 10.3 Summary of compensated foundation working conditions

	JAL	*PC*	*PCC*
Total building weight, MN	92.95	221.37	90.98
No. of piles	54	266	82
Pile capacity, kN	1835.0	1866.0	847.0
Pile group capacity[127], MN	65.19	326.53	45.67
Excavation depth, m	2.9	3.3	8.0
Foundation area, m^2	800.0	2052.0	1730.0
Free field total stress at foundation raft, kPa	46.3	50.0	103.0
Total compensated (excavated) weight, MN	37.04	102.60	178.15
Net load variation at raft level, MN	+55.91	+118.77	-87.17
Net stress variation at raft level, kPa	70.0	58.0	-50.0
Group capacity / total weight ratio	0.7	1.5	0.5
Group capacity / net load at raft level ratio	1.17	2.75	

Table 10.3 indicates that for the JAL and PC buildings the excavated soil is equivalent to 40% and 46% of the total weight of the buildings, respectively. The weight of the excavated soil is 1.96 times the total weight of the PCC building. The PCC is overcompensated and should be heaving, and this assessment remains true even when account is taken of the potential uncertainties regarding the building's weight.

10.3.3 Pile raft load distribution for the case histories

The study of the pile-raft co-participation for the JAL, PC and PCC buildings was carried

---

[127] The efficiency group factor for the JAL, PC and PCC buildings are 1.0, 0.88 and 1.0, respectively.

out with the methodology presented in section 10.2. The raft stiffnesses were computed for rigid and flexible, rectangular and circular rafts supported on finite and semi-infinite elastic homogenous solid using closed form solutions from Poulos and Davies (1974). Pile group stiffnesses were computed using Randolph and Wroth (1978)'s expressions for flexible and rigid single pile stiffness (section 10.2.3), and also using the Equivalent Pier approach (section 10.2.4). Following Poulos (2000), the analyses addressed the short term (undrained, ν=0.5) and long term (drained, ν=0.35) conditions where possible.

The general description of the building foundations was presented in their respective chapter of structural analyses. Table 10.4 shows the predicted percentages of the total building weight taken by the pile groups. Percentages higher that 100% were computed in some cases and where this happened the piles were assumed to take the entire load, limited to 100%. Negative percentages correspond to the raft taking the entire load, they are shown as 0%.

Table 10.4 Percentage of the total building weight carried by the piles in the JAL, PC and PCC buildings foundations

	Short term, undrained			Long term, drained		
Raft type / Pile type	Stiff Pile	Flexible Pile	Equivalent Pier	Stiff Pile	Flexible Pile	Equivalent Pier
JAL						
Circular raft on semi infinite	88	61	95	91	83	97
Circular raft on finite soil	83	33	93	85	68	95
Rectangular raft on semi-infinite	92	78		94	89	
Rectangular raft on finite soil	87	57				
PC						
Circular raft on semi- infinite	92	81	97	94	90	98
Circular raft on finite soil	74	0	92	86	74	95
Rectangular raft on semi-infinite	94	86		95	92	
Rectangular raft on finite soil	86	56				
PCC						
Circular raft on semi infinite	44	0	88	64	48	90
Circular raft on finite soil	100	100	14	100	100	67
Rectangular raft on semi-infinite	62	20		74	64	
Rectangular raft on finite soil	100	100				

The actual condition of the buildings corresponds to a rectangular rigid raft supported on a finite layer. The equivalent pier analysis is applicable only for circular rafts; and no solution was found for $\nu \neq 0.5$ (long term) rectangular raft on finite half space. The analysis indicates that:

i) The lowest long term percentage taken by the pile groups is 48% (PCC building). The average long term pile group contribution for the JAL and PC buildings is 88% and 91%, respectively; the PCC values show scatter.

ii) Under all raft conditions the pile groups are predicted to take most load by the Equivalent Pier approach. The lowest contribution is for the flexible pile condition, with the stiff pile condition falling in between. Hain and Lee (1978) indicated that the effectiveness of a specific pile group in reducing raft settlement and the percentage of total load supported by the group diminishes as the pile compressibility increases; a decrease in the length of the piles has a similar effect.

iii) Rectangular rafts give higher pile loads than circular rafts. This is due to the lower stiffness associated with rectangular raft-soil systems.

iv) Higher pile load participation is predicted under the long term drained conditions than under short term conditions. The long term is characterised by lower soil Poisson ratio (ν) and Young's moduli (E) – which give a softer raft-soil system.

v) The results indicate that for the soft MC soil conditions a large proportion of the structural load is likely to be transmitted directly to the piles – which conforms with Mendoza, et al.'s measurement of an 85% pile contribution. Cooke, et al. (1981) reported that for stiff clays the foundation raft shared about 25%-40% of the total load, while Koizumi and Ito (1967) measured a 20% raft contribution in a sensitive slightly overconsolidated soft clay. Yamashita and Kakurai (1991) found that in clays having an OCR of two, the load carried by the raft was about 49% of the total load at the end of building construction, reducing to 44% one year later.

The percentages in Table 10.4 are applied to the total weight of the building, without reducing the weight of the excavated soil[128]. The applied consideration produces close agreement with Mendoza, et al. (1998) measurements, which indicated that the net contribution of the raft is about 15% of the total building load, while the application of the elastic methodology to Mendoza, et al. foundation indicated 5%.

The application of the percentage in Table 10.4 to the base reactions is presented in Chapter 11. The Author is aware that the application of these percentages does not

---

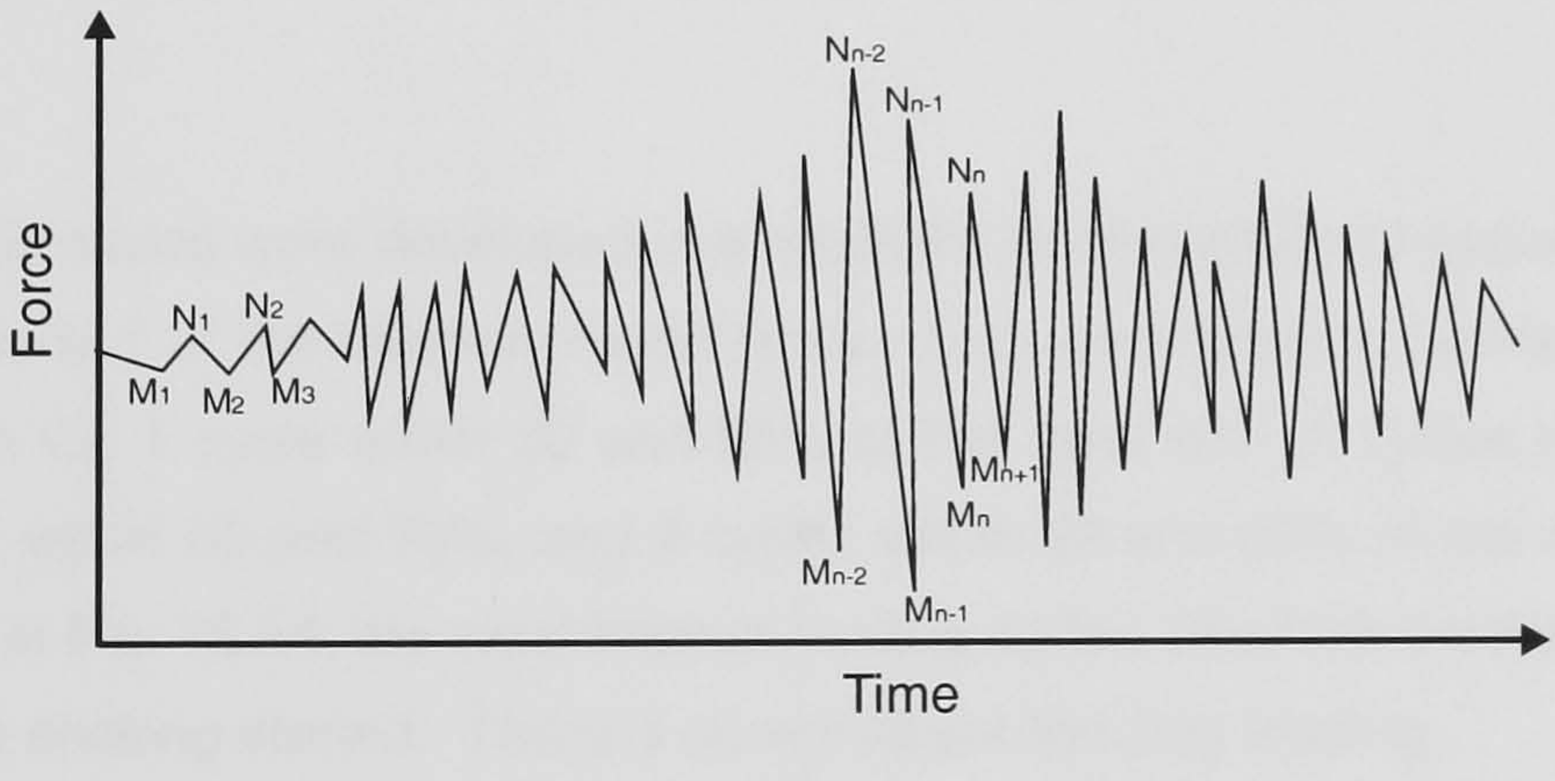
[128] The other alternative is to apply them to the net applied load (building weight minus weight of excavated soil).

consider other conditions applying to the compensated piled-foundation response, among them: rate of regional subsidence, rate of the building settlement (or heave), and pore pressures. A study of the influence of these conditions is out of the scope of this Thesis. The calculated percentages should remain valid provided the structures sink at a faster rate than the regional subsidence. The common construction methodology for compensated piled foundations in MC was presented in section 8.3.

10.4 Processing of the axial seismic base reactions

The structural analyses resulting in the inertial axial reactions acting at the base of the case history buildings were presented in Chapters 7, 8 and 9. Those chapters also provided details of the building dimensions, their foundation characteristics, and the structural model configurations.

This section introduces the processing of the base reactions, in order to describe them in terms of cyclic load amplitude (Q_c), mean load (Q_a), and number of cycles. The cyclic amplitude is defined for every cycle considering a maximum value and two minimum values; the mean load is the maximum less the cyclic amplitude (Fig. 10.13, see also section 2.2). As seen in the following tables, this load characterisation produces a relatively uniform mean reaction.



$$Cyclic\ \ Amplitude = \frac{\left(N_n - \frac{M_n + M_{n+1}}{2} \right)}{2}$$

$$Mean\ Load = N_n \text{ - } cyclic\ amplitude$$

Fig. 10.13 Definition of parameters for the analysis of cyclic base reactions

Characterising the loads in terms of Q_c and Q_a allowed a framework for considering dead loads and earthquake loads acting over specific numbers of cycles. This approach

is more representative than simply comparing the maximum reactions developed during cycling (Q_{max}), and it is easier to compare with the field pile load test data – which are usually reported as Q_a and Q_c normalised against pile ultimate static capacity[129] (Q_{ult}).

The processed base reactions time histories are presented in the following sections using tables that list values of N, Q_a and Q_c. The load cycles are classified according to their Q_c values. A wide range of Q_c amplitudes is included for completeness.

10.4.1 JAL Building

The base reactions resulting from the Masonry model under the calibration 1995 Copala event were presented in Fig. 7.24; Fig. 10.14 shows the results for the best estimate "Masonry" model under Copala motion amplified by a factor of 2 (λ=2)[130]. The processed base reactions for the Bare and Masonry models under the various conditions studied are presented in Tables 10.5 and 10.6. These tables, and the following for the PC building, classify the load at each node according to Q_c. The tables include: (i) the structural model node number, (ii) the cyclic amplitude interval as percentage of the maximum cyclic amplitude, (iii) the number of load cycles in that interval amplitude, (iv) the total number of cycles in the node, (v) the average, maximum and minimum cyclic amplitude (Q_c) multiplied by two, and (vi) the mean force (Q_a) for the interval. (For the sake of clarity, nodes where Q_c is not significant, mainly due to low initial static load, are not shown.)

The largest Q_c values were developed in a relatively small number of cycles (Table 10.5 and 10.6). Node 1 of the Masonry model (under λ=2) undergoes two extreme cycles at the maximum Q_c, 1 cycle within 80 and 90% of the maximum, 2 cycles within 70 and 80%, 1 cycle within 60 and 70%, and 9 cycles within 50 and 60% of the maximum Q_c. As observed in Fig. 10.14, the most intense loading cycles developed around 70 and 80 seconds after shaking started. There is no significant two-way loading.

---

[129] The normalisation of the base reactions against the predicted static capacity is presented in Chapter 11.

[130] The 1985 catastrophic earthquake correspond to λ=5.

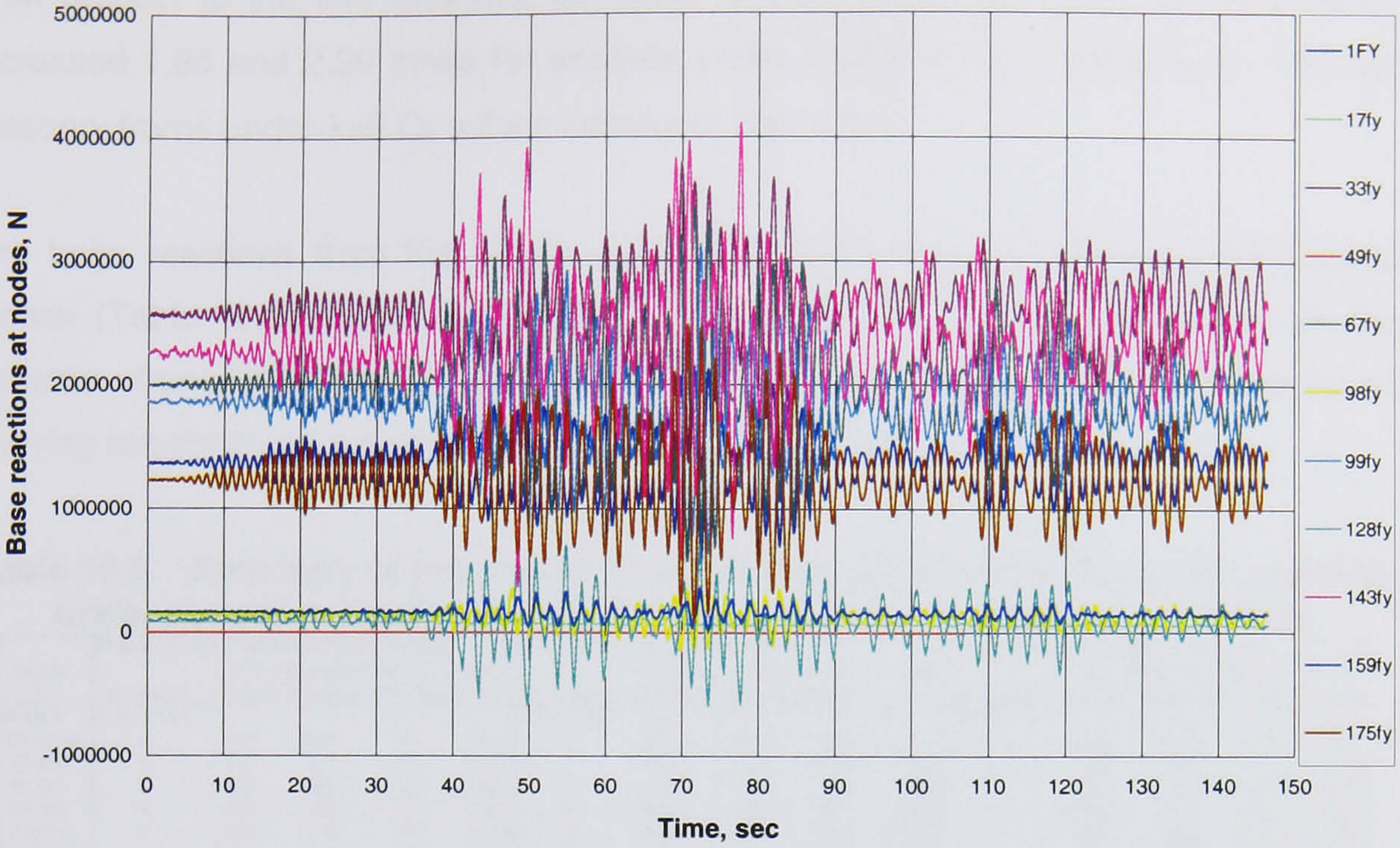


Fig. 10.14 Base reaction from Masonry model under twice amplified input motion

Table 10.5 Summary of processed base reactions on Bare frame JAL building under normal and amplified input motions

Range %	*Bare frame, calibration input motion* 2* Cyclic amplitudes, kN No. Cycles	Average	Maximum	Minimum	Mean Force	*3 times amplified input motion* 2* Cyclic amplitudes, kN No. Cycles	Average	Maximum	Minimum	Mean Force	*5 times amplified input motion* 2* Cyclic amplitudes, kN No. Cycles	Average	Maximum	Minimum	Mean Force
Node 1	Total = 96					Total = 94					Total = 104				
90-100%	1	820.2	820.2	820.2	1378	1	1438.7	1438.7	1438.7	1426	1	1703.0	1703.0	1703.0	1335
80-90%	1	666.1	666.1	666.1	1359	3	1210.9	1248.9	1161.7	1389	1	1522.8	1522.8	1522.8	1393
70-80%	2	648.5	653.8	643.2	1359	2	1091.7	1138.5	1044.9	1429	2	1239.5	1269.1	1210.0	1396
60-70%	4	526.3	547.0	501.9	1360	1	971.4	971.4	971.4	1324	1	1083.6	1083.6	1083.6	1341
50-60%	3	452.1	467.2	425.9	1355	3	835.0	842.5	821.0	1394	9	932.9	995.0	862.4	1378
40-50%	3	378.8	408.9	345.2	1355	9	619.8	671.7	575.5	1395	5	748.1	773.7	719.5	1378
20-40%	26	239.1	306.8	165.6	1370	15	404.7	560.1	295.1	1392	11	518.3	674.5	382.7	1430
Node 33	Total = 139					Total = 134					Total = 130				
90-100%	1	564.5	564.5	564.5	2640	1	1581.8	1581.8	1581.8	2649	1	2191.6	2191.6	2191.6	2653
80-90%	1	456.8	456.8	456.8	2652	0	0.0	0.0	0.0	0	0	0.0	0.0	0.0	0
70-80%	3	424.6	443.2	412.7	2647	1	1186.0	1186.0	1186.0	2685	1	1604.9	1604.9	1604.9	2579
60-70%	1	363.0	363.0	363.0	2608	5	1030.4	1106.2	982.8	2666	5	1432.2	1493.4	1384.1	2727
50-60%	5	323.3	334.2	292.1	2635	2	811.8	831.5	792.0	2611	1	1167.8	1167.8	1167.8	2678
40-50%	9	261.3	273.2	247.3	2615	7	662.5	691.2	639.7	2616	6	1020.7	1076.5	938.6	2649
20-40%	16	165.9	221.9	113.5	2624	16	473.6	604.0	343.2	2605	20	649.9	863.1	442.6	2641
Node 67	Total = 112					Total = 119					Total = 107				
90-100%	1	1219.9	1219.9	1219.9	1877	1	1730.5	1730.5	1730.5	1898	4	1871.3	1950.9	1794.2	1881
80-90%	2	1055.3	1064.9	1045.8	1867	2	1508.0	1534.9	1481.0	1864	1	1592.6	1592.6	1592.6	1959
70-80%	2	898.3	917.6	879.0	1871	2	1317.1	1377.4	1256.8	1857	4	1480.3	1548.1	1423.8	1870
60-70%	4	784.1	818.0	750.8	1856	6	1111.6	1173.2	1046.1	1873	4	1223.7	1263.4	1171.0	1835
50-60%	5	663.1	716.8	630.7	1848	3	988.6	1017.5	931.5	1843	2	1071.2	1094.3	1048.1	1835
40-50%	3	536.9	595.6	502.7	1865	3	775.3	853.1	731.3	1836	8	851.5	936.1	781.0	1874
20-40%	19	357.6	451.8	249.0	1848	23	496.9	678.2	367.4	1931	15	557.3	744.4	403.8	1921
Node 99	Total = 104					Total = 113					Total = 110				
90-100%	3	871.7	929.8	841.6	1746	1	1506.6	1506.6	1506.6	1866	1	1969.3	1969.3	1969.3	1904
80-90%	0	0.0	0.0	0.0	0	4	1309.7	1355.2	1283.7	1793	0	0.0	0.0	0.0	0
70-80%	3	711.9	733.1	685.1	1724	3	1144.1	1170.7	1102.5	1791	4	1507.6	1534.8	1486.4	1749
60-70%	2	624.7	627.8	621.6	1721	3	947.8	963.1	918.6	1747	6	1302.8	1374.2	1233.7	1852
50-60%	6	514.5	552.8	479.7	1718	4	811.4	879.4	767.5	1762	4	1142.6	1179.9	1107.0	1830
40-50%	5	401.1	417.4	374.2	1710	4	690.5	726.6	635.5	1806	4	912.3	941.8	901.8	1872
20-40%	14	282.8	348.0	198.2	1725	13	385.9	587.2	303.4	1796	12	610.2	775.7	406.9	1830
Node 143	Total = 102					Total = 102					Total = 101				
90-100%	3	992.4	1046.0	954.4	2390	4	2356.3	2465.4	2310.6	2442	2	3372.9	3500.8	3245.1	2377
80-90%	2	897.9	929.1	866.7	2370	1	2027.8	2027.8	2027.8	2326	3	3015.5	3137.1	2815.3	2462
70-80%	3	773.2	815.0	734.7	2360	3	1803.9	1883.9	1738.7	2339	2	2564.3	2671.7	2456.8	2456
60-70%	4	658.9	671.2	633.7	2372	3	1533.9	1562.3	1510.5	2316	4	2222.4	2296.6	2116.5	2309
50-60%	6	576.7	618.1	525.2	2352	5	1368.8	1446.3	1264.5	2382	5	1938.4	2066.1	1767.1	2414
40-50%	9	449.1	504.5	419.1	2346	6	1138.5	1230.6	1056.6	2301	6	1560.4	1692.9	1462.4	2294
20-40%	15	276.2	376.1	215.6	2361	17	719.3	983.6	499.8	2345	17	1000.6	1329.7	703.7	2351
Node 175	Total = 100					Total = 92					Total = 96				
90-100%	2	921.6	956.8	886.3	1237	2	1603.9	1677.7	1530.1	1269	1	2004.0	2004.0	2004.0	1349
80-90%	1	830.1	830.1	830.1	1260	2	1431.7	1450.5	1412.9	1219	1	1744.1	1744.1	1744.1	1302
70-80%	4	729.5	745.1	713.2	1231	3	1203.1	1225.4	1185.4	1233	0	0.0	0.0	0.0	0
60-70%	3	625.0	638.6	600.3	1248	1	1124.4	1124.4	1124.4	1275	3	1338.8	1371.5	1317.6	1304
50-60%	4	538.7	570.5	499.5	1221	5	921.6	976.7	845.9	1270	10	1089.7	1183.5	1020.0	1278
40-50%	3	396.2	415.2	383.4	1259	7	760.8	829.9	688.5	1241	6	894.3	971.4	809.6	1226
20-40%	27	267.4	357.9	192.4	1250	18	457.3	665.6	356.6	1271	9	570.9	753.8	449.9	1307

With respect to the λ=1 analysis, the base reaction Q_c predicted by the Bare frame increased 1.86 and 2.39 times for analysis under λ=3 and λ=5, respectively. For the Masonry frame under λ=2 Q_c values increased 1.88 times.

The base reactions from the elastic analysis[131] of the Masonry frame under Copala motion (Table 10.6) indicate an amplification ratio for Q_c of 1.65 with respect to the inelastic structural model under the same event. This indicates the importance of carrying out structural analysis that includes detailed modelling of the structure.

Table 10.6 Summary of processed base reaction on Masonry frame JAL building under normal and amplified input motion and elastic analysis conditions

Range %	Masonry frame, calibration input motion					2 times amplified input motion					Elastic model, calibration motion				
		2* Cyclic amplitudes, kN			Mean		2* Cyclic amplitudes, kN			Mean		2* Cyclic amplitudes, kN			Mean
	No. Cycles	Average	Maximum	Minimum	Force	No. Cycles	Average	Maximum	Minimum	Force	No. Cycles	Average	Maximum	Minimum	Force
Node 1	Total = 115					Total = 105					Total = 52				
90-100%	6	798	842	781	1370	2	1527	1584	1469	1379	6	1583	1666	1547	1378
80-90%	5	717	727	702	1355	1	1378	1378	1378	1380	4	1450	1460	1442	1413
70-80%	2	645	669	622	1367	2	1249	1265	1232	1374	14	1242	1332	1170	1347
60-70%	6	542	586	525	1360	1	957	957	957	1362	10	1093	1146	1001	1352
50-60%	5	445	474	427	1357	9	868	950	822	1357	5	927	982	868	1274
40-50%	9	381	420	347	1356	12	706	786	639	1354	1	790	790	790	1165
20-40%	30	257	333	170	1357	32	437	629	317	1355	3	486	597	415	1291
Node 33	Total = 125					Total = 116					Total = 63				
90-100%	1	1541	1541	1541	2658	2	2370	2415	2325	2527	2	2368	2485	2250	3026
80-90%	0	0	0	0	0	3	2062	2156	1992	2587	3	2138	2215	1990	2814
70-80%	0	0	0	0	0	2	1760	1788	1732	2610	6	1882	1940	1810	2659
60-70%	3	991	1063	955	2582	2	1509	1516	1501	2505	2	1615	1680	1550	2508
50-60%	5	812	832	788	2547	4	1328	1403	1222	2590	12	1361	1485	1250	2474
40-50%	4	706	765	645	2575	10	1098	1179	1007	2608	5	1100	1155	1035	2650
20-40%	36	452	602	313	2518	21	749	964	528	2631	11	862	970	775	2440
Node 67	Total = 112					Total = 116					Total = 50				
90-100%	7	1185	1243	1127	2027	2	2370	2415	2325	2527	1	1975	1975	1975	2263
80-90%	3	1059	1086	1007	2009	3	2062	2156	1992	2587	5	1649	1755	1585	2043
70-80%	2	911	937	885	2012	2	1760	1788	1732	2610	7	1492	1565	1420	1984
60-70%	7	803	850	754	2007	2	1509	1516	1501	2505	14	1299	1370	1195	1957
50-60%	5	688	732	633	1996	4	1328	1403	1222	2590	6	1087	1155	1000	1975
40-50%	11	542	590	500	1993	10	1098	1179	1007	2608	2	940	955	925	2070
20-40%	24	377	484	256	1982	21	749	964	528	2631	4	625	760	495	1945
Node 99	Total = 128					Total = 115					Total = 55				
90-100%	4	967	1007	922	1865	1	2417	2417	2417	1926	3	1416	1462	1325	2062
80-90%	6	848	891	815	1843	1	1934	1934	1934	1950	4	1224	1300	1185	1971
70-80%	1	723	723	723	1864	0	0	0	0	0	2	1082	1139	1025	1849
60-70%	5	652	701	613	1853	3	1577	1631	1471	1877	5	973	1005	930	1850
50-60%	3	545	567	518	1830	10	1315	1395	1228	1860	8	819	860	750	1843
40-50%	5	452	492	403	1820	6	1100	1176	1008	1838	12	654	725	585	1739
20-40%	23	315	395	211	1818	21	652	942	492	1850	7	486	580	315	1784
Node 143	Total = 126					Total = 118					Total = 67				
90-100%	3	1596	1657	1555	2362	4	3040	3112	2965	2437	3	3008	3139	2870	2523
80-90%	1	1350	1350	1350	2294	1	2535	2535	2535	2446	5	2646	2785	2575	2715
70-80%	2	1244	1288	1200	2415	1	2310	2310	2310	2181	2	2373	2475	2270	2324
60-70%	2	1080	1138	1022	2283	2	1936	1996	1875	2304	6	1995	2060	1951	2442
50-60%	3	858	878	833	2340	3	1632	1693	1573	2343	6	1766	1841	1685	2170
40-50%	9	742	820	674	2347	5	1356	1475	1246	2356	5	1428	1480	1330	2466
20-40%	23	514	640	351	2336	27	963	1203	645	2327	12	1019	1210	656	2014
Node 175	Total = 111					Total = 110					Total = 51				
90-100%	3	1173	1217	1131	1255	2	2332	2341	2322	1307	3	1993	2117	1913	1284
80-90%	8	1035	1081	978	1240	1	1928	1928	1928	1292	5	1835	1867	1799	1268
70-80%	4	898	929	865	1244	3	1735	1839	1670	1277	10	1626	1690	1573	1222
60-70%	2	745	746	744	1234	2	1516	1607	1424	1278	16	1381	1459	1274	1229
50-60%	5	700	725	671	1239	5	1249	1359	1191	1248	5	1197	1265	1131	1218
40-50%	16	541	586	503	1224	16	1057	1145	940	1248	3	994	1003	990	1356
20-40%	24	361	467	244	1213	24	651	902	494	1230	2	505	521	490	1297

10.4.2 PC Building

The base reactions resulting from the Selected model under the calibration Copala event were presented in Fig. 8.19; Fig. 10.15 shows the results for the Selected model under the strongest motion analysed successfully, this is the Copala earthquake amplified by

---

[131] Only the first 100 seconds were analysed.

λ=3 factor. The processed base reactions for the Original and Selected frame models under the studied motions are presented in Tables 10.7 and 10.8. (Nodes where the cyclic variation of the load is not significant, due to a low initial static load, are not shown.)

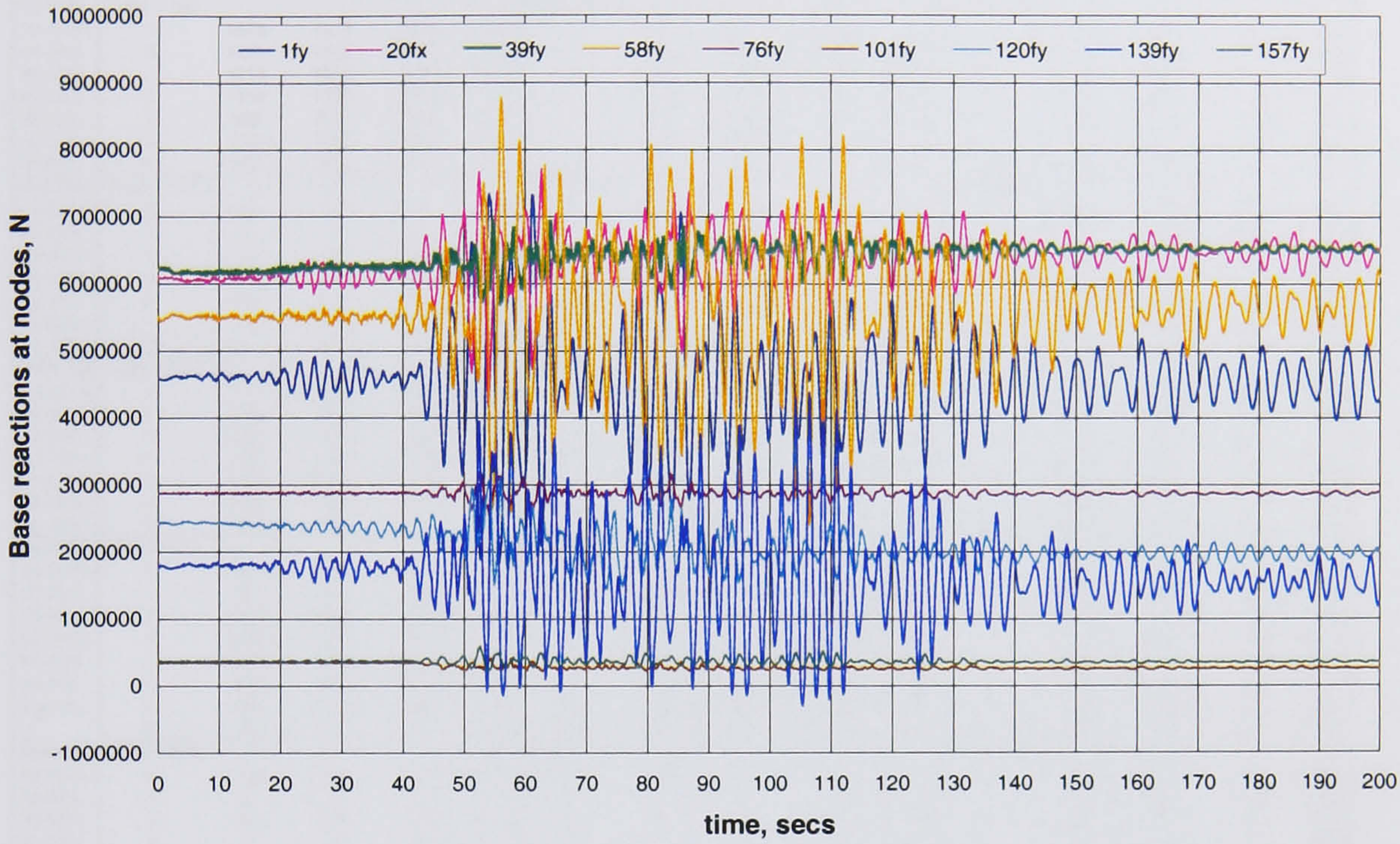


Fig. 10.15 Base reactions from Selected model under input motion amplified three times

For the analysis of the Selected model under λ=3, the node with the highest loads underwent two extreme maximum Q_c, 1 cycle within 80 and 90% of the maximum, 6 cycles within 70 and 80%, 5 cycle within 60 and 70%, and 2 cycles within 50 and 60%. As observed in Fig. 10.15, the maximum amplitudes are seen between 50 and 115 seconds.

Table 10.7 Summary of processed reactions on Original frame PC building under normal and amplified input motions

Range %	Under calibration copala motion					3 times amplified input motion					5 times amplified input motion				
		2* Cyclic amplitudes, kN			Mean		2* Cyclic amplitudes, kN			Mean		2* Cyclic amplitudes, kN			Mean
	No. Cycles	Average	Maximum	Minimum	Force	No. Cycles	Average	Maximum	Minimum	Force	No. Cycles	Average	Maximum	Minimum	Force
Node 1	Total = 84					Total = 91					Total = 96				
90-100%	2	2816	2949	2683	4683	1	4892	4892	4892	4960	3	5191	5439	4975	4909
80-90%	2	2465	2466	2465	4654	4	4171	4379	4058	4638	1	4727	4727	4727	4881
70-80%	1	2132	2132	2132	4587	4	3664	3866	3431	4802	5	4082	4269	3905	4962
60-70%	3	1860	1930	1820	4623	2	3034	3055	3012	5099	2	3624	3646	3602	4761
50-60%	1	1580	1580	1580	4663	1	2839	2839	2839	4599	5	2914	3166	2773	4822
40-50%	7	1269	1388	1180	4630	3	2261	2429	2158	4624	8	2473	2694	2196	4836
20-40%	18	883	1178	599	4606	13	1456	1941	1027	4691	19	1608	2149	1090	4618
Node 20	Total = 105					Total = 127					Total = 137				
90-100%	1	1678	1678	1678	7280	2	2970	3016	2924	7275	3	3262	3384	3094	7392
80-90%	3	1431	1457	1397	7192	1	2450	2450	2450	7280	1	2914	2914	2914	7237
70-80%	1	1213	1213	1213	7271	3	2322	2398	2208	7223	1	2524	2524	2524	7369
60-70%	1	1154	1154	1154	7191	3	1913	1955	1873	7253	4	2234	2340	2102	7155
50-60%	2	888	917	859	7172	1	1546	1546	1546	7173	1	1706	1706	1706	7189
40-50%	6	728	793	676	7213	2	1400	1488	1313	7326	8	1474	1654	1371	7306
20-40%	17	516	663	364	7211	15	884	1185	648	7193	23	1016	1328	704	7211
Node 39	Total = 147					Total = 172					Total = 186				
90-100%	2	720	742	697	7209	1	1473	1473	1473	7258	3	1275	1313	1235	7367
80-90%	0	0	0	0	0	1	1200	1200	1200	7473	2	1065	1077	1053	7435
70-80%	1	576	576	576	7222	0	0	0	0	0	2	1026	1034	1018	7286
60-70%	0	0	0	0	0	1	1013	1013	1013	7444	0	0	0	0	0
50-60%	4	410	438	374	7267	3	771	788	749	7368	3	690	722	672	7589
40-50%	1	311	311	311	7231	2	678	719	636	7472	8	589	626	528	7454
20-40%	22	217	294	156	7249	17	395	562	299	7348	27	373	510	272	7303
Node 139	Total = 132					Total = 131					Total = 131				
90-100%	3	1945	2001	1891	1695	5	3990	4146	3861	1798	2	5222	5363	5082	2169
80-90%	5	1692	1800	1611	1698	1	3718	3718	3718	2050	7	4501	4759	4292	1754
70-80%	3	1485	1585	1417	1674	4	3050	3215	2921	1740	0	0	0	0	0
60-70%	3	1279	1328	1253	1674	3	2591	2659	2507	1770	4	3354	3544	3231	1613
50-60%	4	1094	1151	1038	1682	9	2299	2423	2113	1427	5	2995	3120	2822	1329
40-50%	6	904	958	819	1627	3	1975	2069	1786	1270	7	2485	2673	2295	1320
20-40%	14	600	751	430	1644	17	1175	1594	886	1384	14	1609	2070	1146	1090
Node 58	Total = 121					Total = 134					Total = 137				
90-100%	1	3357	3357	3357	5661	2	6077	6323	5830	5606	3	7053	7304	6688	5634
80-90%	0	0	0	0	0	2	5299	5366	5232	5750	1	6478	6478	6478	5670
70-80%	6	2468	2608	2399	5661	3	4750	4951	4453	5624	2	5715	5749	5680	5947
60-70%	3	2206	2281	2117	5747	4	4001	4285	3882	5815	4	4757	4929	4510	5740
50-60%	3	1874	1976	1751	5706	2	3179	3193	3164	5513	5	4095	4369	3927	5547
40-50%	5	1506	1643	1358	5646	4	2734	2856	2623	5585	4	3435	3636	3076	6112
20-40%	15	1031	1338	690	5668	17	1902	2502	1349	5818	22	2169	2882	1503	6168
<	88	127	631	1	5587	100	284	1258	3	5626	96	268	1351	5	5616
Node 76	Total = 155					Total = 174					Total = 180				
90-100%	4	356	368	339	2916	1	679	679	679	2999	1	649	649	649	2981
80-90%	0	0	0	0	0	0	0	0	0	0	1	546	546	546	2845
70-80%	2	278	284	272	2919	2	514	529	500	2893	5	489	515	473	2956
60-70%	0	0	0	0	0	3	441	463	424	3002	7	414	438	390	2933
50-60%	1	188	188	188	2898	1	367	367	367	2929	8	357	388	338	2912
40-50%	9	163	182	152	2901	5	297	320	273	2962	10	292	321	266	2918
20-40%	18	106	144	74	2892	20	178	240	138	2913	21	197	256	133	2881

With respect to the analysis carried out under λ=1, the base reaction Q_c values predicted by the Original frame increased 1.90 and 2.04 times for analysis under λ=3 and λ=5, respectively. For the Selected frame under λ=3 the Q_c amplitudes increase 2.56 times. The forces obtained from amplified motions show non-linear response.

Table 10.8 Summary of processed base reactions on Selected frame PC building under normal and amplified input motions

Range %	Under calibration copala motion					3 times amplified input motion				
		2* Cyclic amplitudes, kN			Mean		2* Cyclic amplitudes, kN			Mean
	No. Cycles	Average	Maximum	Minimum	Force	No. Cycles	Average	Maximum	Minimum	Force
Node 1	Total = 93					Total = 95				
> 90	2	2646	2707	2584	4607	1	5467	5467	5467	4602
> 80	1	2373	2373	2373	4655	2	4609	4794	4425	4885
> 70	3	2071	2163	1993	4624	2	4103	4105	4101	4509
> 60	3	1743	1842	1667	4633	2	3383	3457	3309	4753
> 50	3	1441	1500	1400	4544	1	3269	3269	3269	4380
> 40	4	1231	1351	1108	4547	6	2431	2605	2211	4588
> 20	17	804	1052	572	4567	18	1540	2166	1107	4562
Node 20	Total = 116					Total = 129				
> 90	2	1550	1619	1481	6273	1	2503	2503	2503	6455
> 80	0	0	0	0	0	0	0	0	0	0
> 70	4	1201	1243	1169	6267	2	1921	1924	1918	6560
> 60	3	998	1001	993	6290	2	1562	1579	1546	6500
> 50	3	893	931	861	6305	10	1377	1478	1294	6428
> 40	4	733	802	671	6344	5	1172	1231	1124	6490
> 20	15	499	591	324	6315	18	699	946	516	6466
Node 120	Total = 136					Total = 127				
> 90	1	562	562	562	2286	1	1482	1482	1482	2353
> 80	1	475	475	475	2128	0	0	0	0	0
> 70	1	414	414	414	2151	3	1140	1146	1129	2252
> 60	5	375	392	343	2196	5	951	989	901	2167
> 50	4	307	328	293	2172	4	770	807	741	2057
> 40	8	249	278	228	2222	4	690	737	643	2112
> 20	18	167	214	117	2186	21	417	558	301	2085
Node 39	Total = 167					Total = 182				
> 90	4	273	286	260	6319	1	1121	1121	1121	6369
> 80	1	230	230	230	6323	0	0	0	0	0
> 70	4	212	222	205	6338	0	0	0	0	0
> 60	2	196	197	195	6328	2	682	689	676	6531
> 50	9	155	166	145	6335	6	642	666	613	6408
> 40	15	127	140	114	6327	5	514	547	494	6342
> 20	36	82	112	59	6301	20	314	443	229	6439
Node 139	Total = 137					Total = 135				
> 90	4	1816	1909	1742	1689	3	4451	4624	4297	2036
> 80	2	1572	1592	1552	1685	4	3945	4132	3749	1906
> 70	2	1428	1461	1395	1803	5	3492	3693	3266	1943
> 60	4	1216	1257	1167	1697	5	2910	2990	2792	1738
> 50	6	1064	1139	982	1706	5	2519	2690	2316	1750
> 40	6	878	946	805	1684	6	2062	2234	1922	1895
> 20	17	514	759	384	1726	13	1312	1761	955	1624
Node 58	Total = 146					Total = 147				
> 90	2	1944	1967	1922	5635	2	5861	6152	5570	5534
> 80	1	1613	1613	1613	5624	1	5209	5209	5209	5596
> 70	2	1453	1499	1407	5627	6	4679	4878	4370	5516
> 60	3	1264	1287	1221	5638	5	3991	4295	3775	5478
> 50	8	1072	1174	985	5620	2	3401	3489	3312	5812
> 40	6	857	909	792	5602	7	2757	3042	2466	5571
> 20	14	567	776	408	5648	14	1796	2234	1266	5614
Node 76	Total = 205					Total = 207				
> 90	1	236	236	236	2881	1	617	617	617	2872
> 80	0	0	0	0	0	0	0	0	0	0
> 70	0	0	0	0	0	1	483	483	483	2884
> 60	4	156	163	148	2885	1	416	416	416	2950
> 50	4	126	135	119	2892	0	0	0	0	0
> 40	2	100	101	99	2880	1	307	307	307	2941
> 20	9	55	68	48	2880	14	164	234	129	2899

10.4.3 PCC Building

As indicated in Chapter 9, the analysis of the seismic base reactions developed by the PCC building is not as reliable as the other two case histories due to the lack of the appropriate data to calibrate the structural models. The results were processed but they are not used in the latter stages of the Thesis.

The base reactions resulting from the Implemented model under the Copala event were presented in Fig. 9.23; Fig. 10.16 shows the results for the Implemented model under the simulated 1985 Michoacan earthquake, which is the 1995 Copala motion amplified by the λ=5 factor. Fig. 10.16 illustrates the inadequacy of the results for the PCC frame model.

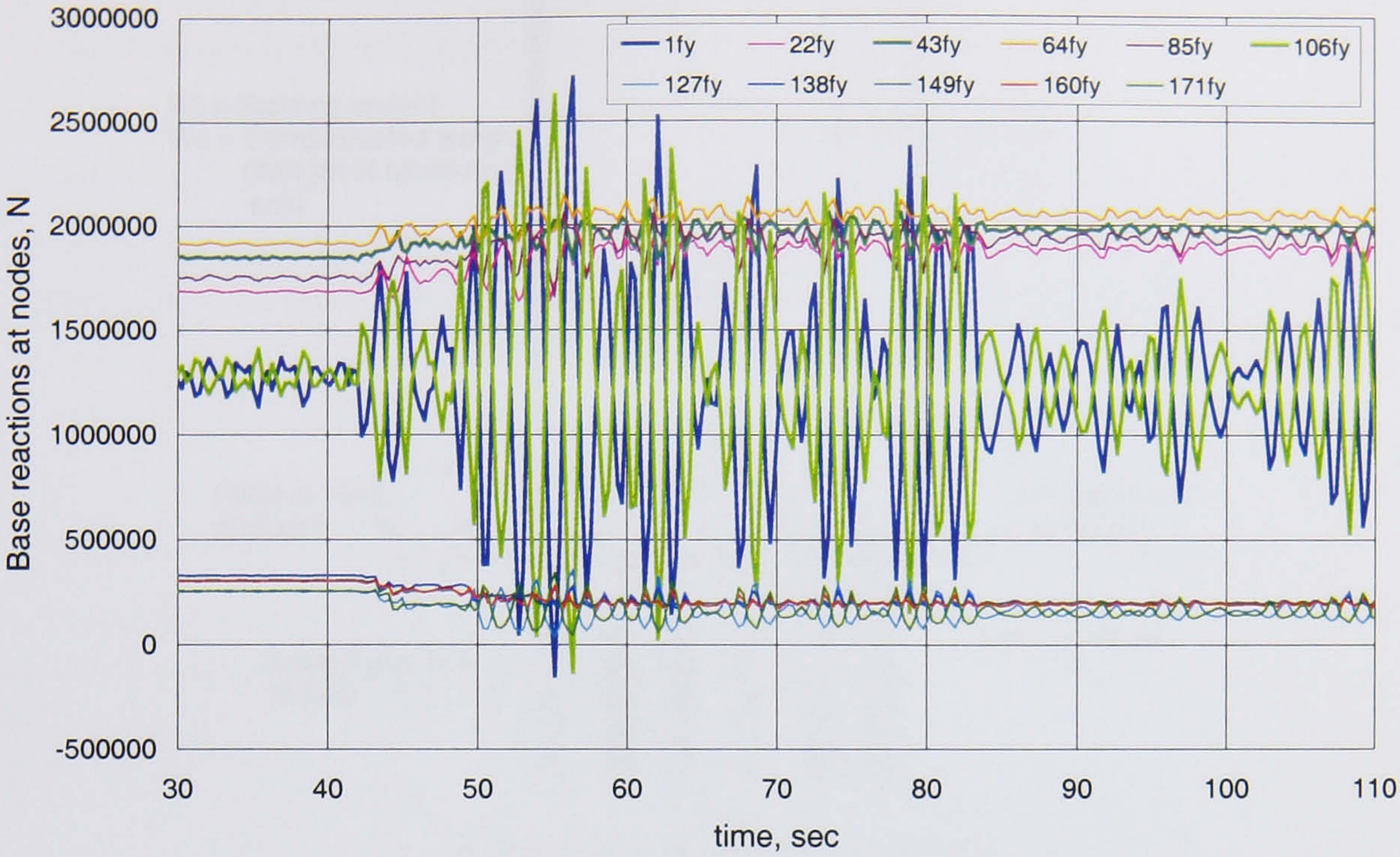


Fig. 10.16 Base reaction from Implemented model under five times amplified Copala input motion

10.5 Assessment of the foundation lateral stability

The earthquake loading of buildings produces basal shear inertial[132] forces in addition to the seismic axial inertial forces already described, although the latter are the focus of this thesis. The permanent and seismic loads transmitted by a foundation box and piles to the soil are, as shown in the Fig. 10.17:

i) The static vertical load reduced by the compensation effect.
ii) The load due to the seismic moment (rocking) which, together with the static load, produces the critical working condition in the piles.
iii) The horizontal shear seismic load, which in general results lower than the passive earth pressure.

In compensated piled foundations, with walls in firm contact with the surrounding soil, the seismic shear forces are taken by: (i) the friction in the soil-basement horizontal and vertical contact areas, (ii) the earth pressure on the vertical walls of the foundation box, and (iii) the reaction of soil adjacent to the piles (Fig. 10.17) (Holguin, et al., 1992; Demenegui, 1986).

---

[132] Function of the seismic acceleration.

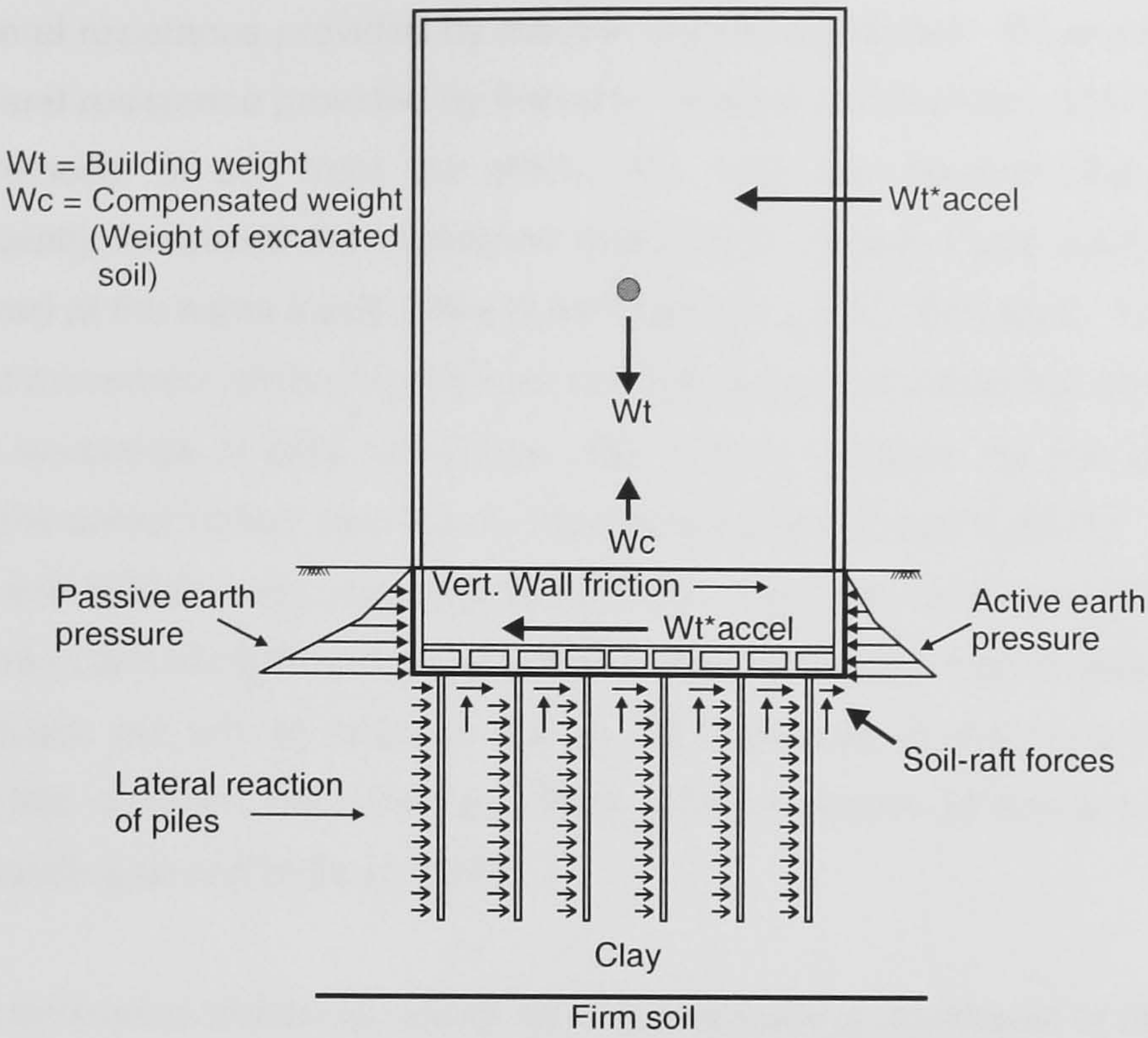


Fig. 10.17 Soil reactions transmitted to the foundation during lateral loading

Jaime, et al. (1988) indicated that in a survey carried out after the 1985 September Michoacan earthquake there was no evidence of foundation damage due to lateral seismic forces, even for a foundation whose raft was 1 m above ground level. In this case the piles took the lateral loads but failed in compression.

10.5.1 Passive earth pressure contribution

As mentioned above, a piled box foundation develops horizontal resistance both along the vertical faces over the embedment depth and along the base of the pile cap. The vertical wall resistance depends primarily on two factors (Mokwa and Duncan, 2001):

i) The stiffness and strength of soil. The passive resistance that can be developed in front of a pile box increases as the strength and stiffness of the backfill soil increase.

ii) The depth of box embedment. At the same load, increasing box depth results in smaller lateral deflections.

Field tests reported in the literature have shown that:

i) The lateral resistance provided by the pile caps is significant. It can be as large as the lateral resistance provided by the piles (Mokwa and Duncan, 2001).

ii) The removal of soil from the sides, the front and beneath the piled boxes significantly increased the measured deflections, rotations and bending moments observed at the same loads (Mokwa and Duncan, 2001; Kim, et al., 1979).

iii) Lateral movement of the cap causes the soil surface to move horizontally and the lateral resistance of piles to reduce; this occurs because the pile and soil have about the same motion near the surface (Mokwa and Duncan, 2001).

iv) If the soil settles away from the base of the pile box, only its vertical faces are effective in providing horizontal support. Additional support is provided by the pile-soil system but this is reduced due to the decrease of the confining pressure. Under this condition the behaviour of the pile-soil system is similar to the case of free-standing piles (De Beer, 1977).

The passive and active pressures under earthquake loading developed at the foundation box of the case history buildings was computed using undrained conditions. The passive earth pressure (p_p) is given by:

$$p_p = \sigma_h = \sigma_v + 2S_u \tag{10.12}$$

The active earth pressure (p_a) is given by:

$$p_a = \sigma_h = \sigma_v - 2S_u \tag{10.13}$$

Consequently, according to Fig. 10.17, the ultimate lateral resistance (Q) is given by:

$$\Delta\sigma_h = p_p - p_a = 4S_u$$

$$Q_{lateral} = \int_0^D 4S_u \tag{10.14}$$

In the above expressions: D = depth of foundation box[133]; S_u = undrained shear strength, a conservative S_u = 26 kPa was applied.

The friction between the vertical walls of the foundation box and the soil was also computed. This was carried out based on S_u and a proportional area of the wall. Table 10.9 shows the comparison between the total computed lateral resistance, and the maximum basal shear force obtained from the building models under the most intense

---

[133] The characteristics of the building foundations are presented in their chapters of structural analysis.

motion (amplifying factor λ=5)[134]. The shear forces are from the JAL Bare frame, the PC Original frame, and the PCC Implemented frame.

Table 10.9 Passive earth pressure resistances on the case history buildings

	JAL Building	PC Building	PCC Building
Box depth (m)	3.3	2.9	8.0
Maximum predicted shear force (kN)	1411	2485	2256
Total lateral resistance (kN)	1656	2507	5085
Ratio resistance/force	1.17	1.01	2.24

The table indicates that the total lateral resistances are equal to or higher than the predicted basal shear forces - Santoyo and Gutierrez (1986) pointed out that this is usually the case. It should be noted that the ultimate shear force resisted by the piles, and the shear stresses developed along the bottom of the box are not included. Therefore, it is considered that the lateral resistances are higher that the lateral loads, even when negative cyclic effects are ignored. No further contributions to the lateral resistance were calculated.

10.5.2 Pile lateral resistance contribution

The contribution of the piles to the resistance of lateral forces was not computed for the case histories, however a brief description of the basic concepts is given below.

The lateral resistance characteristics of piles can be estimated from empirical formulae or loading tests at the site. The resistance varies with pile width, deflection, and the depth below ground surface.

Broms (1964) proposed the failure modes for restrained laterally loaded piles shown in Fig. 10.18. When the length of the pile and the penetration depth are large, failure may take place when two plastic hinges form at the locations of the maximum positive and maximum negative bending moments (Fig. 10.18a). For intermediate length piles, failure may take place after the formation of a plastic hinge at the top end of the pile and the lateral reactions exceed the bearing capacity of the soil along the full length of the pile (Fig. 10.18b). When the length of the piles and the penetration depths are small, failure may take place when the applied lateral load exceeds the resistance of the supporting soil (Fig. 10.18c).

---

[134] The design code seismic coefficient for the case history buildings (5% damping) is 0.3g. This is at least 50% higher than that computed from the Author's structural analyses.

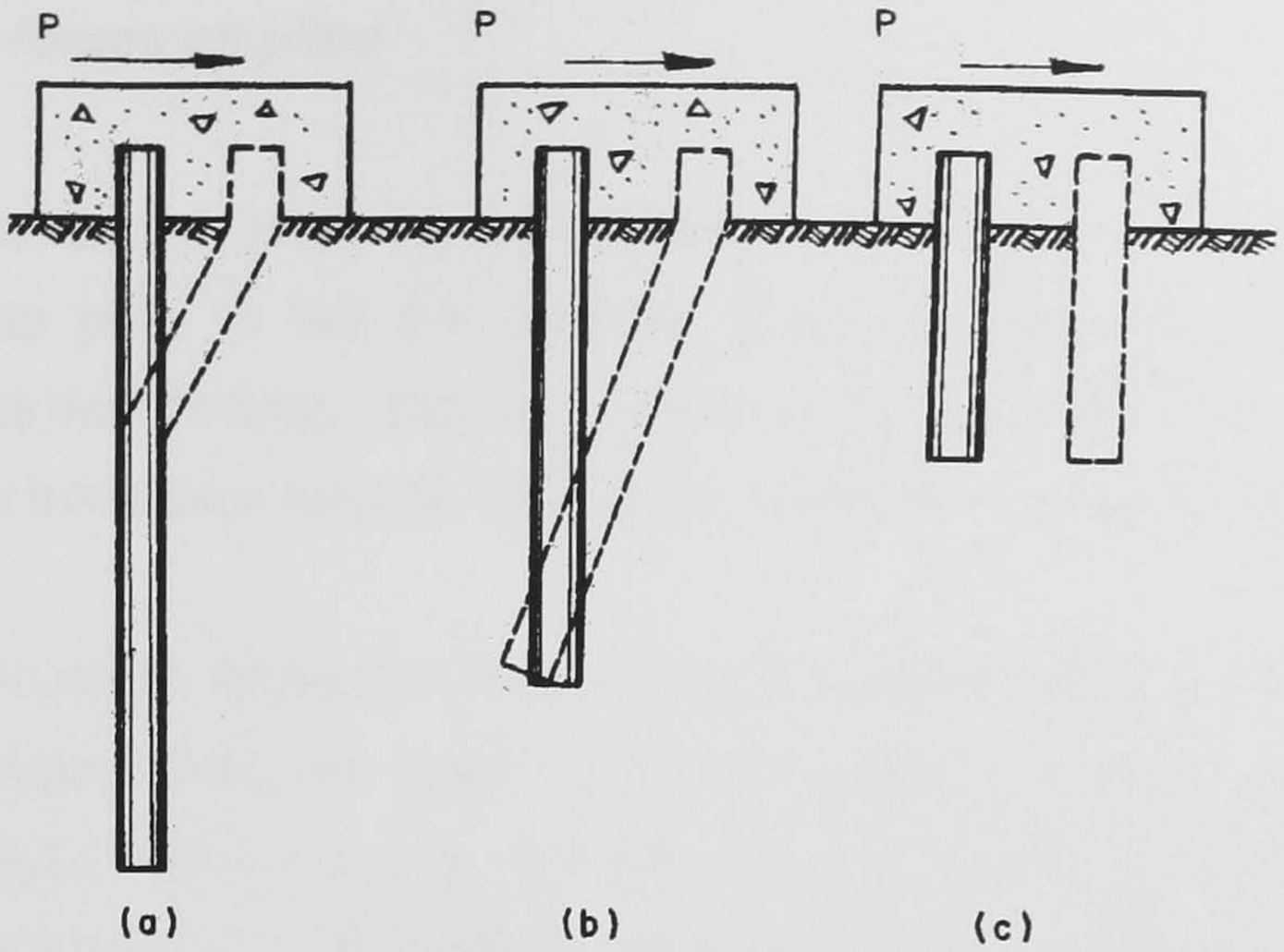


Fig. 10.18 Failure modes for restrained piles (Broms, 1964)

Broms (1964) proposed graphs to compute the ultimate lateral resistance for the three failure modes[135]. The graphs are functions of dimensionless quantities of pile yield moments and ultimate forces and the dimensionless length L/D. In order to use the graphs, definitions of the stiffness and failure mode of the piles are required.

The ultimate lateral pile capacity computed from Broms' graph is modified by group effects, which for lateral loading includes two types of issues. The first is that the ultimate lateral capacity and stiffness of a pile group may be smaller than the ultimate resistance calculated as the sum of the ultimate capacity or stiffness resistances of individual piles[136] (Kim, et al., 1979). The second is concerned with load sharing, within the group the front piles in the moving direction develop larger soil reactions than those further back (De Beer, 1977).

The lateral cyclic loading of piles also influences their modulus and ultimate resistance by gradually decreasing the shear strength and stiffness of the soil located in the immediate vicinity of the loaded pile. Repetitive loading could decrease the ultimate lateral resistance of the soil about one-half of its initial value (Holguin, et al., 1992; Broms, 1964).

---

[135] Broms studied the resistance at working loads assuming that the pile behaves as an ideal elastic member and the supporting soil as an ideal elastic material.

[136] No reduction in lateral resistance was found when the pile spacing exceeded four pile diameters. When piles were closer than approximately two pile diameters the piles and the soil located within the pile group behaves as a unit (Broms, 1964).

10.6 Kinematic forces on piles

The forces generated in piles by an earthquake result from two phenomena: the resistance of the piles to the soil motions during the passage of seismic waves (kinematic interaction forces), and the inertia forces generated by vibration of the structure (inertial interaction forces). The latter are the focus of this Thesis.

Localised high kinematic interaction forces can play a significant role in the magnitude of the forces developed along the length of piles founded in layered soils at any depth where the stiffness of the soil profile changes abruptly (Kayna and Mahzooni, 1996). A survey of pile damage in Japan between 1923 and 1983 by Mizuno (1987), results of shaking table tests by Mizuno, et al. (1984), and finite element analysis of a pile group by Kimura and Zhang (2000) support this observation. Kayna (1997) indicated that, depending on the soil stiffness contrast, the kinematic interaction forces can be as large as the total forces in the piles, and that they can cause damage and should not be ignored.

The inertia interaction depends on the foundation-structure system vibration characteristics – mass, stiffness and geometry. The numerical results reported by Waas and Hartmann (1984) and Masayuki and Shoichi (1991) showed that around the natural frequency of the system the inertial forces of the piles are much larger than their associated kinematic-interaction values (the maximum acceleration of the structure occurs at the same frequency than maximum pile forces). Outside this frequency, the seismic force in a pile is almost identical to its kinematic-interaction value.

Common procedures for the seismic design of piles are based on the consideration of the inertial-interaction forces, while the kinematic-interaction forces are assumed to be negligible. Following these procedures, the piles are designed either for code-specified forces, or inertia forces in the structure obtained from its dynamic analysis (Kayna, 1997; Kayna and Mahzooni, 1996). The analysis in this Thesis follows this criterion.

In this Thesis, the inertial forces were obtained from the structural analysis. The kinematic interaction forces should be small in the soft homogenous MC profiles where the studied buildings are located.

The pile loads are computed by applying the factors and concepts developed in this chapter to the base reactions obtained from the structural analyses. This is presented in Chapter 11.

CHAPTER 11

RELATIONSHIPS BETWEEN STATIC AND DYNAMIC AXIAL PILE CAPACITIES

The criteria adopted to define cyclic pile failure, and consequently pile cyclic capacity, usually involve limiting cyclic or permanent displacements. However, there is no standardised definition of pile cyclic failure, with choices depending on the site soil conditions, the dimensions of the pile, and the characteristics of the cyclic loading. This uncertainty in definitions serves to confuse the discussion between those who consider pile cyclic capacity to be higher than static capacity, and those who consider it to be lower. The low number of pile foundation failures assigned to cyclic action has led many to think that the negative influence of cyclic loading is less significant than the positive rate of loading effects, so that pile capacity under fast cycling is higher than the static capacity.

For example, consider the Bias[137] and Uncertainty factors proposed for seismic axial pile capacity assessment by the API panel[138] responsible for earthquake design (Table 11.1). The Biases are defined as the ratio of the true or expected capacity of the pile subjected to earthquake loading effects to the predicted or design code nominal capacity (generally the static capacity from the API methods). According to the API the expected capacity during an earthquake is 2.5 times the static capacity (e.g. Bea, et al., 1999).

Table 11.1 Piles axial capacity biases and uncertainties (API, draft 1998)

Foundation system	Bias	Uncertainties, COV[139]
Clays	2.5	0.4
Sands	1.0	0.5

---

[137] The biases are reported as being produced from identifying major sources of uncertainty, evaluating them using available field and laboratory test data, integrating them using a probabilistic model, and carrying out a reliability evaluation. The major sources of uncertainty for pile capacity are soil boring, sampling and testing, loading conditions, time effects, and analysis methodology.

[138] Their goals were to assist designers when comparing different API editions and to produce consistent level of safety for different site conditions, pile configurations, and structural and foundation systems.

[139] In this table the coefficient of variation (COV) is a global uncertainty due to all uncertainties in the pile analysis parameters (API, draft 1998). For the definition of COV see Chapter 5.

Objections may be raised to Table 11.1 approach in that: (i) it is not usually clear how the biases and COV's have been derived; and (ii) existing databases do not allow a reliable set of biases and uncertainties to be established. Adopting the mentioned approach would have deep repercussions in the assessment of dynamic pile performance.

This chapter investigates whether any systematic bias can be established between dynamic and static driven pile capacity in Mexico City (MC). The goal is to develop sound evidence to test the assumption of a strong positive bias. The conclusions are obtained from: (i) the comparison between the best estimates of seismic axial pile forces established for the JAL and PC buildings with the static pile capacity predicted by the ICPDM; and (ii) by expressing the best estimate data in cyclic Interaction Diagrams (ID) developed for MC.

11.1 Studies included in the Interaction Diagram for Mexico City

The data sources used by the Author to develop cyclic ID diagrams for MC include:

i) Field cyclic pile tests by Jaime, et al. (1988).
ii) Field cyclic pile test reported in Girault (1986).
iii) The axial pile forces computed from the reactions predicted at the base of the JAL and PC case history buildings. The PCC building pile forces are not included due to the lack of confidence on its seismic analyses (Chapter 9).
iv) Recorded pile forces from Mendoza, et al. (1998)'s instrumented foundation - presented in section 10.1.2.

At a later stage, cyclic direct shear laboratory tests on MC clay by Ovando, et al. (1993) were included to evaluate 2-way cyclic loading conditions.

The load per pile for the JAL and PC buildings is obtained by an analysis that particularly accounts for the raft-pile load sharing and the pile group effects (see Chapter 10). The following criteria were considered:

i) The pile-raft load sharing factors were applied to the total weight of the frames as established in section 10.3.3.
ii) Although measurements have shown that the soil-raft contact pressure and the

pile-raft load sharing[140] are not uniform in the raft area (section 10.1.2), the pile-raft load sharing factors are applied uniformly to the raft. The raft-pile load distribution obtained by applying the mentioned factors to characterise the initial static condition. During an earthquake the system response is more complex and it includes cyclic variations on the pile loads and on the raft contact pressures (Section 10.1.3).

iii) The group efficiency factors were obtained using the Sayed and Bakeer (1992) equation: $\eta_g = 1-(1-\eta_s' K)\rho$. η_g is the efficiency factor; η_s' is the geometry efficiency, equal to the ratio between the perimeter of the pile group and the summation of the perimeters of the individual piles; ρ is the ratio between the ultimate shaft capacity and the total capacity; and K is the group interaction factor. The computed group factors are presented in the following sections.

iv) During an earthquake the piles respond to the complete imposed loading history. However, we cannot input the whole load spectrum into the Interaction Diagram (ID). The "*characteristic pile loads*" developed at each base node of the JAL and PC buildings were assessed for this purpose. These were obtained by selecting the load combination closest to the selected average Q_a and Q_c values and assigning to those values the total number of cycles (these values were obtained considering the pile loads with Q_c higher than 20% of the maximum Q_c; see section 10.4 for definitions). IDs indicating the 90%-100% Q_c load, the 40% to 50% Q_c load, the characteristic pile loads, and the number of cycles they act are presented in the following sections.

The application of curve hopping[141] procedure to the cyclic tests and the seismic loads evaluated for the case histories was investigated, however the lack of key data for the

---

[140] The foundation working conditions has to be considered when studying the pile-raft load sharing, including an inundated foundation box and the regional subsidence. The foundation response to the regional subsidence depends upon the foundation compensation condition, which determines if the foundation emerge, settles or follows the regional subsidence – each response represent a particular working condition of the soil-raft contact.

[141] Curve hopping is a procedure that is often applied in offshore engineering. Jardine (2002) indicates that "the basic hypothesis is that when the cyclic loading level is changed from its initial level the rate of settlement changes abruptly. The settlement now grows, as additional cycles ΔN are applied at the new level, as if they had hopped to a new point on the virgin settlement-N curve applying to the new loading level. This new point corresponds to $N=N^*$, where N^* is defined as the value of N on the new loading curve at which the permanent settlement matches that developed at the end of the last batch of cycles."

cyclic tests and the case histories[142] made the procedure not applicable.

The following sections report the details of the data used to develop the ID.

11.1.1 JAL Building pile data

The pile loads acting at the supports of the Bare and Masonry models during the earthquakes studied are shown in Tables 11.2 and 11.3. Following Chapter 10, these tables, and those following for the PC building, classify the pile loads according to their Q_c amplitude. The Tables include: (i) the structural model node number where the pile is located, (ii) Q_c intervals expressed as percentages of the overall maximum Q_c, (iii) the number of load cycles in that interval, (iv) the total number of significant cycles experienced by the pile during the shaking, (v) the mid interval Q_c multiplied by two and the mean load Q_a applying to each interval, and (vi) the ratio of Q_c and Q_a to the Q_{ult} predicted by the ICPDM. (For the sake of clarity, nodes where Q_c is not significant, mainly due to low initial static load, are not shown.) All the pile loads include:

i) A reduction of 6% (or 5577 kN) from the total weight of the building due to raft participation. The reduction accounts for 15% of the compensated soil weight.
ii) A 6% reduction of the ICPDM predicted pile capacity (Q_{ult}) to 1725 kN in order to account for the calibration explained in Chapter 5 (see also Appendix C).
iii) A group efficiency factor equal to 1.
iv) The base reactions at nodes 1, 67, 99 and 175 (defined in the foundation plan of the JAL building in section 7.3) are carried by one single pile. The reactions at nodes 33 and 143 were distributed between two piles.

---

[142] e.g. number of cycles vs. permanent displacement curves for cyclic tests, or the number and amplitude of seismic loads acting in the case histories since their construction.

Table 11.2 Pile loads (kN) for the JAL building Bare frame model under the Copala and the amplified input motions

Range to max. Qc	Under calibration Copala motion					3 times amplified input motion					5 times amplified input motion -Michoacan				
	Number of cycles	2*Cyclic Amplitude	Mean load	% of pile cap. Cyclic	Mean	Number of cycles	2*Cyclic Amplitude	Mean load	% of pile cap. Cyclic	Mean	Number of cycles	2*Cyclic Amplitude	Mean load	% of pile cap. Cyclic	Mean
Node 1	Total = 96					Total = 94					Total = 104				
90-100%	1	771	1296	0.22	0.75	1	1352	1340	0.39	0.77	1	1601	1255	0.46	0.73
80-90%	1	626	1277	0.18	0.74	3	1138	1306	0.33	0.75	1	1431	1310	0.41	0.76
70-80%	2	610	1278	0.18	0.74	2	1026	1344	0.30	0.78	2	1165	1313	0.34	0.76
60-70%	4	495	1278	0.14	0.74	1	913	1245	0.26	0.72	1	1019	1261	0.29	0.73
50-60%	3	425	1273	0.12	0.74	3	785	1311	0.23	0.76	9	877	1295	0.25	0.75
40-50%	3	356	1274	0.10	0.74	9	583	1311	0.17	0.76	5	703	1295	0.20	0.75
20-40%	26	225	1287	0.06	0.74	15	380	1309	0.11	0.76	11	487	1344	0.14	0.78
Characteristic load											30			0.29	0.73
Node 33	Total = 139					Total = 134					Total = 130				
90-100%	1	265	1241	0.08	0.72	1	743	1245	0.21	0.72	1	1030	1247	0.30	0.72
80-90%	1	215	1246	0.06	0.72	0	0	0	0.00	0.00	0	0	0	0.00	0.00
70-80%	3	200	1244	0.06	0.72	1	557	1262	0.16	0.73	1	754	1212	0.22	0.70
60-70%	1	171	1226	0.05	0.71	5	484	1253	0.14	0.72	5	673	1282	0.19	0.74
50-60%	5	152	1239	0.04	0.72	2	382	1227	0.11	0.71	1	549	1258	0.16	0.73
40-50%	9	123	1229	0.04	0.71	7	311	1229	0.09	0.71	6	480	1245	0.14	0.72
20-40%	16	78	1233	0.02	0.71	16	223	1224	0.06	0.71	20	305	1241	0.09	0.72
Characteristic load											34			0.22	0.7
Node 67	Total = 112					Total = 119					Total = 107				
90-100%	1	1147	1765	0.33	1.02	1	1627	1784	0.47	1.03	4	1759	1768	0.51	1.02
80-90%	2	992	1755	0.29	1.01	2	1417	1752	0.41	1.01	1	1497	1841	0.43	1.06
70-80%	2	844	1759	0.24	1.02	2	1238	1746	0.36	1.01	4	1391	1757	0.40	1.02
60-70%	4	737	1745	0.21	1.01	6	1045	1761	0.30	1.02	4	1150	1725	0.33	1.00
50-60%	5	623	1738	0.18	1.00	3	929	1733	0.27	1.00	2	1007	1725	0.29	1.00
40-50%	3	505	1753	0.15	1.01	3	729	1726	0.21	1.00	8	800	1761	0.23	1.02
20-40%	19	336	1737	0.10	1.00	23	467	1815	0.13	1.05	15	524	1805	0.15	1.04
Characteristic load											38			0.4	1.02
Node 99	Total = 104					Total = 113					Total = 110				
90-100%	3	819	1641	0.24	0.95	1	1416	1754	0.41	1.01	1	1851	1789	0.53	1.03
80-90%	0	0	0	0.00	0.00	4	1231	1685	0.36	0.97	0	0	0	0.00	0.00
70-80%	3	669	1621	0.19	0.94	3	1075	1683	0.31	0.97	4	1417	1644	0.41	0.95
60-70%	2	587	1618	0.17	0.93	3	891	1642	0.26	0.95	6	1225	1741	0.35	1.01
50-60%	6	484	1615	0.14	0.93	4	763	1656	0.22	0.96	4	1074	1720	0.31	0.99
40-50%	5	377	1608	0.11	0.93	4	649	1698	0.19	0.98	4	858	1759	0.25	1.02
20-40%	14	266	1621	0.08	0.94	13	363	1688	0.10	0.98	12	574	1720	0.17	0.99
Characteristic load											31			0.41	0.95
Node 143	Total = 102					Total = 102					Total = 101				
90-100%	3	466	1123	0.13	0.65	4	1107	1148	0.32	0.66	2	1585	1117	0.46	0.65
80-90%	2	422	1114	0.12	0.64	1	953	1093	0.28	0.63	3	1417	1157	0.41	0.67
70-80%	3	363	1109	0.10	0.64	3	848	1099	0.24	0.64	2	1205	1154	0.35	0.67
60-70%	4	310	1115	0.09	0.64	3	721	1088	0.21	0.63	4	1045	1085	0.30	0.63
50-60%	6	271	1105	0.08	0.64	5	643	1119	0.19	0.65	5	911	1134	0.26	0.66
40-50%	9	211	1103	0.06	0.64	6	535	1081	0.15	0.62	6	733	1078	0.21	0.62
20-40%	15	130	1110	0.04	0.64	17	338	1102	0.10	0.64	17	470	1105	0.14	0.64
Characteristic load											39			0.35	0.67
Node 175	Total = 100					Total = 92					Total = 96				
90-100%	2	866	1163	0.25	0.67	2	1508	1193	0.44	0.69	1	1884	1268	0.54	0.73
80-90%	1	780	1185	0.23	0.68	2	1346	1146	0.39	0.66	1	1639	1224	0.47	0.71
70-80%	4	686	1157	0.20	0.67	3	1131	1159	0.33	0.67	0	0	0	0.00	0.00
60-70%	3	587	1173	0.17	0.68	1	1057	1199	0.31	0.69	3	1258	1226	0.36	0.71
50-60%	4	506	1148	0.15	0.66	5	866	1194	0.25	0.69	10	1024	1201	0.30	0.69
40-50%	3	372	1184	0.11	0.68	7	715	1167	0.21	0.67	6	841	1153	0.24	0.67
20-40%	27	251	1175	0.07	0.68	18	430	1194	0.12	0.69	9	537	1229	0.16	0.71
Characteristic load											30			0.36	0.71

Table 11.3 Pile loads (kN) for the JAL building Masonry frame model under calibration Copala and amplified input motions

Range to max. Qc	Under calibration Copala motion					2 times amplified input motion					Elastic model, no amplified motion				
	Number of cycles	2*Cyclic Amplitude	Mean load	% of pile cap. Cyclic	Mean	Number of cycles	2*Cyclic Amplitude	Mean load	% of pile cap. Cyclic	Mean	Number of cycles	2*Cyclic Amplitude	Mean load	% of pile cap. Cyclic	Mean
Node 1	Total = 115					Total = 105					Total = 52				
90-100%	6	750	1288	0.22	0.74	2	1435	1296	0.41	0.75	6	1488	1296	0.43	0.75
80-90%	5	674	1273	0.19	0.74	1	1295	1297	0.37	0.75	4	1363	1328	0.39	0.77
70-80%	2	607	1285	0.18	0.74	2	1174	1291	0.34	0.75	14	1168	1267	0.34	0.73
60-70%	6	509	1278	0.15	0.74	1	900	1280	0.26	0.74	10	1027	1270	0.30	0.73
50-60%	5	419	1276	0.12	0.74	9	816	1275	0.24	0.74	5	872	1198	0.25	0.69
40-50%	9	358	1275	0.10	0.74	12	663	1273	0.19	0.74	1	742	1095	0.21	0.63
20-40%	30	242	1275	0.07	0.74	32	411	1274	0.12	0.74	3	457	1213	0.13	0.70
	63	Characteristic load		0.19	0.74										
Node 33	Total = 125					Total = 116					Total = 63				
90-100%	1	724	1249	0.21	0.72	2	1114	1188	0.32	0.69	2	1113	1422	0.32	0.82
80-90%	0	0	0	0.00	0.00	3	969	1216	0.28	0.70	3	1005	1323	0.29	0.76
70-80%	0	0	0	0.00	0.00	2	827	1227	0.24	0.71	6	884	1250	0.26	0.72
60-70%	3	466	1214	0.13	0.70	2	709	1177	0.20	0.68	2	759	1179	0.22	0.68
50-60%	5	382	1197	0.11	0.69	4	624	1217	0.18	0.70	12	640	1163	0.18	0.67
40-50%	4	332	1210	0.10	0.70	10	516	1226	0.15	0.71	5	517	1246	0.15	0.72
20-40%	36	213	1184	0.06	0.68	21	352	1237	0.10	0.71	11	405	1147	0.12	0.66
	49	Characteristic load		0.13	0.70										
Node 67	Total = 112					Total = 116					Total = 50				
90-100%	7	1114	1905	0.32	1.10	2	2228	2375	0.64	1.37	1	1857	2127	0.54	1.23
80-90%	3	995	1889	0.29	1.09	3	1938	2432	0.56	1.40	5	1550	1921	0.45	1.11
70-80%	2	856	1891	0.25	1.09	2	1654	2454	0.48	1.42	7	1403	1865	0.41	1.08
60-70%	7	755	1886	0.22	1.09	2	1418	2355	0.41	1.36	14	1221	1840	0.35	1.06
50-60%	5	647	1876	0.19	1.08	4	1248	2435	0.36	1.41	6	1022	1856	0.30	1.07
40-50%	11	510	1873	0.15	1.08	10	1032	2451	0.30	1.42	2	884	1946	0.26	1.12
20-40%	24	354	1863	0.10	1.08	21	704	2473	0.20	1.43	4	588	1828	0.17	1.06
	59	Characteristic load		0.25	1.09										
Node 99	Total = 128					Total = 115					Total = 55				
90-100%	4	909	1753	0.26	1.01	1	2272	1810	0.66	1.05	3	1331	1938	0.38	1.12
80-90%	6	797	1732	0.23	1.00	1	1818	1833	0.53	1.06	4	1150	1852	0.33	1.07
70-80%	1	680	1752	0.20	1.01	0	0	0	0.00	0.00	2	1017	1738	0.29	1.00
60-70%	5	613	1742	0.18	1.01	3	1483	1765	0.43	1.02	5	915	1739	0.26	1.00
50-60%	3	512	1720	0.15	0.99	10	1236	1749	0.36	1.01	8	770	1732	0.22	1.00
40-50%	5	425	1711	0.12	0.99	6	1034	1728	0.30	1.00	12	615	1634	0.18	0.94
20-40%	23	296	1709	0.09	0.99	21	613	1739	0.18	1.00	7	457	1677	0.13	0.97
	47	Characteristic load		0.20	1.01										
Node 143	Total = 126					Total = 118					Total = 67				
90-100%	3	750	1110	0.22	0.64	4	1429	1145	0.41	0.66	3	1414	1186	0.41	0.68
80-90%	1	635	1078	0.18	0.62	1	1192	1150	0.34	0.66	5	1243	1276	0.36	0.74
70-80%	2	585	1135	0.17	0.66	1	1086	1025	0.31	0.59	2	1115	1092	0.32	0.63
60-70%	2	508	1073	0.15	0.62	2	910	1083	0.26	0.63	6	938	1148	0.27	0.66
50-60%	3	403	1100	0.12	0.64	3	767	1101	0.22	0.64	6	830	1020	0.24	0.59
40-50%	9	349	1103	0.10	0.64	5	638	1107	0.18	0.64	5	671	1159	0.19	0.67
20-40%	23	242	1098	0.07	0.63	27	453	1094	0.13	0.63	12	479	946	0.14	0.55
	43	Characteristic load		0.18	0.62										
Node 175	Total = 111					Total = 110					Total = 51				
90-100%	3	1103	1179	0.32	0.68	2	2192	1229	0.63	0.71	3	1873	1207	0.54	0.70
80-90%	8	973	1166	0.28	0.67	1	1812	1214	0.52	0.70	5	1725	1192	0.50	0.69
70-80%	4	844	1169	0.24	0.68	3	1631	1200	0.47	0.69	10	1528	1149	0.44	0.66
60-70%	2	700	1160	0.20	0.67	2	1425	1201	0.41	0.69	16	1299	1155	0.38	0.67
50-60%	5	658	1164	0.19	0.67	5	1174	1173	0.34	0.68	5	1125	1145	0.32	0.66
40-50%	16	509	1151	0.15	0.66	16	994	1173	0.29	0.68	3	935	1275	0.27	0.74
20-40%	24	339	1140	0.10	0.66	24	612	1156	0.18	0.67	2	475	1220	0.14	0.70
	62	Characteristic load		0.24	0.68										

The pile loads considered as representing those during the 1985 Michoacan event were obtained for the Bare frame model under λ=5 – third column in Table 11.2. The pile loads during the Copala event are those from the calibrated Masonry frame model – first column in Table 11.3.

In Tables 11.2 and 11.3 several Q_{max} values exceed Q_{ult}. A clear indication of this is given in Figs. 11.1 and 11.2 which show the pile forces during the Copala and Michoacan earthquakes in an ID framework. Both figures show similar Q_a ranges, but the frame under the 1985 Michoacan event shows higher extreme Q_c amplitudes, which act for 1 or 2 cycles in most cases. The characteristic pile load for the 1985 Michoacan earthquake is higher than the static capacity in 4 out of the 6 piles considered with the maximum characteristic Q_{max} amounting to 1.42 times the Q_{ult}. During the 1995 Copala earthquake only 2 nodes suffer loads higher than their piles' static capacity. It is important to note that the Copala event produced on average 54 cycles with Q_c exceeding 20% of the maximum overall Q_c while the Michoacan event produced on

average 34 such cycles.

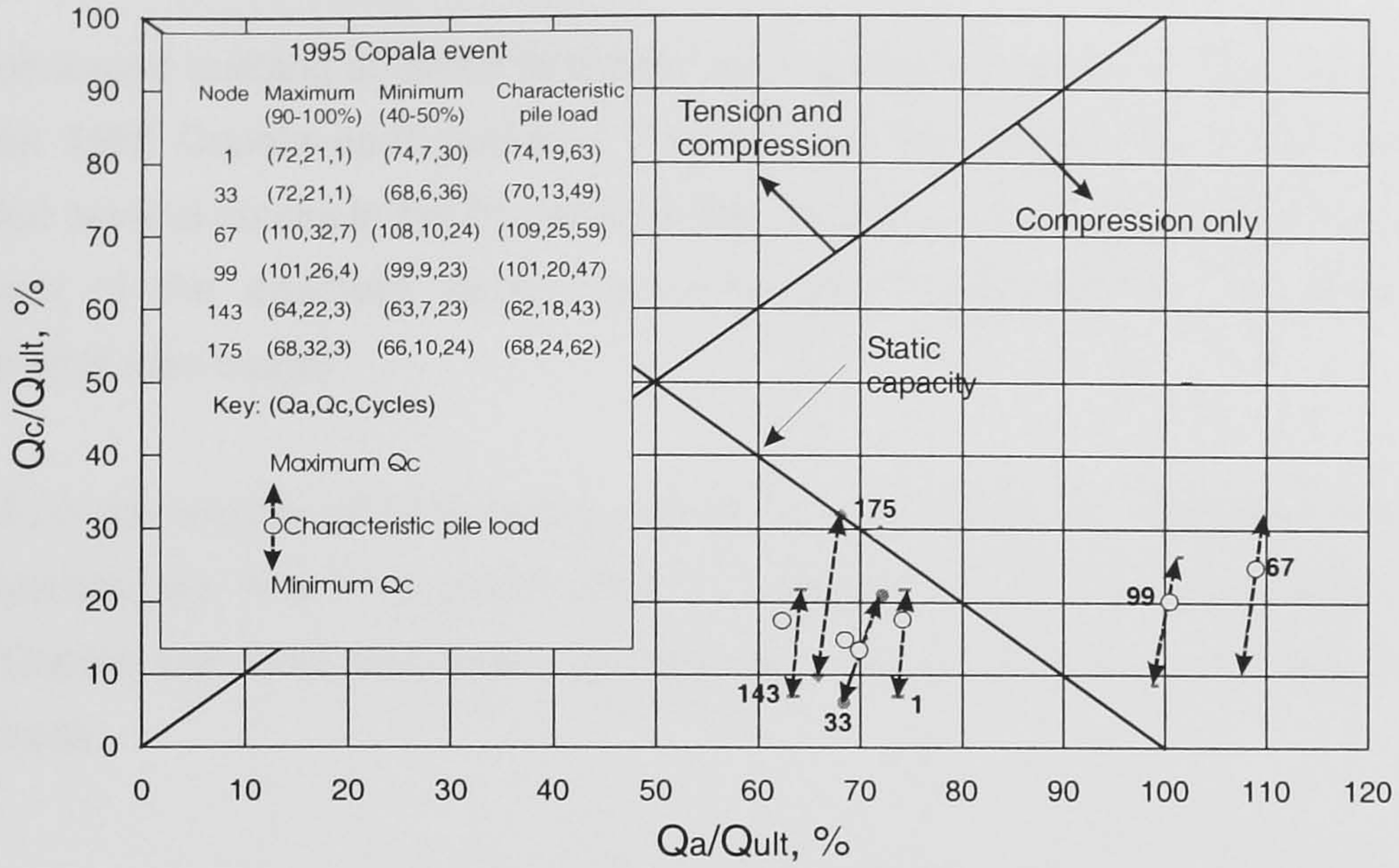


Fig. 11.1 Normalized pile loads for the JAL building Masonry frame model under the Copala (1995) earthquake

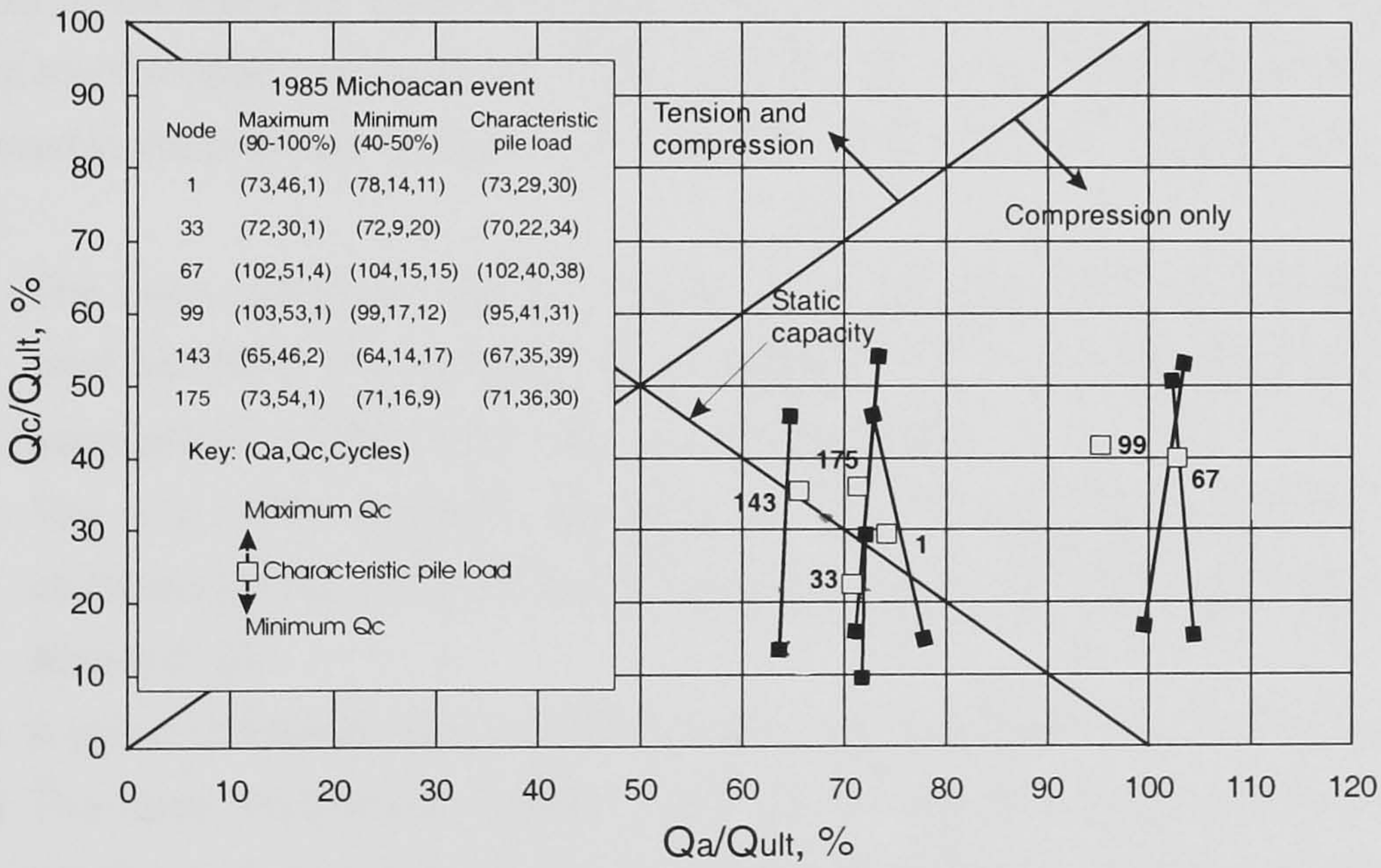


Fig. 11.2 Normalized pile loads for the JAL building Bare frame model under the Michoacan (1985) earthquake

The fundamental frequency of the predicted pile loads for the Michoacan 1985 event was 0.31 Hz (3.2 sec period). The predicted fundamental frequency for the pile load was 0.6 Hz (period of 1.7 sec) for the Copala 1995 event.

During the 1985 Michoacan earthquake the building suffered cracking in many columns, in the ribs of the waffle slab, and in most of the masonry infill walls, but overall

foundation failure was either not reported or absent – the Author assumed the former. As a result of the structural damage, the building was reinforced (section 7.2).

The reinforced building suffered structural damage again during the December 10, 1994 and the 1995 Copala earthquakes. The damage during these two both earthquakes included several cracks in the first two parking levels due to settlement of the structure in the area of the attached section (no information regarding the magnitude of the settlements was found).

Based on the reports of settlements during the December 10, 1994 and 1995 Copala earthquakes, the Author considers that the piles of the JAL building failed under the 1995 Copala and 1985 Michoacan earthquakes – the latter is the event with the highest magnitude.

11.1.2 PC Building pile data

The pile loads acting at the base nodes of the Original and Selected models during the earthquakes studied are shown in Tables 11.4 and 11.5 – the table characteristics were described in the previous section. The pile loads presented in the tables include:

i) The base reactions reduced by 5% (or 11069 kN considering the PC building total weight) due to raft participation (section 10.3.3). The load taken by the raft accounts for 10.8% of the compensated soil weight.
ii) The pile static capacity predicted by the ICPDM reduced by the regional calibration factor of 6%, the pile capacity is then 1754 kN (see Chapter 5 and Appendix C).
iii) A group efficiency factor of 0.88 for the subgroups located below the columns.
iv) The base reactions at nodes 1, 20 and 139 are distributed among 6 piles, the reactions at nodes 39, 58 and 76 are distributed among 4 piles, and the reaction at node 120 is carried by one single pile (see the PC building foundation plan on section 8.3).

Table 11.4 Pile loads (kN) for the PC Building Original frame model under calibration Copala and amplified input motions

Range to max. value	Under calibration 1995 Copala motion					3 times amplified input motion					5 times amplified motion - Michoacan				
	Number of cycles	2*Cyclic Amplitude	Mean load	% of pile cap. Cyclic	Mean	Number of cycles	2*Cyclic Amplitude	Mean load	% of pile cap. Cyclic	Mean	Number of cycles	2*Cyclic Amplitude	Mean load	% of pile cap. Cyclic	Mean
Node 1	Total = 84					Total = 91					Total = 96				
90-100%	2	446	741	0.14	0.48	1	775	785	0.25	0.51	3	822	777	0.27	0.50
80-90%	2	390	737	0.13	0.48	4	660	734	0.21	0.47	1	748	773	0.24	0.50
70-80%	1	338	726	0.11	0.47	4	580	760	0.19	0.49	5	646	786	0.21	0.51
60-70%	3	295	732	0.10	0.47	2	480	807	0.16	0.52	2	574	754	0.19	0.49
50-60%	1	250	738	0.08	0.48	1	450	728	0.15	0.47	5	461	764	0.15	0.49
40-50%	7	201	733	0.06	0.47	3	358	732	0.12	0.47	8	392	766	0.13	0.49
20-40%	18	140	729	0.05	0.47	13	230	743	0.07	0.48	19	255	731	0.08	0.47
Characteristic load											43			0.19	0.49
Node 20	Total = 105					Total = 127					Total = 137				
90-100%	1	266	1153	0.09	0.74	2	470	1152	0.15	0.74	3	516	1170	0.17	0.76
80-90%	3	227	1139	0.07	0.74	1	388	1153	0.13	0.74	1	461	1146	0.15	0.74
70-80%	1	192	1151	0.06	0.74	3	368	1144	0.12	0.74	1	400	1167	0.13	0.75
60-70%	1	183	1139	0.06	0.74	3	303	1148	0.10	0.74	4	354	1133	0.11	0.73
50-60%	2	141	1136	0.05	0.73	1	245	1136	0.08	0.73	1	270	1138	0.09	0.73
40-50%	6	115	1142	0.04	0.74	2	222	1160	0.07	0.75	8	233	1157	0.08	0.75
20-40%	17	82	1142	0.03	0.74	15	140	1139	0.05	0.74	23	161	1142	0.05	0.74
Characteristic load											41			0.13	0.75
Node 39	Total = 147					Total = 172					Total = 186				
90-100%	2	171	1712	0.06	1.11	1	350	1724	0.11	1.11	3	303	1750	0.10	1.13
80-90%	0	0	0	0.00	0.00	1	285	1775	0.09	1.15	2	253	1766	0.08	1.14
70-80%	1	137	1715	0.04	1.11	0	0	0	0.00	0.00	2	244	1731	0.08	1.12
60-70%	0	0	0	0.00	0.00	1	241	1768	0.08	1.14	0	0	0	0.00	0.00
50-60%	4	97	1726	0.03	1.11	3	183	1750	0.06	1.13	3	164	1802	0.05	1.16
40-50%	1	74	1717	0.02	1.11	2	161	1775	0.05	1.15	8	140	1770	0.05	1.14
20-40%	22	52	1722	0.02	1.11	17	94	1745	0.03	1.13	27	89	1734	0.03	1.12
Characteristic load											45			0.08	1.12
Node 139	Total = 132					Total = 131					Total = 131				
90-100%	3	308	268	0.10	0.17	5	632	285	0.20	0.18	2	827	343	0.27	0.22
80-90%	5	268	269	0.09	0.17	1	589	325	0.19	0.21	7	713	278	0.23	0.18
70-80%	3	235	265	0.08	0.17	4	483	275	0.16	0.18	0	0	0	0.00	0.00
60-70%	3	203	265	0.07	0.17	3	410	280	0.13	0.18	4	531	255	0.17	0.16
50-60%	4	173	266	0.06	0.17	9	364	226	0.12	0.15	5	474	210	0.15	0.14
40-50%	6	143	258	0.05	0.17	3	313	201	0.10	0.13	7	393	209	0.13	0.13
20-40%	14	95	260	0.03	0.17	17	186	219	0.06	0.14	14	255	173	0.08	0.11
Characteristic load											39			0.23	0.18
Node 58	Total = 121					Total = 134					Total = 137				
90-100%	1	797	1344	0.26	0.87	2	1443	1331	0.47	0.86	3	1675	1338	0.54	0.86
80-90%	0	0	0	0.00	0.00	2	1258	1366	0.41	0.88	1	1538	1347	0.50	0.87
70-80%	6	586	1344	0.19	0.87	3	1128	1336	0.36	0.86	2	1357	1412	0.44	0.91
60-70%	3	524	1365	0.17	0.88	4	950	1381	0.31	0.89	4	1130	1363	0.36	0.88
50-60%	3	445	1355	0.14	0.88	2	755	1309	0.24	0.85	5	973	1318	0.31	0.85
40-50%	5	358	1341	0.12	0.87	4	649	1327	0.21	0.86	4	816	1452	0.26	0.94
20-40%	15	245	1346	0.08	0.87	17	452	1382	0.15	0.89	22	515	1465	0.17	0.95
Characteristic load											41			0.36	0.88
Node 76	Total = 155					Total = 174					Total = 180				
90-100%	4	85	693	0.03	0.45	1	161	712	0.05	0.46	1	154	708	0.05	0.46
80-90%	0	0	0	0.00	0.00	0	0	0	0.00	0.00	1	130	676	0.04	0.44
70-80%	2	66	693	0.02	0.45	2	122	687	0.04	0.44	5	116	702	0.04	0.45
60-70%	0	0	0	0.00	0.00	3	105	713	0.03	0.46	7	98	696	0.03	0.45
50-60%	1	45	688	0.01	0.44	1	87	696	0.03	0.45	8	85	691	0.03	0.45
40-50%	9	39	689	0.01	0.44	5	70	703	0.02	0.45	10	69	693	0.02	0.45
20-40%	18	25	687	0.01	0.44	20	42	692	0.01	0.45	21	47	684	0.02	0.44
Characteristic load											53			0.04	0.45

The forces considered as best estimates for those acting during the 1985 Michoacan event were those obtained from the Original frame under λ=5 – the third column in Table 11.4. The forces for the 1995 Copala event were obtained from the calibrated Selected model – first column in Table 11.5.

The ID's given in Figs. 11.3 and 11.4 show the pile forces for middle values from the 90% to 100% Q_c and 40% to 50% Q_c intervals, along the characteristic pile loads. These plots clearly indicate that for the Copala and Michoacan earthquakes some cycles involved characteristic Q_{max} values that exceeded Q_{ult}.

Table 11.5 Pile loads (kN) for the PC Building Selected model under calibration Copala and amplified input motions

Range to max. value	Under calibration copala motion					3 times amplified input motion				
	Number of cycles	2*Cyclic Amplitude	Mean load	% of pile cap. Cyclic	Mean	Number of cycles	2*Cyclic Amplitude	Mean load	% of pile cap. Cyclic	Mean
Node 1	Total = 96					Total = 95				
90-100%	2	419	730	0.14	0.47	1	866	729	0.28	0.47
80-90%	1	376	737	0.12	0.48	2	730	773	0.24	0.50
70-80%	3	328	732	0.11	0.47	2	650	714	0.21	0.46
60-70%	3	276	734	0.09	0.47	2	536	753	0.17	0.49
50-60%	3	228	719	0.07	0.46	1	518	693	0.17	0.45
40-50%	4	195	720	0.06	0.46	6	385	727	0.12	0.47
20-40%	17	127	723	0.04	0.47	18	244	722	0.08	0.47
	33	Charcateristic load		0.11	0.47					
Node 20	Total = 116					Total = 129				
90-100%	2	245	993	0.08	0.64	1	396	1022	0.13	0.66
80-90%	0	0	0	0.00	0.00	0	0	0	0.00	0.00
70-80%	4	190	992	0.06	0.64	2	304	1039	0.10	0.67
60-70%	3	158	996	0.05	0.64	2	247	1029	0.08	0.66
50-60%	3	141	998	0.05	0.64	10	218	1018	0.07	0.66
40-50%	4	116	1005	0.04	0.65	5	186	1028	0.06	0.66
20-40%	15	79	1000	0.03	0.65	18	111	1024	0.04	0.66
	31	Charcateristic load		0.06	0.64					
Node 120	Total = 136					Total = 127				
90-100%	1	534	2172	0.17	1.40	1	1408	2235	0.45	1.44
80-90%	1	451	2022	0.15	1.31	0	0	0	0.00	0.00
70-80%	1	393	2043	0.13	1.32	3	1083	2140	0.35	1.38
60-70%	5	356	2087	0.11	1.35	5	903	2059	0.29	1.33
50-60%	4	291	2063	0.09	1.33	4	732	1954	0.24	1.26
40-50%	8	236	2111	0.08	1.36	4	655	2006	0.21	1.30
20-40%	18	158	2077	0.05	1.34	21	396	1981	0.13	1.28
	38	Charcateristic load		0.11	1.35					
Node 39	Total = 167					Total = 182				
90-100%	4	65	1501	0.02	0.97	1	266	1513	0.09	0.98
80-90%	1	55	1502	0.02	0.97	0	0	0	0.00	0.00
70-80%	4	50	1505	0.02	0.97	0	0	0	0.00	0.00
60-70%	2	46	1503	0.02	0.97	2	162	1551	0.05	1.00
50-60%	9	37	1505	0.01	0.97	6	153	1522	0.05	0.98
40-50%	15	30	1503	0.01	0.97	5	122	1506	0.04	0.97
20-40%	36	20	1497	0.01	0.97	20	75	1529	0.02	0.99
	71	Charcateristic load		0.02	0.97					
Node 139	Total = 137					Total = 135				
90-100%	4	288	267	0.09	0.17	3	705	322	0.23	0.21
80-90%	2	249	267	0.08	0.17	4	625	302	0.20	0.19
70-80%	2	226	285	0.07	0.18	5	553	308	0.18	0.20
60-70%	4	193	269	0.06	0.17	5	461	275	0.15	0.18
50-60%	6	168	270	0.05	0.17	5	399	277	0.13	0.18
40-50%	6	139	267	0.04	0.17	6	327	300	0.11	0.19
20-40%	17	81	273	0.03	0.18	13	208	257	0.07	0.17
	41	Charcateristic load		0.07	0.18					
Node 58	Total = 146					Total = 147				
90-100%	2	462	1338	0.15	0.86	2	1392	1314	0.45	0.85
80-90%	1	383	1336	0.12	0.86	1	1237	1329	0.40	0.86
70-80%	2	345	1336	0.11	0.86	6	1111	1310	0.36	0.85
60-70%	3	300	1339	0.10	0.86	5	948	1301	0.31	0.84
50-60%	8	255	1335	0.08	0.86	2	808	1380	0.26	0.89
40-50%	6	203	1330	0.07	0.86	7	655	1323	0.21	0.85
20-40%	14	135	1341	0.04	0.87	14	427	1333	0.14	0.86
	36	Charcateristic load		0.10	0.86					
Node 76	Total = 205					Total = 207				
90-100%	1	56	684	0.02	0.44	1	146	682	0.05	0.44
80-90%	0	0	0	0.00	0.00	0	0	0	0.00	0.00
70-80%	0	0	0	0.00	0.00	1	115	685	0.04	0.44
60-70%	4	37	685	0.01	0.44	1	99	701	0.03	0.45
50-60%	4	30	687	0.01	0.44	0	0	0	0.00	0.00
40-50%	2	24	684	0.01	0.44	1	73	698	0.02	0.45
20-40%	9	13	684	0.00	0.44	14	39	689	0.01	0.44
	20	Charcateristic load		0.01	0.44					

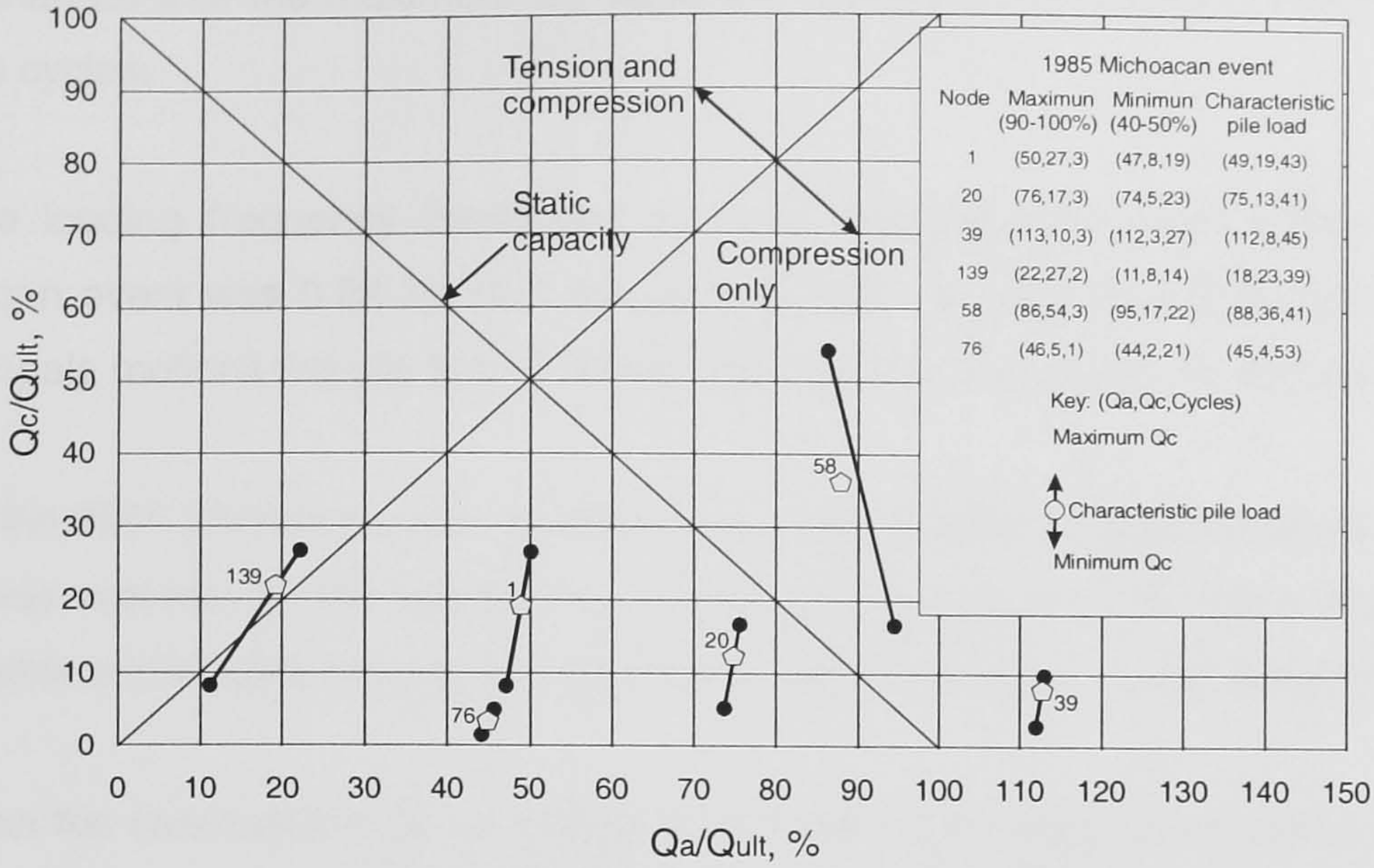


Fig. 11.3 Pile loads for the PC building Original frame model under the 1985 Michoacan earthquake

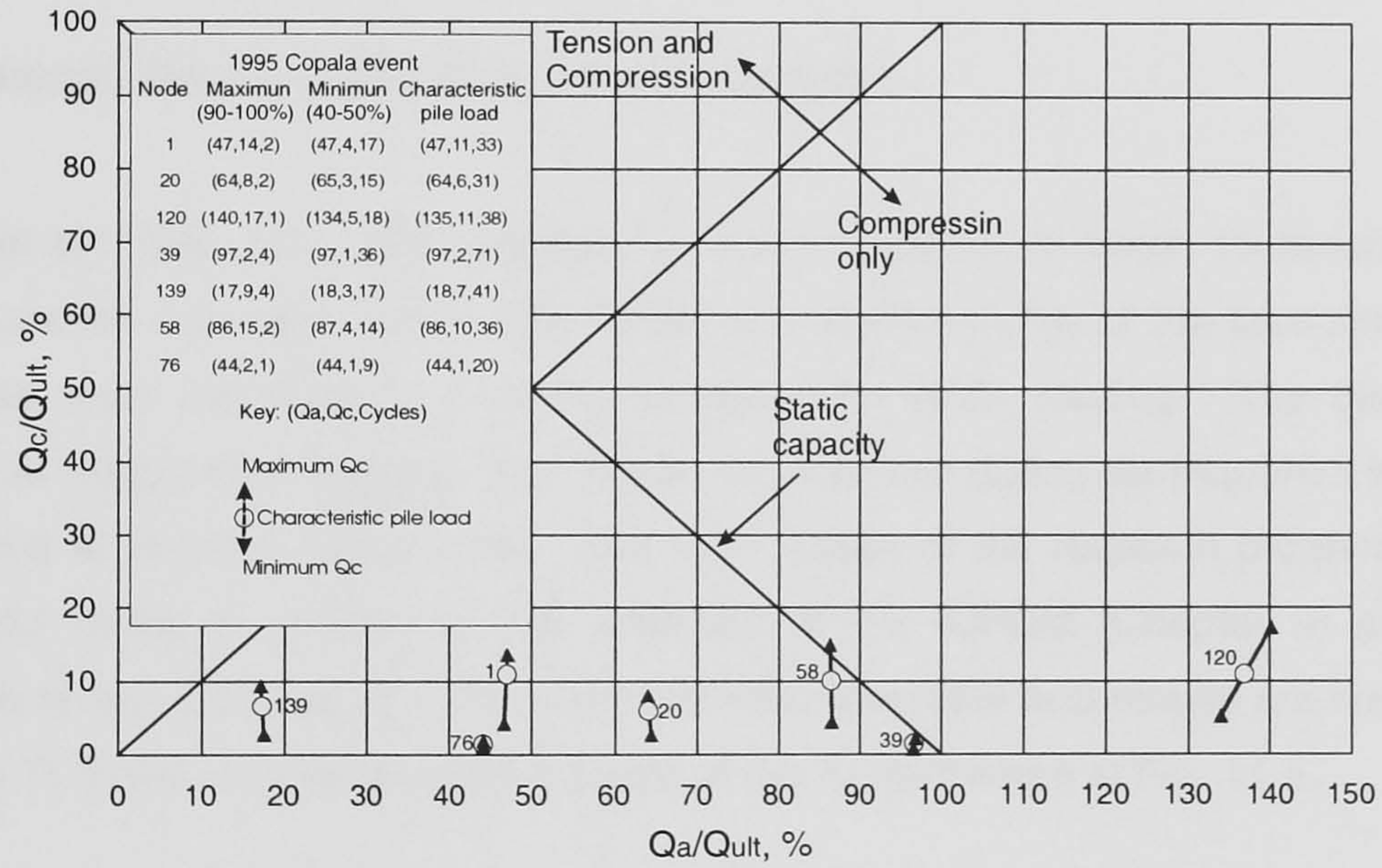


Fig. 11.4 Pile loads for the PC building Selected frame model under the Copala earthquake

As for the JAL building results the main difference between the response under the two events is the greater Q_c amplitude developed in the 1985 Michoacan event. The predicted characteristic pile load for the 1985 Michoacan earthquake is higher than the static capacity in 2 out of 6 piles, with the maximum Q_{max} being 1.24 times higher that Q_{ult}. During the 1995 Copala earthquake only node 120 is predicted to experience a characteristic pile load higher than Q_{ult}, with a ratio of $Q_{max} = 1.46\ Q_{ult}$, mainly due to high static load[143]. The Copala event produced on average 39 cycles with Q_c amplitudes

---

[143] The high Q_a on node 120 reflects the fact that this structural node is supported by one single

higher than 20% of the maximum Q_c, while the Michoacan event produced on average 44 such cycles.

The pile loading frequency developed by the Original frame model under the 1985 Michoacan event was 0.24 Hz (4.2 sec period). For the Selected frame model under 1995 Copala motions the pile load fundamental frequency was 0.33 Hz (3.0 sec period).

During the 1985 Michoacan earthquake the building sustained light structural damage, which was repaired by the addition of reinforced concrete walls in some frames. No appreciable settlements have been reported for the PC building during any earthquake.

Based on the observations of no settlements of the PC building during eathquakes, the Author considers that the piles of the PC building did not fail under the 1985 Michoacan or 1995 Copala eartquakes.

11.1.3 Jaime, Resendiz and Romo cyclic pile tests

Jaime, et al. (1990 and 1988) studied the cyclic response of three, 10 m long, 30 cm square section concrete friction piles driven in a typical profile of the lake zone in MC. The piles were subjected to one-way compression cyclic loading. The cycles were applied at frequencies ranging from those experienced during earthquakes in the MC Lake zone to values 6 times lower. The main results of the research programme were discussed earlier in relation to the validation of the ICPDM (Chapter 5) and in the literature review (Chapter 2). The main test characteristics and results are summarized in Table 11.6 and are represented in terms of the ID framework in Fig. 11.5.

The ultimate static pile capacity (Q_{ult}) was 552 kN, obtained from a maintained load pile test conducted over 22 hours on Pile No. 2 before any cyclic loading. Jaime, et al. defined cyclic failure as a sharp increase in the magnitude or the rate of accumulation of permanent displacement ($d_a \approx 1$ mm/cycle).

---

pile.

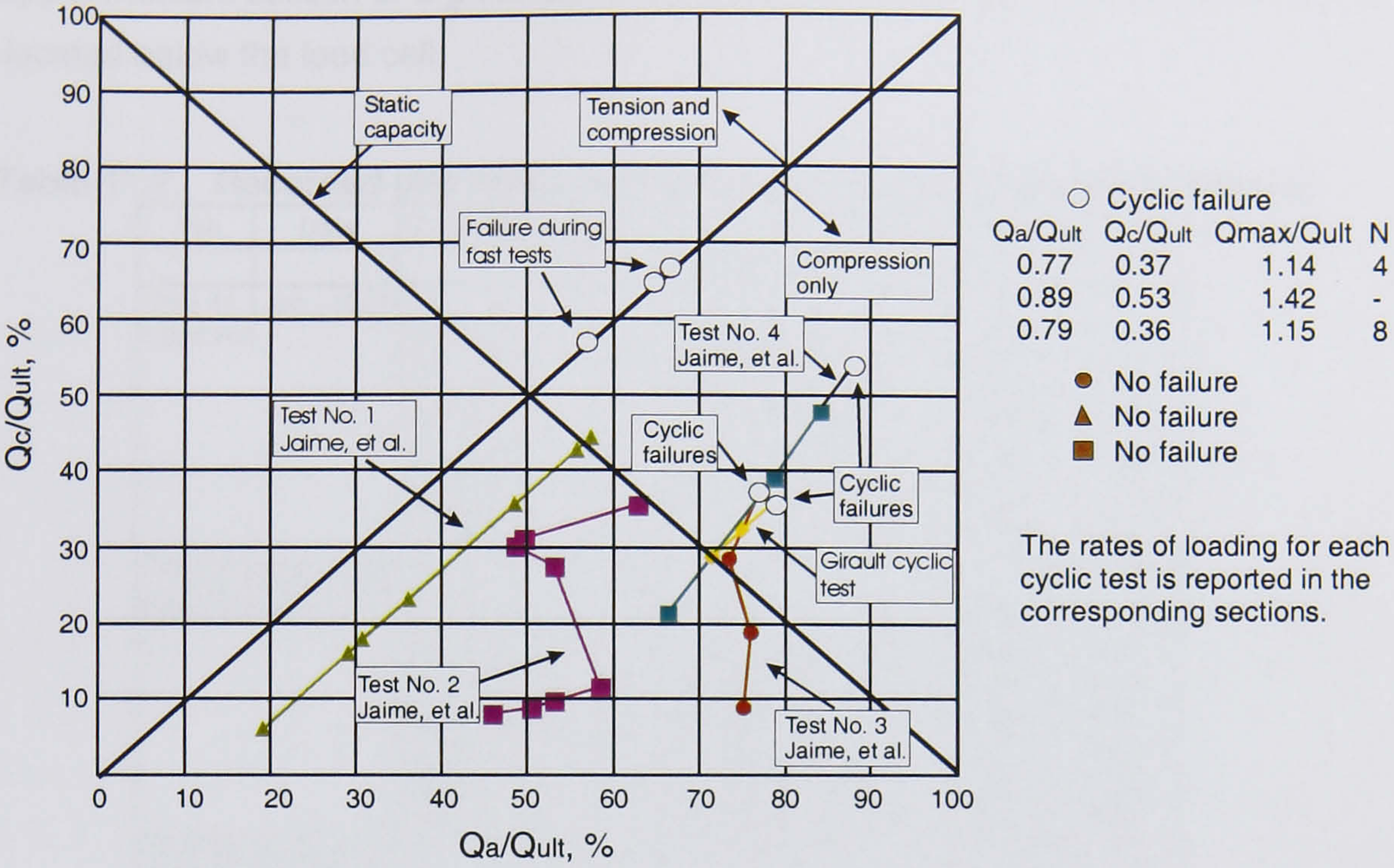
Table 11.6 Summary of the cyclic pile tests carried out in Mexico City clay by Jaime, et al. (1988)

Test	Date	Cycles	Period	Q_{min}	Q_{max}	Q_a	Q_c	d_a	d_c	Q_a/Q_{ult}	Q_c/Q_{ult}	Q_{max}/Q_{ult}
(No)		(No.)	(sec)	(kN)	(kN)	(kN)	(kN)	(mm)	(mm)			
1	2/2/88	30	1.0	71.9	138.6	105.3	33.4	0.0	-	0.19	0.06	0.25
Pile 2		30	2.7	71.9	248.5	160.2	88.3	0.4	-	0.29	0.16	0.45
		30	4.3	71.9	268.1	170.0	98.1	0.3	-	0.31	0.18	0.49
		30	5.3	71.9	327.0	199.4	127.5	0.5	1.5	0.36	0.23	0.59
		30	6.3	71.9	464.3	268.1	196.2	0.6	3.9	0.49	0.36	0.84
		30	9.1	71.9	542.8	307.4	235.4	2.3	6.1	0.56	0.43	0.98
	No failure	30	8.3	71.9	562.4	317.2	245.3	2.7	6.0	0.57	0.44	1.02
2	3/16/88	30	3.1	209.3	297.5	253.4	44.1	0.0	1.4	0.46	0.08	0.54
Pile 1		30	2.3	228.9	327.0	277.9	49.1	0.0	1.7	0.50	0.09	0.59
		30	3.0	238.7	346.6	292.6	54.0	0.0	2.0	0.53	0.10	0.63
		30	4.0	258.3	385.8	322.1	63.8	0.7	2.0	0.58	0.12	0.70
		30	7.5	140.6	444.7	292.6	152.1	0.0	5.9	0.53	0.28	0.81
		30	10.8	101.3	434.9	268.1	166.8	0.0	6.6	0.49	0.30	0.79
		30	9.4	101.3	444.7	273.0	171.7	0.2	6.8	0.49	0.31	0.81
	No failure	30	9.9	150.4	542.8	346.6	196.2	0.8	7.6	0.63	0.36	0.98
3	4/12/88	30	3.6	366.2	464.3	415.3	49.1	1.0	1.5	0.75	0.09	0.84
Pile 3		30	7.2	317.2	523.2	420.2	103.0	2.6	3.9	0.76	0.19	0.95
		30	8.3	248.5	562.4	405.5	157.0	0.2	6.9	0.73	0.28	1.02
	Failure	**4**	**11.6**	**219.1**	**631.1**	**425.1**	**206.0**	**25.5**	**8.9**	**0.77**	**0.37**	**1.14**
4	4/21/88	30	4.2	248.5	483.9	366.2	117.7	0.4	3.8	0.66	0.21	0.88
Pile 1		30	8.0	219.1	650.7	434.9	215.8	0.6	7.5	0.79	0.39	1.18
		30	12.5	199.4	729.2	464.3	264.9	3.6	9.2	0.84	0.48	1.32
Jaime's extrapolated failure				*199.4*	*788.0*	*493.7*	*294.3*	-	-	*0.89*	*0.53*	*1.43*
Fast compression tests												
Pile 1				716.1 kN			15.0 mm		55 sec			
Pile 3				627.8 kN			11.5 mm		32 sec			

11.1.4 Girault cyclic pile test

Girault (1986) reported limited information from a cyclic compression pile test carried out on a typical profile of the Lake zone of MC (although no information is reported on the pile length and cross sectional dimensions). The pre-cycling static pile capacity (Q_{ult}) was 140 tons (1373 kN). The first cyclic load stage consisted of 8 cycles of Q_a/Q_{ult} = 0.71 and Q_c/Q_{ult} = 0.29, at the end of which the permanent displacement reached 1.5 mm. The second and third cyclic stages consisted of the following combinations Q_a/Q_{ult} = 0.75, Q_c/Q_{ult} = 0.32, and Q_a/Q_{ult} = 0.79, Q_c/Q_{ult} = 0.36, respectively – according to Girault the latter produced pile failure. The cyclic loading period for the three load combinations was 16 sec.

Girault's (1986) and Jaime, et al.'s (1990) cyclic pile tests are presented in terms of the ID framework in Fig. 11.5. These test results indicated that failure is not observed during cyclic loading before Q_{max} exceeds Q_{ult} and that there is a threshold Q_{max} after which the pile displacements increase at very high rates, as was also observed in cyclic undrained simple shear tests on samples from the same site (Jaime, et al., 1990). The three cyclic failures, and the static failure induced by fast monotonic loading, show Q_{max} values ranging between 1.14 and 1.42 Q_{ult}. The number of cycles and characteristics of the loads imposed during the three tests that underwent cyclic failure are included in Fig.



○ Cyclic failure

Qa/Qult	Qc/Qult	Qmax/Qult	N
0.77	0.37	1.14	4
0.89	0.53	1.42	-
0.79	0.36	1.15	8

● No failure
▲ No failure
■ No failure

The rates of loading for each cyclic test is reported in the corresponding sections.

Fig. 11.5 Cyclic pile tests on Mexico City clay presented in a cyclic Interaction Diagram framework

11.1.5 Mendoza, Romo, Calderon, and Rodriguez instrumented piled foundation

Section 10.1.2 presented a detailed description of Mendoza, et al.'s (1998) instrumented piled viaduct foundation. The piles considered for the current analysis are pile 41 and 4 as loaded during the January 1997 event (Fig. 10.7); and pile 40 during the June 1999 event[144] (Fig. 10.9) (Mendoza, et al. 1997 and 2000a).

Table 11.7 shows the axial loads developed in the mentioned piles[145]. Following from the previous analysis, Table 11.7 classifies the load at each pile according to Q_c. The tables include: (i) the pile number and position of the load cell in each pile, (ii) the Q_c interval as a percentage of the maximum Q_c, (iii) the number of load cycles in the Q_c interval, (iv) the average values of Q_a and Q_c for the interval, and (v) the ratio of average Q_c and Q_a to the Q_{ult} predicted by the ICPDM.

---

[144] The foundatiuon time–settlement curves showed a step of 20 mm at axis 11 after the June 1999 event (Fig. 10.12).

[145] The pile load were scaled from figures given in the mentioned papers, some minor inconsistencies with the values reported by Mendoza, et al. might be noted.

An estimate of the pile's static capacity Q_{ult} = 1110 kN[146] was obtained from the ICPDM. The Q_{ult} estimates used to normalized the pile loads obtained from load cells located in the upper medium section of a given pile is calculated considering only the section of the pile located below the load cell.

Table 11.7 Recorded pile loads in Mendoza, et al. instrumented foundation

Pile	Date	Q_c range	Cycles	Q_c	Q_a	Q_c/Q_{ult}	Q_a/Q_{ult}	Q_{max}/Q_{ult}
			(No.)	(kN)	(kN)			
Pile 41	Jan., 1997							
Head cell		90-100%	5	22.3	533.7	0.02	0.48	0.50
		80-90%	1	19.3	533.7	0.02	0.48	0.50
		70-80%	1	16.9	533.7	0.02	0.48	0.50
		60-70%	5	14.6	533.7	0.01	0.48	0.49
		50-60%	6	12.5	533.7	0.01	0.48	0.49
		40-50%	9	10.5	533.7	0.01	0.48	0.49
		20-40%	16	7.2	533.7	0.01	0.48	0.49
Pile 4	Jan., 1997							
Upper-medium cell		90-100%	5	83.0	471.5	0.09	0.52	0.61
		80-90%	2	70.8	471.4	0.08	0.52	0.60
		70-80%	6	62.9	465.4	0.07	0.51	0.58
		60-70%	8	54.2	475.9	0.06	0.52	0.58
		50-60%	9	46.8	465.5	0.05	0.51	0.56
		40-50%	3	38.4	483.0	0.04	0.53	0.57
		20-40%	5	23.0	463.8	0.03	0.51	0.54
Pile 40	June, 1999							
Upper-medium cell		90-100%	3	118.0	561.6	0.13	0.62	0.75
		80-90%	2	103.8	540.2	0.11	0.60	0.71
		70-80%	9	91.8	571.3	0.10	0.63	0.73
		60-70%	6	79.3	581.8	0.09	0.64	0.73
		50-60%	13	67.6	570.1	0.07	0.63	0.70
		40-50%	9	55.5	569.7	0.06	0.63	0.69
		20-40%	16	36.1	589.2	0.04	0.65	0.69

Table 11.7 indicates low Q_c amplitudes, with piles 4 and 40 experiencing maximum Q_c loads of around 10% Q_{ult}. Mendoza, et al. reported that the loads carried by piles 4 and 40 fell gradually during shaking, while Pile 41 remained steady. The axial loads for all the piles under analysis varied with a 0.24 Hz fundamental frequency (Mendoza, et al. 2000a). These piles transferred part of their shaft resistance to the foundation raft; their loading data were not plotted in the Author's ID, although we note that applying 20 to 30 cycles in the Q_c/Q_{ult}=0.13, Q_a/Q_{ult}=0.62 region causes no damage. The piles did not undergo failure.

---

[146] Reduced 6% according to the validation presented in Chapter 5.

11.2 Interaction Diagram for Mexico City

11.2.1 Summary of the data used to develop an Interaction Diagram for driven piles in Mexico City

The characteristic single pile loads developed at each base node of the JAL and PC building frames have been obtained by averaging Q_a and Q_c and assigning to these mean values the total number of cycles. The characteristic pile loads were presented in Fig. 11.1 to Fig. 11.4, they are also presented in Table 11.8 and indicated as empty symbols in Fig. 11.6.

In order to characterise the response of each complete frame the characteritic pile loads at the frame nodes were averaged, obtaining one single point per analyzed frame and earthquake. These load combinations are shown in Table 11.8 using bold font, and indicated as shadowed symbols in Fig. 11.6.

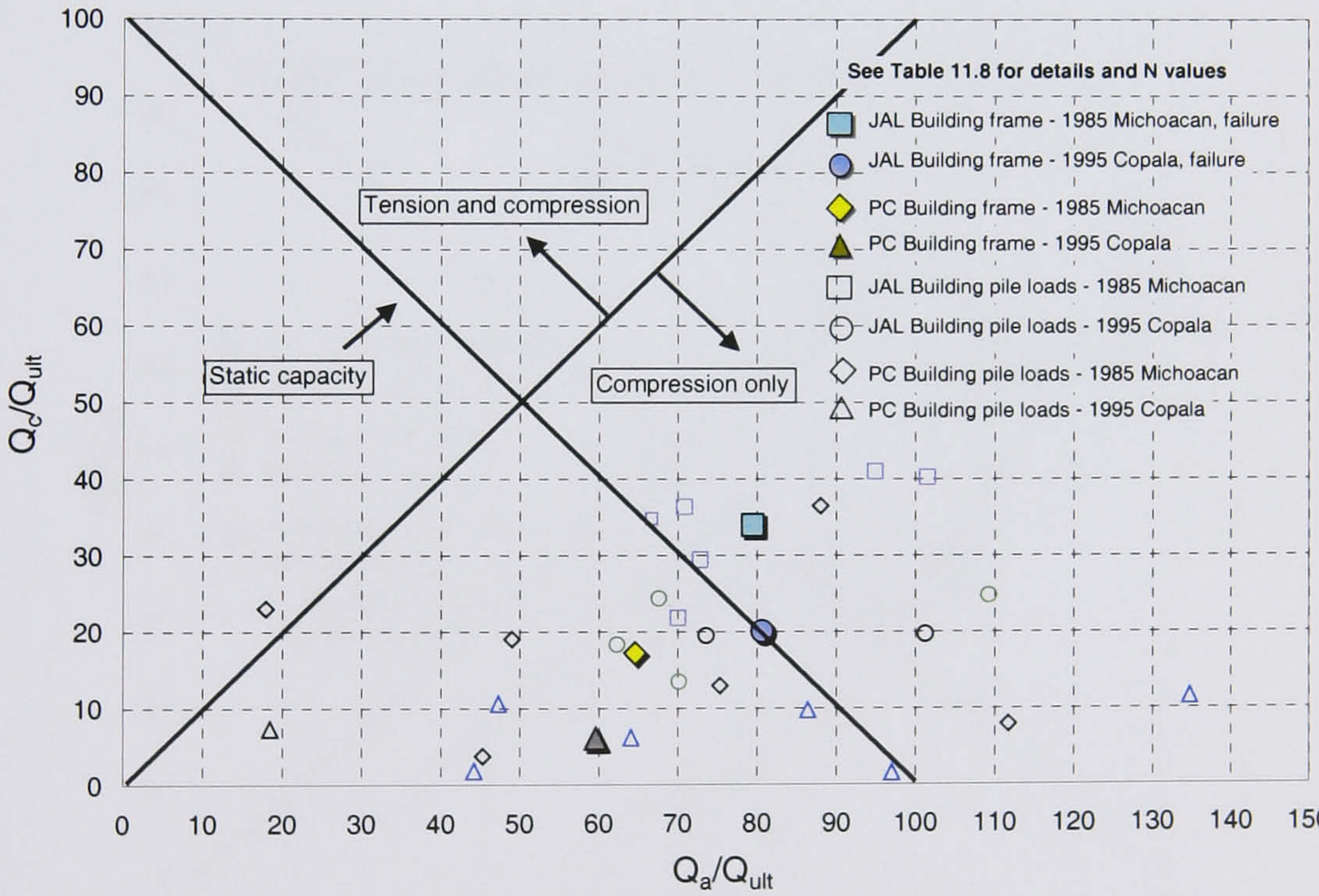


Fig. 11.6 Frame loads from pile loads

Table 11.8 Pile characteristic loads and frame mean loads for JAL and PC buildings

	Q_a/Q_{ult} (%)	Q_c/Q_{ult} (%)	Cycles (No.)		Q_a/Q_{ult} (%)	Q_c/Q_{ult} (%)	Cycles (No.)
	JAL under 1985 Michoacan				**JAL under 1995 Copala**		
Node 1	73	29	30		74	19	63
Node 33	70	22	34		70	13	49
Node 67	102	40	38		109	25	59
Node 99	95	41	31		101	20	47
Node 143	67	35	39		62	18	43
Node 175	71	36	30		68	24	62
Frame	**79**	**34**	**34**		**81**	**20**	**54**
	PC under 1985 Michoacan				**PC under 1995 Copala**		
Node 1	49	19	43		47	11	33
Node 20	75	13	41		64	6	31
Node 120					135	11	38
Node 39	112	8	45		97	2	71
Node 139	18	23	39		18	7	41
Node 58	88	36	41		86	10	36
Node 76	45	4	53		44	1	20
Frame	**65**	**17**	**44**		**60**	**6**	**39**

Fig. 11.7 includes the average points for the frames of the JAL and PC buildings and the load combinations for Girault and Jaime, et al.'s cyclic pile tests. (The symbols for the load combinations producing failure are indicated in the figure). Table 11.9 shows the load combination for failure under cyclic or fast tests.

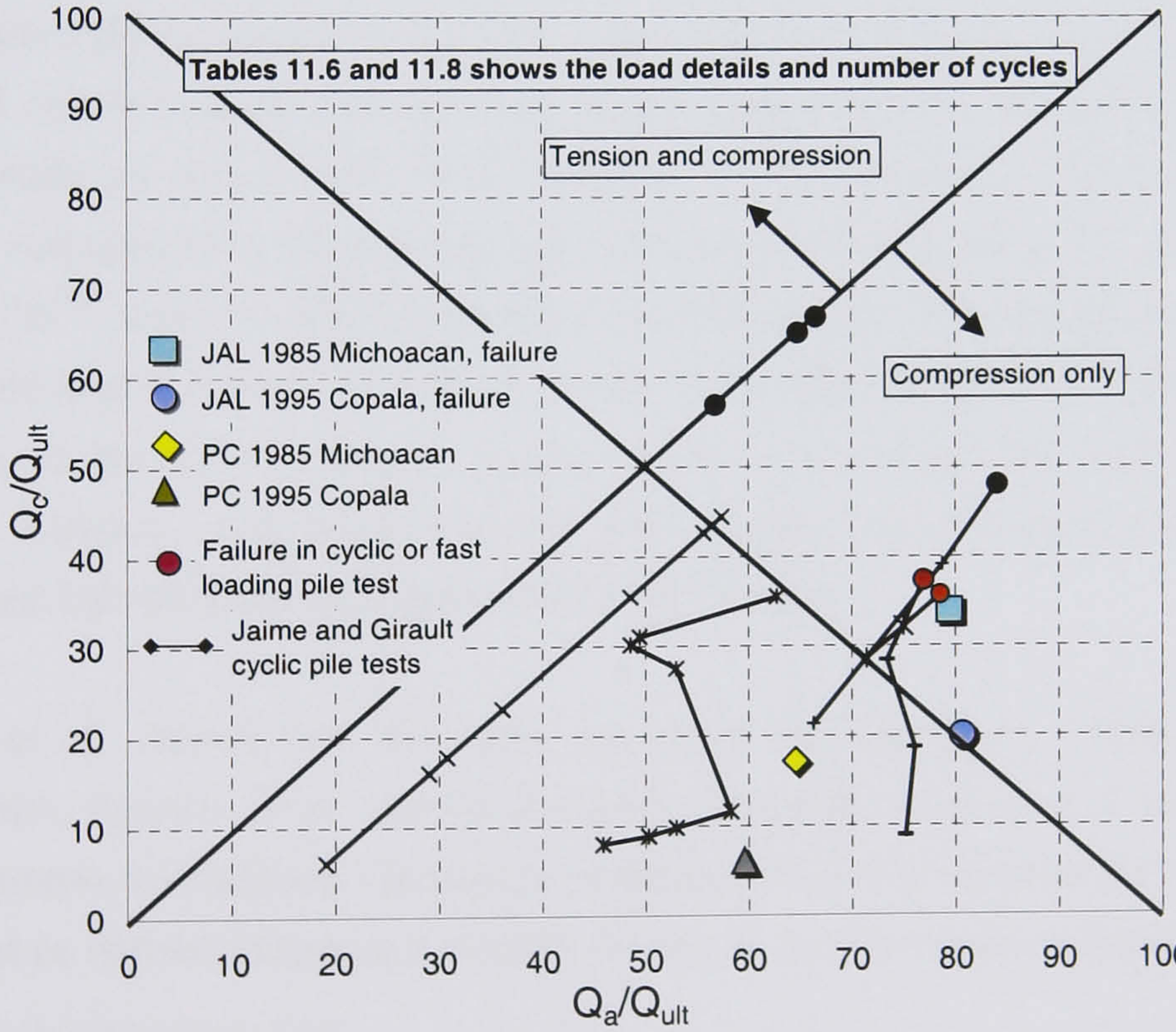


Fig. 11.7 JAL and PC building frame loads and cyclic piles test results in MC

Table 11.9 Failure loads for Jaime, et al. and Girault cyclic pile tests

	Q_a/Q_{ult} (%)	Q_c/Q_{ult} (%)	Cycles (No.)
Girault	79	36	8
Jaime, et al.	77	37	4
	89	53	-
	57	57	1
	65	65	1
	67	67	1

An additional point to establish the failure countours was obtained by identifying the point in the Q_a axis corresponding to Q_c=0. When Q_c approaches zero the cyclic test becomes a sustained static load test. Thus, the number of cycles contour that intersects the Q_a/Q_{ult} axis is given by the relation between the time the static sustained failure load level acts and the cyclic load period (Karlsrud, et al., 1987). Considering that for Jaime, et al.'s static test Q_{ult} acted for 1 minute[147] before failure, and a seismic load period of 2.3 sec, the N = 26 (60/2.3) failure contour would intersect the Q_a/Q_{ult} axis at Q_a/Q_{ult} = 1.0.

The data described previously do not allow the two-way loading pile response to be defined. Since two way cyclic pile tests have not been performed on MC, an estimate of the expected pile response is obtained from undrained two-way cyclic load controlled Direct Shear (DS) tests carried out in MC clay samples by Ovando, et al. (1993)[148]. The use of DS results to obtain a rough idea of cyclic pile response has been advocated by following Karlsrud, et al. (1987) who compared an ID developed from cyclic pile tests against a corresponding ID obtained from constant rate of strain (CRS) and sustained load (SL) DS[149] tests on undisturbed and remoulded reconsolidated (RR) clay. Karlsrud, et al. found that the shaft resistance at the cyclic pile capacity (Q_{max}/Q_{ult}) is closely analogous to the cyclic strength (τ_{max}/τ_f) seen on laboratory DS tests on RR clay samples. Karlsrud, et al. found that the ratio between undisturbed and remoulded re-consolidated DS test shear strengths was 0.7 for his clays.

Ovando, et al. carried out DS tests on intact MC samples. After full sample consolidation, Ovando, et al. applied sinusoidal deformation cycles of 2 sec period and variable maximum amplitude, recording the number of cycles necessary to reach failure. Ovando, et al. defined failure as a sudden change in the rate of permanent displacement

---

[147] The maintained load test was carried out by applying 5 tons every 2 hours. Rojas, et al. (1999) report that the Q_{ult} acted 1 minute before failure.

[148] Ovando, et al. modified a simple shear apparatus in order to carry out direct shear tests. All the test consisted of symmetrical two way cyclic loading.

[149] Karlsrud, et al. used a direct simple shear (DSS) apparatus adapted for cyclic loading and with high control mechanism, which is used to maintain constant the volume of the specimen.

accumulation[150]. As noted by Karlsrud, et al. (1987), the ratio between shear strength for intact and reconsolidated remoulded samples of MC clay was around 0.7.

The results from Ovando, et al.'s two-way cyclic direct shear tests used to tentatively define response under two-way cyclic loading are summarized in Fig. 11.8, where the ratio between the shear strength obtained in static and cyclic tests (τ_d/τ_{ult}) is plotted against the number of cycles to failure. Since all the cyclic DS tests by Ovando, et al. were carried out on intact samples, the shear strength ratios are transformed to their equivalent remoulded strength by reducing them by 30% when introduced in the Author's ID.

Karlsrud and Haugen (1983) and Jardine (1985) have identified reductions in capacity for piles under two-way loading that agree with those established by the above analogy. Jardine indicates that two-way cycling produces higher reductions on the radial effective stress (σ_v'). See section 2.4.2.

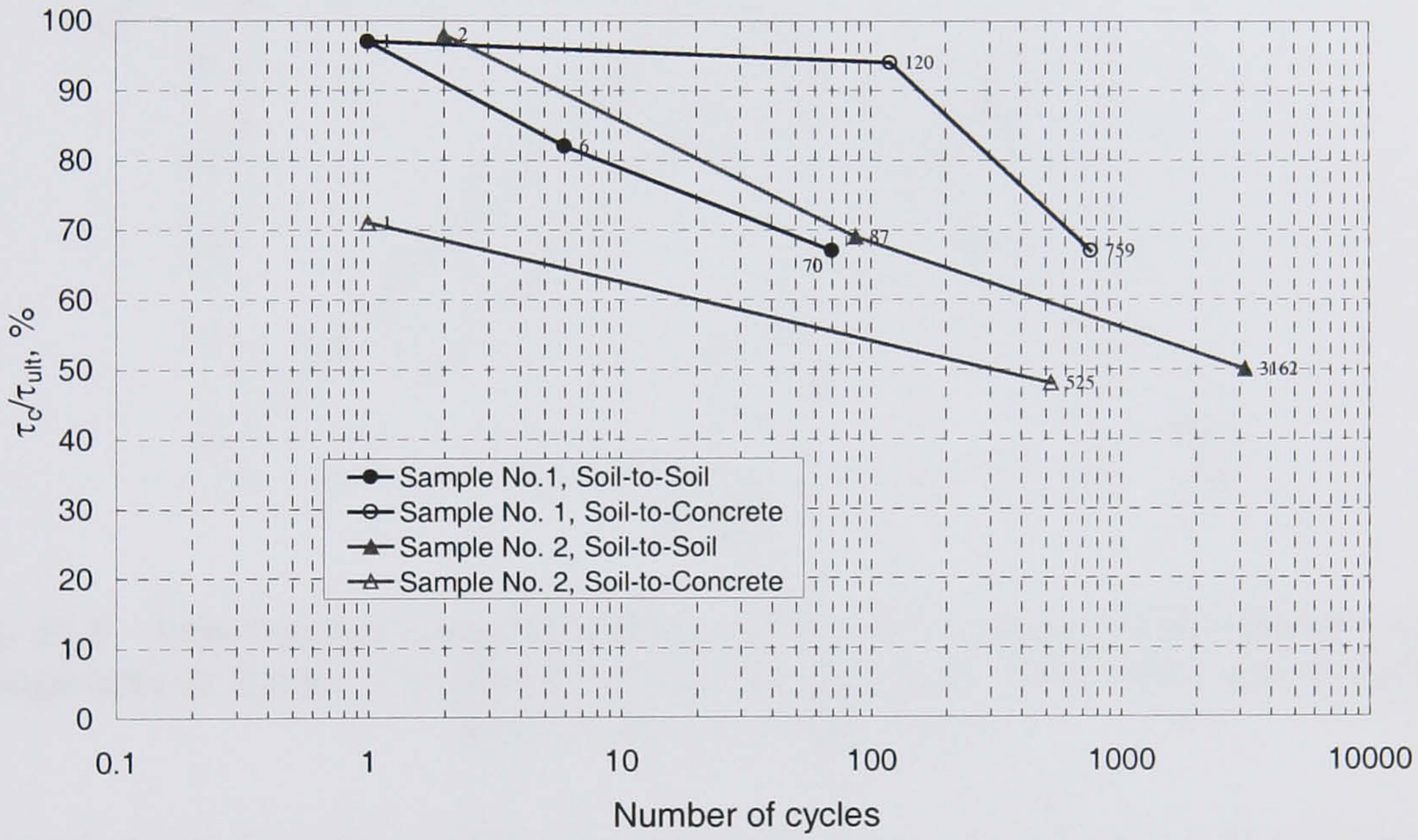


Fig. 11.8 Number of cycles to failure under different constant cyclic load combinations for 4 MC clay samples (Ovando, et al., 1993)

11.2.2 Failure countours in the ID for Mexico City

The failure contours for the ID were established using the failure load combinations established for each pile study in the previous sections. The lack of original load-displacement or time-displacement records made it difficult to maintain a consistent

---

[150] In general, when a critical number of cycles is reached the stiffness degrade rapidly and the sample fails after some few cycles.

cyclic failure criterion. With regard to the building case histories, the JAL building is considered to have failed under the 1995 Copala and the 1985 Michoacan earthquakes, while the PC building was considered as a non-failure.

The complete set of points used to stablish the IDs contours is presented in Fig. 11.9. These data are not corrected for the differences in rate of loading.

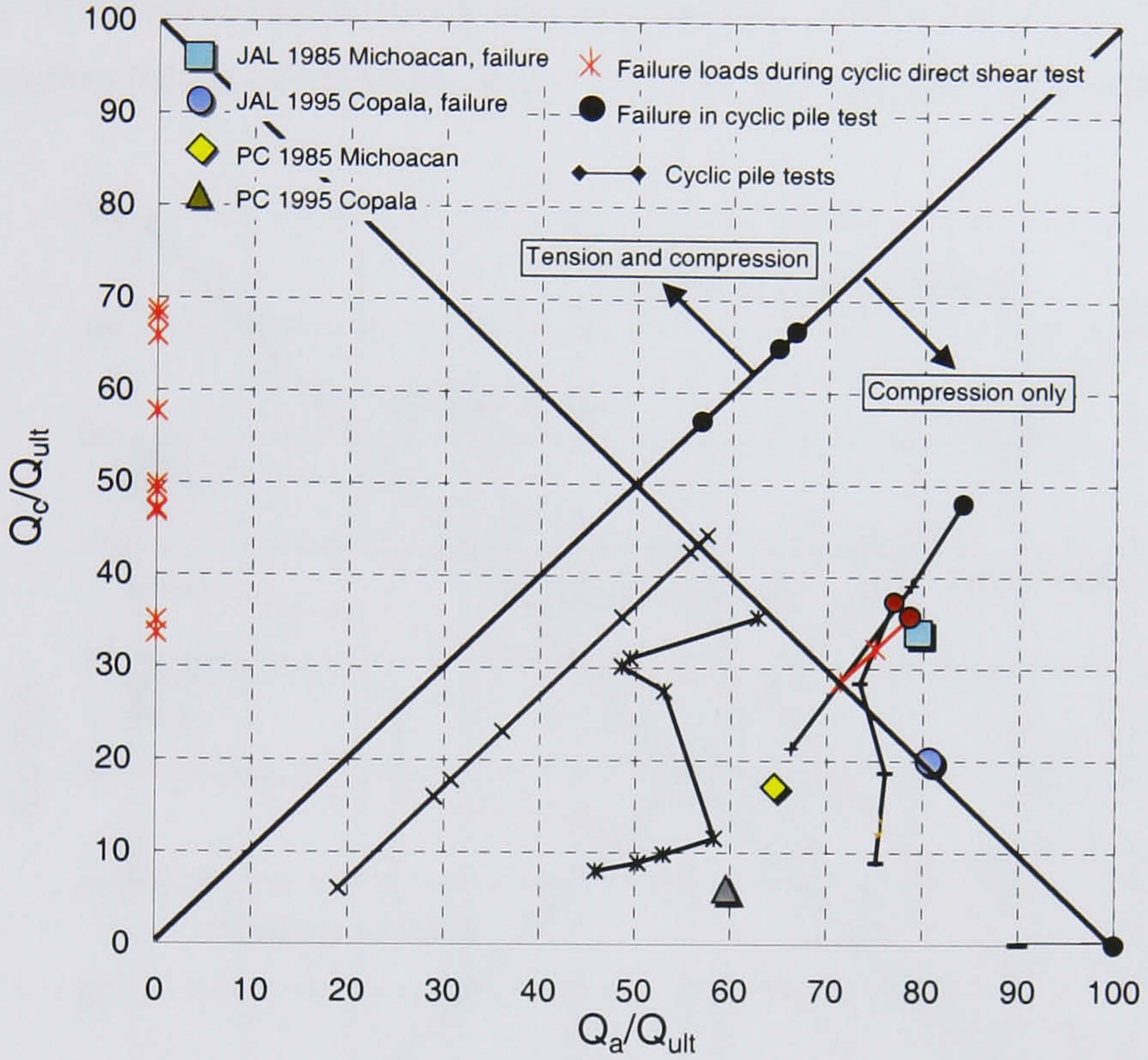


Fig. 11.9 Information used to developed the ID for MC and interpolation points through use of Surfer programme – data from seismic and slower cyclic tests not normalized for loading rate

Fig. 11.10 shows the failure points from the Fig. 11.9 transformed to a rate of loading[151] of 84.8 ton/sec ($0.45Q_{ult}$/sec), which is the pile load rate for the JAL building under the Michoacan 1985 earthquake[152]. Fig. 11.10 shows also the proposed contours of number to cycles to failure (the supporting information is not presented). The contours were

---

[151] The load rate effects were taken into account considering Jaime, et al. (1990) who established that in MC pile capacity increases 12% per order of magnitude increment in rate of loading. The reference static test was carried out in 22 hrs, while the load period for most of the points in the ID is a few seconds. The analysis indicated reductions between 39% and 63% in Q_c when the rate is scale down to static values. The application of a rate correction does not take into account the uncertainties described in section 11.3.2. Rate effects are considered only in the cyclic load component Q_c.

[152] Jaime's cyclic pile test No. 4 was not included since it corresponds to a re-test.

derived through applying the surfer programme to the data points, and then simplifying the output into a bilinear scheme. Figs. 11.11 and 11.12 present the auxiliary information and the proposed N contour lines for the ID under the rate of loading asociated with Jaime et al.'s static maintained load test.

Fig. 11.10 indicates that during a seismic event there exists an over (static) pile capacity of around 30% for N=1 in one-way loading. For two-way cycling a 20% under capacity is observed. The overcapacity during one-way loading is eliminated after 60 cycles. When a slow loading rate is considered (Fig. 11.12) no over capacity is represented.

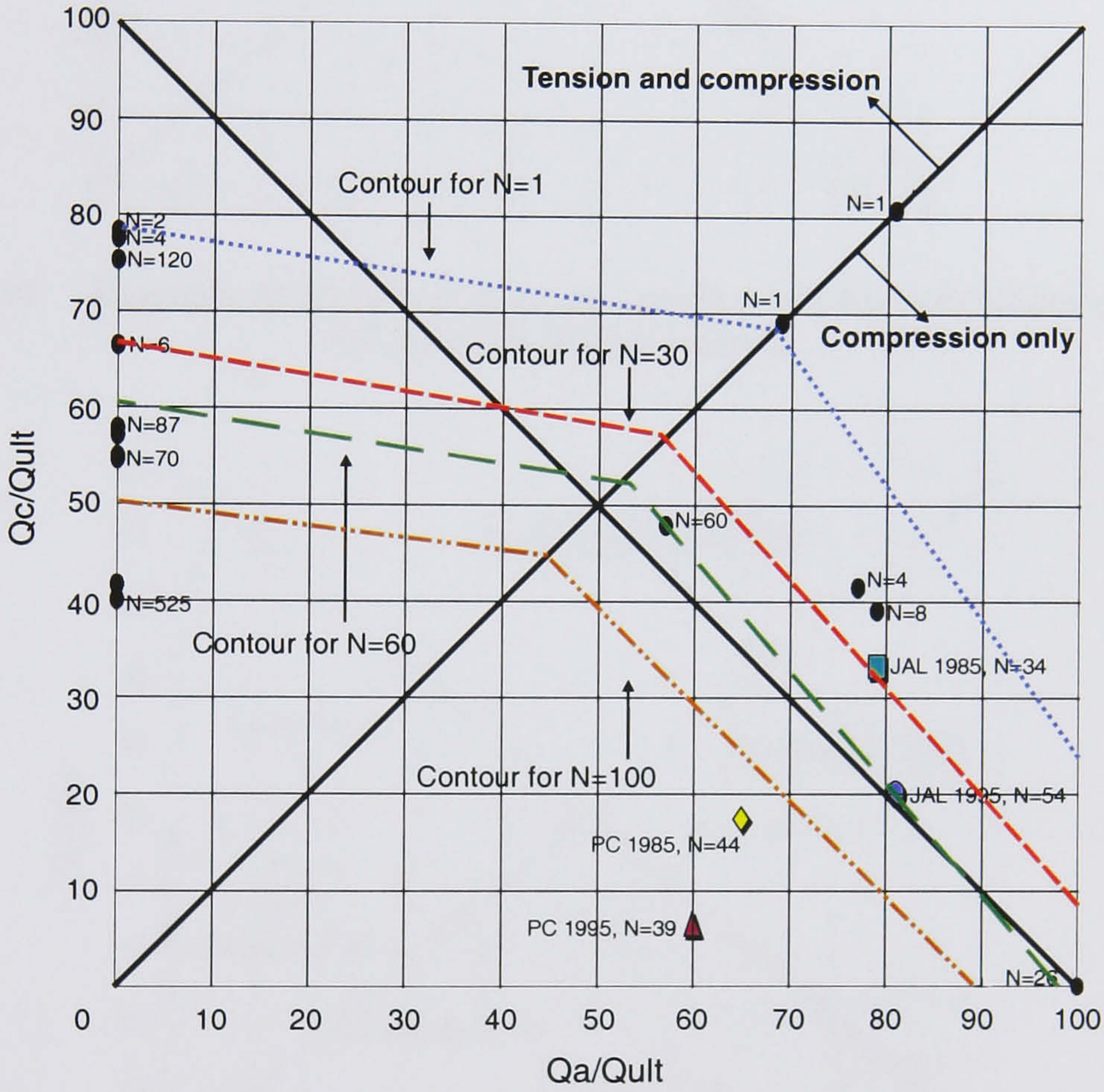


Fig. 11.10 Proposed ID for MC for 84.8 ton/sec ($0.45Q_{ult}$/sec) loading rate (2.3 sec period)

The contouring for N was allocated considering that: (i) as Q_a increases the Q_c to produce cyclic failure reduces; (ii) as Q_c levels increase, fewer cycles are required to lose a given amount of capacity; and (iii) the reduction in capacity towards two-way loading occurs gradually.

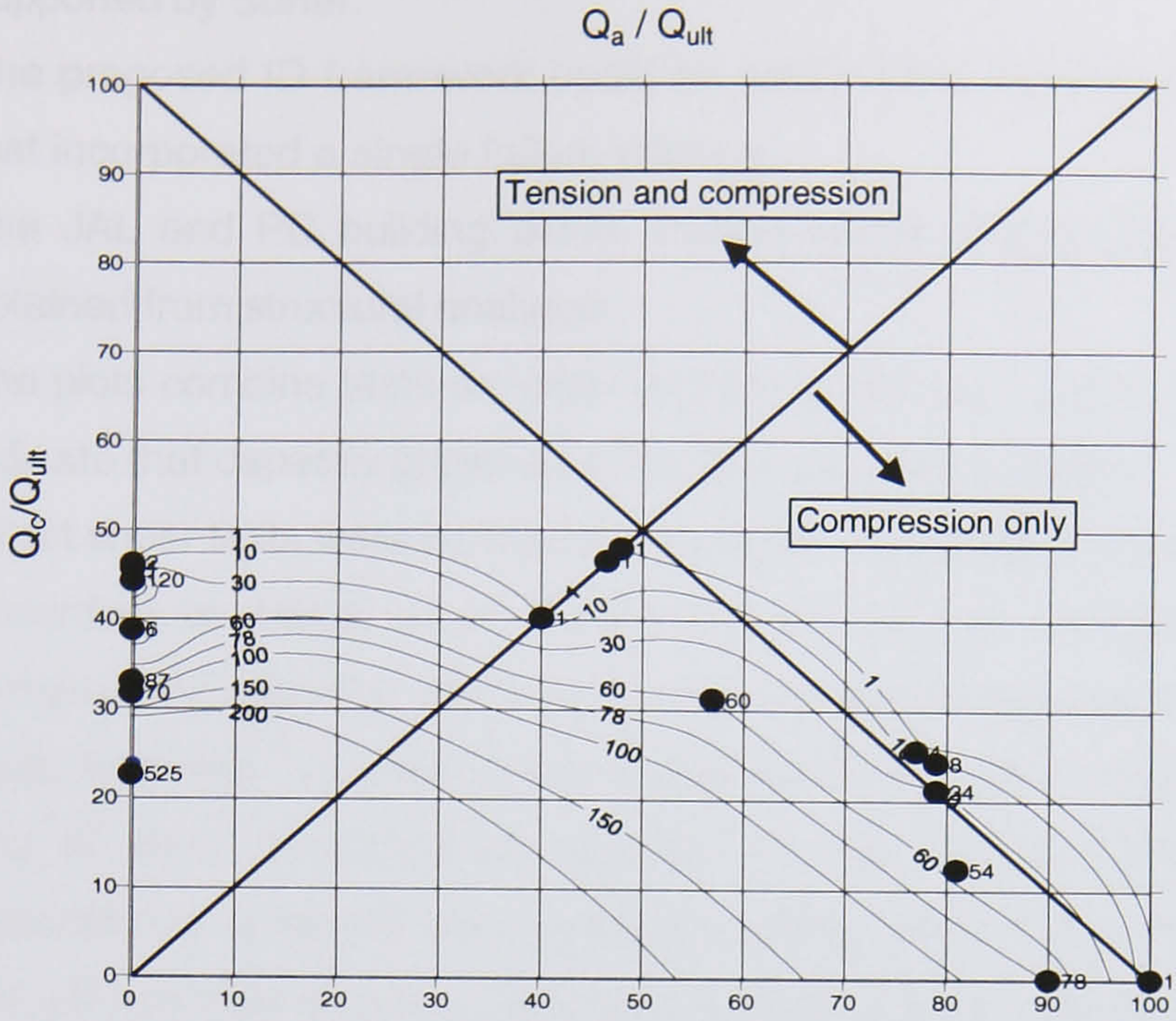


Fig. 11.11 Example of surfer out put data used to develop the failure contours for the slow loading rate ID

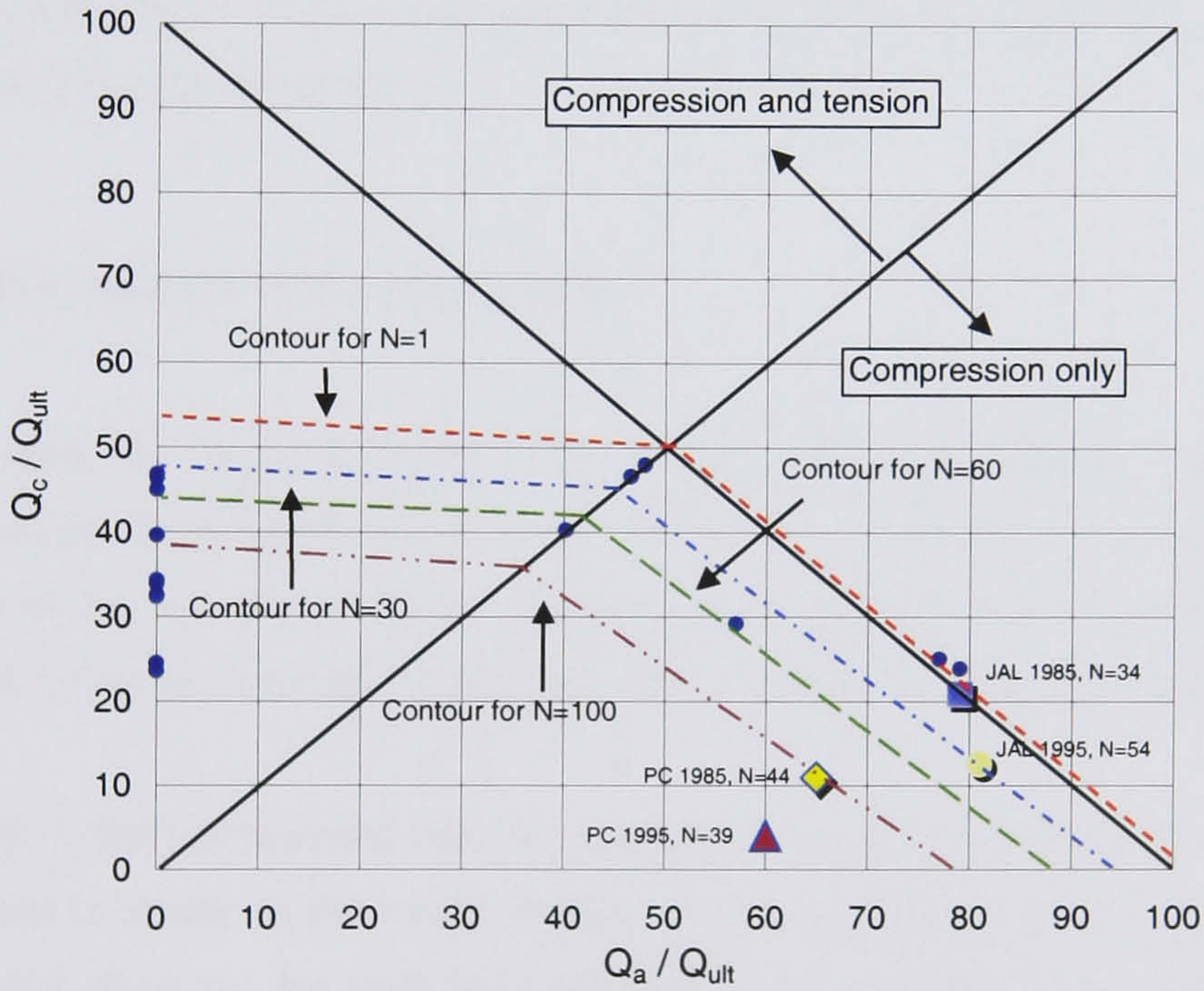


Fig. 11.12 ID extrapolating for slow cyclic or static loading – with 22 hrs nominal loading

The following issues have to be considered in relation to the proposed failure contours:

i) The IDs offer an interpretation based on a relatively small data set. A more reliable interpretation would require an extensive programme of pile cyclic tests.

ii) The contour lines represent the Author best estimates established by eye

supported by Surfer.

iii) The proposed ID framework could be made more rigorous if supported by tests that incorporated a single failure criterion.

iv) The JAL and PC building points correspond to average cyclic loads and were obtained from structural analyses.

v) The plots combine tests on virgin and pre-failed piles. Jaime, et al. (1988)'s data indicate that capacity grows as a result of prior cyclic failure.

vi) Direct shear tests were included to cover two way loading conditions.

vii) According to Jaime, et al. (1988) the tension pile capacity is lower than the compression capacity, this would mean a non-symmetrical ID with respect to the cyclic load axis. This was not included due to the lack of tension cyclic pile tests.

viii) The ID load combinations reported for the JAL and PC buildings include uncertainties related to the predicted seismic forces, the static pile capacity (Q_{ult}), the raft-pile load shearing, and the pile group effects. Quantifying the uncertainty in the JAL and PC data points would involve a complex process that is out of the scope of this work, Section 6.3 describes the uncertainty in the structural analyses. The Author estimates that the uncertainty for the ID load combinations is around ±30%. The results included from cyclic pile tests are considered as involving low uncertainties.

11.2.3 Dynamic versus static pile capacity

When comparing the "cyclic capacity" (Q_{ultc}) against the static ultimate capacity (Q_{ult}) the former is usually associated to the maximum cyclic load (Q_{max}) at failure, with no consideration of the number of cycles involved. An approach that includes the influence of the number of cycles, and load characteristics is introduced in the following sections.

Karlsrud, et al. (1987) concluded that the average accumulated displacement in one-way cyclic load tests is similar to the creep displacement associated with the effective time the cyclic peak load stays on, for both field pile load tests and laboratory cyclic direct shear (DS) tests. Jaime, et al., in MC, also showed that d_c is similar to the short-term displacements seen in static tests when creep movements are subtracted. Fig. 11.13 shows the close relation between the cyclic displacement amplitude (d_c) and Q_c for Jaime, et al. tests in MC[153].

---

[153] Diaz and Casales (1986) also concluded that the deformation of soil samples under cyclic loads could be computed through the static application of a similar magnitude load. Diaz and Casales carried out small amplitude cyclic load oedometer tests on MC clay.

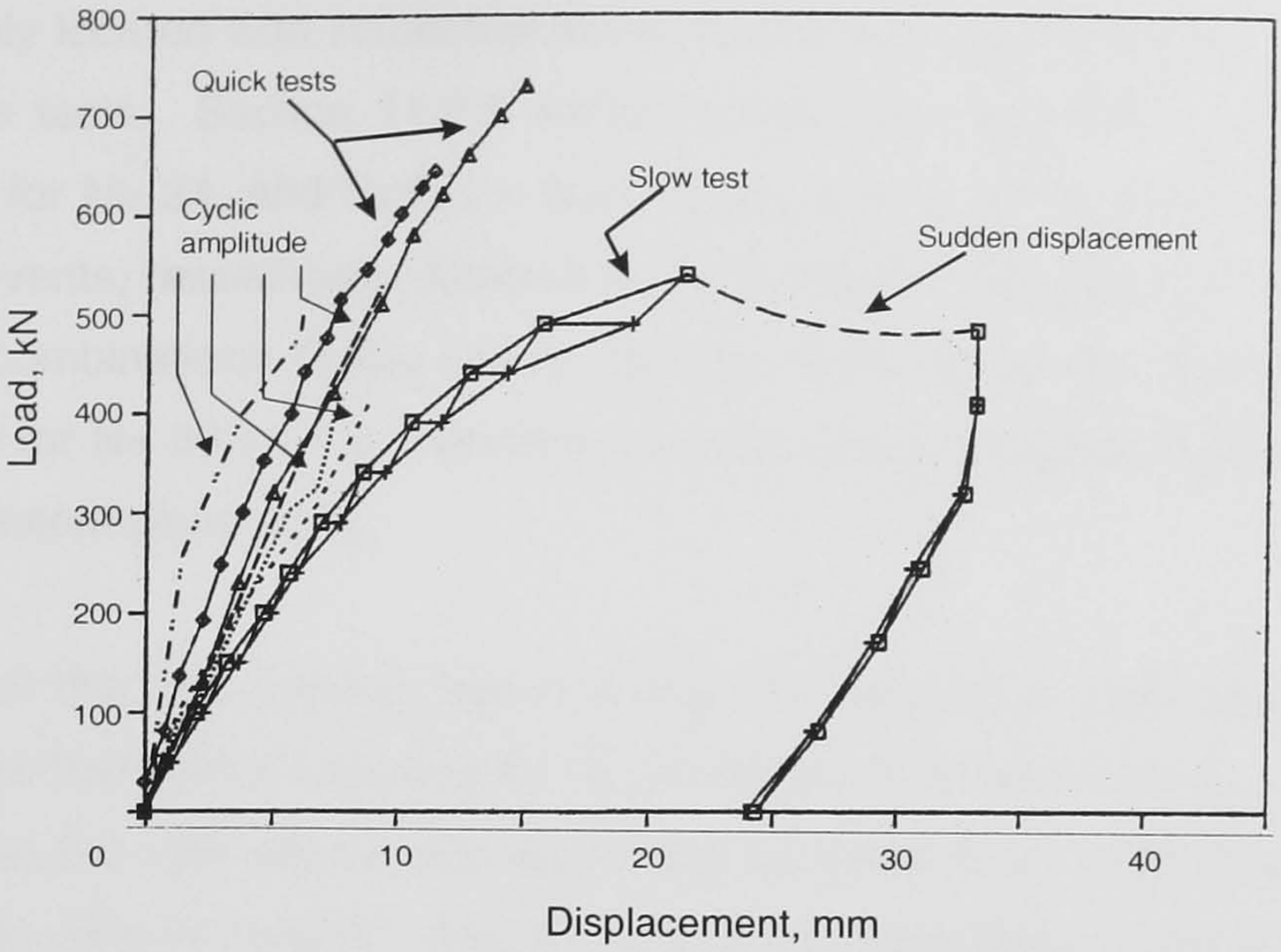


Fig. 11.13 Cyclic amplitude and displacements from static and cyclic tests, after Jaime, et al. (1990)

It follows that for a specific Q_c/Q_{ult} greater than zero the frequency of loading (duration of peak load) governs the number of cycles (time) to reach a failure defined in terms of displacement (Karlsrud, et al., 1987). For Jaime, et al.'s cyclic tests, considering that the peak cyclic load acts for one-fourth of the 2.3 sec period and that the Q_{ult} acted for 1.0 minutes in the reference static test before failure (Fig. 11.8), the N contour that best relates cyclic and static failure is N= 104 cycles. The following relative cyclic to static capacities are obtained from Figs. 11.10 and 11.12:

Table 11.10 Normalized dynamic pile capacities with and without rate effects

Load conditions	For 22 hrs loading	For Period = 2.3 sec
Symmetrical two-way loading	0.50	0.39
Non-symmetrical two-way loading; $Q_c = 2Q_a$	0.71	0.55
One-way cyclic loading; $Q_c = Q_a$	0.89	0.70
One-way cyclic loading; $Q_c = 0.5\ Q_a$	0.89	0.74

The ID for period of 2.3 sec indicates that in one-way loading the seismic pile reaction to produce cyclic failure is higher that the static capacity when the number of cycles is lower than around 60. This over-capacity is considered to be due to rate effects, since when the projection is made to cover slow cycling (loading on 22 hrs) the over-capacity disappears. When the comparison is carried out on the basis introduced above (at N=104), the seismic capacity is lower than the static for all load combinations, when rate effects are accounted for.

The load combination and N corresponding to the JAL and PC building frames in the ID are adequately located with reference to the failure and non-failure areas defined with the cyclic pile tests. Section 11.2.1 indicates that the combinations of Q_c/Q_{ult}= 0.34, Q_a/Q_{ult}= 0.79 for N= 34, and Q_c/Q_{ult} = 0.20, Q_a/Q_{ult} = 0.81 for N= 54 for the Michoacan and Copala events, respectively, locate the JAL building in the failure zone. For the PC building the combinations Q_c/Q_{ult}= 0.17, Q_a/Q_{ult}= 0.65 for N= 44, and Q_c/Q_{ult} = 0.06, Q_a/Q_{ult} = 0.60 for N= 39 for the Michoacan and Copala events, respectively, located the building in the non-failure zone.

The results for the JAL building frame during the Michoacan 1985 and Copala 1995 events indicate that failure occurred for Q_{max} between 1.01 and 1.13 Q_{ult}, including rate effects. When the rate effects are accounted for there is no indication of pile over-capacity during seismic events. It is concluded that there is no support for a 2.5 bias (API, draft 1998) in the capacity of the piles of the JAL building.

11.3 Analysis of results according to the state of the knowledge

The capacity and load-displacement response of piles subjected to seismic loading in MC are analyzed based on the proposed ID and the literature review in Chapter 2.

11.3.1 Effects of load cycles on pile response

Redistribution of soil reactions and cyclic and permanent displacements characterize the response of piles to seismic load cycles. This response depends on the number of load cycles, the loading frequency and direction, and the Q_c/Q_{ult} ratio.

Loss of pile shaft friction as a result of seismic loading has been recorded in MC by Mendoza, et al. (2000, see Chapter 10)[154] and Auvinet and Hanell (1981)[155]. Further evidence of loss of pile shaft friction during earthquakes[156] is the slippage of the soil surrounding end bearing piles, which have emerged due to regional subsidence, occurring during seismic shaking. The loss of shear transfer capacity is a temporary

---

[154] Mendoza, et al. show evidences of reductions in static capacity after around 50 one-way low load level cycles at around 4 sec period (Table 11.7).

[155] During negative skin friction tests on piles in Mexico City.

[156] The earthquake produces the total or partial disappearance of negative friction without damage to the pile.

phenomenon since it recovers to some extend with time, maybe as a result of thixotropic effects and soil bond restoration (Jaime, et al., 1988; Mendoza, et al., 1998; Chapter 2).

Intense two-way pile cyclic loading can reduce the shaft capacity to a value observed during and immediately after pile installation and very close to the remoulded shear strength (Chapter 2; Grosch and Reese, 1980; Karlsrud and Haugen, 1985; and Bogard and Matlock, 1998a, 1990a and b). An approximation of the shaft capacity lost due to intense two-way loading in MC can be obtained from Zeevaert (1957) who reported a 40% reduction in shear strength in material obtained close to the pile shaft after installation. Jaime, et al. (1988) observed a 45% reduction in shear strength when testing a sample in simple shear under several two-way deformation cycles. These data support the location of the number of cycles to failure contours for two-way loading in the Author proposed ID (Figs. 11.10 and 11.12).

Due to the high initial axial static forces, the seismic cycling of building piles usually involves one-way loading only. However, local pile shaft capacity loses can be produced during one-way cyclic loading when the shear stresses at shallow pile depths exhibited stress reversals (Chapter 2). This phenomenon, attributed to long compressible steel piles under relatively short period load cycles, is not considered relevant for the short stiff reinforced concrete piles used in MC.

Apart from the pore pressure on the degradation of shaft shear capacity, which is discussed in section 11.3.2, the degradation of shaft shear capacity can derive from:

i) The destruction by cycling of soil inter-particle bonds and soil-pile interface bonds produced after pile driving into the clay. For MC conditions two observations contradict this argument: (a) MC clay shows no degradation even when subjected to large strains (see Chapter 3); and (b) the reductions in shaft capacity observed by Mendoza, et al. and Auvinet and Hanell occurred under low intensity loading.
ii) Residual shear surfaces produced by the alignment of clay particles in the direction of shearing. This is not considered a dominant factor since statically re-tested piles by Hjort and Carrillo (1985) produced full capacity recovery – therefore not showing evidences of residual surfaces. Furthermore, MC clay has a turbulent shearing response (Chapter 4).
iii) Reductions in radial effective stress (σ_{rc}'). Karlsrud and Haugen indicated that during long term cyclic axial loading variations on effective radial stress arose from reductions on total radial stress and increments in pore pressure. Hardy

(2001) has predicted, using FE analyses, horizontal total stress reductions at the surface of a single pile in soft soil under earthquake loading. Cyclic pile tests by Chow (1997) at Pentre and analytical studies by Jardine (1991) have also supported reduction on σ_{rc}' during cyclic axial loading. Hjort and Carrillo (1985) carried out total lateral stress measurements on a pile shaft in MC. However, such measurements are very difficult to make accurately and there is no conclusive evidence to support reductions in total lateral stresses during seismic events in MC.

From the three introduced options, the reduction of radial effective stresses by either $\Delta\sigma_r$ or Δu is the most likely explanation for the pile shear transfer degradation. This can be modelled using an effective stress approach.

11.3.2 Loading rate effect on pile response

The foregoing analysis shows that pile capacity increases due to rate effects and that this increment is at least partially erased by load cycling (Figs. 11.10 and 11.12).

Tests on piles driven in MC have shown increases of 12% on peak capacity and 20% in pile-soil stiffness per order of magnitude increment in loading rate. However, the application of these results requires considering of the following:

i) The Q_a/Q_{ult} ratio. Applying a higher loading rate over just the final stages of a pile loading test does not generate the same capacity enhancement as applying the rate for the whole test (Kraft, 1981a). The higher the load at which the rate is increased, the lower the rate effect. This is relevant for foundation piles that work at $Q_a \approx Q_{ult}$.

ii) The static pressure transmitted by the foundation raft to the soil. High contact pressures can be transferred back through the ground and augment the shaft shear stresses at greater depth and so reduce the potential overall rate effect (Auvinet and Mendoza, 1987).

iii) The relative proportion of load carried by the tip and shaft of the pile. The greater the percentage taken by pile shaft, the higher the rate dependency. Typical piles in MC develop between 75 and 80% of their capacity from shaft resistance.

iv) The dependency of rate effects on pile loading history. Kraft (1981a) indicated greater increases in capacity with rate in piles that have not been severely pre-

loaded. The effects on the rate effects of repetitive seismic loads and consolidation cycles are not known.

Bond (1989), Lehane (1992) and Chow (1997) indicated that effects of rate on pile capacity were closely related to residual strength fabric phenomena that were well represented in laboratory ring shear tests performed at the same rates (see Chapter 2). Karlsrud and Haugen (1985) and Kraft (1981a) pointed out that the rate increment observed in their pile tests agreed closely with the rate effect observed in undrained triaxial laboratory tests, reflecting different processes. In MC, good agreement exists between Jaime, et al. cyclic pile tests (12% per order of magnitude) and isotropically consolidated undrained triaxial test (10%) (Chapter 3). The Author's ring shear tests on MC clay showed no increase or small reduction in residual shear for rates lower than 50 mm/min, and decrements for higher rates (Chapter 4).

The rate or frequency of loading, together with the drainage conditions, are the controlling factors of the amplitude of pore pressure fluctuations during pile cyclic loading (Chapter 2). The influence of pore pressure in pile load transfer degradation and pile displacements during cyclic loading is not always clear. Most of the evidence indicating pore pressure influence on pile load transfer degradation has been obtained from small-scale laboratory tests, for which the drainage conditions are not compatible with field conditions. Some researches did not record pore pressure increments during pile cyclic tests because they applied long period load cycles (e.g. Chow, 1997). Also pore water pressure measurements are difficult to make reliably in field tests on piles.

The pore pressure generation does not seem to be the main cause of pile capacity reduction under cyclic loading because:

i) Degradation of pile shaft capacity has been observed during field cyclic pile testing[157] in normally consolidated soils with only small variations in pore pressure at the pile shaft (Puech and Jezequel, 1980). (In MC Mendoza, et al. (2000) registered pile shaft capacity degradation occurring during small pore pressure variations in the soil mass.)
ii) It has been observed that some soils show a decrease in pore pressure as the shear transfer degraded. This is observed for OC soils showing fatigue (Chapter 3).

---

[157] Q_{max} = 62% Q_{ult} at a 14 s period.

11.3.3 Test sequence effect on pile response

Static tests following cyclic tests show more extended near "linear" portions in their load displacement curves, and the displacements required to reach peak are around half those for a previous static test. The comparison of d_c for two successive one-way cyclic tests by Jaime, et al. (1990) (Fig 11.7) indicates slightly higher stiffness and higher capacity for the second test carried out after a 5 weeks pause[158]. From the cyclic re-testing by Jaime, et al. (1990) it is possible to conclude:

i) Cyclic pre-loading to less than 75-80% Q_{ult} does not have a significant effect upon G_{cp} (Fig. 11.14), or degradation of peak capacity. Any capacity degradation could have been regained through consolidation and thixotropic effects during a rest period lasting 5 weeks. The recovery of pile capacity after cyclic loading in MC reported by Mendoza, et al. (2000a) and Jaime, et al. (1990) indicates that important residual fabric changes are not produced.

ii) Cyclic pre-testing leads to smaller permanent displacements in re-tests made later under similar cyclic load amplitude (as observed by Bouckavalas, 1996 – see Chapter 2).

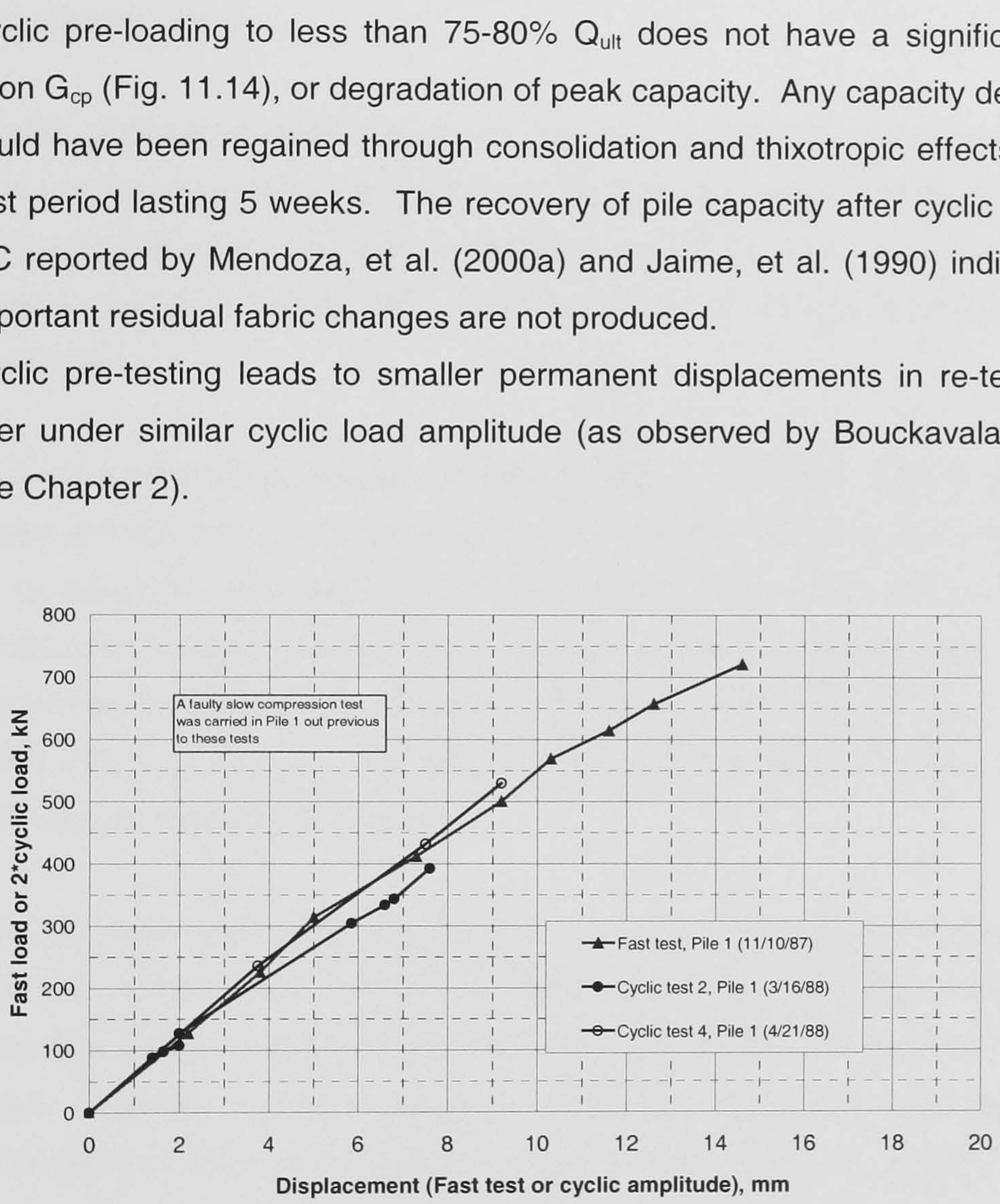


Fig. 11.14 Load-displacement response for Jaime, et al. (1990) test program

---

[158] Notice that the first cyclic test underwent a higher number of cycles at low load amplitudes – every point in the figure represents a 30 cycles stage.

11.4 Implications for seismic design of piles in MC

11.4.1 Application of the interaction diagram to the seismic design of piles

The current understanding of the cyclic and seismic response of piles has been insufficient to recommend a detailed and generalised approach to cyclic pile design. Designers who are concerned about cyclic loading effects often apply irregular empirical rules that are based on the relationship between Q_c, Q_{max}, and the type of loading (one- or two-way) (Section 2.9).

In MC the piles undergoing cyclic loading are designed using a capacity reduction factor that does not consider explicitly the characteristics of cyclic loading. Jaime, et al. (1988) and Auvinet and Mendoza (1987) have proposed methodologies to compute a more rational seismic capacity of piles in MC. However, they also fail to consider all the cyclic load characteristics.

The adoption of a generalised seismic ID (such as Figs. 11.10 and 11.12) for pile design in MC would address the key loading factors that control the pile response to cyclic loading[159], would reduce uncertainties and would produce more consistent safety levels. The application of the proposed ID for the JAL and PC buildings adequately indicates that the former is unsafe and the later safe. According to the proposed ID, the seismic safety of the JAL would improve by changing the pile distribution, increasing the pile length or increasing the number of piles.

The typical MC piled foundation box solution is sensitive to the equilibrium of loads between the raft and the piles. In these conditions the use of an ID – which indicates the pile capacity degradation – would assist in the determination of the increment of load at the raft level. However, a detailed modelling of the raft response to static and seismic conditions would have to be carried out to evaluate the ratios of Q_a/Q_{ult} and Q_c/Q_{ult}.

Under certain dynamic loads combination the ID can indicate that the pile can produce over capacity during a dynamic cyclic loading. However, it has to be recognised that this over-capacity is transitory and that could disappear depending on the cyclic load characteristics. Based on the time the peak load acts, using the comparison in section

---

[159] e.g. the influence of one-way or two-way cyclic loading, and the influence of the mean load, and rate of loading.

11.2.3, the design dynamic capacity can be obtained from the static capacity.

It is important to consider that when a new tool is introduced to the design process, the process requires a complete re-evaluation. If an ID is introduced to the seismic pile design, the main aspects to re-evaluate are the structural analysis and the static pile design.

11.4.2 The importance of the static pile design on the seismic pile design based on ID

The application of the standard MC α method to the computation of pile capacity in MC shows scatter and overprediction[160] (Hjort and Carrillo, 1985; see Chapter 5). This situation results in shorter piles, reducing Q_{ult}, and increasing Q_c/Q_{ult} and Q_a/Q_{ult} ratios, therefore reducing safety factor against seismic (and static) loading. This could have contributed to the friction piles' bad performance during earthquakes in MC. The static ICPDM produced better predictions in MC than the α method specified by MC code and its application, after further validation, could contribute to a more certain "seismic" safety factor.

The proposed ID is based on static pile capacity obtained from pile tests or the ICPDM predictions. If the α method is used with the ID, Q_{ult} will be overstimated so the pile will be less safe.

The implementation of the new ID approach should not impede research into other factors that were identified as contributors to the poor performance of friction pile foundations during the 1985 Michoacan earthquake, among them (Auvinet and Mendoza, 1987):

i) Distribution of loads. Excentric or non-uniform loads produce differential settlements and reduce the structure's capacity to withstand eartquakes and creates favourable conditions for local failure. Stiff foundation boxes concentrate loads at their borders and corners.
ii) Distribution of piles in the foundation. The seismic actions must be taken into account when locating the foundation piles.

---

[160] Mendoza, et al. (2000) have also indicated the lack of correlation between the undrained shear strength and the shaft capacity in MC.

iii) The action of negative skin friction on piles.

11.4.3 Implications for the structural analysis of buildings

The rational design of piles subjected to cyclic loads requires a comprehensive analysis and understanding of the soil-structure interaction under dynamic loading (Bea, 1992; Karlsrud and Haugen, 1985; Puech and Jezequel, 1980; Sangrey, 1977).

The structural configuration of a building has a significant influence on the distribution of static loads on the base and on the magnitude and frequency of the seismic base loads. Since simple linear structural models are not capable of reproducing these conditions accurately, complex modelling tools, validated through calibration procedures, become necessary. The application of simple structural analyses that are not checked against measured responses can produce erroneous conclusions regarding the dynamic loads imposed on piles.

The three case history calibrations made of the JAL, PC and PCC structural models in this thesis indicated that base reaction amplitudes and dominant frequencies were sensitive to the competence of the structural elements, the modelling technique, and the input motion (see section 11.1). The analysis for the JAL building, Chapter 7, indicated that forces predicted by elastic analysis are 65% higher than those for more realistic inelastic analysis. The inelastic behaviour seen during two earthquakes was proven to modify the response characteristics of the buildings – including their fundamental periods.

CHAPTER 12

CONCLUSIONS

The thesis dealt with the strong need for physical evidence on the performance of pile foundations under earthquake loading through the use of case histories that include both good and poor seismic performance. The research focused on case histories from Mexico City (MC) where an important number of friction pile foundations failed during the September 19 1985 Michoacan earthquake.

The research intended to improve knowledge concerning the relation between the dynamic and static capacities of displacement piles, with the aim of facilitating the development of a design method for piles under cyclic loads. This chapter summarizes the main conclusions of the research in the following areas:

i) Ring shear response and intrinsic properties of MC clay
ii) Validation of the Imperial College pile design method (ICPDM) for MC conditions
iii) Seismic response of buildings and its influence on the seismic pile loads of the case history buildings
iv) Cyclic response of piles in MC
v) Application of Interaction Diagrams (ID) to the cyclic design of piles, in specific their application in MC, and the comparison between static and dynamic pile capacities.

12.1 Pile response to cyclic loading

The pile performance under cyclic loading is influenced by the interaction of loading rate, number of load cycles, magnitude of cyclic and sustained loads, and loading history. Each of these factors influences pile performance in a complex manner, and their individual and combined effects can be significant.

The most relevant concepts on the behaviour of piles subjected to repeat axial load obtained from the review of the available literature were:

i) The behaviour of piles under cyclic loading can be analysed using an effective stress approach.

ii) The cyclic shear stresses produced by cyclic loading of piles may lead to a gradual increase in pore pressure and reduction in radial total stress. This response in combination with the destruction of soil particle bonds may reduce the shear strength of the soil. However, since pile capacity degradation can appear even without build up of pore pressure at the soil-pile interface, the reduction in total radial stresses seems to control the degradation of the pile cyclic capacity – for the case when residual failure surfaces are not developing actively.

iii) Increments in pile capacity during cyclic loading can appear due to rate effects, however these increments can be overwhelmed after certain number of cycles. Increases in pile capacity due to consolidation after cyclic loading disappear at a lower number of cycles.

iv) The threshold cyclic load producing a reduction in a pile's ultimate capacity, or stiffness, increases with plasticity index. Although it is usually considered as 0.7 Q_{ult}, it can reach 1.0 Q_{ult}.

v) Existing pile design methods are not considered adequate for general soil profiles and cyclic loading conditions. The possible effects of cyclic loading are usually not addressed explicitly in current pile design practice and designers who are concerned about cyclic effect on piles take them into account using highly approximate "rules of thumb".

12.2 Mexico City clay properties

The research included a critical review of the properties of the clay in MC that assisted in the ICPDM validation and the seismic analyses. The following sections summarize the main conclusions from the Author original laboratory tests.

12.2.1 Intrinsic properties study

i) The correlations for e_{100}^* and C_c^* proposed by Burland did not predict MC's intrinsic properties closely. Nagaraj, et al. (1986)'s expression for the determination of e and C_c in fine grain uncemented normally consolidated soils produced better correlations. The study also indicated the importance of following Burland's procedure for the determination of the intrinsic properties.

ii) The in situ void index framework applies well to the consolidation history and naturally cemented state of typical MC clay profiles.

iii) The determination of sensitivity from oedometer tests gives good correlations in

relation to traditional undrained triaxial tests.

12.2.2 Ring Shear study

i) The large strain shearing of MC clay involves a transitional (with tendency to turbulent) mode of behaviour, which is dominated by the silt sized particles.
ii) The clay mineralogy appears dominated by illites and kaolinites.
iii) MC clay partially developed residual shear surfaces that looked striated and orientated in the direction of shear, but they did not shine. The failure surface usually showed residues of fine sand or silt size material, which could have migrated during shearing.
iv) MC clay developed very high δ' and ϕ_r' values that plotted well away from the ranges indicated by current PI-δ' correlations. The shear mechanism of MC clay is better predicted by criteria based on the shape and size of its components.

12.3 Validation of the Imperial College design method

The ICPDM was validated for MC Lake zone profile using a database of 26 static load tests on friction piles. The following points are relevant:

i) The statistical analysis of the validation indicated satisfactory results for the ICPDM. The method showed a slightly tendency to overpredict (6%), with a standard deviation of ±16%. The marginal overprediction could be originated from the large displacement associated with peak capacity in most pile tests in MC. This large displacement could locally reduce δ' to an ultimate value, while the predictions considered that peak δ' applied along the whole pile length.
ii) The ICPDM showed no clear skew with pile embedded length-equivalent radius ratio (L/R), but it tends to overpredict slightly with reducing S_t and YSR.
iii) The statistical analysis indicated that the MC code recommended pile design method overpredicts pile static capacity by around 20%. This trend slightly increases with L and YSR, and slightly reduces with increasing S_t.
iv) By providing what appears to be an unbiased and more reliable prediction of the medium term fully equalized pile capacity, the ICPDM seems to have an advantage over the MC code suggested design method.
v) The study of the pile test database showed well known responses when evaluated for α vs. Su, and α, β and τ_{rz} vs. L.

12.4 Dynamic structural analysis of case histories

A methodology to predict the seismic reactions at the base of the case history buildings was introduced. The more important assumptions were:

i) The forces at pile head level in a soil-structure system can be computed by analyzing the structure as a sub-system. The structure sub-system is subjected to prescribed earthquake accelerations recorded at basement level on instrumented buildings. The pile-soil sub-system is not included.
ii) The recorded input accelerations at building basement contain the kinematic and inertial effects of soil-structure interaction (SSI), including the influence of the piles and the structure sub-systems.

The structural analytical work was carried out using the finite element computer code ADAPTIC. The main observations from the structural analyses were:

i) The structure inelastic response has a significant influence on the pile static and seismic (magnitude and frequency) loads. The modification of the structural models results on changes in static and seismic reactions at the base of a model; this should be considered when designing foundations.
ii) Simple structural models are not capable of reproducing a building's response to earthquake loading. A purely elastic structural analysis produced base loads that were 1.65 times higher than those for the inelastic structural model under the same event.
iii) The response of the buildings to earthquake loading is complex. The uncertainties involved in seismic analyses necessitate a calibration procedure in which some of the assumptions on mass distribution and stiffness were modified in a parametric fashion until the most plausible results are obtained. Due to the non-linear response of the buildings, the calibrated model is strictly valid only for the event under which it is calibrated.
iv) The forces at the base showed their highest amplitude for the fundamental frequencies of the input motion and the super-structure.

12.5 Seismic loads and Interaction Diagram

The pile raft load-sharing, the foundation lateral stability, and the kinematic forces on piles are involved on the static and seismic response of the piles in the case history buildings. The main conclusions on these topics were:

i) The soft clay typical of the MC profile produces a pile-raft load transfer mechanism in which the piles take most of the load, in both static and seismic conditions. There are records that indicate that for static condition in MC the piles shared 85% of the total load with the remainder carried by the foundation raft. The predicted average long-term pile contributions for the JAL and PC buildings were 88% and 91%, respectively.

ii) For the compensated piled foundations of the case histories, the reaction obtained from the passive earth pressure and the friction on the lateral vertical walls of the basements are higher than the predicted basal shear forces.

iii) The piles forces associated to kinematic-interaction should be small in the non-layered homogeneous soft clay profile of MC. The Author's study of only the inertial forces follows a common procedure for the seismic design of piles in which the kinematic-interaction forces are assumed to be negligible.

The relevant concerning the ID developed for MC were:

i) The development of a data base from field cyclic pile tests, the recorded pile forces from an instrumented foundation, cyclic direct shear tests, and the axial pile forces computed for the JAL and PC case history buildings. These were crucial to the production of a synthetised ID.

ii) The study of the influence of seismic loads on pile response was based on an equivalent number of cycles that corresponds to the time Q_{ult} acted during a reference static load test.

iii) The ID indicates that in one-way loading the seismic pile reaction is higher that the static capacity when the number of cycles is lower than around 60 for a load period of 2 sec - this over-capacity may be due to rate effects. When the comparison is carried out on the basis of the equivalent number of cycles (N=104), the seismic capacity is lower than the static for all load combinations, even when rate effects are allowed.

iv) The responses of the JAL and PC building frames during the Michoacan 1985 and Copala 1995 events are adequately located with reference to the failure and non-failure areas, respectively, of the ID defined with the cyclic pile tests.

v) The results do not indicate that piles can sustain loads far above their static capacities during seismic events. For the JAL building limited failure occurred for a Q_{max} between 1.01 and 1.13 Q_{ult}. There is no evidence to support the positive bias of 2.5 that was suggested to apply to the seismic capacity of piles during an API committee meeting (API, 1998).

12.6 Analysis of the seismic performance of piles in Mexico City

The capacity and load-displacement response of friction piles subjected to seismic loading in MC were analyzed based on the proposed ID and the literature review in Chapter 2. The conclusions are:

i) The reduction of radial total stresses is the most likely explanation for the pile shear transfer degradation observed in MC. The destruction of soil bonds might also be involved. Pore pressure generation seems not to be the main cause of pile capacity reduction under cyclic loading since degradation of pile shaft capacity has been observed during field cyclic pile testing with only small variations in pore pressure.
ii) The loss of shear transfer capacity produced by cyclic loading is a temporary phenomenon since it recovers with time. The recovery may be the result of thixotropic effects and soil bond restoration.
iii) The seismic cycling of piles on regular shape heavy buildings usually involves only one-way loading due to the high initial static forces. Shear stress reversal during one-way cyclic loading should not be relevant for the short stiff reinforced concrete piles used in MC.
iv) Rate effects of 12% in pile capacity per log rate of loading increment appear to apply, which are in good agreement with results obtained from isotropically consolidated undrained triaxial tests (10%). The Author's tests show that Ring Shear experiments do not match this rate dependency.

12.7 Implications for seismic design of piles

12.7.1 Application of the interaction diagram on the seismic design of piles

The current understanding of the cyclic and seismic response of piles is insufficient to

propose a generalised approach to practical pile design that makes detailed and specific recommendations for dynamic axial capacities. The benefits of introducing an ID into the cyclic or seismic design of piles are:

i) They offer a simple procedure to assist in the assessment of pile capacity under cyclic loading. This procedure includes the soil and load characteristics.
ii) A more rational design method that reduces uncertainties and gives more consistent safety levels is obtained.
iii) The design dynamic pile capacity can be obtained from the static pile capacity.
iv) The ID would assist in the determination of the pile-raft load transfer during earthquakes. This would improve the design of typical MC piled foundation box solution, which is sensitive to the equilibrium of loads between the raft and the piles.
v) It is difficult to establish if the application of an ID for the seismic design of piles will result in more conservative design, however the resulting design will include fewer uncertainties.

It is important to stress that when a new tool is introduced to the design process, the latter requires a complete re-evaluation. The introduction of the ID to the seismic pile design requires changes also in structural analysis approach and the static design procedures applied to piles.

12.7.2 Implications of the seismic design of piles based on an ID for the static design of piles and the structural analysis of buildings

i) The application of the α method to the computation of pile capacity in MC shows scatter and overprediction. This situation results in shorter piles, reducing Q_{ult}, and increasing the actual Q_c/Q_{ult} and Q_a/Q_{ult} ratios, therefore reducing the safety factor against seismic (and static) loading. The static ICPDM produced better predictions than the α method (suggested by MC code) and its application could contribute to a more certain "seismic" safety factor.
ii) In addition to pile-soil response to cyclic loading, the rational design of piles subjected to cyclic loads requires a comprehensive analysis and understanding of the structure and foundation behaviour under dynamic loading. The application of simple structural analysis that are not compared to actual measurements or validated against measured responses can produce erroneous conclusions on the dynamic capacity of piles.

12.8 Recommendations for future research

i) The complete validation of a design method is a time consuming procedure, and experience is required before practitioners can feel fully confident in its use. The presented validation of the ICPDM considered a small number of tests; further comparisons against an extensive as possible data base would aid the confidence building process.

ii) A clear need exists to improve cyclic pile design methods to obtain economies in some cases and enhance performance, and safety, in others. The development of a cyclic pile design method need to be co-ordinated with parallel developments in reliability theory and the characterisation on environmental loading.

iii) There is a strong need for more physical data on the performance/behaviour of pile foundations under earthquake loading. Such physical data would ideally emerge from detailed case histories that include instances of both good and poor performance. The procedure followed in this research could be applied to buildings without instrumentation.

iv) Further research could extend the application of the ID to different site conditions; this can be carried out using the database of available cyclic pile tests. A model ID could be created from which ID for other sites could be produced. A further aspect to consider when describing piled foundation behaviour under seismic loads is the variation in the stress state in the soil mass, including the soil self weight, wave propagating stresses, and stresses imposed by the base of the buildings.

v) The implementation of a new tool should not stop the study of other static factors that were identified as contributors to the poor performance of friction pile foundations during the 1985 Michoacan earthquake. Among them (Auvinet and Mendoza, 1987): (i) concentration of loads and local failures produced by the stiff foundation boxes; (ii) the action of negative skin friction on piles.

vi) A complete programme of cyclic full-scale pile tests in MC would appear a cost-effective way of completing and refining the proposed ID. Also, the testing of piles that had supported buildings through prior cyclic loading events (carried perhaps after demolition) would provide a valuable information on the effects of seismic actions on piles and ageing. These tests could aim to identify the origin of rate effects on piles.

vii) Further parametric studies of structural models would help to identify the circumstances under which structural changes have a significant impact on the seismic pile loads.

REFERENCES

Alberro, J. A. and Santoyo, E.V. (1973), Long term behaviour of Mexico City Clay, Proc. 8th ICSMFE, Vol. 1, pp. 1-9.

Alcantara, L., Almora D., Castro, G., Macias, M., Vazquez, R., Ylizaliturri, J., Velasco, J. M., Sandoval, H., Soto, U., and Carmona, G. (1999), The earthquake of June 15 1999 in the Plaza Cordoba Building, Recorded accelerations, Institute of Engineering, UNAM. In Spanish.

American Petroleum Institute (1986), RP2A: Recommended practice of planning, designing and constructing fixed offshore platforms, 16th Edition, Washington, pp. 59-61.

American Petroleum Institute (1991), RP2A: Recommended practice of planning, designing and constructing fixed offshore platforms, 19th Edition, Washington.

American Petroleum Institute (1993), RP2A: Recommended practice of planning, designing and constructing fixed offshore platforms, Washington.

American Petroleum Institute, API (1998), Minutes API RG7/ISO Meeting Thursday 7th May 1998, Report by NGI on foundation bias and uncertainties for seismic design, Houston.

Ang, A. H. and Newmark, N. M. (1977), A probabilistic seismic safety assessment of the Diablo Canyon Nuclear power plant, report to the US Nuclear Regulatory Commission (Cited by FEMA, 1995).

Aubeny, C. P. (1992), Rational interpretation of in-situ tests in cohesive soils, PhD Thesis, Massachusetts Institute of Technology.

Audibert, J. M. E. and Hamilton, T. K. (1998), West Delta 58A Site Selection and Characterization, Proc. Offshore Technology Conference, Houston, Texas, OTC 8764, pp. 415-431.

Auvinet, G. and Hanell, J. J. (1981), Negative skin friction on piles in Mexico City clay, Proc. 10th ICSMFE, Stockholm, Vol. 1, pp. 559-604.

Auvinet, G. and Mendoza, M. J. (1987), Considerations on the behaviour of friction piles in seismic regions, Proc. VII National conference on Seismic Engineering, C 223-239, Queretaro, Mexico. In Spanish.

Auvinet, G. and Mendoza, M. J. (1987), Reponse of diverse foundation types in the Lake zone of Mexico City during the 19 September 1985 earthquake, Proc. Conf. "The earthquakes of 1985: soils mechanics experiences", Mexican Society of soil Mechanics, Mexico, D. F., pp. 227-240. In Spanish.

Banerjee, P. K. and Sen, R. (1987), Dynamic behaviour of axially and laterally loaded piles and pile groups, in "Dynamic behaviour of foundations and buried structures, Soil dynamics: an overview", Developments in soil mechanics and foundation engineering – 3.

Bardet, J. P., Idriss, I. M., and O'Rourke, T. D. (1996), Performance of pile foundations, Chapter 7 of the Proc. of the North America - Japan Workshop on the Geotechnical Aspects of the Kobe, Loma Prieta, and Northridge Earthquakes, Osaka, Japan, pp. 38-43.

Bea, R. G. (1980), Dynamic response of piles in offshore platforms, Proc. Dynamic response of pile foundations, Analytical aspects, ASCE, pp. 80-109.

Bea, R. G. (1992), Pile capacity for axial cyclic loading, J. of Geotech. Engng. ASCE, Vol. 118, No. 1, pp. 34-50.

Bea, R. G. and Audibert, J. M. E. (1979), Performance of dynamically loaded pile foundations, Proc. 2nd Int. Conf. on Behaviour of offshore structures, Vol. 3, London, England, pp. 728-745.

Bea, R. G., Litton, R. W., Nour-Omid, S., and Chang, J. Y. (1984), Specialised design and research tool for the modelling of near-field pile-soil interactions, 16th Offshore Technology Conference, OTC 4806, Houston, Texas, pp. 249-262.

Bea, R. G., Jin, Z., Valle, C. and Ramos, R. (1999), Evaluation of reliability of platform pile foundations, J. of Geotec. and Geoenviron. Engng., ASCE, Vol. 125, pp. 696-704.

Bergdahl, U. and Hult, G. (1981), Load tests on friction piles in clay, Proc. 10th ICSMFE, Stockholm, pp. 625-630.

Bishop, A. W., Green, G. E., Garga, V. K., Andresen, A. and Brown, J. D. (1971), A new ring shear apparatus and its application to the measurement of the residual strength, Geotechnique 21, No. 4, 273-328.

Bogard, J. D. and Matlock, H. (1990a), In-situ pile segment model experiments at Empire, Lousiana, Offshore Technology Conference, OTC 6323, Houston, Texas, pp. 459-467.

Bogard, J. D. and Matlock, H. (1990b), In-situ pile segment model experiments at Harvey, Lousiana, Offshore Technology Conference, OTC 6324, Houston, Texas, pp. 469-477.

Bogard, D. and Matlock, H. (1998a), Lateral Pressure Measurements During a 2.5 Year Period of Consolidation and Setup, Proc. Offshore Technology Conference, Houston, Texas, OTC 8765, pp. 433-444.

Bogard, D. and Matlock, H. (1998b), Experimental Methods and Qualification of the Data, Proc. Offshore Technology Conference, Houston, Texas, OTC 8766, pp. 445-454.

Bogard, D. and Matlock, H. (1998c), Static and Cyclic Load Testing of a 30-inch-Diameter Pile Over a 2.5-year Period, Proc. Offshore Technology Conference, Houston, Texas, OTC 8767, pp. 455-468.

Bond, A. J. (1989), Behaviour of displacement piles in overconsolidated clays, PhD Thesis, University of London, Imperial College.

Bouckovalas, G. (1996), Evaluation of cyclic model tests on anchor piles in clay, Soils and foundations, vol. 36, No. 4, pp. 57-70.

Briaud, J. L. and Felio, G. Y. (1986), Cyclic axial loading of piles: analysis of existing data, Canadian Geotech. J., Vol. 23, pp. 362-371.

Briaud, J. L. and Tucker, L. M. (1988), Measured and predicted axial load response of 98 piles, J. Geotech. Engng., ASCE, Vol. 114, pp. 984-1001.

British Standard Institution (1998), BS 8110 issue 2, Structural use of concrete, Part 1 Code of practice for design and construction.

Bromhead, E. N. (1979), A simple ring shear apparatus, Ground Engineering, Vol. 12, No. 5, pp. 40-44.

Broms, B. B. (1964), Lateral resistance of piles in cohesive soils, Journal of the Soil Mech. and Foundations Div., ASCE, Vol. 90, pp. 27-63.

Burland, J. B. (1990), On the compressibility and shear strength of natural clays, Geotechnique 40, No. 3, pp. 329-378.

Butterfield, R. and Banerjee, P. K. (1971), The problem of pile group-pile cap interaction, Geotechnique 21, pp. 135-142.

Butterfield, R. and Douglas, R. A. (1981), Flexibility coefficients for the design of piles and pile groups, Construction Industry Research and Information Association, Technical Note 108. (Cited by Horikoshi and Randolph, 1999).

Carrillo, N. (1948), Influence of artesian wells on the sinking of Mexico City, Proc. of the 2nd ICSMFE, Holland, Vol. 7, pp. 156-159.

Cassaro, M. A. and Martinez-Romero, E. (1986), Prologue to the ASCE Conference "The Mexico Earthquakes –1985, Factors involved and Lessons learned", edited by Michael A. Cassaro and Enrique Martinez Romero, ASCE, pp. V-VII.

Castellanos, J. E. (1998), Behaviour of soil-pile interface in Mexico City clay, MSc thesis, UNAM, Mexico. In Spanish.

Chan, J. H-C and Birrell, N. D. (1998), Project Overview and Organization – Tension Pile Study, Proc. Offshore Technology Conference, Houston, Texas, OTC 8762, pp. 399-406.

Charlie, W. A., Turner, J. P., and Kulhawy, F. H. (1985), Review of repeated axial load tests on deep foundations, in "Drilled pier and caissons II", Baker, J. Editor, ASCE. New York, pp. 129-150.

Chellis, R. D. (1961), Pile foundations, McGraw Hill.

Chow, F. C. (1997), Investigation into the behaviour of displacement piles for offshore foundations, PhD. Thesis, Imperial College.

Clancy, P. and Randolph, M. F. (1993), An approximate analysis procedure for piled raft foundations, J. for numerical and analytical methods in geomechanics, Vol. 17, pp. 849-869.

Clancy, P. and Randolph, M. F. (1996), Simple design tools for piled raft foundations, Geotechnique 46, pp. 313-328.

Clark, J. I. And Meyerhof, G. G. (1972), The behaviour of piles driven in clay, An investigation of soil stress and pore water pressure as related to soil properties, Canadian Geotech. J., Vol. 9, pp. 351-373.

Complementary Technical Norms for the design and construction of foundations (2001), Mexico, D. F.

Cooke, R. W., Price, G. and Tarr, K. (1980), Jacked piles in London clay: interaction and group behaviour under working conditions, Geotechnique 30, pp. 97-136.

Cooke, R. W., Bryden-Smith, D. W, Gooch, M. N., and Sillett, D. F. (1981), Some observations of the foundation loading and settlement of a multi-storey building on a piled raft foundation in London clay, Proc. I.C.E. (70), part 1, pp. 433-468.

Cowley, R. C. (1998), The effect of pile geometry on the design of piles using the new Imperial College Pile Design Method, MSc Dissertation, Imperial College.

Coyle, H. M. and Reese, L. C. (1966), Load transfer for axially-loaded piles in clay, J. Soil Mechanics and Foundation Division, ASCE, Vol. 92, No. 2, pp. 1-26.

Craig, R. F. (1997), Soil mechanics, 6th Edition, E & FN SPON, pp. 179-201.

De Beer, E. E. (1977), The effects of horizontal loads on piles, due to surcharge or seismic effects, Specialty session 10, 9th ICSMFE, Tokyo, Vol. III, pp. 547-558.

Demeneghi, A. (1986), Seismic behaviour of foundations in Mexico City, Proc. of the Symposium "The earthquakes of 1985: Soil mechanics cases", Mexico City, Mexican Society of Soil Mechanics, pp. 297-299. In Spanish.

Det Norske veritas (2000a), Design of offshore steel structures, Offshore Standard DNV-OS-C101.

Det Norske veritas (2000b), Structural design of TLPs, Offshore Standard DNV-OS-C105.

Diaz, J. A. and Casales, C. (1986), Unidimensional deformation of the Mexico City clay by vibrations, Proc. Conf. "The earthquakes of 1985: Soils mechanics experiences", Mexican Society of soil Mechanics, Mexico, D. F., pp. 301-308. In Spanish.

Diaz, J. A. and Cordoba, G. (1986), Strength of Mexico City clay under cyclic loading, Proc. Conf. "The earthquakes of 1985: Soils mechanics experiences", Mexican Society of soil Mechanics, Mexico, D. F., pp. 309-313. In Spanish.

Diaz-Rodriguez, J. A., Lozano, R., Giron, V, Vallejo, E. (1995), Mineralogy and Geotechnical properties of Mexico City Clay, Proc. X Pan-American Conf. of Soil Mechanics and Foundation Engineering, Vol. I, Guadalajara, Mexico, pp. 102-113.

Dobry, R., and Vucetic, M. (1988), Dynamic properties and seismic response of soft clay deposits, Proc. of the Int. Symposium on Geotech. Engng. of Soft Soils, SMMS, Vol. 2, Mexico, D.F., pp. 49-85.

Doyle, E. H. and Pelletier, J. H. (1985), Behaviour of a large scale pile test in silty clay, Proc. 11th ICSMFE, San Francisco, Vol. 3, pp. 1595-1598.

Dunnavant, T. W., Clukey, E. C. and Murff, J. D. (1990), Effects of cyclic loading and pile flexibility on axial pile capacities in clay, Proc. XXII Offshore Technology Conference, OTC 6378, Vol. 3, Houston Texas, pp. 289-298.

Durrani, A. J., Mau, S. T., AbouHashish, A. A. (1994), Earthquake response of flat-slab buildings, Journal of Structural Engineering, ASCE, Vol. 120, pp. 947-965.

Elnashai, A. S. and Izzuddin, B. A. (1993), Modelling of material non-linearities in steel structures subjected to transient dynamic loading, Earthquake Engineering and Structural Dynamics, Vol. 22, pp. 509-532.

Earthquake Spectra, (1990), Loma Prieta reconnaissance report, Supplement to Vol. 6, Geotechnical aspects, pp. 81-125.

EUROCODE 8 (1994), The design provisions for earthquake resistance of structures – Part 5

Fearon, R. (1998), The behaviour of a structurally complex clay from an Italian landslide, PhD Thesis, City University, London.

FEMA, Federal Emergency Management Agency (1995), Recommended provisions for seismic regulations for new buildings, Part 2 Commentary, National Earthquake Hazards Reduction Program (NEHRP), Building seismic safety council, 1994 Edition, Washington, D.C., pp. 1-5.

Finn, W. D. L., Wu, G., and Thavaraj, T. (1997), Soil-pile-structure interaction, in "Seismic analysis and design for soil-pile-structure interaction"; Geotech. special publicacion, No. 70, Edited by Shamsher Prakash, pp. 1-22.

Fleming, W. G. K., Weltman, A. J., Randolph, M. F. and Elson, W. K. (1992), Piling Engineering, 2nd edition, Surrey University Press.

Focht, J. A. and O'Neill, M. W. (1985), Piles and other foundations, 11th ICSMFE, Vol. 1, San Francisco, pp. 187- 209.

Foutch, D. A. (1978), The vibrational characteristics of a twelve-story steel frame building, Earthquake Engng. and Structural Dynamics, Vol. 6, pp. 265-294.

Fraser, R. A. and Wardle, L. J. (1976), Numerical analysis of rectangular rafts on layered foundations, Geotechnique 26, pp. 613-630.

Gallagher, K. A. and St. John, H. G. (1980), Field scale model studies of piles as anchorages for buoyant platforms, Proc. European Offshore Petroleum Conference and Exhibition, London.

Gamboa, V. and Muria, D. (1996), Computation of the structural response of JAL building during the Copala earthquake, X National Congress on structural engineering, Yucatan, Mexico. In Spanish.

Garcia-Ranz, F. and Gomez, R. (1988), The Mexico earthquake of September 19, 1985 – Live load specifications on the 1976 and 1987 Mexico City Building Codes, Earthquake Spectra, Vol. 4, pp. 461-467.

Garga, V. K. (1970), Residual shear strength under large strains and the effect of sample size on the consolidation of fissured clay, PhD thesis, University of London.

Gazetas, G. (1983), Analysis of machine foundation vibrations - State of the art, Soil dynamics and earthquake engineering, Vol. 2, No. 1, pp. 2-42.

Gazetas, G. (1987), Dynamic behaviour of foundations and buried structures, in Soil dynamics: an overview, Developments in soil mechanics and foundation engineering –3.

Giraldo, M. (1996), Evaluation of an elasto-plastic model for Mexico City clay, MSc Thesis, UNAM, Mexico. In Spanish.

Girault, P. (1986), Foundation failures during earthquakes in Mexico City, Proc. Conf. "The earthquakes of 1985: soils mechanics experiences", Mexican Society of Soil Mechanics, Mexico, D. F., pp. 355-358.

Gomez-Looh, R. (1987), X ray diffraction analyses of Mexico City clay, BSc Thesis, UNAM, Mexico. In Spanish.

Grosch, J. J. and Reese, L. C. (1980), Field tests of small-scale pile segments in a soft clay deposit under repeated axial loading, Proc. 12th Offshore Technology Conference, OTC 3869, Houston, Texas, pp. 143-151.

Hain, S. J. and Lee, I. K. (1978), The analysis of flexible raft-pile systems, Geotechnique 28, pp. 65-83.

Han, Y. and Cathro, D. (1997), Seismic behaviour of tall buildings supported on pile foundations, Seismic analysis and design for soil-pile-structure interaction, Geotech. Special Publication No. 70, ASCE, Edited by Shamher Prakash, pp. 36-51.

Handbook to British Standard BS 8110:1985 - Structural used of concrete (1987), Palladium publications LTD, London, page 49.

Hansbo, S. and Jendeby, L. (1983), A case study of two alternative foundation principles: conventinal friction piling and creep piling, Vag ocht Vattenbyggaren, No. 7-8. Cited by Mendoza and Romo (1997).

Harding, B. O. and Drnevich, V. P. (1972), Shear modulus and damping in soils: design equations and curves, Journal of the geotechnical Engineering division, ASCE, Vol. 98, GT7, pp. 667-692.

Hardy, S. (2001), Personal communication

Hemsley, J. A. (2000), Developments in raft analysis and design, in "Design applications of raft foundations"; J. A. Hemsley editor, Thomas Telford, pp. 487-605.

Hight, D.W. (1993), A review of sampling effects in clays and sands, Advances in underwater technology, ocean science and offshore engineering, Vol. 28, Offshore site investigation and foundation behaviour, pp. 115-146.

Hight, D.W., Jardine, R. J. and Gens, A. (1987), The behaviour of soft clays, Embankments on soft clays, Public works research center, Athens, Chapter 2, pp. 33-158.

Hight, D. W., Bennell, J. D., Chana, B., Davis, P. D., Jardine, R. J. and Porovic, E. (1997), Wave velocity and stiffness measurements of the Crag and Lower London Tertiaries at Sizewell, Geotechnique 47, No. 3, pp. 451-474.

Hjort, E. and Carrillo, G. (1985), Acquisition process and bearing capacity of friction piles, BSc Thesis, Engineering Faculty, UNAM. In Spanish.

Holguin, E., Gutierrez, C. E., Cuevas, A., and Segovia, J. A. (1992), Geotechnical design of foundations, TGC Geotecnia, page 51. In Spanish.

Holmquist, D. V. and Matlock, H. (1976), Resistance-displacement relationships for axially-loaded piles in soft clay, Proc. 8th Offshore technology conference, Vol. 1, Houston, Texas, pp. 553-569.

Horikoshi, K. and Randolph, M. F. (1996), Centrifuge modelling of piled raft foundations on clay, Geotechnique 46, pp. 741-752.

Horikoshi, K. and Randolph, M. F. (1999), Estimation of overall settlement of piled rafts, Soils and Foundations 39, pp. 59-68.

Idriss, I. M., Dobry, R. and Singh, R. D. (1978), Nonlinear behaviour of soft clays during cycling loading, Journal of the Geotechnical Division, ASCE, vol. 104, No. 12, pp. 1427-1447.

International Standard ISO 19900, Petroleum and Natural Gas Industries, Offshore Structures. This first edition of ISO 19900 cancels and replaces ISO 13819-1:1995.

Ishihara, K. (1996), Soil behaviour in earthquake geotechnics, Clarendon Press-Oxford, New York-USA, Chapters 6 to 9, pp. 87-207.

Izzuddin, B. A. (1991), Non-linear dynamic analysis of framed structures, PhD Thesis, Imperial College.

Izzuddin, B. A. and Elnashai, A. S. (1989), ADAPTIC, a program for adaptive large displacement elastoplastic dynamic analysis of steel, concrete and composite frames. Research report ESEE-89/7, Engineering Seismology and Earthquake Engineering Section, Imperial College, London.

Izzuddin, B. A. and Elnashai, A. S. (1993), ADAPTIC, a program for static and dynamic large displacement nonlinear analysis of space frames by adaptive mesh refinement, User and example manual.

Jaime, A. (1987), Dynamic characteristics of the Mexico Valley clay, PhD Thesis, UNAM, Mexico, pp. 10-99. In Spanish.

Jaime, A. (1988), Foundation Engineering in Mexico City: General aspects and subsoil conditions, Proc. Int. Symposium on Geotech. Engng. of Soft Soils, Mexican Society of Soil Mechanics, Vol. 2, Mexico, D.F., pp. 225-243.

Jaime, A., Romo, M. P., and Resendiz, D. (1988), Behaviour of friction piles in the Valley of Mexico clay, Engineering Institute publication No. 515, UNAM. In Spanish.

Jaime, A., Romo, M. P. and Resendiz, D. (1990), Behaviour of friction piles in Mexico City clay, J. of Geotech. Engng., ASCE, Vol. 116, pp. 915-931.

Jaime, A., Rojas, E. and Legorreta, H. (1991), Friction piles driven in soft clay: Behaviour under static load, Engineering Institute Publication, UNAM Mexico. In Spanish.

Jardine, R. J. (1985), Investigation of pile-soil behaviour, with special reference to the foundation of offshore structures, PhD Thesis, University of London, Imperial College.

Jardine, R. J. (1991), The cyclic behaviour of large piles with special reference to offshore structures, Chapter 5 in "Cyclic loading of soils", Edited by M. P. O'Reilly and S. F. Brown, Glasgow.

Jardine, R. J. (2002), Report for Rail link engineering on cyclic axial loading response of piles installed for CTRL contract 310, Imperial College Consultants, February.

Jardine, R. J. (2002), Personal communication.

Jardine, R. J. and Chow, F. C. (1996), New design method for offshore piles, MTD Publication 96/103, Marine Technology Directorate, London.

Jardine, R. J., Chow, F. C., Matsumoto, T. and Lehane, B. M. (1998), A new design procedure for driven piles and its application to two Japanese clays, Soils and Foundations, Vol. 38, pp. 207-219.

Jardine, R. J. and Saldivar, E. E. (1999), An alternative interpretation of the West Delta 58A tension-pile research results, OTC Conference, OTC 10827, Houston, Texas.

Kanji, M. A. (1974), Unconventional laboratory tests for the determination of the shear strength of soil-rock contacts, Proc. 3rd Congr. Int. Conf. Rock Mech., Denver 2A, 241-247.

Karlsrud, K. and Haugen, T. (1983), Cyclic loading of piles and pile anchors – Field model tests, Final report, Summary and evaluation of test results, Norwegian Geotechnical Institute, Report 40018-11.

Karlsrud K and Haugen, T. (1985), Behaviour of piles in clay under cyclic axial loading – results of field model tests, Behaviour of offshore structures Conference, Amsterdam, pp. 589-600.

Karlsrud, K., Nadim, F. and Haugen, T. (1987), Piles in clay under cyclic axial loading – Field tests and computational modelling, Norwegian Geotechnical Institute, Publication No. 169.

Katzenbach, R., Arslan, U., Moorman, C. and Reul, O. (1998), Piled raft foundation: interaction between piles and raft, Darmstadt Geotechnics (Daarmstadt University of Technology), No. 4, pp. 279-296.

Kayna, A. M. (1997), Earthquake induced forces in piles in layered soil media, in "Seismic analysis and design for soil-pile-structure interactions", Geotech. special publication No. 70, Edited by Shamsher Prakash, pp. 85-95.

Kayna, A. M and Mahzooni, S. (1996), Forces in pile foundations under seismic loading, J. of Engng. Mechanics , Vol. 122, ASCE, pp. 46-53.

Kenney, T. C. (1967), The influence of minerological composition on the residual strength of natural soils, Proc. of the Oslo Geotechnical Conference on the shear strength properties of natural soils and rocks, Vol. I, pp. 123-129.

Kimura, M. and Zhang, F. (2000), Seismic evaluations of pile foundations with three different methods based on three-dimensional elastoplastic finite element analysis, Soils and Foundations, Vol. 40, pp. 113-132.

Kim, J. B., Singh, P., and Brungraber, R. J. (1979), Pile cap soil interaction from full-scale lateral load tests, J. Geotech. Engng. Div. ASCE, Vol. 105, pp. 643-653.

Koizumi, Y. and Ito, K. (1967), Field tests with regard to pile driving and bearing capacity of piled foundations, Soil and Foundations, Vol. 7, No. 3, pp. 30-53.

Kraft, L. M, Cox, W. R. and Verner, E. A. (1981a), Pile load tests: cyclic loads and varying load rates, J. of the Geotech. Engng. Div., ASCE, Vol. 107, pp. 1-19.

Kraft, L. M., Ray, R. P. and Kagawa, T. (1981b), Theoretical t-z curves, J. of the Geotech. Engng. Div., ASCE, Vol. 107, pp. 1543-1561.

Lehane, B. M. (1992), Experimental investigation of pile behaviour using instrumented field piles, PhD Thesis, Imperial College.

Lemos, L. J. (1986), The effects of rate on the residual strength of soil, PhD Thesis, University of London, Imperial College.

Lemos, L. J., Skempton, A. W. and Vaughan, P. R. (1985), Earthquake loading of shear surfaces in slopes, Proc. 11th ICSMFE, San Francisco, Vol. 4, pp. 1955-1958.

Lemos, L. J. and Vaughan, P. R. (2000), Clay-interface shear resistance, Geotechnique 50, No. 1, 55-64.

Littleton, I. (1976), An experimental study on the adhesion between clay and steel, J. Terramechanics 13, No. 3, 141-152.

Leon, J. L., Jaime, A., and Rabago, A. (1974), Dynamic properties of soils – preliminary study, Institute of Engineering, UNAM. In Spanish. Cited by Dobry and Vucetic (1988).

Leonards, G. and Girault, P. (1961), A study of the one dimensional consolidation test, Proc. 5th ICSMFE, Vol. 1, pp. 213-218.

Lo, K. Y. (1962), Shear strength properties of a sample of volcanic material of the Valley of Mexico, Geotechnique 12, No. 4, 303-318.

Luco, J. E. (1980), Linear soil-structure interaction, UCRL-15262, Lawrence Livermore National Laboratory, Livermore, California.

Lupini, J. F. (1981), The residual strength of soils, PhD thesis, Imperial College.

Lupini, J. F., Skinner, A. E. and Vaughan, P. R. (1981), The drained residual strength of cohesive soils, Geotechnique 31, No. 2, 181-213.

Madas, P. and Elnashai, A. S. (1992), A new passive confinement model for the analysis of concrete structures subjected to cyclic and transient dynamic loading, Earthquake Engng. and Structural Dynamics, Vol. 21, pp. 409-431.

Mander, J. B., Priestley, M. J. N. and Park, R. (1988), Observed stress-strain behaviour of confined concrete, J. of Structural Engng., ASCE, Vol. 114, pp. 1827-1849.

Mandolini, A. and Viggiani, C. (1997), Settlement of piled foundations, Geotechnique, Vol. 47, pp. 791-816.

Marchetti, S. (1980), In-situ tests by flat dilatometer, J. of Geotech. Engng., ASCE, Vol. 106, No. GT3, pp. 291-321.

Marsal, R. J. (1985), Geotechnical notes on the effects of Mexico's 1985 earthquakes, in "The Mexico Earthquake 1985, Factors involved and lessons learned", Edited by Michael A. Cassaro and Enrique Martinez R., ASCE, pp. 78-95.

Marsal, R. J. and Mazari, Y.M. (1962), The subsoil of Mexico City, 2nd. Edition, UNAM, Mexico. In Spanish.

Marsal, R. J. (1986), Notes about the design and construction of foundations in the Distrito Federal, Federal Commission of Electricity, Mexico. In Spanish.

Martinez-Rueda, E. (1997), Energy dissipation devices for seismic upgrading of reinforced concrete structures, PhD Thesis, Imperial College.

Martins, J. P. (1983), Shaft resistance of axially loaded piles in clay, PhD thesis, Imperial College.

Matlock, H. and Foo, S. H. C. (1979), Axial analysis of piles using a hysteretic and degrading soil model, Proc. Conf. on numerical methods in offshore piling, Institute of Civil Engineers, London.

Matlock, H., Bogard, D. and Chan, J. H-C. (1998), Technical Program Tension Pile Study, Proc. Offshore Technology Conference, Houston, Texas, OTC 8763, pp. 407-413.

Mayne, P. W. and Kulhawy, F. H. (1982), k_0-OCR relationship in soils, J. Getechnical Engng. Div., ASCE 108, pp. 851-872.

Mayne, P. W. and Poulos, H. (1999), Approximate displacement influence factors for elastic shallow foundations, J. Geotech. Geoenviron. Engng. 125, pp. 453-460.

Masayuki, H. and Shoichi, N. (1991), A study on pile forces of a pile group in layered soil under seismic loading, Proc. 2nd Int. Conf. on recent advances in Geotech. earthquake engineering and soil dynamics, Vol. 3, pp. 2079-2086.

McAnoy, R. P. L., Chasman, A.C. and Purvis, D. (1982), Cyclic tensile testing of a pile in glacial till, Proc. Recent developments in the design and construction of offshore structures Conference, Institute of Civil Engineers, London.

Meli, R. and Bazan, E. (1992), "Manual for the seismic design of buildings", LIMUSA.

Meli, R., Faccioli, E., Muria-Vila, D., Quaas, R., and Paolucci, R. (1998), A study of site effects and seismic response of an instrumented building in Mexico City, J. of Earthquake Engineering, Vol. 2, No. 1, pp. 89-111.

Mendoza, M. J. (1990), Foundation engineering in Mexico City: Behaviour of foundations, Proc. Int. Symposum on Geotech. Engng. of Soft Soils, Mexico, Vol. 2, pp. 351-367.

Mendoza, M.J. and Hernandez, V.M. (1992), Experimental study of the development of pore pressure and permanent deformations in Mexico City clay, Engineering Institute Internal Report, UNAM, Mexico. In Spanish.

Mendoza, M. J., Romo, M. P., Dominguez, L., Orozco, M., Noriega, I., Velasco, J. M. (1996), Instrumentation and performance of a friction pile-box foundation in Mexico City during its construction and beginning of operation, Proc. XIII Soil Mechanics National Conference, Mexico, pp. 143-159. In Spanish.

Mendoza, M. J., Romo, M. P., Orozco, M., Dominguez, L., Velasco, J. M., Noriega, I. (1997), First experience of seismic-geotechnical instrumentation of a foundation box and friction pile foundation in Mexico, Proc. of the XI National Conference on Seismic Engineering, Mexico, Vol. 1, pp. 75-84. In Spanish.

Mendoza, M. J. and Romo, M. P. (1997), Behaviour of a friction pile-box foundation in Mexico City during construction, Proc. 14th ICSMFE, Hamburg, Vol. 2, pp. 1119-1124.

Mendoza, M. J. and Auvinet, G. (1988), The Mexico Earthquake of September 19, 1985 – Behaviour of Building foundations in Mexico City, Earthquake Spectra, Vol. 4, No. 4, pp. 835-853.

Mendoza, M. J., Romo, M. P., Orozco, M., Dominguez, L., Velasco, J., Noriega, I. (1998), Pile loads and contact and pore pressures in a box-pile foundation in Mexico City, XIX National Conf. on Soil Mechanics, Puebla, Mexico, pp. 358-367. In Spanish.

Mendoza, M. J., Romo, M. P., Dominguez, L., Orozco, M., Noriega, I. (2000a), Static and seismic behaviour of a friction pile foundation in Mexico City after 5 years of beginning of construction, Proc. of the XX National Conference on Soil Mechanics, Oaxaca, Mexico, Vol. 1, pp. 329-340. In Spanish.

Mendoza, M. J., Romo, M. P., Orozco, M., and Dominguez, L. (2000b), Static and seismic behaviour of a friction pile-box foundation in Mexico City clay, Soils and Foundations, Vol. 40, pp. 143-154.

Mesri, G., Rokhsar, A. and Bohar, B.F. (1975), Composition and compressibility of typical samples of Mexico City clay, Geotechnique 25, pp. 527-554.

Mexican Society of Seismic Engineering (SMIS) - (1997), Database of strong earthquakes, CD 1, Edited by University of Colima.

Meyerhof, G. G. (1976), Bearing capacity and settlement of pile foundations, The 11th Terzaghi Lecture, J. of Geotech. Engng. Div., ASCE, Vol. 120, pp. 197-228.

Mizuno, H. (1987), Pile damage during earthquakes in Japan (1923-1983), in "Dynamic response of piles foundations – experiments, analysis and observations", Geotech. special publication No. 11, T. Nogami, ASCE, New York, pp. 53-78.

Mizuno, H., Iiba, M. and Kitagawa, Y. (1984), Shaking table testing of seismic building-pile-two layered soil interaction, Proc. 8th WCEE, San Francisco, Vol. 3, pp. 649-656.

Mitchell, J. K. (1976), "Fundamental of soils behaviour", John Willey and Sons, New York.

Mokwa, R. L. and Duncan, J. M. (2001), Experimental evaluation of lateral-load resistance of pile caps, J. of Geotech. and Geoenviron. Div., ASCE, Vol. 127, pp. 185-192.

Mooser, F. (1990), Stratigraphy and structure of the Valley of Mexico, Proc. Symposium "The subsoil of the Valley of Mexico and its relation to foundation engineering 5 year after the 1985 earthquake", Mexican Society of Soil Mechanics, pp. 29-36. In Spanish.

Muria-Vila, D. (1997), Instrumented buildings, Chapter 9 in "The Macro-earthquake of Manzanillo of the 9 October 1995", Tena Arturo Editor, Mexican Society of Seismic

Engineering, pp. 197-232. In Spanish.

Muria-Vila, D. and Del Toro, M. (1998), Effects of several seismic events recorded at a building founded on soft soil, 11th European Conf. on Earthquake Engng., Balkema, Rotterdam.

Muria-Vila, D., Macias, M. A., Rodriguez, G. and Soto, U. (2000), Analysis of the records obtained at PC Building from 1990 to 1999, Internal report, Engineering Institute, UNAM. In Spanish.

Mylonakis (2001), W inkler modulus for axially loaded piles, Geotechnique, Vol. 51, No. 5, pp. 455-461.

Nagaraj, T. S. and Srinivasa Murthy, B. R. (1986), A critical reapraisal of compression index equations, Geotechnique 36, No. 1, pp. 27-32.

Newmark, N. and Rosenblueth, E. (1971), "Fundamentals of earthquake engineering", Prentice Hall, page 220.

Nilson, A. H. and Winter, G. (1986), "Design of concrete structures", Chapter 8 and 9, 10th edition, McGrow Hill.

Novak, M. (1991), Piles under dynamic loads: state of the art, Proc. 2nd Int. Conf. On recent advances in geotechnical earthquake engineering and soil dynamics, St. Louis, Vol. 3, 2433-2456.

Nowatzki, E. A. (1966), Fabric changes accompanying shear strains in a cohesive soil, PhD. Thesis, University of Arizona (Cited by Grosch and Reese, 1980).

O'Neill, M. W., Hawkins, R. A. and Mahar, L. J. (1982), Load transfer mechanism in piles and pile groups, J. of the Geotech. Engng. Div., ASCE, Vol. 108, No. 12, pp. 1605-1623.

O'Neill, M. W., Caputo, V., De Cock, F., Hirtikainen, J. and Mets, M. (1996), Case histories of pile supported rafts, Report for ISSMFE, Technical Committee TC18, Univ. of Houston, Texas. (Cited by Mendoza, et al., 2000b)

Ovando, E., Cuanalo, O., and Roque, G. (1993), Dynamic behaviour of soil-pile interfaces, Proc. of the X National Congress on Seismic Engineering, Puerto Vallarta, Mexico, pp.

940-948. In Spanish.

Paolucci, R. (1993), Soils-structure interaction effects on an instrumented building in Mexico City, European Earthquake engineering, No. 3, pp. 33-45.

Papageorgiou, A. A. and Lin, B. (1990), Analysis of recorded earthquake response and identification of a multi-story structure accounting for foundation interaction effects, Computation Mechanics, pp. 55-64.

Parathiras, A. N. (1994), Displacement rate effects on the residual strength of soils, PhD thesis, Imperial College.

Pellew, A. (2002), Field investigation into piles in clay, PhD Thesis, Imperial College.

Peralta and Faby, R. (1989), About the origin of some mechanical properties of the Upper Clay Formation of the Valley of Mexico, Proc. Symposium "Geologic topics of Valley of Mexico basin", Mexican Society of Soil Mechanics, pp. 43-53. In Spanish.

Pinho, R. (2000), Selective retrofitting of reinforced concrete structures in seismic areas, PhD Thesis, Imperial College.

Potyondy, J. G. (1961), Skin friction between various soils and construction materials, Geotechnique 11, No.11, No. 4, pp. 339-353.

Poulos, H. G. (1988), Cyclic stability diagram for axially loaded piles, J. Geotech. Engng. ASCE, Vol. 114, pp. 877-895.

Poulos, H. G. (1989), Pile behaviour – theory and application, Geotechnique 39, No. 3, pp. 365-415.

Poulos, H. G. (2000), Practical design procedures for piled raft foundations, in "Design applications of raft foundations", J. A. Hemsley editor, Thomas Telford, pp. 425-467.

Poulos, H. G. (2001), Piled raft foundations: design and applications, Geotechnique 51, pp. 95-113.

Poulos, H. G. and Davis, E. H. (1974), Elastic solutions for soil and rock mechanics, Wiley, New York.

Poulos, H. G. and Davis, E. (1980), Pile foundation analysis and design, John Wiley and Sons, New York.

Poulos, H. G., Small, J. C., Ta, L. D., Sinha, J. and Chen, L. (1997), Comparison of some methods for analysis of piled rafts, Proc. 14th ICSMFE, Hamburg, Vol. 2, pp. 1119-1124.

Puech A. and Jezequel, J. F. (1980), The effects of long time cyclic loadings on the behaviour of a tension pile, 12th Offshore Technology Conference, OTC 3870, Houston Texas, pp. 153-162.

Ramsey, N., Jardine, R. J., Lehane, B. M. and Ridley, A.M. (1998), A Review of Soil-steel Interface Testing with the Ring-shear Apparatus, Proc. Conf. Offshore Site Investigations and Foundation behaviour, Society for Underwater Technology (SUT), London, pp. 237-258.

Randolph, M. F. (1983), Design of piled raft foundations, Proc. Int. Symp. on recent developments in laboratory and field tests and analysis of geotechnical problems, Bangkok, pp. 525-537.

Randolph, M. F. (1994), Design methods for pile groups and piled rafts: state of the art report, Proc. 13th ICSMFE, New Delhi, Vol. 5, pp. 61-82.

Randolph, M. F. and Wroth, C. P. (1978), Analysis of deformation of vertically loaded piles, J. Geotech. Engng. Div., ASCE, Vol. 104 GT, pp. 1465-1488.

Randolph, M. F. and Murphy, B. J. (1985), Shaft capacity of driven piles in clay, Proc. 17th Offshore Technology Conference, Houston, Texas, Vol. I, pp. 371-378.

Resendiz, D. (1964), Field study on reinforced concrete piles, Engineering Magazine, vol. XXXIV. In Spanish.

Resendiz D., and Auvinet G. (1973), Analysis of pile foundations in consolidating soil, Proc. 8th ICSMFE, Moscow, pp. 211-218.

Reyes, A. and Luco, E., The PCC's building strong motion array, Structural response, data processing and identification of dynamic characteristics, 12th ASCE Conference.

Reyes, A., Diaz de Cossio, G., Rocha, E., Delgadillo, H., and Ballesteros, C. (1995), Records obtained at the PCC building from the 9 October 1995 earthquake originated at the Colima Coast, Final Report, CICESE. In Spanish.

Reyes, A., Rocha, E. and Diaz de Cossio, G. (1997), Acelerometer array at the PCC Building, Catalogue of records obtained in 1995, CICESE. In Spanish.

Rigden, W. J. and Semple, R. M. (1983), Design and installation of the Magnus foundations; predictions of pile behaviour, in "Design in offshore structures", Thomas Telford, Ltd., London, pp. 29-43.

Rodriguez, N. (1991) Dynamic interaction of foundations on soft soils, Proc. "Soil-structure interaction and structural design of foundations" Mexican Society of Soil Mechanics, pp. 119-129.

Roesset, J. M. (1980), A review of soil-structure interaction, UCRL-15262, Lawrence Livermore National Laboratory, Livermore, California.

Roesset, J. M. and Angelides, C. (1979), Dynamic stiffness of piles, Proc. Numerical methods in offshore piling, London, pp. 75-81.

Rojas, E., Romo, M. P. and Hiriart, G. (1987), Stress-strain behaviour of Mexico City clay, Internal report, Engineering Institute, UNAM. In Spanish.

Rojas, E., Valle, C., and Romo, M. P. (1999), Soil-pile interface model for axially loaded single piles, Soils and Foundations, Vol. 39, pp. 35-45.

Romo, M. P. (1980), Dynamic analysis of soil-structure systems and earth embankments, X National Conf. on Soil Mechanics, Mexico, pp. 112-133. In Spanish.

Romo, M. P. (1995), Clay behaviour, ground response and soil-structure interaction studies in Mexico City, State of the art paper, 3rd Int. Conf. on recent advances in geotechnical earthquake engineering and soil dynamics, St. Louis Missouri (USA), Vol. 2, pp. 1039-1051.

Romo, M. P. and Jaime, A. (1986), Dynamic characteristics of Mexico Valley clays and soil seismic response, Internal report, Engineering Institute, UNAM, Mexico. In Spanish.

Romo, M. P. and Seed, H.B. (1987), Analytical modelling of dynamic soil response in the Mexico Earthquake of September 19, 1985, Proc. of the Int. Conf. The Mexico Earthquake – 1985, Factors involved and lessons learned, Edited by Cassaro, M. A. and Martinez Romero, E., ASCE, Mexico, pp. 148-161.

Romo, M. P., Jaime, A., Resendiz, D. (1988), The Mexico Earthquake of September 19, 1985 - General soil conditions and clay properties in the Valley of Mexico, Earthquake Spectra, Vol. 4, No. 4, pp. 731-752.

Romo, M. P. and Barcena, A. (1993), Dynamic soil-structure interaction and its impact on foundation engineering, X National Conference on Earthquake Engineering, Mexico. In Spanish.

Romo, M. P. and Ovando, E. (1994), Dynamic and static behaviour of the soil of the Alameda project, Report from the Engineering Institute UNAM to Reichmann International. In Spanish. Cited by Romo (1995).

Romo, M. P., Mendoza, M. J., and Garcia, S. R. (2000), Geotechnical factors in seismic design of foundations, Proc. of the 12th WCEE, New Zealand, State-of-the-art report, No. 2832, 24 pp.

Rosenblueth, E. (1965), Note on the use of friction piles in the Valley of Mexico, April 1965, Revista de Ingenieria, UNAM. In Spanish.

Sangrey, D. A. (1977), Response of offshore piles to cyclic loading, Proceedings, 9th Offshore Technology Conference, OTC 2944, Houston, Texas, pp. 507-512.

Santoyo, E. V. (1989), "The cone penetration test in geotechnical exploration", TGC Geotecnia, Mexico, pp. 123-171. In Spanish.

Santoyo, E. and Gutierrez (1986), Re-foundation of buildings on friction piles, Proc. of the Symposium The earthquakes of 1985: Soil mechanics cases, Mexico City, Mexican Society of Soil Mechanics, pp. 403-409. In Spanish.

Santoyo, E. and Gutierrez, C. E. (1990), Stratigraphy and sampling of the lacustrine soils of the Valley of Mexico, Proc. Symposium "The subsoil of the Valley of Mexico and his relation with foundation engineering 5 year after the 1985 earthquake", Mexican Society of

Soil Mechanics, Mexico, pp. 37-55. In Spanish.

Sayed, S. M. and Bakeer, R. M. (1992), Efficiency formula for pile groups, J. of Geotch. Engng., Vol. 118, pp. 278 - 299.

Scarlat, A. S. (1996), "Approximate methods in structural seismic design", E & FN SPON, pp. 160-169.

Seed, H. B., Romo, M.P., Sun, J. Y., Jaime, A., and Lysmer, J. (1988), The Mexico Earthquake of September 19, 1985 - Relationships between soil conditions and earthquake ground motions, Earthquake Spectra, Vol. 4, No. 4. pp. 687-729.

Semple, R. M. and Rigden, W. J. (1984), Shaft capacity of driven piles in clay, Proc. Symp. on codes and standards, ASCE National Conv., San Francisco.

Singh, S. K. and Suarez, G. (1986), Review of the seismicity of Mexico with emphasis on the September 1985, Michoacan Earthquakes, "The Mexico Earthquakes –1985, Factors involved and Lessons learned", edited by Michael A. Cassaro and Enrique Martinez Romero, ASCE, pp. 7-18.

Smith, P.R. (1992), The properties of high compressibility clay with special reference to construction on soft ground, PhD. Thesis, Imperial College.

Stark, T. D. and Vettel, J. J. (1992), Bromhead ring shear test procedure, Geotech. testing J., Vol. 15, No. 1, pp. 24-32.

Stuckrath, L. (1992), A study of pile behaviour in different soil types including installation effects, PhD Thesis, Ecole Polytechnique Federale de Lausanne.

Sugimura, Y., Fujiwara, K., Ohgi, T., and Karkee, M (1997), Seismic behaviour of piles supporting tall buildings and the consideration of ground response effects in design, 4th Conf. on tall buildings in seismic regions, Los Angeles, pp. 303-317.

Taylor Hobson, A guide to surface texture parameters.

Taylor, P.N. (1971), The properties of soils under dynamic stress conditions, with applications to the design of foundations in seismic areas, PhD Thesis, University of Auckland (cited by Grosch and Reese, 1980).

Tika, T. M. (1989), The effect of rate on the residual strength of soil, PhD Thesis, Imperial College.

Tika-Vassilikos, T. (1991), Clay-on-steel ring shear tests and their implications for displacement piles, Geotech. Testing J., Vol. 14, No. 4, pp. 457-463.

Tika, T. E., Vaughan, P. R., Lemos, L. J. (1996), Fast shearing of pre-existing shear zones in soil, Geotechnique 46, No. 2, 197-233.

Tomazevic, M. (1999), "Earthquake-resistance design of masonry buildings", Vol. 1, Imperial College Press.

Tsubakihara, Y. and Kishida, H. (1993), Frictional behaviour between normally consolidated clay and steel by two direct shear type apparatuses, Soils and Foundations, Vol. 33, No. 2, pp. 1-13.

Veletsos, A. S. (1977), Dynamics of structure-foundation systems, Structural and Geotechnical Mechanics, Edited by W. J. Hall, Prentice-Hall, pp. 333-361.

Vucetic, M. and Dobry, R. (1991), Effect of soil plasticity on cyclic response, Journal of geotechnical engineering, 117, pp. 89-107, cited by Ishihara 1996.

Waas, G. and Hartmann, H. G. (1984), Seismic analysis of pile foundations including pile-soil-pile interaction, Proc. 8th WCEE, Vol. 5, San Francisco, U.S.A. pp. 55-62.

Wang, S., Kutter, B. L., Chacko, M. J., Wilson, D. W., Boulanger, R. W., and Abbas A. (1998), Non-linear seismic soil-pile structure interaction, Earthquake Spectra, Vol. 14, No. 2, pp. 377-396.

Wolf, J. P. (1985), "Dynamic soil-structure interaction", Prentice Hall.

Wood, D. M. (1982), "Laboratory investigations of the behaviour of soils under cyclic loading: A review, Soil Mechanics - transient and cyclic loads, Edited by G.N. Ponde and O.C. Zienkiewicz, John Wiley and sons, pp. 513-582.

Yamashita, k. and Kakurai, M. (1991), Settlement behaviour of raft foundation with friction piles, Proc. 4th Int. DFI Conf. Balkena, pp. 461-466. Cited by Mendoza, et al.

(2000b).

Zeevaert, L. (1949), An investigation of the engineering characteristics of the volcanic lacustrine clay deposits beneath Mexico City, PhD thesis, University of Illinois, (Cited by Mesri, et al., 1975).

Zeevaert, L. (1957), Compensated friction-pile foundation to reduce the settlement of buildings on the highly compressible volcanic clay of Mexico City, Proc. 4th ICSMFE, Vol. 3, pp. 81-86.

Zeevaert, L. (1982), Foundation engineering for difficult subsoil conditions, Van Nostrand-Reinhold Co., New York, N. Y.

Zeevaert, L. (1988), Seismo-geodynamics of the ground surface, Mexico City Government, Mexico, pp. 1-20.

APPENDIX A

DATABASE OF LABORATORY TESTS ON MEXICO CITY CLAY

This appendix gives details from tests conducted on Mexico City (MC) clay. The tests comprise ring shear on Bishop and Bromhead apparatus, and oedometer tests on intact, remoulded and reconstituted samples. Table A1 shows the experimental programme.

The main goal of the ring shear tests was to obtain the effective stress soil-to-concrete interface angles of friction for MC clay. This angles are applied in the Imperial College pile design method validation exercise. The ring shear study was extended to cover the response of this highly unusual clay to different rates of shearing, interfaces, apparatus and overconsolidation ratios.

The main features of the ring shear tests were described in Chapter 4. The details of the tests on Bromhead apparatus are presented in Table A2; the details of the tests on Bishop apparatus are presented in Tables A3 to A6.

The oedometer tests were performed in order to study the intrinsic properties of MC clay and their application to compute the sensitivity of MC clay (Chapter 3).

Table A1 Summary of laboratory tests on Mexico City clay samples

Sample	Atterberg limits	Hydro-meter	Oedometer Intact	Oedometer Recons.	Bishop ring shear: Soil-to-soil FS	Soil-to-soil RED	Soil-to-soil OC	Soil-to-soil CD	Soil-to-concrete FS	Soil-to-concrete RED	Soil-to-concrete OC	Soil-to-concrete CD	Soil-to-steel FS	Soil-to-steel RED	Soil-to-steel OC	Soil-to-steel CD
C134 SMC2 15.1-15.3	206-68				■	■	■		■	■		■	■	■		■
C142 SMC1 8.3-8.5	426-134		2		■				■	■						
M151 SMS-1 14.5-14.7	355-145	■			■		■	■	■	■			■	■	■	■
M162 SMS-1 17.2-17.4	275-130	■			■		■	■	■	■	■		■			

Sample	Bromhead ring shear: Soil-to-soil FS	Soil-to-soil RED	Soil-to-soil OC	Soil-to-soil CD	Soil-to-concrete FS	Soil-to-concrete RED	Soil-to-concrete OC	Soil-to-concrete CD	Soil-to-steel FS	Soil-to-steel RED	Soil-to-steel OC	Soil-to-steel CD
C134 SMC2 15.1-15.3	■				■				2			
C142 SMC1 8.3-8.5	2				1 1	■			■			
M151 SMS-1 14.5-14.7	■				■				■			
M162 SMS-1 17.2-17.4	■				2				■			

FS = Fast shearing previous slow shearing
RED = Rate effects study
OC = Evaluation of overconsolidation effect
CD = Slow shearing under change of shearing direction
A shaded square means that a test was carried out under the that condition

Table A2 Summary of Bromhead ring shear test results

Sample		P	PD	R	RD	FD	RR	S	IVD	FVD
		Soil-to-Soil								
C134		31.9	3.02	31.4	5.3	32.0	0.024	100	0.44	1.33
SMC2		C. 2								
15.1-15.3										
C142	2	33.9	6.31	33.8	8.55	33.6	0.025	72	0.94	2.02
SMC1		35.3	12.39	35.3	12.39	12.6	0.024	72	0.76	1.13
8.3-8.5		C. No orientated failure surface								
M151		32.5	7.9	32.5	7.9	36.0	0.024	100	0.53	1.46
SMS-1		C. 2, Surface material did not show orientation.								
14.5-14.7		C. 3, from 0.63 mm or 24.5° to 0.73 mm								
M162		33.5	12.2	33.2	12.2	104.9	0.024	100	0.85	2.6
SMS-1		C. 2, Material stuck to the top cap								
17.2-17.4										
		P	PD	R	RD	FD	RR	S	IVD	FVD
		Soil-to-Concrete								
C134		32.9	2.66	32.9	2.66	25.51	0.024	83.3	0.5	1.03
SMC2										
15.1-15.3										
C142		36.3	4.95	35.5	26.92	26.92	0.024	83.3	0.66	1.3
SMC1		C. 3 at 0.39 mm or 18.5°								
8.3-8.5		36.1	7.14	36.1	9.22	32.79	0.024	83.3	2.233	2.53
		C. Two FS cycles were applied								
M151		33.0	2.67	32.9	6.65	25.5	0.024	83.3	0.5	1.03
SMS-1										
14.5-14.7										
M162	2	32.4	4.5	29.4	33.75	142.1	0.024	100	0.59	1.12
SMS-1		C. 1, 3 from 0.4 mm or 19.9° to 0.82 mm								
17.2-17.4		34.3	2.99				0.024	100	0.672	0.836
		C. 3 at 0.5 mm or 19°								
		P	PD	R	RD	FD	RR	S	IVD	FVD
		Soil-to-Steel								
C134	2	33.1	2.35	31.6	5.99	33.76	0.024	100	0.29	0.42
SMC2		C. 1	The tests show racketing							
15.1-15.3		33.3	3.0	31.7	5.99	35.47	0.024	100	0.31	0.76
		C. 1 and 3 at 0.64 mm (or 25.9°) to 0.91 mm								
C142		34.0	9.37	33.95	9.87	36.3	0.024	100	0.63	1.07
SMC1		C. 3 at 0.41mm or 20.7° to 0.6mm								
8.3-8.5										
M151		32.5	7.9	32.3	7.91	42.4	0.024	100	0.89	1.43
SMS-1		C. 3 at 0.74 mm or 24.7° to 1.12 mm								
14.5-14.7										
M162		32.7	10.8	32.5	10.8	69.1	0.024	100	0.47	1.00
SMS-1		C. 1. No fine size particles at interface.								
17.2-17.4										

Normally consolidated tests

P = Peak friction angle
R = Residual friction angle
PD = Displacement at peak, mm
RD = Displacement at residual state, mm
FD = Final displacement
FS = Fast shearing
RR = Rate of shearing, mm/min
S = Vertical stress, kPa
IVD = Shearing initial vertical displacement, mm
FVD = Shearing final vertical displacement, mm

C = comments
C1. Failure at interface
C2. Failure in soil mass
C3. Plateau at start of test
C4. Fast shearing, pulse of 267 mm at 500 mm/min

Table A3 Bishop ring shear test results on sample Chapultepec 13-4

Soil-to-Soil								
	P	PD	R	RD	FD	RR	S	
RED	35.3	10.08	19.0	92.6	112.6	0.011	150	
	25.75	46.67	25.4		299.6	9.4	150	
	32.11	0.34	20.1	27.6	39.9	0.012	150	
	29.28	7.14	29.6		297.5	47.0	150	
	36.3	0.47	20.0	37.4	37.4	0.012	150	
	28.39	5.06	7.4		300.1	184.0	150	
	33.73	0.52	20.4	22.8	22.8	0.012	150	
	28.24	7.66	8.6		301.2	278.0	150	
	34.46	0.45	19.9	30.6	41.5	0.012	150	
	28.56	13.37	8.9		304.1	365.0	150	
	33.36	0.56	19.3	46.5	64.2	0.012	150	
Surface looked aligned and with some polished areas.								
1st and 2nd FS showed light trend to a low bound just after								
fast peak. 1st, 2nd and 4th slow shearing stages showed								
plateau at the start of shearing.								
OC	34.7	14.73	33.8	30.6	30.6	0.010	400	
	39.7	0.78	29.67	35.66	35.66	0.011	300	
	36.4	0.38	28.6	25.01	35.01	0.011	200	
	35.27	0.28	26.78	59.16	74.94	0.009	100	
After 16 hours of finishing the shearing the test was dismantled.								
The surface looked irregular with a thin layer of fine granular								
particles. The surface was aligned but this was not continuous for								
more than 1/4 of the perimeter.								
The higher the OCR the faster the residual is obtained.								
There were plateaus at the start of all the slow shearing, this								
were function of axial stress but did not show an specific trend.								

Soil-to-Concrete								
FS	P	PD	R	RD	FD	RR	S	
RED	32.05	2.74	28.7	15.81	55.6	0.011	150	
	29.3	1.3	19.49		293.5	55	150	
	31.81	0.35	25.09	25.09	27.78	0.01	150	
	25.3	3.07	12.19		300.82	150	150	
	33.33	0.36	24.91	45.9	48.6	0.01	150	
	26.58	3.8	10.91		305	305	150	
	32.22	0.44	26.55	41.56	45.12	0.01	150	
	21.55	7.08	10.2		304.58	425	150	
	31.25	0.36	25.9	36.79	48.66	0.01	150	
	26.29	7.24	10.47		305.06	543	150	
	31.73	0.48	24.4	63.2	68.28	0.01	150	NoC
	-	-	9.87		404.41	202	150	NoC
	26.0	0.62	30.9	23.25	36	0.011	150	NoC
	26.6	4.97	22.61	47.92	50.91	0.01	150	NoC-ChDir
The ring of soil separated in one piece from the top porous								
stone. The sample didn't show any type of disturbance at								
its sides. The surface was plane, with fine grains and								
it was not polished.								

Soil-to-Steel								
	P	PD	R	RD	FD	RR	S	
RED	31.5	3.6	29.0	19.33	32.72	0.01	150	
	33.2	0.5	32.0		295.74	3.5	150	
	38.4	0.5	32.8	62.8	74.28	0.01	150	
	37.0	4.9	32.2		299.2	17.1	150	
	39.8	0.4	33.7	16.33	29.41	0.01	150	
	41.4	0.9	32.6		298.5	53	150	
	40.6	0.46	33.9	14.66	32.25	0.01	150	
	x	2.3	30.8		300.63	138	150	
	37.9	0.44	33.6	5.55	45.11	0.01	150	NoC
	31.5	2.07	32.8	41.44	46.21	0.01	150	NoC-ChDir
The surface was not polished. Fine granular particles								
appeared at the failure surface, which looked waivy.								
It was difficult to separate interface and soil.								
Failure surface was soil-on-soil.								
The 2nd, 3rd and 4th FS showed an initial residual strength lower								
than slow residual and then recover to residual								

P = Peak friction angle
R = Residual friction angle
PD = Displacement at peak, mm
RD = Displacement at the end of test, mm
FS = Fast shearing
RR = Rate of shearing, mm/min
S = Vertical stress, kPa
NoC = Shearing without consolidation
Ch.Dir = Change of direction of shearing
OC = Evaluation of over-consolidation effects

The peak values at rates higher than 50 mm/min could not be recorded

Fast shearing consists of 200 mm pulse at 500 mm/min

Table A4 Bishop ring shear test results on sample Chapultepec 14-2

Soil-to-soil								
FS	P	PD	R	RD	FD	RR	S	
	37.11	20.3	37.5	22.2	94.3	0.009	104.8	
	Failure surface aligned and with fine particles at the failure surface.							

Soil-to-concrete							
P	PD	R	RD	FD	RR	S	
38	2.4	35.5	16.1	20.96	0.009	102.3	
4 FS pulses simulating pile installation were applied previous to drained shearing.							

Soil-to-steel							
P	PD	R	RD	RR	S		

P = Peak friction angle
R = Residual friction angle
PD = Displacement at peak, mm
RD = Displacement at the end of test (residual), mm
FS = Fast shearing
RR = rate of shearing, mm/min
S = Vertical stress, kPa
NoC = Shearing without consolidation

Ch. Dir. = Change of direction of shearing
Ch. RR = Changing rate
Fast shearing, 500 mm/min, for 200 mm

The peak values at rates higher than 50 mm/min were not recorded.

Table A5 Bishop ring shear test results on sample Piedad 15-1

Soil-to-soil									
		P	PD	R	RD	FD	RR	S	
	RED	35.4	13.7	35.0	15.9	37.6	0.012	150	
		38.6	0.7	29.3		299.7	3.8	150	
		38.17	0.7	35.0	24.7	86.5	0.012	150	
		40.17	0.59	28.3		297.7	17.9	150	
		39.43	0.45	35.8	11.2	34.1	0.012	150	
		40.8	1.6	25.9		276.0	47.9	150	
		40.02	0.48	36.6	7.7	37.7	0.012	150	
		41.51	2.08	16.9		297.6	125.0	150	
		37	0.67	35.3	6.6	53.2	0.012	150	No.C
		34.8	4.23	33.0	11.5	50.6	0.0	150	No.C
									ChDir
		1st FS showed low residual after peak.							
		All the initial slow shearings showed plateau at the start.							
		The two sample halves separated easily. The surface							
		was not polished and it was concaved.							
		39.0	8.49	39.13	11.2	11.2	0.008	104.2	
		From the side was possible to see the location of the							
		failure surface. The failure surface looked orientated but							
		didn't shine.							
Soil-to-Concrete									
		P	PD	R	RD	FD	RR	S	
		37.5	1.4	31.2	17.42	20.96	0.009	87.95	
		5 FS pulses were applied previous the slow shearing.							
		Sample separated easily from interface. Soil-to-soil							
		failure.							
Soil-to-Steel									
		P	PD	R	RD	FD	RR	S	
	RED	36.6	9.662	36.1	15.1	16.5	0.012	150	
		41.8	0.66	35.3		199.4	3.8	150	
		44.6	0.408	35.1	4.3	68.8	0.012	100	
		42.2	0.389	31.4		183.9	3.9	100	
		40.8	0.29	34.0	6.0	39.2	0.012	100	
		41.8	6.11	32.1		298.2	17.9	100	
		40.6	0.29	32.2	13.5	29.2	0.012	100	
		38.4	0.785	26.6		299.4	46.9	100	
		33.9	0.23	31.8	9.4	236.2	0.012	100	No.C
									ChDir
		The interface separated easily from the sample. The soil							
		surface is orientated but not shining. Fine granular particles							
		were at the failure surface. Failure soil-to-soil.							
		It was observed a reduction in shear strength with							
		increasing rate.							
		2nd, 3rd and 4th slow shearing shown plateou at start.							
		1st, 3rd and 4th FS show low after peak and then recovery.							
		34.8	5.33	34.47	14.01	14.01	0.009	87.6	
		Material strongly bound to interface.							
		Show plateau at the start.							
		35.5	2.57	35.52	4.23	13.67	0.009	88.0	
		Show plateau at the start							

P = Peak friction angle
R = Residual friction angle
PD = Displacement at peak, mm
RD = Displacement at the end of test (residual), mm
FS = Fast shearing
RED = Rate effects study
RR = rate of shearing, mm/min
S = Vertical stress, kPa

NoC = consolidation

Ch. Di of shearing

Ch. RR = Changing rate
Fast shearing, 500 mm/min, for 200 mm

The peak values at rates higher than 50 mm/min might not be recorded

Table A6 Bishop ring shear test results on sample Piedad 16-2

Soil-to-Soil									
		P	PD	R	RD	FD	RR	S	
	OC	36.19	11.42	35.8	13.7	13.7	0.009	400	
		53.0	0.359	40.2	27.3	27.3	0.010	100	
		No well defined failure surface, which has flocks of degraded material. The lower section of the sample became concaved. It seems from the deformed blades that the two porous stone could have been in contact. 1st drained shearing showed small plateau at the start.							
		35.69	10.09	35.5	19.5	701.6	0.011	105	ChRR
		The two halves of the sample separated when dismantling it. The surface showed aligment but doesn't shine. The sample failure surface was concave. No signals of shearing were seen at the sides of the sample.							
Soil-to-Concrete									
		P	PD	R	RD	FD	RR	S	
	OC	36.71	3.45	36.38	6.45	30.36	0.009	100	
		34.25	6.298	32.4	24.81	26.39	0.008	400	
		35.6	0.275	31.86	28.03	31.59	0.01	200	
		36.02	0.353	31.62	21.57	30.148	0.01	300	
		3 pulses of FS were applied previous to first slow shearing. The first slow shearing shows plateau at the start. The interface and the sample separated easily. The sample surface is aligned. At the top there is a very thin layer of fine granular material not continuous and very loose that shine as it were wet. The irregularities on the concrete surface produced chanels (until 3 mm wide) during shearing. From a lateral view is possible to observe some loose material at the interface and soil contact. In some of the chanels the surface was polished.							
Soil-to-Steel									
		P	PD	R	RD	FD	RR	S	
		35.8	27.18	37.1	39.1	142.8	0.009	100	ChRR
		Reduction of strength with increment of slow rate was observed. When the sample was removed a very thin layer of soil was left stick to the interface. The soil failure surface was aligned.							

P = Peak friction angle
R = Residual friction angle
PD = Displacement at peak, mm
RD = Displacement at the end of test, mm
FS = Fast shearing
OC = evaluation of overconsolidaiton effects.
RR = Rate of shearing, mm/min
S = Vertical stress, kPa
NoC = Shearing without consolidation
Ch. Dir. = Change of direction of shearing
Ch. RR = Change of rate of shearing
Fast shearing: 500 mm/min, for 200 mm
The peak values at rates higher than 50 mm/min might not be recorded

APPENDIX B

APPLICATION OF THE IMPERIAL COLLEGE PILE DESIGN METHOD TO THE WD58A TENSION PILE RESEARCH RESULTS

B1 Introduction

This appendix presents a detailed description of the application of the Imperial College (IC) pile design method to the WD58A pile test programme (Chan and Birrell, 1998; Matlock, et al., 1998; Audibert, and Hamilton, 1998; Bogard and Matlock, 1998a, b, c). The case history is important because it represents a full scale offshore loading test to failure that included cyclic loading stages.

Dr. Jean Audibert from Fugro kindly provided information on the original WD58A test programme and soil samples from a nearby site. This validation follows from the alternative interpretation of these tests involving the IC method that was presented in Jardine and Saldivar (1999). Special feature was underconsolidated initial conditions.

The IC method calculations are presented in the following pages. The assumptions and soil properties are explained and referred to in the related figures and spread sheets. Where scatter exists, the interpretation made for the analyses are shown in red.

Three spreadsheets are presented. Sheet B1 includes the predictive analysis presented by Jardine and Saldivar (1999), when no information on δ values was available. Sheet B2 and B3 present the revised predictions made in 2000, the only change being (i) the adoption of the measured δ values and (ii) account being taken of progressive failure influencing the position of the operational δ values between the limits of the observed peak and residual angles.

The IC method predicts the pile capacity for the "fully equalised" condition. The WD 58A pile test that most closely matches this state was carried out 16 months after driving.

Following Bogard and Matlock (1998c) it was assumed that the reported pile loads have been corrected for the weight of the pile.

B2 Evaluation of pile capacity

These notes present the calculations shown in the spreadsheets, following Jardine and Chow (1996).

E Shaft capacity of closed-ended piles in clay

E1 Shaft capacity: Integral of local shear stresses along the embedded shaft length

$$Q_s = \pi D \int \tau_f dz$$

The pile parameters are presented in spreadsheet B1, while Figs. B1 and B2 define the soil profile. The number and lengths of sections into which the pile was divided for analysis are presented in columns A and B of spreadsheet B1, respectively. The average shear stress (τ_f) acting on each section, and its contribution to capacity (Q) are shown in columns L and M of this sheet.

E2 Local shear stress: Coulomb failure criterion

$$\tau_f = \sigma'_{rf} \tan\delta_f$$

$$\sigma'_{rf} = 0.8\sigma'_{rc}$$

A laboratory study in the Bishop Ring Shear apparatus was carried out with samples of Gulf of Mexico clay provided by Dr. Audibert. The results of these tests are presented in Figs. B3 to B7.

E3 Local radial effective stress: For closed ended piles σ_{rc}' is a function of free-field effective overburden pressure, σ_{v0}'; I_{vr} and ΔI_{vy}; YSR; and h/R ratio.

F3 Modified radius, R^*: For open-ended piles K_c is taken from either of the expressions given in Step E3, but with $R^* = (R^2_{outer} - R^2_{inner})^{1/2}$ substituted for R in the h/R terms. Lower limit: $h/R^* = 8$. The cross sectional area of the instrumentation was taken into account for these calculations.

Spread sheet B1 shows: σ_{v0}' in column E, σ_{vy}' in column F, S_t in column G, h/R^* in column H, YSR in column I, and K_c and σ_{rc}' values in columns J and K respectively. Profiles of S_t and σ_{vy}' are shown in Figs. B8 and B9. As explained in OTC 10827, YSR is obtained considering $\sigma_{v0}' = \sigma_{vy}'$.

E4 Interface angle of friction: δ should be measured in interface ring shear test. The operational values depend on the degree of progressive failure, pile roughness, clay type and shearing history.

The procedure applied to determine δ is explained in Fig. B3. The approach followed in allowing for progressive failure is summarised below. The δ values are shown in column S of spreadsheets B2 and B3.

Progressive failure

The effect of progressive failure on the long and relatively flexible WD58A piles was taken into account using the following simplified *t-z* procedure:

- Firstly, the pile capacity was estimated taking $\delta = 19^{o}$ along the entire pile, as in Jardine and Saldivar (1999). Column N in spreadsheets B2 and B3 shows the computed axial loads (F) at each pile section.
- The axial loads were then used to calculate the local elastic strain ($d\lambda$) in the pile:

$$d\lambda = \frac{F}{(AE)_p} L$$

L is the length of each subsection. The stiffness (AE) was obtained from the slope of the axial strain vs. axial load curves presented in Bogard and Matlock (1998b) – see paper for details. AE values are shown in column O of the spreadsheets B2 and B3.

- Using the total displacement at pile head and pile base reported in Bogard and Matlock (1998c), the distribution of soil-pile relative movement with depth was computed. The displacement at mudline level for peak capacity determined from Fig. B9 was 25.37 mm, while for residual condition the displacement at pile base level determined from Fig. B11b was 42.16 mm – column P in spreadsheets B2 and B3 shows the soil-pile relative displacements (d).
- Ring shear test data was used to check the rate of post peak softening. For computing peak capacity it was considered that peak transfer of load occurred at a displacement of 8.7 mm along the entire pile. Applying this condition, the so-called corrected displacements were computed (column R) and the operational δ values modified to reflect any post peak movement and the accompanying reduction from peak δ. The following criteria were applied:

  If d < peak displacement then δ_{peak} is taken as in API ISO Draft #3B

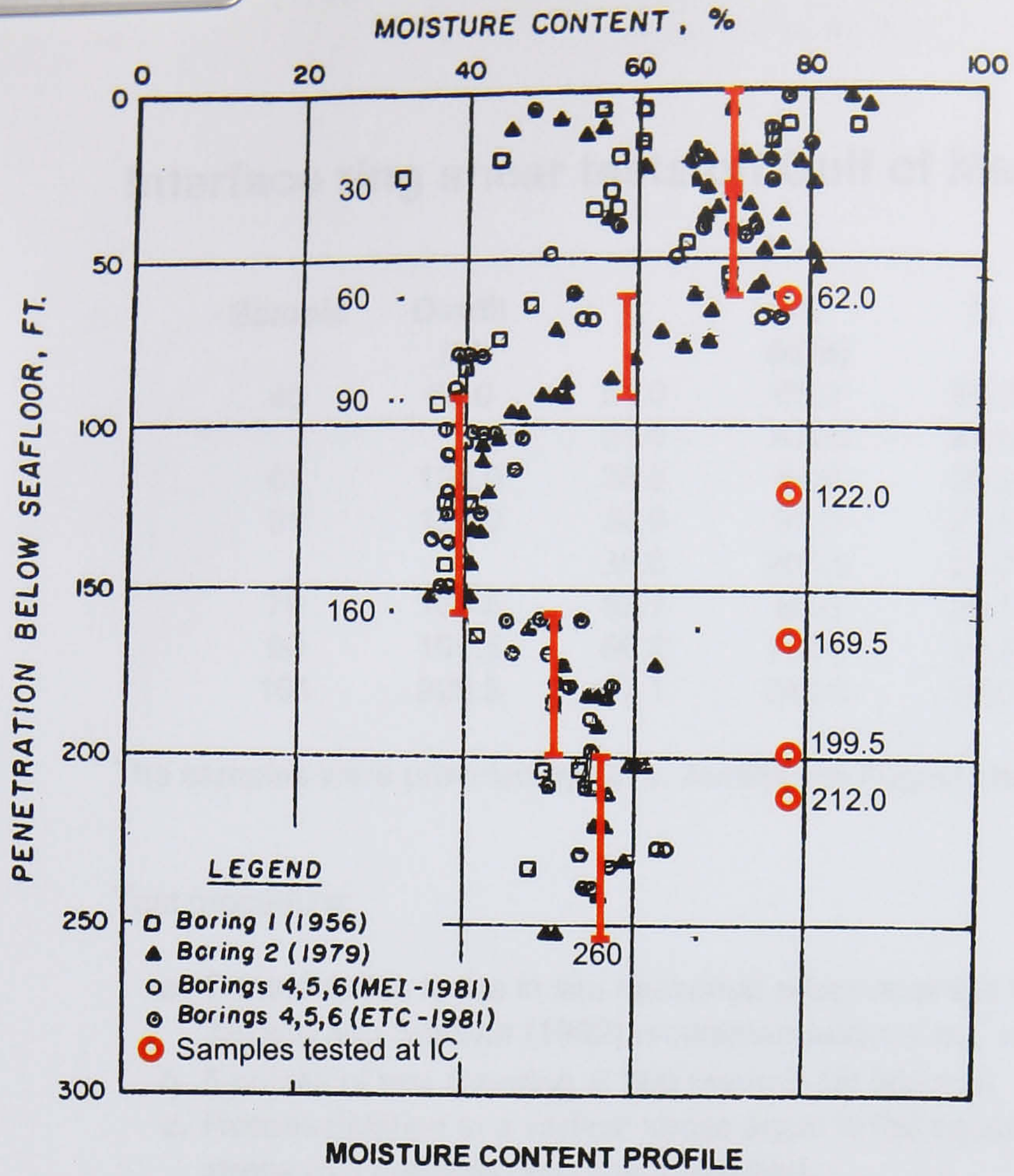
  If d > displacement to residual then $\delta_{residual}$ is taken

If d is in between, the non-linear trend in the ring-shear is applied to δ.

The modified δ values are presented in column S. Figs. B3 to B7 show the location of the peak and ultimate δ values.

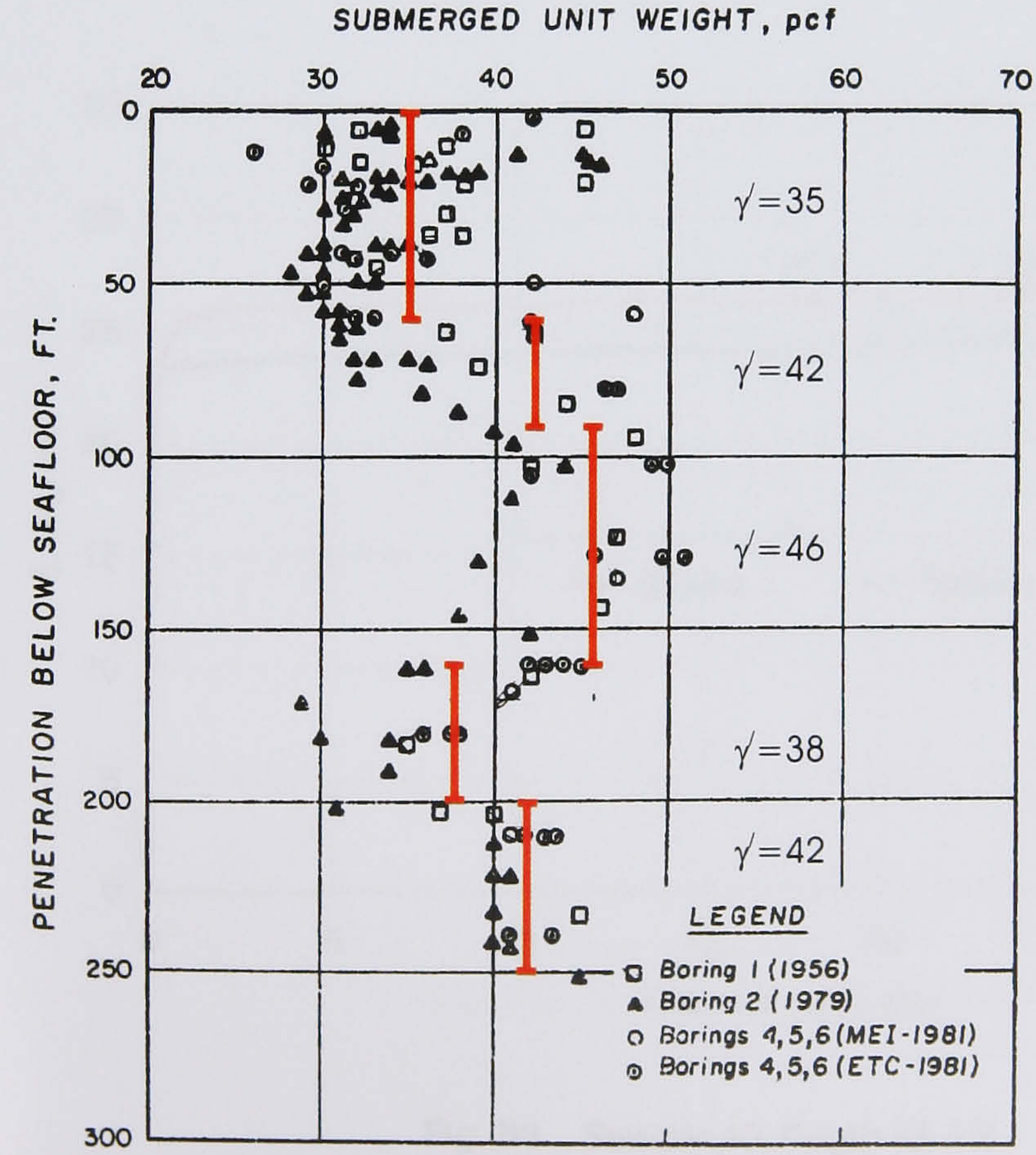
Conclusions

- The IC pile design method is demonstrated and verified using data from the pile test programme at the Gulf of Mexico WD58A site, which involved tests on large instrumented driven piles.
- The analysis presented included measured δ values and allowance for the progressive failure mechanism. This analysis confirmed that the IC pile design method produced good predictions for the tension pile test carried out on April 1985 at the WD 58A site. The method predicts the peak capacity within 4% and the residual within 8%. Fig. B10 shows a summary of the static WD58A test results and the predictions using the IC design method.
- Progressive failure was included considering a simplified t-z method based on the API ISO draft.
- The samples from WD58A showed a range of δ values, some of which were higher than might be expected for "plastic" clays. The three shallower samples, for example, showed high δ values and no significant post-peak softening of δ.
- As mentioned in Jardine and Saldivar (1999), a good match between the predicted and measured σ_r' profiles was obtained.
- Overall, very good agreement was obtained with the field measurements. However, we emphasize that the site's underconsolidated initial stress conditions must be accounted for, as described in Jardine and Saldivar (1999), when assessing the σ_{v0}' and σ_{vy}' profiles adopted for analysis.



MOISTURE CONTENT PROFILE

Fig. B1 Moisture content vs depth profile (Audibert and Hamilton, 1998)



SUBMERGED UNIT WEIGHT PROFILE

Fig. B2 Submerged unit weight vs depth profile (Audibert and Hamilton, 1998)

Interface ring shear tests on Gulf of Mexico samples

Sample	Depth (ft)	I_p	σ_v' (kPa)	δ_p	δ_u
40	62.0	51.0	65.0	26.3	26.3
		51.0	100.0	24.6	24.6
61	122.0	36.0	64.0	33.0	33.0
61	122.0	36.0	99.0	27.2	27.2
		36.0	201.0	24.0	24.0
79	169.5	52.7	82.0	23.1	22.9
90	199.5	69.2	144.0	19.3	12.2
101	229.5	67.1	262.0	18.0	13.2

The samples were provided by Dr. J. Audibert of Fugro Limited.

Test procedure:

a. Consolidation to the in situ horizontal effective stress following Jardine and Saldivar (1999) recommendation of $\sigma_{v0}' = \sigma_{vy}'$ and k_0=0.5.
b. 5 pulses of fast shearing at 500 mm/min for 200 mm.
c. Reconsolidation at a vertical stress equal to the equalized effective radial stress (σ_r') predicted with the IC method.
d. Slow shearing at 0.005 mm/min
e. Sand blasted steel interfaces were used as interfaces.

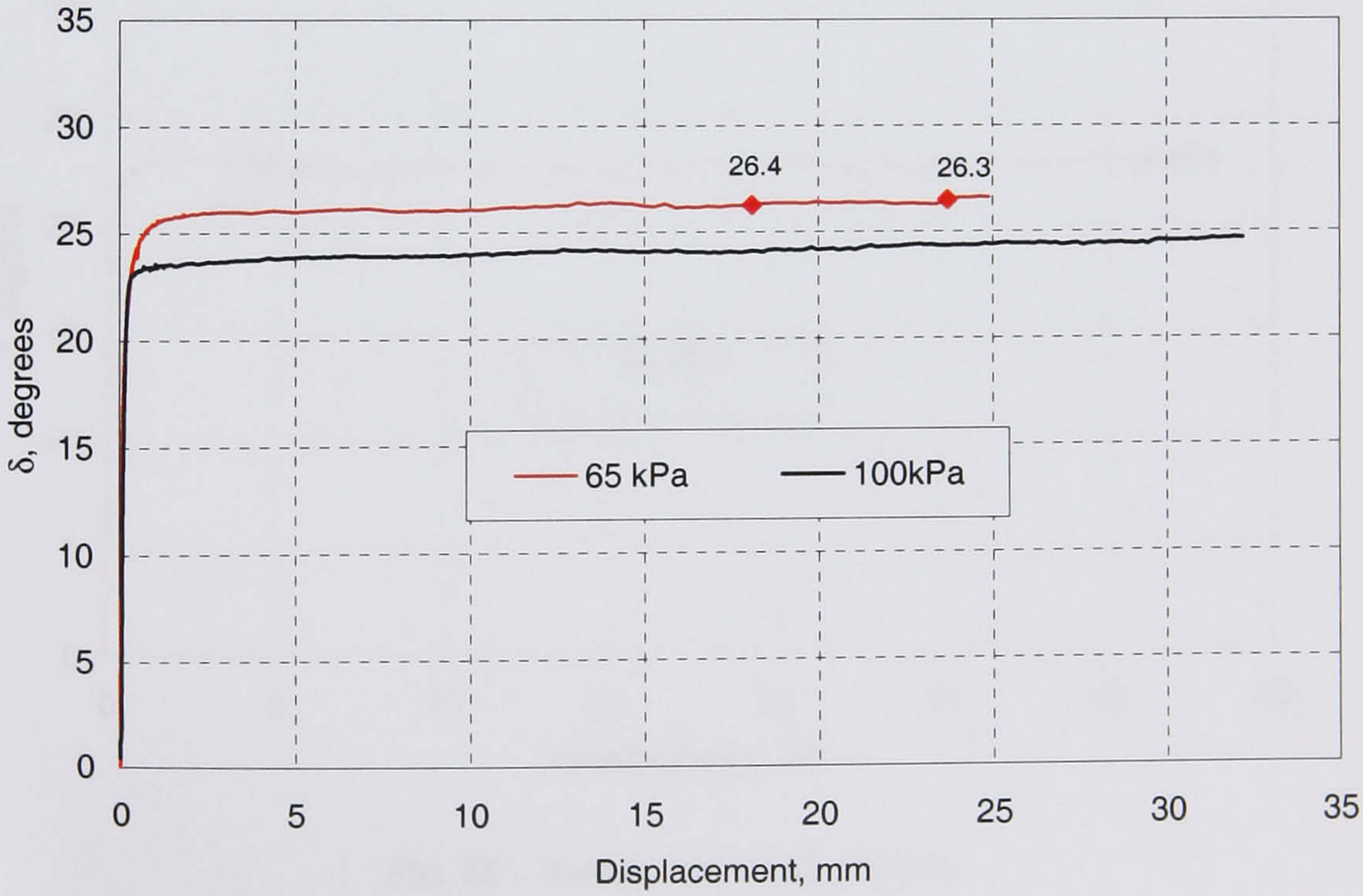


Fig. B3 Sample 40, Depth 62.0 ft

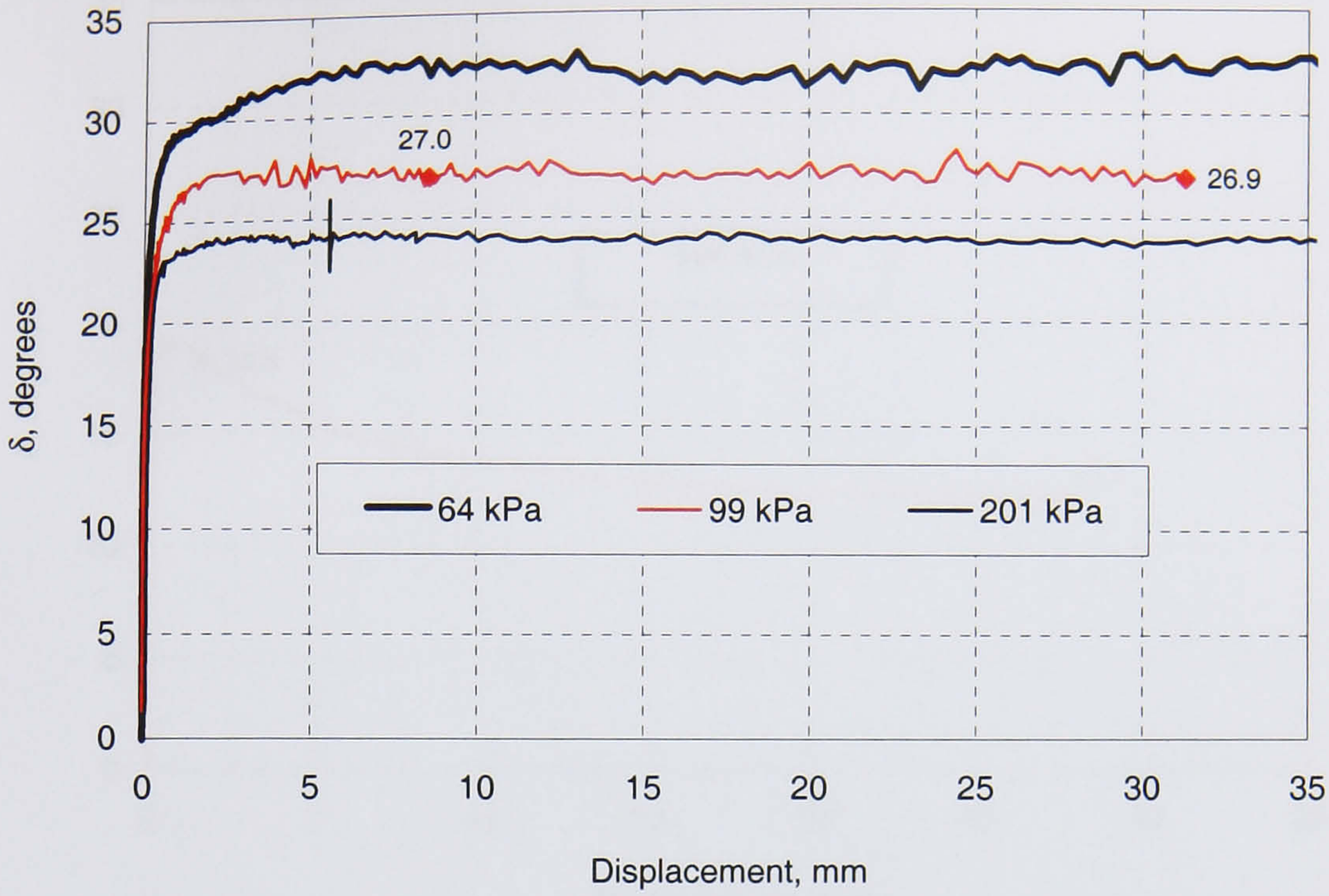


Fig. B4 Sample 61, Depth 122 ft

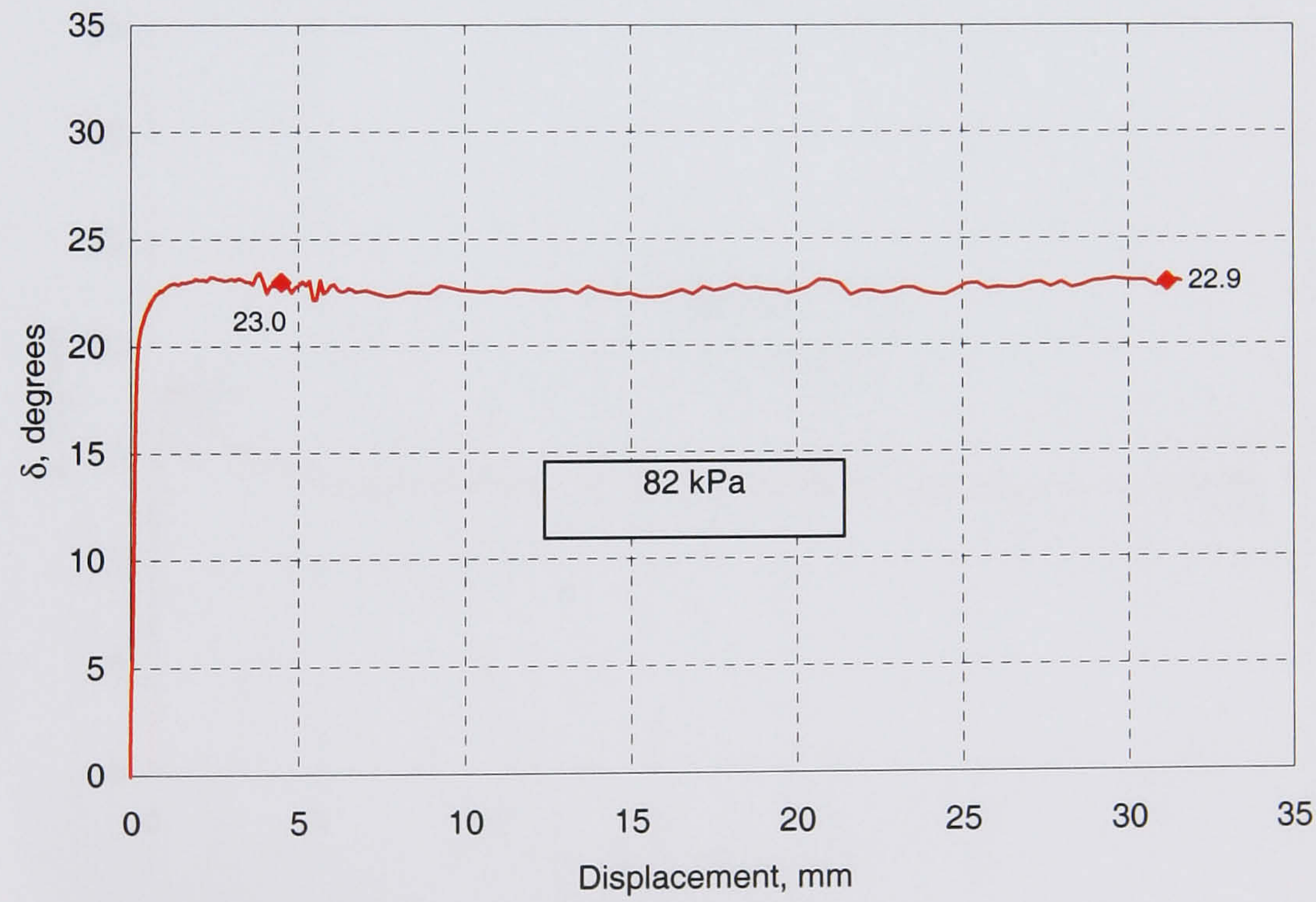


Fig. B5 Sample 79, Depth 169.5 ft

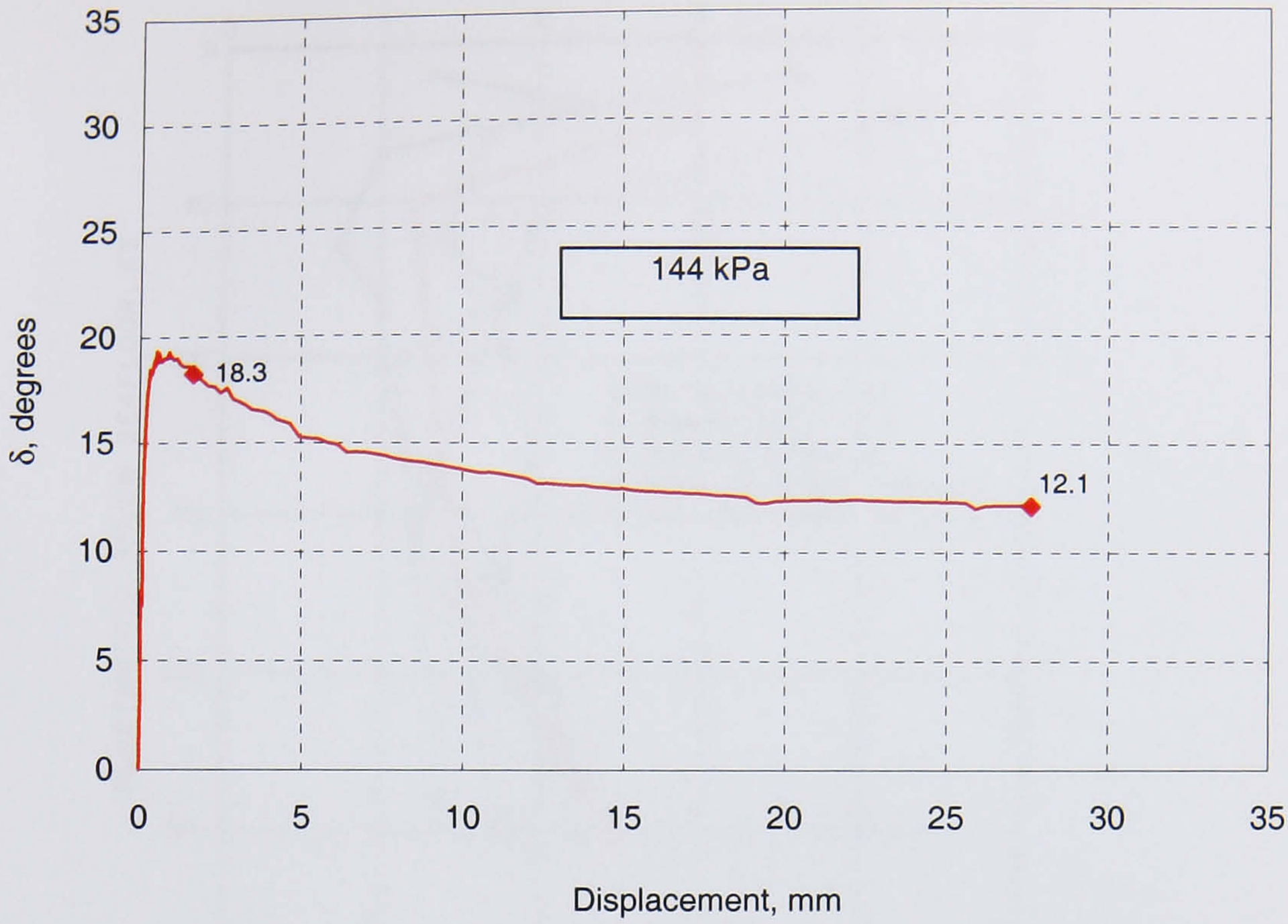


Fig. B6 Sample 90, Depth 199.5 ft

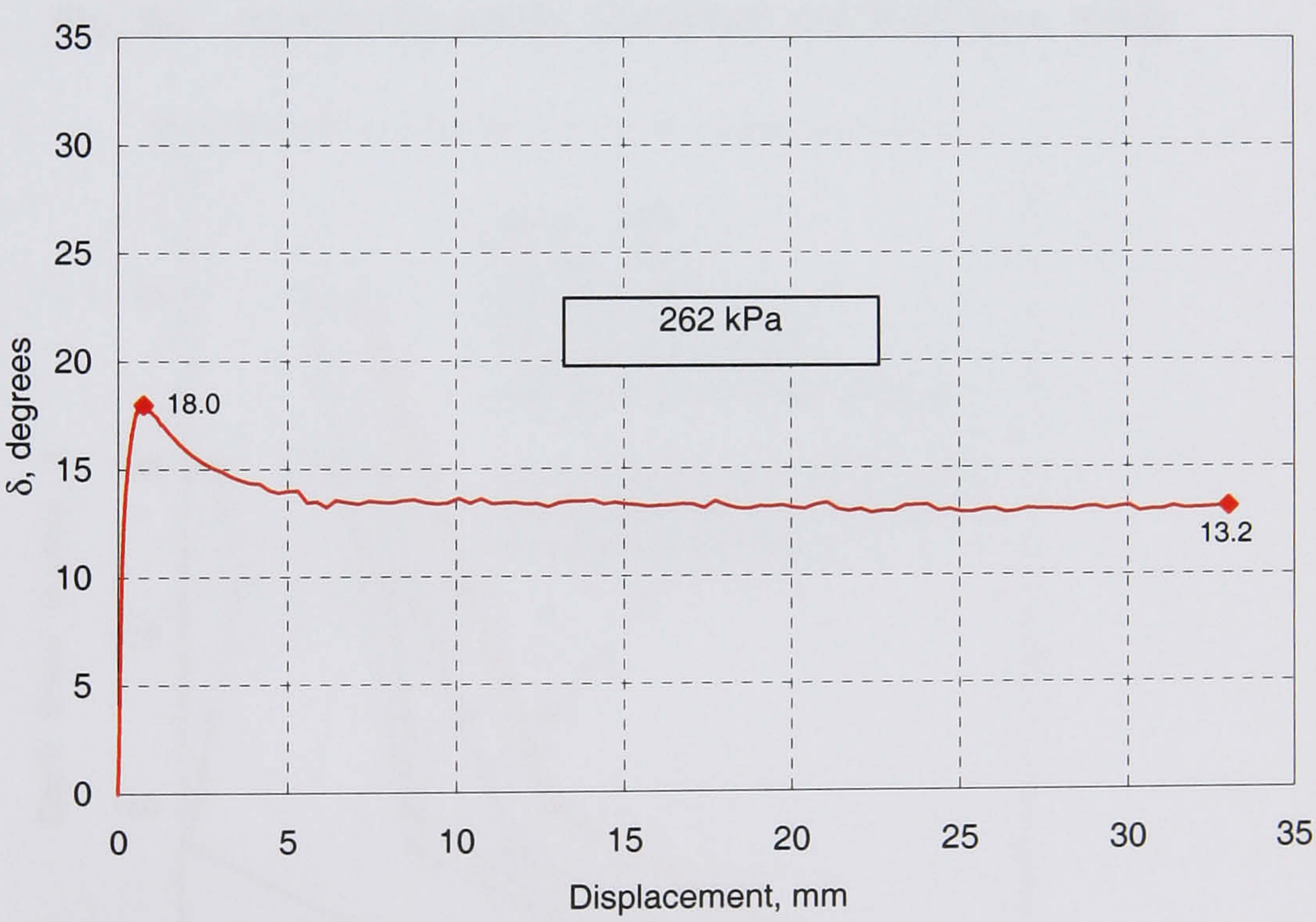


Fig. B7 Sample 101, Depth 229.5 ft

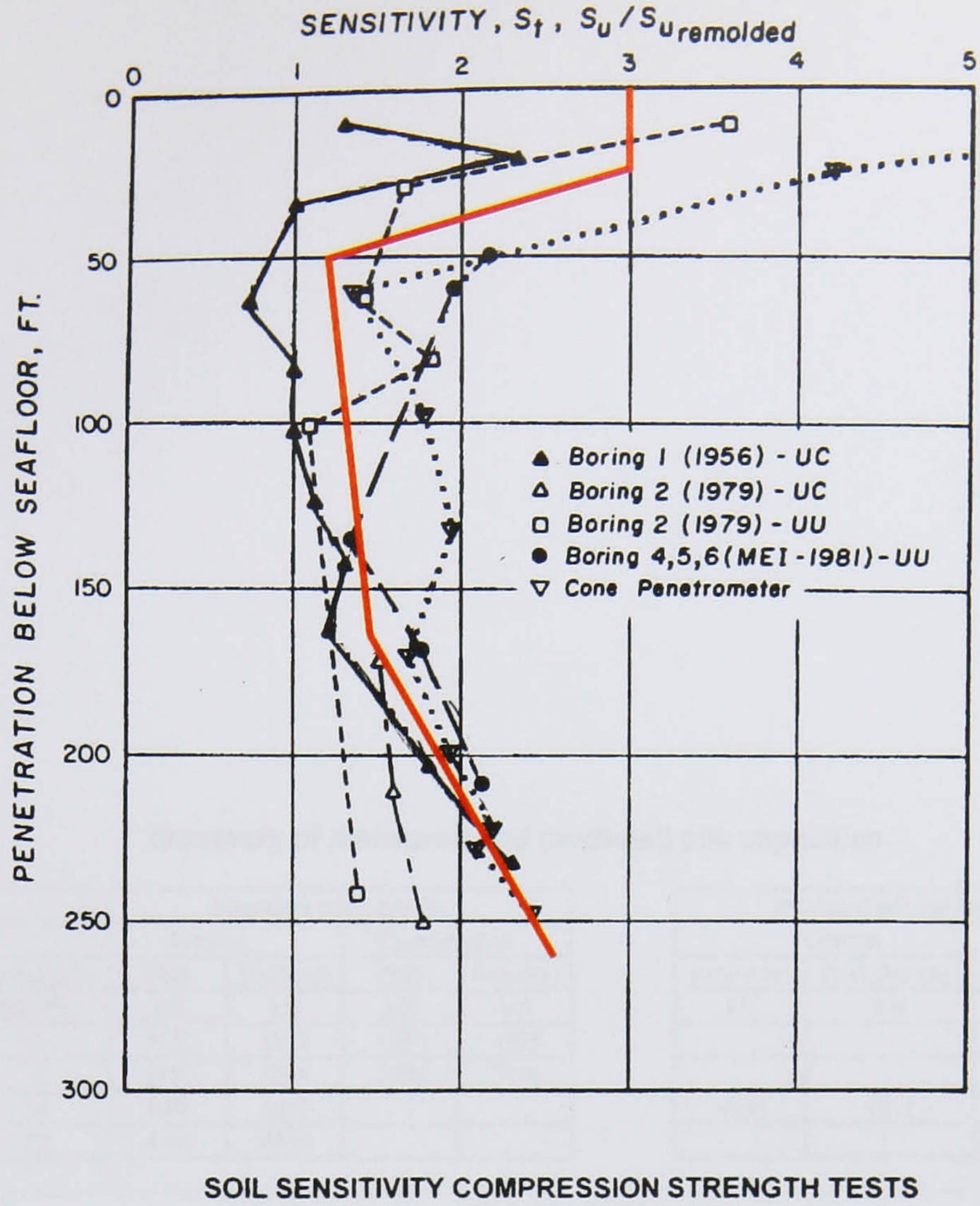


Fig. B8 Sensitivity profile (Audibert and Hamilton, 1998)

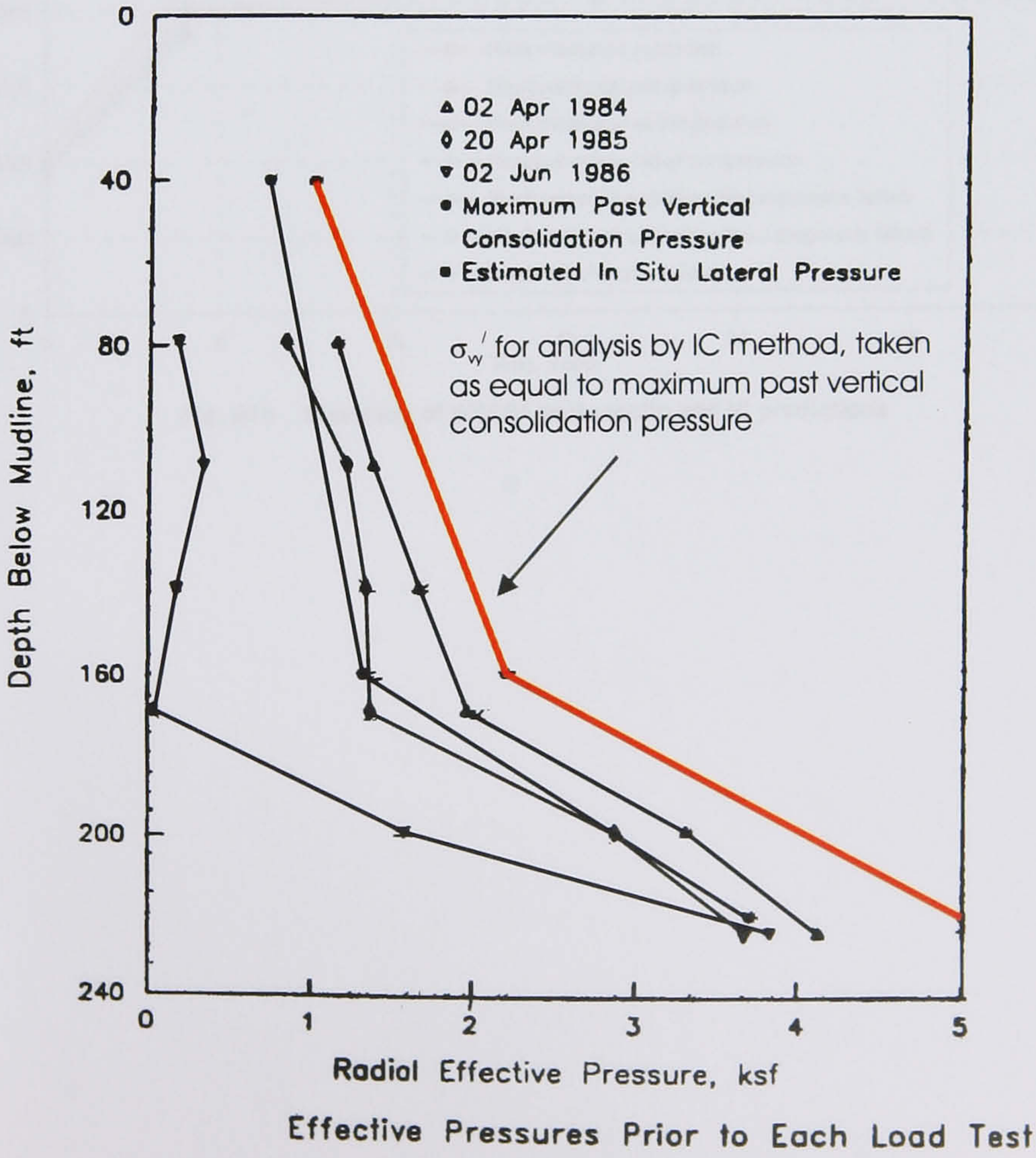


Fig. B9 Yield stress profile (Bogard and Matlock, 1998a)

Summary of measured and predicted pile capacities

	Measured pile capacity			
	Tension		Compression	
Set up time	Peak	Residual	Peak	Residual
Months	kN	kN	kN	kN
0	2132	1972	1903	1903
4	4403	4014	3858	3714
16	4955	4473		
29	4742	4349		

Predicted pile capacity		
Tension		
Peak-Pro.	Peak-No pro.	Residual
kN	kN	kN
4804	4871	4133

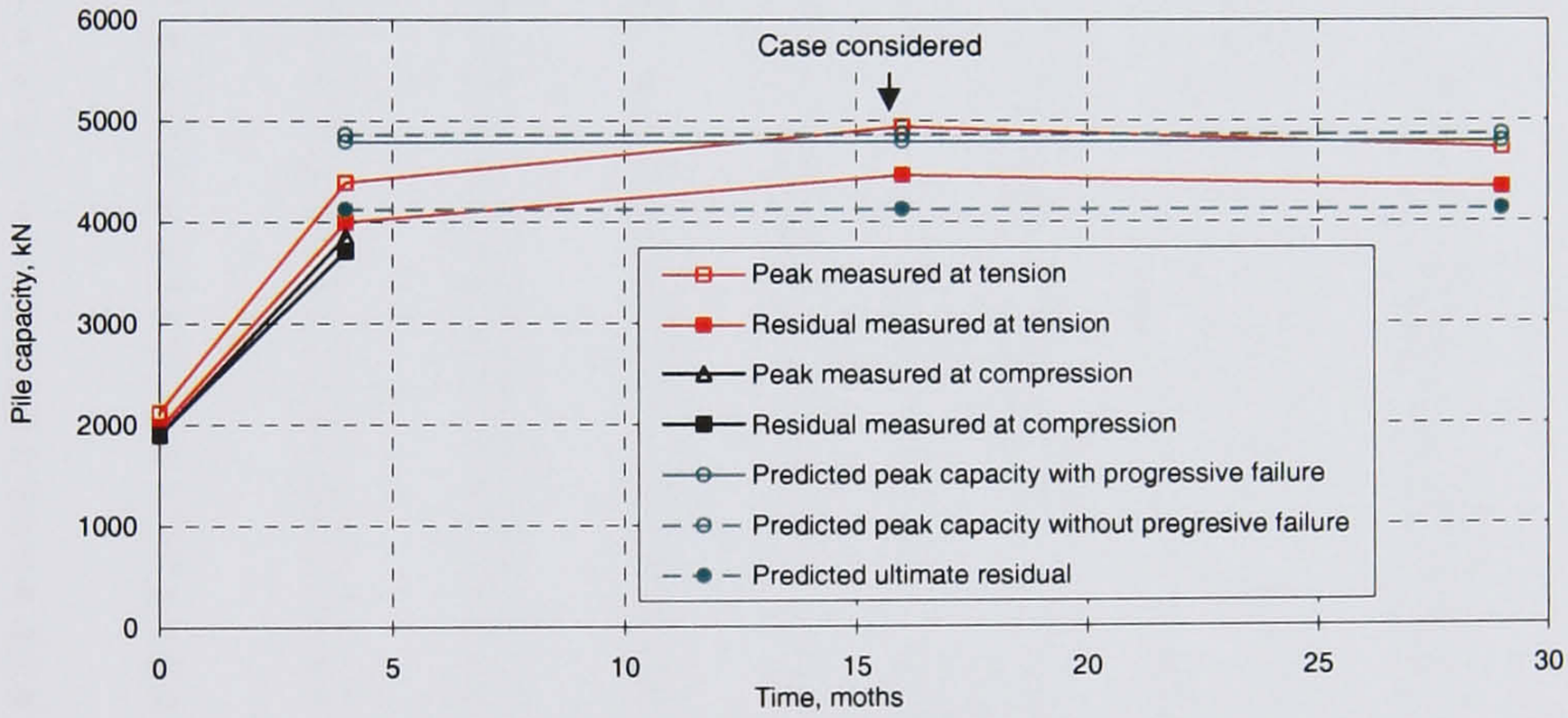


Fig. B10 Summary of WD58A test results and IC predictions

IMPERIAL COLLEGE PILE DESIGN METHOD

Tension test on open ended steel pile by CONOCO

West Delta 58A site

SPREAD SHEET B1 - 1999 OTC PAPER ANALYSIS

Friction angle = 19

Pile diameter (m) = 0.762 Pile length (m) = 71.3 $\sigma_{v0}'=\sigma_{vy}$

Wall thickness (m) = 0.019 Equivalent radius, R* (m) = 0.155 *Friction angle to match the test result*

A	B	C	D	E	F	G	H	I	J	K	L	M
Section No.	Thickness m	Mean depth m	ft	σ_{v0}' kPa	σ_y kPa	S_t	h/R*	YSR	k_c	Radial stress (kPa)	Shear stress (kPa)	Section cap. (kN)
1	4.6	2.3	7.5	11.27	11.27	3.0	445.1	1.0	0.53	4.80	1.65	18.07
2	4.6	6.9	22.5	30.18	30.18	3.0	415.6	1.0	0.54	13.02	4.48	49.06
3	4.6	11.4	37.5	48.9	48.9	2.0	386.1	1.0	0.59	23.23	8.00	87.53
4	4.6	16.0	52.5	53.8	53.8	1.2	356.7	1.0	0.66	28.53	9.82	107.51
5	3.0	19.8	65.0	61.1	61.1	1.2	332.1	1.0	0.67	32.86	11.32	82.57
6	3.0	22.9	75.0	66	66	1.3	312.4	1.0	0.68	35.68	12.28	89.64
7	4.6	26.7	87.5	73.3	73.3	1.3	287.9	1.0	0.69	40.22	13.85	151.58
8	4.6	31.2	102.5	80.6	80.6	1.3	258.4	1.0	0.70	44.82	15.43	168.91
9	3.0	35.1	115.0	88	88	1.4	233.8	1.0	0.71	49.72	17.12	124.92
10	3.0	38.1	125.0	92.9	92.9	1.4	214.2	1.0	0.72	53.21	18.32	133.68
11	3.0	41.1	135.0	95.8	95.8	1.4	194.5	1.0	0.73	55.79	19.21	140.17
12	3.0	44.2	145.0	100.2	100.2	1.4	174.9	1.0	0.74	59.61	20.53	149.77
13	3.0	47.2	155.0	105.1	105.1	1.4	155.2	1.0	0.76	63.71	21.94	160.06
14	3.0	50.3	165.0	118.5	118.5	1.5	135.6	1.0	0.77	73.43	25.29	184.50
15	3.0	53.3	175.0	141.7	141.7	1.6	115.9	1.0	0.79	89.31	30.75	224.39
16	3.0	56.4	185.0	163.7	163.7	1.7	96.3	1.0	0.81	105.65	36.38	265.44
17	3.0	59.4	195.0	188.2	188.2	1.8	76.6	1.0	0.84	125.79	43.31	316.03
18	3.0	62.5	205.0	216.7	216.7	1.9	57.0	1.0	0.88	151.82	52.27	381.42
19	3.0	65.5	215.0	237	237	2.0	37.3	1.0	0.94	178.95	61.62	449.60
20	1.2	67.7	222.0	254	254	2.1	23.6	1.0	1.03	209.08	71.99	210.12
21	1.8	69.2	227.0	266.3	266.3	2.2	13.7	1.0	1.14	242.40	83.47	365.41
22	1.5	70.9	232.5	278.6	278.6	2.2	8.0	1.0	1.26	281.05	96.77	353.05
	71.6		235								**Shaft capacity =**	**4213.4**

IMPERIAL COLLEGE PILE DESIGN METHOD
Tension test on open ended steel pile by CONOCO
West Delta 58A site
SPREAD SHEET B2 - 2000 ANALYSIS

PREDICTED PEAK CAPACITY CONSIDERING MEASURED δ AND PROGRESSIVE FAILURE

N	O	P	Q	R	S	T	U	V	W	X
Axial load	AE	Pile deformation		Correction		Shear stress	Section cap.	Axial load	Pile deformation	
(kN)	kN	mm	in	mm	δ	(kPa)	(kN)	(kN)	mm	in
4195.37	1.42E+07	25.37	0.999	18.74	*26.4*	2.38	26.05	4778.10	26.38	1.039
4146.31	1.42E+07	24.02	0.946	17.39	*26.4*	6.46	70.73	4707.37	24.84	0.978
4058.78	1.42E+07	22.68	0.893	16.05	*26.4*	11.53	126.20	4581.18	23.32	0.918
3951.26	1.42E+07	21.37	0.842	14.74	*26.4*	14.16	155.00	4426.18	21.85	0.860
3868.69	1.42E+07	20.10	0.791	13.47	*26.4*	16.31	119.04	4307.14	20.42	0.804
3779.06	1.20E+07	19.27	0.759	12.64	*26.4*	17.71	129.23	4177.91	19.49	0.767
3627.48	1.20E+07	18.30	0.721	11.65	27.0	20.49	224.30	3953.61	18.43	0.726
3458.56	1.19E+07	16.92	0.666	10.27	27.0	22.84	249.95	3703.66	16.92	0.666
3333.64	1.19E+07	15.58	0.614	8.93	27.0	25.33	184.86	3518.80	15.49	0.610
3199.96	1.19E+07	14.73	0.580	8.08	27.0	27.11	197.82	3320.98	14.59	0.574
3059.79	1.19E+07	13.91	0.547	7.26	27.0	28.43	207.42	3113.56	13.73	0.541
2910.02	1.19E+07	13.12	0.517	6.47	27.0	30.37	221.62	2891.94	12.93	0.509
2749.96	1.19E+07	12.37	0.487	5.72	*23.0*	27.04	197.32	2694.63	12.19	0.480
2565.47	1.19E+07	11.67	0.459	5.02	*23.0*	31.17	227.44	2467.19	11.50	0.453
2341.07	1.19E+07	11.01	0.433	4.36	*23.0*	37.91	276.62	2190.56	10.86	0.428
2075.64	1.19E+07	10.41	0.410	2.66	17.6	33.51	244.54	1946.03	10.30	0.406
1759.61	1.19E+07	9.87	0.389	2.12	*17.7*	40.14	292.91	1653.11	9.80	0.386
1378.19	1.19E+07	9.42	0.371	1.67	18.3	50.21	366.35	1286.76	9.38	0.369
928.58	1.19E+07	9.07	0.357	1.11	*17.5*	56.42	411.70	875.07	9.05	0.356
718.47	1.19E+07	8.83	0.348	0.87	*17.9*	67.53	197.10	677.97	8.82	0.347
353.05	1.19E+07	8.75	0.345	0.79	*18.0*	78.76	344.82	333.15	8.75	0.345
0.00	1.19E+07	8.70	0.343	0.74	*18.0*	91.32	333.15	0.00	8.70	0.343
						Shaft capacity =	**4804.2**			

IMPERIAL COLLEGE PILE DESIGN METHOD

Tension test on open ended steel pile by CONOCO

West Delta 58A site

SPREAD SHEET B3 - 2000 ANALYSIS

PREDICTED RESIDUAL CAPACITY CONSIDERING MEASUREDδ AND PROGRESSIVE FAILURE

N	O	P	Q	R	S	T	U	V	W	X
Axial load	AE	Pile deformation		Correction		Shear stress	Section cap.	Axial load	Pile deformation	
(kN)	kN	mm	in	mm	δ	(kPa)	(kN)	(kN)	mm	in
4195.37	1.42E+07	58.84	2.316	53.29	*26.3*	2.37	25.94	4106.89	56.50	2.224
4146.31	1.42E+07	57.48	2.263	51.93	*26.3*	6.43	70.42	4036.47	55.18	2.172
4058.78	1.42E+07	56.15	2.211	50.60	*26.3*	11.48	125.64	3910.83	53.88	2.121
3951.26	1.42E+07	54.84	2.159	49.29	*26.3*	14.10	154.32	3756.51	52.61	2.071
3868.69	1.42E+07	53.56	2.109	48.01	*26.3*	16.24	118.52	3637.99	51.40	2.024
3779.06	1.20E+07	52.73	2.076	47.18	*26.3*	17.63	128.66	3509.33	50.62	1.993
3627.48	1.20E+07	51.77	2.038	46.20	26.9	20.41	223.34	3285.99	49.73	1.958
3458.56	1.19E+07	50.38	1.984	44.81	26.9	22.74	248.87	3037.12	48.47	1.908
3333.64	1.19E+07	49.05	1.931	43.48	26.9	25.23	184.06	2853.06	47.30	1.862
3199.96	1.19E+07	48.19	1.897	42.62	26.9	26.99	196.97	2656.09	46.57	1.833
3059.79	1.19E+07	47.37	1.865	41.80	26.9	28.30	206.53	2449.56	45.88	1.806
2910.02	1.19E+07	46.58	1.834	41.01	26.9	30.24	220.66	2228.90	45.25	1.782
2749.96	1.19E+07	45.84	1.805	40.27	*22.9*	26.91	196.36	2032.54	44.68	1.759
2565.47	1.19E+07	45.13	1.777	39.56	*22.9*	31.02	226.34	1806.21	44.16	1.739
2341.07	1.19E+07	44.47	1.751	38.90	*22.9*	37.73	275.28	1530.92	43.70	1.720
2075.64	1.19E+07	43.87	1.727	37.20	12.1	22.65	165.26	1365.66	43.30	1.705
1759.61	1.19E+07	43.34	1.706	36.67	12.1	26.97	196.76	1168.90	42.95	1.691
1378.19	1.19E+07	42.88	1.688	36.21	12.1	32.55	237.48	931.42	42.65	1.679
928.58	1.19E+07	42.53	1.674	35.65	*13.1*	41.64	303.85	627.57	42.41	1.670
718.47	1.19E+07	42.29	1.665	35.41	*13.1*	48.65	142.00	485.56	42.25	1.663
353.05	1.19E+07	42.22	1.662	35.34	*13.1*	56.41	246.96	238.60	42.20	1.661
0.00	1.19E+07	42.16	1.660	35.28	*13.1*	65.40	238.60	0.00	42.16	1.660
						Shaft capacity =	**4132.8**			

APPENDIX C

APPLICATION OF THE IMPERIAL COLLEGE PILE DESIGN METHOD TO THE PILES OF THE CASE HISTORY BUILDINGS

This appendix presents the description of the application of the Imperial College pile design method (ICPDM, Jardine and Chow, 1996) to the piles of the case history buildings.

The details of the piles and the main features of the computation process are presented in Tables C1 and C2. The tables include the predicted shaft and base capacities using the ICPDM and the total stress approach suggested by the Mexico City design code. The relevant topics are:

i) The selection of soil parameters and the procedures to include pre-boring and pile cross section effects are those used for the validation study in Chapter 5.

ii) The soil-to-concrete interface δ values are obtained from the results presented in Chapter 4. The sensitivity and the profiles of vertical effective stress and YSR are obtained from the nearest available geotechnical study.

iii) The piles from the JAL and PC building have triangular cross section. The cross section for the PCC original piles could not be verified, therefore its capacity calculation is not presented. Sections 7.3 and 8.3 comment on the individual piles and soil conditions for the JAL and PC buildings, respectively.

Table C1 JAL Building, Pile capacity
Triangular closed ended concrete pile

Imperial College approach

Sand lenses friction angle = 30
Clay peak friction angle= 36 Reduction factor for section shape = 0.65
Triangular Pile side length= 0.6 m Equivalent radius = 0.286

SHAFT CAPACITY

Section No.	Thickness m	h m	σo kPa	σvy	St	h/R	YSR	kc	Radial stress (kPa)	Shear stress (kPa)	Section cap. (kN)	Cross section effect	Reduction
1	1.7	26.65	32.87	82.524	3	93.03	2.51	1.09	28.53	20.73	63.44	41.23	22.20
2	1.5	25.05	42.42	76.17	7	87.44	1.80	0.78	26.50	19.25	51.99	33.79	18.20
3	1.5	23.55	51.37	70.213	8	82.20	1.37	0.68	27.86	20.24	54.66	35.53	19.13
4	1.0	22.30	58.83	65.248	8	77.84	1.11	0.63	29.46	21.41	38.53	25.05	13.49
5	1.0	21.30	64.79	73.705	8	74.35	1.14	0.64	33.11	24.06	43.30	28.15	15.16
6	1.0	20.30	70.76	79.368	8	70.86	1.12	0.64	36.29	26.36	47.46	30.85	16.61
7	1.0	19.30	76.73	85.031	3	67.37	1.11	0.81	49.77	36.16	65.09	42.31	22.78
8	1.0	18.30	82.86	90.694	3	63.88	1.09	0.82	54.04	39.26	70.67	45.94	24.73
9	1.0	17.30	89.66	96.357	3	60.39	1.07	0.82	58.67	42.63	76.73	49.87	26.86
10	1.0	16.30	96.47	102.02	18	56.90	1.06	0.51	39.60	28.77	51.79	33.67	18.13
11	1.0	15.30	103.27	107.68	18	53.41	1.04	0.52	42.68	31.01	55.81	36.28	19.53
12	1.0	14.30	110.07	113.35	18	49.92	1.03	0.52	45.85	33.32	59.97	38.98	20.99
13	1.0	13.30	116.88	119.01	8	46.43	1.02	0.67	62.56	45.45	81.81	53.18	28.63
14	1.0	12.30	123.68	124.67	8	42.94	1.01	0.68	66.95	48.64	87.56	56.91	30.64
15	1.0	11.30	130.48	130.34	8	39.44	1.00	0.69	71.56	51.99	93.58	60.83	32.75
16	1.0	10.30	137.29	136	8	35.95	0.99	0.70	76.43	55.53	99.95	64.97	34.98
17	1.0	9.30	144.09	141.66	8	32.46	0.98	0.71	81.60	59.29	106.72	69.37	37.35
18	1.0	8.30	150.89	147.32	8	28.97	0.98	0.72	87.16	63.33	113.99	74.09	39.89
19	1.0	7.30	157.70	158.83	3	25.48	1.01	0.95	119.26	86.65	155.97	101.38	54.59
20	0.5	6.55	162.80	vs=	570	22.86	Δσr=	173.41	31.70	118.42	106.58	69.28	37.30
21	0.5	6.05	167.68	vs=	570	21.12	Δσr=	173.41	32.80	119.05	107.15	69.65	37.50
22	0.5	5.55	172.06	177.42	3	19.37	1.03	1.01	138.85	100.88	90.79	59.01	31.78
23	0.5	5.05	176.44	182.74	3	17.63	1.04	1.03	145.37	105.62	95.06	61.79	33.27
24	0.5	4.55	180.83	188.05	11	15.88	1.04	0.77	110.86	80.55	72.49	47.12	25.37
25	0.5	4.05	185.21	193.36	11	14.14	1.04	0.79	116.42	84.59	76.13	49.48	26.64
26	0.5	3.55	189.60	198.67	11	12.39	1.05	0.81	122.56	89.04	80.14	52.09	28.05
27	0.5	3.05	193.98	203.98	11	10.65	1.05	0.83	129.45	94.05	84.65	55.02	29.63
28	0.5	2.55	198.36	209.29	11	8.90	1.06	0.87	137.41	99.83	89.85	58.40	31.45
29	0.5	2.05	202.75	214.6	11	8.00	1.06	0.89	143.67	104.38	93.95	61.06	32.88
30	0.5	1.55	207.13	219.91	11	8.00	1.06	0.89	146.97	106.78	96.10	62.47	33.64
31	0.5	1.05	211.52	225.23	11	8.00	1.06	0.89	150.27	109.18	98.26	63.87	34.39
32	0.5	0.55	215.90	230.54	11	8.00	1.07	0.89	153.57	111.58	100.42	65.27	35.15
33	0.3	0.15	219.41	242.71	3	8.00	1.11	1.24	217.79	158.23	85.45	55.54	29.91
27.5									**Shaft capacity =**	**1752.4**	**1752.4**		943.60
BASE CAPACITY			qc= 1500 kPa						**Base capacity=**	187.06			
Base capacity, drained conditions									**TOTAL PILE CAPACITY=**	**1939.5**			

Design approach recommended by Mexico City design code

Qt = Qf + Qt

Qf = cPL

c = cohesion from UU test; P: perimeter, L = pile length
alfa is considered as 1
Cuu from CPT tests profile, factor = 13

Qt = c NcAp

Nc = bearing capacity factor, = 9
Usually Qt is not include in pile design in Mexico city

Depth	Average Cohesion	Capacity	Average Cohesion			
3.3 - 14.4	26.3	525.5	291.9	c=	108	kPa
14.4- 19.7	45.65	435.5	241.9	Qt =	174.96	kN
19.7- 27	66.0	867.2	481.8	Total capacity =	2618.8	kN
27 - 30.8	90.0	615.6	342.0	Including pile weight =	2514.0	kN
	Total:	2443.8	49.37		**256.3**	**Ton**

If the cross section effect is considered, pile capacity = 1658.7 kN
169.1 Ton

SUMMARY OF VALIDATION

Pile characteristics
Concrete pile
Triangular section of 60 cm side and 28 m long.
Pile weigth = 104.8 kN

Predictions: Imperial College design method

Base capacity (kN) =	187.06	kN
Shaft capacity (kN) =	1752.4	kN
Total capacity (kN) =	1939.5	kN
Base contribution ratio =	0.10	
Capacity less pile weight =	1834.7	kN
	187.0	Ton

Notes:
St values determined according water content, and liquit limit
Equivalent radius for triangular pile based on triangule perimeter: R* = 3L/2Pi
Reduction due to cross section shape from Jaime, et al., (1991): Ff = 0.5 (1+b/180)

Table C2 PC Building, Pile capacity
Triangular closed ended concrete pile

Imperial College approach

Sand lenses friction angle = 30 — Reduction factor for pre-boring = 0.99
Clay peak friction angle= 36 — Reduction factor for section shape = 0.65
Triangular Pile side length= 0.65 m — Equivalent radius = 0.310 Base on perimeter

SHAFT CAPACITY

Section No.	Thickness m	h m	σo kPa	σvy	St	h/R	YSR	kc	Radial stress (kPa)	Shear stress (kPa)	Section cap. (kN)	Cross section effect	Reduction
1	1.5	25.40	32.28	82.921	3	81.84	2.57	1.12	29.04	21.10	61.71	39.71	22.00
2	1.5	23.90	41.23	76.964	7	77.01	1.87	0.81	26.88	19.53	57.11	36.75	20.36
3	1.5	22.40	50.18	71.007	8	72.18	1.42	0.71	28.36	20.60	60.27	38.78	21.48
4	1.0	21.15	57.63	66.043	8	68.15	1.15	0.65	30.06	21.84	42.59	27.41	15.18
5	1.0	20.15	63.60	62.071	8	64.93	0.98	0.61	31.26	22.71	44.28	28.50	15.79
6	1.0	19.15	69.57	78.236	8	61.70	1.12	0.66	36.72	26.68	52.02	33.48	18.55
7	1.0	18.15	75.53	83.899	3	58.48	1.11	0.83	50.45	36.66	71.48	46.00	25.48
8	1.0	17.15	81.50	89.562	3	55.26	1.10	0.84	54.81	39.82	77.65	49.97	27.68
9	1.0	16.15	88.30	95.225	3	52.04	1.08	0.84	59.62	43.31	84.46	54.35	30.11
10	1.0	15.15	95.11	100.89	18	48.82	1.06	0.53	40.31	29.29	57.12	36.75	20.36
11	1.0	14.15	101.91	106.55	18	45.59	1.05	0.53	43.52	31.62	61.65	39.67	21.98
12	1.0	13.15	108.71	112.21	18	42.37	1.03	0.54	46.85	34.04	66.37	42.71	23.66
13	1.0	12.15	115.52	117.88	8	39.15	1.02	0.69	64.03	46.52	90.72	58.38	32.34
14	1.0	11.15	122.32	123.54	8	35.93	1.01	0.70	68.67	49.89	97.29	62.61	34.69
15	1.0	10.15	129.12	129.2	8	32.70	1.00	0.71	73.57	53.45	104.24	67.08	37.16
16	1.0	9.15	135.93	134.87	8	29.48	1.00	0.73	79.05	57.43	112.00	72.07	39.93
17	1.0	8.15	142.73	140.53	8	26.26	1.00	0.74	84.95	61.72	120.36	77.45	42.91
18	1.0	7.15	149.53	146.19	8	23.04	1.00	0.76	91.36	66.38	129.44	83.29	46.15
19	0.5	6.40	154.64	150.44	3	20.62	1.00	0.98	121.63	88.37	86.16	55.44	30.72
20	0.5	5.90	158.04	153.27	3	19.01	1.00	1.00	126.34	91.79	89.50	57.59	31.91
21	0.5	5.40	161.44	vs=	570	17.40	Δσr=	160.07	35.13	112.70	109.88	70.71	39.17
22	0.5	4.90	165.92	vs=	570	15.79	Δσr=	160.07	36.58	113.54	110.70	71.23	39.46
23	0.5	4.40	170.31	175.3	3	14.18	1.03	1.07	146.18	106.20	103.55	66.63	36.91
24	0.5	3.90	174.69	180.61	3	12.57	1.03	1.10	153.89	111.81	109.01	70.15	38.86
25	0.5	3.40	179.07	185.92	3	10.96	1.04	1.13	162.44	118.02	115.07	74.05	41.02
26	0.5	2.90	183.46	191.23	3	9.34	1.04	1.17	172.09	125.03	121.90	78.44	43.46
27	0.5	2.40	187.84	196.54	11	8.00	1.05	0.88	132.45	96.23	93.82	60.37	33.45
28	0.5	1.90	192.23	201.86	11	8.00	1.05	0.88	135.75	98.63	96.16	61.88	34.28
29	0.5	1.40	196.61	207.17	11	8.00	1.05	0.88	139.05	101.03	98.50	63.38	35.12
30	0.3	1.00	200.12	211.42	11	8.00	1.06	0.89	141.69	102.94	60.22	38.75	21.47
31	0.3	0.70	202.75	214.6	11	8.00	1.06	0.89	143.67	104.38	61.06	39.29	21.77
32	0.3	0.40	205.38	217.79	11	8.00	1.06	0.89	145.65	105.82	61.91	39.84	22.07
33	0.25	0.13	207.79	220.71	11	8.00	1.06	0.89	147.47	107.14	52.23	33.61	18.62
	26.15									**Shaft capacity =**	**1776.3**	**1776.3**	984.10

BASE CAPACITY — qc= 1350 kPa — **Base capacity=** 197.58
Base capacity, drained conditions — **TOTAL PILE CAPACITY=** 1973.9

Design approach recommended by Mexico City design code

Qt = Qf + Qt
Qf = cPL
c = cohesion from UU test; P: perimeter, L = pile length
alfa is considered as 1
Cuu from CPT test profile, Factor = 13.

Qt = c NcAp
Nc = bearing capacity factor, = 9
Usually Qt is not include in pile design in Mexico city

Depth	Average Cohesion	Capacity	Average Cohesion
3.3 - 14.4	26.3	569.3	291.9
14.4- 19.7	45.65	471.8	241.9
19.7- 27	66.0	939.5	481.8
27 - 29.45	90.0	666.9	220.5
	Total =	2647.5	44.95

c= 108 kPa
Qt = 174.96 kN

Total capacity = 2822.4 kN
Including pile weight = 2714.1 kN
276.7 Ton

Icluding reduction for preboring and shape of section = 1770.3 kN
180.5 Ton

SUMMARY OF VALIDATION

Pile characteristics
Concrete pile
Triangular section of 65 cm side and 26.15 m long.
Pile weigth = 108.3 kN

Prediction: Imperial College approach

Base capacity (kN) =	197.6	kN
Shaft capacity (kN) =	1776.3	kN
Total capacity (kN) =	1973.9	kN
Base/total capacity ratio =	0.10	
Capacity less pile weight =	1865.6	kN
	190.2	Ton

Notes:
St values determined according water content, and liquit limit
Equivalent radius for triangular pile based on triangule perimeter: $R^* = 3L/2Pi$
Reduction due to cross section shape from Jaime, et al., 1991: $Ff = 0.5\ (1+b/180)$

BIBL. LONDON UNIV.